# Controls on the distribution of gas hydrates in sedimentary basins

Matteo Paganoni

Thesis submitted to the University of Oxford

for the degree of Doctor of Philosophy (DPhil)

*Trinity Term 2017*




Supervised by Professor Joe A. Cartwright

and Professor Bruce K. Levell

# *Declaration*

I declare that the work presented in this thesis is wholly my own, except where otherwise stated. The views and interpretations expressed herein are mine, and do not represent those of any other person or group except where this is cited to be the case.

# *Author's note*

Parts of this thesis have been presented as talks and posters at the following conferences:

- Paganoni, M., Foschi, M., Cartwright, J.A., Van Rensbergen, P. & Shipp, R.C. Stable Gas Hydrates Beneath a BSR: Implications for Resource Inventories and Shallow Hydrocarbon Fluid Flow. *AGU Fall Meeting 2015*.

- Paganoni, M., Cartwright, J.A., Foschi, M., Van Rensbergen, P. & Shipp, R.C. Controls on hydrates distribution in active thermogenic settings: Insights from Sabah (NW Borneo). *Gordon Research Seminar (New Frontiers in Gas Hydrate Behavior at the Macro- and Micro-Scales) and Conference (Interfacial Science Advances Towards Understanding and Monitoring Gas Hydrate Systems) 2016*.

Parts of this thesis have been published, accepted for publication, or are under submission as scientific papers, as described below:

- Paganoni, M., Cartwright, J.A., Foschi, M., Shipp, R.C. & Van Rensbergen, P. 2016. Structure II gas hydrates found below the bottom-simulating reflector. *Geophysical Research Letters*, 43. (**Chapter 3** of the thesis).

- Paganoni, M., Cartwright, J.A., Foschi, M., Shipp, R.C. & Van Rensbergen, P. 2018. Relationship between fluid-escape pipes and hydrate distribution in offshore Sabah (NW Borneo). *Marine Geology*, 395, 82-103. (**Chapter 4** of the thesis).

- Paganoni, M., Cartwright, J.A. &Van Rensbergen, P. Three-dimensional seismic evidence of extensive gas hydrate deposits linked with large free gas columns suggests long-range advection mechanisms. Accepted for publication in *Marine and Petroleum Geology*. (**Chapter 6** of the thesis)

*Controls on the distribution of gas hydrates in sedimentary basins*

# Abstract

Natural gas hydrates store a substantial portion of the Earth's organic carbon, although their occurrence is restricted by thermobaric boundaries and the availability of methane-rich fluids. The complexity of geological systems and the multiphase flow processes promoting hydrate formation can result in a mismatch between the predicted and the observed hydrate distribution.

The purpose of this research is to achieve a better comprehension of the factors that influence the distribution of gas hydrates and the mechanism of fluid movements beneath and across the gas hydrate stability zone (GHSZ). Therefore, this study integrates seismic, petrophysical and geochemical data from different gas hydrate provinces.

This work provides evidence that hydrates can occur below bottom-simulating reflectors, in the presence of sourcing thermogenic hydrocarbons. The relationship between fluid-escape pipes and gas hydrates is further explored, and pipe-like features are suggested to host a significant volume of hydrates. The host lithology also represents a critical factor influencing hydrate and free gas distribution and, in evaluating a natural gas hydrate system, needs to be considered in conjunction with the spatial variability in the methane supply.

The three-dimensional distribution of gas hydrate deposits in coarse-grained sediments, representing the current target for hydrate exploration, is shown to be correlated with that of the underlying free gas zone, reflecting sourcing mechanisms dominated by a long-range advection. In such systems, the free gas invasion into the GHSZ appears controlled by the competition between overpressure and sealing capacity of the gas hydrate-bearing sediments.

Globally, the thickness of the free gas zones is regulated by the methane supply and by different multi-phase flow processes, including fracturing, capillary invasion and possibly diffusion.

In conclusion, this research indicates that geological, fluid flow and stability factors interweave at multiple scales in natural gas hydrate systems.

# Extended abstract

Natural gas hydrates, on Earth, host between a few hundred and a few thousand gigatons of carbon, mainly in the form of methane. Therefore, they represent a critical component in the organic carbon cycle. The stability of gas hydrates is controlled by temperature, pressure, water chemistry, and gas composition, and their occurrence is further limited by the presence of an adequate gas supply. These restrictions make natural gas hydrates stable only in well-defined portions of subaquatic basins and permafrost regions, with the first of these two environments hosting the vast majority of the global hydrate reservoir. Importantly, the composition of the gas entrapped in the hydrate cage constitutes a crucial control on the vertical extension of the gas hydrate stability zone and results in the presence of different crystallographic hydrate structures, having different stability boundaries.

These well-defined stability conditions make the hydrate reservoir sensitive to modifications in temperature and pressure. For this reason, natural gas hydrate systems could be impacted by climate changes, tectonic events and drilling operations. The concern about the present-day global warming, as well as the potential natural and operational geohazards associated with gas hydrate dissociation and dissolution have driven, in the last 20 years, both the scientific community and industry towards a better understanding of natural gas hydrate systems. The massive volumes of methane entrapped in the form of hydrate on Earth further raised the awareness that natural gas hydrate deposits could constitute a potential unconventional target. Some countries have invested considerably in assessing natural gas hydrates as a potential economic resource, and commercial drilling operations have recently been accomplished.

For all of these reasons, understanding the factors that govern the distribution of gas hydrates in sedimentary basins is critical. Notwithstanding the enormous amount of research in this field, the lack of a dense data coverage and integration has often lead to over-

simplistic assessments of the gas hydrate distribution, where a major unknown is represented by the evaluation of the physical and geochemical mechanisms fostering hydrate formation.

Thus, this work aims to integrate different types of data with an approach that takes into account the whole suite of the physical and geochemical processes of fluid flow in sedimentary basins, to better explain the occurrence of natural gas hydrates. This project utilises a multi-scale approach, where seismic data is often integrated with petrophysical, core and geochemical information.

A literature review on natural gas hydrates is provided in **Chapter 1**, to equip the reader with the essential tools to interpret the data presented in the following chapters. At the end of **Chapter 1**, the major topics tackled in this work are presented, to provide a better understanding of the questions that have been tried to be answered in this thesis. In **Chapter 2**, the geological framework of the two principal study areas of this PhD project is presented. The key results and related discussions are then shown in **Chapters 3** to **7**.

**Chapter 3**, by the use of data collected in offshore NW Borneo, shows and discuss the discovery of structure II and potentially structure H hydrates below a bottom-simulating reflector (BSR), observed at the crest of a system of thrust-cored anticlines (named GKL Dome), trapping oil and gas in deep reservoirs. The BSR conventionally constitutes the primary seismic indicator of the base of hydrate stability in continental margins. However, the results of this work challenge this interpretation, by presenting petrophysical, core and geochemical evidence that the base of gas hydrate stability can extend indeed much deeper (about 100 m) than what inferred from simple geophysical observations.

In the study area, the BSR approximates the boundary between structure I hydrates above and structure II and H hydrates below, where these latter two structures coexist with free gas. At this location, gas hydrates occur with a fracture-filling morphology in homogeneous fine-grained sediments, therefore complicating the estimates of gas hydrate saturation. Nevertheless, by integrating resistivity and pore water chlorinity measurements with the results of pressure core degassing experiments, it is assuredly shown that hydrate

saturation below the BSR is higher than above. Moreover, a process of molecular fractionation of the migrating free gas is responsible for the structure II/H to I transition.

The results from gas hydrate stability modelling and the remarkable similarity between the compositions of the gas released from pressure core samples near the base of structure II and H stability and the gas trapped within an underlying deep-seated reservoir indicate that thermogenically-sourced hydrocarbons efficiently leaked through hundreds of metres of fine-grained sequences with minimal geochemical changes *'en-route'*. The observed '*layered'* configuration of gas hydrate structures can be typical of those basins interested by fluxes of thermogenic fluids towards the gas hydrate stability zone. This work finally suggests revisiting global estimates of the carbon stored in the form of hydrates, particularly if further research and exploration activity will reveal that basins with a thermogenic production of methane-rich fluids constitute critical sources for natural gas hydrate systems.

**Chapter 4** extends the analysis of the natural gas hydrate system at the crest of the GKL Dome. This work integrates a three-dimensional seismic interpretation of a system of vertical cross-stratal fluid flow features, interpreted as fluid-escape pipes, with the petrophysical and geochemical information presented in **Chapter 3**. In natural gas hydrate systems, fluid-escape pipes serve both as conduits for methane-rich fluids towards the water column and as preferred locations for the formation of gas hydrates. The aim is to investigate the controls on the occurrence of fluid-escape pipes and their impact on hydrate distribution in a system dominated by the vertical leakage of thermogenic hydrocarbons.

The pipes are observed within and beneath the gas hydrate stability zone and are restricted to an area with evidence of free gas-bearing sediments, suggesting a causative link where the free gas promotes the build-up of critical fluid pressures. The stacking of the upper terminus of fluid-escape pipes at discrete stratigraphic intervals suggests that fluid flow to the seabed has been episodically enhanced. Possible triggers for cyclical increases of pore fluid pressures are sea-level and temperature fluctuations, tectonic activity and gas leakage from deep reservoirs. This fluid flow system further impacts the gas hydrate distribution.

The fluid-escape pipes can be locations where hydrates occur at high concentrations up to the seafloor. Therefore, the observed up-bending of the stratigraphic reflections along the pipes are interpreted as a combination of a net volume increase of the host sediment owing to hydrate formation and seismic velocity pull-up effects. Away from the pipes, hydrates do not occur until 65-152 mbsf and are present only at low to moderate concentrations.This work suggests that, at this site of focused fluid flow, although fluid-escape pipes constitute, by volume, only 7-11% of the gas hydrate occurrence zone, they could host between 17.5 and 58.0% of the whole hydrate volume. It is therefore likely that, in similar systems, a volumetrically significant portion of the total hydrate reservoir is contained within fluid-escape pipes. The distribution of these features should thus be considered as a critical parameter for hydrate volume estimates.

**Chapter 5** continues the analysis of the natural gas hydrate system presented in **Chapters 3** and **4**, in this case showing and discussing the hydrate and free gas distribution at the flanks of the GKL Dome, where a thick sedimentary sequence, dominated by mud-prone mass-transport deposits, completely covers the fold and thrust belt. In this study, three-dimensional seismic data are integrated with well-log and core information.

At the eastern flank of the GKL Dome, core and geochemical data, as well as hydrate stability modelling, indicate that only structure I hydrates occur, in contrast to what has been observed at the crest. The sourcing mechanism for these hydrates is difficult to constrain. Several mechanisms are discussed, including the roles played by primary and secondary methane generation, where the latter process involves a degradation of an originally purely thermogenic fluid. The base of hydrate stability is here seismically expressed as a system of patchily distributed enhanced amplitude reflections. The distribution of such reflections suggests that free gas accumulates at and near the three-phase boundary in association with particular seismic facies. However, hydrates are shown to occur even in the absence of such geophysical indicators.

Regardless the mud-rich sedimentary sequence, hydrates at the eastern flank of the GKL Dome are present with a pore-filling morphology, and preferentially fill 5-10 cm thick beds, most likely rich in silt and sand. The integration between P-wave velocity measurements on pressure cores and estimates of hydrate saturation from pore water chlorinity, in conjunction with existent theoretical rock-physics models, corroborates this interpretation on hydrate morphology. At the northwestern flank of the GKL Dome, where the recent sedimentary sequence does not overlie deep hydrocarbon accumulations, there is no clear evidence of hydrates. This observation points out the importance, in this area, of deep leaky reservoirs in charging the shallow hydrocarbon plumbing systems. Overall, the lithological heterogeneities, as well as the lateral variations in gas geochemistry and supply impact the architecture of this natural gas hydrate system.

**Chapter 6** analyses the natural gas hydrate system in the outer fold belt of the Guajira Basin (offshore Northern Colombia), which is interpreted to be characterised by concentrated hydrate deposits within coarse-grained sediments, on the basis of compelling seismic evidence. Importantly, the mechanisms associated with the accumulation of natural gas hydrates in coarse-grained sediments are largely unconstrained, although an improved understanding of such processes is crucial to efficiently prospect for hydrate resources. The integration between observations on seismic cross-section and seismic attribute maps help in imaging the three-dimensional extension of these coarse-grained gas hydrate-bearing sediments and their relationship with the underlying free gas zone.

Specifically, these gas hydrate-bearing sediments are seismically expressed as segments of enhanced stratigraphic reflections, comparable in amplitude but opposite in polarity to the reflections observed in the underlying free gas zone. This geophysical character is highly diagnostic for the occurrence of gas hydrates at high saturation (≥50% of the pore space) in sandy/silty sediments. Observations in seismic sections and amplitude maps of a bottom-simulating reflection and key horizons indicate that the distribution of hydrates and free gas is largely affected by the structural setting of the study area, where

hydrates and free gas further have markedly diverse extents in different anticlines. We recognise a link between hydrates and free gas, such that the most extensive hydrate accumulations and the largest (up to 570 m) free gas columns occur along the same dipping horizons, cross-cutting the base of gas hydrate stability. These observations suggest that a long-range advection of free gas operates with varying effectiveness in these structures.

It is hypothesised that these hydrate deposits form by overpressure-controlled pulses of free gas invasion into the gas hydrate stability zone along dipping stratal conduits. This process implies that hydrate-bearing sediments constitute an efficient but dynamic membrane seal for large buoyant free gas columns. This coupling between free gas and hydrate accumulations represents an extraordinary example of hydrate distribution governed by advective processes illustrated in three dimensions.

Finally, **Chapter 7** reviews the controlling mechanisms on the vertical extent of the free gas zone underlying hydrate stability, its critical status (i.e. the existence of significant overpressures at the base of hydrate stability), as well as the related fluid migration mechanisms and gas hydrate distribution. In this study, more than thirty gas hydrate provinces have been analysed, extracting information on the tectonic setting, the depth of the BSR, the thickness of the free gas zone, and the geothermal gradient. The use of core and logging-while-drilling data from thirteen sedimentary basins further allowed extrapolating information on the lithostatic stress. Such information has been coupled with theoretical failure criteria for hydraulic/pneumatic fracturing and fault reactivation, as well as with pressure thresholds for the initiation of a multiphase flow through capillary invasion. This integration of multiple scenarios for fluid flow with real data allowed assessing a natural gas hydrate system, with regard to the overpressures developed beneath the three-phase boundary. The most critical unknowns and uncertainties in this study are represented by the effective presence of overpressures at the base of gas hydrate stability, the quantification of the tensile strength at the base of hydrate stability, as well as the validity of the assumed seismic velocities, underlining the need for further research in this field.

Despite these uncertainties and contrary to previous studies, this review suggests that the critical status of the free gas zone is largely independent of the regional tectonic framework, although convergent margins display a wider range of free gas zone thicknesses and BSR depths, compared to passive margins and actively extensional settings. Local factors, such as the methane supply at the km-scale, are instead inferred to play a critical role. This review, by making specific examples from well-known gas hydrate provinces, also highlights the importance of evaluating the occurrence of multiple sources of overpressure in a natural gas hydrate systems, as well as the presence of pre-existent preferential pathways for fluid flow (e.g. a fracture system).

The primary processes of fluid flow in natural gas hydrate systems are also discussed. Moreover, based on the relationship between the thickness of free gas zones and the geothermal gradient, it is hypothesised that the formation of large free gas columns could be inhibited in the presence of high geothermal gradients (more than ~60-70 °C/km), owing to the presence of steep methane solubility gradients, beneath and above the three-phase boundary. Finally, a classification of free gas zones is proposed, based on lithology, fluid flux, the dip of stratigraphic layering, the three-dimensional shape of the base of gas hydrate stability and the geothermal gradient. This classification helps in distinguishing natural gas hydrate systems with different impact on climate dynamics, geohazard and prospectivity.

The conclusive chapter (i.e. **Chapter 8**) firstly provides a holistic short discussion on the key controls on hydrate distribution in sedimentary basins, as a result of the interplay through time between stability factors, geological framework, and fluid flow. Lastly, a summary of the results of the thesis is presented, with particular reference to the critical topics stated at the end of the introductory chapter. In conclusion, this PhD research has contributed towards a better understanding of natural gas hydrates, by analysing and discussing the controls on their complex vertical and lateral distribution. Future studies in this field should focus on the temporal evolution of hydrate reservoirs, on the origin and

distribution of overpressures beneath the base of hydrate stability, and on the global assessment of thermogenically-sourced natural gas hydrate systems.

# *Acknowledgements*

Firstly, I would like to thank my supervisor Joe Cartwright. He has been an excellent guide during this PhD. He helped me a lot in acquiring research skills that I did not have before. But most importantly, he taught me the importance to observe natural phenomena, to think in the four dimensions and at multiple scales of observations.

Martino Foschi merita un ringraziamento speciale per avermi sopportato nei momenti di stress, per i consigli (tecnici e meno tecnici), e per essere diventato un grande amico. A special acknowledgement is also deserved by my fantastic *'Lab'* friends (Ben, Chris, Claudia, James and Victoria, in rigorous alphabetical order), to Professor Bruce Levell, and to all the other people in the department who spent some time with me in these years. An important acknowledgement goes to my sponsor (Shell), which allowed me to live this beautiful experience in such a great university. In this sense, I need to particularly thank Pieter Van Rensbergen, who has been such an important mentor and friend, as well as Craig Shipp, who provided me with one of the best datasets on gas hydrate systems. Special thanks also go to the Shell Exploration Team in Houston (Sandro Mercio and William Lyons), who allowed me to publish the results of Chapter 6, as well as to Borders & Southern Petroleum plc and New Zealand Petroleum & Minerals, who provided me with seismic data, used in Chapter 7. A particular acknowledgement goes to Geotek (Melanie Holland and Peter Schultheiss), who helped me greatly (by e-mail and in person), in understanding the processes of core recovery and interpretation. Thanks also to Prof. Carlos Santamarina, Marco Terzariol, Katie Taladay, Michael Nole, Ann Cook, Ingo Pecher, and all the other *'hydrate scientists'* who I have met, directly and indirectly, throughout these years. A very special thank goes to all the IODP Expedition 372 scientific and non-scientific party. I will never forget you.

Infine, voglio ringraziare più di tutti la mia fidanzata e compagna di avventure Lara. Non è stato per niente facile sopportarmi e supportarmi in questi anni e mi chiedo come tu possa sempre averlo fatto con amore e con il sorriso. Si volta pagina ora e si guarda avanti, insieme come sempre, pronti ad iniziare nuove esperienze e vivere giorni felici e spensierati.

***This work is dedicated to curious people and to all those who spent and will spend some time in trying to answer challenging scientific questions***

# Table of Contents

**Abstract…… iii**

**Extended abstract…… v**

**List of Figures…… xix**

**List of Tables…… xxvii**

**List of Abbreviations and Symbols…… xxix**

**Chapter 1. Introduction and literature review…… 1**

**1.1. Gas hydrate crystallography and molecular composition…… 2**
**1.2. Discovery history of natural gas hydrates…… 6**
**1.3. Occurrence and origin of natural gas hydrates…… 9**
**1.4. Acoustic properties, thermal properties, and morphology of gas hydrate-bearing sediments…… 20**
**1.5. Borehole detection of gas hydrate-bearing sediments…… 28**
**1.6. Core detection of gas hydrate-bearing sediments…… 38**
**1.7. The seismic expression of natural gas hydrates…… 42**
*1.7.1. Origin and characteristics of the bottom-simulating reflector…… 42*
*1.7.2. Other seismic indicators of a natural gas hydrate* system…… 46
*1.7.3. Quantitative seismic analyses, multibeam surveys and ROV observations.* 47
**1.8. Other geophysical methods: CSEM surveys…… 60**
**1.9. The importance of natural gas hydrates…… 62**
**1.10. Controls on gas hydrate distribution: key topics…… 66**
*1.10.1. The vertical distribution of gas hydrates…… 66*
*1.10.2. The coexistence between hydrates and free gas…… 67*
*1.10.3. The Geochemical changes in hydrates and free gas within the GHSZ…… 67*
*1.10.4. The impact of focused fluid flow on hydrate distribution and the triggering events…… 68*
*1.10.5. The physical mechanisms of hydrocarbon migration…… 68*
*1.10.6. The role of free gas in influencing gas hydrate distribution and the sealing capacity of gas hydrate-bearing sediments…… 69*
**1.11. Appendix: geochemistry of gas hydrates…… 70**

**Chapter 2. Geological setting of the study areas…… 87**

**2.1. Introduction…… 88**
**2.2. Offshore Sabah (NW Borneo)…… 88**
**2.3. Offshore Guajira Basin (Northern Colombia)…… 90**

**Chapter 3. Structure II and H gas hydrates found below the bottom-simulating reflector……..……..…… 97**

**3.1. Introduction……..…….. 98**
**3.2. Data and Methods……..…….. 100**
**3.3. Results……..……..... 104**
*3.3.1. Key seismic and geological observations*…….…….…….…. 104
*3.3.2. Evidence of gas hydrates and saturation estimates*…….…….…… 106
*3.3.3. Evidence of free gas*…….…….…….…. 116
*3.3.4. Gas geochemistry*…….…….…….…. 116
**3.4. Gas hydrate stability modelling……..…….…… 120**
**3.5. Discussion……..……..……..……..... 121**
*3.5.1. Origin of gas hydrates and molecular fractionation*…….…….... 121
*3.5.2. Stacked bases of hydrate stability and occurrence of free gas*…….…….... 123
*3.5.3. Reservoir characteristics of gas hydrate-bearing sediments*…….…….... 125
*3.5.4. Thermogenic hydrate provinces: impact on carbon inventories*…….…….... 126
**3.6. Conclusions…… 127**
**3.7. Appendix……..……..……... 128**
*3.7.1. Methods to estimate gas hydrate saturation*…….…….…….... 128
*3.7.2. Supplementary tables*…….…….…….…. 130

**Chapter 4. Relationship between fluid-escape pipes and hydrate distribution in offshore Sabah (NW Borneo)…..……..... 137**

**4.1. Introduction……..…. 138**
**4.2. Data and Methods……..……..….. 140**
**4.3. Geological setting……..…….. 145**
*4.3.1. Major structures of the study area*…….…….…….…. 145
*4.3.2. Stratigraphic framework*…….…….…….…. 146
**4.4. Results…… 147**
*4.4.1. The bottom-simulating reflector and the free gas zone*…….…….…. 147
*4.4.2. Occurrence of gas hydrates*…….…….…….…. 148
*4.4.3. Fluid-escape pipes*…….…….…….…. 153
*4.4.4. Morphology and amplitude anomalies at and near the seafloor*…….…….…. *156*
**4.5. Discussion……..…….. 161**
*4.5.1. Controls on the distribution of fluid-escape pipes*…….…….…….. 161
*4.5.2. Episodicity and triggering events*…….…….…….…. 165
*4.5.3. Gas hydrates along fluid-escape pipes?*…….…….…….…. 167
*4.5.4. Fluid flow and gas hydrate distribution*…….…….…….…. 169
**4.6. Conclusions…… 173**
**4.7. Appendix……..……..…… 175**
*4.7.1. Supplementary figure*…….…….…….…. 175
*4.7.2. Gas hydrate volumes within vs outside the pipe-zones*…….…….…. 176

**Chapter 5. Investigating the impact of gas composition, migration and lithology on the distribution of gas hydrates and free gas… 180**

**5.1. Introduction……... 181**
**5.2. Data and Methods…….. 184**
*5.2.1. 3D seismic, well-log and core data*…… 184
*5.2.2. Seismic interpretation and calibration of amplitude anomalies*…… 185
*5.2.3. Gas hydrate saturation*…… 186
**5.3. Geological setting……. 189**
*5.3.1. Seafloor geomorphology and major structures*…… 189
*5.3.2. The flanks of the GKL Dome: seismic stratigraphy*…… 190
**5.4. Results……... 197**
*5.4.1. Distribution of the amplitude anomalies*…… 197
*5.4.2. Gas hydrate distribution at the flanks of the GKL Dome*…… 202
*5.4.2.1. Evidence from core data*…… 202
*5.4.2.2. Gas geochemistry*…… 207
*5.4.2.3. Evidence from well-log data*…… 208
**5.5. Discussion…….. 214**
*5.5.1. Controls on the thickness of the GHSZ and origin of the gas*…… 214
*5.5.2. Reservoir characteristics of gas hydrate-bearing sediments*…… 218
*5.5.3. Significance of the seismic expression of the natural gas hydrate system*…… 221
**5.6. Conclusions…… 224**
**5.7. Appendix…… 226**
*5.7.1. Supplementary figures*…… 226
*5.7.2. Supplementary tables*…… 229

**Chapter 6. Three-dimensional seismic evidence of extensive gas hydrate deposits linked with large free gas columns suggests long-range advection mechanisms……. 236**

**6.1. Introduction……... 237**
**6.2. Data and Methods…….. 238**
**6.3. Geological Setting……... 239**
**6.4. Results: seismic observations and interpretations…….. 244**
*6.4.1. Seismic evidence of gas hydrates and free gas*……*244*
*6.4.2. Distribution of gas hydrates and free gas*……*246*
**6.5. Discussion……... 267**
*6.5.1. Long-range advection feeding hydrate formation*…… 267
*6.5.2. Overpressure-driven migration through hydrate seals*…… 270
*6.5.3. Global implications*…… 276
**6.6. Conclusions……... 277**
**6.7. Appendix: capillary invasion and free gas buoyancy at the BGHSZ…... 278**

**Chapter 7. A review of the critical state and the fluid flow processes associated with free gas zones beneath hydrate stability…. 281**

**7.1. Introduction……..……..…… 282**
**7.2. Seismic expression of the free gas zone…… 286**
**7.3. Data and methods…….. 287**
*7.3.1. Critical status of the free gas zone and fluid flow mechanisms*…… 289
*7.3.2. Impact of the gas solubility and geothermal gradient*…… 292
**7.4. Results…… 296**
*7.4.1. Thickness of free gas zones in sedimentary basins*…… 296
*7.4.1.1. Convergent margins*…… 296
*7.4.1.2. Continental margins with gravity, shale, salt and far-field tectonics*…… 298
*7.4.1.3. Passive and actively extensional margins*…… 299
*7.4.1.4. General observations*…… 300
*7.4.2. Mechanisms of free gas migration: significant examples*…… 324
*7.4.2.1. Hydrate Ridge (Cascadia margin)*…… 324
*7.4.2.2. Blake Ridge (offshore south Carolina)*…… 325
*7.4.2.3. GKL Dome (offshore Sabah, NW Borneo)*…… 325
*7.4.2.4. Vestnesa Ridge (Fram Strait)*…… 326
*7.4.2.5. Walker Ridge (Terrebonne Basin, Gulf of Mexico)*…… 327
*7.4.2.6. Frontal anticlines of the Guajira Basin (Colombian margin)*…… 327
*7.4.3. Impact of methane solubility on the formation of a free gas zone*…… 330
**7.5. Discussion……..…… 335**
*7.5.1. Critically pressured free gas zones: controlling factors*…… 335
*7.5.2. Fluid migration processes*…… 338
*7.5.2.1. Free gas advection: hydraulic fracturing vs capillary invasion*…… 338
*7.5.2.2. Advection of methane-rich water*…… 343
*7.5.2.3. Diffusion processes and methane solubility near the base of hydrate stability*..... 343
*7.5.2.4. Colloidal flow of isolated free gas bubbles*…… 345
*7.5.3. Triggering events*…… 346
*7.5.4. Classification of free gas zones*…… 350
*7.5.4.1. Type-A free gas zones (FGZs-A)*…… 350
*7.5.4.2. Type-B free gas zones (FGZs-B)*…… 352
*7.5.4.3. Type-C free gas zones (FGZs-C)*…… 354
*7.5.4.4. Type-D free gas zones (FGZs-D)*…… 356
**7.6. Conclusions…… 359**
**7.7. Appendix…… 361**
*7.7.1. Hydraulic fracturing*…… 361
*7.7.2. Fault reactivation*…… 365
*7.7.3. Supplementary figures*…… 367

**Chapter 8. Final discussion and conclusions…… 373**

**8.1. Multi-scale controls on hydrate distribution……..…. 374**
*8.1.1. Controls from the pore- to the core-scale*…… 375
*8.1.2. Controls at the prospect-scale*…… 376

*8.1.3. Controls at the basin-scale*…… 377
**8.2. Final conclusions……..…… 381**
*8.2.1. Summary of the results*…… 381
*8.2.2. Contribution to the understanding of natural gas hydrate systems*…… 388
*8.2.3. Guidelines for future research*…… 390

**References……... 393**

# List of Figures

## Chapter 1

**1.1.** **(a)** Schematic cartoon and showing the three naturally-occurring hydrate crystal structures. **(b)** Crystallographic properties and gas guest molecules of $S_I$, $S_{II}$ and $S_H$ hydrates……..……. 4

**1.2.** **(a)** Simplified example of the predicted depth of the base of the gas hydrate stability zone (BGHSZ) along the continental slope of the Gulf of Mexico. **(b)** Gas hydrate stability conditions for different structures and chemical composition of the feeding gas……..…….. 5

**1.3.** Theoretical examples of gas hydrate stability boundaries, at varying pressure, temperature and feeding gas composition, assuming a constant pore water salinity (3.0% NaCl eq.)…….……. 6

**1.4.** Vintage seismic reflection lines, showing some of the first observed bottom-simulating reflectors (BSRs)…… 8

**1.5.** Schematic representations of the temperature and pressure conditions leading to gas hydrate stability in permafrost regions **(a)** and subaquatic environments **(b**)…….... 13

**1.6.** Schematic map showing the locations where hydrates have been recovered or inferred to occur, on the basis of geophysical and petrophysical evidence……..... 14

**1.7.** Schematic representation of the relationships between gas hydrate stability, gas (methane) solubility and hydrate occurrence……... 14

**1.8.** **(a)** Seismic reflection profile along the Blake Ridge Diapir, showing the impact of a conductive salt body on the shape of the BGHSZ. **(b)** and **(c)** Gas flares (plumes) at the Hydrate Ridge (offshore Oregon) and schematic model showing that the shallowest occurrences of the gas flares coincide with the top of the GHSZ.……..…… 15

**1.9.** $C_1/C_2+$ *vs* $\delta^{13}C$ of CH4 (‰) plot based on an updated dataset of recovered gas hydrate samples or gas hydrate-bearing cores. ……. 16

**1.10.** $\delta^{13}C$ *vs* $\delta$ D of CH4 (‰) based on an updated dataset of recovered gas hydrate samples or gas hydrate-bearing cores.…… 17

**1.11.** **(a)** Cartoon showing the biogeochemical zonations plus the $CH_4$, $CO_2$ and $SO_4$ concentration within shallow sediments in a marine NGHS. **(b)** Cartoon showing the relationship between methane flux and depth of the SMTZ. **(c)** Sulphate concentration at the Tunica Mound (Northern Gulf of Mexico), chirp seismic reflection profile and sketches showing the predicted depths of the BGHSZ……... 18

**1.12.** Schematic representations of natural gas hydrate systems developed in homogeneous **(a-c)** and heterogeneous **(d-f)** geological settings. ……... 19

**1.13.** Predicted relationship between compressional velocity and *Sh* for different hydrate habits.…… 24

**1.14.** Examples of grain-displacing and pore-filling hydrate morphologies (core-scale)……...…… 25

**1.15.** **(a)** Photograph (left) and IR image (right) of a gas hydrate-bearing core. **(b)** Photographs of grain-displacing sub-horizontal hydrate lenses. **(c)** Photograph of a gas hydrate pingo……. 26

**1.16.** Photographs showing different types of different hydrate morphologies…….…. 27

**1.17.** Well-log data showing gas hydrate-bearing sediments in different provinces…….…….. 32

**1.18.** **(a)** Gas hydrate and free gas saturatio at Blake Ridge. **(b)** P-wave velocity *vs Sh* for hydrate-bearing sediments in the Nankai Through……..……. 33

**1.19.** **(a)** *Sh vs* depth profile at Site GC955-H, in the Green Canyon (Northern Gulf of Mexico), characterised by hydrate-filled fractures. **(b)** Schematic models for hydrate growth in the pore space and impact on the saturation index…… 34

**1.20.** Examples of resistivity image logs from Northern Cascadia **(a)** and the Krishna-Godavari Basin **(b)**...35

**1.21.** **(a)** Well-log data including the NMR log (borehole Mallik 5L-38, onshore northern Canada). **(b)** CPTu data acquired near the seafloor, in a pockmark system offshore Nigeria……..36, 37

**1.22.** **(a)** Core photographs, IR images and particle size measurements of core samples from the Ulleung Basin. **(b)** Salinity, chlorinity and *Sh* profiles, extrapolated from cores recovered in the Northern Cascadia margin…… 40

**1.23.** **(a)** X-ray images from a pressure core acquired in the Krishna-Godavari Basin. **(b, c)** Pressure *vs* cumulative volume of expelled gas *vs* time plot, representing a core degassing experiment accomplished on a pressure core recovered at the Hydrate Ridge, and molecular composition of the expelled gas… 41

**1.24.** **(a)** Simplified P-wave velocity (Vp) profile in a marine setting characterised by free gas beneath the BGHSZ and schematic synthetic seismogram. **(b)** Velocity (P- and S-wave) *vs Sg* plot. **(c)** Seismic profile and P-wave velocities at the Blake Ridge…….. 49

**1.25.** **(a)** Seismic reflection profile with superimposed 3D bathymetry along the Vestnesa Ridge (offshore Svalbard), showing a BSR and an FGZ. **(b)** P-wave velocity along the same profile shown in **(a)**, obtained with a velocity analysis of pre-stack multichannel seismic reflection data…….……...……. 50

**1.26.** **(a)** Seismic reflection profile in the Lake Baikal, highlighting a clear cross-cutting relationship between a BSR (blue arrows) and the stratigraphy. **(b)** Seismic reflection profile in the Terrebonne Basin (Northern Gulf of Mexico) displaying a discontinuous BSR…….…… 51

**1.27.** Seismic profiles, showing anomalous BSRs. **(a)** Discontinuous BSR in the Opouawe Bank (Hikurangi margin). **(b)** Profile form the Garden Banks (Northern Gulf of Mexico). **(c)** Profile and seafloor bathymetric map from the Vesntesa Ridge (Fram Strait, offshore Svalbard)……...……. 52

**1.28.** Gas hydrate phase boundaries, showing the impact of capillary effects in small pores on hydrate stability…….. 53

**1.29.** **(a)** Seismic reflection profile from the continental slope offshore Mauritania showing the *'hydrate wedge'*. **(b)** Bathymetric map showing a pockmark field developed above the *'hydrate wedge'* on the continental slope offshore Svalbard……..…. 54

**1.30.** Schematic cartoons showing the processes that can lead to the upward shift of the BGHSZ, and re-equilibration at new conditions……...……... 55

**1.31.** Examples of multiple BSRs: **(a)** Norwegian margin. **(b)** Hydrate Ridge. **(c)** Danube Fan……... 56

**1.32.** Examples of seismically visible GHBS. **(a, b)** GHBS at high *Sh* along segments of coarse-grained stratigraphic intervals. **(c, d)** GHBS at high *Sh* along portions of cross-stratal pathways in fine-grained sediments……... 57

**1.33.** Seafloor mounds (hydrate pingoes) and depressions at the seafloor associated with active methane seepage **(a)** Gas hydrate pingoes in the Kwanza Basin (offshore Angola). **(b)** Gas hydrate pingo in the Santa Monica Basin (offshore California). **(c)** Seafloor depression at the Hydrate Ridge…… 58

**1.34.** Examples of blanking in NGHSs. **(a)** Crest of the Blake Ridge. **(b)** Offshore Vancouver Island (Cascadia margin)**. (c)** Pegasus Basin (Hikurangi margin)…….……... 59

**1.35.** **(a)** Schematic representation of a marine CSEM system. **(b)** Velocity inversion integrated with CSEM results in offshore Norway……. 61

**1.36.** **(a)** Gas hydrate resource pyramid. **(b)** Reservoir quality (i.e. intrinsic reservoir permeability) *vs Sh* (schematic plot). **(c)** Reservoir quality (expressed as the sand content of GHBS) *vs Sh* (real data)….. 65

## Chapter 2

**2.1.** Modified images from Google Earth, showing the present-day plate-scale geological settings of the study areas. **(a)** Sabah (offshore NW Borneo) (**Chapters 3-5**). **(b)** Guajira Basin (offshore Northern Colombia) **(Chapter 6)**……. 92

**2.2.** Detailed Tectonic map of NW Borneo……...… 93

**2.3.** **(a)** Regional NW-SE seismic reflection line across the NW Borneo margin, offshore Sabah. **(b)** and **(c)** Examples of BSRs at the crests of the thrust-cored anticlines offshore Sabah and in The seismic the nearby Brunei margin…… 94

**2.4.** **(a)** Regional NW-SE seismic reflection line along the Guajira Basin. **(b)** and **(c)** Examples of BSRs along the South Caribbean Deformed Belt……...……. 95

**2.5.** Bathymetric maps of the study areas. **(a)** Sabah and **(b)** Guajira Basin……. 96

## Chapter 3

**3.1.** **(a)** Seafloor map with borehole locations and projection of the BSR. **(b)** Seismic section showing the BSR and $R_{II}$ plus the phase-shift, deep smoothed resistivity (Res.) and the gamma-ray (GR) logs along boreholes DC_E and DC_F. **(c)** DC_E well log data……... 103

**3.2.** **(a)** Seismic section, showing the BSR (blue arrows) at the top of the anticline and its cross-cutting relationship with the host stratigraphy. **(b)** Instantaneous frequency section along the same path of **Fig. 3.1b**……. 105

**3.3.** Phase shift deep smoothed resistivity (Res.) and gamma-ray (GR) data for wells DC_E, M_1, DC_F and L_2…..…….. 105

**3.4.** **(a)** and **(b)** X-ray images, MSCL data and *Sh* estimates of FPC-E#08 and FPC-E#11. **(c)** and **(d)** Blow-ups of the X-ray images of the two pressure cores…… 107

**3.5.** **(a)** Chlorinity and sulphate profiles at DC_E. **(b)** Gas hydrate saturation profile. **(c)** IR thermal image of FC cores……... 108

**3.6.** Resistivity images (static) at DC_E. **(a)** General view. **(b)** and **(c)** Detailed view of two selected intervals……... 110

**3.7.** Resistivity *vs* depth profile at DC_F……..…… 111

**3.8.** Horizontal and vertical resistivity *vs* depth profile at DC_F……..... 112

**3.9.** Gas hydrate saturation and stability modelling……..... 114, 115

**3.10.** $C_1/C_{2+}$ ratio extrapolated from the molecular composition of gases within FC and FPC cores from onboard and onshore analyses at DC_E……... 117

**3.11.** Onshore geochemical analyses. Relative concentrations of $C_1$-$C_{6+}$ gases collected from FPC and HRC cores at DC_E and of the gases present within the gas cap of the Gumusut-Kakap reservoir……. 118

**3.12.** Relative concentrations of $C_1$-$C_4$ gases collected from FC-E#16 at DC_E and of the gas of the GK reservoir…….. 119

**3.13.** Excess pore pressure profile at DC_E…..... 121

**3.14.** Porosity profiles at DC_E and DC_F…..... 129

## Chapter 4

**4.1.** **(a)** Regional low-resolution NW-SE seismic line, showing the main tectonic features and the stratigraphic units of the study area. **(b)** and **(c)** Blow-ups extracted from **(a)**, showing the BSRs at the crests of the Kikeh structure **(b)** and the GKL Dome **(c)**. **(a)** Blended TWT and variance seafloor map of the study area covered by the low-resolution seismic survey……... 143

**4.2.** Blended TWT and variance seafloor map of the area investigated by the high-resolution seismic survey. This map shows the projection of the BSR, the GOC in the GK reservoir, the area with EARs within MTD3, the whole area characterised by evidence of free gas at the crest of the GKL Dome and the fluid-escape pipes……..……. 144

**4.3.** Detailed view of the BSR at the crest of the GKL Dome and calibration with WL velocity data…... 150

**4.4.** Main stratigraphic elements and fluid flow features in the study area. **(a)** High-resolution NW-SE seismic line. **(b)** Variance extraction of the lines shown in **(a)**. **(c)** Interpreted geological section….. 151

**4.5.** **(a)** SW-NE seismic line showing the push-down effect (white arrows) associated with the EARs present within and below $MTD_3$…….. 152

**4.6.** **(a, b)** Variance maps of the base of the recent drape interval **(a)** and the base of Unit 1 **(b)** at the crest of the GKL Dome. The maps show the plan-view of both the normal faults and the pipe-zones. **(c)** Blow-up of **(b)**, showing a detail of some pipe-zones. **(d)** Rose diagrams, showing the dominant strike directions of the normal faults at the crest of the GKL Dome and the maximum axis of the 41 sub-circular to elliptical pipe-zones. **(e)** Schematic cartoon representing a pipe-zone, and the interpreted geometric relationship with a normal fault…….. 157

**4.7.** **(a)** Wireline P- and S-wave velocity logs at DC_E. **(b)** 3D borehole shape along DC_E. **(c)** *Sh* and sulphate concentration profiles at DC_E. **(d)** NW-SE seismic section, showing the location of borehole

L_2 (vertical red-black line), drilled very close to many pipe-zones. **(e-g)** *Sh* profiles, extrapolated from resistivity data at M_1, DC_F and L_2……..... 158

**4.8.** **(a-c)** Relationships between fluid-escape pipes and stratigraphy. **(d)** RMS amplitude map of horizon H, which shows different zones of enhanced amplitude. **(e)** RMS amplitude map of the seafloor showing the areas with enhanced reflectivity. **(f)** Map of the study area indicating the location of the sections shown in **(a-c)** plus detailed dip map showing evidence of fluid expulsion at the seafloor……..... 159

**4.9.** **(a, b)** NW-SE seismic sections, showing the different stratigraphic levels of the termini of the pipes…… 160

**4.10.** **(a, c)** NW-SE and SW-NE seismic sections, showing the crest of the Kikeh structure. (**b, d)** Variance extractions of the seismic lines shown in **(a)** and **(b)**……..... 161

**4.11.** **(a, b)** Schematic representation of two gas hydrate-bearing cores, depicting the interpreted hydrate distribution outside **(a)** and inside **(b)** a pipe-zone……... 172

**4.12.** **(a)** Regional NW-SE seismic profiles, showing Pipe-α at the crest of the GKL Dome. **(b)** Regional NW-SE seismic profiles showing that the studied structures become buried moving towards the northeast…….. 175

## Chapter 5

**5.1.** Bathymetric map of the study area interested by the high-resolution seismic survey. The map indicates the main structural elements of the study area, as well as the projection of the anomalies associated with shallow free gas……...… 188

**5.2.** Low-resolution regional NW-SE seismic sections, showing the main structures and hydrocarbon reservoirs of the study area, as well as the possible seismic expression of the BSIGHSZ in the structural lows, characterised by mass-transport deposition……..... 192

**5.3.** Representative high-resolution NW-SE **(a, b)** and SW-NE **(c)** seismic sections, covering the study area and passing through the locations of DC_A **(a)**, DC_B **(b)** and DC_C **(c)**…….. 193

**5.4.** SW-NE seismic sections, passing through the borehole locations DC_E, DC_A and DC_B and showing the main features at the crest and the eastern flank of the GKL Dome, as well as the tied resistivity and gamma-ray logs (DC_A and DC_B)……...……. 194, 195

**5.5.** Gamma-ray, porosity (density and neutron), resistivity and velocity data extrapolated from LWD and WL logs acquired at DC_A **(a)**, DC_B **(b)** and DC_C **(c)**. The figure includes a lithological interpretation……... 196

**5.6.** **(a-c)** Gas hydrate stability modelling in relation to the depth of three EARs observed at different water depths along the eastern flank of the GKL Dome…….…… 199

**5.7.** Amplitude characteristics of the EARs at the eastern flank of the GKL Dome…… 200

**5.8.** Attribute maps of the base of Unit 2 and of Horizon 3 (H3)……...……. 201

**5.9.** Core evidence of gas hydrates at DC_A……... 203

**5.10.** Core evidence of gas hydrates at DC_B……... 205

**5.11.** Sulphate profiles at DC_A, DC_B and DC_E……..... 206

**5.12.** **(a-d)** P-wave velocity vs hydrate saturation (*Sh*) estimated from selected MSCL and chlorinity measurements on FPC cores at DCA_ and DC_B. This data is integrated with theoretical models, calibrated with in-situ mineralogical information, at ~zero to very low (0.22 MPa) effective stress conditions. **(e)** P-wave velocity vs effective stress plot at 0% *Sh* (i.e. 100% water-saturated sediment), extrapolated using the input parameters for the sediment and water physical properties shown in **Tab. 5.3**, and following the effective-medium theory used to extrapolate the curves shown in **(a-d)** ….... 207

**5.13.** Molecular hydrocarbon composition of gases within FC and FPC cores from onboard and onshore analyses expressed as $C_1/C_2$ for DC_A and DC_B **(a, b**) and as $C_1/C_{2+}$ for DC_E……..…… 208

**5.14.** Resistivity images (Static) (left panels), borehole 3D profiles (central panel) and average caliper log (right panels), obtained with the STAR WL device at DC_A **(a)**, DC_B **(b)** and DC_C **(c)**……..… 212

**5.15.** Gas hydrate saturation (*Sh*) estimated from LWD resistivity measurements with an Archie approach at DC_A **(a)**, DC_B **(b)** and DC_C **(c)**……. 213

**5.16.** Schematic plot showing the relationship between the intrinsic reservoir quality of the gas hydrate reservoirs at the crest and the flanks of the GKL Dome, the observed *Sh* and the availability of gas in the system (charge)…….. 224

**5.17.** $R_w$ profiles for DC_A and DC_B……. 226

**5.18.** Pickett plots for DC_A **(a)**, DC_B **(b)** and DC_C **(c)**……... 227

**5.19.** CTD and borehole temperature data with extrapolated geothermal gradients for DC_A, DC_B and DC_E……... 228

## Chapter 6

**6.1.** Seismic-trace conceptual model for gas hydrate-bearing sediments with variable saturation and reservoir interval thickness…….……...……..… 241

**6.2.** **(a)** Schematic map of the Northern South America. **(b)** Bathymetric map of the offshore Guajira Basin. **(c)** Line drawing of a 2D regional line, showing the tectonic domains of the Guajira Basin. **(d)** Detailed depth-converted bathymetric map of the study area…..... 242

**6.3.** **(a)** 3D view of the seafloor of the study area, superimposed on the velocity model used to convert the TWT data into depth. **(b)** Composite seismic line, passing across the two main anticlines of the study area ($A_1$ and $A_2$). **(c)** Average P-wave velocity along the same path of **(b)**..... 243

**6.4.** **(a)** Detailed depth-converted bathymetric map of the study area, showing the areal occurrence of the BSR. **(b)** Frequency histogram showing the range of depths below the seafloor of the BSR. **(c)** BSR depth (mbsf) *vs* seafloor depth (mbsl), with overlapped methane hydrate stability boundary conditions…..... 247

**6.5.** NW-SE Seismic section, passing through $A_4$, $A_1$ and $A_3$. **(a)** Uninterpreted version. **(b)** Interpreted version……. 248, 249

**6.6.** SW-NE seismic section, showing the crest of $A_1$. **(a)** Uninterpreted version; **(b)** Interpreted version..... 250

**6.7.** NW-SE seismic section, passing through $A_5$, $A_2$, $A_3$ and the seaward front of the South Caribbean Deformed Belt. **(a)** Uninterpreted version; **(b)** Interpreted version…..... 251, 252

**6.8.** NW-SE seismic section, passing through $A_2$, $A_3$ and the seaward front of the South Caribbean Deformed Belt. **(a)** Uninterpreted version; **(b)** Interpreted version..... 253, 254

**6.9.** SW-NE seismic section, showing the crest of $A_2$. **(a)** Uninterpreted version; **(b)** Interpreted version..... 255

**6.10.** Seismic wavelet extraction from selected portions of seismic sections, and interpretation of the high amplitude anomalies as due to either gas hydrates or free gas.....… 256

**6.11.** Portions of the seismic sections shown in **Figs. 6.5, 6.7** and **6.8**, showing interpreted polarity reversals near and at the interpreted BGHSZ (i.e. the BSR), at the backlimb of $A_1$ **(a)** and $A_2$ **(b, c)**.....… 257

**6.12.** RMS amplitude maps of the area of BSR occurrence.....… 258

**6.13.** **(a)** Mean amplitude map of Hα. **(b)** Variance map of Hα.....… 263

**6.14.** **(a)** Mean amplitude map of Hα. **(b)** Variance map of Hβ…..... 264

**6.15.** W-E seismic section passing through $A_4$, $A_5$ and $A_2$. **(a)** Uninterpreted version; **(b)** Interpreted version.....…..... 265, 266

**6.16.** **(a)** Sketch of the natural gas hydrate system in the study area. **(b)** Schematic view of the geophysical character of the gas hydrate and free gas-bearing sediments in the study area.....… 273

**6.17.** Schematic representation, showing the process of capillary invasion of free gas inhibited by gas hydrates near the BGHSZ……..…….. 274

**6.18.** Conceptual model, describing the processes of fluid flow from the free gas zone towards and throughout the GHSZ in the study area…….. 275

**6.19.** Thickness of the free gas column *vs* pore throat radius…… 279

**6.20.** Plots of hydrostatic, overburden and free gas buoyancy pressures, in relation to the free gas zone developed beneath the BGHSZ along Hα (left) and Hβ (right), at the backlimb of $A_1$…..... 280

## Chapter 7

**7.1.** Cartoons displaying the possible origins of a free gas zone in a natural gas hydrate system……... 285

**7.2.** **(a)** Variation of the lithostatic pressure (***Pv***) with depth in the 13 analysed locations. **(b)** Variation of the gas pressure (***Pg***) *vs* the thickness of the free gas column…….. 294

**7.3.** Variation of the critical $\boldsymbol{Th_{FGZ}}$ required to initiate hydraulic fracturing in relation to the thickness of the overburden expressed as the depth of the BSR ($\boldsymbol{D_{BSR}}$)……..… 295

**7.4.** Examples of FGZs in the Guajira Basin……..… 306, 307

**7.5.** Other examples of FGZs from the Guajira Basin……. 308

**7.6.** Examples of FGZs from the South Falkland Basin…….. 309

**7.7.** Other examples of FGZs from the South Falkland Basin……. 310

**7.8.** Examples of FGZs from the Pegasus Basin, along the Hikurangi margin…… 311, 312

**7.9.** Examples of FGZs from the fold and thrust belt offshore Sabah (NW Borneo)…….. 313

**7.10.** Examples of FGZs from different convergent margins……..... 314

**7.11.** Examples of FGZs from continental margins dominated by shale/gravity **(a)** or salt **(b-e)** tectonics.. 316

**7.12.** Examples of FGZs from active extensional basins **(a, b)** and old rifted passive margins **(c-f)**…… 317

**7.13.** $Th_{FGZ}$ *vs* $D_{BSR}$ for convergent margins **(a)** and other geological settings **(b-e)**……..… 319-323

**7.14.** FGZs plotted with the hydraulic fracturing, fault reactivation and capillary invasion thresholds, calibrated with in-situ information and reasonable ranges for the Poisson ratio ($\nu$), the gas density ($\rho_g$), and the interfacial tension ($\gamma$)……... 329

**7.15.** ***GTG*** *vs* $P_{BSR}$ for convergent margins **(a)** and other geological settings **(b-e)**…….. 331-333

**7.16.** **(a)** $Th_{FGZ}$ *vs* ***GTG*** (°C/km) and **(b)** $Th_{FGZ}$ *vs* $\Delta_{SOL}$ ($10^{-5}$ mol. $CH_4$ $kg^{-1}$ $m^{-1}$)……. 334

**7.17.** **(a)** Variation of $Th_{FGZ}$ *vs* that of the pore throat size (***a***), required to initiate a capillary invasion of free gas in a water-bearing sediment. **(b)** Variation of $Th_{FGZ}$ at varying $D_{BSR}$, required to initiate hydraulic fracturing, plus ranges of $Th_{FGZ}$ required to initiate capillary invasion at discrete values of ***a***.... 341, 342

**7.18.** Water overpressure generated by **(a)** a sea level drop of 100 m **(a)** and **(b)** a tidal excursion of 5 m, at various $S_g$ and hydrostatic pressures above a given free gas accumulation……..… 349

**7.19.** Sketches displaying the principal characteristics of each class of FGZ……..... 358

**7.20.** **(a)** Relationship between ***Pf/Ph*** and ***Pf/Pv***. **(b)** Relationship between ***Ph/Pv*** and ***Pf/Pv***……. 364

**7.21.** Effect of the increase in ***Ph***, expressed as ***Ph/Pv***, on the increase in ***Pfault***, expressed as $P_{fault}/Pv$…. 366

**7.22.** Density plots from core and LWD data from different locations worldwide……..... 367-371

**7.23.** Solubility of methane, (mol/kg) at varying temperature (0-30 °C) and pressure (0-60 MPa)..……... 371

**7.24.** **(a)** Relationship (almost linear) between ***GTG*** and $\Delta_{SOL}$. **(b)** Relationship between the $Th_{FGZ}/D_{BSR}$ ratio and ***GTG***…….. 372

## Chapter 8

**8.1.** Schematic representation of the major controls on hydrate distribution at different scales……. 379

# List of Tables

## Chapter 1

**1.1.** Elastic Constants of methane gas, water, ice, $S_I$ methane hydrates and selected sediment components... 24

**1.2.** Compilation of geochemical data ($C_1/C_{2+}$, $\delta^{13}C$ of methane ($C_1$) and $\delta D$ methane ($C_1$)) of recovered gas hydrate samples and gas evolved from gas hydrate-bearing sediments in cores at *'seep'* and *'non-seep'* sites worldwide……. 70-86

## Chapter 3

**3.1.** Onboard analyses on gas samples obtained from conventional and pressure cores at DC_E…….. 130

**3.2.** Onshore analyses on gas samples obtained from conventional and pressure cores at DC_E……..… 131

**3.3.** Temperatures measured at DC_E…..... 132

**3.4.** Chloride and sulphate concentration data for DC_E…..... 133-135

**3.5.** Parameters used to calculate hydrate saturation from chlorinity…..... 135

**3.6.** Compilation of *Sh* from all the recovered core samples at DC_E, from chlorinity measurements and mass-balance calculations……... 136

## Chapter 4

**4.1.** Parameters used to calculate the volume of the pipe-zones (pipe terminus plus maximum and minimum axes of the pipe)……... 178

**4.2.** Extent of the zones interested by free gas anomalies, of the GHOZ within *vs* outside the pipe-zones and of hydrate volumes within *vs* outside the pipe-zones……..…. 179

## Chapter 5

**5.1.** Summary table of the main characteristics of each borehole location (DC_A, DC_B, DC_C and DC_E)……. 213

**5.2.** Temperatures measured at DC_A and DC_B..... 229

**5.3.** Parameters used to extrapolate the theoretical Vp *vs Sh* trends for the pore-filling and load-bearing models……. 229

**5.4.** Chloride and sulphate concentration data for DC_A…….....…. 230, 231

**5.5.** Chloride and sulphate concentration data for DC_B…….....….. 232, 233

**5.6.** Compilation of *Sh* from all the recovered core samples, from chlorinity measurements and mass-balance calculations at DC_A…….…. 234

**5.7.** Compilation of *Sh* from all the recovered core samples, from chlorinity measurements and mass-balance calculations at DC_B……... 235

## Chapter 6

**6.1.** Parameters used to compute the free gas buoyancy pressure, the hydrostatic pressure, the lithostatic pressure and the capillary pressure…….. 280

## Chapter 7

**7.1.** Summary table with the location, geological settings and references for each gas hydrate province considered in this study……..... 288

**7.2.** Location, sites and data used to extrapolate the ***Pv*** *vs* depth functions used in this study……..... 295

**7.3.** Detailed dataset used for this study…… 301-305

**7.4.** **(a)** Characteristics of each type of FGZ, based on the five main considered factors; **(b)** Prospectivity for gas hydrates, geohazard and climate sensitivity related to each class of FGZ…… 357

**7.5.** Parameters used to calculate ***Pf/Ph***, ***Pf/Pv*** and ***Ph/Pv*** in **Fig. 7.20**…….. 363

## Chapter 8

**8.1.** Detailed list of the controls of gas hydrate distribution at different scales……... 380

# List of Abbreviations and Symbols

- ***NGHS(s)***= Natural gas hydrate system(s)
- ***$S_I$ hydrates***= Structure I hydrates
- ***$S_{II}$ hydrates***= Structure II hydrates
- ***$S_H$ hydrates***= Structure H hydrates
- ***$S_{II/H}$ hydrates*=** Structure II and structure H hydrates
- ***GHSZ***= Gas hydrate stability zone
- ***BGHSZ***= Base of the gas hydrate stability zone
- ***$BS_IGHSZ$***= BGHSZ for $S_I$ hydrates
- ***$BS_{II}GHSZ$***= BGHSZ for $S_{II}$ hydrates
- ***$BS_{II/H}GHSZ$***= BGHSZ for $S_{II}$ and $S_H$ hydrates
- ***GHBS***= Gas hydrate-bearing sediments
- ***C-GHBS*=** Coarse-grained gas hydrate-bearing sediments at high concentrations
- ***FGZ(s)***= Free gas zone(s)
- ***GWC***= Gas-water contact
- ***GOC***= Gas-oil contact
- ***SMTZ***= Sulphate-methane transition zone
- ***AOM***= Anaerobic methane oxidation
- ***$C_{2+}$***= Heavier than methane (referred to a mixture of hydrocarbons)
- ***mbsf***= Metres below the seafloor
- ***ms TWT bsf*=** ms two-way-time below the seafloor
- ***mbsl***= Metres below the sea level
- ***$Th_{FGZ}$*=** Vertical thickness of the FGZ (measured from the BGHSZ)
- ***$D_{BSR}$***= Depth of the BSR (mbsf)
- ***Sh***= Gas hydrate saturation (% of pore space)
- ***Sg***= Free gas saturation (% of pore space)
- ***BSR(s)***= Bottom-simulating reflector(s)
- ***EAR(s)***= Enhanced amplitude reflection(s)
- ***ZSW(s)***= Zone(s) of seismic wipeout
- ***HRA(s)***= High-reflectivity area(s) at the seafloor
- ***RMS amplitud***e= Root-mean-square amplitude
- ***TWT***= Two-way time
- ***MTD(s)***= Mass-transport deposit(s)

- ***GTG(s)***= Geothermal gradient(s)
- ***FC***= Fugro corer
- ***FPC***= Fugro pressure corer
- ***HRC***= Hyace rotary corer
- ***LWD*** = Logging-while-drilling
- ***WL***= Wireline
- ***XMAC***= Cross-Multipole Array Acoustic log
- ***STAR***= Simultaneous Acoustic and Resistivity Imager device
- ***MSCL***= Multi-sensor core logger
- ***FPWS***= Fugro pore water sampler
- ***TCPT***= Temperature cone penetration equilibrium tests
- ***Cm***= Measured chlorinity
- ***Cb***= Measured chlorinity
- ***Ø***= Porosity
- $R_{deep}$= Deep Resistivity
- $R_t$= Measured resistivity
- $R_w$= Resistivity of the pore water
- $R_o$= Resistivity of a fully water-saturated sediment
- ***a***= Tortuosity factor (Archie equations); pore throat radius (Young-Laplace equation)
- ***m***= Cementation index
- ***n***= Saturation index
- ***IR***= infra-red
- ***GR***= Gamma-ray
- ***HI***= Hydrogen index
- ***Pv***= Lithostatic stress (lithostatic pressure)
- ***Ph***= Minimum horizontal stress
- ***Pw***= Hydrostatic stress (hydrostatic pressure) measured from the seafloor
- ***Pg***= Free gas buoyancy pressure
- ***P'v***= Effective lithostatic pressure (stress)
- ***OP***= Overpressure
- ***Pf***= Pore fluid pressure
- $Pf_{tot}$= Total pore fluid pressure
- ***Pc***= Capillary entry pressure
- $\gamma_{gw}$= Interfacial tension between methane as free gas and water

- $\boldsymbol{\varphi}$= Contact angle against the solid between methane as free gas and water
- $\boldsymbol{g}$= Gravity acceleration
- $\boldsymbol{\rho_w}$= Density of the pore water
- $\boldsymbol{\rho_b}$= Density of the bulk sediment
- $\boldsymbol{\rho_g}$= Density of the free gas
- $\boldsymbol{\rho_h}$= Density of pure gas hydrate
- $\Delta\boldsymbol{\rho_{(w-g)}}$= Density difference between pore water and free gas
- $\boldsymbol{h}$= Vertical interval of reference (e.g. from the seafloor to a specific interface in the overburden)
- ***GK***= Gumusut-Kakap
- ***GKL Dome*=** Gumusut-Kakap and Limbayong Dome (i.e. the bathymetric ridge overlying the thrust-cored anticlines shown in **Chapters 3-5**)

# Chapter 1. Introduction and literature review

Natural gas hydrates are clathrate compounds, constituted by a solid hydrogen-bounded water lattice, able to encage other molecules under particular thermobaric conditions (Kvenvolden, 1993; Sloan Jr, 2003; Collett *et al.*, 2009). Natural gas hydrates are similar to water-ice to the naked eye, but some physical properties and the stability conditions are different (Waite *et al.*, 2009). On Earth, methane is the most common guest molecule naturally enclathrated within the hydrate structure. Methane is a powerful greenhouse gas, naturally produced during the microbially and thermogenically-mediated organic matter diagenesis in sedimentary basins, on- and offshore (Rice and Claypool, 1981; Schoell, 1983; Wallmann *et al.*, 2006a; Collett *et al.*, 2009; Boswell and Collett, 2011; Stolper *et al.*, 2014).

## 1.1. Gas hydrate crystallography and molecular composition

The size of the guest molecules is crucial to determine the structure of the hydrogen-bonded water cavity, where the molecules are non-stoichiometrically entrapped by van der Waals interactions (Sloan Jr, 2003; Hester and Brewer, 2009). Three natural gas hydrate structures have been discovered in geological systems so far: structure I ($S_I$), II ($S_{II}$) and H ($S_H$) (**Fig. 1.1a**). In natural systems, $S_{II}$ and $S_H$ hydrates can include a wider spectrum of guest molecules compared to $S_I$ hydrates (Sassen *et al.*, 2001d; Collett *et al.*, 2009). A pentagonal dodecahedron is the water-made building block of all the three naturally occurring hydrate structures. However, it is necessary to incorporate other face types (i.e. hexagonal and squared) to stabilise the whole clathrate structure and avoid a bond breakage (Sloan Jr, 2003). $S_I$ hydrates have a body-centred (primitive) cubic structure whereas $S_{II}$ hydrates have face-centred diamond cubic structure. Finally, $S_H$ hydrates have a hexagonal lattice structure.

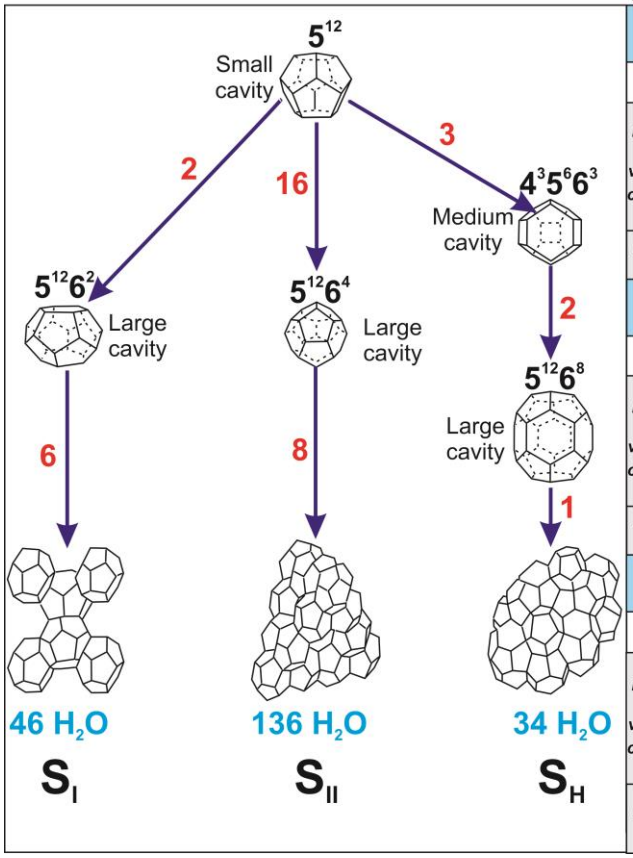
Naturally occurring $S_I$ and $S_{II}$ hydrates host relatively small gas molecules. In particular, $S_I$ hydrates host molecules with diameters of 0.4-0.55 nm, usually methane and occasionally ethane, carbon dioxide and hydrogen sulphide. $S_{II}$ hydrates can include larger molecules (up to 0.7 nm), including propane and iso-butane. Finally, $S_H$ hydrates can be associated with heavier order hydrocarbon gases (up to 0.9 nm), such as pentanes and hexanes, thanks to a large icosahedral cavity (**Fig. 1.1b**) (Sloan Jr, 2003; Lu *et al.*, 2007; Hester and Brewer, 2009; Koh *et al.*, 2012). Noble gases (e.g. Argon, Krypton and Xenon) have also been found as traces in a few hydrate samples (Winckler *et al.*, 2002).

$S_I$ is the most common hydrate structure, given that methane is by far the most abundant hydrate-forming gas in natural environments. Nevertheless, if molecules larger and heavier than methane are present even in relatively small quantities (i.e. a few mol. %), the other two structures can be formed. (Kvenvolden, 1993; Sassen *et al.*, 2000 and 2001a; Milkov, 2005). Multiple hydrate structures have been found to coexist in the same geological

system (Sassen and MacDonald, 1994; Paull *et al.*, 2005; Kida *et al.*, 2006; Lu *et al.*, 2007; Klapp *et al.*, 2010). Mixtures of methane and ethane can further be included in both $S_I$ and $S_{II}$ hydrates, depending on their reciprocal abundance (Ballard and Sloan Jr, 2000; Subramanian *et al.*, 2000; Sassen *et al.*, 2001b; Kida *et al.*, 2006). Importantly, given an initial feeding gas mixture, some gases are more favourably crystallised as hydrates than others, depending on their fugacity and Langmuir constants (i.e. on the gas capacity to be adsorbed). This effect is evident for $S_{II}$ and $S_H$ hydrates, commonly more enriched in $C_{2+}$ components than the original feeding gas (Sassen *et al.*, 2001a). $S_{II}$ and $S_H$ hydrates are more stable than $S_I$ hydrates at pressure and temperature conditions typical of sedimentary basins (Milkov and Sassen, 2000; Lu *et al.*, 2007) (**Fig. 1.2**). The same hydrate structure can also display a broad spectrum of thermobaric stability conditions, depending on the relative abundance of the guest molecules (Lu *et al.*, 2007). For instance, even 1.0 mol. % of propane added to a formerly pure methane gas determines a transition from $S_I$ to $S_{II}$ hydrate. Increasing the relative quantity of propane with respect to methane widens the hydrate stability conditions (**Fig. 1.3**). The changes in hydrate stability conditions are ultimately controlled by the relative amounts of the guest molecules entering in the hydrate cavities, by the guest molecule to hydrate cavity size ratios, and by the guest molecule shape (for $S_H$ hydrates) (Sloan Jr and Koh, 2007).

In natural samples, not all the hydrate cages are filled with a gas molecule. If all the cages were filled, the hydration number would be 5.75 for a 100% $CH_4$ $S_I$ hydrate (Uchida *et al.*, 1999a; Sloan Jr, 2003). However, in both natural and laboratory samples, this number is equal or higher than 6.0, implying that gas hydrates are non-stoichiometric compounds (Uchida *et al.*, 1999a; Chazallon *et al.*, 2007; Kida *et al.*, 2009 and 2015; Liu *et al.*, 2015). Regardless of the cage occupancy, the gas hydrate structure is capable of hosting a significant amount of gas. The dissociation of one cubic metre of gas hydrate is thought to liberate 150-180 cubic metres of free gas at ambient conditions (Kvenvolden, 1993; Collett *et al.*, 2009).

a




b

| Structure I<br>$2(5^{12})+6(5^{12}6^2)\cdot 46\ H_2O$ | | |
|---|---|---|
| **Cavity** | **Small** | **Large** |
| average radius (nm) | 0.395 | 0.433 |
| radius variation (%) | 3.4 | 14.4 |
| coordination number | 20 | 24 |
| possible guests | $C_1$, $C_2$, $CO_2$, $H_2S$, $Ar^*$, $Kr^*$, Xe | |

| Structure II<br>$16(5^{12})+8(5^{12}6^4)\cdot 136\ H_2O$ | | |
|---|---|---|
| **Cavity** | **Small** | **Large** |
| average radius (nm) | 0.391 | 0.473 |
| radius variation (%) | 5.5 | 1.73 |
| coordination number | 20 | 28 |
| possible guests | $C_1$, $C_2$, $C_3$, n-$C_4$, i-$C_4$, cyclopentane, benzene?, $Co_2$, $Ar^*$, $Kr^*$ | |

| Structure H<br>$3(5^{12})+2(4^35^66^3)+1(5^{12}6^8)\cdot 34\ H_2O$ | | | |
|---|---|---|---|
| **Cavity** | **Small** | **Medium** | **Large** |
| average radius (nm) | 0.394 | 0.404 | 0.579 |
| radius variation (%) | 4.0 | 8.5[b] | 15.1 |
| coordination number | 20 | 20 | 26 |
| possible guests | $C_1$, n-$C_5$, i-$C_5$, neo-$C_5$?, 2-methylpent., 3-methylpent., n-hexane, methylcyclopent., cyclohex., methylcyclohex. | | |

**Figure 1.1. (a)** Schematic representation, showing the three naturally-occurring hydrate crystal structures. The $S_I$ hydrate unit crystal structure has 46 water molecules and is composed of 2 pentagonal dodecahedron ($5^{12}$) water cages, which form small cavities for the guest gases, and 6 tetrakaidekahedral ($5^{12}6^2$) water cages, which form large cavities for the guest gas. The $S_{II}$ hydrate unit crystal structure has 136 water molecules and is composed of 16 $5^{12}$ small cavities and 8 hexakaidecahedral ($5^{12}6^4$) large cavities. Finally, the $S_H$ hydrate unit crystal structure is composed of 3 $5^{12}$ small cavities, 2 irregular dodecahedral ($4^35^66^3$) medium cavities and one icosahedral ($5^{12}6^8$) large cavity. **(b)** Principal crystallographic properties and gas guest molecules of the $S_I$, $S_{II}$ and $S_H$ hydrates (modified after Sloan Jr, 2003 and Sloan Jr and Koh, 2007). *= Ar and Kr have been found in traces in natural almost ~100% methane $S_I$ hydrates at Hydrate Ridge. However, they form $S_{II}$ hydrates if they represent the sole guest molecule (Davidson *et al.*, 1984; Winckler *et al.*, 2002).

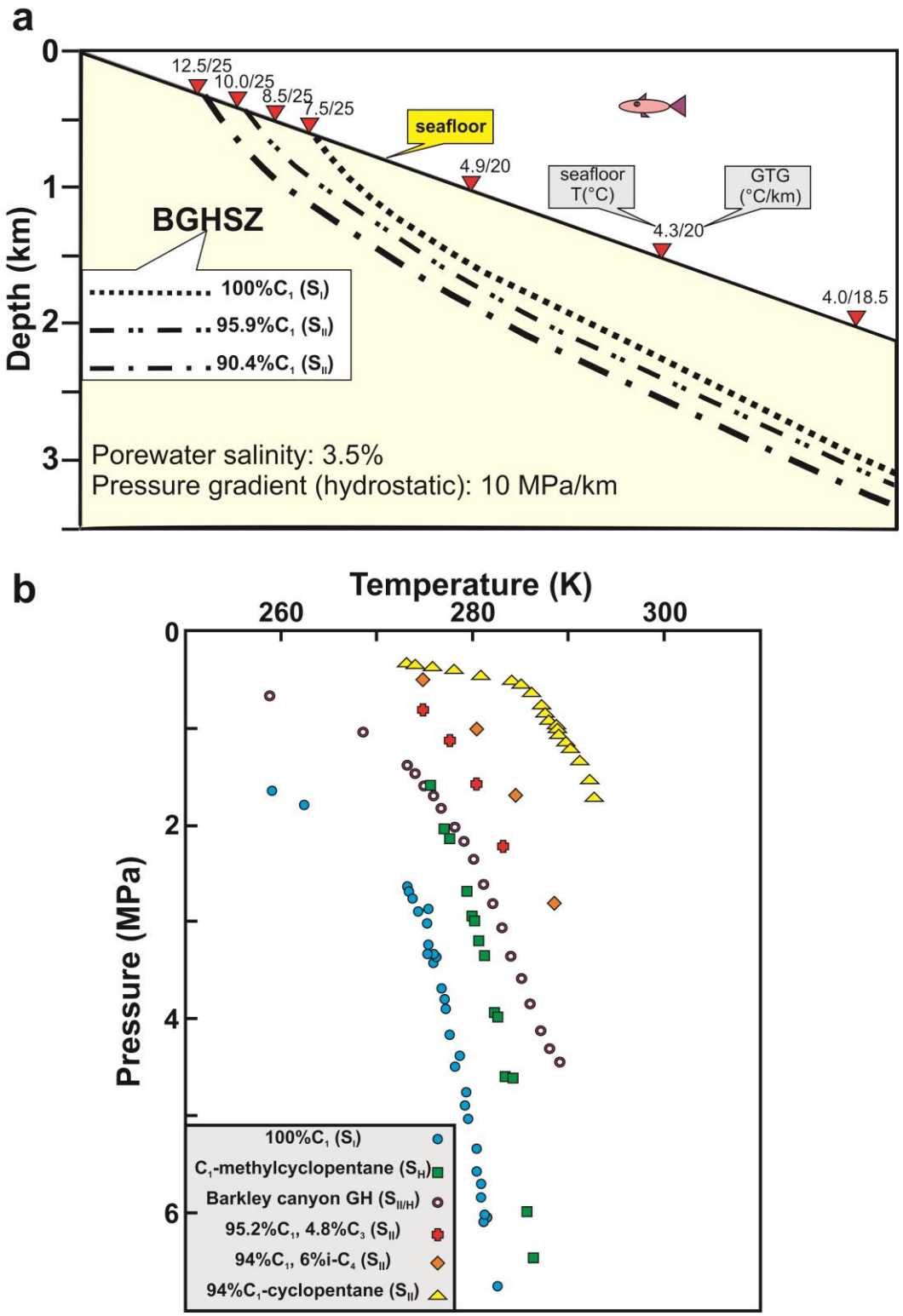



**Figure 1.2. (a)** Simplified example of the predicted depth of the base of the gas hydrate stability zone (BGHSZ) along the continental slope of the Gulf of Mexico (modified after Milkov and Sassen, 2000). Note that with decreasing methane ($C_1$) in the feeding gas composition, the depth along the slope at which the BGHSZ pierces the seafloor is shallower, indicating wider stability conditions for gas mixture with respect to pure methane. GTG= Geothermal gradient **(b)** Gas hydrate stability conditions for different structures and chemical composition of the feeding gas. Hydrates are stable on the left sides of the curves. Note that $S_{II}$, $S_H$ and mixed $S_{II}$ and $S_H$ hydrates ($S_{II/H}$) are more stable than $S_I$ pure methane hydrates (modified after Lu *et al.*, 2007). $C_1$= methane; $C_3$= propane; i-$C_4$= iso-butane.

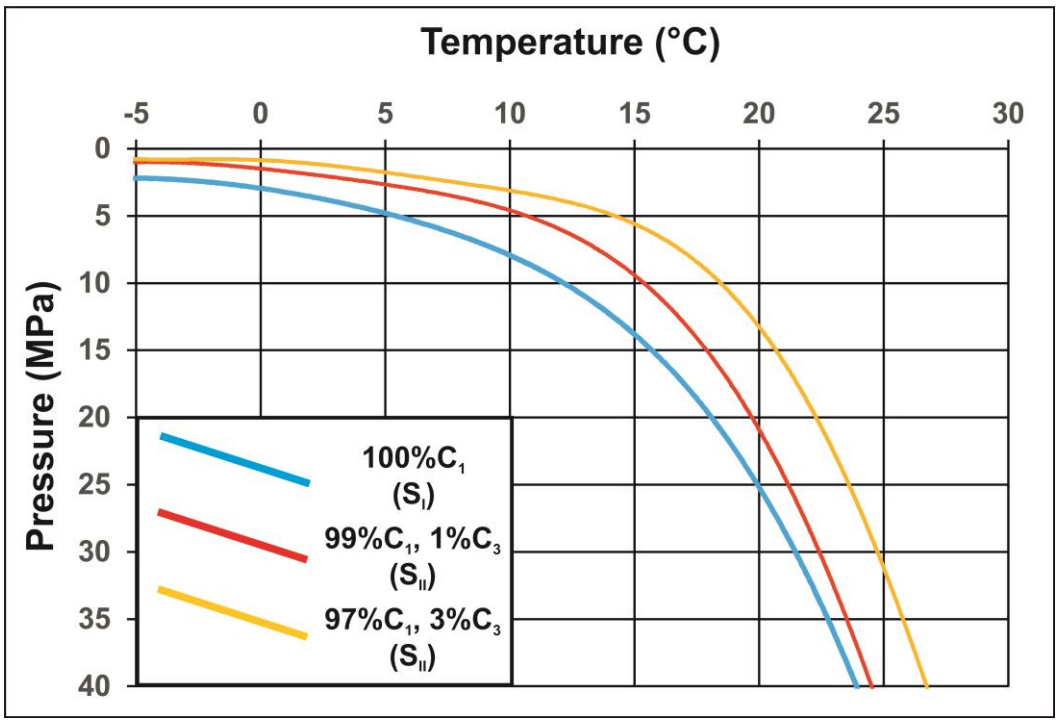



**Figure 1.3.** Theoretical examples of gas hydrate stability curves (coloured curves), at varying pressure, temperature and feeding gas composition, assuming a constant pore water salinity (3.0% NaCl eq.). Hydrates are stable on the left sides of the curves. $C_1$= methane; $C_3$= propane. Note that hydrate stability increases with increasing propane content. The curves have been constructed with CSMHyd (Sloan Jr and Koh, 2007).

## 1.2. Discovery history of natural gas hydrates

The laboratory discovery of clathrate compounds is dated between the late eighteenth and early nineteenth century while the observation of natural gas hydrates in pipelines goes back to 1934 (Makogon *et al.*, 2007). However, the natural occurrence of gas hydrates in sediments was firstly inferred in the sixties, where the gas field of Messoyakha was discovered in the Siberian permafrost (Makogon and Omelchenko, 2013) and, later, in the seventies, where well-log data suggested hydrate occurrence in the Canadian and Alaskan permafrost regions (Bily and Dick, 1974; Kvenvolden and McMenamin, 1980). Concurrently, the presence of natural gas hydrates was also hypothesised in marine environments. The first indirect evidence (i.e. geophysical) and direct recovery of marine natural gas hydrates coincided with pioneering offshore geophysical surveys and the onset of scientific drilling projects (i.e. the DSDP Legs) and along continental margins (Markl *et al.*, 1970; Shipley *et al.*, 1979; von Huene *et al.*, 1980; Kvenvolden *et al.*, 1993).

The widespread recognition of bottom-simulating reflectors (BSRs), approximating the base of hydrate stability in seismic profiles, contributed to raise the attention towards marine gas hydrates. The first BSRs were imaged at the Blake Ridge, offshore N Carolina and along the Middle-America Pacific and Colombian accretionary prisms (Shipley *et al.*, 1979) (**Fig. 1.4**). Since those days, enormous efforts were made to increase our knowledge of naturally-occurring gas hydrates. Hence, the number of localities, both onshore and offshore, exhibiting indirect and direct evidence of hydrates has continuously increased (e.g. Brooks *et al.*, 1991; Miller *et al.*, 1991; Collett, 1994; MacKay *et al.*, 1994; Paull *et al.*, 1995).

The significant improvement of geophysical, well-logging and coring techniques in the last 15-20 years, has provided a further improvement in the understanding of the distribution of natural gas hydrates, especially when a multi-scale and multidisciplinary approach is taken. This approach has been the key to the success of the several ODP, IODP, academic, national and industry-leaded campaigns that have investigated naturally-occurring gas hydrates, both off- and onshore, in active and passive margins (e.g. Holbrook *et al.*, 1996; Tréhu *et al.*, 2004b; Pecher *et al.*, 2005; Sultan *et al.*, 2007; Torres *et al.*, 2008; Hustoft *et al.*, 2009; Riedel *et al.*, 2010b; Bahk *et al.*, 2011; Collett *et al.*, 2011; Boswell *et al.*, 2012a; Lee *et al.*, 2013; Kumar *et al.*, 2014; Wang *et al.*, 2014; Crutchley *et al.*, 2015; Fujii *et al.*, 2015).

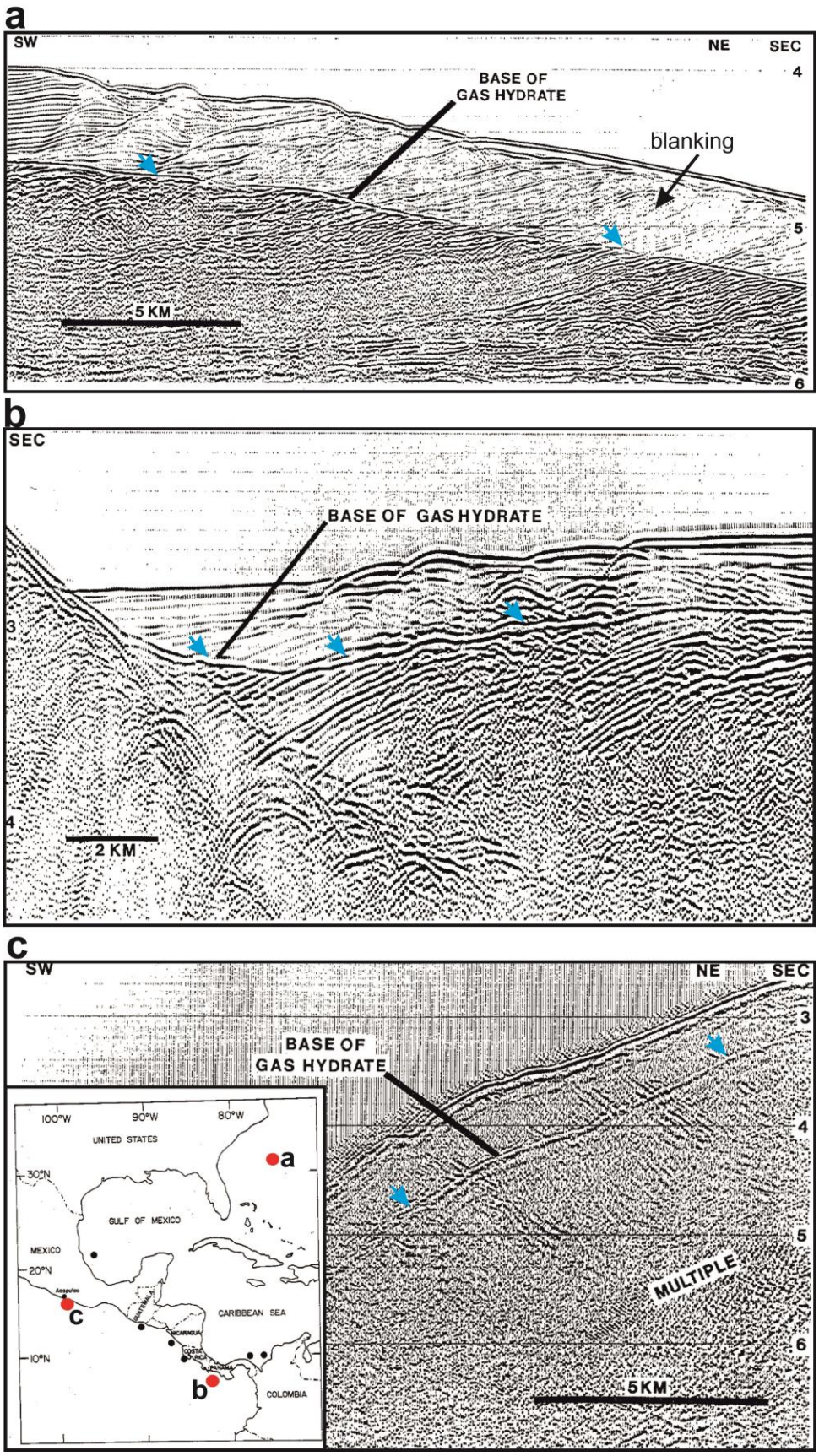



**Figure 1.4.** Vintage seismic reflection lines, showing bottom-simulating reflectors (BSRs, blue arrows) along the continental margins of Blake Ridge **(a)**, Panama **(b)** and the Middle America Trench (Mexico) **(c)** (Shipley *et al.*, 1979). The inset map in **(c)** shows the geographic locations of the lines (red circles). The black circles indicate other areas where the occurrence of hydrates was suspected in 1979.

## 1.3. Occurrence and origin of natural gas hydrates

The physical and chemical factors that control gas hydrate formation and stability restrict the occurrence of natural gas hydrate to specific portions of **(1)** subaquatic basins and **(2)** permafrost regions. In these settings, a combination of relatively high pore fluid pressures and low temperatures makes gas hydrates stable (**Fig. 1.5**). Nowadays, the presence of natural gas hydrates is inferred or ascertained through core recovery along most of the continental margins, at different latitudes, as well as in the Arctic and Himalayan permafrost (Kvenvolden, 1993; Collett *et al.*, 2009; Lu *et al.*, 2011) (**Fig. 1.6**). The sedimentary basins beneath the Antarctic ice-sheets likely constitute another significant methane hydrate province (Wadham *et al.*, 2012) although so far there is no direct recovery or geophysical evidence. Furthermore, hydrates have been found to occur also in few lacustrine basins, such as the Lake Baikal and the Caspian Sea (Ginsburg and Soloviev, 1994; Kida *et al.*, 2009).

The gas hydrate stability zone (GHSZ) represents the volume of the sedimentary and water columns where hydrate stability conditions are satisfied. However, **(1)** the availability of water and **(2)** the presence of enough gas molecules in the system to exceed the required supersaturation threshold in the pore water constitute further limiting conditions for hydrate formation (Xu and Ruppel, 1999; Davie *et al.*, 2004; Milkov *et al.*, 2004b; Liu and Flemings, 2006; Chand *et al.*, 2008) (**Fig. 1.7**). Offshore, along continental margins, hydrates are stable at water depths greater than about 300-500 m (i.e. at pore fluid pressures higher than ~3-5 MPa). Going deeper, the GHSZ extends down to a few hundred of metres in the overburden (Kvenvolden *et al.*, 1993; Milkov and Sassen, 2000; Rajan *et al.*, 2012; Brothers *et al.*, 2014) (see **Fig. 1.2a**). In contrast, the low temperatures and thermal gradients associated with permafrost grounds make the GHSZs in these onshore regions up to ~1000-2000 m thick (e.g. Collett *et al.*, 2011). Along those continental shelves at high-latitudes where a

submarine relict permafrost occurs, the stability zones for marine and permafrost hydrates can approach each other (Collett *et al.*, 2011; Riedel *et al.*, 2017).

Natural gas hydrates can form **(1)** within the sediment and, in marine and lacustrine environments, **(2)** at the sediment-water interface and **(3)** in the water column, in the form of free gas-coating rims (Greinert *et al.*, 2006; Sauter *et al.*, 2006). Within the GHSZ, from the seafloor down to the base of the GHSZ (BGHSZ), the volume of sediment that effectively contains gas hydrates is termed gas hydrate occurrence zone (GHOZ). The GHOZ can be constituted by a single or multiple intervals, where hydrates partially or entirely occupy the pore space (e.g. Malinverno *et al.*, 2008) **(Fig. 1.7**).

The geothermal gradient (GTG) is a critical control on the vertical extent of the GHSZ. At a fixed water depth (or ground surface in permafrost regions), the higher the GTG is, then the shallower the BGHSZ will be. The regional tectonic history is a primary influence on the GTG. However, local anomalies can occur due to focused fluid flow, the presence of conductive salt bodies and an irregular/highly faulted basement geometry (e.g. Taylor *et al.*, 2000; Macelloni *et al.*, 2015). In subaquatic hydrate provinces, within the water column down to the sediment-water interface, the top of the GHSZ is controlled by the water temperature, which varies with latitude, ocean circulation patterns and climate changes (Heeschen *et al.*, 2003; Mienert *et al.*, 2005; Phrampus and Hornbach, 2012) (**Figs. 1.5, 1.8**).

The availability and the preservation of organic matter in the sedimentary section are crucial for the formation of natural hydrocarbon gases (Müller and Suess, 1979; Hedges and Keil, 1995). Ultimately, this limits the areal extent of the occurrence of gas hydrates to those continental margins characterised by efficient processes of microbial and thermogenic natural gas formation and migration (Milkov, 2005). In contrast, permafrost-related hydrate accumulations are dominantly fed by leaky thermogenically-sourced petroleum systems (Collett *et al.*, 2011; Wang *et al.*, 2015). Moreover, It has been argued that hydrates can be

locally fed by abiotic methane, derived from the reaction between $CO/CO_2$ and $H_2$, produced by the serpentinisation of the oceanic crust (see Johnson *et al.*, 2015).

The thermogenic gases leaking from conventional hydrocarbon reservoirs are characterised by variable amounts of $C_{2+}$ hydrocarbons (usually around 1-15%). Therefore, they may form mixtures of $S_I$, $S_{II}$ and $S_H$ hydrates (Sassen *et al.*, 2001d; Chen and Cathles, 2003; Kida *et al.*, 2006; Klapp *et al.*, 2010). Conversely, the sole presence of $S_I$ hydrates suggests a microbially-derived source of methane (Kvenvolden and Lorenson, 2001; Milkov, 2005), of primary or secondary origin. The thickness of the GHSZ is therefore usually increased in the presence of a thermogenic source (cf. **Figs. 1.2, 1.3**). Nevertheless, the existence of a dry (i.e. with trace amounts of $C_{2+}$ hydrocarbon) thermogenic source, capable of generating $S_I$ hydrates solely, must not be ruled out (De Prunelé *et al.*, 2017). Only by combining isotopic and compositional analyses, the two different sources can be clearly distinguished, being that microbially-sourced gas hydrates have a lighter methane $\delta^{13}C$ and D isotopic signatures than thermogenically-sourced ones (Kvenvolden, 1995; Sassen *et al.*, 2001a and b; Mazurenko *et al.*, 2002; Milkov, 2005; Pohlman *et al.*, 2005). The geochemical signatures that fall in between these end-members are frequently interpreted indicate a mixture of shallow microbial and deep thermogenic sources (Kida *et al.*, 2006; Pape *et al.*, 2010a; Liu *et al.*, 2015).

**Figures 1.9** and **1.10** show, respectively, the relationship between the carbon isotope ratio ($\delta^{13}C$) of methane and the gas wetness ($C_1/C_{2+}$) and between the carbon and the hydrogen isotope ratios ($\delta^{13}C$ and $\delta D$) of methane. The data plotted in these figures have been updated in this thesis from most of the known gas hydrate provinces where hydrates have been successfully sampled (**Tab 1.2** in **paragraph 1.11**). The majority of naturally occurring gas hydrates appear biogenically sourced, although there is an emerging consensus on the importance of hydrates sourced by thermogenic hydrocarbon systems (e.g. Ostanin *et al.*, 2013; Serié *et al.*, 2016; De Prunelé *et al.*, 2017; Plaza-Faverola *et al.*, 2017).

The salinity of the pore water represents another control on the extent of the GHSZ, being inversely correlated to gas hydrate stability. This effect is relevant in regions of salt tectonism (**Fig. 1.8a**), in basins subject to variations in the hydrogeologic system (e.g. freshwater to salt-water time shifts) and, at smaller scales and transiently, during the migration of free gas across the GHSZ (Clennell *et al.*, 1999; Henry *et al.*, 1999; Taylor *et al.*, 2000; Liu and Flemings, 2007; Chand *et al.*, 2008; Riboulot *et al.*, 2018).

The processes of formation and dissociation of gas hydrates are, respectively exothermic and endothermic (Tréhu *et al.*, 2004b; Waite *et al.*, 2009). In natural systems, the temperature increase induced by hydrate formation may transiently shift the phase boundary, allowing the localised migration of free gas throughout the GHSZ (Smith *et al.*, 2014a). Importantly, hydrate dissociation should not be confused with hydrate dissolution. Both these processes naturally occur but, while the former is related to conditions that bring hydrates outside their stability field, inducing the liberation of free gas and pure water, the latter is associated with a lack of adequate gas supply (e.g. Waite *et al.*, 2009; Sultan *et al.*, 2010; Brothers *et al.*, 2014).

In subaquatic gas hydrate provinces, from the seafloor down to a few up to tens of metres below, methane is oxidised. This oxidation is accompanied by the reduction of sulphate, which is mostly driven by anaerobic bacteria and archaea (Borowski *et al.*, 1996; Boetius *et al.*, 2000) through the following reaction: $\mathbf{CH_4 + SO_4 \rightarrow HCO_3^- + HS^- + H_2O}$. In addition, sulphate may be reduced by microbially-induced organic-matter breakdown processes, with the following simplified reaction: $\mathbf{2(CH_2O) + SO4 \rightarrow 2HCO_3^- + H_2S}$.

The lowermost depth where the anaerobic methane oxidation (AOM) occurs marks a specific interface in the sedimentary column, called the sulphate-methane transition zone (SMTZ). Below this zone, methane (and other hydrocarbon gases) are not oxidised, and hydrates can be preserved. Below the SMTZ, methane may be produced at shallow depth through $CO_2$ reduction and acetate fermentation (Claypool and Kaplan, 1974). The

effectiveness of the reduction of sulphate is related to the amount of methane in the system. Therefore, the depth of the SMTZ has been quantitatively correlated with diffusive methane fluxes (Borowski *et al.*, 1999). However, high advective fluxes of hydrocarbon gases may shift the SMTZ up to the seafloor and gas hydrates can form at shallow depths. Consequently, these regions of high fluid fluxes allow the formation of cold seeps and sustain the survival of chemosynthetic communities (Paull *et al.*, 2005; Boetius and Wenzhöfer, 2013) **(Fig. 1.11)**.

The analysis of the physical and chemical controls on hydrate stability and formation has been combined, in recent years, with a classical petroleum system approach. The term gas hydrate petroleum system (or natural gas hydrate system, NGHS) is now widely used and accounts for **(1)** the P-T stability conditions and their 3D variability; **(2)** the 3D variability of pore water and gas composition, as well as their availability in adequate amounts in the system; **(3)** the 3D variability in the host lithology properties (i.e. the gas hydrate reservoir quality) **(4)** the gas migration pathways below and throughout the GHSZ and **(5)** the changes, through time, of these factors (Collett *et al.*, 2009) (**Fig. 1.12**).

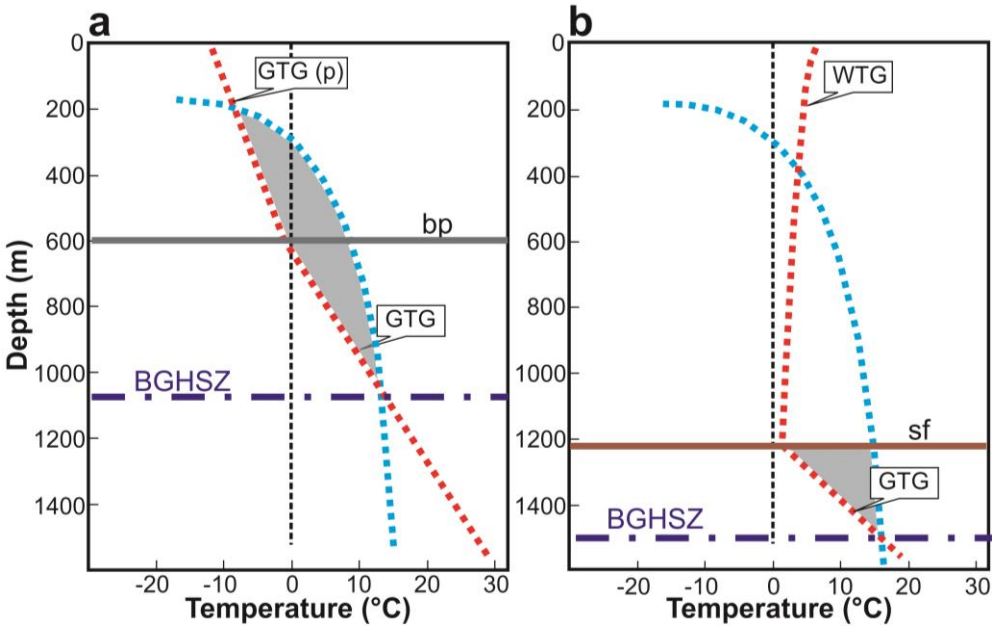



**Figure 1.5.** Schematic representations of the temperature and pressure conditions leading to gas hydrate stability in **(a)** permafrost regions and **(b)** subaquatic environments (modified after Collett *et al.*, 2009). The red-dotted area indicates the thermal gradient whereas the blue-dotted area is an arbitrary gas hydrate stability curve. The grey-zones indicate where hydrates are stable in the sediments. GTG (p) = geothermal gradient in the permafrost zone; GTG = geothermal gradient; WTG = thermal gradient in the water column; bp = base of the permafrost layer; sf = seafloor; BGHSZ = base of the GHSZ.

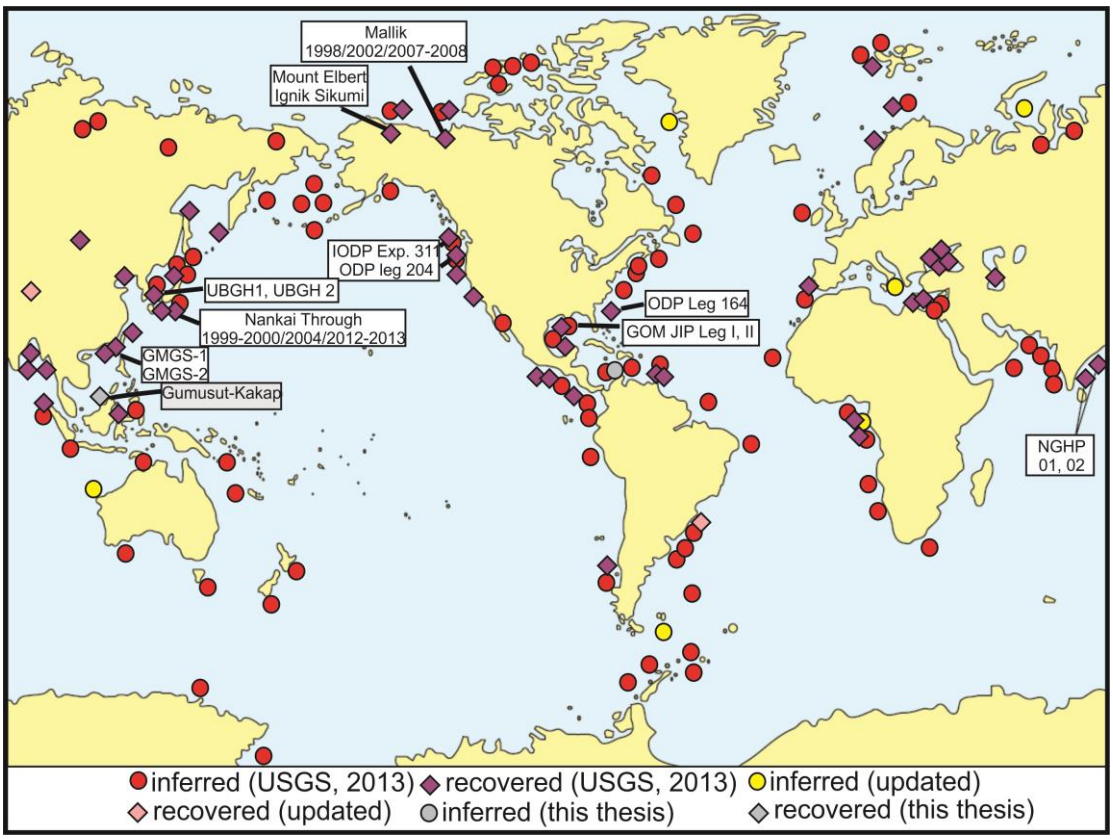



**Figure 1.6** Schematic map showing the locations where hydrates have been recovered (rhombi) or inferred to occur (circles), from geophysical and petrophysical evidence. The grey rhombi and circles represent the hydrate provinces analysed in this thesis (source of the map: USGS, https://woodshole.er.usgs.gov/project-pages/hydrates/primer.html).

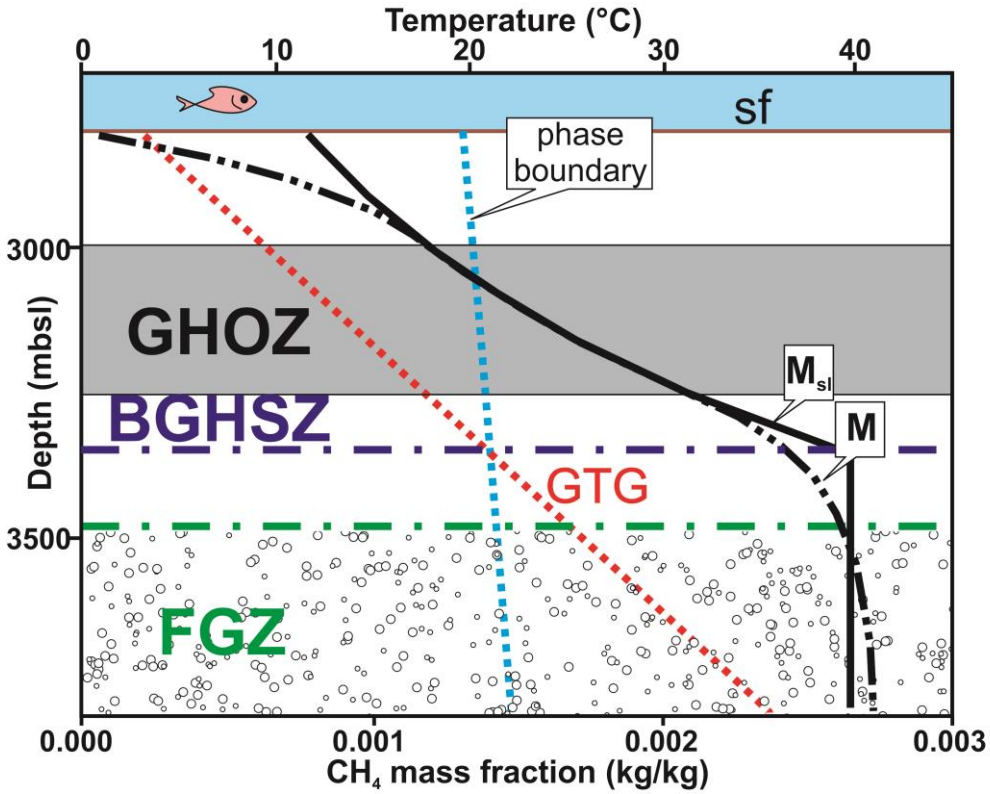



**Figure 1.7.** Relationships between gas hydrate stability, gas (methane) solubility and hydrate occurrence (modified after Xu and Ruppel, 1999). Gas hydrate and free gas form where the methane concentration in the system (M) exceeds the supersaturation thresholds defined by the methane solubility curve ($M_{sl}$). It is theoretically possible that the gas hydrate occurrence zone (GHOZ) and the free gas zone (FGZ) are separated in a natural system GTG= geothermal gradient; BGHSZ= base of gas hydrate stability zone; sf= seafloor.

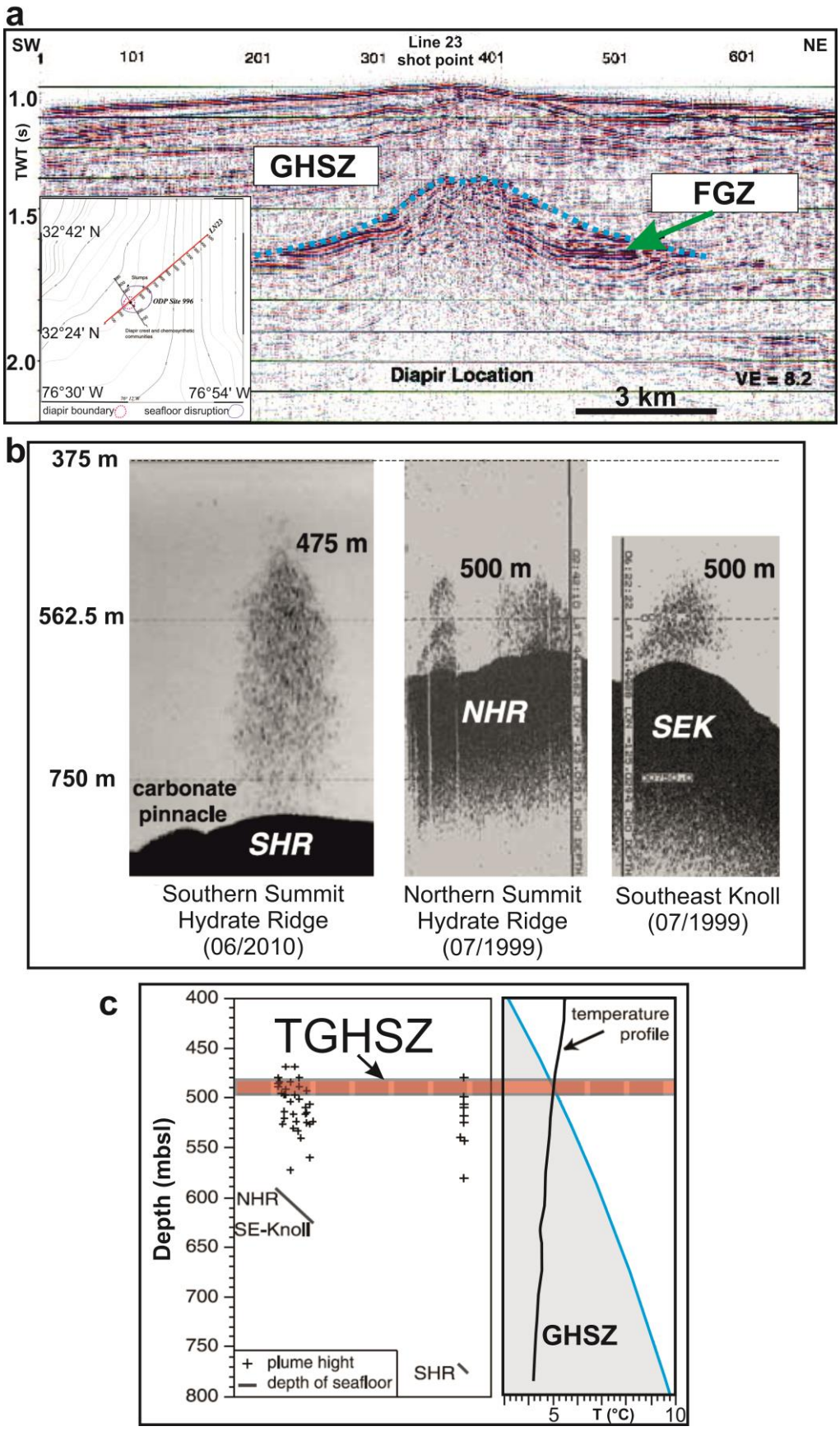



**Figure 1.8. (a)** Seismic reflection profile along the Blake Ridge Diapir, showing the impact of a salt body on the shape of the BGHSZ (modified after Taylor *et al.*, 2000). The high thermal conductivity of the diapir, together with the associated increase in salinity, determine a shallower BGHSZ (blue dotted line) above it. The free gas zone (FGZ) is marked with a green arrow. **(b)** Gas flares (plumes) at the Hydrate Ridge (offshore Oregon), expressed as acoustic disruptions in the water column. **(c)** The shallowest occurrences of the gas flares are at ~475-500 metres below the sea level (mbsl). This range of depths coincide with the top of the GHSZ (TGHSZ)**.** The blue line represents the hydrate phase boundary (modified after Heeschen *et al.*, 2003).

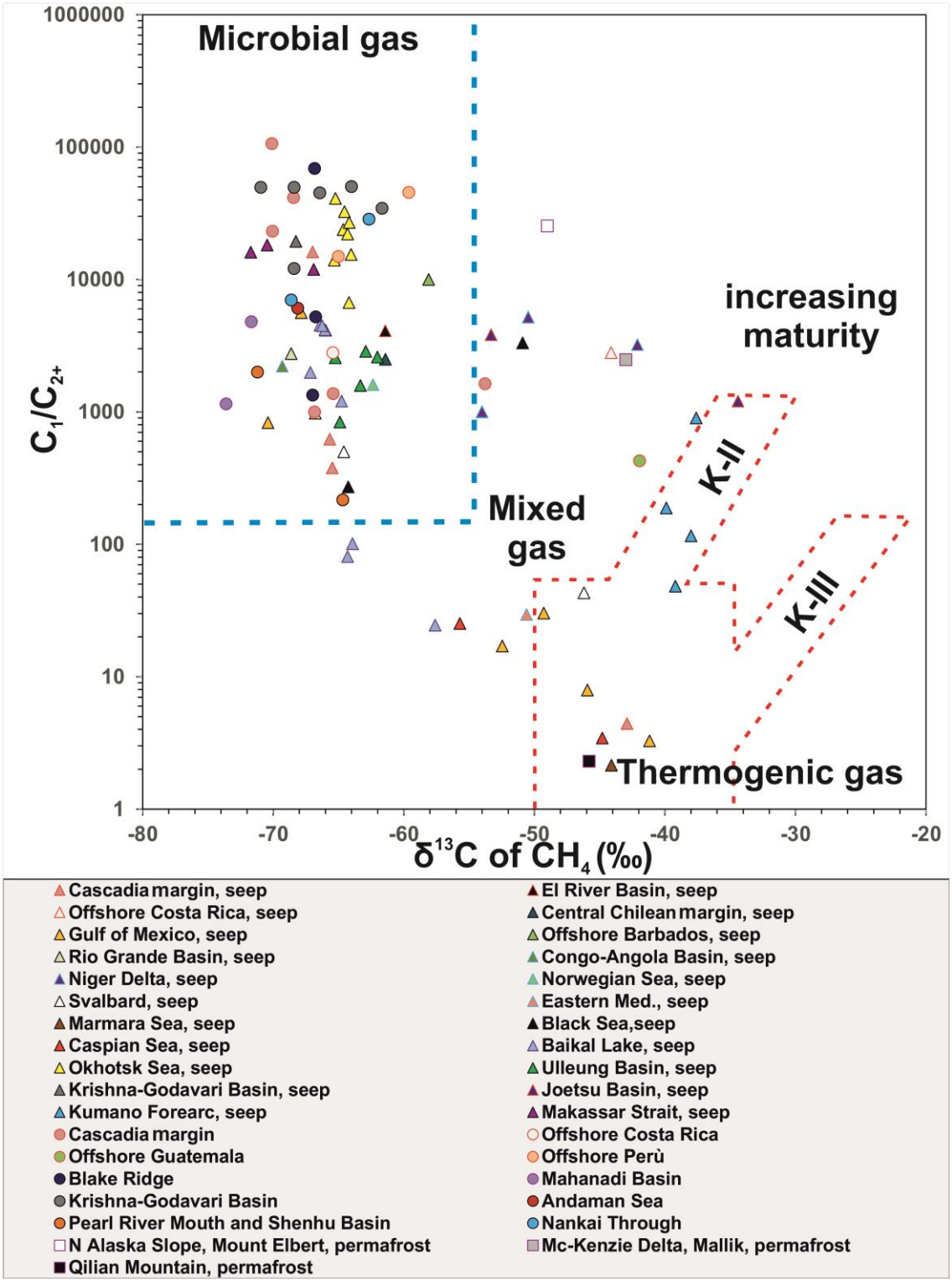
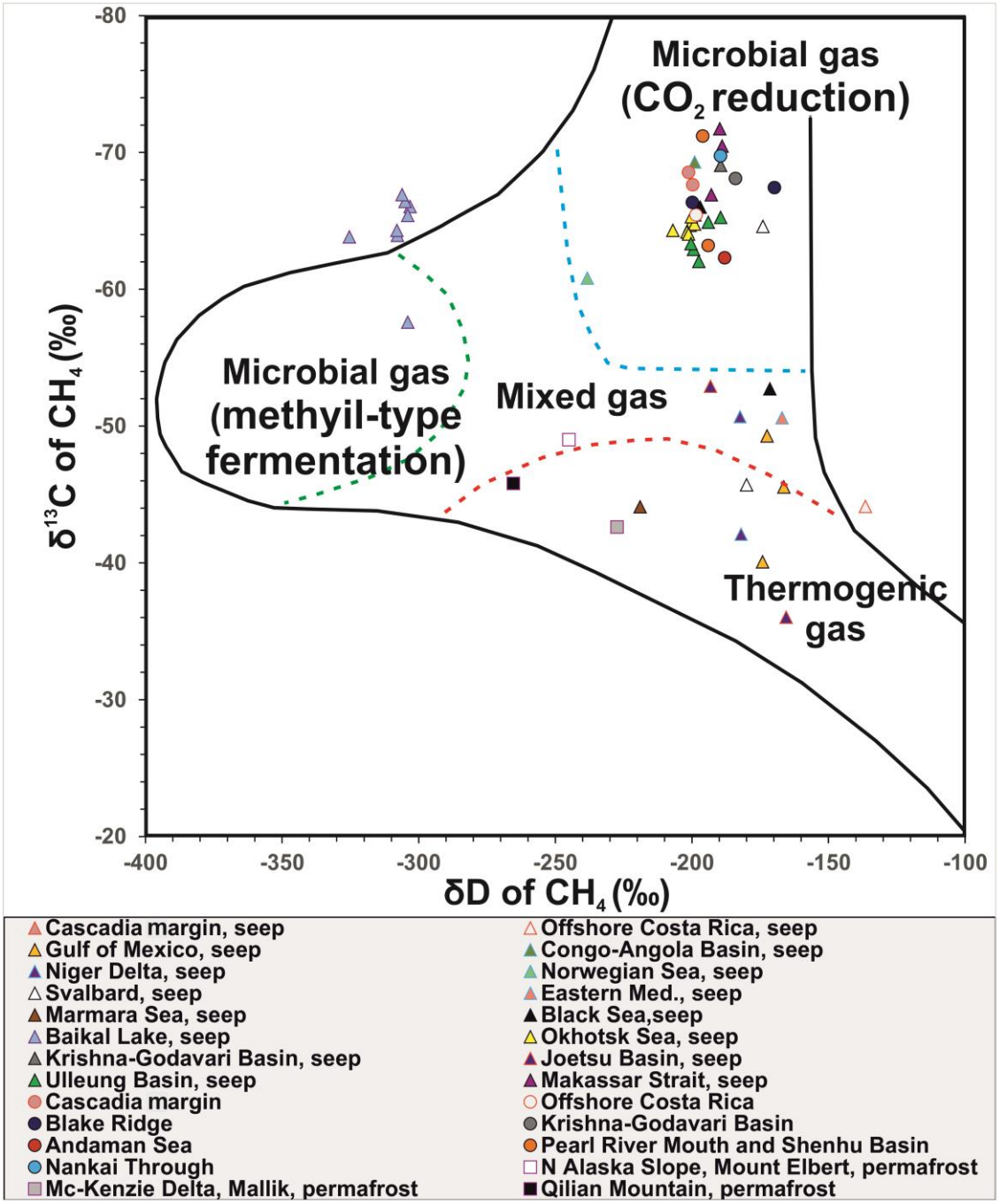

Microbial gas
Mixed gas
Thermogenic gas
increasing maturity
K-II
K-III
C1/C2+
δ13C of CH4 (‰)
1000000
100000
10000
1000
100
10
1
-80
-70
-60
-50
-40
-30
-20
Cascadia margin, seep
Offshore Costa Rica, seep
Gulf of Mexico, seep
Rio Grande Basin, seep
Niger Delta, seep
Svalbard, seep
Marmara Sea, seep
Caspian Sea, seep
Okhotsk Sea, seep
Krishna-Godavari Basin, seep
Kumano Forearc, seep
Cascadia margin
Offshore Guatemala
Blake Ridge
Krishna-Godavari Basin
Pearl River Mouth and Shenhu Basin
N Alaska Slope, Mount Elbert, permafrost
Qilian Mountain, permafrost
El River Basin, seep
Central Chilean margin, seep
Offshore Barbados, seep
Congo-Angola Basin, seep
Norwegian Sea, seep
Eastern Med., seep
Black Sea,seep
Baikal Lake, seep
Ulleung Basin, seep
Joetsu Basin, seep
Makassar Strait, seep
Offshore Costa Rica
Offshore Perù
Mahanadi Basin
Andaman Sea
Nankai Through
Mc-Kenzie Delta, Mallik, permafrost

**Fig. 1.9**




**Figures 1.9 (See the previous page) and 1.10 (This page).** $C_1/C_2+$ *vs* $\delta^{13}C$ of CH4 (‰) and $\delta^{13}C$ *vs* $\delta$ D of CH4 (‰) plots of recovered gas hydrate samples. These plots represent updated versions after the work of Milkov (2005). The observed values are the result of an average of different data for the same locality. Where available, geochemical data from direct hydrate samples has been accounted. In other cases, pressure core or gas void data from gas hydrate-bearing sediments have been used. The localities followed by *'seep'* indicate sites with evidence of present-day or recent free gas migration throughout the GHSZ up to the water column. At these locations, hydrate or hydrate-bearing sediments have been sampled at or in the vicinity of a mud volcano, an active fault, a pockmark or a hydrate pingo. Refer to **Tab. 1.2** in **paragraph 1.11** (Appendix) for the sources of data and the references. K-II= kerogen type-II; K-III= kerogen type-III.

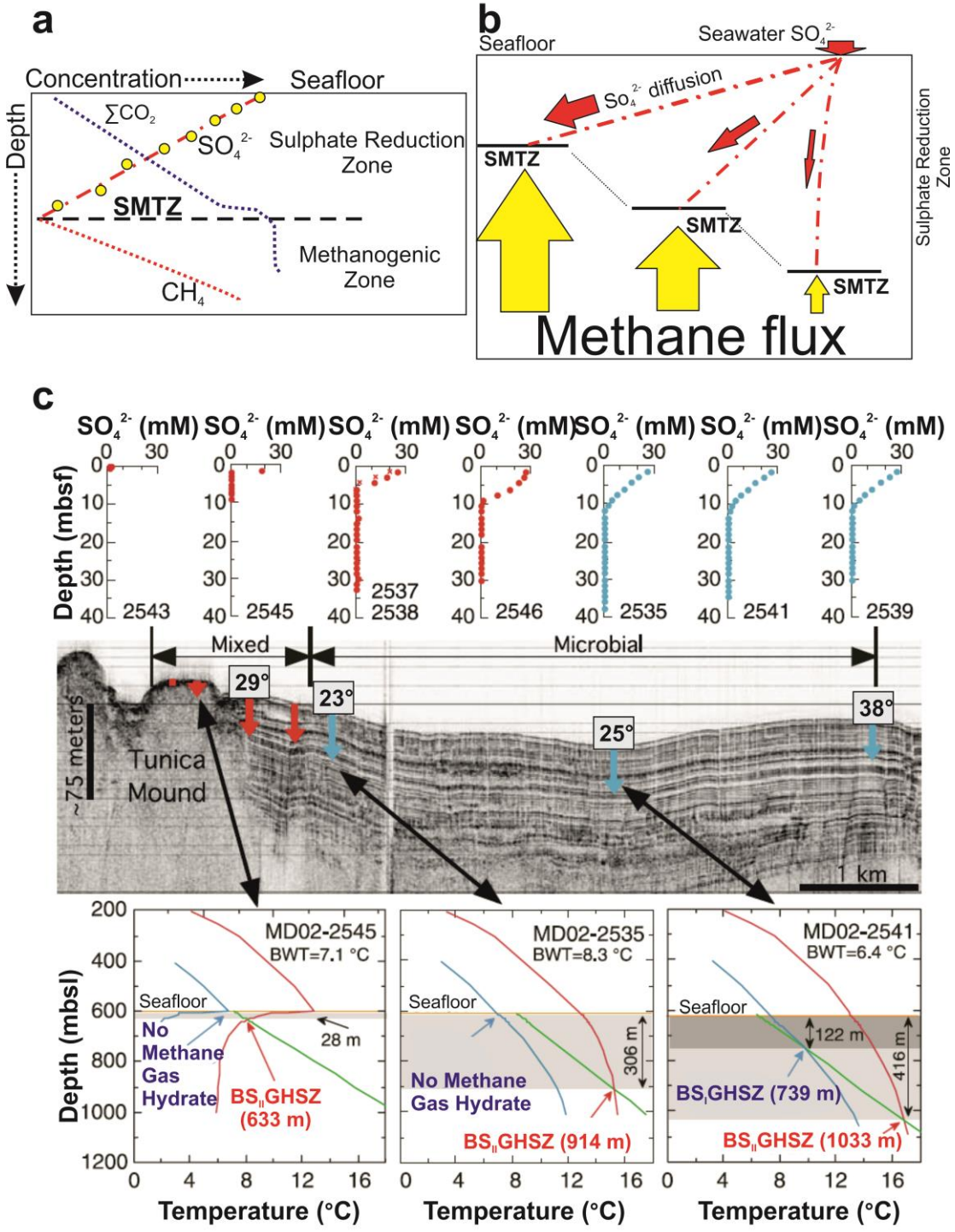



**Figure 1.11. (a)** Schematic cartoon, showing the biogeochemical zonations plus the $CH_4$, $CO_2$ and $SO_4$ concentration trends within shallow sediments in a marine NGHS. SMTZ= sulphate-methane transition zone. Methane is oxidised in the sulphate reduction zone whereas it is preserved and/or generated in-situ in the methanogenic zone (modified after Borowski *et al.*, 1999). **(b)** Cartoon showing the relationship between methane flux (directly proportional to the size of the yellow arrows) and depth of the SMTZ. The higher is the flux of methane (left), then the shallower the depth of the SMTZ will be (modified after Borowski *et al.*, 1996). **(c)** Sulphate concentration at the Tunica Mound (Northern Gulf of Mexico), chirp seismic reflection profile and sketches showing the predicted depths of the BGHSZ for $S_I$ 100% methane hydrates ($BS_IGHSZ$) and $S_{II}$ $C_{2+}$-rich hydrates ($BS_{II}GHSZ$). Blue and red colours indicate mixed (thermogenic + microbial) and purely microbial sources of gas (modified after Paull *et al.*, 2005).

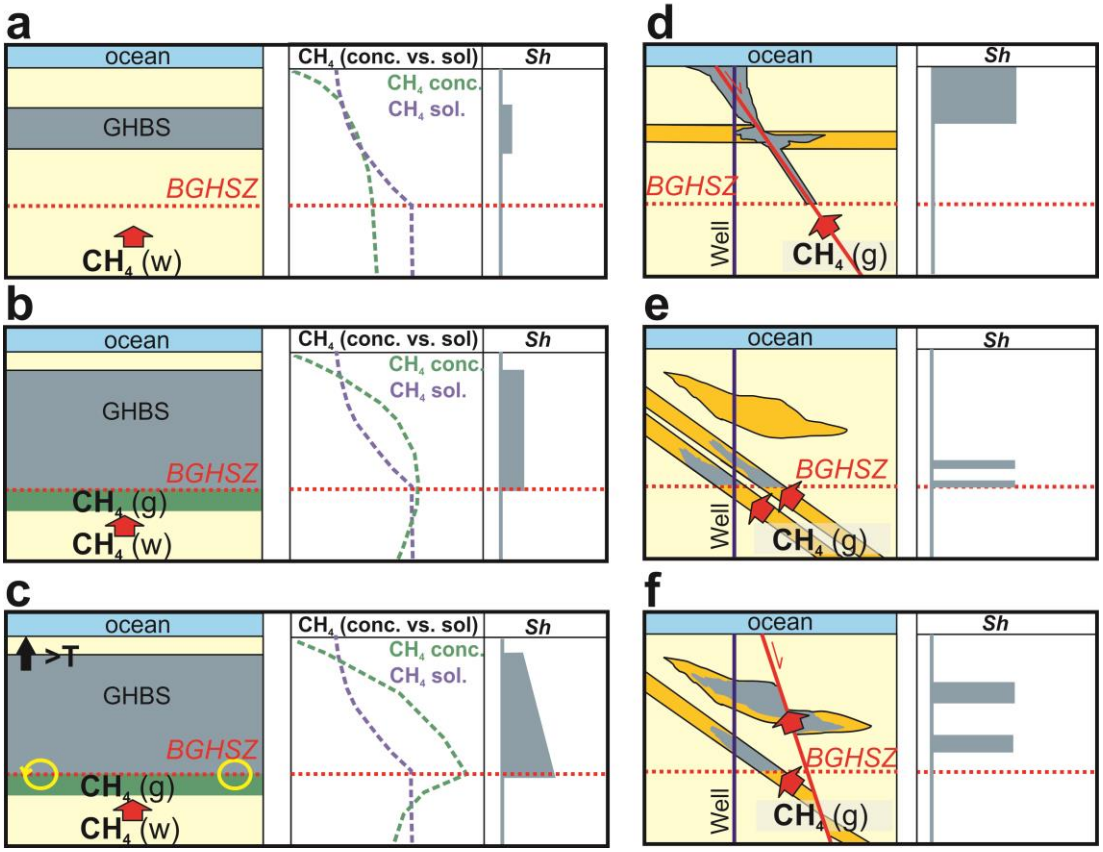



**Figure 1.12.** Schematic representations of natural gas hydrate systems developed in homogeneous **(a-c)** and heterogeneous **(d-f)** geological settings. $CH_4$ conc.= methane concentration profile (green-dotted lines); $CH_4$ sol.= methane solubility profile (purple-dotted lines); *Sh* (grey-shaded areas)= hydrate saturation profiles. **(a)** Natural gas hydrate system (NGHS) characterised by upward migration of methane dissolved in water, exceeding the solubility threshold within the GHSZ, without forming a free gas zone (FGZ). **(b)** NGHS characterised by upward migration of methane dissolved in water, exceeding solubility thresholds below the BGHSZ, leading to the formation of an FGZ. **(c)** Continuation of **(b)**: sedimentation, temperature increases or uplift determine the upward movement of the BGSHZ and the recycling of gas hydrates at the BGHSZ. Hydrates, therefore, dissociate into free gas and water, with the free gas capable of migrating again towards the GHSZ. **(d)** Methane advectively migrates as free gas or dissolved in water along a fault and leads to a concentrated hydrate deposit. **(e)** Methane advectively migrates as free gas or dissolved in water along carrier beds and leads to a concentrated hydrate deposit. **(f)** Mixed fault and carrier-bed methane migration and hydrate accumulation. The *Sh* profiles in **(d)**, **(e)** and **(f)** are referred to those encountered along hypothetical wells (blue lines). Dark-yellow coloured zones represent sand-rich deposits, where hydrate preferentially occur. Methane in the pore waters exceeds solubility along these structural and stratal pathways, up to the top of the zones of hydrate occurrence (modified after Collett *et al.*, 2009).

## 1.4. Acoustic properties, thermal properties, and morphology of gas hydrate-bearing sediments

Considering that there are approximately six molecules of water per molecule of gas, the solid structure of gas hydrates resembles that of ice. Hence, some physical and mechanical properties, such as the density, as well as the bulk and shear moduli, are fairly similar (Koh, 2002; Sloan Jr and Koh, 2007; Waite *et al.*, 2009). Consequently, the P- and S-wave velocities of pure hydrates are much higher compared to those of the sediments that characterise the first hundreds of metres of overburden in marine and lacustrine basins (Hamilton, 1971; Prasad, 2002; Avseth *et al.*, 2010). As a result, gas hydrate-bearing sediments (GHBS) have a higher bulk modulus, shear modulus but also lower density compared to hydrate-free sediments (e.g. Guerin *et al.*, 1999; Helgerud *et al.*, 1999 and 2009; Winters *et al.*, 2004; Yun *et al.*, 2005; Waite *et al.*, 2009; Riedel *et al.*, 2014) (**Tab. 1.1**). Moreover, in contrast to pore waters, but similarly to hydrocarbons, natural gas hydrates are electrical insulators (i.e. resistive materials). Thus, hydrates can dramatically change the electrical properties of the sediments, in a way that depends on the hydrate saturation and mode of occurrence (e.g. Spangenberg, 2001; Collett and Lee, 2011).

The capacity of gas hydrates to transfer heat (i.e. the thermal conductivity) is 0.55-0.60 W $m^{-1}$ $K^{-1}$, similar to that of liquid water but higher than that of oil and gas, and lower than that of ice (2.3 W $m^{-1}$ $K^{-1}$) and other materials, such as salt (~6W $m^{-1}$ $K^{-1}$) (Ruppel, 2000; Waite *et al.*, 2009). However, hydrates and free gas, if present in the sediments at low to moderate saturation, do not considerably impact the heat transfer in the shallow portions of sedimentary basins. To a first order approximation, geothermal gradients and heat flow estimates can neglect the presence of gas hydrates (Grevemeyer and Villinger, 2001).

Gas hydrates affect the sound properties of sediments (i.e. P- and S-wave velocities), in a way that depends on **(1)** the mode of occurrence of gas hydrates in the sediments; **(2)** the gas hydrate saturation (*Sh*, % of pore space) and **(3)** the nature of the host sediments, in

terms of mineralogy, porosity, grain size, etc. The mode of hydrate occurrence can be evaluated at the pore-scale and the core-scale. At the pore-scale four main micro-habits have been recognised (Helgerud *et al.*, 1999; Dvorkin *et al.*, 2000; Rees, 2009; Dai *et al.*, 2012) (**Fig. 1.13**): **(1)** Hydrate forms as a particle suspension in the pore space (i.e. within the fluid), without being in contact with the sediment grains; **(2)** Hydrate forms in the pore space but supports the sediment frame (i.e. load-bearing); **(3)** Hydrate forms at grain contacts as a cement (i.e. contact-cement); **(4)** Hydrate forms as a circumgranular cement around the grains (i.e. grain-coating). In the first two habits, the hydrate grows in the pore space whereas in the last two it cements the grains (Priest *et al.*, 2009; Spangenberg *et al.*, 2014).

P- and S-wave velocities are weakly to moderately influenced by the presence of hydrates in the case of particle suspension or load-bearing micro-habits, until *Sh* becomes moderately high (i.e. >30-40%). Conversely, a low saturation (i.e. <5-10%) is enough to increase P- and S-wave velocities of gas hydrate-bearing sediments significantly, in the case of cementing micro-habits (Priest *et al.*, 2005; Yun *et al.*, 2005; Winters *et al.*, 2007; Priest *et al.*, 2009; Waite *et al.*, 2009) (**Fig. 1.13**). Dai *et al.* (2012) further suggested that GHBS can be patchily filled with hydrates, with zones without hydrates (0% saturation) alternating with zones characterised by 100% gas hydrate saturation. The calibration between petrophysical observations and rock-physics models suggest that the suspension and load-bearing micro-habits are very common in nature. This was interpreted as evidence that hydrates often form from an aqueous supersaturated fluid (Helgerud *et al.*, 1999; Winters *et al.*, 2004; Lee and Waite, 2008; Spangenberg *et al.*, 2014). In contrast, cementing micro-habits can form either in the presence of high fluxes of free gas across the GHSZ or at the three-phase boundary (Guerin *et al.*, 1999; Waite *et al.*, 2009; Spangenberg *et al.*, 2014). One micro-habit can further evolve into another at increasing *Sh* (e.g. from particle suspension to load-bearing or cementing) (Yun *et al.*, 2005; Waite *et al.*, 2009).

At the core-scale, field observations of GHBS indicate two primary hydrate morphologies, named **(1)** pore-filling (or disseminated) and **(2)** grain-displacing (Holland *et al.*, 2008) (**Fig. 1.14-1.16**). Pore-filling hydrates can exhibit, at the pore-scale, the four micro-habits mentioned above. In contrast, grain-displacing hydrates are characterised by continuous masses of hydrate that **(1)** are volumetrically bigger than the sediment grains and the associated primary pore space, **(2)** have elevated aspect ratios, **(3)** can be oriented discordant with respect to the stratigraphy and **(4)** are generated by external and/or internal forces able to create secondary spaces where hydrates can crystallise. For these reasons, grain-displacing hydrates exhibit diverse variety sub-morphologies, such as massive hydrates, nodular or lensoid hydrates and fracture-filling hydrates (Cook *et al.*, 2008; Daigle and Dugan, 2010b; Riedel *et al.*, 2010a; Chun *et al.*, 2011; Rees *et al.*, 2011; Wei *et al.*, 2015; Matsumoto *et al.*, 2017). In addition, massive metre-sized hydrate outcrops have been indirectly and directly detected at the seafloor. These almost pure hydrate outcrops, referred to as hydrate mounds or pingoes, reflect high rates of methane flux and may be associated with authigenic minerals and chemosynthetic communities (Sassen *et al.*, 2001a; Pohlman *et al.*, 2005; Paull *et al.*, 2008a; Serié *et al.*, 2012) (**Fig. 1.15c**).

As a simple rule of thumb, pore-filling hydrates usually form within coarse-grained sediments (e.g. siliciclastic and volcanic sands and silts) whereas grain-displacing hydrates are found in fine-grained clay-rich sediments (e.g. Cook *et al.*, 2008 and 2014; Holland *et al.*, 2008; Bahk *et al.*, 2011; Boswell *et al.*, 2012b; Lee and Collett, 2012; Fujii *et al.*, 2015). However, the presence of diatom oozes, biogenic opal and early diagenetic cements can further complicate the relationship between lithology, gas hydrate distribution and *Sh*, resulting in an unexpected increase in the reservoir quality in fine-grained sediments. For example, in the South China Sea, abundant gas hydrates occur within intervals with calcareous fossils and forams, which enhance the reservoir quality of the sediment (Wang *et al.*, 2011). In the Ulleung Basin, hydrates are observed to occur as *'disseminated'* in the pore space within thin fine-grained intervals rich in diatom fossils (Bahk *et al.*, 2013). At

the Blake Ridge, a hydrate-rich interval has been associated with an increased reservoir quality, resulting from an enrichment in silica-rich sediments (Kraemer *et al.*, 2000). Finally, in the Andaman Sea, an anomalous porosity is preserved owing to early calcite diagenesis, with cement grains counteracting the mechanical compaction. Ultimately, this has enhanced the permeability and facilitated hydrate accumulation in ash-rich layers (Rose *et al.*, 2014). An additional control on hydrate morphology appears played by the effective stress. Dai *et al.* (2012) observed that massive or nodular hydrate morphologies form at relatively low effective stress conditions whereas, deeper in the overburden, pore-filling and fracture-filling hydrates occur. In this view, the massive hydrate outcrops, which form at the seafloor at zero effective stress, represent an extreme end-member in this classification.

| MATERIAL | Vp (m/s) | Vs (m/s) | K (GPa) | G (GPa) | ρ (g/cm$^3$) |
|---|---|---|---|---|---|
| **Methane gas (10 MPa, 273 K)** | 412 | 0 | 0.015 | 0 | 0.90 |
| **Water** | 1500 | 0 | 2250 | 0 | 1.00 |
| **Ice (5 MPa, 273 K)** | 3870 | 1940 | 9.09 | 3.46 | 0.917 |
| **Methane hydrate ($S_I$) (5 MPa, 273 K)** | 3770 | 1960 | 8.41 | 3.54 | 0.925 |
| **Clay** | 3410 | 1630 | 20.9 | 6.85 | 2.58 |
| **Quartz** | 6040 | 4120 | 36.6 | 45 | 2.65 |
| **Calcite** | 6640 | 3440 | 76.8 | 32 | 2.71 |

**Table 1.1** Elastic properties of methane gas, water, ice, $S_I$ methane hydrates and selected sediment components. The data is taken from Waite *et al.* (2009) and Mavko *et al.* (2009). Note that these properties, for gas hydrates, ice and methane gas, are dependent on pressure and temperature. The elastic properties of $S_I$ hydrate further differ slightly than those of $S_{II}$ hydrates (Helgerud *et al.*, 2009).

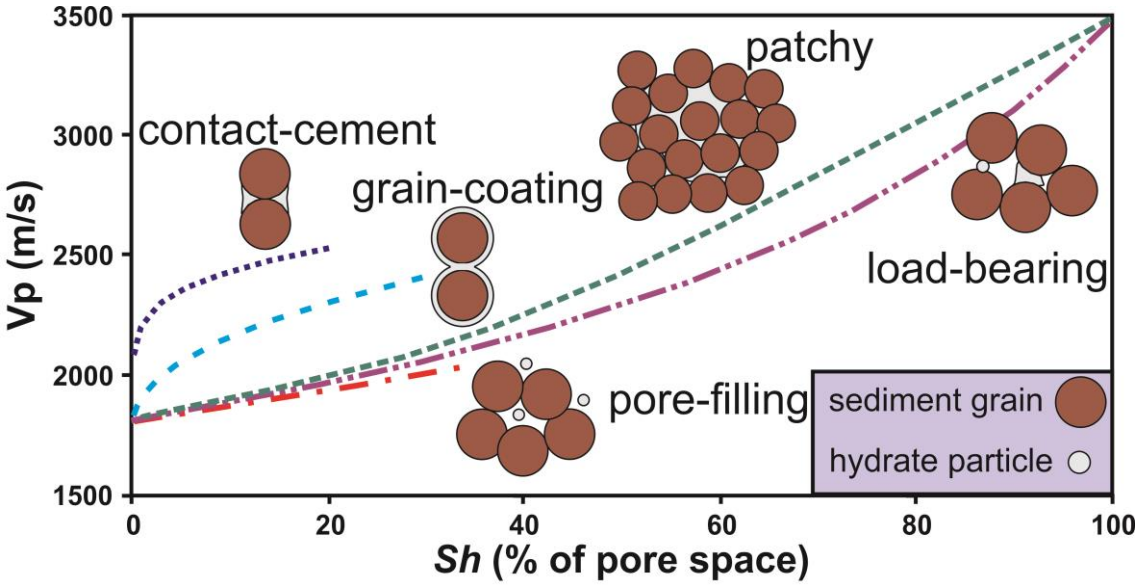



**Figure 1.13**. Predicted relationship between compressional velocity and *Sh* for different hydrate micro-habits. The P-wave velocity at 0% *Sh* depends on the lithology and its porosity. Therefore, this value can vary in different geological settings at various overburden depths (i.e. stress conditions) (modified after Dai *et al.*, 2012).

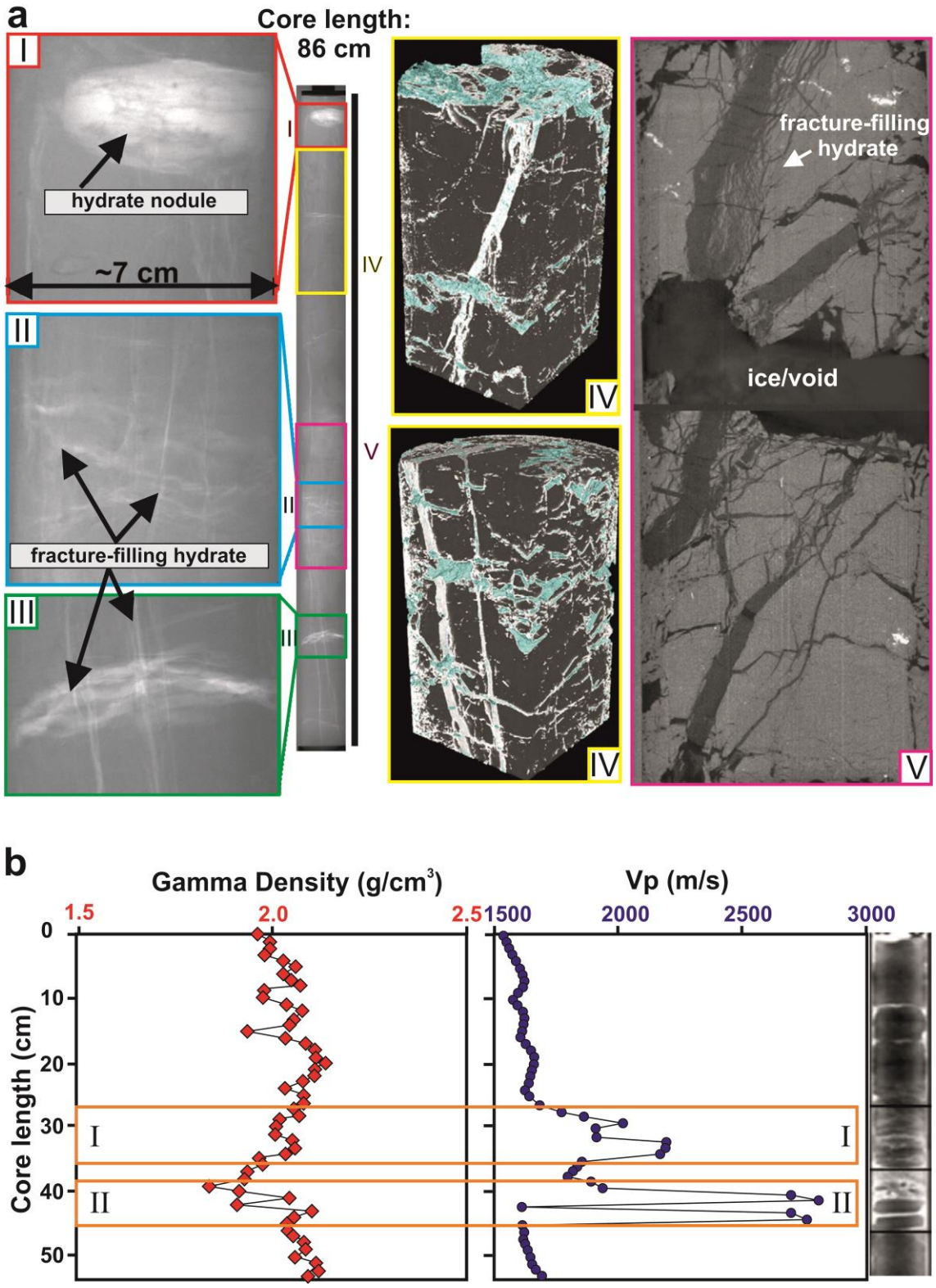



**Figure 1.14.** Examples of grain-displacing and pore-filling hydrate morphologies at the core-scale. **(a)** Fracture-filling and nodular hydrates in a pressure core recovered along the Krishna-Godavari Basin (offshore India) (Site NGHP-01-10B, 50 mbsf). The X-ray image of the whole core is shown in the centre. I-III are detailed blow-ups. IV and V are 3D detailed x-ray CT images displaying the fracture geometry. In IV, the blue-coloured fractures are filled with ice and represent artefacts whereas the white-coloured fractures are filled with hydrates and are interpreted to represent the original hydrate morphology. The locations along the core of the detailed images (I-V) is marked with coloured boxes (modified after Riedel *et al.*, 2010a; Rees *et al.*, 2011). **(b)** Non-destructive measurements of physical properties (gamma density and P-wave velocity) along a pressure core with pore-filling hydrates (X-ray image on the right) within turbidite-rich sediments, recovered in the Nankai Trough, at 296 mbsf. *Sh* is 38% and 54% in the upper (I) and lower (II) interval, respectively (modified after Konno *et al.*, 2015).

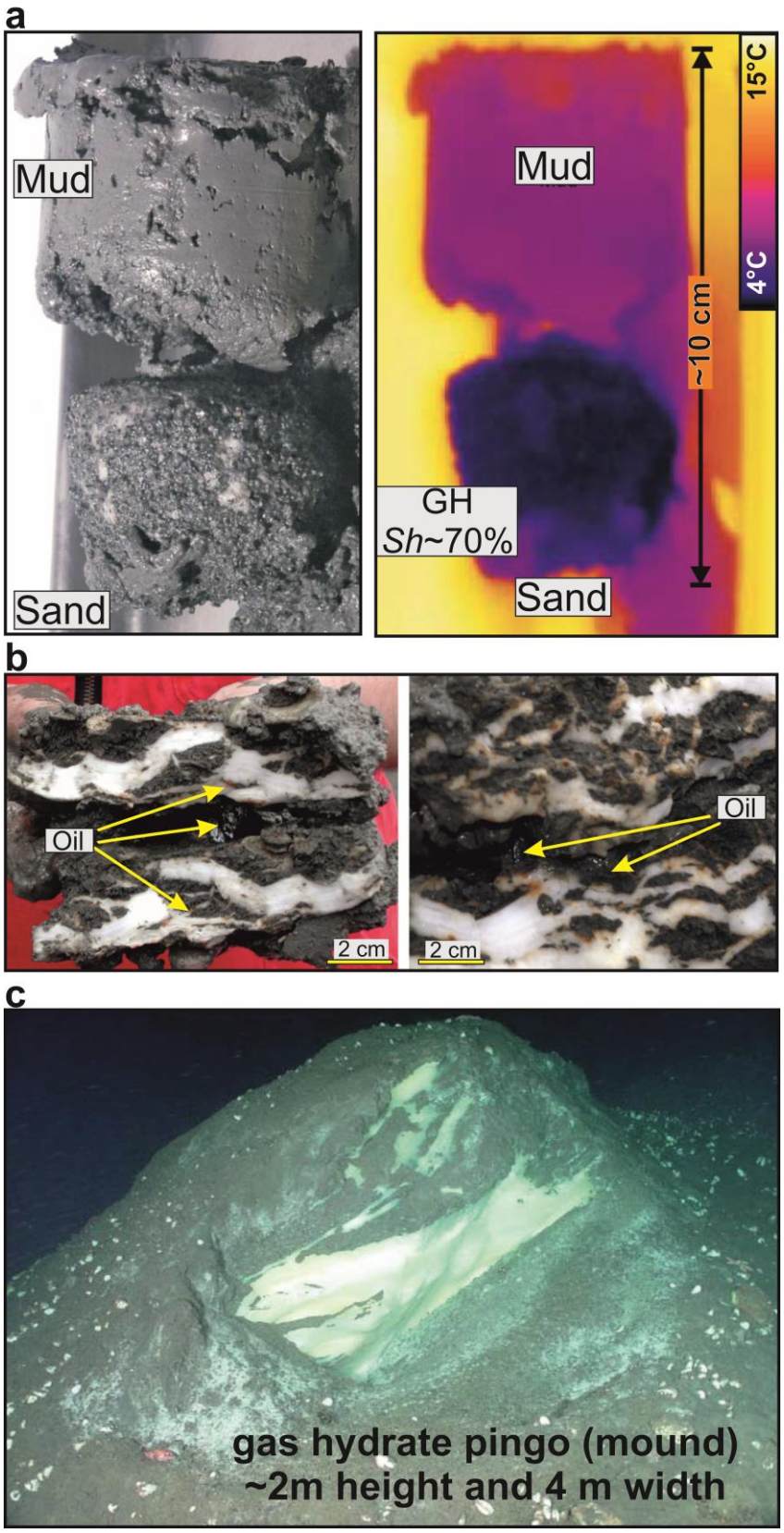



**Figure 1.15. (a)** Photograph (left) and IR image (right) of a gas hydrate-bearing sediment. Hydrates are concentrated in the lower sand-rich interval. The core has been retrieved along the Cascadia margin (IODP Expedition 311) (modified after Riedel *et al.*, 2010b). **(b)** Photographs of grain-displacing sub-horizontal hydrate lenses coated with oil in a muddy sediment. These hydrates have been recovered in the Gulf of Mexico (Bush Hill) (modified after Klapp *et al.*, 2010). **(c)** Photograph of a gas hydrate pingo in the Northern Cascadia margin (Berkley Canyon) (modified after Pohlman *et al.*, 2005).

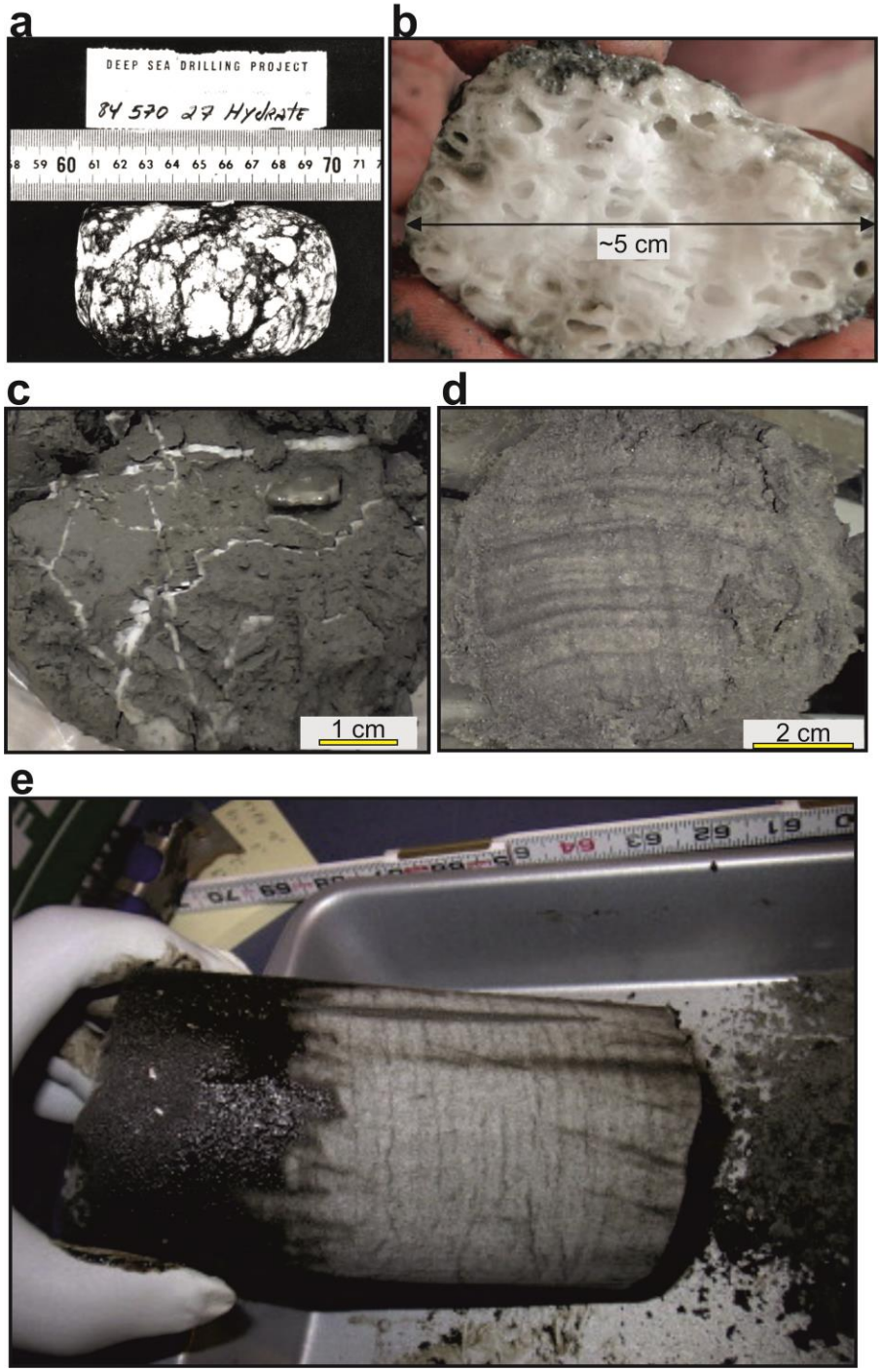



**Figure 1.16.** Photographs showing different types of hydrate morphologies. **(a)** Massive (nodular?) gas hydrates (white) recovered offshore Guatemala during the DSDP Leg 84 (Kvenvolden *et al.*, 1984). **(b)** Bubbly gas hydrate piece recovered at the top of a pockmark offshore Nigeria (Sultan *et al.*, 2014). **(c)** and **(d)** Fracture-filling and pore-filling hydrates, recovered respectively within mud-rich and sand-rich sediments, in the Ulleung Basin (Chun *et al.*, 2011). **(e)** Gas hydrate-bearing sandy sediments in a core retrieved along the Mount Elbert Gas Hydrate Stratigraphic Test Well (onshore Alaska) (Winters *et al.*, 2011).

## 1.5. Borehole detection of gas hydrate-bearing sediments

The unique physical properties of gas hydrates make their presence within the sediments detectable with standard well-log techniques. The penetration of boreholes throughout the GHSZ during scientific and industrial drilling has provided crucial information on the vertical distribution and three-dimensional architecture of GHBS.

Both wireline (WL) and logging-while-drilling (LWD) techniques have been successfully applied in NGHSs (Collett and Lee, 2011). With WL, the measurements along the borehole are performed shortly after that the section has been drilled whereas LWD allows the measurements to be carried out during the well penetration, with sensors positioned above the drill bit. Thus, with WL, data is acquired at fixed depth intervals whereas with LWD data is acquired at fixed time intervals, depending on the drilling rate (Goldberg *et al.*, 2010). Both the techniques have advantages and disadvantages For example, while the WL acquisition offers, in principle, better vertical resolutions, the LWD is not affected by changes potentially occurring between drilling and data acquisition (Goldberg *et al.*, 2010; Collett *et al.*, 2012). Furthermore, WL data cannot often be acquired within the first ~50-100 mbsf because drill casings are used to increase the wellbore stability within this interval, usually constituted by poorly consolidated sediments (Goldberg *et al.*, 2010). The borehole condition is then evaluated with caliper logs (see Guerin *et al.*, 1999; Collett *et al.*, 2012; Wang *et al.*, 2014).

GHBS are particularly sensitive to acoustic and resistivity logs, which have been therefore extensively used in drilling projects (e.g. Guerin *et al.*, 1999; Cook *et al.*, 2008; Lee and Waite, 2008; Collett and Lee, 2011; Riedel *et al.*, 2014) **(Fig. 1.17)**. To quantify *Sh* from P- and S-wave velocity logs, an adequate rock physics model must be applied. Approaches using e.g. the Effective Medium Theory and three-phase Biot-type equations have been proved to be successful in estimating *Sh* in GHBS with a pore-filling morphology (**Fig. 1.18**). More complicated methods exist for grain-displacing hydrates, taking into

account the anisotropy induced by the presence of e.g. hydrate-filled fractures (e.g. Helgerud *et al.*, 1999; Lee, 2002; Lee and Collett, 2009, 2012 and 2013; Ghosh *et al.*, 2010). In addition, velocity data from vertical seismic profiling may be similarly used to estimate *Sh* (e.g. Holbrook, 2001).

The electrical properties of GHBS are also influenced by the hydrate morphology. Pore-filling hydrates commonly result in isotropic electrical properties, and accurate estimates of *Sh* can be easily performed with the Archie relationship (Archie, 1942). This method, if some in-situ information such as the pore water resistivity and lithology are well-constrained (Malinverno *et al.*, 2008), provides good estimates of *Sh*. Laboratory measurements have further suggested that the saturation exponent depends on *Sh* and varies between ~2 and ~4, due to the interplay between growing hydrate crystals and capillary water in the pores (Spangenberg and Kulenkampff, 2006) **(Figs. 1.17c, 1.19)**.

In contrast, grain-displacing hydrates are electrically anisotropic, and the relationship between electrical resistivity and *Sh* is not straightforward. A simple Archie approach would overestimate *Sh* in these GHBS unless the saturation exponent is highly but not realistically enhanced. This problem has been solved by taking into account for the fracture orientation with respect to the resistivity tool (e.g. Lee and Collett, 2009, 2011, 2012 and 2013; Cook *et al.*, 2010). The fracture characterisation is commonly achieved with the interpretation of resistivity image logs, where resistive fracture-like features appear as sinusoids in a typical 0-360 degree plain display (Riedel *et al.*, 2010a; Kim *et al.*, 2013a; Cook *et al.*, 2014) (**Fig. 1.20**). A further indicator for the presence of resistive fracture-filling hydrates is the separation between resistivity values extrapolated with different methods (e.g. attenuation and phase) and at various transmitter-receiver spacing (Cook *et al.*, 2010 and 2014). Such differences reflect the anisotropic electrical conductivity of grain-displacing GHBS (i.e. the horizontal and vertical resistivity of the formation are different).

Nuclear magnetic resonance (NMR) logs are occasionally used to estimate *Sh* and provide precise estimates (Kleinberg *et al.*, 2005; Lee and Waite, 2008; Bauer *et al.*, 2015; Fujii *et al.*, 2015) (**Fig. 1.21a**). NMR logs are primarily influenced by the hydrogen molecules in the pore space (Collett and Lee, 2011). However, in contrast with classical density and neutron porosity measurements, the hydrate is detected as part of the solid frame and not as part of the pore space, given that the NMR transverse magnetisation relaxation time of water molecules within the hydrate cage is similar to that of solid grains (~0.01 ms). Hence, by comparing the standard density and NMR logs can be used to assess *Sh* (Collett and Lee, 2011). The presence of clay-rich sediments can complicate these estimates, due to the clay-bound water effect on relaxation times (Lee and Collett, 2008), but more sophisticated approaches (e.g. signal classification of the transverse relaxation time) may solve these issues (Bauer *et al.*, 2015).

The density and neutron logs are commonly used to evaluate the porosity of the sediment. Both the density and the hydrogen index (1.059 for $S_I$ hydrates) of hydrates are very similar to those of water (~0.97-1.00, depending on salinity). Thus, the density log can unequivocally detect the hydrates only at very high *Sh* whereas the neutron log is almost unaffected by hydrates (Collett and Lee, 2011). Nevertheless, the density and neutron logs, in combination with gamma-ray measurements provide instead invaluable information of the host sediment lithology (e.g. Cook *et al.*, 2008; Boswell *et al.*, 2011).

Natural gas hydrate systems have also been investigated with in-situ geotechnical tools, such as the cone penetration and pore pressure tests with piezocone (piezocone CPTu), (Sultan *et al.*, 2007 and 2011). This test allows evaluating the soil geotechnical properties, by the interpreting the piezocone resistance ($q_c$), friction ($f_s$) and pore water pressure ($u_2$), measured during the continuous penetration of the piezocone (Lunne *et al.*, 1997; Peuchen, 2000; Robertson, 2009). GHBS are typically characterised by high cone resistance and friction. The pore pressure, upon penetration of GHBS, can display values both higher and

lower than hydrostatic (**Fig. 1.21b**). Further measurements, including acoustic velocity and density, can be accomplished during CPTu tests and can improve the understanding of hydrate and free gas distribution (Long *et al.*, 2007; Sultan *et al.*, 2007, 2010, 2011 and 2014). Piezocone CPTu tests have further been accomplished in the laboratory, on recovered undisturbed pressurised samples (Santamarina *et al.*, 2015). In addition, the in situ pore pressure can be measured, through a piezoprobe, with dissipation tests carried on when the cone penetration is interrupted. The dissipation test can further be used to interpret the sediment properties (e.g. the permeability) (Long *et al.*, 2007; Sultan *et al.*, 2011; Riboulot *et al.*, 2013).

Finally, the combination of acoustic, resistivity and neutron logs is also important to detect and evaluate the free gas distribution and saturation in the sediments underlying the BGHSZ. However, the complex relationship between free gas saturation (*Sg*), distribution (e.g. uniform *vs* patchy) and the response of the velocity and resistivity well-logs makes a quantitative assessment always complicated and subject to uncertainties (Domenico, 1976; Guerin *et al.*, 1999; Lee, 2004; Lee and Collett, 2006).

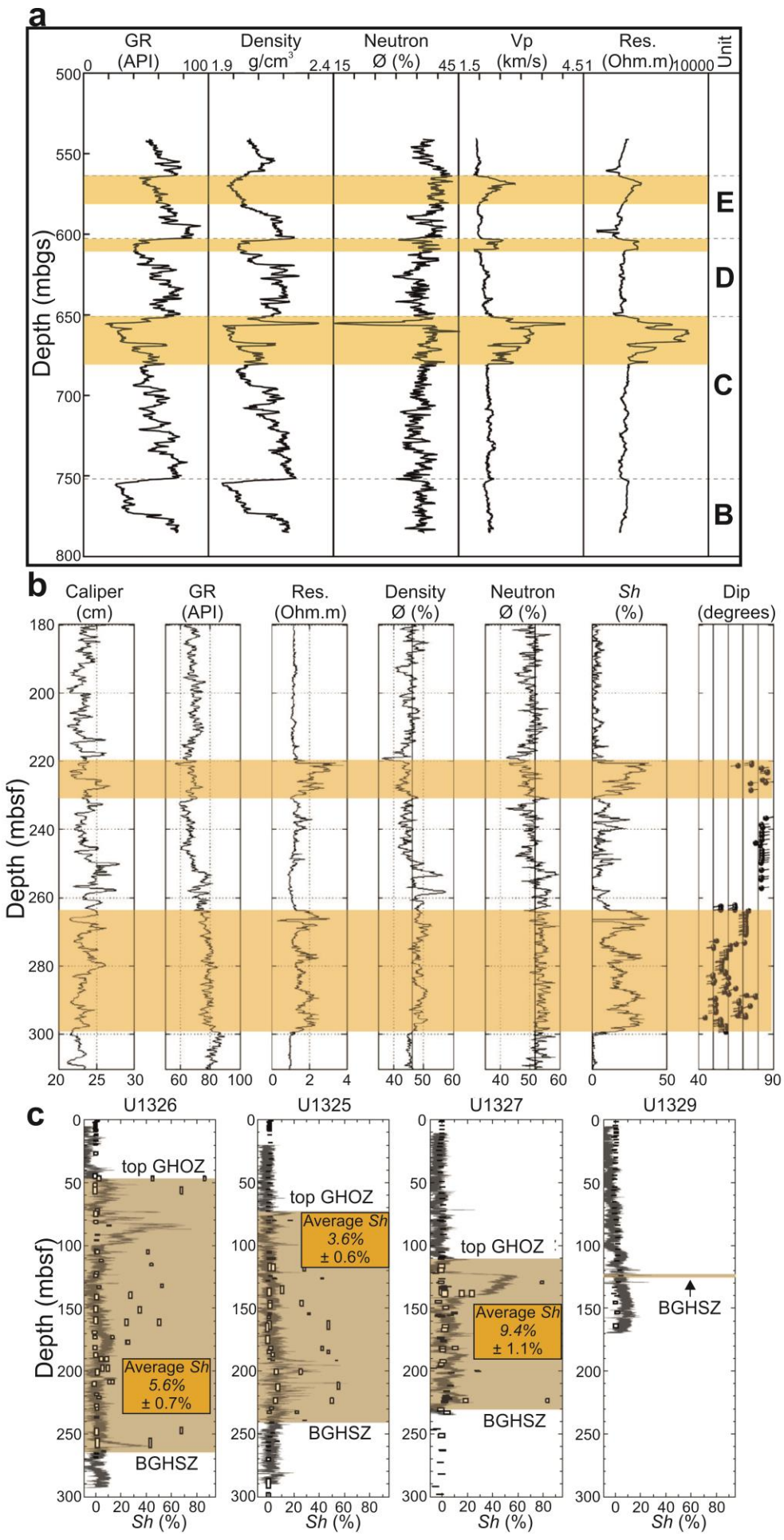

a
GR (API)
Density g/cm³
Neutron Ø (%)
Vp (km/s)
Res. (Ohm.m)
Unit
Depth (mbgs)
E
D
C
B
b
Caliper (cm)
GR (API)
Res. (Ohm.m)
Density Ø (%)
Neutron Ø (%)
Sh (%)
Dip (degrees)
Depth (mbsf)
c
U1326
U1325
U1327
U1329
top GHOZ
Average Sh 5.6% ± 0.7%
Average Sh 3.6% ± 0.6%
Average Sh 9.4% ± 1.1%
BGHSZ
Depth (mbsf)
Sh (%)

**Figure 1.17 (See the previous page).** Well-log data, showing gas hydrate-bearing sediments in different provinces. **(a)** Gamma-ray (GR), density, neutron, velocity (Vp) and resistivity (Res.) logs in the Northwest Eileen State-2 well (Alaska North Slope) (Collett *et al.*, 2011). mbgs= metres below the ground surfaces. **(b)** Caliper, GR, resistivity and neutron logs from Hole 3 in the Keathley Canyon (Gulf of Mexico). The interpreted *Sh* and dip of hydrate-filled fractures are also shown on the right (modified after Cook *et al.*, 2008). **(c)** *Sh* profiles extrapolated from resistivity (continuous black lines) and chlorinity (white rectangles) data at various sites of the Cascadia margin (IODP 311) (Malinverno *et al.*, 2008). The yellow areas in indicate the zones of hydrate occurrence.

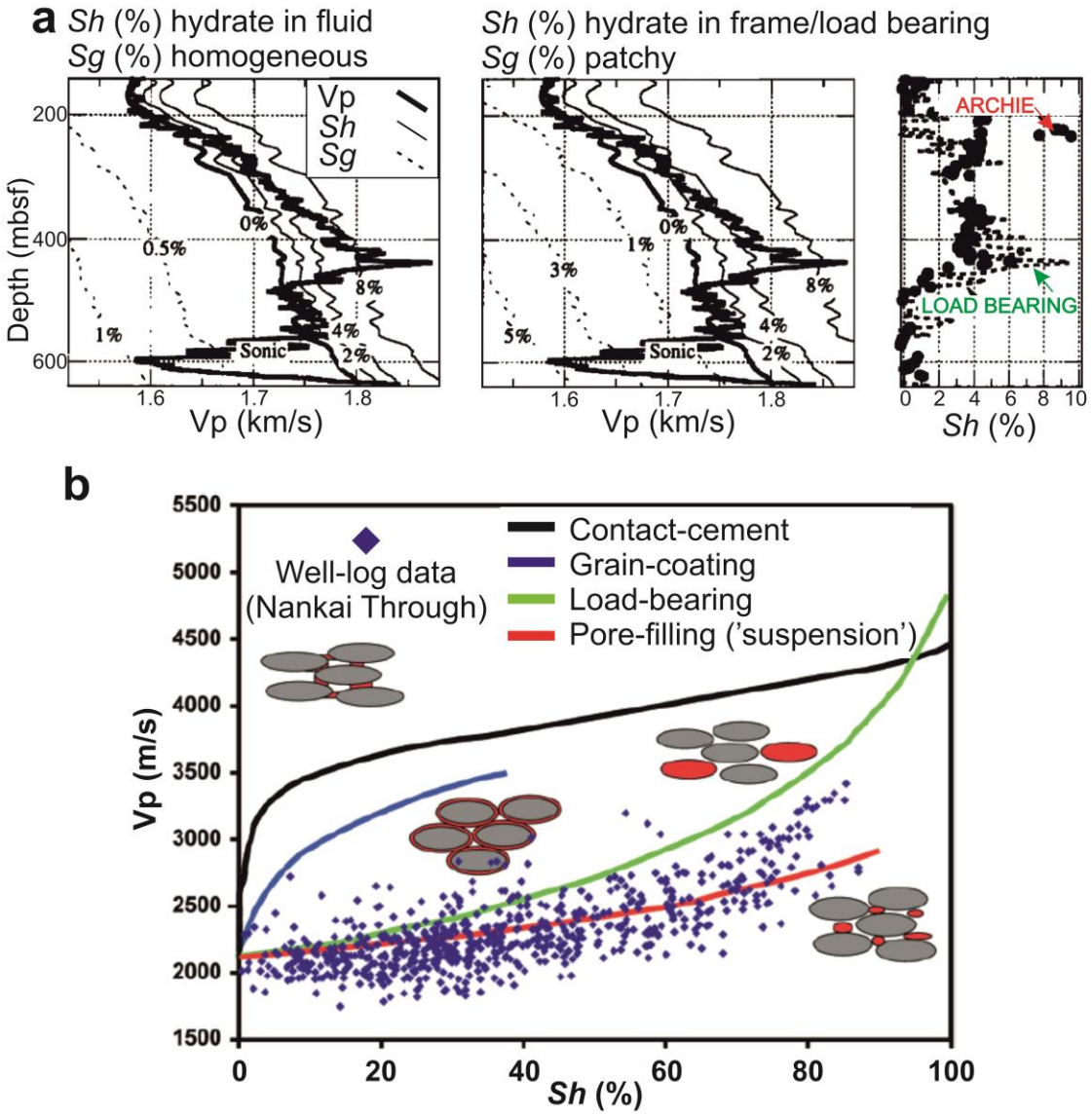



**Figure 1.18. (a)** Gas hydrate and free gas saturation at Blake Ridge (ODP Leg 164, Site 995). *Sh* (continuous lines) is estimated assuming the gas hydrate as floating particles in the fluid (left) and as part of the frame/load-bearing (middle), by the use of P-wave velocity (Vp) data (solid black lines). The free gas saturation (dotted lines) has also been estimated assuming both a homogeneous (left) and a patchy distribution (middle). The *Sh* estimated from resistivity (Archie approach), and velocity data (load-bearing model) are compared in the right panel (modified after Helgerud *et al.*, 1999). **(b)** P-wave velocity *vs Sh* for hydrate-bearing sediments in the Nankai Trough. *Sh* has been estimated by combining resistivity and NMR well-log data. The trend of increasing Vp with increasing *Sh* suggests that hydrates adopt a pore-filling to load-bearing morphology at the pore-scale (modified after Murray *et al.*, 2006).

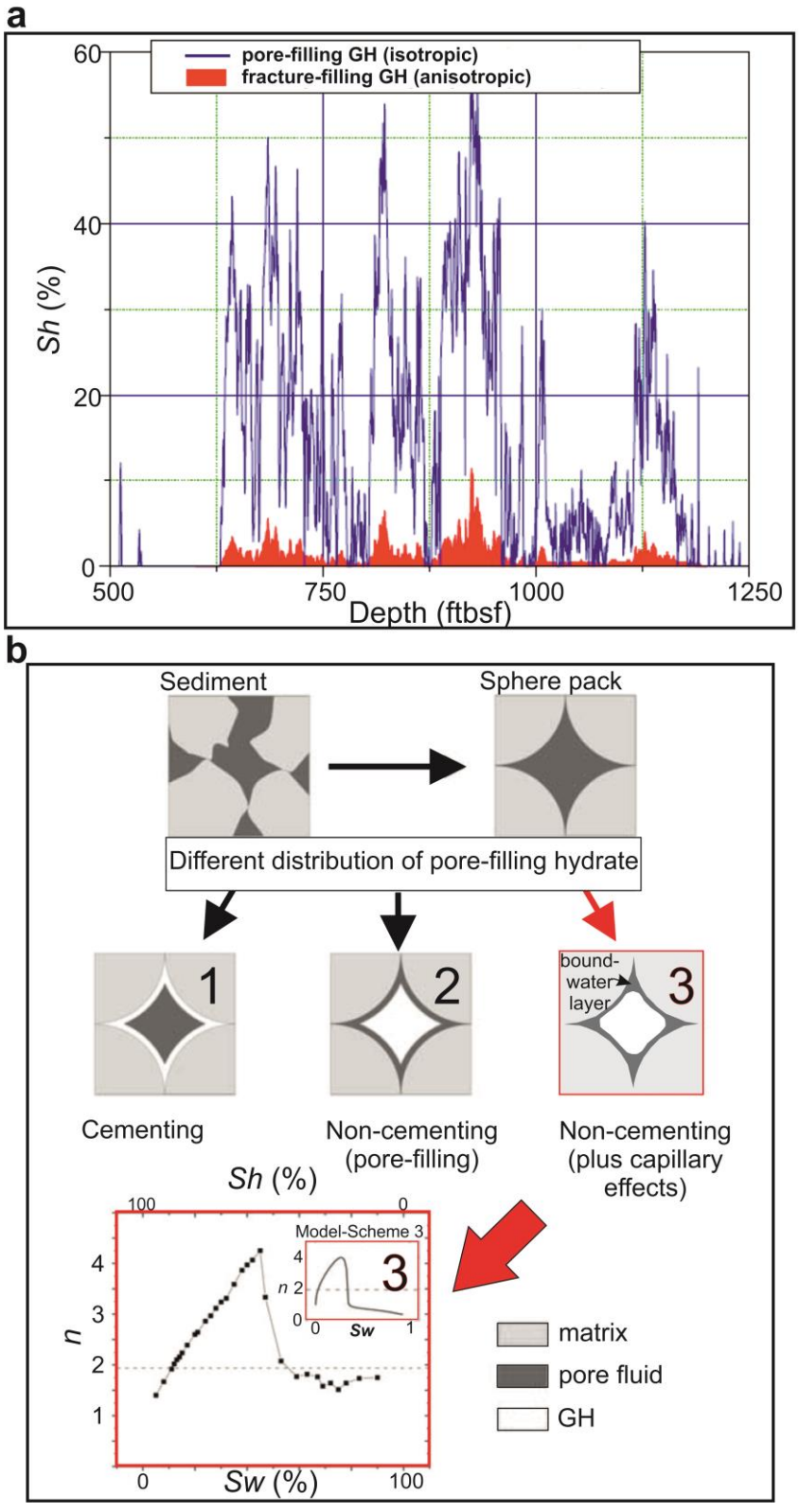



**Figure 1.19. (a)** *Sh vs* depth profile at Site GC955-H, in the Green Canyon (Northern Gulf of Mexico). Blue indicates *Sh* estimated assumed a pore-filling hydrate morphology (isotropic) whereas red indicates *Sh* calculated considering a fracture-filling morphology (anisotropic). The interval shown in the figure is characterised by fracture-filling hydrates in clay-rich sediments. Therefore the anisotropic model provides a more realistic estimate (modified after Lee and Collett, 2012). **(b)** Schematic models for hydrate growth in the pore space. Experimental data (bottom-left) indicate that the saturation exponent (*n*) varies with different *Sh* (red square). This suggests that model 3, which considers a non-cementing hydrate particle in the pore space with the development of capillary effects at increasing *Sh* is the most appropriate (modified after Spangenberg and Kulenkampff, 2006). *Sw* = water saturation.

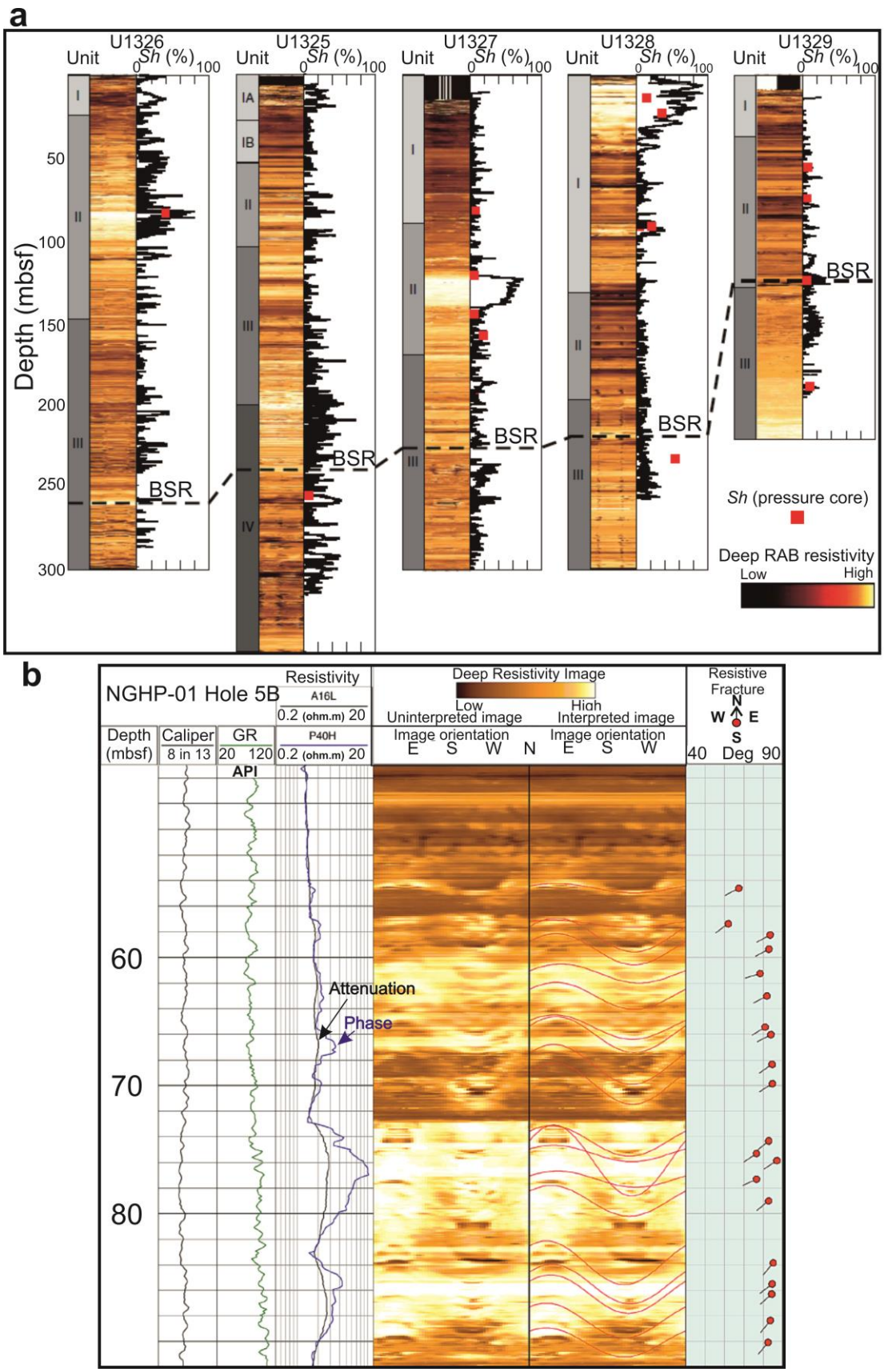



**Figure 1.20.** Resistivity image logs from two gas hydrate provinces. GHBS are characterised by brighter colours and, if a fracture-filling morphology is present, by bright sinusoids. **(a)** Northern Cascadia margin (IODP 311). The image logs are accompanied with *Sh* estimates (Riedel *et al.*, 2010b). **(b)** Krishna-Godavari Basin (Site NGHP-01-05B). The image log is accompanied with the caliper, gamma-ray, as well as attenuation and phase resistivity logs. The interpreted orientation and dip angle of the hydrate-filled fracture is further indicated in the panel on the right (Cook *et al.*, 2014).

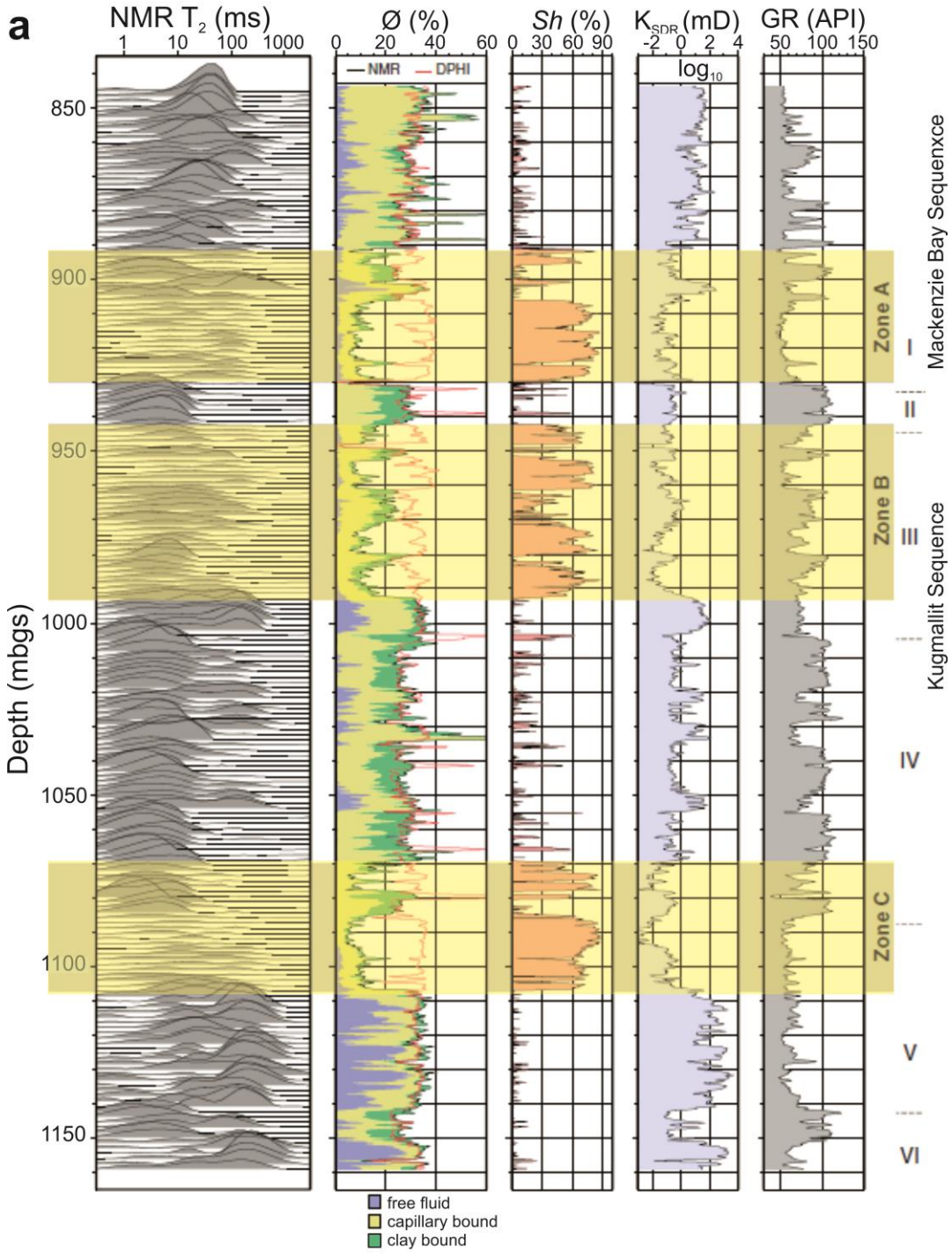

a
NMR T2 (ms)
1 10 100 1000
Ø (%)
0 20 40 60
NMR DPHI
Sh (%)
0 30 60 90
KSDR (mD)
-2 0 2 4
log10
GR (API)
50 100 150
Depth (mbgs)
850
900
950
1000
1050
1100
1150
Zone A
Zone B
Zone C
I
II
III
IV
V
VI
Mackenzie Bay Sequenxce
Kugmallit Sequence
free fluid
capillary bound
clay bound

**Fig. 1.21a**

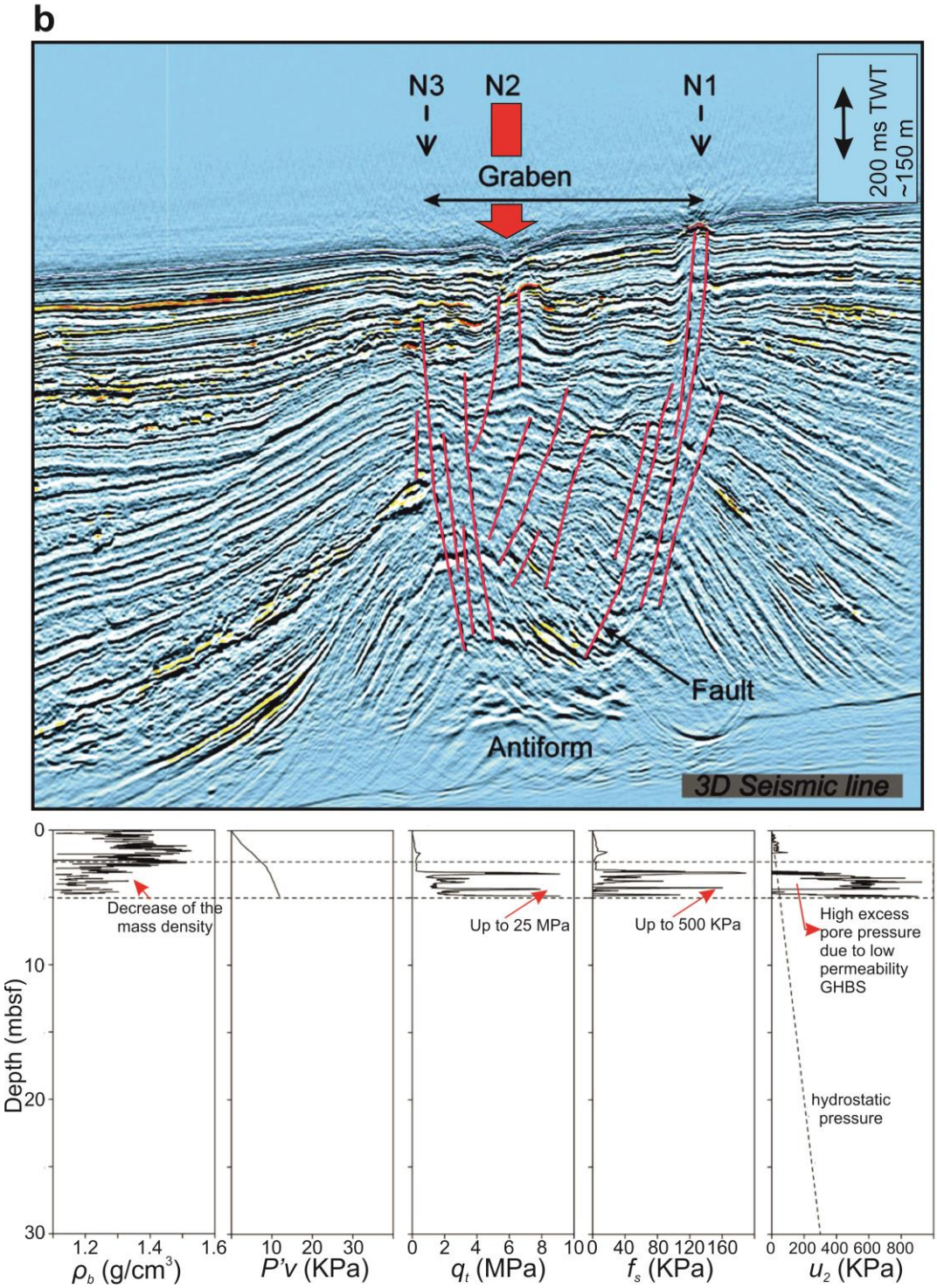



**Figure 1.21 (See the previous page for a). (a)** Well-log data acquired along the borehole Mallik 5L-38 (onshore northern Canada). The NMR $T_2$ log (transverse nuclear magnetic relaxation time) is shown on the left panel. Note that gas hydrate-bearing sediments are characterised by lower $T_2$ amplitudes and NMR porosities than hydrate-free sediments (compare the $T_2$ and the *Sh* panels) (modified after Bauer *et al.*, 2015) **(b)** Seismic reflection profile acquired offshore Nigeria showing a shale-cored anticline with a faulted crest. A gas hydrate system is developed near the seafloor. CPTu data (bottom) has been acquired close to the depression indicated by the red arrow. This data shows high $q_t$, $f_s$ and $u_2$, diagnostic for massive hydrate-bearing sediments. The density and effective stress (*P'v*) are also shown on the left (modified after Sultan *et al.*, 2007). Note the decrease in mass density associated with massive hydrates.

## 1.6. Core detection of gas hydrate-bearing sediments

Although well-log and in-situ CPTu data provide reliable information on the vertical distribution of gas hydrates and their saturation, a successful core recovery is the only way to gain more detailed insights about hydrate morphology and distribution at the cm-scale. Both non-pressurised and pressurised cores have been retrieved in gas hydrate systems. Non-pressurised cores are obtained without maintaining the core under gas hydrate stability conditions. Therefore, gas hydrates will dissociate, although massive hydrates pieces could occasionally be preserved upon core recovery (Tréhu *et al.*, 2004b). Although non-pressurised cores are not particularly representative of the in-situ physical properties of the sediments, the dissociation of gas hydrates from non-pressurised cores provokes a relevant two-fold effect:

**(1)** It decreases the core temperature where hydrates were formerly present (e.g. Tréhu *et al.*, 2004b; Torres *et al.*, 2008; Bahk *et al.*, 2011) **(Figs. 1.15a, 1.22a)**;

**(2)** It releases fresh water, previously trapped within the hydrate structure, decreasing the salinity (Ussler and Paull, 2001; Malinverno *et al.*, 2008) **(Figs. 1.17c, 1.22b)**.

Consequently, *Sh* can be evaluated by analysing the thermal anomalies in these cores (named *'cold spots'*) (Long *et al.*, 2010), and especially by quantitatively evaluating the difference between the measured pore water chlorinity and the estimated *'baseline'* chlorinity, which reflects the chlorinity conditions in-situ, prior to hydrate dissociation (Egeberg and Dickens, 1999; Ussler and Paull, 2001).

Pressure cores are recovered at pressures and temperatures within the hydrate stability field (Schultheiss *et al.*, 2008). In the last 15-20 years, there have been significant advances in the development of pressure coring apparatus (Dickens *et al.*, 1997; Schultheiss *et al.*, 2006, 2008 and 2011; Santamarina *et al.*, 2012; Dai and Santamarina, 2014). The successful retrieval of pressurised samples has massively improved our understanding of sediment-hosted gas hydrates.

Pressure cores can be CT-scanned and the obtained X-ray images provide detailed insights into hydrate morphology and distribution, particularly for grain-displacing hydrates (e.g. Holland *et al.*, 2008; Riedel *et al.*, 2010a; Rees *et al.*, 2011; Lee *et al.*, 2013; Holland and Schultheiss, 2014) (**Fig. 1.14a**). Additionally, by the use of multi-sensor core logging (MSCL) tools on pressure cores, it is possible to measure the in-situ physical properties of GHBS and, importantly, detect disseminated hydrates, which are invisible in X-ray. The bulk P-wave velocity and density are the most common parameter acquired by MSCL tools (**Fig. 1.14b**). Occasionally, also the electrical conductivity, S-wave velocity and undrained shear strength are measured (e.g. Yun *et al.*, 2010; Lee *et al.*, 2013; Konno *et al.*, 2015) (**Fig. 1.23a**). Although *Sh* can be estimated by CT-intensity analysis in grain-displacing hydrate morphologies (Holland and Schultheiss, 2014), the state of the art technique involves a mass balance calculation which follows the depressurisation of the core and the quantification of the evolved gas volume **(Fig. 1.23b, c**). Then, by comparing the measured volume with the in-situ gas solubility thresholds, it is possible to constrain the amount of gas in excess and precisely calculate *Sh*.

The analysis of the released gas volume, upon controlled dissociation, provides information on the geochemistry of the hydrate-forming gases (e.g. Dickens *et al.*, 1997 and 2000; Milkov *et al.*, 2004b; Heeschen *et al.*, 2007). The geochemical data from experiments on pressurised and non-pressurised cores (e.g. geochemical analysis on void gas samples), as well as the direct measurements on gas hydrate pieces (X-ray diffraction and Raman spectroscopy) are crucial to constrain the sourcing gas origin and the hydrate structure (Sassen *et al.*, 2001a; Charlou *et al.*, 2004; Milkov *et al.*, 2004b; Heeschen *et al.*, 2007; Lu *et al.*, 2007; Klapp *et al.*, 2010; Lorenson *et al.*, 2011; Liu *et al.*, 2015) (**Figs. 1.9, 1.10**).

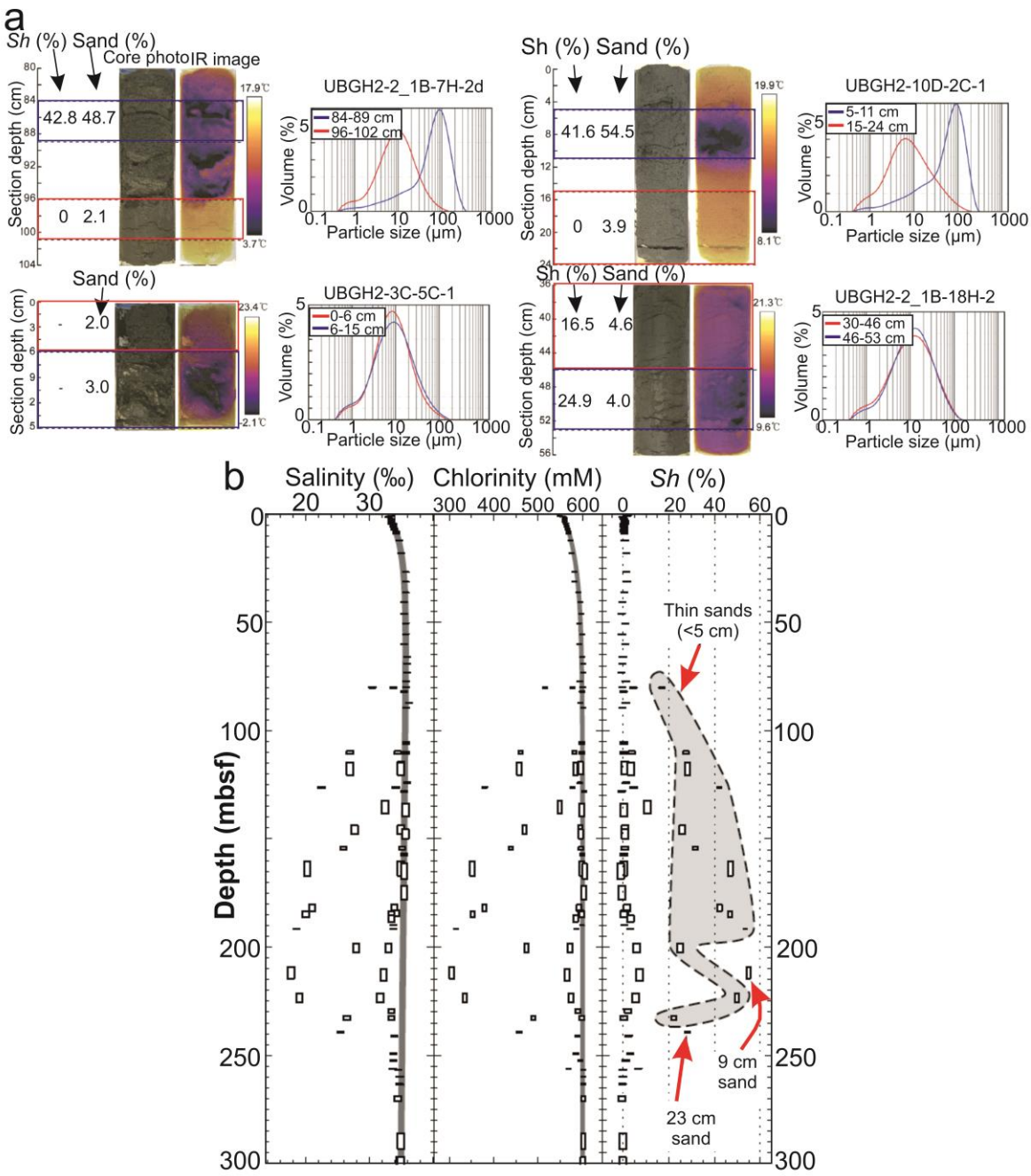



**Figure 1.22. (a)** Core photographs, IR images and particle size measurements of core samples from the Ulleung Basin. The *'cold spots'* (purple areas) indicate formerly gas hydrate-bearing sediments. The upper two samples contain sandy intervals with concentrated hydrates and bimodal particle size distributions. The lower two samples represent fine-grained diatom oozes with pore-filling disseminated hydrates (left) and fracture-filling hydrates within muddy sediments (modified after Bahk *et al.*, 2013). **(b)** Salinity, chlorinity and *Sh* profiles, extrapolated from cores recovered in the Northern Cascadia margin (Site U1325, IODP 311). The continuous grey lines on the left and central panels represent the extrapolated *'baseline'* trends (modified after Malinverno *et al.*, 2008).

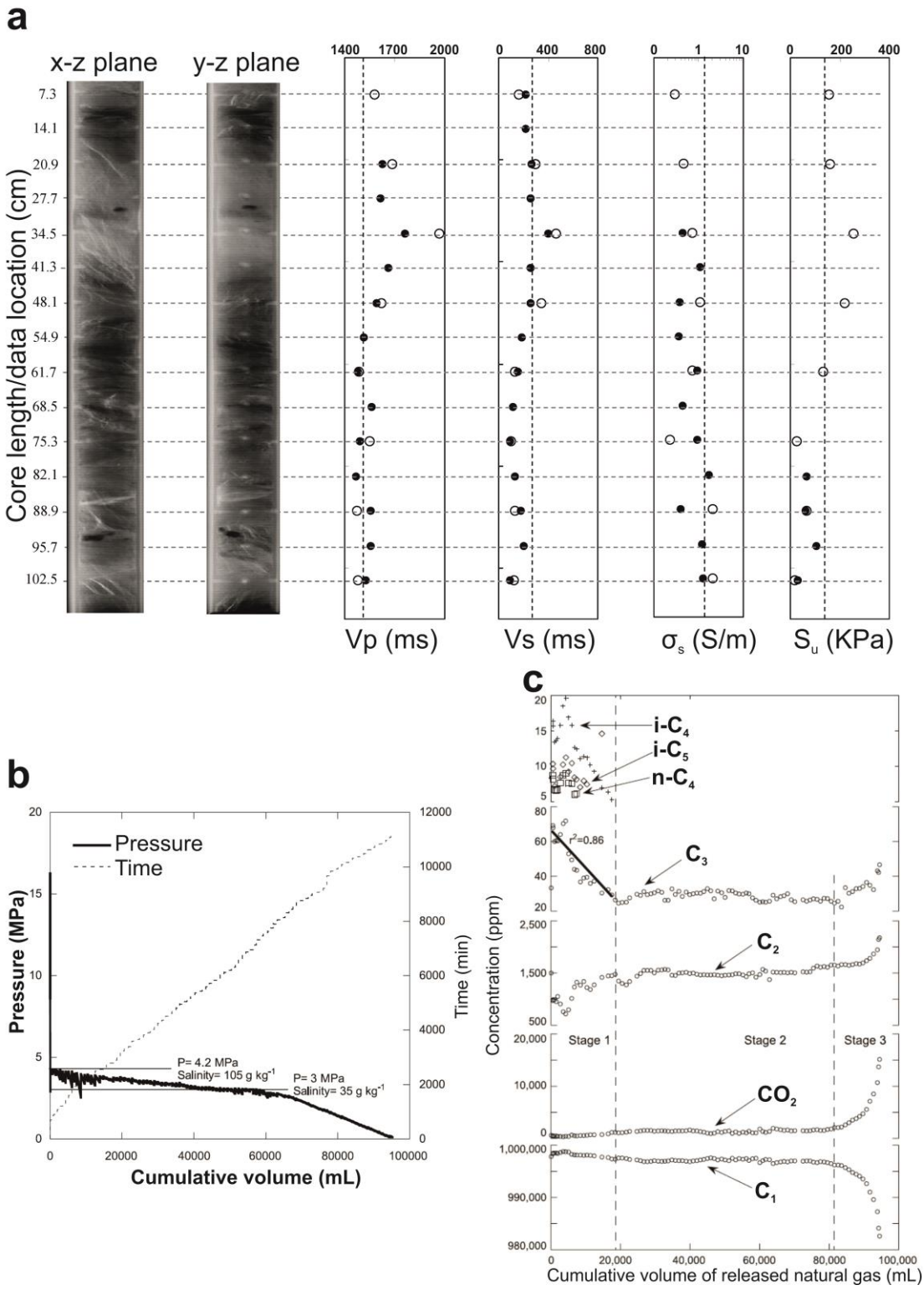



**Figure 1.23. (a)** X-ray images from a pressure core, acquired in the Krishna-Godavari Basin (Site NGHP-01-21) and the associated physical property measurements (Vp= P-wave velocity; Vs= S-wave velocity; $\sigma_s$= sediment conductivity and $S_u$= undrained shear strength) (Yun *et al.*, 2010). **(b)** Pressure *vs* cumulative volume of expelled gas *vs* time plot, representing the results of a core degassing experiment accomplished on a pressure core (204-1249F-4P) retrieved in at Site 1249 at the Hydrate Ridge (ODP Leg 204), at 13.5 mbsf. This core released ~95 l of gas upon degassing (Milkov *et al.*, 2004b) **(c)** Molecular composition of the gas released during the degassing of core 204-1249F-4P. $C_1$= methane; $CO_2$= carbon dioxide; $C_2$= ethane; $C_3$= propane; n-$C_4$= n-butane; i-$C_5$= iso-pentane; i-$C_4$= iso-butane, (Milkov *et al.*, 2004b).

## 1.7. The seismic expression of natural gas hydrates

### *1.7.1. Origin and characteristics of the bottom-simulating reflector*

The concentration of the hydrate-forming gases needs to exceed the solubility thresholds in the pore water to form hydrates (Xu and Ruppel, 1999; Davie *et al.*, 2004). In many marine NGHSs, this condition is satisfied at the BGHSZ and immediately beneath, leading to the formation of the so-called free gas zone (FGZ) (Bangs *et al.*, 1993; Holbrook *et al.*, 1996; Plaza-Faverola *et al.*, 2012a) **(Figs. 1.12, 1.24a)**. The presence of free gas within the pore space, particularly at shallow depths, produces huge effects on the P-wave velocity of sediments, given the extremely low bulk modulus and density of hydrocarbon gases (Domenico, 1976; Lee, 2004). In contrast to the S-wave velocity, which is mostly unaffected by free gas, even a *Sg* of 0.5-5% dramatically influences the P-wave velocity in shallow and poorly consolidated sediments (Helgerud *et al.*, 1999; Sain *et al.*, 2000; Holbrook, 2001) **(Fig. 1.24b)**.

For this reason, the BGHSZ can be easily imaged in seismic reflection data as a high amplitude anomaly which follows the phase boundary, if the free gas exceeds at this interval its supersaturation thresholds **(Figs. 1.4, 1.24c, d, 1.25)**. In subaquatic gas hydrate provinces, at constant water depths (i.e. equal hydrostatic pressure and seafloor temperature), the BGHSZ is roughly parallel to the seabed interface. Thus, the BGHSZ is detectable as a high-amplitude reflection, parallel to the seafloor but with opposite polarity, given the negative acoustic impedance contrast between hydrate and free gas-bearing sediments (e.g. Haacke *et al.*, 2007) **(Figs. 1.4, 1.24b, c, 1.25).** This reflection is named bottom-simulating reflector or reflection (BSR) and is a good approximation for the BGHSZ in natural gas hydrate systems (e.g. Hovland *et al.*, 1997; Ashi *et al.*, 2002).

In contrast to the free gas, hydrates exert an impact on the acoustic character of the sediment only at elevated concentrations (Lee *et al.*, 2009). Hence, the seismic character of BSRs is mostly due to the presence of free gas beneath the three-phase boundary (Bangs *et*

*al.*, 1993; Holbrook *et al.*, 1996; Andreassen *et al.*, 1997; Bünz and Mienert, 2004). This has been corroborated by the fact that gas hydrates have been recovered or inferred in areas lacking a BSR and, vice-versa, a BSR may exist without the presence of hydrates above it (Holbrook *et al.*, 1996; Tsuji *et al.*, 2009; Boswell *et al.*, 2012a; Shedd *et al.*, 2012). Therefore, BSRs are not indicative of the detailed gas hydrate distribution. However, they still represent the best seismic indicator for the existence of **(1)** pressure and temperature conditions suitable for hydrate stability and **(2)** adequate amounts of hydrocarbon gases in the system to support hydrate formation. Moreover, excluding the cases where free gas escapes throughout the GHSZ (Wood *et al.*, 2002; Liu and Flemings, 2006 and 2007; Smith *et al.*, 2014a), the BSR represents, in a regional sense, the top of the FGZ, i.e. the shallowest free gas occurrence in the sediments (Hillman *et al.*, 2017b).

BSRs can further display a cross-cutting relationship with stratigraphic reflections, either **(1)** if the latter are discordant with respect to the seafloor or **(2)** in the presence of rapid changes in the bathymetry. In some circumstances, it is possible to identify a polarity reversal at the intersections between the BSR and stratigraphic reflections. The depth of this reversal is indicative of the BGHSZ (e.g. Vanneste *et al.*, 2001; Bünz and Mienert, 2004; Fohrmann and Pecher, 2012; Hillman *et al.*, 2017b) **(Fig. 1.26)**. The frequency of acquisition further needs to be considered, as the continuity of BSRs decreases at increased seismic frequencies, owing to either the impact of the velocity dispersion or the occurrence of a transitional BGHSZ (Lee, 2007).

The tectonic activity, sedimentary processes, as well as heat and fluid flow perturbations further complicate the seismic expression of BSRs, which can lose their continuity and/or their bottom-simulating character (e.g. Wood *et al.*, 2002; Pecher *et al.*, 2005; Bangs *et al.*, 2010; Shedd *et al.*, 2012) **(Figs. 1.8a, 1.26b, 1.27)**. Typical geological features that may impact the bottom-simulating character of BSRs are thrust-cored anticlines, fluid-escape pipes/chimneys, faults, salt diapirs and mud volcanoes (Taylor *et al.*,

2000; Wood *et al.*, 2002; Vanneste *et al.*, 2003; Pecher *et al.*, 2010; Pape *et al.*, 2011; Crutchley *et al.*, 2014). Further complications derive from lateral variability in the molecular composition of the feeding gas (Sassen *et al.*, 2001d; Macelloni *et al.*, 2015). Stratigraphic heterogeneities also impact the seismic expression of a BSR. In such cases, the BSR can appear as a discontinuous reflection, where the amplitude is enhanced only along those stratigraphic reflections which represent permeable free gas-bearing carrier beds (e.g. Boswell *et al.*, 2012b; Boswell *et al.*, 2016) **(Fig. 1.26b)**.

The host lithology further controls the kinetics of gas hydrate nucleation and stability. Capillary effects are considered particularly important in fine-grained sediments and can impact the solubility thresholds for hydrate and free gas formation, ultimately shifting the BSR position upward or downward **(Fig. 1.28)**. The presence of capillary effects may also result in a relatively thick zone of three-phase equilibria, favoured within sediments with a broad pore size distribution (Clennell *et al.*, 1999; Liu and Flemings, 2011).

BSRs become shallower with shallower water depths along continental slopes because of the decreasing pore pressures (Gorman and Senger, 2010; Davies *et al.*, 2015). Ultimately, the BSR can pierce the seafloor along the slope and gas hydrates are no more stable. The region where the BGHSZ evidently thins towards the seafloor is termed *'hydrate wedge'* or *'feather-edge'* of gas hydrates. Above this region, free gas can migrate towards the seafloor without forming hydrates. This process has been recognised thanks to the abundant evidence of pockmarks and flares above this zone along many continental slopes (Hustoft *et al.*, 2009; Rajan *et al.*, 2012; Brothers *et al.*, 2014) **(Figs. 1.25a, 1.29)**.

The hydrate stability conditions are inevitably transient on geological scales of thousands of years, due to sedimentation, erosion, uplift and sea level cycles. The result is a re-equilibration of the BGHSZ, involving gas hydrate dissociation and free gas migration (Mienert *et al.*, 2005). Consequently, BSRs are predicted to *'migrate'* over time as well. Eventually, relict or paleo BSRs, indicating past gas hydrate stability conditions, may be

preserved and be visible in seismic data **(Figs. 1.30, 1.31)**. At some point, the free gas trapped within a paleo BSR will either dissolve in an undersaturated pore water or advectively migrate upward, towards the present-day BGHSZ. In the case of a downward shift of the BGHSZ, free gas will be converted into hydrate. Foucher *et al.* (2002) suggested that a paleo BSR may be seismically preserved for a maximum of a few thousand years (~1000-10000), depending on the methane concentration in the system relative to its solubility, in the absence of active fluid flow and solely in the presence of diffusive processes.

In theory, multiple/secondary BSRs may also occur, thanks to the presence of stacked zones of hydrate occurrence, each zone characterised by different hydrate structures (i.e. $S_I$, $S_{II}$ and $S_H$), overlying layers of free gas. In the absence of in-situ data or precise geological constraints (e.g. sedimentation and uplift rates, sea level changes over time), discerning between these contrasting interpretations is challenging. Multiple BSRs have been identified in different sedimentary basins, including the Nankai Trough, the Cascadia margin, the Peruvian margin, the Norwegian margin, the Hikurangi margin and the Danube Fan in the Black Sea (Andreassen *et al.*, 2000; Foucher *et al.*, 2002; Bangs *et al.*, 2005; Popescu *et al.*, 2006; Pecher *et al.*, 2014; Auguy *et al.*, 2017) **(Fig. 1.30)**. So far, a complete borehole penetration through multiple BSRs is lacking.

Finally, BSRs may also indicate diagenetic fronts, for instance, related to mineral dehydration processes and phase boundaries for different polymorphs. For example, the opal-A/opal-CT transition occurs in biosiliceous oozes at temperatures comprised between ~25 and 50°C, depending on the basin history, pore water chemistry and sediment properties (Lee *et al.*, 2003; Berndt *et al.*, 2004; Davies and Cartwright, 2007). These temperatures are higher than those commonly characterising the BGHSZ (less than ~25 °C). Moreover, this diagenetic front, contrarily to *'hydrate stability BSRs'*, generates a positive acoustic impedance contrast in seismic data.

### *1.7.2. Other seismic indicators of a natural gas hydrate system*

In addition to the BSR, there are other seismic indicators for the presence of an NGHS. Importantly, the free gas is not solely located beneath the BGHSZ but can be stratigraphically or structurally trapped deeper in the overburden. Alternatively, free gas can transiently occur along vertical cross-stratal migration pathways, either below or across the GHSZ. Seismically, these manifestations of free gas-bearing sediments can be expressed as **(1)** enhanced amplitude reflections, with negative acoustic impedance contrasts, **(2)** flat spots, **(3)** zones of seismic wipeout and **(4)** fluid-escape pipes/chimneys (e.g. Gorman *et al.*, 2002; Wood *et al.*, 2002; Gay *et al.*, 2007; Davies and Clarke, 2010; Petersen *et al.*, 2010; Koch *et al.*, 2016) **(Fig. 1.27a, c).** Contextualising these features into the geological framework provides information on the migration pathways used by gas to migrate towards and across the GHSZ.

Within the GHSZ, it is possible to identify amplitude anomalies properly related to gas hydrate deposits. GHBS at high *Sh* can be expressed as enhanced reflections with a positive acoustic impedance contrast at their interface with the overlying hydrate-free sediment. These reflections can indicate either **(1)** GHBS at high *Sh* hosted in permeable coarse-grained sediments, if occurring along segments of stratigraphic intervals, or **(2)** accumulations associated with vertical fluid flow pathways passing through the GHSZ (Chun *et al.*, 2011; Boswell *et al.*, 2012b and 2016; Ho *et al.*, 2012; Zhang *et al.*, 2012; Fujii *et al.*, 2015) **(1.32)**. In the latter case, the formation of shallow massive hydrates at and near the seafloor can result in the genesis of gas hydrate pingoes (Hovland and Svensen, 2006; Paull *et al.*, 2008a; Serié *et al.*, 2012), reflecting a volume expansion owing to either hydrate decomposition (Paull *et al.*, 2007) or the formation of hydrates at elevated *Sh* (Paull *et al.*, 2008a). An acoustically reflective seafloor can further indicate pockmarks, mud/asphalt volcanoes, chemosynthetic communities and authigenic carbonate mounds (MacDonald *et al.*, 2004; Roberts *et al.*, 2006; Sultan *et al.*, 2014). The presence of hydrate outcrops at or near the seafloor can be transient: hydrate dissociation, dissolution, or fluid migration can

result in the collapse of shallow hydrate accumulation and the genesis of complex pockmarks (Paull *et al.*, 2015; Riboulot *et al.*, 2016) **(Fig. 1.33)**. These features are preferred locations for geochemical sampling, which can reveal information about the origin and composition of the migrating fluids (Sassen *et al.*, 2004; Serié *et al.*, 2016).

In other cases, a reduction of the seismic amplitudes within the GHSZ, named amplitude blanking, can be observed **(Fig. 1.34)**. It has been attributed to a *'homogenisation effect'*, induced by the formation of hydrates in the more porous sediments, resulting in a reduced acoustic impedance contrast (Lee and Dillon, 2001). However, amplitude blanking can also be caused by fairly homogeneous sediments overlying highly reflective FGZs (Holbrook *et al.*, 1996). Other studies (Vanneste *et al.*, 2001; Riedel *et al.*, 2002; Horozal *et al.*, 2009) demonstrated that hydrate distribution is relatively independent of blanking, which is instead related to seismic frequency. Other elements associated with blanking include mass-transport deposits (MTDs), zones of homogenised sediment due to fluid flow and fracturing, and transmission artefacts (Riedel *et al.*, 2002). Amplitude blanking has been identified along large portions of the Blake Ridge whereas elsewhere (e.g. Hydrate Ridge, Hikurangi margin, Ulleung Basin), it is instead localised along and in the vicinity of vertical fluid flow pathways (Riedel *et al.*, 2002; Plaza-Faverola *et al.*, 2011; Fraser *et al.*, 2016).

### *1.7.3. Quantitative seismic analyses, multibeam surveys and ROV observations*

2D and 3D seismic data have been used to quantitatively or semi-quantitatively evaluate an NGHS. All the methods are based on those rock-physics models that constrain the impact of gas hydrates on the acoustic properties of the sediments. Standard approaches include amplitude *vs* offset analysis (AVO analysis), the full-waveform inversion of pre-stack data and empirical relationships between seismic amplitudes and well-log data. These methods provide first-order evaluations on the distribution and saturation of gas hydrate- and free gas-bearing sediments. These analyses recognised that the free gas and its distribution are the primary cause for the generation of BSRs and, occasionally, have helped

in identifying concentrated hydrate deposits (e.g. Andreassen *et al.*, 1997; Ecker *et al.*, 1998; Carcione and Tinivella, 2000; Dai *et al.*, 2004; Fohrmann and Pecher, 2012; Zhang *et al.*, 2012; Qian *et al.*, 2014).

The detailed acquisition of bathymetry morphology (e.g. multibeam surveys), frequently coupled with ultra-high resolution seismic data (e.g. deep-towed and autonomous underwater vehicle (AUV) acoustic systems), and visual observations with remotely operating vehicles (ROV), provides further information on gas hydrate distribution (Riedel *et al.*, 2002; Wood *et al.*, 2002; Hovland and Svensen, 2006; Paull *et al.*, 2008a and 2015; Simonetti *et al.*, 2013) **(Fig. 1.33)**.

Finally, the hydrocarbon migration above the sediment-water interface, in the form of hydrate-coated hydrocarbon bubbles, has been detected with single and multibeam echosounder data in many gas hydrate provinces, in the form of acoustic gas flares (Heeschen *et al.*, 2003; Greinert *et al.*, 2006; Smith *et al.*, 2014b) **(Figs. 1.7b, 1.27c)**. These flares are observed above actively venting cold seeps and can extend for hundreds of metres in the water column, up to the top of the GHSZ. At this interface, the hydrate skins which coat the rising free gas bubbles dissociate and the formerly trapped gas is dissolved into water, although the presence of liquid hydrocarbon films can preserve the bubbles even shallower. The spatial and temporal detection of these features provides a better understanding of the episodicity of hydrocarbon fluid flow (Naudts *et al.*, 2010; Kannberg *et al.*, 2013).

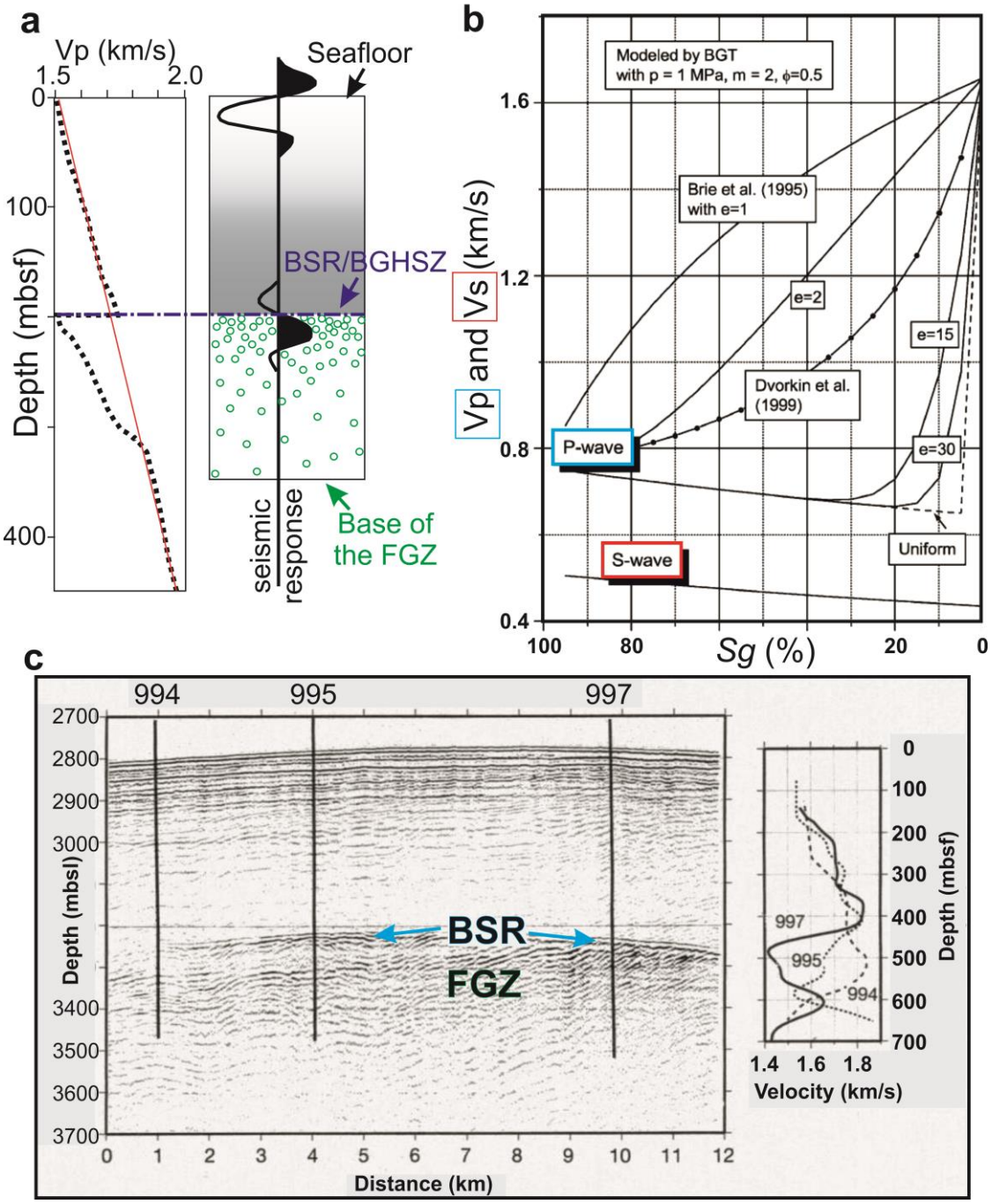



**Figure 1.24. (a)** (Left) Simplified P-wave velocity (Vp) profile (black-dotted line) in a hypothetical marine setting, characterised by a ~100 m thick free gas zone (FGZ) beneath the base of the gas hydrate stability zone (BGHSZ). (Right) Schematic synthetic seismogram (Phase-shifted by 90°, N. American polarity convention), highlighting the opposite seismic response of the seafloor and the BSR (modified after Haacke *et al.*, 2007). **(b)** Velocity (P- and S-wave) *vs Sg* plot, for a 50% porosity sediment at conditions of 1 MPa of effective stress (modified after Lee, 2004). Note the considerable variability in *Sg*, at a given Vp, depending on the used model and the calibration constant **e** (Brie *et al.*, 1995). **(c)** Seismic profile acquired at the Blake Ridge (left) indicating a BSR (blue arrows) at ~450 mbsf. An FGZ, exceeding 200 m of thickness, is developed below the BSR and provokes a marked decrease in the P-wave velocities, detected with vertical seismic profiling (right) (modified after Holbrook *et al.*, 1996).

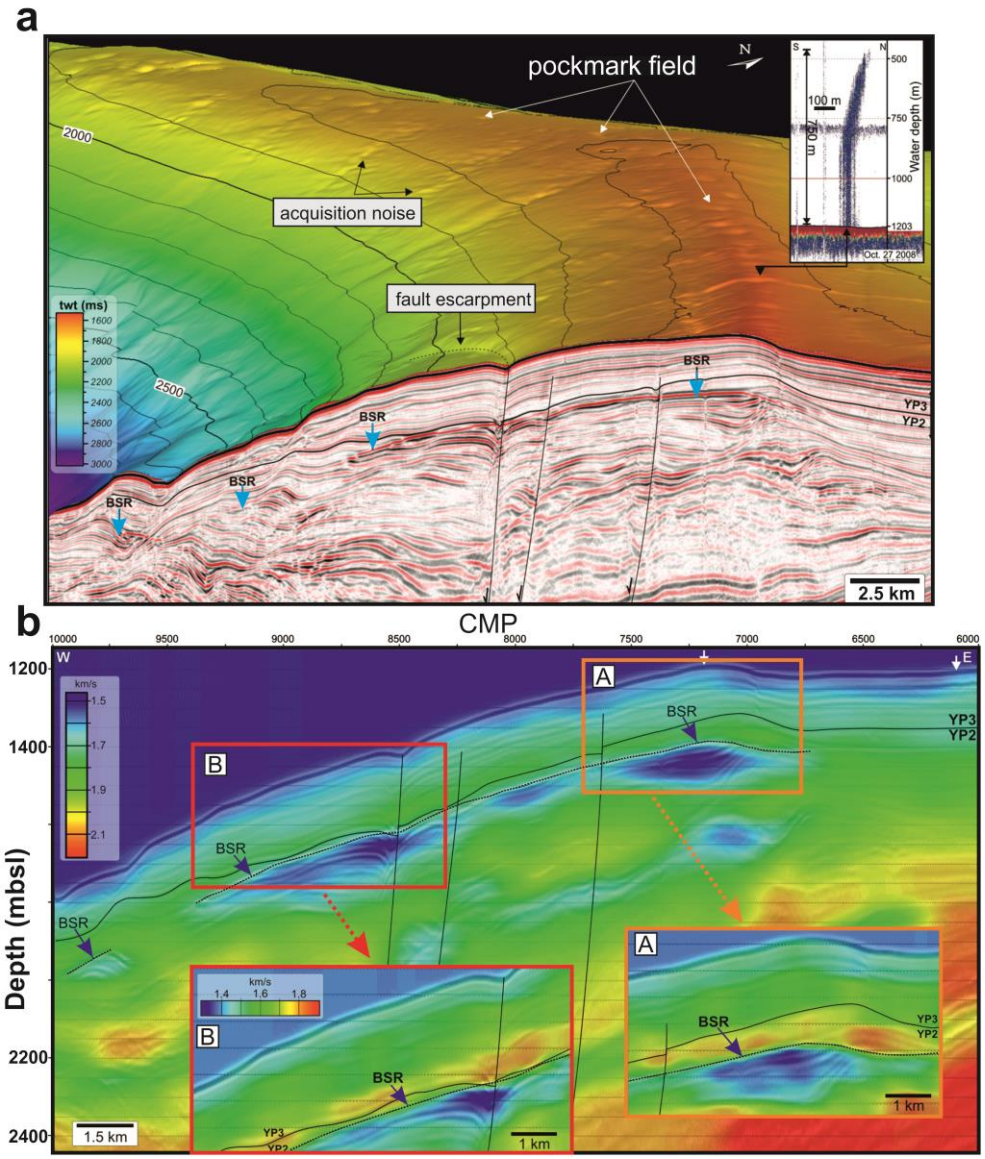



**Figure 1.25. (a)** Seismic reflection profile with superimposed 3D bathymetry along the Vestnesa Ridge (offshore Svalbard, Fram Strait), showing a BSR (blue arrows) and the underlying free gas zone, seismically expressed as a series of enhanced reflections. Along the slope, the shallower limit of the BSR coincides with a pockmark field, which is the seafloor expression of methane escape from the seafloor. The migration of methane in the water column is detected as an acoustic flare in echosounder data (top-right corner of the image). **(b)** P-wave velocity along the same profile shown in **(a)**, obtained with a velocity analysis of pre-stack multichannel seismic reflection data. Note the low velocities (less than ~1500 m/s) associated with the free gas zone and imaged as blue-coloured zones (Hustoft *et al.*, 2009).

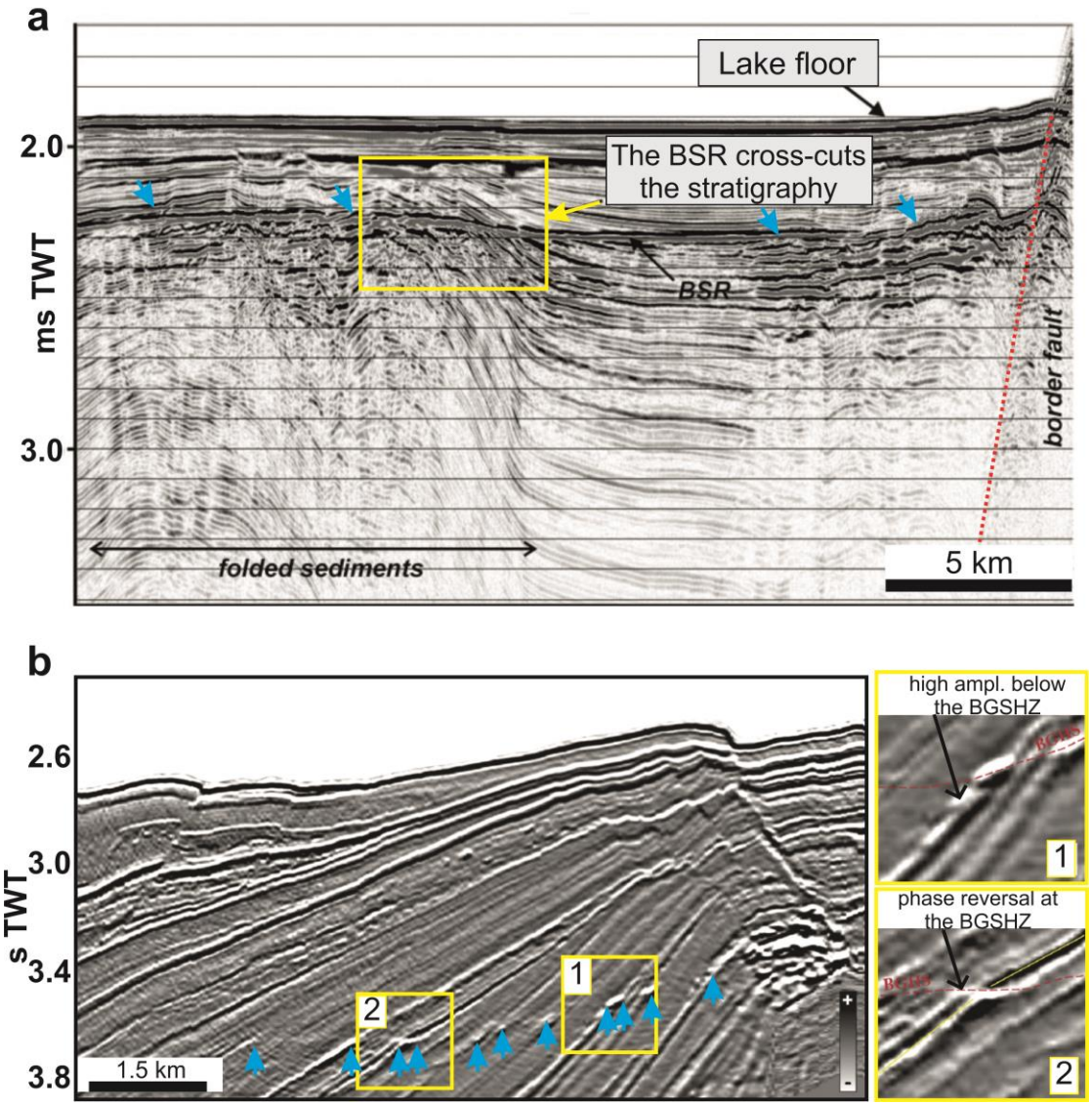



**Figure 1.26. (a)** Seismic reflection profile in the Lake Baikal, highlighting a clear cross-cutting relationship between a BSR (blue arrows) and the stratigraphic reflections (modified after Vanneste *et al.*, 2001). **(b)** Seismic reflection profile in the Terrebonne Basin (Northern Gulf of Mexico), displaying a discontinuous BSR. This discontinuous BSR results from the alignment of the upper terminations of segments of stratigraphic reflections with enhanced amplitudes, which represent gas-charged horizons (top-right panel, 1). Occasionally, a phase reversal at the BGHSZ is observed (bottom-right panel, 2) (modified after Hillman *et al.*, 2017b).

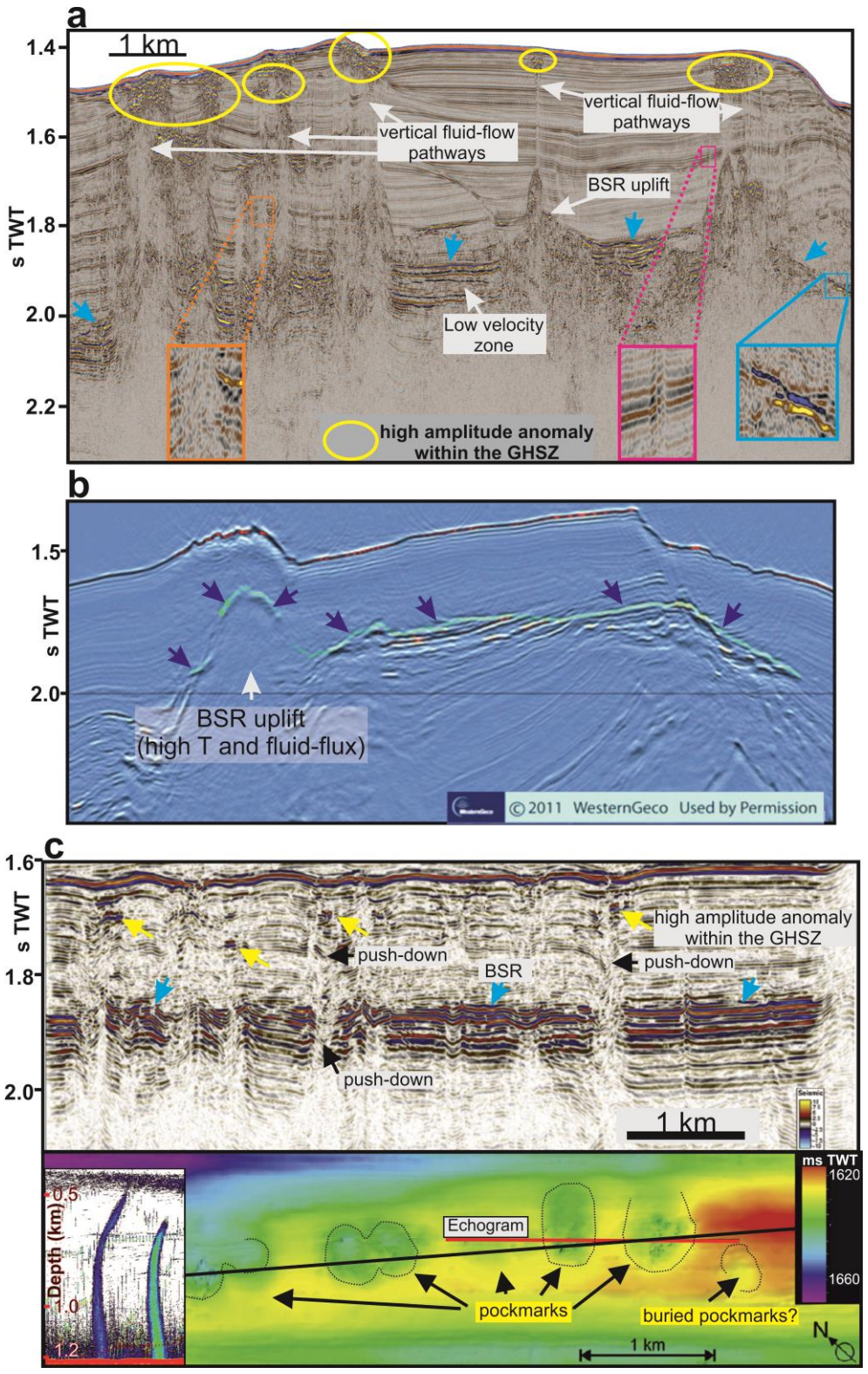



**Figure 1.27.** Seismic profiles, showing anomalous BSRs. **(a)** Discontinuous BSR in the Opouawe Bank (Hikurangi margin). The BSR is cut by vertical fluid flow features (fluid-escape pipes), serving as pathways for free gas throughout the GHSZ. A low-velocity zone, representing free gas-bearing sediments, occurs beneath the BSR. High amplitude anomalies, indicating free gas, massive hydrates or carbonates are observed near the seafloor, at the top of the fluid flow pathways (yellow circles) (modified after Koch *et al.*, 2016). **(b)** Profile from the Garden Banks (Northern Gulf of Mexico), showing a BSR that is uplifted above a salt diapir, due to changes in heat flow and pore water salinity (modified after Shedd *et al.*, 2012). **(c)** Profile (top) and seafloor bathymetric map (bottom) from the Vesntesa Ridge (offshore Svalbard, Fram Strait), showing a BSR and an FGZ, both disrupted by vertical fluid flow pathways (fluid-escape pipes), expressed as pockmarks at the seafloor. Free gas can migrate in the water column from these pockmarks and is detected as vertical flares in echosounder data (modified after Bünz *et al.*, 2012).

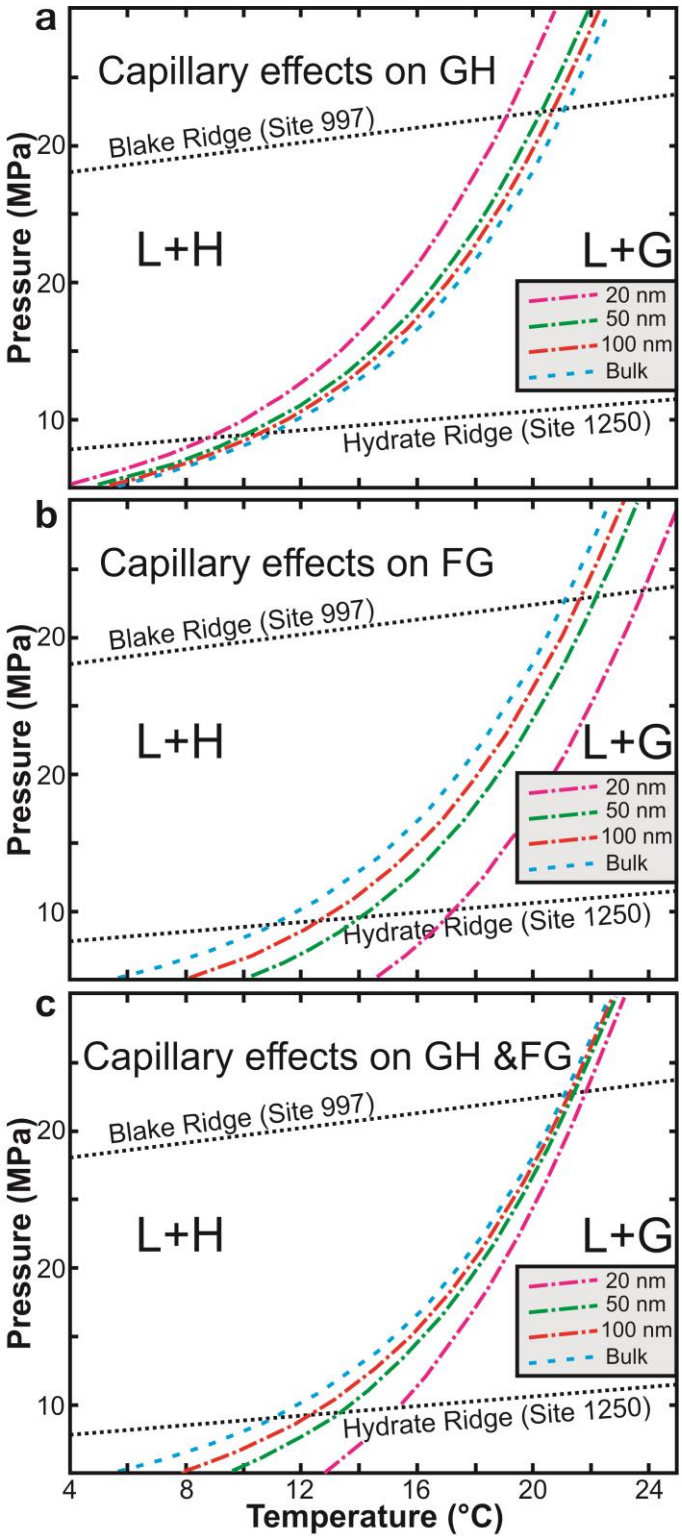



**Figure 1.28.** Gas hydrate phase boundaries, showing the impact on hydrate stability of capillary effects in small pores of 20, 50 and 100 nm. Bulk conditions (i.e. no capillary effects) are highlighted with blue dotted lines. **(a)** Capillary effects act only on the hydrate phase. **(b)** Capillary effects act only on the free gas phase. **(c)** Capillary effects act both on the hydrate and free gas phases. The shift from bulk conditions increases with decreasing pore size. The P-T conditions at Blake Ridge (Site 997) and Hydrate Ridge (Site 1250) are indicated by black dotted lines. The examples are valid for uniform pore distribution and do not consider systems with a range of pore sizes (modified after Liu and Flemings, 2011). GH= gas hydrate; FG= free gas; L+H= methane is stable in the liquid state (dissolved in water) and as hydrate; L+G= methane is stable in the liquid state (dissolved in water) and as free gas.

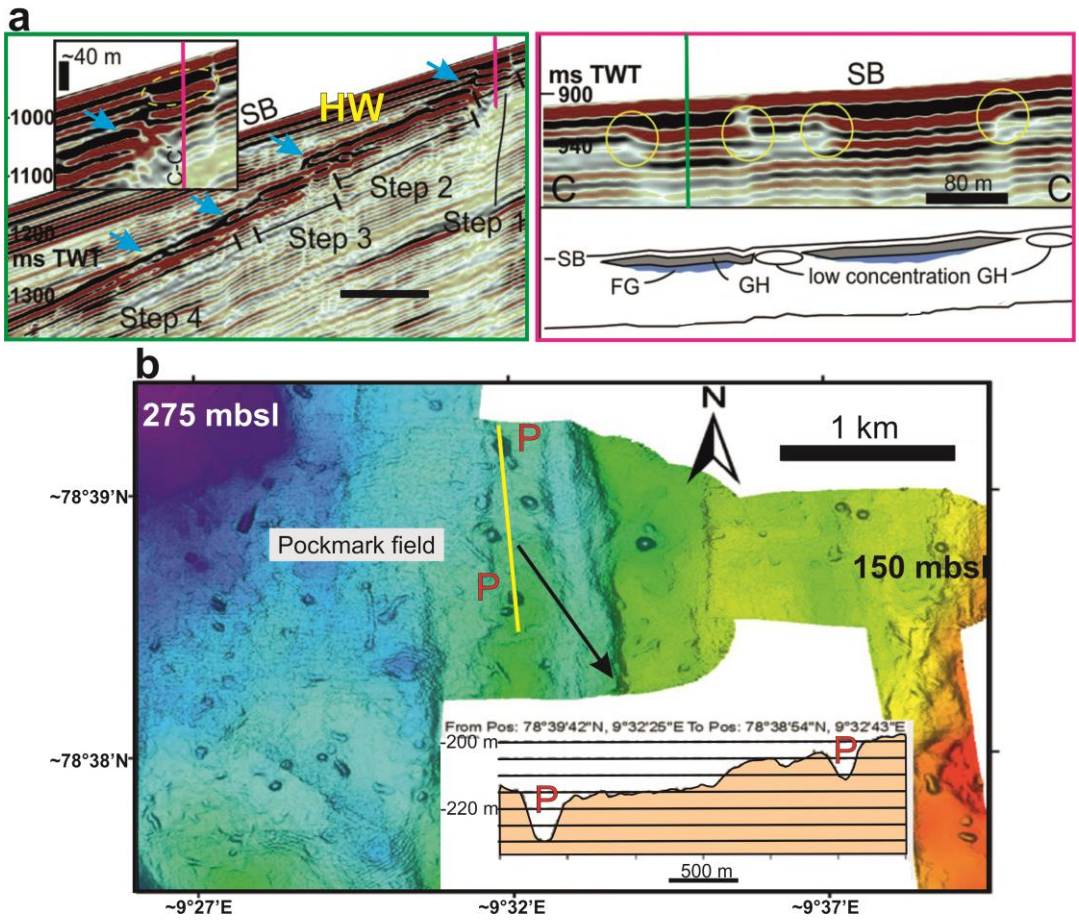



**Figure 1.29. (a)** Seismic reflection profiles from the continental slope offshore Mauritania, showing the *'hydrate wedge'* (HW) (left). The BSR (i.e. the BGHSZ) becomes progressively shallower along the slope until it pierces the seabed (SB). In the crossline (i.e. parallel to the shelf-break) (right), it is possible to see that the free gas irregularly accumulates in patches beneath the GHSZ (modified after Davies *et al.*, 2015). The purple and the green vertical lines show, respectively, the traces of the sections shown on the right and on the left. **(b)** Bathymetric map showing a pockmark field developed above the *'hydrate wedge'* on the continental slope offshore Svalbard. The inset topographic profile follows the yellow line, from N (left) to S (right), and indicates an irregular seafloor surface, with two main pockmarks (P) (modified after Rajan *et al.*, 2012).

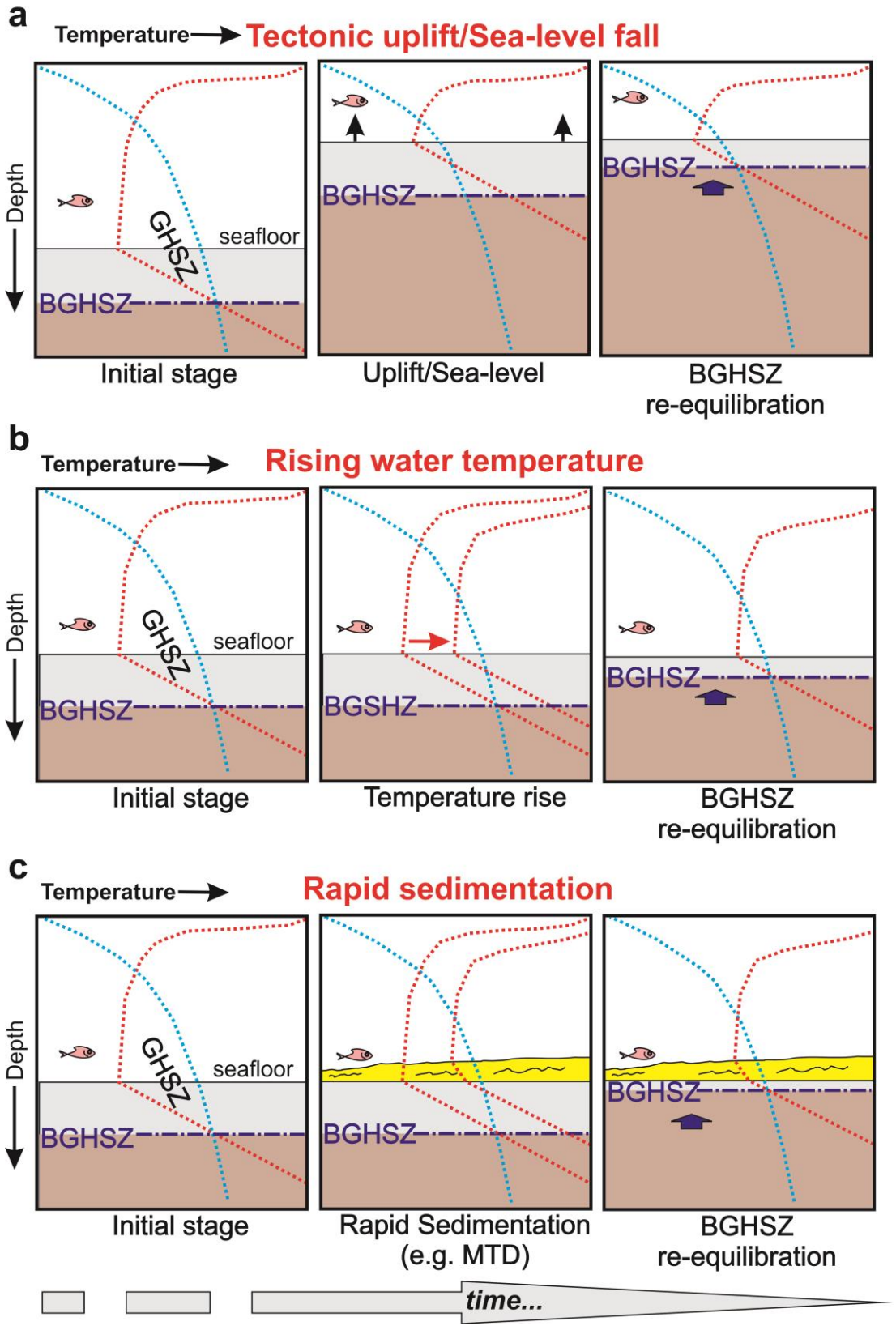



**Figure 1.30.** Schematic cartoons, showing the processes that can shift the BGHSZ at new equilibrium conditions. The blue-dotted curves represent the hydrate phase boundary whereas the red-dotted curves represent thermal gradients. **(a)** Re-equilibration after a tectonic uplift or a sea level fall. **(b)** Re-equilibration after an increase in the water temperature. **(c)** Re-equilibration after a rapid sedimentation event (e.g. an MTD) (modified after Bangs *et al.*, 2005).

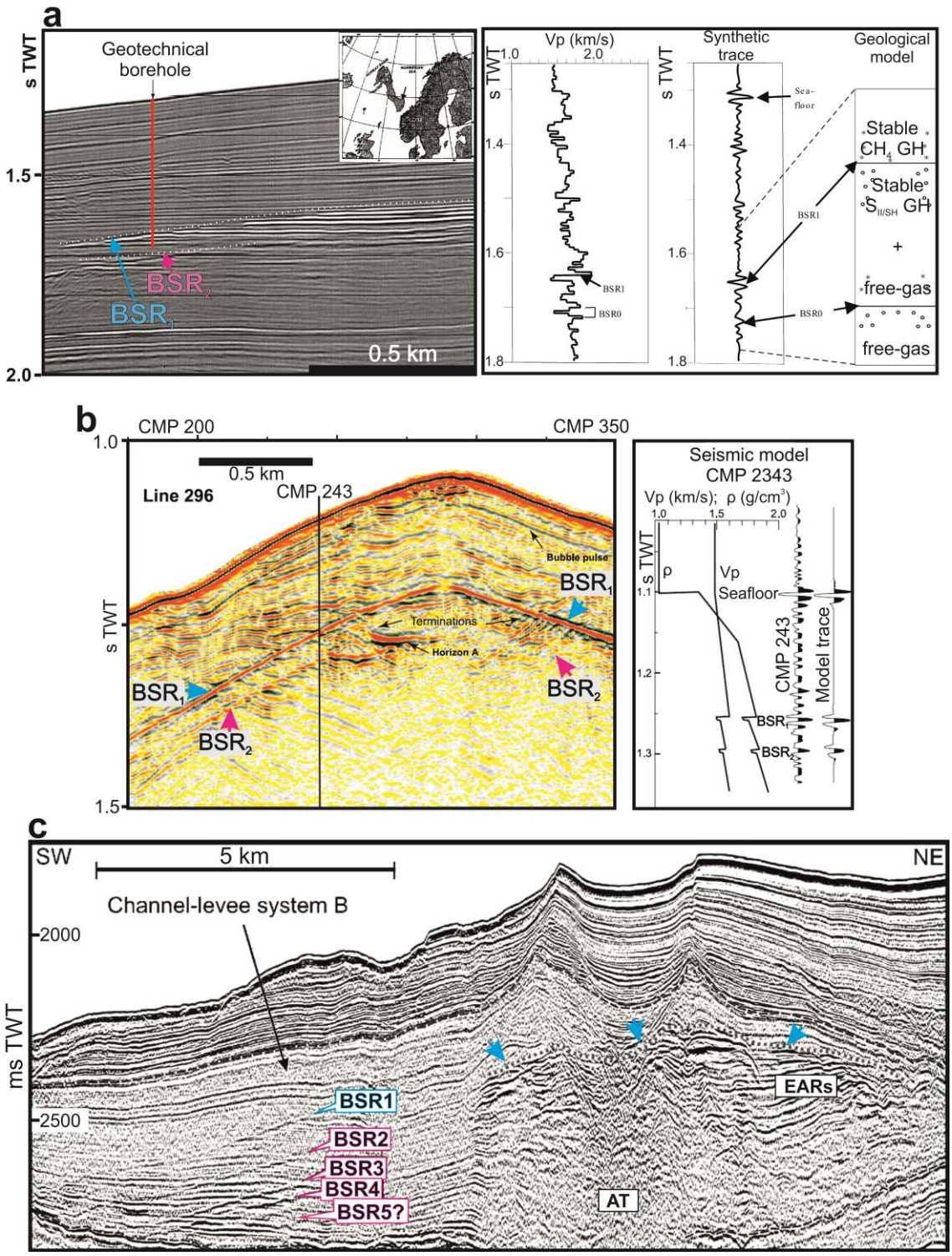



**Figure 1.31. (a)** Multiple BSRs along the Norwegian margin. A seismic reflection profile is shown on the left, with two BSRs ($BSR_1$ and $BSR_2$), indicated by a blue and a purple arrow, respectively. The modelled seismic velocity of the sediments, a synthetic seismogram and the geological interpretation are shown on the right. The BSRs are interpreted as the BGHSZ for different hydrate structures (modified after Andreassen *et al.*, 2000). **(b)** Multiple BSRs at the Hydrate Ridge (Cascadia margin). Two BSRs have been identified in seismic reflection data (left). Seismic model, compared with the real seismic trace at CMP 243, highlighting that the two BSRs are likely due to P-wave velocity decreases with respect to a normal trend. Here, the BSRs are interpreted to reflect the climate changes which followed the Last Glacial Maximum (modified after Bangs *et al.*, 2005). **(c)** Multiple BSRs in the Danube Fan (Black Sea). Five BSRs ($BSR_{1-5}$) are identified in seismic reflection data and have been interpreted to indicate multiple shifts in the BGHSZ. Similarly to the Hydrate Ridge, these BSRs are thought to reflect climate variations. EARs= enhanced amplitude reflections; AT= acoustic turbidity (modified after Popescu *et al.*, 2006).

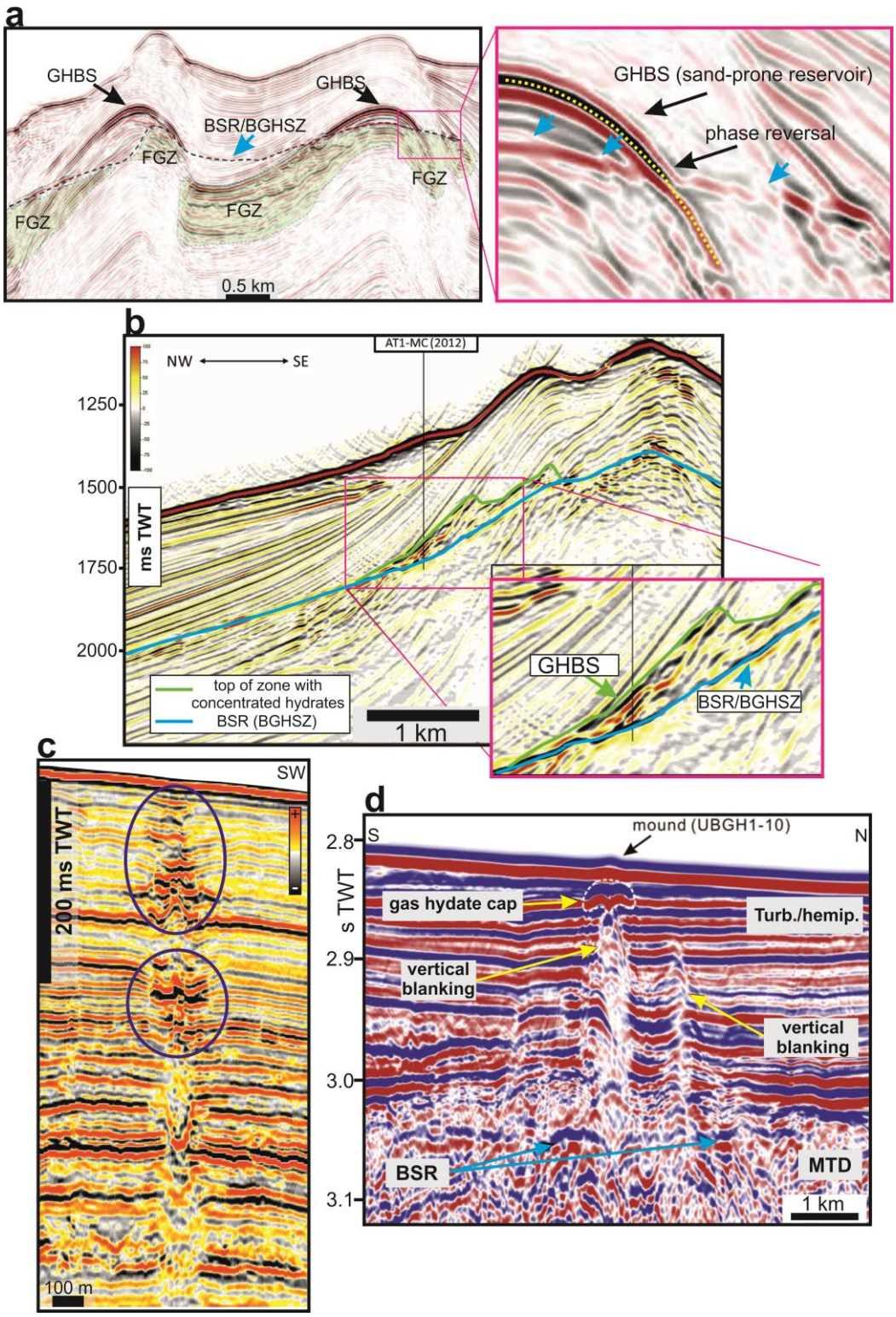



**Figure 1.32.** Examples of seismically visible gas hydrate-bearing sediments (GHBS) at high saturation. **(a)** Example from a fold and thrust belt in a compressive margin. A phase-reversal (or polarity reversal) is identified at the BSR (i.e. the BGHSZ). The high amplitudes along the stratigraphic reflections are maintained within the GHSZ and suggest the presence, above an FGZ, of hydrates at high saturation within carrier beds, probably representing sand-prone lithologies (modified after Boswell *et al.*, 2016). **(b)** Concentrated zone of gas hydrate accumulation at the Daini-Atsumi Knoll (Nankai Trough). A green line indicates the top of this zone (modified after Fujii *et al.*, 2015). **(c)** Possible zones with concentrated hydrates and authigenic carbonates (blue circles), expressed as high amplitude anomalies, along a fluid-escape pipe in the Lower Congo Basin (offshore Angola) (modified after Ho *et al.*, 2012). **(d)** High amplitude anomaly at the top of a fluid-escape pipe in the Ulleung Basin (Site UBGH1-10), interpreted as a buried massive gas hydrate mound (modified after Chun *et al.*, 2011). FGZ= free gas zone; MTD= mass-transport deposit.

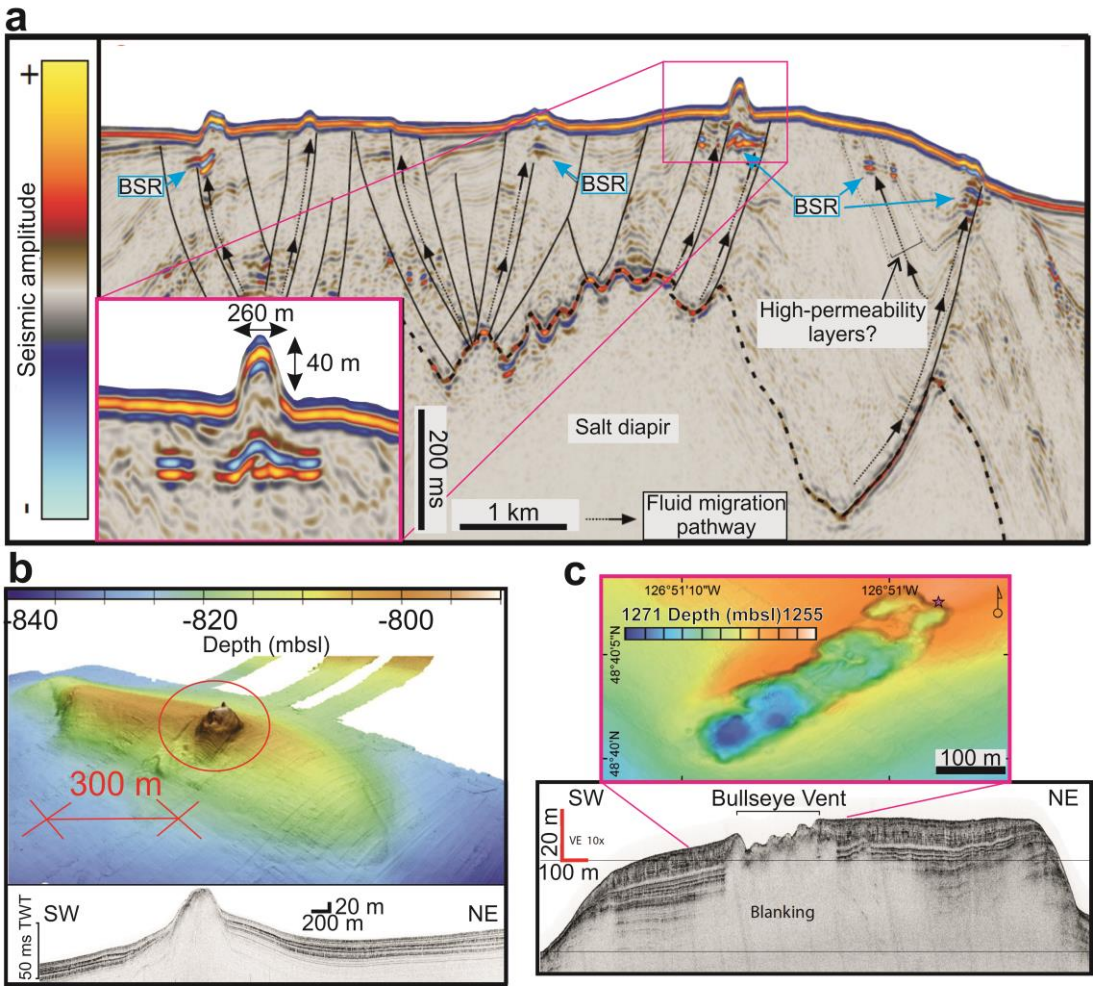



**Figure 1.33. (a)** Gas hydrate pingoes, imaged in seismic reflection data in the Kwanza Basin (offshore Angola) (modified after Serié *et al.*, 2012). **(b)** and **(c)** High-resolution multibeam bathymetry maps and chirp seismic reflection profiles, acquired in the Santa Monica Basin (offshore California) **(b)** and at the Hydrate Ridge (Cascadia margin) **(c)**, respectively showing a gas hydrate pingo and a depression. Both these seafloor morphologies are diagnostic for a gas hydrate system characterised by methane seepage and possible hydrate occurrence at the seafloor (Paull *et al.*, 2008a and 2015).

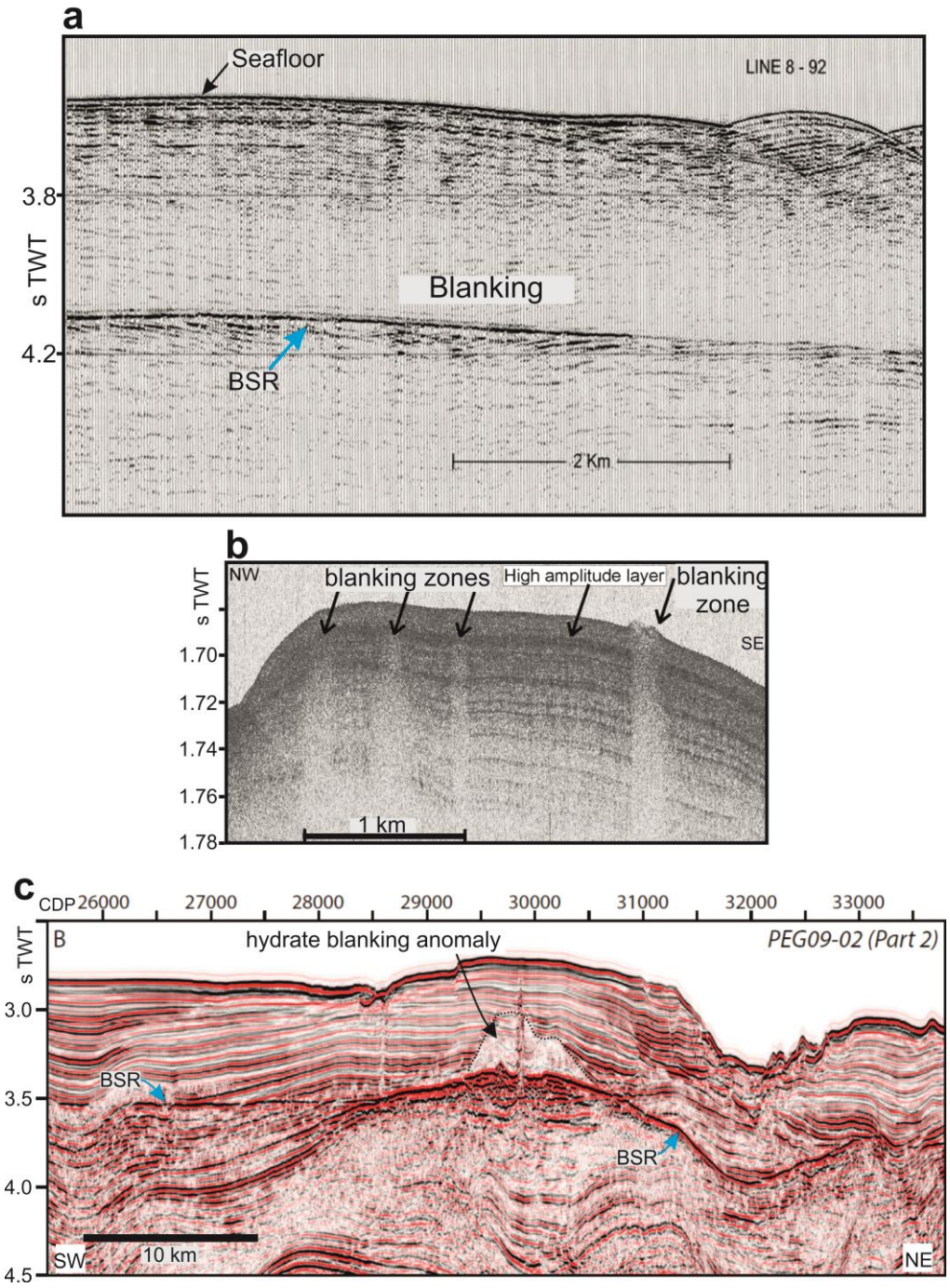



**Figure 1.34.** Examples of blanking in NGHSs. **(a)** Blanking within the GHSZ at the crest of the Blake Ridge (Lee and Dillon, 2001). **(b)** Blanking associated with vertical fluid-escape pipes offshore Vancouver Island (Cascadia margin) (Riedel *et al.*, 2002). **(c)** Blanking at the margins of a fluid-escape pipe in the Pegasus Basin (Hikurangi margin) (Fraser *et al.*, 2016).

## 1.8. Other geophysical methods: CSEM surveys

In addition to seismic techniques, other large-scale geophysical methods can detect and quantify sediment-hosted gas hydrates. For example, the use of large-scale electromagnetic surveys can reveal resistivity anomalies in the shallow subsurface. Successful controlled-source marine electromagnetic (CSEM) methods have been applied in some of the best-known gas hydrate provinces (e.g. the Blake Ridge, the Cascadia margin, the Hikurangi margin and the Norwegian margin).

The CSEM method is based on the acquisition of the electric field of the investigated section of overburden, with an electric dipole transmitter and various receivers, at different frequencies and ranges, **(Fig.1.35)**. Although the BSR cannot be imaged with this technique because both hydrates and free gas are electrical insulators, the vertical extent of the GHSZ can be assessed by integrating CSEM methods with seismic data. Then, hydrate saturation can be estimated from the resistivity anomalies. Importantly, this approach has been used to constrain the internal character of complex fluid flow features like fluid-escape pipes/chimneys (e.g. Schwalenberg *et al.*, 2010; Weitemeyer and Constable, 2010; Attias *et al.*, 2016). These features have been shown to be highly resistive and therefore likely associated with elevated concentrations of gas hydrates (Attias *et al.*, 2016). CSEM surveys also imaged the occurrence of GHBS in areas lacking BSRs (Yuan and Edwards, 2000; Schwalenberg *et al.*, 2005). Finally, this method permits to map the distribution of seafloor resistive features, like mounds and faults, which are essential components of shallow hydrocarbon plumbing systems (Ellis *et al.*, 2008).

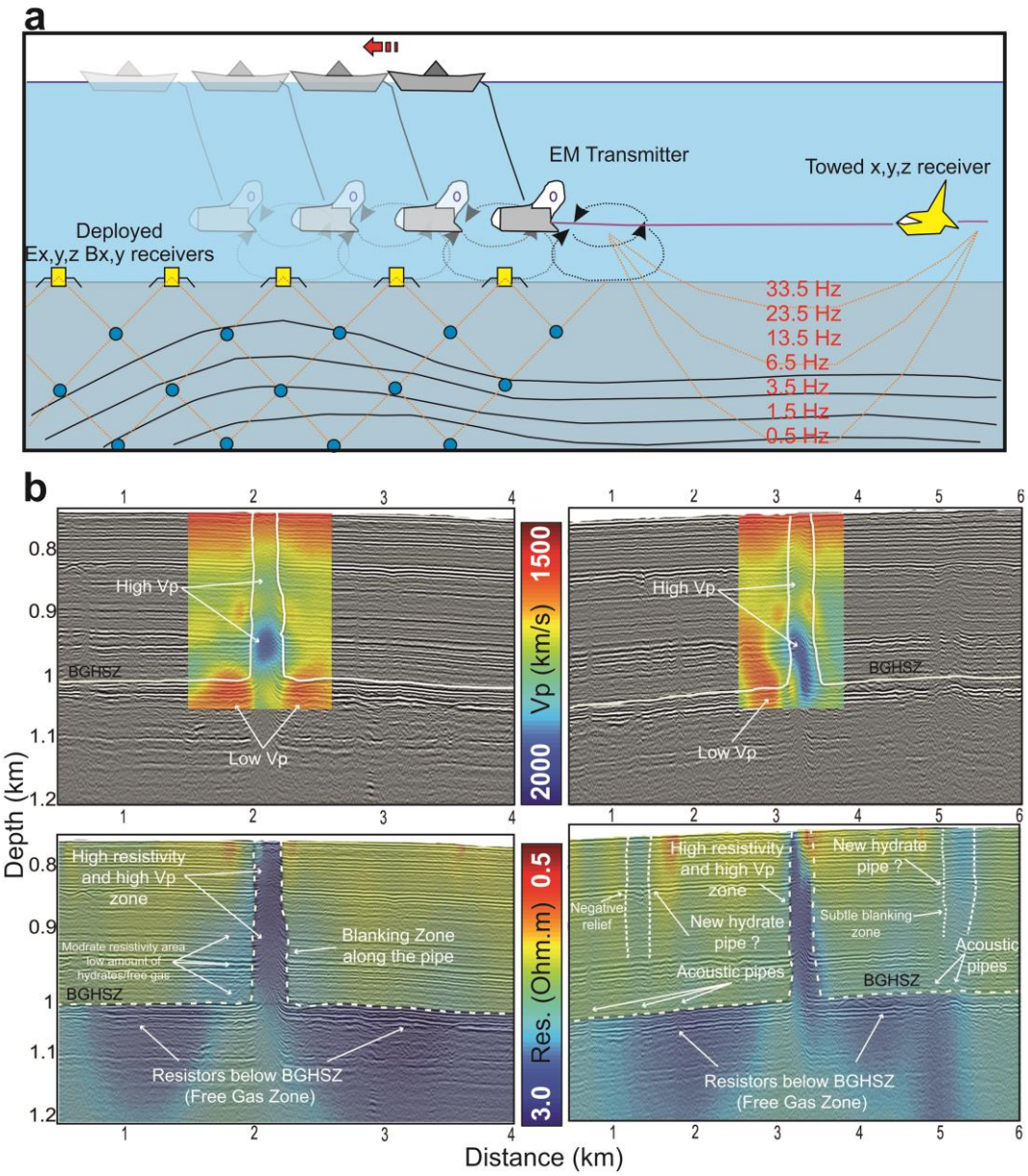



**Figure 1.35. (a)** Schematic representation of a marine CSEM system. The receivers can be placed either at the seafloor or follow the transmitter, which can work at different frequencies (modified after Weitemeyer and Constable, 2010). **(b)** Velocity inversion results (upper sections) used to constrain the results from a CSEM survey (lower section), carried out offshore Norway, in a gas hydrate province characterised by fluid-escape pipes. Note that the pipes have zones of high velocity and resistivity, suggesting the presence of hydrates. Below the base of the gas hydrate stability zone (BGHSZ), a zone of low velocity and high resistivity indicates free gas (Attias *et al.*, 2016).

## 1.9. The importance of natural gas hydrates

Natural gas hydrates probably constitute the largest organic carbon reservoir on Earth. The most recent estimates suggest that the global amount of methane at standard temperature and pressure stored within hydrates is in the order of $10^{15}$-$10^{16}$ $m^3$ (or $10^2$-$10^4$ Gt of carbon). This volume is at least a few times greater than the world's conventional gas endowment (e.g. Milkov, 2004; Archer *et al.*, 2009; Boswell and Collett, 2011; Burwicz *et al.*, 2011; Piñero *et al.*, 2013). Therefore, natural gas hydrates represent:

**(1)** An important reservoir in the global carbon cycle, in terms of volumes and geochemical processes at the solid-liquid-gas interfaces, within the GHSZ and at its boundaries. For these reasons, gas hydrates have been invoked to take part, actively and passively, in many short- and long-term processes linked to past climate changes (Hesselbo *et al.*, 2000; Kennett *et al.*, 2000; Dickens, 2003; Jenkyns, 2003; Maslin *et al.*, 2004; Majorowicz *et al.*, 2014). Additionally, researchers have argued that the present-day global warming could affect the hydrate stability, particularly along the continental shelves at high latitudes and in permafrost regions (Archer, 2007; Ruppel, 2011; Frederick and Buffett, 2014; Phrampus *et al.*, 2014; Andreassen *et al.*, 2017; Serov *et al.*, 2017).

**(2)** A potential energy resource, especially for countries like India, China, Japan and the United States which either do not have high amounts of conventional hydrocarbon resources or have high energy demand (Sloan Jr, 2003; Collett *et al.*, 2009; Boswell and Collett, 2011; Koh *et al.*, 2012). Natural gas production from hydrates has been tested in the North America Arctic permafrost (Mallik and Mount Elbert sites) and offshore, in the Nankai Trough (Daini-Atsumi Knoll site) and the South China Sea (Shenhu area). Methane production from hydrates and has been further successful in the Messoyakha Field in the Siberian permafrost. In all these cases, the depressurisation of the reservoir

was the preferred production technique (Moridis *et al.*, 2004 and 2011; Collett *et al.*, 2009; Makogon and Omelchenko, 2013; Fujii *et al.*, 2015).

**(3)** A potential geohazard which is natural, if associated with hydrate dissociation or dissolution in response to geological and climate-related events (e.g. fluid flow and overpressure, sediment loading, earthquakes, sea level drops, global warming). The geohazard can further be operational if connected with drilling through the GHSZ. Drilling may impact the geotechnical properties of the sediments, as well as the in-situ pressure and temperature. Thus, it could induce small or large-scale failures and gas blowouts (Hovland and Gudmestad, 2001; Maslin *et al.*, 2004; Sultan *et al.*, 2004; Mienert *et al.*, 2005; McConnell *et al.*, 2012; Wegner and Campbell, 2014).

**(4)** An indicator for the occurrence of deeper conventional petroleum systems and reservoirs. The study of NGHSs can provide evidence of the processes of hydrocarbon leakage from deep sources, as well as information on the hydrocarbons trapped in deeper conventional accumulations (e.g. Sassen *et al.*, 2001b and d; Warren *et al.*, 2010; Ruffine *et al.*, 2013).

The evaluation of natural gas hydrates as a future energy resource requires the understanding of the relation between the different types of hydrate morphologies and the host lithology, as well as their volumetric importance. It is accepted that the majority of the gas trapped within hydrates is hosted in fine-grained sediments, disseminated in the pore space. In contrast, a smaller but largely unquantified percentage is thought to be stored in fine-grained reservoirs with grain-displacing morphologies, within the pore space of porous lithologies, or as massive hydrate outcrops at the seafloor. This relation between hydrate morphologies and relative abundances defines the *'hydrate resource pyramid'* (**Fig. 1.36a**), where the most abundant morphologies are also the most difficult to recover and exploit.

The quality of a gas hydrate reservoir can be intuitively evaluated by plotting the intrinsic reservoir permeability against *Sh* (Boswell and Collett, 2006; Boswell and Collett, 2011; Boswell *et al.*, 2016). In this plot (**Fig. 1.36b**), assuming an adequate methane supply,

the pore-filling morphologies (**A**, **B**) are represented by a relatively straight zone of increasing *Sh* with increasing intrinsic reservoir permeability. Where the limiting factor is the intrinsic permeability, the hydrate morphology will be instead grain-displacing, and such hydrate deposits will plot in the lower portion of this graph (**C**). In contrast, if the limiting factor is the methane flux, it is possible to encounter reservoirs with lower *Sh* than permitted by their intrinsic quality (**D**). A similar plot has been constructed with real data in **Fig. 1.36c**, where the sand content approximates the reservoir quality. The zones indicating a low charge (i.e. a scarce methane supply) can result from a limited methane generation potential in the sourcing intervals or absence of permeable pathways that connect the reservoirs with the methane sources. Conversely, moderately high *Sh* can occur in sediments where porosity has been anomalously preserved (see **paragraph 1.4**) or within fractured mud-prone sediments, due to the presence of high fluxes of methane-rich fluids (i.e. a high charge). At a fixed rate of charge of methane-rich fluids towards the GHSZ, a linear trend of increased saturation with increased reservoir quality would be expected.

Nowadays, the gas hydrates stored within sand-rich deposits, both onshore and offshore (e.g. in the Arctic permafrost and the Nankai Trough) are of particular interest, for their relatively high reservoir quality and similarity to conventional reservoirs. All the natural gas production tests from hydrates carried out so far and planned in the future are related to this type of reservoir (Boswell *et al.*, 2011; Boswell *et al.*, 2012b; Fujii *et al.*, 2015; Boswell *et al.*, 2016). These deposits, globally, could contain up to $3 \cdot 10^{14} m^3$ of technically recoverable methane gas at standard pressure and temperature (Boswell and Collett, 2011).

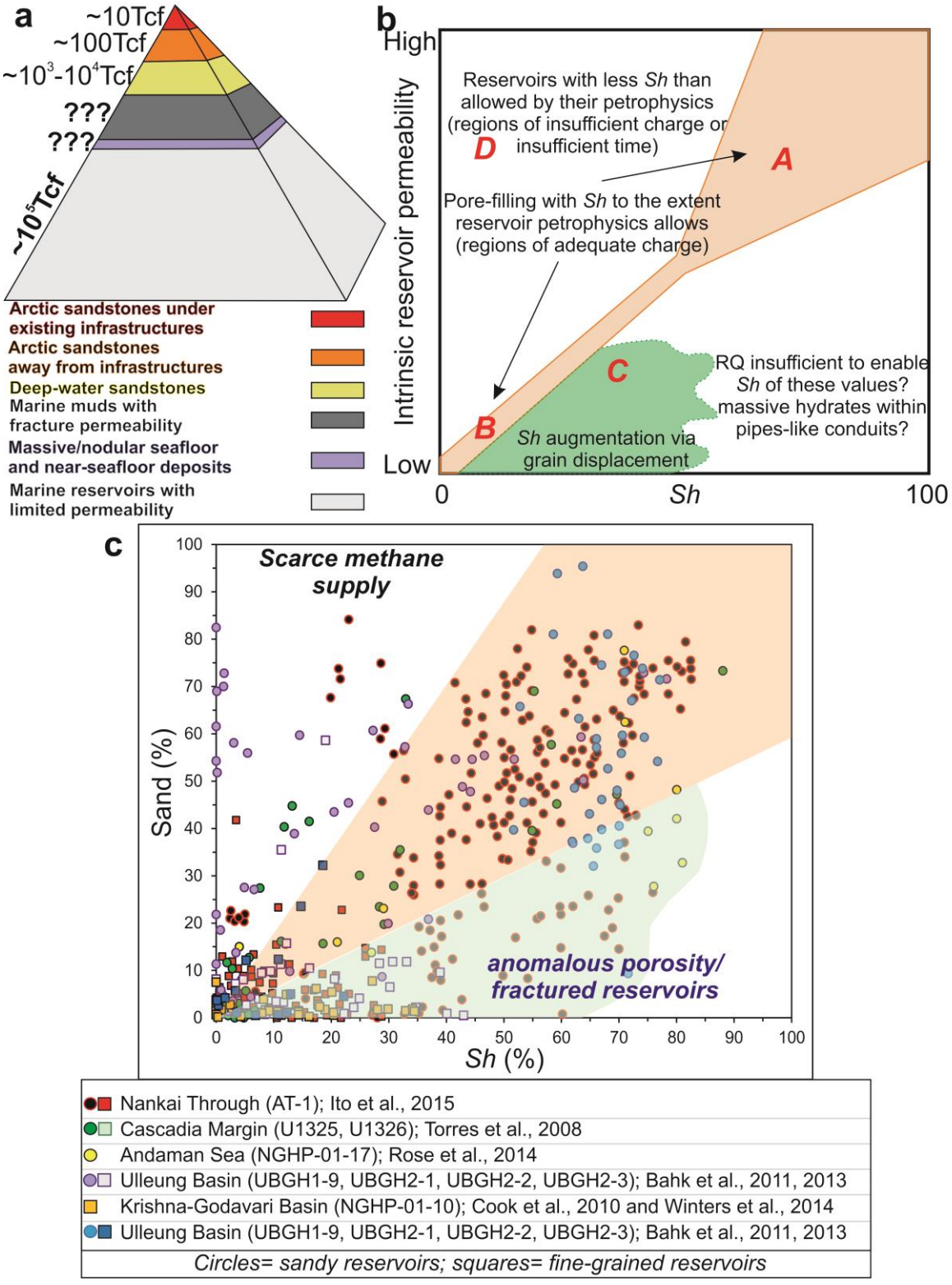



**Figure 1.36 (a)** Gas hydrate resource pyramid (modified after Boswell and Collett, 2006). Tcf= Trillion cubic feet; 1 Tcf~$2.8 \cdot 10^{10} m^3$. **(b)** Reservoir quality (i.e. intrinsic reservoir permeability) *vs Sh*. The orange area represents situations where the charge (supply of methane) is not a limiting factor, and an increase in reservoir quality is accompanied by an increase in *Sh* (A and B). The green area (C) represents hydrate reservoirs within sediments having a low intrinsic permeability (e.g. clay-rich fine-grained sediments). In a different scenario, the presence of an insufficient charge, reservoirs with high reservoir quality could have low *Sh* (D) (modified after Boswell *et al.*, 2016). **(c)** Reservoir quality (expressed as the sand content of GHBS) *vs Sh*. Similarly to **(b)**, the orange area represents situations where an increase in reservoir quality is accompanied by an increase in *Sh*. The green area represents GHBS with anomalously preserved porosity or mud-prone sediments with grain-displacing hydrates. The white area in the top-left indicates cases where the low methane charge is a limiting factor.

## 1.10. Controls on gas hydrate distribution: key topics

The previous paragraphs have reviewed the principal characteristics of natural gas hydrate systems, as well as the most common methods of detection and evaluation of gas hydrate reservoirs. Notwithstanding the enormous amount of research in this field, there are still elements that require a better understanding. Therefore, the objective of this thesis is to analyse the controls on gas hydrate distributions at different scales to solve or at least to focus on the following key topics:

### *1.10.1. The vertical distribution of gas hydrates*

The simplest models explaining the mechanisms of gas hydrate formation and accumulation, and their resulting vertical distribution (Xu and Ruppel, 1999; Liu and Flemings, 2007; Daigle and Dugan, 2010a), have identified two opposite end-member systems: In the former, the GHSZ is sourced by limited fluid fluxes, dominated by aqueous fluids rich in methane, which become oversaturated at the BGHSZ or above, depending on its initial concentration. In contrast, the latter system is sourced by higher fluxes of free gas and saturated pore waters, capable of creating overpressures at the BGHSZ. More recent two-dimensional models have taken into account the influence of both lithological heterogeneities and diffusion-driven concentration gradients (Chatterjee *et al.*, 2014; Nole *et al.*, 2016 and 2017).

In this thesis (**Chapter 3**), I will contribute towards a better understanding of the vertical distribution of gas hydrates, by providing evidence that hydrates can be stable below BSRs, coexisting with free gas. I will further discuss why this surprising finding can be common in certain gas hydrate provinces. The impact of vertical fluid flow pathways (**Chapter 4**), complex lithologies, like MTDs (**Chapter 5**) and dipping carrier beds (**Chapter 6**) and on the resulting hydrate distribution will also be discussed.

### *1.10.2. The coexistence between hydrates and free gas*

It is recognised that free gas can migrate throughout the GHSZ, implying the coexistence between three phases (methane as free gas, as hydrate and dissolved in the pore water). This migration is allowed by a suite of possible processes, including: **(1)** Suitable kinetics conditions, such as a rapid fluid flow; **(2)** The limitation of water supply, due to the growth of a hydrate film around a migrating gas string, for instance along a fault or a fracture system; **(3)** The local perturbation of hydrate stability due to an increase in temperature, caused either by the migration of warm fluids or to the release of heat during hydrate formation and **(4)** The local perturbation of the stability boundary conditions due to salt ion exclusion from hydrate formation (Gorman *et al.*, 2002; Tréhu *et al.*, 2004b; Liu and Flemings, 2007; Daigle and Dugan, 2010a; Smith *et al.*, 2014a):

This coexistence of three-phases frequently results in the formation of massive hydrate accumulations near the seafloor and the delivery of free gas up to the sediment-water interface, a process crucial for local and global carbon cycle dynamics and the persistence of chemosynthetic ecosystems. Seismically, the zones of gas migration throughout the GHSZ are imaged as fluid escape-pipes/chimneys. This thesis provides new seismic examples of multi-phase fluid flow across the GHSZ (**Chapters 4** and **6**), as well as evidence of the coexistence of free gas and hydrates *'at equilibrium'* (i.e. not during a transient event of fluid flux) (**Chapter 3**).

### *1.10.3. The Geochemical changes in hydrates and free gas within the GHSZ*

The chemical composition of the gas entrapped into the hydrate cage usually differs from that of the original feeding gas (see **paragraph 1.1**). This evidence comes, so far, from seafloor sampling of massive gas hydrate outcrop at seepage sites (Sassen *et al.*, 2001a). Theoretical models suggest that these geochemical modifications are influenced by the fluid flux (Chen and Cathles, 2003). However, there is little evidence of how hydrate geochemistry changes from the BGHSZ to the seafloor and laterally (e.g. Pape *et al.*, 2010a).

The following chapters (**Chapters 3-5**) will show examples of vertical and lateral geochemical changes across the GHSZ in a system dominated by thermogenic fluxes. It will be demonstrated that these geochemical variations are responsible for a change in the hydrate structure within a zone of hydrate occurrence. The impact of fluid flux on these geochemical changes will also be discussed. The geochemical sampling at the seafloor has recently become a routine process in the evaluation of petroleum systems, but such sampling needs to account for the geochemical modifications which affect migrating hydrocarbons.

### *1.10.4. The impact of focused fluid flow on hydrate distribution and the triggering events*

The presence of focused routes for fluid flow towards and across the GHSZ is an essential control on gas hydrate distribution (e.g. Crutchley *et al.*, 2013; Crutchley *et al.*, 2015; Fraser *et al.*, 2016). In this work, I will show examples that indicate how both **(1)** vertical fluid flow pathways and **(2)** stratigraphic heterogeneities control hydrocarbon migration and the resulting architecture of the hydrate reservoir (**Chapters 4-6**). I will discuss how the mutual importance of these two factors change laterally and I provide evidence of the impact of fluid flow on hydrate accumulation in high- and low-permeability reservoirs. Tectonic movements, sedimentation and sea level fluctuations can profoundly impact the dynamics of hydrocarbon migration (Plaza-Faverola *et al.*, 2011; Riboulot *et al.*, 2013 and 2014). For this reason, the triggering processes for fluid flow are discussed as well (**Chapters 4** and **7**).

### *1.10.5. The physical mechanisms of hydrocarbon migration*

An adequate supply of hydrocarbon gases is crucial for hydrate formation. Understanding the physical mechanism of gas migration can allow a better prediction of the resulting hydrate distribution. So far, a range of processes has been recognised although, in many cases, there is uncertainty around the dominant mechanism in a given system. Gas hydrates can be sourced either internally (i.e. from within the GHSZ), through in-situ

methane generation processes, or from deeper sources, by either a short- or a long-range advection (Crutchley *et al.*, 2015; Malinverno and Goldberg, 2015; Nole *et al.*, 2016). The observation and the interpretation of the processes at the interfaces, i.e. at the BGHSZ, is crucial to get better insights into these fluid supply dynamics. This thesis will discuss how the supply processes impact hydrate distribution (**Chapters 4-6**). The predominance of one process above the others has a dramatic lateral km-scale variability and further changes from the km-scale to the pore-scale.

### *1.10.6. The role of free gas in influencing gas hydrate distribution and the sealing capacity of gas hydrate-bearing sediments*

The common observation of free gas reservoirs associated with NGHSs suggests a relationship between the gas hydrate accumulations and the underlying free gas. How the free gas distribution affects the overlying hydrate accumulations? Is the FGZ at a critical pressure state and sealed beneath GHBS? These questions have received attention in the last years (e.g. Flemings *et al.*, 2003; Hornbach *et al.*, 2004; Haacke *et al.*, 2007; Plaza-Faverola *et al.*, 2012a). A common belief recognises substantial differences between the FGZ in active and in passive margins (Hornbach *et al.*, 2004; Haacke *et al.*, 2007). In this work, I suggest that more local km-scale processes can challenge this simplistic view. I provide seismic evidence of a buoyant free gas accumulation mechanically trapped beneath the BGHSZ (**Chapter 6**). Finally, I review the role of the BGHSZ as a sealing interface for the underlying free gas, as well as the processes leading to hydrocarbon migration throughout the GHSZ (**Chapter 7**).

# 1.11. Appendix: geochemistry of gas hydrates

| Reference | Basin | Site/ Sample and hydrate habit | Depth (mbsf) | $C_1/C_{2+}$ | $\delta^{13}C$ of $C_1$ (‰) | $\delta D$ of $C_1$ (‰) |
|---|---|---|---|---|---|---|
| Milkov *et al.* (2005) | Hydrate Ridge, Cascadia margin | ODP 204, 1244-C, Hydrate-bound gas, pore-filling hydrates | 65.0 | 24999.0 | -67.1 | - |
| | Hydrate Ridge, Cascadia margin | ODP 204, 1244-C, Hydrate-bound gas, pore-filling hydrates | 85.0 | 49999.0 | -69.5 | - |
| | Hydrate Ridge, Cascadia margin | ODP 204, 1244-E, Hydrate-bound gas, pore-filling hydrates | 50.0 | 49999.0 | - | - |
| | Hydrate Ridge, Cascadia margin | ODP 204, 1244-E, Hydrate-bound gas, pore-filling hydrates | 74.2 | 49999.0 | -68.3 | -208.0 |
| | Hydrate Ridge, Cascadia margin | ODP 204, 1245-B, Hydrate-bound gas, pore-filling hydrates | 54.5 | 49770.0 | -69.1 | -203.0 |
| | Hydrate Ridge, Cascadia margin | ODP 204, 1245-B, Hydrate-bound gas, pore-filling hydrates | 85.0 | 49880.0 | -67.5 | -188.0 |
| | Hydrate Ridge, Cascadia margin | ODP 204, 1245-C, Hydrate-bound gas, pore-filling hydrates | 53.4 | 50000.0 | - | - |
| | Hydrate Ridge, Cascadia margin | ODP 204, 1245-C, Hydrate-bound gas, pore-filling hydrates | 101.4 | 49806.0 | -67.8 | -205.0 |
| | Hydrate Ridge, Cascadia margin | ODP 204, 1245-C, Hydrate-bound gas, pore-filling hydrates | 105.1 | 33170.0 | -68.2 | - |
| | Hydrate Ridge, Cascadia margin | ODP 204, 1247-B, Hydrate-bound gas, pore- and fracture-filling hydrates (Seep site) | 93.0 | 24999.0 | -70.0 | -202.0 |
| | Hydrate Ridge, Cascadia margin | ODP 204, 1248-B, Hydrate-bound gas, pore- and fracture-filling hydrates (Seep site) | 0.5 | 536.1 | -68.1 | -202.0 |
| | Hydrate Ridge, Cascadia margin | ODP 204, 1248-B, Hydrate-bound gas, pore- and fracture-filling hydrates (Seep site) | 2.0 | - | -67.1 | - |
| | Hydrate Ridge, Cascadia margin | ODP 204, 1248-B, Hydrate-bound gas, pore- and fracture-filling hydrates (Seep site) | 2.2 | 530.3 | -67.2 | - |
| | Hydrate Ridge, Cascadia margin | ODP 204, 1248-B, Hydrate-bound gas, pore- and fracture-filling hydrates (Seep site) | 7.4 | 95.9 | -66.2 | - |
| | Hydrate Ridge, Cascadia margin | ODP 204, 1248-C, Hydrate-bound gas, pore- and fracture-filling hydrates (Seep site) | 1.5 | 726.5 | -65.9 | - |
| | Hydrate Ridge, Cascadia margin | ODP 204, 1248-C, Hydrate-bound gas, pore- and fracture-filling hydrates (Seep site) | 2.2 | 564.3 | -66.1 | - |
| | Hydrate Ridge, Cascadia margin | ODP 204, 1248-C, Hydrate-bound gas, pore- and fracture-filling hydrates (Seep site) | 22.4 | 733.6 | -67 | -193.0 |
| | Hydrate Ridge, Cascadia margin | ODP 204, 1248-C, Hydrate-bound gas, pore- and fracture-filling hydrates (Seep site) | 22.4 | 724.4 | - | - |
| | Hydrate Ridge, Cascadia margin | ODP 204, 1248-C, Hydrate-bound gas, pore- and fracture-filling hydrates (Seep site) | 49.7 | 1991.3 | - | - |
| | Hydrate Ridge, Cascadia margin | ODP 204, 1248-C, Hydrate-bound gas, pore- and fracture-filling hydrates (Seep site) | 74.6 | 2924.9 | -66.3 | - |
| | Hydrate Ridge, Cascadia margin | ODP 204, 1248-C, Hydrate-bound gas, pore- and fracture-filling hydrates (Seep site) | 74.6 | 2687.8 | - | - |
| | Hydrate Ridge, Cascadia margin | ODP 204, 1248-C, Hydrate-bound gas, pore- and fracture-filling hydrates (Seep site) | 87.0 | 1876.5 | -67.8 | -204.0 |
| | Hydrate Ridge, Cascadia margin | ODP 204, 1248-C, Hydrate-bound gas, pore- and fracture-filling hydrates (Seep site) | 38.3 | 280.9 | -64.8 | - |
| | Hydrate Ridge, Cascadia margin | ODP 204, 1248-C, Hydrate-bound gas, pore- and fracture-filling hydrates (Seep site) | 1.1 | 1059.7 | -66.2 | - |
| | Hydrate Ridge, Cascadia margin | ODP 204, 1248-C, Hydrate-bound gas, pore- and fracture-filling hydrates (Seep site) | 2.0 | 808.7 | -65.3 | - |
| | Hydrate Ridge, Cascadia margin | ODP 204, 1248-C, Hydrate-bound gas, pore- and fracture-filling hydrates (Seep site) | 2.0 | 489.8 | -63.3 | - |
| | Hydrate Ridge, Cascadia margin | ODP 204, 1248-C, Hydrate-bound gas, pore- and fracture-filling hydrates (Seep site) | 5.0 | - | -66.4 | - |
| | Hydrate Ridge, Cascadia margin | ODP 204, 1248-C, Hydrate-bound gas, pore- and fracture-filling hydrates (Seep site) | 6.1 | 588.3 | -67.0 | -200.0 |
| | Hydrate Ridge, Cascadia margin | ODP 204, 1248-C, Hydrate-bound gas, pore- and fracture-filling hydrates (Seep site) | 18.0 | 562.1 | -66.0 | - |
| | Hydrate Ridge, Cascadia margin | ODP 204, 1248-C, Hydrate-bound gas, pore- and fracture-filling hydrates (Seep site) | 19.6 | 269.3 | -65.4 | - |
| | Hydrate Ridge, Cascadia margin | ODP 204, 1248-C, Hydrate-bound gas, pore- and fracture-filling hydrates (Seep site) | 20.8 | 426.6 | - | - |
| | Hydrate Ridge, Cascadia margin | ODP 204, 1249-D, Hydrate-bound gas, pore- and fracture-filling hydrates (Seep site) | 2.1 | 621.1 | -68.0 | - |
| | Hydrate Ridge, Cascadia margin | ODP 204, 1249-D, Hydrate-bound gas, pore- and fracture-filling hydrates (Seep site) | 10.5 | 699.0 | -66.8 | - |
| | Hydrate Ridge, Cascadia margin | ODP 204, 1249-E, Hydrate-bound gas, pore- and fracture-filling hydrates (Seep site) | 0.0 | 727.1 | -68.0 | - |
| | Hydrate Ridge, Cascadia margin | ODP 204, 1249-E, Hydrate-bound gas, pore- and fracture-filling hydrates (Seep site) | 10.3 | 962.5 | -65.3 | - |
| | Hydrate Ridge, Cascadia margin | ODP 204, 1249-F, Hydrate-bound gas, pore- and fracture-filling hydrates (Seep site) | 0.0 | 897.9 | -68.0 | - |
| | Hydrate Ridge, Cascadia margin | ODP 204, 1249-F, Hydrate-bound gas, pore- and fracture-filling hydrates (Seep site) | 2.0 | | -67.2 | - |
| | Hydrate Ridge, Cascadia margin | ODP 204, 1249-F, Hydrate-bound gas, pore- and fracture-filling hydrates (Seep site) | 16.1 | 597.2 | -63.2 | -198.0 |
| | Hydrate Ridge, Cascadia margin | ODP 204, 1249-F, Hydrate-bound gas, pore- and fracture-filling hydrates (Seep site) | 16.3 | - | -63.2 | - |
| | Hydrate Ridge, Cascadia margin | ODP 204, 1249-F, Hydrate-bound gas, pore- and fracture-filling hydrates (Seep site) | 17.6 | 349.3 | -64.2 | - |

| | | | | | | |
|---|---|---|---|---|---|---|
| | Hydrate Ridge, Cascadia margin | ODP 204, 1249-F, Hydrate-bound gas, pore- and fracture-filling hydrates (Seep site) | 17.6 | 267.1 | - | - |
| | Hydrate Ridge, Cascadia margin | ODP 204, 1249-F, Hydrate-bound gas, pore- and fracture-filling hydrates (Seep site) | 17.7 | - | -64.6 | - |
| | Hydrate Ridge, Cascadia margin | ODP 204, 1249-F, Hydrate-bound gas, pore- and fracture-filling hydrates (Seep site) | 32.9 | - | -66.4 | - |
| | Hydrate Ridge, Cascadia margin | ODP 204, 1249-F, Hydrate-bound gas, pore- and fracture-filling hydrates (Seep site) | 33.0 | 425.9 | -63.5 | - |
| | Hydrate Ridge, Cascadia margin | ODP 204, 1250-C, Hydrate-bound gas, pore- and fracture-filling hydrates (Seep site) | 1.4 | 1159.7 | -66.0 | - |
| | Hydrate Ridge, Cascadia margin | ODP 204, 1250-C, Hydrate-bound gas, pore- and fracture-filling hydrates (Seep site) | 1.4 | 1108.5 | - | - |
| | Hydrate Ridge, Cascadia margin | ODP 204, 1250-C, Hydrate-bound gas, pore- and fracture-filling hydrates (Seep site) | 6.5 | 1507.2 | -64.8 | -194.0 |
| | Hydrate Ridge, Cascadia margin | ODP 204, 1250-C, Hydrate-bound gas, pore- and fracture-filling hydrates (Seep site) | 86.7 | 24854.5 | -67.4 | - |
| | Hydrate Ridge, Cascadia margin | ODP 204, 1250-C, Hydrate-bound gas, pore- and fracture-filling hydrates (Seep site) | 92.5 | - | -66.8 | - |
| | Hydrate Ridge, Cascadia margin | ODP 204, 1250-D, Hydrate-bound gas, pore- and fracture-filling hydrates (Seep site) | 1.0 | 1329.4 | -65.5 | -193.0 |
| | Hydrate Ridge, Cascadia margin | ODP 204, 1250-D, Hydrate-bound gas, pore- and fracture-filling hydrates (Seep site) | 1.6 | 1159.5 | -65.6 | -193.0 |
| | Hydrate Ridge, Cascadia margin | ODP 204, 1250-D, Hydrate-bound gas, pore- and fracture-filling hydrates (Seep site) | 1.6 | 1026.8 | - | - |
| | Hydrate Ridge, Cascadia margin | ODP 204, 1250-D, Hydrate-bound gas, pore- and fracture-filling hydrates (Seep site) | 1.6 | 1185.2 | - | - |
| | Hydrate Ridge, Cascadia margin | ODP 204, 1250-D, Hydrate-bound gas, pore- and fracture-filling hydrates (Seep site) | 81.5 | 49742.0 | -69.4 | -200.0 |
| | Hydrate Ridge, Cascadia margin | ODP 204, 1250-F, Hydrate-bound gas, pore- and fracture-filling hydrates (Seep site) | 100.2 | 33238.3 | -70.2 | -202.0 |
| Whiticar *et al.* (1995); Kastner *et al.* (1998) | Hydrate Ridge, Cascadia margin | ODP 146, 892-A, pure massive/macrocrystalline hydrate (rich in $H_2S$) | 3.7 | 999.3 | -64.8 | - |
| | Hydrate Ridge, Cascadia margin | ODP 146, 892-A., pure massive/macrocrystalline hydrate (rich in $H_2S$) | 17.0 | 1749.0 | -66.0 | -198.0 |
| Pohlman *et al.* (2005) | Northern Cascadia margin | Barkley Canyon, massive hydrate at the seafloor (hydrate pingo) | 0.0 | 5.7 | -43.4 | -143.0 |
| | Northern Cascadia margin | Barkley Canyon, massive hydrate at the seafloor (hydrate pingo) | 0.0 | 4.5 | -42.6 | -139.0 |
| | Northern Cascadia margin | Barkley Canyon, massive hydrate at the seafloor (hydrate pingo) | 0.0 | 5.4 | -42.9 | -138.0 |
| | Northern Cascadia margin | Barkley Canyon, massive hydrate at the seafloor (hydrate pingo) | 0.0 | 2.1 | -42.7 | -140.0 |
| Pohlman *et al.* (2009b) | Northern Cascadia margin | IODP 311, U1325, void gas from hydrate-bearing intervals (cf. Malinverno et al., 2008). Pore-filling hydrates. | 74.9 | 156800.0 | -71.2 | - |
| | Northern Cascadia margin | IODP 311, U1325, void gas from hydrate-bearing intervals. Pore-filling hydrates. | 80.8 | 140900.0 | -72.4 | - |
| | Northern Cascadia margin | IODP 311, U1325, void gas from hydrate-bearing intervals. Pore-filling hydrates. | 85.3 | 156700.0 | -71.7 | - |
| | Northern Cascadia margin | IODP 311, U1325, void gas from hydrate-bearing intervals. Pore-filling hydrates. | 88.8 | 167000.0 | -72.1 | - |
| | Northern Cascadia margin | IODP 311, U1325, void gas from hydrate-bearing intervals. Pore-filling hydrates. | 104.4 | 128800.0 | -70.3 | - |
| | Northern Cascadia margin | IODP 311, U1325, void gas from hydrate-bearing intervals. Pore-filling hydrates. | 109.6 | 97600.0 | -71.7 | - |
| | Northern Cascadia margin | IODP 311, U1325, void gas from hydrate-bearing intervals. Pore-filling hydrates. | 114.8 | 83100.0 | -71.0 | - |
| | Northern Cascadia margin | IODP 311, U1325, void gas from hydrate-bearing intervals. Pore-filling hydrates. | 123.0 | 107900.0 | -69.9 | - |
| | Northern Cascadia margin | IODP 311, U1325, void gas from hydrate-bearing intervals. Pore-filling hydrates. | 125.8 | 83400.0 | -70.9 | - |
| | Northern Cascadia margin | IODP 311, U1325, void gas from hydrate-bearing intervals. Pore-filling hydrates. | 128.0 | 115100.0 | -70.3 | - |
| | Northern Cascadia margin | IODP 311, U1325, void gas from hydrate-bearing intervals. Pore-filling hydrates. | 131.5 | 117000.0 | -70.8 | - |
| | Northern Cascadia margin | IODP 311, U1325, void gas from hydrate-bearing intervals. Pore-filling hydrates. | 145.3 | 88700.0 | -70.9 | - |
| | Northern Cascadia margin | IODP 311, U1325, void gas from hydrate-bearing intervals. Pore-filling hydrates. | 157.6 | 105000.0 | -68.9 | - |
| | Northern Cascadia margin | IODP 311, U1325, void gas from hydrate-bearing intervals. Pore-filling hydrates. | 160.3 | 80700.0 | -70.2 | - |
| | Northern Cascadia margin | IODP 311, U1325, void gas from hydrate-bearing intervals. Pore-filling hydrates. | 179.9 | 62000.0 | -69.9 | - |
| | Northern Cascadia margin | IODP 311, U1325, void gas from hydrate-bearing intervals. Pore-filling hydrates. | 182.7 | 71800.0 | -69.3 | - |
| | Northern Cascadia margin | IODP 311, U1325, void gas from hydrate-bearing intervals. Pore-filling hydrates. | 190.7 | 104900.0 | -69.0 | - |
| | Northern Cascadia margin | IODP 311, U1325, void gas from hydrate-bearing intervals. Pore-filling hydrates. | 208.4 | 95500.0 | -69.2 | - |
| | Northern Cascadia margin | IODP 311, U1325, void gas from hydrate-bearing intervals. Pore-filling hydrates. | 210.3 | 205300.0 | -68.7 | - |
| | Northern Cascadia margin | IODP 311, U1325, void gas from hydrate-bearing intervals. Pore-filling hydrates. | 220.2 | 85100.0 | -69.2 | - |
| | Northern Cascadia margin | IODP 311, U1325, void gas from hydrate-bearing intervals. Pore-filling hydrates. | 221.7 | 82800.0 | -68.9 | - |
| | Northern Cascadia margin | IODP 311, U1325, void gas from hydrate-bearing intervals. Pore-filling hydrates. | 230.1 | 97100.0 | -68.7 | - |

| | | | | | | |
|---|---|---|---|---|---|---|
| | Northern Cascadia margin | IODP 311, U1325, void gas from hydrate-bearing intervals. Pore-filling hydrates. | 233.8 | 50500.0 | -69.0 | - |
| | Northern Cascadia margin | IODP 311, U1325, void gas from hydrate-bearing intervals. Pore-filling hydrates. | 238.9 | 61800.0 | -68.3 | - |
| | Northern Cascadia margin | IODP 311, U1326, void gas from hydrate-bearing intervals. Pore-filling hydrates. | 52.7 | 17100.0 | -73.9 | - |
| | Northern Cascadia margin | IODP 311, U1326, void gas from hydrate-bearing intervals. Pore-filling hydrates. | 70.9 | 15200.0 | -72.3 | - |
| | Northern Cascadia margin | IODP 311, U1326, void gas from hydrate-bearing intervals. Pore-filling hydrates. | 72.0 | 21000.0 | -72.0 | - |
| | Northern Cascadia margin | IODP 311, U1326, void gas from hydrate-bearing intervals. Pore-filling hydrates. | 93.6 | 40100.0 | -71.0 | - |
| | Northern Cascadia margin | IODP 311, U1326, void gas from hydrate-bearing intervals. Pore-filling hydrates. | 94.4 | 50300.0 | -71.0 | - |
| | Northern Cascadia margin | IODP 311, U1326, void gas from hydrate-bearing intervals. Pore-filling hydrates. | 103.0 | 59100.0 | -70.6 | - |
| | Northern Cascadia margin | IODP 311, U1326, void gas from hydrate-bearing intervals. Pore-filling hydrates. | 109.2 | 28700.0 | -71.1 | - |
| | Northern Cascadia margin | IODP 311, U1326, void gas from hydrate-bearing intervals. Pore-filling hydrates. | 118.7 | 26600.0 | -71.0 | - |
| | Northern Cascadia margin | IODP 311, U1326, void gas from hydrate-bearing intervals. Pore-filling hydrates. | 123.1 | 19300.0 | -70.9 | - |
| | Northern Cascadia margin | IODP 311, U1326, void gas from hydrate-bearing intervals. Pore-filling hydrates. | 129.9 | 20400.0 | -70.5 | - |
| | Northern Cascadia margin | IODP 311, U1326, void gas from hydrate-bearing intervals. Pore-filling hydrates. | 132.9 | 26200.0 | -70.3 | - |
| | Northern Cascadia margin | IODP 311, U1326, void gas from hydrate-bearing intervals. Pore-filling hydrates. | 137.7 | 33700.0 | -70.3 | - |
| | Northern Cascadia margin | IODP 311, U1326, void gas from hydrate-bearing intervals. Pore-filling hydrates. | 140.4 | 33500.0 | -70.1 | - |
| | Northern Cascadia margin | IODP 311, U1326, void gas from hydrate-bearing intervals. Pore-filling hydrates. | 148.8 | 20600.0 | -70.3 | - |
| | Northern Cascadia margin | IODP 311, U1326, void gas from hydrate-bearing intervals. Pore-filling hydrates. | 156.1 | 10700.0 | -70.3 | - |
| | Northern Cascadia margin | IODP 311, U1326, void gas from hydrate-bearing intervals. Pore-filling hydrates. | 158.2 | 16500.0 | -70.1 | - |
| | Northern Cascadia margin | IODP 311, U1326, void gas from hydrate-bearing intervals. Pore-filling hydrates. | 167.8 | 17300.0 | -69.5 | - |
| | Northern Cascadia margin | IODP 311, U1326, void gas from hydrate-bearing intervals. Pore-filling hydrates. | 177.1 | 15900.0 | -69.3 | - |
| | Northern Cascadia margin | IODP 311, U1326, void gas from hydrate-bearing intervals. Pore-filling hydrates. | 179.3 | 39600.0 | -69.4 | - |
| | Northern Cascadia margin | IODP 311, U1326, void gas from hydrate-bearing intervals. Pore-filling hydrates. | 186.5 | 22600.0 | -69.3 | - |
| | Northern Cascadia margin | IODP 311, U1326, void gas from hydrate-bearing intervals. Pore-filling hydrates. | 196.9 | 8700.0 | -70.0 | - |
| | Northern Cascadia margin | IODP 311, U1326, void gas from hydrate-bearing intervals. Pore-filling hydrates. | 198.6 | 21000.0 | -69.2 | - |
| | Northern Cascadia margin | IODP 311, U1326, void gas from hydrate-bearing intervals. Pore-filling hydrates. | 204.3 | 12000.0 | -69.6 | - |
| | Northern Cascadia margin | IODP 311, U1326, void gas from hydrate-bearing intervals. Pore-filling hydrates. | 208.4 | 16600.0 | -69.2 | - |
| | Northern Cascadia margin | IODP 311, U1326, void gas from hydrate-bearing intervals. Pore-filling hydrates. | 214.6 | 26800.0 | -68.8 | - |
| | Northern Cascadia margin | IODP 311, U1326, void gas from hydrate-bearing intervals. Pore-filling hydrates. | 217.0 | 27600.0 | -68.4 | - |
| | Northern Cascadia margin | IODP 311, U1326, void gas from hydrate-bearing intervals. Pore-filling hydrates. | 226.6 | 24800.0 | -68.7 | - |
| | Northern Cascadia margin | IODP 311, U1326, void gas from hydrate-bearing intervals. Pore-filling hydrates. | 228.7 | 23700.0 | -69.1 | - |
| | Northern Cascadia margin | IODP 311, U1326, void gas from hydrate-bearing intervals. Pore-filling hydrates. | 237.3 | 23800.0 | -68.6 | - |
| | Northern Cascadia margin | IODP 311, U1326, void gas from hydrate-bearing intervals. Pore-filling hydrates. | 244.5 | 7500.0 | -69.0 | - |
| | Northern Cascadia margin | IODP 311, U1326, void gas from hydrate-bearing intervals. Pore-filling hydrates. | 245.5 | 7500.0 | -68.8 | - |
| | Northern Cascadia margin | IODP 311, U1326, void gas from hydrate-bearing intervals. Pore-filling hydrates. | 252.3 | 6200.0 | -69.1 | - |
| | Northern Cascadia margin | IODP 311, U1327, void gas from hydrate-bearing intervals. Pore-filling hydrates. | 113.5 | 5600.0 | -58.0 | - |
| | Northern Cascadia margin | IODP 311, U1327, void gas from hydrate-bearing intervals. Pore-filling hydrates. | 128.5 | 3200.0 | -58.5 | - |
| | Northern Cascadia margin | IODP 311, U1327, void gas from hydrate-bearing intervals. Pore-filling hydrates. | 155.3 | 2100.0 | -55.5 | - |
| | Northern Cascadia margin | IODP 311, U1327, void gas from hydrate-bearing intervals. Pore-filling hydrates. | 157.0 | 1900.0 | -55.6 | - |
| | Northern Cascadia margin | IODP 311, U1327, void gas from hydrate-bearing intervals. Pore-filling hydrates. | 163.1 | 1500.0 | -55.1 | - |
| | Northern Cascadia margin | IODP 311, U1327, void gas from hydrate-bearing intervals. Pore-filling hydrates. | 172.7 | 1400.0 | -54.6 | - |
| | Northern Cascadia margin | IODP 311, U1327, void gas from hydrate-bearing intervals. Pore-filling hydrates. | 176.1 | 1100.0 | -54.3 | - |
| | Northern Cascadia margin | IODP 311, U1327, void gas from hydrate-bearing intervals. Pore-filling hydrates. | 181.9 | 1400.0 | -53.9 | - |
| | Northern Cascadia margin | IODP 311, U1327, void gas from hydrate-bearing intervals. Pore-filling hydrates. | 184.5 | 1000.0 | -54.1 | - |
| | Northern Cascadia margin | IODP 311, U1327, void gas from hydrate-bearing intervals. Pore-filling hydrates. | 191.3 | 1200.0 | -52.7 | - |

| | | | | | | |
|---|---|---|---|---|---|---|
| | Northern Cascadia margin | IODP 311, U1327, void gas from hydrate-bearing intervals. Pore-filling hydrates. | 194.1 | 1100.0 | -53.0 | - |
| | Northern Cascadia margin | IODP 311, U1327, void gas from hydrate-bearing intervals. Pore-filling hydrates. | 200.6 | 800.0 | -53.7 | - |
| | Northern Cascadia margin | IODP 311, U1327, void gas from hydrate-bearing intervals. Pore-filling hydrates. | 210.0 | 1100.0 | -52.2 | - |
| | Northern Cascadia margin | IODP 311, U1327, void gas from hydrate-bearing intervals. Pore-filling hydrates. | 214.1 | 1400.0 | -52.1 | - |
| | Northern Cascadia margin | IODP 311, U1327, void gas from hydrate-bearing intervals. Pore-filling hydrates. | 220.0 | 900.0 | -48.7 | - |
| | Northern Cascadia margin | IODP 311, U1327, void gas from hydrate-bearing intervals. Pore-filling hydrates. | 224.6 | 1100.0 | -46.9 | - |
| | Northern Cascadia margin | IODP 311, U1327, void gas from hydrate-bearing intervals. Pore-filling hydrates. | 229.8 | 900.0 | -55.2 | - |
| Pohlman *et al.* (2009a) | Northern Cascadia margin | Bullseye Vent, PGC0208. Gas hydrate sample at the seafloor (Vent site) | 0.0 | 475.2 | -64.6 | -178.0 |
| | Northern Cascadia margin | Bullseye Vent, PGC0208. Gas hydrate sample at the seafloor (Vent site) | 0.0 | 713.6 | -63.2 | -173.0 |
| | Northern Cascadia margin | Bullseye Vent, PGC0208. Gas hydrate sample at the seafloor (Vent site) | 0.0 | 302.1 | -63.8 | -175.0 |
| Riedel *et al.* (2006) | Northern Cascadia margin | Bullseye Vent, PGC00-02. Massive gas hydrate sample near the seafloor (Vent site) | 2.6 | 163.1 | -65.4 | - |
| | Northern Cascadia margin | Bullseye Vent, PGC00-02. Disseminated gas hydrates near the seafloor (Vent site) | 6.7 | 239.5 | -70.4 | - |
| Brooks *et al.* (1991) | Offshore California, Eel River Basin | ER-82. Hydrate nodules, layered hydrates and disseminated (Vent Site) | 0.0 | 2209.0 | -59.6 | - |
| | Offshore California, Eel River Basin | ER-83. Hydrate nodules, layered hydrates and disseminated (Vent Site) | <1.5 | 5158.0 | - | - |
| | Offshore California, Eel River Basin | ER-105. Hydrate nodules, layered hydrates and disseminated (Vent Site) | 0.0 | 10591.0 | -57.6 | - |
| | Offshore California, Eel River Basin | ER-139. Hydrate nodules, layered hydrates and disseminated (Vent Site) | 1.8-2 | 803.0 | -61.1 | - |
| | Offshore California, Eel River Basin | ER-148. Hydrate nodules, layered hydrates and disseminated (Vent Site) | 0-1.8 | 5324.0 | -59.7 | - |
| | Offshore California, Eel River Basin | ER-202. Hydrate nodules, layered hydrates and disseminated (Vent Site) | 2.2-2.8 | 1603.0 | -69.1 | - |
| Schmidt *et al.* (2005) | Offshore Costa Rica | MV-11, GH-01. Hydrate patches within silty clays (MV site) | 2.0 | 3069.0 | -43.3 | -125.0 |
| | Offshore Costa Rica | MV-11, GH-02. Hydrate patches within silty clays (MV site) | 2.0 | 2150.0 | -45.2 | -135.0 |
| | Offshore Costa Rica | MV-11, GH-03. Hydrate patches within silty clays (MV site) | 2.0 | 3027.0 | -43.4 | -143.0 |
| | Offshore Costa Rica | MV-11, GH-04. Hydrate patches within silty clays (MV site) | 2.0 | 2972.0 | -44.6 | -143.0 |
| Lückge *et al.* (2002) | Offshore Costa Rica | ODP 170, 1041a. Solid pieces of hydrates and disseminated hydrates | 120.0 | 4693.9 | -67.7 | -189.2 |
| | Offshore Costa Rica | ODP 170, 1041a. Solid pieces of hydrates and disseminated hydrates | 131.0 | 4925.1 | -66.9 | -200.0 |
| | Offshore Costa Rica | ODP 170, 1041b. Solid pieces of hydrates and disseminated hydrates | 160.0 | 3716.4 | -66.0 | -204.0 |
| | Offshore Costa Rica | ODP 170, 1041b. Solid pieces of hydrates and disseminated hydrates | 189.8 | 2303.2 | -64.9 | -198.0 |
| | Offshore Costa Rica | ODP 170, 1041b. Solid pieces of hydrates and disseminated hydrates | 196.1 | 2201.5 | -64.7 | -206.0 |
| | Offshore Costa Rica | ODP 170, 1041b. Solid pieces of hydrates and disseminated hydrates | 207.6 | 1711.3 | - | - |
| | Offshore Costa Rica | ODP 170, 1041b. Solid pieces of hydrates and disseminated hydrates | 218.7 | 1549.5 | - | - |
| | Offshore Costa Rica | ODP 170, 1041b. Solid pieces of hydrates and disseminated hydrates | 234.5 | 984.2 | -64.1 | -196.6 |
| | Offshore Costa Rica | ODP 170, 1041b. Solid pieces of hydrates and disseminated hydrates | 258.5 | 765.3 | -63.7 | -195.2 |
| Pohlman *et al.* (2009a) | Central Chilean margin | Concepción Methane Seep, CHL-1004. Solid piece of hydrate. | 0.0 | 2500 | -61.4 | - |
| Pohlman *et al.* (2005) | Green Canyon, Northern Gulf of Mexico | GC234, massive hydrate at the seafloor (Seep site) | 0.0 | 2.2 | -48.8 | -179.0 |
| | Green Canyon, Northern Gulf of Mexico | GC234, massive hydrate at the seafloor (Seep site) | 0.0 | 1.7 | -49.5 | -192.0 |
| | Green Canyon, Northern Gulf of Mexico | GC234, massive hydrate at the seafloor (Seep site) | 0.0 | 1.9 | -50.0 | -153.0 |
| Sassen *et al.* (2001b) | Mississippi Fan Foldbelt, Northern Gulf of Mexico | AT 425-1, massive hydrate at the seafloor (Seep site) | 0.0 | 3.4 | -49.3 | -148.0 |
| | Mississippi Fan Foldbelt, Northern Gulf of Mexico | AT 425-2, massive hydrate at the seafloor (Seep site) | 0.0 | 7.6 | -49.4 | -183.0 |
| | Mississippi Fan Foldbelt, Northern Gulf of Mexico | AT 425-3, massive hydrate at the seafloor (Seep site) | 0.0 | 16.2 | -48.4 | -183.0 |
| | Mississippi Fan Foldbelt, Northern Gulf of Mexico | AT 425-4, massive hydrate at the seafloor (Seep site) | 0.0 | 19.0 | -50.1 | -171.0 |
| | Mississippi Fan Foldbelt, Northern Gulf of Mexico | AT 425-5, massive hydrate at the seafloor (Seep site) | 0.0 | 36.0 | -46.9 | -177.0 |
| | Mississippi Fan Foldbelt, Northern Gulf of Mexico | AT 425-6, massive hydrate at the seafloor (Seep site) | 0.0 | 99.0 | -51.6 | -173.0 |
| Brooks *et al.* (1986) | Orca Basin, Northern Gulf of Mexico | -, massive hydrate at the seafloor (Seep site) | 0.0 | 159.8 | -71.3 | - |
| | Green Canyon, Northern Gulf of Mexico | GC184, massive hydrate at the seafloor (Seep site) | 0.0 | 2.8 | -44.6 | - |
| | Green Canyon, Northern Gulf of Mexico | GC204, massive hydrate at the seafloor (Seep site) | 0.0 | 1.6 | -56.5 | - |

| | | | | | | |
|---|---|---|---|---|---|---|
| | Green Canyon, Northern Gulf of Mexico | GC234, massive hydrate at the seafloor (Seep site) | 0.0 | 3.5 | -43.2 | - |
| | Green Canyon, Northern Gulf of Mexico | GB388, massive hydrate at the seafloor (Seep site) | 0.0 | 829.2 | -70.4 | - |
| | Green Canyon, Northern Gulf of Mexico | GC257, massive hydrate at the seafloor (Seep site) | 0.0 | 10000.0 | -69.2 | - |
| | Green Canyon, Northern Gulf of Mexico | GC320, massive hydrate at the seafloor (Seep site) | 0.0 | 1246.3 | -66.5 | - |
| | Mississippi Canyon, Northern Gulf of Mexico | -, massive hydrate at the seafloor (Seep site) | 0.0 | 37.4 | -48.2 | - |
| McGee *et al.* (2009) | Mississippi Canyon, Northern Gulf of Mexico | MC118, massive hydrate at the seafloor (Seep site) | 0.0 | 2.3 | -46.7 | -169.0 |
| Sassen *et al.* (2001a) | Green Canyon, Northern Gulf of Mexico | GC185, massive hydrate at the seafloor (Seep site) | 0.0 | 5.0 | -42.9 | -163.0 |
| | Green Canyon, Northern Gulf of Mexico | GC185, massive hydrate at the seafloor (Seep site) | 0.0 | 2.7 | -42.2 | -190.0 |
| | Green Canyon, Northern Gulf of Mexico | GC185, massive hydrate at the seafloor (Seep site) | 0.0 | 4.3 | -43.5 | -177.0 |
| | Green Canyon, Northern Gulf of Mexico | GC185, massive hydrate at the seafloor (Seep site) | 0.0 | 2.7 | -42.5 | -193.0 |
| | Green Canyon, Northern Gulf of Mexico | GC185, massive hydrate at the seafloor (Seep site) | 0.0 | 6.3 | -42.9 | -115.0 |
| | Green Canyon, Northern Gulf of Mexico | GC185, massive hydrate at the seafloor (Seep site) | 0.0 | 2.8 | -43.6 | -167.0 |
| Sassen *et al.* (1999) | Green Canyon, Northern Gulf of Mexico | Bush Hill, GC185, massive hydrate at the seafloor (Seep site) | 0.0 | 4.9 | -42.9 | -163.0 |
| | Green Canyon, Northern Gulf of Mexico | Bush Hill, GC185, massive hydrate at the seafloor (Seep site) | 0.0 | 2.5 | -42.2 | -190.0 |
| | Green Canyon, Northern Gulf of Mexico | Bush Hill, GC185, massive hydrate at the seafloor (Seep site) | 0.0 | 4.1 | -43.5 | -177.0 |
| | Green Canyon, Northern Gulf of Mexico | Bush Hill, GC185, massive hydrate at the seafloor (Seep site) | 0.0 | 2.6 | -42.5 | -193.0 |
| | Green Canyon, Northern Gulf of Mexico | Bush Hill, GC185, massive hydrate at the seafloor (Seep site) | 0.0 | 6.0 | -42.9 | -115.0 |
| | Green Canyon, Northern Gulf of Mexico | GC234, massive hydrate at the seafloor (Seep site) | 0.0 | 2.8 | -48.4 | -203.0 |
| Sassen *et al.* (2004) | Green Canyon, Northern Gulf of Mexico | GC234, massive hydrate at the seafloor (Seep site) | 0.0 | 3.1 | -46.8 | -161.0 |
| | Green Canyon, Northern Gulf of Mexico | GC234, massive hydrate at the seafloor (Seep site) | 0.0 | 2.6 | -48.3 | -173.0 |
| | Green Canyon, Northern Gulf of Mexico | GC234, massive hydrate at the seafloor (Seep site) | 0.0 | 3.0 | -46.5 | -202.0 |
| | Green Canyon, Northern Gulf of Mexico | GC234, massive hydrate at the seafloor (Seep site) | 0.0 | 2.8 | 48.4 | -203.0 |
| Sassen *et al.* (2001c) | Mississippi Canyon, Northern Gulf of Mexico | MC853, massive hydrate at the seafloor (Seep site) | 0.0 | 3.2 | -44.7 | -173.0 |
| | Mississippi Canyon, Northern Gulf of Mexico | MC853, massive hydrate at the seafloor (Seep site) | 0.0 | 2.5 | -46.5 | -183.0 |
| | Mississippi Canyon, Northern Gulf of Mexico | MC853, massive hydrate at the seafloor (Seep site) | 0.0 | 3.4 | -49.9 | -171.0 |
| | Mississippi Canyon, Northern Gulf of Mexico | MC853, massive hydrate at the seafloor (Seep site) | 0.0 | 3.0 | -45.1 | -148.0 |
| Wilson *et al.* (2014) | Mississippi Canyon, Northern Gulf of Mexico | MC118, Woolsey Mound, layered hydrate near the seafloor (Seep site) | 1.2 | 3.8 | -40.4 | -154 |
| MacDonald *et al.* (2004) | Campeche Knolls, Southern Gulf Of Mexico | Chapopote Knoll, massive hydrate at the seafloor (Seep site with asphalt volcanism) | 0.0 | 13.4 | -50.1 | - |
| Klapp *et al.* (2010) | Campeche Knolls, Southern Gulf Of Mexico | Chapopote Knoll, TVG-6, massive hydrate at the seafloor (Seep site with asphalt volcanism) | 0.0 | 50.5 | - | - |
| | Campeche Knolls, Southern Gulf Of Mexico | Chapopote Knoll, GC-6#1, massive hydrate at the seafloor (Seep site with asphalt volcanism) | 0.0 | 16.1 | - | - |
| | Campeche Knolls, Southern Gulf Of Mexico | Chapopote Knoll, GC-6#2, massive hydrate at the seafloor (Seep site with asphalt volcanism) | 0.0 | 40.2 | - | - |
| | Green Canyon, Northern Gulf of Mexico | GC185, Bush Hill, massive hydrate at the seafloor (Seep site) | 0.0 | 2.6 | - | - |
| | Green Canyon, Northern Gulf of Mexico | GC185, Bush Hill, massive hydrate at the seafloor (Seep site) | 0.0 | 2.5 | - | - |
| | Green Canyon, Northern Gulf of Mexico | GC415, massive hydrate at the seafloor (Seep site) | 0.0 | 2.9 | - | - |
| | Green Canyon, Northern Gulf of Mexico | GC415, massive hydrate at the seafloor (Seep site) | 0.0 | 4.6 | - | - |
| Schubotz *et al.* (2011) | Campeche Knolls, Southern Gulf Of Mexico | Chapopote Knoll, GeoB10618, massive and dispersed hydrates with pure asphalt near the seafloor (Seep site with asphalt volcanism) | 1.0 | 20.7 | -54.8 | - |
| Henry *et al.* (1996) | Offshore Barbados | Atlante MV, core KS20, Piece of hydrate observed near the seafloor (MV site) | <6.0 | 10000 | -58.1 | - |
| Miller *et al.* (2015) | Rio Grande Cone, Offshore Brazil | PC 76, hydrate nodules and veins recovered with Pistone cores in muds (Seep site) | 5.0-9.0 | 2832 | -69.3 | - |
| | Rio Grande Cone, Offshore Brazil | PC 76, hydrate nodules and veins recovered with Pistone cores in muds (Seep site) | 5.0-9.0 | 3210 | -68.1 | - |
| | Rio Grande Cone, Offshore Brazil | PC 76, hydrate nodules and veins recovered with Pistone cores in muds (Seep site) | 5.0-9.0 | 2957 | -68.1 | - |
| | Rio Grande Cone, Offshore Brazil | PC 76, hydrate nodules and veins recovered with Pistone cores in muds (Seep site) | 5.0-9.0 | 2040 | -69 | - |
| | Rio Grande Cone, Offshore Brazil | PC 67, hydrate nodules and veins recovered with Pistone cores in muds (Seep site) | 5.0-13.0 | 1352 | -67 | - |
| | Rio Grande Cone, Offshore Brazil | PC 67, hydrate nodules and veins recovered with Pistone cores in muds (Seep site) | 5.0-13.0 | 999 | -66.7 | - |

| | | | | | | |
|---|---|---|---|---|---|---|
| | Rio Grande Cone, Offshore Brazil | PC 67, hydrate nodules and veins recovered with Pistone cores in muds (Seep site) | 5.0-13.0 | 890 | -66.9 | - |
| | Rio Grande Cone, Offshore Brazil | PC 67, hydrate nodules and veins recovered with Pistone cores in muds (Seep site) | 5.0-13.0 | 446 | -66.7 | - |
| | Rio Grande Cone, Offshore Brazil | PC 67, hydrate nodules and veins recovered with Pistone cores in muds (Seep site) | 5.0-13.0 | 958 | -66.7 | - |
| | Rio Grande Cone, Offshore Brazil | PC 67, hydrate nodules and veins recovered with Pistone cores in muds (Seep site) | 5.0-13.0 | 1222 | -66.7 | - |
| Norwegian Charlou *et al.* (2004) | Congo-Angola Basin | Pockmark, gravity core KZR-42, massive/layered hydrates within a pockmark (Seep site) | 12.0 | 2217.0 | -69.3 | -199.0 |
| Cunningham and Lindholm (2000) | Niger Delta, Offshore Nigeria | Gas hydrate mound (massive hydrate?) (Seep site) | n.a. (likely seafloor) | 999.0 | -54.0 | - |
| Ruffine *et al.* (2013) | Niger Delta, Offshore Nigeria | Irregular pockmark, Calypso core, massive/layered/porous hydrates within a pockmark (Seep site) | 4.0-8.0 | 3219.4 | -42.1 | -182.0 |
| De Prunelé *et al.* (2017) | Niger Delta, Offshore Nigeria | Irregular pockmark, Calypso core, massive/layered/porous hydrates within a pockmark (Seep site) | 7.7-20 | 4981.0 | -50.5 | -182.0 |
| Lein *et al.* (1999); Milkov (2005) | Norwegian Sea | Håkon Mosby MV, site 25, hydrates plates/flakes within MV sediments (MV site) | 1.3 | 1281.1 | -61.9 | -242.0 |
| | Norwegian Sea | Håkon Mosby MV, site 25, hydrates plates/flakes within MV sediments (MV site) | 1.9 | 1213.6 | -61.8 | -241.0 |
| | Norwegian Sea | Håkon Mosby MV, site 25, hydrates plates/flakes within MV sediments (MV site) | 2.3 | 2378.6 | -61.7 | -240.0 |
| | Norwegian Sea | Håkon Mosby MV, site 25, hydrates plates/flakes within MV sediments (MV site) | 3 | 1580.5 | -61.9 | -239.0 |
| | Norwegian Sea | Håkon Mosby MV, site 28, hydrates plates/flakes within MV sediments (MV site) | 1.25-1.3 | 2307.2 | -61.4 | -238.0 |
| | Norwegian Sea | Håkon Mosby MV, site 28, hydrates plates/flakes within MV sediments (MV site) | 2.2-2.3 | 3192.3 | -56.0 | -237.0 |
| | Norwegian Sea | Håkon Mosby MV, site 28, hydrates plates/flakes within MV sediments (MV site) | 2.4 | 4803.8 | - | -236.0 |
| | Norwegian Sea | Håkon Mosby MV, site 32, hydrates plates/flakes within MV sediments (MV site) | 0.7-0.8 | 2484.1 | - | -235.0 |
| | Norwegian Sea | Håkon Mosby MV, site 33, hydrates plates/flakes within MV sediments (MV site) | 0.6 | 903.8 | - | -234.0 |
| | Norwegian Sea | Håkon Mosby MV, site 45, hydrates plates/flakes within MV sediments (MV site) | 0.0-0.05 | 1403.2 | - | -233.0 |
| | Norwegian Sea | Håkon Mosby MV, site 45, hydrates plates/flakes within MV sediments (MV site) | 0.4-0.45 | 3292.7 | - | -232.0 |
| | Norwegian Sea | Håkon Mosby MV, site 45, hydrates plates/flakes within MV sediments (MV site), visible and/or disseminated hydrates in MV sediments (MV site) | 0.9-1 | 1973.3 | -61.0 | -231.0 |
| Pape *et al.* (2011) | Norwegian Sea | Håkon Mosby MV, DAPC pressure core 2, visible and/or disseminated hydrates in MV sediments (MV site) | 0.0-2.4 | 1018.0 | -63.9 | - |
| | Norwegian Sea | Håkon Mosby MV, DAPC pressure core 1, visible and/or disseminated hydrates in MV sediments (MV site) | 0.0-2.5 | 1144.0 | -63.9 | - |
| | Norwegian Sea | Håkon Mosby MV, DAPC pressure core 3, visible and/or disseminated hydrates in MV sediments (MV site) | 0.0-2.7 | 1542.0 | -63.9 | - |
| | Norwegian Sea | Håkon Mosby MV, DAPC pressure core 4, visible and/or disseminated hydrates in MV sediments (MV site) | 0.0-2.7 | 1066.0 | -63.9 | - |
| | Norwegian Sea | Håkon Mosby MV, DAPC pressure core 5, visible and/or disseminated hydrates in MV sediments (MV site) | 0.0-2.6 | 1533.0 | -63.9 | - |
| | Norwegian Sea | Håkon Mosby MV, DAPC pressure core 6, visible and/or disseminated hydrates in MV sediments (MV site) | - | 1095.0 | -63.9 | - |
| | Norwegian Sea | Håkon Mosby MV, DAPC pressure core 7, visible and/or disseminated hydrates in MV sediments (MV site) | 00.0-1.7 | 1195.0 | -63.9 | - |
| | Norwegian Sea | Håkon Mosby MV, hydrate samples U I-II from gravity cores, visible and/or disseminated hydrates in MV sediments (MV site) | 0.0 | 1133.0 | - | - |
| Smith *et al.* (2014b) | Offshore Svalbard, Vestnesa Ridge | Vestnesa Ridge, GC 929, hydrate recovered in a gravity core | 2.0-4.0 | 26.2 | -46.7 | - |
| Graves *et al.* (2017) | Offshore Svalbard, Vestnesa Ridge | Vestnesa Ride, 26 GC, hydrate recovered in a gravity core | >1.3 | 60 | -45.7 | -180 |
| | Offshore Svalbard, Pockmark field on the continental slope | Pockmark Site, 33 GC, hydrate recovered in a gravity core | >1.9 | 500 | -64.6 | -174 |
| Pape *et al.* (2010b) | Mediterranean Sea | Anaximander Mountains, Amsterdam MV, GC 01, solid hydrate piece (MV site) | 1.0-2.0 | 28.9 | - | - |
| | Mediterranean Sea | Anaximander Mountains, Amsterdam MV, DAPC pressure core 01, hydrate dispersed in mud breccia (MV site) | 1.0-2.0 | 32.7 | -50.7 | - |
| | Mediterranean Sea | Anaximander Mountains, Amsterdam MV, DAPC pressure core 02, hydrate dispersed in mud breccia (MV site) | 1.0-2.0 | 25.5 | - | - |

| | | | | | | |
|---|---|---|---|---|---|---|
| | Mediterranean Sea | Anaximander Mountains, Amsterdam MV, DAPC pressure core 03, hydrate dispersed in mud breccia (MV site) | 1.0-2.0 | 31.2 | -50.6 | -167.0 |
| | Mediterranean Sea | Anaximander Mountains, Amsterdam MV, DAPC pressure core 05, solid hydrate piece (MV site) | 1.0-2.0 | 24.7 | -50.5 | - |
| Bourry *et al.* (2009) | Sea of Marmara, Offshore Turkey | Western High, MNTKS 27, small hydrate inclusions in mud breccia (Seep site) | ~0.0-10.0 | 2.1 | -44.1 | -219.0 |
| Milkov (2005) | Sorokin Through, Black Sea | Mud Diapir, probably visible hydrate pieces in mud breccia (MV site) | 0.0-1.0 | 4719.0 | -63.4 | - |
| Blinova *et al.* (2003) | Sorokin Through, Black Sea | Mud Diapir, probably visible hydrate pieces in mud breccia (MV site) | 0.0-1.0 | 2183.0 | -61.8 | - |
| | Sorokin Through, Black Sea | Dvurechenskii MV, small hydrate inclusions in mud breccia (MV site) | 0.0 | 242.2 | -66.0 | -202.0 |
| | Sorokin Through, Black Sea | Dvurechenskii MV, small hydrate inclusions in mud breccia (MV site) | 0.0 | 379.4 | -66.0 | - |
| | Sorokin Through, Black Sea | Dvurechenskii MV, small hydrate inclusions in mud breccia (MV site) | 0.0 | 261.7 | - | - |
| | Sorokin Through, Black Sea | Dvurechenskii MV, small hydrate inclusions in mud breccia (MV site) | 0.0 | 184.2 | - | - |
| | Sorokin Through, Black Sea | Dvurechenskii MV, small hydrate inclusions in mud breccia (MV site) | 0.0 | 211.2 | -62.0 | -185.0 |
| | Sorokin Through, Black Sea | Dvurechenskii MV, small hydrate inclusions in mud breccia (MV site) | 0.0 | 255.0 | -63.0 | -209.0 |
| | Sorokin Through, Black Sea | Dvurechenskii MV, small hydrate inclusions in mud breccia (MV site) | 0.0 | 268.6 | - | - |
| Pape *et al.* (2010a) | SE Black Sea, Offshore Georgia | Batumi Seep, GC 14, layered gas hydrates (Seep site) | ~1.5 | 2318.0 | -51.5 | - |
| | SE Black Sea, Offshore Georgia | Batumi Seep, GC 04, layered gas hydrates (Seep site) | ~1.5 | 3920.0 | -50.9 | - |
| | SE Black Sea, Offshore Georgia | Batumi Seep, GC 06, layered gas hydrates (Seep site) | ~1.5 | 4212.0 | -50.5 | - |
| | SE Black Sea, Offshore Georgia | Batumi Seep, GC 08, layered gas hydrates (Seep site) | ~1.5 | 3323.0 | -51.7 | - |
| | SE Black Sea, Offshore Georgia | Batumi Seep, GC 13, layered gas hydrates (Seep site) | ~1.5 | 3058.0 | -50.2 | - |
| | SE Black Sea, Offshore Georgia | Batumi Seep, GC 18, layered gas hydrates (Seep site) | ~1.5 | 3509.0 | -50.3 | - |
| | SE Black Sea, Offshore Georgia | Batumi Seep, GC 23, layered gas hydrates (Seep site) | ~1.5 | 2944.0 | -51.2 | - |
| Pape *et al.* (2010a), data extracted from Figure 5c | SE Black Sea, Offshore Georgia | Batumi seep, layered gas hydrates (Seep site) | ~1.5 | - | -52.3 | -152.0 |
| | SE Black Sea, Offshore Georgia | Batumi seep, layered gas hydrates (Seep site) | ~1.5 | - | -52.9 | -172.0 |
| | SE Black Sea, Offshore Georgia | Batumi seep, layered gas hydrates (Seep site) | ~1.5 | - | -53.0 | -190.5 |
| Ginsburg and Soloviev (1994) | Caspian Sea | Buzdag MV, hydrate inclusions in mud breccia (MV site) | 0.0 | 3.4 | -44.8 | - |
| | Caspian Sea | Elm MV, hydrate inclusions in mud breccia (MV site) | 0.0 | 25.2 | -55.7 | - |
| | South Baikal Basin, Lake Baikal | Malenky MV, Sample A, massive hydrates and veins in silty clays (MV site) | 0.0 | 3593.0 | -66.6 | -304.0 |
| | South Baikal Basin, Lake Baikal | Bolshoy MV, Sample B, massive hydrates and veins in silty clays (MV site) | 1.0 | 4732.0 | -66.5 | -302.0 |
| | Central Baikal Basin, Lake Baikal | Kukuy K-2 MV, Sample C-1, massive hydrates and veins in silty clays (MV site) | 2.0-3.0 | 5.8 | -57.4 | -303.0 |
| | Central Baikal Basin, Lake Baikal | Kukuy K-2 MV, Sample C-2, massive hydrates and veins in silty clays (MV site) | 2.0-3.0 | 29.6 | -57.6 | -303.0 |
| | Central Baikal Basin, Lake Baikal | Kukuy K-2 MV, Sample C-3, massive hydrates and veins in silty clays (MV site) | 2.0-3.0 | 25.6 | -57.0 | -304.0 |
| Hachikubo *et al.* (2010a) | South Baikal basin | Malenky MV, 2005St3GC1, massive, layered and fracture-filling hydrates (MV site) | 1.2 | 3786.9 | -65.7 | -306.3 |
| | South Baikal basin | Malenky MV, 2005St3GC1, massive, layered and fracture-filling hydrates (MV site) | 1.2 | 5463.5 | -66.0 | -306.8 |
| | South Baikal basin | Malenky MV, 2005St3GC1, massive, layered and fracture-filling hydrates (MV site) | 1.3 | 3483.3 | -65.1 | -308.4 |
| | South Baikal basin | Malenky MV, 2005St3GC1, massive, layered and fracture-filling hydrates (MV site) | 1.3 | 3596.1 | -65.9 | -307.6 |
| | South Baikal basin | Malenky MV, 2005St3GC2, massive, layered and fracture-filling hydrates (MV site) | 1.2 | 4544.5 | -67.0 | -306.9 |
| | South Baikal basin | Malenky MV, 2005St3GC2, massive, layered and fracture-filling hydrates (MV site) | 1.5 | 5987.0 | -65.8 | -301.3 |
| | South Baikal basin | Malenky MV, 2005St3GC2, massive, layered and fracture-filling hydrates (MV site) | 1.5 | 7041.3 | -65.4 | -305.5 |
| | South Baikal basin | Malenky MV, 2005St3GC2, massive, layered and fracture-filling hydrates (MV site) | 1.5 | 9008.0 | -65.8 | -307.7 |
| | South Baikal basin | Malenky MV, 2005St3GC2, massive, layered and fracture-filling hydrates (MV site) | 1.8 | 4423.8 | -65.7 | -303.6 |
| | South Baikal basin | Malenky MV, 2005St3GC2, massive, layered and fracture-filling hydrates (MV site) | 1.8 | 4423.8 | -66.0 | -304.5 |
| | South Baikal basin | Malenky MV, 2005St3GC2, massive, layered and fracture-filling hydrates (MV site) | 1.8 | 4716.0 | -65.6 | -307.5 |
| | South Baikal basin | Malenky MV, 2005St3GC4, massive, layered and fracture-filling hydrates (MV site) | 1.2 | 2665.7 | -67.4 | -303.0 |

| | | | | | | |
|---|---|---|---|---|---|---|
| | South Baikal basin | Malenky MV, 2005St3GC4, massive, layered and fracture-filling hydrates (MV site) | 1.2 | 6848.3 | -66.9 | -302.4 |
| | South Baikal basin | Malenky MV, 2005St3GC4, massive, layered and fracture-filling hydrates (MV site) | 2.3 | 3235.2 | -67.3 | -304.2 |
| | South Baikal basin | Malenky MV, 2005St3GC5, massive, layered and fracture-filling hydrates (MV site) | 0.7 | 4503.5 | -66.8 | -300.4 |
| | South Baikal basin | Malenky MV, 2005St3GC5, massive, layered and fracture-filling hydrates (MV site) | 0.7 | 6943.4 | -67.1 | -302.0 |
| | South Baikal basin | Malenky MV, 2005St3GC5, massive, layered and fracture-filling hydrates (MV site) | 0.8 | 3423.7 | -67.2 | -303.2 |
| | South Baikal basin | Malenky MV, 2005St3GC5, massive, layered and fracture-filling hydrates (MV site) | 0.8 | 6171.8 | -67.0 | -303.0 |
| | South Baikal basin | Malenky MV, 2005St3GC5, massive, layered and fracture-filling hydrates (MV site) | 0.8 | 3730.3 | -67.2 | -307.7 |
| | South Baikal basin | Malenky MV, 2005St3GC6, massive, layered and fracture-filling hydrates (MV site) | 0.7 | 2211.4 | -67.4 | -306.7 |
| | South Baikal basin | Malenky MV, 2005St3GC6, massive, layered and fracture-filling hydrates (MV site) | 0.7 | 3412.0 | -67.1 | -304.2 |
| | South Baikal basin | Malenky MV, 2005St3GC6, massive, layered and fracture-filling hydrates (MV site) | 0.7 | 3104.6 | -66.5 | -305.5 |
| | South Baikal basin | Malenky MV, 2005St3GC6, massive, layered and fracture-filling hydrates (MV site) | 0.7 | 2380.0 | -65.4 | -308.0 |
| | South Baikal basin | Bolshoy MV, 2005St1GC3, massive, layered and fracture-filling hydrates (MV site) | - | 4463.3 | -66.2 | -300.4 |
| | South Baikal basin | Bolshoy MV, 2005St1GC3, massive, layered and fracture-filling hydrates (MV site) | -! | 4254.3 | -65.9 | -305.4 |
| | South Baikal basin | Bolshoy MV, 2005St1GC3, massive, layered and fracture-filling hydrates (MV site) | 1.0 | 4346.8 | -65.9 | -304.1 |
| | South Baikal basin | Bolshoy MV, 2005St1GC3, massive, layered and fracture-filling hydrates (MV site) | 1.0 | 3057.1 | -65.7 | -303.8 |
| | South Baikal basin | Bolshoy MV, 2005St1GC3, massive, layered and fracture-filling hydrates (MV site) | 1.0 | 5318.1 | - | -307.2 |
| | South Baikal basin | Malyutka MV, 2006St7GC1, massive, layered and fracture-filling hydrates (MV site) | 1.3 | 4503.5 | -67.1 | - |
| | South Baikal basin | Malyutka MV, 2006St7GC1, massive, layered and fracture-filling hydrates (MV site) | 1.4 | 4443.4 | -65.4 | -304.0 |
| | South Baikal basin | Malyutka MV, 2006St7GC1, massive, layered and fracture-filling hydrates (MV site) | 1.7 | 5523.9 | - | -305.0 |
| | South Baikal basin | Peschanka P-2 MV, 2007St2GC2, massive, layered and fracture-filling hydrates (MV site) | 2.3 | 1386.0 | -66.1 | -310.2 |
| | South Baikal basin | Peschanka P-2 MV, 2007St2GC2, massive, layered and fracture-filling hydrates (MV site) | 2.4 | 1221.5 | -67.8 | - |
| | South Baikal basin | Peschanka P-2 MV, 2007St2GC2, massive, layered and fracture-filling hydrates (MV site) | 2.5 | 1509.6 | -65.2 | -311.8 |
| | South Baikal basin | Peschanka P-2 MV, 2007St2GC5, massive, layered and fracture-filling hydrates (MV site) | 3.0 | 1889.4 | -66.8 | -305.5 |
| | South Baikal basin | Peschanka P-2 MV, 2007St2GC5, massive, layered and fracture-filling hydrates (MV site) | 4.2 | 2251.3 | -67.9 | - |
| | South Baikal basin | Peschanka P-2 MV, 2007St2GC5, massive, layered and fracture-filling hydrates (MV site) | 4.2 | 1810.6 | -67.7 | -306.1 |
| | South Baikal basin | Peschanka P-2 MV, 2007St2GC6, massive, layered and fracture-filling hydrates (MV site) | - | 2687.2 | -67.0 | -304.8 |
| | South Baikal basin | Peschanka P-2 MV, 2007St2GC11, massive, layered and fracture-filling hydrates (MV site) | 4.1 | 1693.9 | -68.1 | - |
| | South Baikal basin | Peschanka P-2 MV, 2007St2GC14, , massive, layered and fracture-filling hydrates (MV site) | 1.3 | 2665.7 | - | -308.6 |
| | South Baikal basin | Peschanka P-2 MV, 2007St2GC14, massive, layered and fracture-filling hydrates (MV site) | 1.5 | 2701.7 | -67.2 | -306.3 |
| | South Baikal basin | Peschanka P-2 MV, 2007St2GC14, massive, layered and fracture-filling hydrates (MV site) | 1.7 | 2716.4 | -67.3 | -304.9 |
| | South Baikal basin | Peschanka P-2 MV, 2007St2GC14, massive, layered and fracture-filling hydrates (MV site) | 2.5 | 1487.1 | - | -302.7 |
| | South Baikal basin | Peschanka P-2 MV, 2007St2GC14, massive, layered and fracture-filling hydrates (MV site) | 2.7 | 1720.2 | -67.6 | -304.3 |
| | South Baikal basin | Peschanka P-2 MV, 2007St2GC14, massive, layered and fracture-filling hydrates (MV site) | 2.9 | 2082.3 | - | -301.2 |
| | South Baikal basin | Peschanka P-2 MV, 2007St2GC14, massive, layered and fracture-filling hydrates (MV site) | 2.9 | 2073.7 | -67.4 | -303.1 |
| | South Baikal basin | Peschanka P-2 MV, 2007St2GC14, massive, layered and fracture-filling hydrates (MV site) | 2.9 | 2131.2 | -66.9 | -303.9 |
| | South Baikal basin | Goloustnoye G-1 2007St8GC1, massive, layered and fracture-filling hydrates (MV site) | 2.9 | 103.9 | -63.9 | -306.0 |
| | South Baikal basin | Goloustnoye G-1 2007St8GC1, massive, layered and fracture-filling hydrates (MV site) | 2.9 | 101.5 | -64.3 | -308.5 |
| | South Baikal basin | Goloustnoye G-1 2007St8GC3, massive, layered and fracture-filling hydrates (MV site) | 1.7 | 150.1 | -64.1 | -306.9 |
| | South Baikal basin | Goloustnoye G-1 2007St8GC3, massive, layered and fracture-filling hydrates (MV site) | 1.7 | 148.8 | -64.4 | -308.0 |
| | South Baikal basin | Goloustnoye G-1 2007St8GC3, massive, layered and fracture-filling hydrates (MV site) | 1.7 | 148.1 | -64.4 | -308.7 |
| | South Baikal basin | Goloustnoye G-1 2007St8GC3, massive, layered and fracture-filling hydrates (MV site) | 1.7 | 146.9 | -64.3 | -306.9 |
| | South Baikal basin | Goloustnoye G-1 2007St8GC6, massive, layered and fracture-filling hydrates (MV site) | 1.9 | 117.2 | -64.3 | -307.3 |
| | South Baikal basin | Goloustnoye G-1 2007St8GC2, massive, layered and fracture-filling hydrates (MV site) | 1.3 | 83.6 | -63.4 | -306.0 |
| | South Baikal basin | Goloustnoye G-1 2007St8GC2, massive, layered and fracture-filling hydrates (MV site) | 1.3 | 84.7 | -63.3 | -306.4 |

| | | | | | | |
|---|---|---|---|---|---|---|
| | South Baikal basin | Goloustnoye G-1 2007St8GC2, massive, layered and fracture-filling hydrates (MV site) | 1.3 | 86.0 | -63.2 | -306.9 |
| | South Baikal basin | Goloustnoye G-1 2008St8wHGC3, massive, layered and fracture-filling hydrates (MV site) | 0.9 | 55.9 | -63.8 | -309.2 |
| | South Baikal basin | Goloustnoye G-1 2008St8wHGC3, massive, layered and fracture-filling hydrates (MV site) | 0.9 | 57.1 | -63.8 | -309.7 |
| | South Baikal basin | Goloustnoye G-1 2008St8wHGC3, massive, layered and fracture-filling hydrates (MV site) | 0.9 | 58.3 | -63.9 | -309.8 |
| | South Baikal basin | Goloustnoye G-1 2008St8wHGC3, massive, layered and fracture-filling hydrates (MV site) | 0.9 | 73.9 | -64.0 | -308.8 |
| | South Baikal basin | Goloustnoye G-2 2008St2GC1, massive, layered and fracture-filling hydrates (MV site) | 1.3 | 80.0 | -64.4 | -308.8 |
| | South Baikal basin | Goloustnoye G-2 2008St2GC1, massive, layered and fracture-filling hydrates (MV site) | 1.3 | 81.5 | -64.2 | -307.1 |
| | Central Baikal Basin | Kukuy K-0 MV, 2006St6GC1, massive, layered and fracture-filling hydrates (MV site) | 2.0 | 1039.6 | -65.9 | - |
| | Central Baikal Basin | Kukuy K-0 MV, 2006St6GC1, massive, layered and fracture-filling hydrates (MV site) | 2.3 | 1084.8 | -64.8 | - |
| | Central Baikal Basin | Kukuy K-0 MV, 2006St6GC3, massive, layered and fracture-filling hydrates (MV site) | 0.9 | 1149.7 | -66.4 | - |
| | Central Baikal Basin | Kukuy K-0 MV, 2006St6GC3, massive, layered and fracture-filling hydrates (MV site) | 1.1 | 1314.8 | -64.1 | -326.3 |
| | Central Baikal Basin | Kukuy K-0 MV, 2006St6GC3, massive, layered and fracture-filling hydrates (MV site) | 1.5 | 1276.1 | -64.3 | -325.3 |
| | Central Baikal Basin | Kukuy K-0 MV, 2006St6GC3, massive, layered and fracture-filling hydrates (MV site) | 2.0 | 1382.1 | -63.1 | -324.5 |
| | Central Baikal Basin | Kukuy K-0 MV, 2006St6GC3, massive, layered and fracture-filling hydrates (MV site) | 2.6 | 1323.5 | - | - |
| | Central Baikal Basin | Kukuy K-2 MV, 2006St6GC5, massive, layered and fracture-filling hydrates (MV site) | 2.5 | 6.2 | -57.3 | -299.5 |
| | Central Baikal Basin | Kukuy K-2 MV, 2006St6GC5, massive, layered and fracture-filling hydrates (MV site) | 2.5 | 5.9 | -57.5 | -303.8 |
| | Central Baikal Basin | Kukuy K-2 MV, 2006St6GC5, massive, layered and fracture-filling hydrates (MV site) | 2.7 | 26.9 | -57.5 | -305.9 |
| | Central Baikal Basin | Kukuy K-2 MV, 2006St6GC5, massive, layered and fracture-filling hydrates (MV site) | 2.7 | 43.0 | -58.3 | -308.5 |
| | Central Baikal Basin | Kukuy K-2 MV, 2006St6GC5, massive, layered and fracture-filling hydrates (MV site) | 2.7 | 28.4 | -57.9 | -306.2 |
| | Central Baikal Basin | Kukuy K-2 MV, 2006St6GC7, massive, layered and fracture-filling hydrates (MV site) | 2.5 | 6.1 | -58.0 | -302.8 |
| | Central Baikal Basin | Kukuy K-2 MV, 2006St6GC7, massive, layered and fracture-filling hydrates (MV site) | 2.6 | 6.2 | -57.6 | -308.1 |
| | Central Baikal Basin | Kukuy K-2 MV, 2006St6GC7, massive, layered and fracture-filling hydrates (MV site) | 2.7 | 30.3 | -58.2 | -302.6 |
| | Central Baikal Basin | Kukuy K-2 MV, 2006St6GC7, massive, layered and fracture-filling hydrates (MV site) | 2.8 | 30.6 | -57.3 | -302.5 |
| | Central Baikal Basin | Kukuy K-2 MV, 2006St6GC7, massive, layered and fracture-filling hydrates (MV site) | 2.8 | 32.0 | -58.0 | -303.1 |
| | Central Baikal Basin | Kukuy K-2 MV, 2006St6GC8, massive, layered and fracture-filling hydrates (MV site) | 1.6 | 36.8 | -57.0 | -304.2 |
| | Central Baikal Basin | Kukuy K-2 MV, 2006St2GC22, massive, layered and fracture-filling hydrates (MV site) | 2.8 | 6.1 | -58.2 | -303.5 |
| | Central Baikal Basin | Kukuy K-2 MV, 2006St2GC22, massive, layered and fracture-filling hydrates (MV site) | 2.9 | 39.9 | -57.4 | -303.2 |
| | Central Baikal Basin | Kukuy K-2 MV, 2006St2GC22, massive, layered and fracture-filling hydrates (MV site) | 3.0 | 39.0 | -59.1 | -305.9 |
| | Central Baikal Basin | Kukuy K-2 MV, 2006St2GC23, massive, layered and fracture-filling hydrates (MV site) | 1.7 | 6.3 | -56.7 | -304.1 |
| | Central Baikal Basin | Kukuy K-2 MV, 2006St2GC23, massive, layered and fracture-filling hydrates (MV site) | 1.8 | 21.3 | -56.5 | -303.4 |
| | Central Baikal Basin | Kukuy K-2 MV, 2006St2GC23, massive, layered and fracture-filling hydrates (MV site) | 1.9 | 62.1 | -58.4 | -301.0 |
| | Central Baikal Basin | Kukuy K-2 MV, 2006St2GC25, massive, layered and fracture-filling hydrates (MV site) | 3.3 | 6.0 | -57.9 | -304.7 |
| | Central Baikal Basin | Kukuy K-2 MV, 2006St2GC30, massive, layered and fracture-filling hydrates (MV site) | 0.9 | 6.3 | -56.7 | -303.6 |
| | Central Baikal Basin | Kukuy K-2 MV, 2006St2GC30, massive, layered and fracture-filling hydrates (MV site) | 2.0 | 50.3 | -58.0 | -301.2 |
| | Central Baikal Basin | Kukuy K-2 MV, 2006St2GC30, massive, layered and fracture-filling hydrates (MV site) | 2.4 | 56.2 | -56.8 | -305.1 |
| | Central Baikal Basin | Kukuy K-2 MV, 2006St2GC32, massive, layered and fracture-filling hydrates (MV site) | 1.1 | 6.2 | -57.6 | -307.3 |
| Ginsburg *et al.* (1993) | Offshore Sakhalin Island, Okhotsk Sea | Gas Vent Field 1, Core 91-02-40, hydrate lenses and layers (Seep site) | 0.0 | 22068.2 | -64.3 | -207.0 |
| Mazurenko *et al.* (2009) | Offshore Sakhalin Island, Okhotsk Sea | Kitami, hydrate lenses and layers (Seep site) | 0.0-1.67 | 26168.4 | -65.0 | - |
| | Offshore Sakhalin Island, Okhotsk Sea | Hieroglyph, hydrate lenses and layers (Seep site) | 0.0-1.60 | 20695.8 | -64.6 | - |
| | Offshore Sakhalin Island, Okhotsk Sea | Chaos, hydrate lenses and layers (Seep site) | 0.0-4.90 | 25394.9 | -64.4 | - |
| | Offshore Sakhalin Island, Okhotsk Sea | Chaos, hydrate lenses and layers (Seep site) | 0.0-1.60 | 41370.8 | -64.0 | - |
| Hachikubo *et al.* (2010b) | Offshore Sakhalin Island, Okhotsk Sea | Kitami, hydrate lenses and layers (Seep site), $H_2S$ present in the hydrate | 0.0 | 39331.0 | -65.6 | -198.8 |
| | Offshore Sakhalin Island, Okhotsk Sea | Kitami, hydrate lenses and layers (Seep site) | 0.0 | 47887.0 | -65.4 | -199.4 |
| | Offshore Sakhalin Island, Okhotsk Sea | Hieroglyph, hydrate lenses and layers (Seep site) | 0.0 | 42056.0 | -65.1 | -200.9 |

| | | | | | | |
|---|---|---|---|---|---|---|
| | Offshore Sakhalin Island, Okhotsk Sea | Hieroglyph, hydrate lenses and layers (Seep site) | 0.0 | 49423.0 | -65.1 | -201.8 |
| | Offshore Sakhalin Island, Okhotsk Sea | Hieroglyph, hydrate lenses and layers (Seep site) | 0.0 | 1516.0 | -65.3 | -198.6 |
| | Offshore Sakhalin Island, Okhotsk Sea | Chaos, hydrate lenses and layers (Seep site) | 0.0 | 8728.0 | -65.0 | -200.2 |
| | Offshore Sakhalin Island, Okhotsk Sea | Chaos, hydrate lenses and layers (Seep site) | 0.0 | 10687.0 | -65.7 | -199.7 |
| | Offshore Sakhalin Island, Okhotsk Sea | Kopri, hydrate lenses and layers (Seep site) | 0.0 | 13199.0 | -65.8 | -198.0 |
| | Offshore Sakhalin Island, Okhotsk Sea | Kopri, hydrate lenses and layers (Seep site) | 0.0 | 8000.0 | -65.7 | -199.1 |
| | Offshore Sakhalin Island, Okhotsk Sea | Kopri, hydrate lenses and layers (Seep site) | 0.0 | 35175.0 | -65.1 | -198.1 |
| | Offshore Sakhalin Island, Okhotsk Sea | Kopri, hydrate lenses and layers (Seep site) | 0.0 | 18140.0 | -65.7 | -196.7 |
| | Offshore Sakhalin Island, Okhotsk Sea | Vniiokeangeologia, hydrate lenses and layers (Seep site) | 0.0 | 39629.0 | -63.6 | -199.3 |
| | Offshore Sakhalin Island, Okhotsk Sea | Poi, hydrate lenses and layers (Seep site) | 0.0 | 38212.0 | -65.0 | -201.1 |
| | Offshore Sakhalin Island, Okhotsk Sea | Poi, hydrate lenses and layers (Seep site) | 0.0 | 19429.0 | -63.2 | -202.3 |
| | Offshore Sakhalin Island, Okhotsk Sea | Poi, hydrate lenses and layers (Seep site) | 0.0 | 20444.0 | -64.6 | -200.5 |
| Kim *et al.* (2011) | Ulleung Basin | Site 07GHP-10, hydrate pieces recovered in a piston core (Seep site) | 2.5-5.2 | 2404.5 | -63.6 | -189 |
| | Ulleung Basin | Site 07GHP-10, hydrate pieces recovered in a piston core (Seep site) | 2.5-5.2 | 2735.3 | -66.9 | -190 |
| Kim *et al.* (2013b) | Ulleung Basin | Site UBGH1-10B, Core 5R, fracture-filling hydrates in pressure cores (Seep site) | 42.0 | 1371.8 | -64.1 | -199.0 |
| | Ulleung Basin | Site UBGH1-10B, Core 12P, fracture-filling hydrates in pressure cores (Seep site) | 109.0 | 1618.1 | -63.2 | -201.7 |
| | Ulleung Basin | Site UBGH1-10B, fracture-filling hydrates in pressure cores (Seep site) Core 14R | 118.0 | 1553.0 | -63.2 | -199.3 |
| | Ulleung Basin | Site UBGH1-10B, Core 17P, fracture-filling hydrates in pressure cores (Seep site) | 136.0 | 1781.8 | -62.8 | -201.3 |
| | Ulleung Basin | Site UBGH2-11B, Core 23P, fracture-filling hydrates in pressure cores (Seep site) | 128.5 | 2599.7 | -62.0 | -197.5 |
| Choi *et al.* (2013) | Ulleung Basin | Site UBGH2-7, solid pieces of hydrate (Seep site) | 6.5 | 1488.8 | -63.9 | -197.0 |
| | Ulleung Basin | Site UBGH2-7, solid pieces of hydrate (Seep site) | 14.0 | 1037.8 | -64.5 | -194.0 |
| | Ulleung Basin | Site UBGH2-7, solid pieces of hydrate (Seep site) | 24.7 | 782.5 | -67.9 | -194.0 |
| | Ulleung Basin | Site UBGH2-7, solid pieces of hydrate (Seep site) | 35.4 | 636.1 | -66.0 | -190.0 |
| | Ulleung Basin | Site UBGH2-7, solid pieces of hydrate (Seep site) | 45.1 | 620.5 | -63.7 | -189.0 |
| | Ulleung Basin | Site UBGH2-7, solid pieces of hydrate (Seep site) | 73.0 | 462.6 | -63.4 | -200.0 |
| | Ulleung Basin | Site UBGH2-11, solid pieces of hydrate (Seep site) | 30.0 | 838.1 | -64.9 | -194.0 |
| | Ulleung Basin | Site UBGH2-11, solid pieces of hydrate (Seep site) | 53.4 | 3338.7 | -63.3 | -197.0 |
| | Ulleung Basin | Site UBGH2-11, solid pieces of hydrate (Seep site) | 70.4 | 3128.8 | -62.5 | -201.0 |
| | Ulleung Basin | Site UBGH2-11, solid pieces of hydrate (Seep site) | 99.5 | 1740.1 | -63.2 | -201.0 |
| | Ulleung Basin | Site UBGH2-11, solid pieces of hydrate (Seep site) | 111.1 | 3530.1 | -63.6 | -198.0 |
| Stern and Lorenson (2014) | Krishna-Godavari Basin | NGHP-01-10B, HYD 7, hydrate sample, fracture-filling hydrates and hydrate nodules; locally vugs filled with hydrates (Seep site) | 25.6 | 50000.0* | -71.2 | - |
| | Krishna-Godavari Basin | NGHP-01-10B, HYD 29, hydrate sample, fracture-filling hydrates and hydrate nodules; locally vugs filled with hydrates (Seep site) | 110.0 | 50000.0* | -66.3 | - |
| | Krishna-Godavari Basin | NGHP-01-10D, HYD 71, hydrate sample, fracture-filling hydrates and hydrate nodules; locally vugs filled with hydrates (Seep site) | 102.1 | 9239.1 | -69.2 | -194.0 |
| | Krishna-Godavari Basin | NGHP-01-10D, HYD 82, hydrate sample, fracture-filling hydrates and hydrate nodules; locally vugs filled with hydrates (Seep site) | 131.3 | 7710.6 | -69.1 | -196.0 |
| | Krishna-Godavari Basin | NGHP-01-10D, HYD 41, hydrate sample, fracture-filling hydrates and hydrate nodules; locally vugs filled with hydrates (Seep site) | 34.9 | 3866.8 | -68.8 | -183.0 |
| | Krishna-Godavari Basin | NGHP-01-10D, HYD 55, hydrate sample, fracture-filling hydrates and hydrate nodules; locally vugs filled with hydrates (Seep site) | 52.6 | 11054.5 | -69.1 | -185.0 |
| | Krishna-Godavari Basin | NGHP-01-12, HYD 92, hydrate sample, fracture-filling hydrates and hydrate nodules; locally vugs filled with hydrates (Seep site) | 143.1 | 50000.0* | -61.4 | - |

| | | | | | | |
|---|---|---|---|---|---|---|
| | Krishna-Godavari Basin | NGHP-01-14, HYD 96, hydrate sample, pore-filling/disseminated hydrates with small isolated pieces | 104.7 | 50000.0 | -68.1 | -184.0 |
| | Andaman Sea | NGHP-01-17, hydrate sample, pore-filling hydrates (vugs and moldes) | 525.0 | 955.0 | -62.3 | -188.0 |
| (Lorenson and Collett, under review)** | Krishna-Godavari Basin | NGHP-01-10, analysis on pressure core, dominantly fracture-filling hydrates (Seep site) | 78.8 | 50000.0 | -69.2 | - |
| | Krishna-Godavari Basin | NGHP-01-10, analysis on pressure core, dominantly fracture-filling hydrates (Seep site) | 165.4 | 1667.0 | -68.2 | - |
| | Krishna-Godavari Basin | NGHP-01-10, gas hydrate sample, dominantly fracture-filling hydrates (Seep site) | 64.9 | - | -65.4 | - |
| | Krishna-Godavari Basin | NGHP-01-10, gas hydrate sample, dominantly fracture-filling hydrates (Seep site) | 25.7 | - | -69.3 | - |
| | Krishna-Godavari Basin | NGHP-01-10, gas hydrate sample, dominantly fracture-filling hydrates (Seep site) | 46.5 | 3923.8 | -70.1 | - |
| | Krishna-Godavari Basin | NGHP-01-10, gas hydrate sample, dominantly fracture-filling hydrates (Seep site) | 51.8 | - | -65.6 | - |
| | Krishna-Godavari Basin | NGHP-01-10, void gas analysis in hydrate occurrence interval, dominantly fracture-filling hydrates (Seep site) | 28.05 | 2100.0 | -75.0 | - |
| | Krishna-Godavari Basin | NGHP-01-10, analysis on pressure core, dominantly fracture-filling hydrates (Seep site) | 117.4 | 4700.0 | -68.2 | - |
| | Krishna-Godavari Basin | NGHP-01-10, analysis on pressure core, dominantly fracture-filling hydrates (Seep site) | 175.1 | 7100.0 | -67.6 | - |
| | Krishna-Godavari Basin | NGHP-01-10, analysis on pressure core, dominantly fracture-filling hydrates (Seep site) | 69.47 | 6600.0 | -68.6 | - |
| | Krishna-Godavari Basin | NGHP-01-10, analysis on pressure core, dominantly fracture-filling hydrates (Seep site) | 164.4 | 1300.0 | -67.9 | - |
| | Krishna-Godavari Basin | NGHP-01-21, void gas analysis in hydrate occurrence interval, dominantly fracture-filling hydrates (Seep site) | 48.4 | 7091.8 | -65.9 | - |
| | Krishna-Godavari Basin | NGHP-01-21, void gas analysis in hydrate occurrence interval, dominantly fracture-filling hydrates (Seep site) | 78.5 | 44216.8 | -66.9 | - |
| | Krishna-Godavari Basin | NGHP-01-21, gas hydrate sample, dominantly fracture-filling hydrates (Seep site) | 84 | 50000.0 | -66.5 | - |
| | Krishna-Godavari Basin | NGHP-01-21 gas hydrate sample, dominantly fracture-filling hydrates (Seep site) | 79.6 | - | -66.7 | - |
| | Krishna-Godavari Basin | NGHP-01-10, gas hydrate sample, dominantly fracture-filling hydrates (Seep site) | 64.9 | - | -65.4 | - |
| | Krishna-Godavari Basin | NGHP-01-12, analysis on pressure core, dominantly fracture-filling hydrates (Seep site) | 93.3 | 8000.0 | -67.9 | - |
| | Krishna-Godavari Basin | NGHP-01-14, void gas analysis in hydrate occurrence interval, pore-filling/disseminated hydrates | 69.1 | 49200.0 | -68.7 | - |
| | Krishna-Godavari Basin | NGHP-01-03, analysis on pressure core, pore-filling/disseminated hydrates | 176.0 | 49400.0 | -70.9 | - |
| | Krishna-Godavari Basin | NGHP-01-03, analysis on pressure core, pore-filling/disseminated hydrates | 184.0 | 49800.0 | -71.0 | - |
| | Krishna-Godavari Basin | NGHP-01-05, void gas analysis in hydrate occurrence interval, pore-filling/disseminated hydrates | 61.9 | 50000.0 | -67.9 | - |
| | Krishna-Godavari Basin | NGHP-01-05, void gas analysis in hydrate occurrence interval, pore-filling/disseminated hydrates | 70.7 | 50000.0 | -67.9 | - |
| | Krishna-Godavari Basin | NGHP-01-05, void gas analysis in hydrate occurrence interval, pore-filling/disseminated hydrates | 72.4 | 50000.0 | -67.9 | - |
| | Krishna-Godavari Basin | NGHP-01-05, void gas analysis in hydrate occurrence interval, pore-filling/disseminated hydrates | 22.9 | 50000.0 | -64.5 | - |
| | Krishna-Godavari Basin | NGHP-01-05, void gas analysis in hydrate occurrence interval, pore-filling/disseminated hydrates | 27.9 | 50000.0 | -66.6 | - |
| | Krishna-Godavari Basin | NGHP-01-05, analysis on pressure core, pore-filling/disseminated hydrates | 86.0 | 96300.0 | -67.2 | - |
| | Krishna-Godavari Basin | NGHP-01-05, analysis on pressure core, pore-filling/disseminated hydrates | 84.9 | 24900.0 | -65.6 | - |
| | Krishna-Godavari Basin | NGHP-01-05, analysis on pressure core, pore-filling/disseminated hydrates | 84.9 | 24900.0 | -65.5 | - |
| | Krishna-Godavari Basin | NGHP-01-05, analysis on pressure core, pore-filling/disseminated hydrates | 84.9 | 24900.0 | -65.7 | - |
| | Krishna-Godavari Basin | NGHP-01-05, analysis on pressure core, pore-filling/disseminated hydrates | 84.9 | 29400.0 | -65.5 | - |
| | Krishna-Godavari Basin | NGHP-01-07, void gas analysis in hydrate occurrence interval, fracture-filling hydrates | 71.6 | 32607.0 | -65.1 | - |
| | Krishna-Godavari Basin | NGHP-01-07, void gas analysis in hydrate occurrence interval, fracture-filling hydrates | 129.4 | 51707.0 | -64.3 | - |
| | Krishna-Godavari Basin | NGHP-01-07, analysis on pressure core, fracture-filling hydrates | 148.2 | 66549.0 | -62.6 | - |
| | Krishna-Godavari Basin | NGHP-01-15, void gas analysis in hydrate occurrence interval, pore-filling/disseminated hydrates | 78.8 | 12100.0 | -68.4 | - |
| | Krishna-Godavari Basin | NGHP-01-16, void gas analysis in hydrate occurrence interval, pore-filling/disseminated hydrates | 129.7 | 97100.0 | -62.3 | - |

| | | | | | | |
|---|---|---|---|---|---|---|
| | Krishna-Godavari Basin | NGHP-01-16, void gas analysis in hydrate occurrence interval, pore-filling/disseminated hydrates | 157.3 | 16400.0 | -61.9 | - |
| | Krishna-Godavari Basin | NGHP-01-16, void gas analysis in hydrate occurrence interval, pore-filling/disseminated hydrates | 187.1 | 16000.0 | -61.1 | - |
| | Krishna-Godavari Basin | NGHP-01-16, void gas analysis in hydrate occurrence interval, pore-filling/disseminated hydrates | 214.1 | 24500.0 | -60.8 | - |
| | Krishna-Godavari Basin | NGHP-01-16, analysis on pressure core, pore-filling/disseminated hydrates | 163.2 | 18300.0 | -62.2 | - |
| | Andaman Sea | NGHP-01-17, void gas analysis in hydrate occurrence interval, pore-filling/disseminated hydrates | 590.3 | 646.7 | -68.5 | - |
| | Andaman Sea | NGHP-01-17, void gas analysis in hydrate occurrence interval, pore-filling/disseminated hydrates | 267.12 | 8900.0 | -70.1 | - |
| | Andaman Sea | NGHP-01-17, void gas analysis in hydrate occurrence interval, pore-filling/disseminated hydrates | 278.33 | 12300.0 | -69.1 | - |
| | Andaman Sea | NGHP-01-17, void gas analysis in hydrate occurrence interval, pore-filling/disseminated hydrates | 290.87 | 12100.0 | -70.3 | - |
| | Andaman Sea | NGHP-01-17, void gas analysis in hydrate occurrence interval, pore-filling/disseminated hydrates | 323.76 | 15800.0 | -69.5 | - |
| | Andaman Sea | NGHP-01-17, void gas analysis in hydrate occurrence interval, pore-filling/disseminated hydrates | 335.08 | 2700.0 | -69.5 | - |
| | Andaman Sea | NGHP-01-17, void gas analysis in hydrate occurrence interval, pore-filling/disseminated hydrates | 351.08 | 20000.0 | -65.2 | - |
| | Andaman Sea | NGHP-01-17, void gas analysis in hydrate occurrence interval, pore-filling/disseminated hydrates | 358.16 | 13200.0 | -66.6 | - |
| | Andaman Sea | NGHP-01-17, void gas analysis in hydrate occurrence interval, pore-filling/disseminated hydrates | 370.05 | 6200.0 | -69.0 | - |
| | Andaman Sea | NGHP-01-17, void gas analysis in hydrate occurrence interval, pore-filling/disseminated hydrates | 373.44 | 7600.0 | -68.8 | - |
| | Andaman Sea | NGHP-01-17, void gas analysis in hydrate occurrence interval, pore-filling/disseminated hydrates | 399.57 | 6200.0 | -68.6 | - |
| | Andaman Sea | NGHP-01-17, void gas analysis in hydrate occurrence interval, pore-filling/disseminated hydrates | 418.53 | 8000.0 | -68.4 | - |
| | Andaman Sea | NGHP-01-17, void gas analysis in hydrate occurrence interval, pore-filling/disseminated hydrates | 424.8 | 6400.0 | -68.6 | - |
| | Andaman Sea | NGHP-01-17, void gas analysis in hydrate occurrence interval, pore-filling/disseminated hydrates | 445.76 | 3000.0 | -66.9 | - |
| | Andaman Sea | NGHP-01-17, void gas analysis in hydrate occurrence interval, pore-filling/disseminated hydrates | 454.93 | 20000.0 | -67.2 | - |
| | Andaman Sea | NGHP-01-17, void gas analysis in hydrate occurrence interval, pore-filling/disseminated hydrates | 474.95 | 6700.0 | -67.9 | - |
| | Andaman Sea | NGHP-01-17, void gas analysis in hydrate occurrence interval, pore-filling/disseminated hydrates | 493.22 | 3700.0 | -68.1 | - |
| | Andaman Sea | NGHP-01-17, void gas analysis in hydrate occurrence interval, pore-filling/disseminated hydrates | 515.46 | 5800.0 | -68.2 | - |
| | Andaman Sea | NGHP-01-17, void gas analysis in hydrate occurrence interval, pore-filling/disseminated hydrates | 531.38 | 4900.0 | -68.0 | - |
| | Andaman Sea | NGHP-01-17, void gas analysis in hydrate occurrence interval, pore-filling/disseminated hydrates | 562.65 | 1100.0 | -68.3 | - |
| | Andaman Sea | NGHP-01-17, void gas analysis in hydrate occurrence interval, pore-filling/disseminated hydrates | 573.18 | 900.0 | -66.1 | - |
| | Andaman Sea | NGHP-01-17, void gas analysis in hydrate occurrence interval, pore-filling/disseminated hydrates | 584.09 | 1600.0 | -67.6 | - |
| | Andaman Sea | NGHP-01-17, void gas analysis in hydrate occurrence interval, pore-filling/disseminated hydrates | 600.01 | 800.0 | -68.3 | - |
| | Andaman Sea | NGHP-01-17, void gas analysis in hydrate occurrence interval, pore-filling/disseminated hydrates | 617.78 | 1000.0 | -68.6 | - |
| | Andaman Sea | NGHP-01-17, void gas analysis in hydrate occurrence interval, pore-filling/disseminated hydrates | 635.25 | 800.0 | -68.2 | - |
| | Andaman Sea | NGHP-01-17, void gas analysis in hydrate occurrence interval, pore-filling/disseminated hydrates | 656.03 | 800.0 | -68.3 | - |

| | | | | | | |
|---|---|---|---|---|---|---|
| | Andaman Sea | NGHP-01-17, void gas analysis in hydrate occurrence interval, pore-filling/disseminated hydrates | 676.18 | 800.0 | -68.1 | - |
| | Andaman Sea | NGHP-01-17, void gas analysis in hydrate occurrence interval, pore-filling/disseminated hydrates | 684.53 | 600.0 | -67.6 | - |
| | Andaman Sea | NGHP-01-17, analysis on pressure core, pore-filling/disseminated hydrates | 329 | 11600.0 | -69.6 | - |
| | Andaman Sea | NGHP-01-17, analysis on pressure core, pore-filling/disseminated hydrates | 412.7 | 7400.0 | -69.9 | - |
| | Andaman Sea | NGHP-01-17, analysis on pressure core, pore-filling/disseminated hydrates | 586.3 | 1600.0 | -68.5 | - |
| | Mahanadi Basin | NGHP-01-18, void gas analysis in hydrate occurrence interval, pore-filling/disseminated hydrates | 141.8 | 5026.2 | -72.1 | - |
| | Mahanadi Basin | NGHP-01-18, void gas analysis in hydrate occurrence interval, pore-filling/disseminated hydrates | 168.9 | 3009.1 | -71.8 | - |
| | Mahanadi Basin | NGHP-01-18, void gas analysis in hydrate occurrence interval, pore-filling/disseminated hydrates | 139.6 | 4800.0 | -72.2 | - |
| | Mahanadi Basin | NGHP-01-18, void gas analysis in hydrate occurrence interval. Pore-filling/disseminated hydrates | 150.5 | 3700.0 | -71.6 | - |
| | Mahanadi Basin | NGHP-01-18, void gas analysis in hydrate occurrence interval, pore-filling/disseminated hydrates | 160.7 | 8300.0 | -71.6 | - |
| | Mahanadi Basin | NGHP-01-18, void gas analysis in hydrate occurrence interval, pore-filling/disseminated hydrates | 177.8 | 3900.0 | -70.7 | - |
| | Mahanadi Basin | NGHP-01-19, void gas analysis in hydrate occurrence interval, pore-filling/disseminated hydrates | 198.5 | 1395.6 | -72.8 | - |
| | Mahanadi Basin | NGHP-01-19, void gas analysis in hydrate occurrence interval, pore-filling/disseminated hydrates | 182.2 | 1200.0 | -73.1 | - |
| | Mahanadi Basin | NGHP-01-19, analysis on pressure core, pore-filling/disseminated hydrates | 126.0 | 1300.0 | -75.4 | - |
| | Mahanadi Basin | NGHP-01-19, analysis on pressure core, pore-filling/disseminated hydrates | 195.3 | 700.0 | -73.1 | - |
| Hachikubo *et al.* (2015) | Umitaka Spur, Joetsu Basin | MD179-3305G, probably massive/layered hydrates (Seep site) | - | 3158.0 | -36.6 | -167.0 |
| | Umitaka Spur, Joetsu Basin | MD179-3305G, probably massive/layered hydrates (Seep site) | - | 3389.0 | -36.0 | -164.0 |
| | Umitaka Spur, Joetsu Basin | MD179-3305G, probably massive/layered hydrates (Seep site) | - | 3086.0 | -36.0 | -164.0 |
| | Umitaka Spur, Joetsu Basin | MD179-3305G, probably massive/layered hydrates (Seep site) | - | 2859.0 | -34.6 | -167.0 |
| | Umitaka Spur, Joetsu Basin | MD179-3306, probably massive/layered hydrates (Seep site) | 4.5 | 3176.0 | -37.3 | -164.0 |
| | Umitaka Spur, Joetsu Basin | MD179-3306, probably massive/layered hydrates (Seep site) | 4.5 | 4213.0 | -35.7 | -167.0 |
| | Joetsu Knoll, Joetsu Basin | MD179-3317, probably massive/layered hydrates (Seep site) | 31.5 | 5783.0 | -56.4 | -194.0 |
| | Joetsu Knoll, Joetsu Basin | MD179-3317, probably massive/layered hydrates (Seep site) | 31.5 | 6446.0 | -54.6 | -195.0 |
| | Joetsu Knoll, Joetsu Basin | MD179-3317, probably massive/layered hydrates (Seep site) | 31.5 | 5758.0 | -54.8 | -194.0 |
| | Joetsu Knoll, Joetsu Basin | MD179-3317, probably massive/layered hydrates (Seep site) | 31.5 | 5810.0 | -54.8 | -194.0 |
| | Joetsu Knoll, Joetsu Basin | MD179-3317, probably massive/layered hydrates (Seep site) | 31.5 | 4819.0 | -57.1 | -194.0 |
| | Joetsu Knoll, Joetsu Basin | MD179-3317, probably massive/layered hydrates (Seep site) | 31.5 | 4713.0 | -55.4 | -195.0 |
| | Joetsu Knoll, Joetsu Basin | MD179-3317, probably massive/layered hydrates (Seep site) | 31.5 | 4603.0 | -54.8 | -194.0 |
| | Joetsu Knoll, Joetsu Basin | MD179-3318C, probably massive/layered hydrates (Seep site) | 1.5 | 6257.0 | -44.0 | -189.0 |
| | Joetsu Knoll, Joetsu Basin | MD179-3318C, probably massive/layered hydrates (Seep site) | 1.5 | 2328.0 | - | -188.0 |
| | Joetsu Knoll, Joetsu Basin | MD179-3318C, probably massive/layered hydrates (Seep site) | 1.5 | 2172.0 | -44.3 | -190.0 |
| | Joetsu Knoll, Joetsu Basin | MD179-3318C, probably massive/layered hydrates (Seep site) | 1.5 | 9682.0 | -43.9 | - |
| Hachikubo *et al.* (2015), data extracted from Figure 3a | Umitaka Spur, Joetsu Basin | Probably massive/layered hydrates (Seep site) | - | 968.0 | -34.9 | - |
| | Umitaka Spur, Joetsu Basin | Probably massive/layered hydrates (Seep site) | - | 2369.0 | -39.1 | - |
| | Umitaka Spur, Joetsu Basin | Probably massive/layered hydrates (Seep site) | - | 2321.3 | -37.9 | - |
| | Umitaka Spur, Joetsu Basin | Probably massive/layered hydrates (Seep site) | - | 5131.5 | -38.0 | - |
| | Umitaka Spur, Joetsu Basin | Probably massive/layered hydrates (Seep site) | - | 165.5 | -39.3 | - |

| | | | | | | |
|---|---|---|---|---|---|---|
| | Umitaka Spur, Joetsu Basin | Probably massive/layered hydrates (Seep site) | - | 135.0 | -36.7 | - |
| | Umitaka Spur, Joetsu Basin | Probably massive/layered hydrates (Seep site) | - | 66.3 | -36.0 | - |
| | Umitaka Spur, Joetsu Basin | Probably massive/layered hydrates (Seep site) | - | 2.0 | -32.5 | - |
| | Umitaka Spur, Joetsu Basin | Probably massive/layered hydrates (Seep site) | - | 9.1 | -32.8 | - |
| | Umitaka Spur, Joetsu Basin | Probably massive/layered hydrates (Seep site) | - | 12.2 | -30.5 | - |
| | Umitaka Spur, Joetsu Basin | Probably massive/layered hydrates (Seep site) | - | 20.3 | -33.9 | - |
| | Umitaka Spur, Joetsu Basin | Probably massive/layered hydrates (Seep site) | - | 23.9 | -33.1 | - |
| | Umitaka Spur, Joetsu Basin | Probably massive/layered hydrates (Seep site) | - | 24.2 | -31.6 | - |
| | Umitaka Spur, Joetsu Basin | Probably massive/layered hydrates (Seep site) | - | 24.9 | -31.3 | - |
| | Umitaka Spur, Joetsu Basin | Probably massive/layered hydrates (Seep site) | - | 30.3 | -31.3 | - |
| | Umitaka Spur, Joetsu Basin | Probably massive/layered hydrates (Seep site) | - | 45.3 | -30.2 | - |
| | Umitaka Spur, Joetsu Basin | Probably massive/layered hydrates (Seep site) | - | 36.1 | -31.9 | - |
| | Umitaka Spur, Joetsu Basin | Probably massive/layered hydrates (Seep site) | - | 44.0 | -31.8 | - |
| | Umitaka Spur, Joetsu Basin | Probably massive/layered hydrates (Seep site) | - | 41.4 | -32.6 | - |
| | Umitaka Spur, Joetsu Basin | Probably massive/layered hydrates (Seep site) | - | 41.4 | -32.8 | - |
| | Joetsu Knoll, Joetsu Basin | Probably massive/layered hydrates (Seep site) | - | 263.3 | -57.9 | - |
| | Joetsu Knoll, Joetsu Basin | Probably massive/layered hydrates (Seep site) | - | 568.8 | -55.4 | - |
| | Joetsu Knoll, Joetsu Basin | Probably massive/layered hydrates (Seep site) | - | 694.8 | -54.2 | - |
| | Joetsu Knoll, Joetsu Basin | Probably massive/layered hydrates (Seep site) | - | 1112.6 | -51.8 | - |
| | Joetsu Knoll, Joetsu Basin | Probably massive/layered hydrates (Seep site) | - | 3026.2 | -53.7 | - |
| | Joetsu Knoll, Joetsu Basin | Probably massive/layered hydrates (Seep site) | - | 2125.8 | -56.6 | - |
| | Joetsu Knoll, Joetsu Basin | Probably massive/layered hydrates (Seep site) | - | 2722.0 | -56.6 | - |
| Pape *et al.* (2014) | Kumano Forearc, Nankai Trough | MV#2 16764-1. Disseminated hydrate in mud breccia (MV site) | 0.0 | 225.7 | - | - |
| | Kumano Forearc, Nankai Trough | MV#2 16771-1. Disseminated hydrate in mud breccia (MV site) | 0.0 | 155.8 | -39.5 | - |
| | Kumano Forearc, Nankai Trough | MV#2 16772-1. Disseminated hydrate in mud breccia (MV site) | 0.0 | 162.9 | -40.5 | - |
| | Kumano Forearc, Nankai Trough | MV#2 16788-1. Disseminated hydrate in mud breccia (MV site) | 0.0 | 221.2 | -39.7 | - |
| | Kumano Forearc, Nankai Trough | MV#2 16788-2. Disseminated hydrate in mud breccia (MV site) | 0.0 | 196.9 | -39.9 | - |
| | Kumano Forearc, Nankai Trough | MV#4 16722-2. Disseminated hydrate in mud breccia (MV site) | 0.0 | 34.0 | -39.4 | - |
| | Kumano Forearc, Nankai Trough | MV#4 16725-1. Disseminated hydrate in mud breccia (MV site) | 0.0 | 54.4 | -38.9 | - |
| | Kumano Forearc, Nankai Trough | MV#4 16736-1. Disseminated hydrate in mud breccia (MV site) | 0.0 | 66.8 | -39.3 | - |
| | Kumano Forearc, Nankai Trough | MV#5 16746-1. Disseminated hydrate in mud breccia (MV site) | 0.0 | 901.0 | -37.6 | - |
| | Kumano Forearc, Nankai Trough | MV#10 16716-2. Disseminated hydrate in mud breccia (MV site) | 0.0 | 116.0 | -38.0 | - |
| Sassen and Curiale (2006) | Northern Makassar Strait | Site 1 gas hydrate nodules (Seep site) | 0.0-0.2 | 11933.2 | -66.9 | -192.9 |
| | Northern Makassar Strait | Site 1 gas hydrate nodules (Seep site) | 5.0-5.2 | 39370.1 | -69.9 | -181.4 |
| | Northern Makassar Strait | Site 1 gas hydrate nodules (Seep site) | 5.2-5.4 | 9658.7 | -70.1 | -193.5 |
| | Northern Makassar Strait | Site 1 gas hydrate nodules (Seep site) | 5.8-6.0 | 5634.4 | -71.4 | -191.9 |
| | Northern Makassar Strait | Site 1 gas hydrate nodules (Seep site) | 6.2-6.4 | 20292.2 | -71.3 | -185.8 |
| | Northern Makassar Strait | Site 1 gas hydrate nodules (Seep site) | 6.2-6.4 | 11466.6 | -71.9 | -189.8 |
| | Northern Makassar Strait | Site 1 gas hydrate nodules (Seep site) | 6.2-6.4 | 10384.6 | -71.3 | -193.0 |
| | Northern Makassar Strait | Site 1 gas hydrate nodules (Seep site) | 6.2-6.4 | 22153.3 | -72.4 | -190.7 |
| Kvenvolden *et al.* (1984) | Offshore Guatemala | DSDP 84, 170. Massive hydrates. | 249.0 | 414.2 | -41.4 | - |
| | Offshore Guatemala | DSDP 84, 170. Massive hydrates. | 249.0 | 451.9 | -43.0 | - |
| | Offshore Guatemala | DSDP 84, 170. Massive hydrates. | 249.0 | 414.1 | -41.4 | - |
| Kvenvolden and Kastner (1990) | Offshore Peru | ODP 112, 685. Small hydrate nodules. | 165.6 | 14924.4 | -65.0 | - |

| | | | | | | |
|---|---|---|---|---|---|---|
| | Offshore Peru | ODP 112, 688. Small hydrate nodules. | 141.0 | 45453.5 | -59.6 | - |
| Brooks *et al.* (1983) | Blake Ridge, offshore N Carolina | DSDP 76, Site 533, layered hydrate | 238.0 | 6000.0 | -68.0 | - |
| | Blake Ridge, offshore N Carolina | DSDP 76, Site 533, disseminated hydrates, inferred from pressure core degassing | 333.0 | 5600.0 | -66.0 | - |
| | Blake Ridge, offshore N Carolina | DSDP 76, Site 533, disseminated hydrates, inferred from pressure core degassing | 361.0 | 5200.0 | -64.0 | - |
| | Blake Ridge, offshore N Carolina | DSDP 76, Site 533, disseminated hydrates, inferred from pressure core degassing | 392.0 | 4100.0 | -69.0 | - |
| Borowski (2004) | Blake Ridge, offshore N Carolina | ODP 164, Site 994, nodular hydrate piece | 259.9 | 11225.0 | -67.0 | - |
| | Blake Ridge, offshore N Carolina | ODP 164, Site 994, nodular hydrate piece | 259.9 | 55511.1 | -69.7 | - |
| | Blake Ridge, offshore N Carolina | ODP 164, Site 994, nodular hydrate piece | 259.9 | 142814.3 | -67.4 | -205.0 |
| | Blake Ridge, offshore N Carolina | ODP 164, Site 994, nodular hydrate piece | 259.9 | - | -63.5 | - |
| | Blake Ridge, offshore N Carolina | ODP 164, Site 994, nodular hydrate piece | 261.1 | 4331.1 | - | - |
| | Blake Ridge, offshore N Carolina | ODP 164, Site 994, nodular hydrate piece | 262.5 | - | - | - |
| | Blake Ridge, offshore N Carolina | ODP 164, Site 996, nodular hydrate piece | 0.1 | 971.7 | - | - |
| | Blake Ridge, offshore N Carolina | ODP 164, Site 996, hydrate veins | 52.5 | 1293.5 | -63.9 | - |
| | Blake Ridge, offshore N Carolina | ODP 164, Site 996, hydrate veins | 63.8 | 1313.4 | -67.4 | - |
| | Blake Ridge, offshore N Carolina | ODP 164, Site 996, nodular hydrate piece | 0.2 | 730.7 | - | 199.7c |
| | Blake Ridge, offshore N Carolina | ODP 164, Site 996, nodular hydrate piece | 0.2 | 1179.2 | - | - |
| | Blake Ridge, offshore N Carolina | ODP 164, Site 996, nodular hydrate piece | >0.0 | 1369.4 | -65.9 | - |
| | Blake Ridge, offshore N Carolina | ODP 164, Site 996, nodular hydrate piece | 1.5 | 1143.8 | - | - |
| | Blake Ridge, offshore N Carolina | ODP 164, Site 996, nodular hydrate piece | 2.4 | - | -65.9 | - |
| | Blake Ridge, offshore N Carolina | ODP 164, Site 996, nodular hydrate piece | 0.2 | - | -65.8 | -136.0 |
| | Blake Ridge, offshore N Carolina | ODP 164, Site 996, nodular hydrate piece | 0.2 | - | -66.6 | -175.0 |
| | Blake Ridge, offshore N Carolina | ODP 164, Site 996, hydrate veins | 22.6 | - | - | - |
| | Blake Ridge, offshore N Carolina | ODP 164, Site 996, hydrate veins | 32.1 | 1302.2 | - | - |
| | Blake Ridge, offshore N Carolina | ODP 164, Site 996, hydrate veins | 41.7 | 1319.4 | - | - |
| | Blake Ridge, offshore N Carolina | ODP 164, Site 996, hydrate veins | 45.9 | - | -66.6 | -175.0 |
| | Blake Ridge, offshore N Carolina | ODP 164, Site 996, nodular hydrate piece | 46.7 | 1319.4 | - | - |
| | Blake Ridge, offshore N Carolina | ODP 164, Site 996, nodular hydrate piece | 61.3 | 1373.5 | 70.7 | -193.0 |
| | Blake Ridge, offshore N Carolina | ODP 164, Site 997, nodular hydrate piece | 331.0 | 4926.4 | -65.8 | -196.0 |
| | Blake Ridge, offshore N Carolina | ODP 164, Site 997, nodular hydrate piece | 331.0 | 52621.1 | -66.2 | -201.0 |
| | Blake Ridge, offshore N Carolina | ODP 164, Site 997, nodular hydrate piece | 331.0 | 49975.0 | -66.1 | - |
| | Blake Ridge, offshore N Carolina | ODP 164, Site 997, nodular hydrate piece | 331.0 | 90881.8 | -66.5 | -206.0 |
| | Blake Ridge, offshore N Carolina | ODP 164, Site 997, nodular hydrate piece | 331.0 | 142842.9 | -65.9 | - |
| | Blake Ridge, offshore N Carolina | ODP 164, Site 997, nodular hydrate piece | 331.0 | - | -65.8 | -191.0 |
| Liu *et al.* (2015) | South China Sea, Pearl River Mouth Basin | PRM GMGS2-08F | 71.1 | 1999.0 | -71.2 | -196.0 |
| | South China Sea, Shenhu Area | SH-2, pore filling/disseminated hydrate | 191.0 | 195.0784 | -63.2 | -194 |
| Liu *et al.* (2012) | South China Sea, Shenhu Area | SH-2, pore filling/disseminated hydrate | ~200.0 | 293.1176 | -65.7 | - |
| | South China Sea, Shenhu Area | SH-7, pore filling/disseminated hydrate | ~200.0 | 160.2903 | -65.1 | - |
| Kida *et al.* (2015) | Daini-Atsumi Knoll, Eastern Nankai Trough, | AT1-C-8P. Gas released by pore-filling gas hydrates | 279.2 | 279.2 | 33231.0 | - |
| | Daini-Atsumi Knoll, Eastern Nankai Trough, | AT1-C-8P. Gas released by pore-filling gas hydrates | 279.3 | 279.3 | 99441.0 | - |
| | Daini-Atsumi Knoll, Eastern Nankai Trough, | AT1-C-8P. Gas released by pore-filling gas hydrates | 279.3 | 279.3 | 60789.0 | - |
| | Daini-Atsumi Knoll, Eastern Nankai Trough, | AT1-C-8P. Gas released by pore-filling gas hydrates | 279.4 | 279.4 | 55095.0 | - |
| | Daini-Atsumi Knoll, Eastern Nankai Trough, | AT1-C-8P. Gas released by pore-filling gas hydrates | 279.9 | 279.9 | 63758.0 | -62.0 |
| | Daini-Atsumi Knoll, Eastern Nankai Trough, | AT1-C-10P. Gas released by pore-filling gas hydrates | 284.2 | 284.2 | 13550.0 | - |
| | Daini-Atsumi Knoll, Eastern Nankai Trough, | AT1-C-10P. Gas released by pore-filling gas hydrates | 284.6 | 284.6 | 20535.0 | -65.0 |

| | | | | | | |
|---|---|---|---|---|---|---|
| | Daini-Atsumi Knoll, Eastern Nankai Trough, | AT1-C-10P. Gas released by pore-filling gas hydrates | 285.8 | 285.8 | 19459.0 | -69.0 |
| | Daini-Atsumi Knoll, Eastern Nankai Trough, | AT1-C-12P. Gas released by pore-filling gas hydrates | 290.1 | 290.1 | 14305.0 | - |
| | Daini-Atsumi Knoll, Eastern Nankai Trough, | AT1-C-12P. Gas released by pore-filling gas hydrates | 290.2 | 290.2 | 18422.0 | - |
| | Daini-Atsumi Knoll, Eastern Nankai Trough, | AT1-C-12P. Gas released by pore-filling gas hydrates | 290.3 | 290.3 | 14003.0 | - |
| | Daini-Atsumi Knoll, Eastern Nankai Trough, | AT1-C-12P. Gas released by pore-filling gas hydrates | 291.4 | 291.4 | 13902.0 | -68.0 |
| | Daini-Atsumi Knoll, Eastern Nankai Trough, | AT1-C-12P. Gas released by pore-filling gas hydrates | 291.5 | 291.5 | 12019.0 | -68.0 |
| | Daini-Atsumi Knoll, Eastern Nankai Trough, | AT1-C-12P. Gas released by pore-filling gas hydrates | 292.0 | 292.0 | 8470.0 | -66.0 |
| | Daini-Atsumi Knoll, Eastern Nankai Trough, | AT1-C-13P. Gas released by pore-filling gas hydrates | 294.3 | 294.3 | 3584.0 | - |
| | Daini-Atsumi Knoll, Eastern Nankai Trough, | AT1-C-14P. Gas released by pore-filling gas hydrates | 296.3 | 296.3 | 54581.0 | -59.0 |
| | Daini-Atsumi Knoll, Eastern Nankai Trough, | AT1-C-18P. Gas released by pore-filling gas hydrates | 308.5 | 308.5 | 21753.0 | - |
| | Daini-Atsumi Knoll, Eastern Nankai Trough, | AT1-C-18P. Gas released by pore-filling gas hydrates | 309.7 | 309.7 | 19274.0 | -59.0 |
| | Daini-Atsumi Knoll, Eastern Nankai Trough, | AT1-C-18P Gas released by pore-filling gas hydrates | 310.1 | 310.1 | 14693.0 | -57.0 |
| | Daini-Atsumi Knoll, Eastern Nankai Trough, | AT1-C-20P. Gas released by pore-filling gas hydrates | 314.1 | 314.1 | 3413.0 | - |
| | Daini-Atsumi Knoll, Eastern Nankai Trough, | AT1-C-20P. Gas released by pore-filling gas hydrates | 315.3 | 315.3 | 3863.0 | -58.0 |
| | Daini-Atsumi Knoll, Eastern Nankai Trough, | AT1-C-20P. Gas released by pore-filling gas hydrates | 315.4 | 315.4 | 4933.0 | -65.0 |
| | Daini-Atsumi Knoll, Eastern Nankai Trough, | AT1-C-20P. Gas released by pore-filling gas hydrates | 315.8 | 315.8 | 5352.0 | - |
| | Daini-Atsumi Knoll, Eastern Nankai Trough, | AT1-C-20P. Gas released by pore-filling gas hydrates | 316.1 | 316.1 | 3636.0 | - |
| | Daini-Atsumi Knoll, Eastern Nankai Trough, | AT1-C-20P. Gas released by pore-filling gas hydrates | 316.1 | 316.1 | 3157.0 | - |
| | Daini-Atsumi Knoll, Eastern Nankai Trough, | AT1-C-20P. Gas released by pore-filling gas hydrates | 316.1 | 316.1 | 2825.0 | - |
| | Daini-Atsumi Knoll, Eastern Nankai Trough, | AT1-C-20P. Gas released by pore-filling gas hydrates | 316.3 | 316.3 | 4033.0 | -65.0 |
| | Daini-Atsumi Knoll, Eastern Nankai Trough, | AT1-C-20P. Gas released by pore-filling gas hydrates | 316.6 | 316.6 | 4357.0 | - |
| Milkov (2005) | MITI Site, Eastern Nankai Trough | Pore-filling gas hydrates | 236.0 | 10000.0 | -70.2 | -186.0 |
| | MITI Site, Eastern Nankai Trough | Pore-filling gas hydrates | 239.0 | 4996.5 | -70.5 | - |
| | MITI Site, Eastern Nankai Trough | Pore-filling gas hydrates | 248.0 | 4997.0 | -66.4 | - |
| | MITI Site, Eastern Nankai Trough | Pore-filling gas hydrates | 257.0 | 4997.5 | -66.7 | - |
| | MITI Site, Eastern Nankai Trough | Pore-filling gas hydrates | 259.0 | 10000.0 | -69.3 | -193.0 |
| Lu *et al.* (2013) | Qinghai, Tibet Plateau | Well DK-1, sample G-5-1-1, fracture-filling hydrates in hard rocks | 134.0 | 2.3 | -50.5 | -262.0 |
| | Qinghai, Tibet Plateau | Well DK-1, sample G-6-1-1, fracture-filling hydrates in hard rocks | 143.0 | 1.6 | -39.5 | -266.0 |
| | Qinghai, Tibet Plateau | Well DK-1, sample S-1-2 (from drilling mud), fracture-filling hydrates in hard rocks | - (from drilling mud) | 3.0 | -47.4 | -268.0 |
| Lorenson (1999) | McKenzie Delta, Beaufort Sea region | Mallik field, JAPEX/JNOC/GSC Mallik 2L-38 gas hydrate research well, pore filling hydrates at high saturation in coarse sands | 898.0 | 766.6 | -48.7 | -231.0 |
| | McKenzie Delta, Beaufort Sea region | Mallik field, JAPEX/JNOC/GSC Mallik 2L-38 gas hydrate research well, pore filling hydrates at high saturation in coarse sands | 898.0 | 1994.8 | - | - |
| | McKenzie Delta, Beaufort Sea region | Mallik field, JAPEX/JNOC/GSC Mallik 2L-38 gas hydrate research well, pore filling hydrates at high saturation in coarse sands | 904.8 | 4981.5 | -41.2 | -220.0 |
| | McKenzie Delta, Beaufort Sea region | Mallik field, JAPEX/JNOC/GSC Mallik 2L-38 gas hydrate research well, pore filling hydrates at high saturation in coarse sands | 904.8 | 1661.3 | - | - |
| | McKenzie Delta, Beaufort Sea region | Mallik field, JAPEX/JNOC/GSC Mallik 2L-38 gas hydrate research well, pore filling hydrates at high saturation in coarse sands | 911.8 | 3329.0 | -40.8 | -242.0 |
| | McKenzie Delta, Beaufort Sea region | Mallik field, JAPEX/JNOC/GSC Mallik 2L-38 gas hydrate research well, pore filling hydrates at high saturation in coarse sands | 914.6 | 2220.5 | -39.6 | -230.0 |
| | McKenzie Delta, Beaufort Sea region | Mallik field, JAPEX/JNOC/GSC Mallik 2L-38 gas hydrate research well, pore filling hydrates at high saturation in coarse sands | 898.0 | 766.6 | -48.7 | -231.0 |
| | | | | | | |

| | | | | | | |
|---|---|---|---|---|---|---|
| Uchida *et al.* (1999b) | McKenzie Delta, Beaufort Sea region | Mallik field, JAPEX/JNOC/GSC Mallik 2L-38 gas hydrate research well, pore filling hydrates at high saturation in coarse sands | 898.0 | 766.6 | -48.7 | -231.0 |
| | McKenzie Delta, Beaufort Sea region | Mallik field, JAPEX/JNOC/GSC Mallik 2L-38 gas hydrate research well, pore filling hydrates at high saturation in coarse sands | 898.0 | 1994.8 | - | - |
| | McKenzie Delta, Beaufort Sea region | Mallik field, JAPEX/JNOC/GSC Mallik 2L-38 gas hydrate research well, pore filling hydrates at high saturation in coarse sands | 904.8 | 4981.5 | -41.2 | -220.0 |
| | McKenzie Delta, Beaufort Sea region | Mallik field, JAPEX/JNOC/GSC Mallik 2L-38 gas hydrate research well, pore filling hydrates at high saturation in coarse sands | 904.8 | 1661.3 | - | - |
| | McKenzie Delta, Beaufort Sea region | Mallik field, JAPEX/JNOC/GSC Mallik 2L-38 gas hydrate research well, pore filling hydrates at high saturation in coarse sands | 911.8 | 3329.0 | -40.8 | -242.0 |
| | McKenzie Delta, Beaufort Sea region | Mallik field, JAPEX/JNOC/GSC Mallik 2L-38 gas hydrate research well, pore filling hydrates at high saturation in coarse sands | 914.6 | 2220.5 | -39.6 | -230.0 |
| Lorenson *et al.* (2011) | Alaska North Slope | Mount Elbert Gas Hydrate Stratigraphic Test Well (cutting gas composition in hydrate-bearing intervals); Unit C, pore filling hydrates at high saturation in coarse sands | 618.8 | 40733.3 | -49.5 | -237.0 |
| | Alaska North Slope | Mount Elbert Gas Hydrate Stratigraphic Test Well (cutting gas composition in hydrate-bearing intervals); Unit C, pore filling hydrates at high saturation in coarse sands | 619.9 | 42553.1 | -49.6 | -235.0 |
| | Alaska North Slope | Mount Elbert Gas Hydrate Stratigraphic Test Well (cutting gas composition in hydrate-bearing intervals); Unit C, pore filling hydrates at high saturation in coarse sands | 620.0 | 26015.7 | -49.0 | -243.0 |
| | Alaska North Slope | Mount Elbert Gas Hydrate Stratigraphic Test Well (cutting gas composition in hydrate-bearing intervals); Unit C, pore filling hydrates at high saturation in coarse sands | 626.0 | 40830.4 | -49.5 | -243.0 |
| | Alaska North Slope | Mount Elbert Gas Hydrate Stratigraphic Test Well (cutting gas composition in hydrate-bearing intervals); Unit D, pore filling hydrates at high saturation in coarse sands | 655.0 | 30102.7 | -48.8 | -232.0 |
| | Alaska North Slope | Mount Elbert Gas Hydrate Stratigraphic Test Well (cutting gas composition in hydrate-bearing intervals); Unit D, pore filling hydrates at high saturation in coarse sands | 657.0 | 19305.6 | -48.8 | -249.0 |
| | Alaska North Slope | Mount Elbert Gas Hydrate Stratigraphic Test Well (cutting gas composition in hydrate-bearing intervals); Unit D, pore filling hydrates at high saturation in coarse sands | 659.3 | 18375.6 | -48.9 | -243.0 |
| | Alaska North Slope | Mount Elbert Gas Hydrate Stratigraphic Test Well (cutting gas composition in hydrate-bearing intervals); Unit D, pore filling hydrates at high saturation in coarse sands | 660.2 | 38525.6 | -48.9 | -242.0 |
| | Alaska North Slope | Mount Elbert Gas Hydrate Stratigraphic Test Well (cutting gas composition in hydrate-bearing intervals); Unit D, pore filling hydrates at high saturation in coarse sands | 661.0 | 11103.8 | -48.8 | -251.0 |
| | Alaska North Slope | Mount Elbert Gas Hydrate Stratigraphic Test Well (cutting gas composition in hydrate-bearing intervals), pore filling hydrates at high saturation in coarse sands; Unit D | 661.1 | 12763.3 | -48.6 | -260.0 |
| | Alaska North Slope | Mount Elbert Gas Hydrate Stratigraphic Test Well (cutting gas composition in hydrate-bearing intervals); Unit D, pore filling hydrates at high saturation in coarse sands | 663.9 | 10484.3 | -48.9 | -250.0 |
| | Alaska North Slope | Mount Elbert Gas Hydrate Stratigraphic Test Well (cutting gas composition in hydrate-bearing intervals); Unit D, pore filling hydrates at high saturation in coarse sands | 664.5 | 29202.1 | -49.2 | -248.0 |
| | Alaska North Slope | Mount Elbert Gas Hydrate Stratigraphic Test Well (cutting gas composition in hydrate-bearing intervals); Unit D, pore filling hydrates at high saturation in coarse sands | 664.5 | 9865.1 | -48.5 | -252.0 |

**Table 1.2.** Compilation of geochemical data ($C_1/C_{2+}$, $\delta^{13}C$ of methane ($C_1$) and δD methane ($C_1$)) of recovered gas hydrate samples and gas evolved from gas hydrate-bearing sediments in cores at *'seep'* and *'non-seep'* sites worldwide. MV= Mud volcano.
* = Assumed value (no detectable $C_{2+}$ hydrocarbons).
** = The data included here comes from analyses on void gas data within the zones of hydrate occurrence, based on Kumar *et al.* (2014).

# Chapter 2. Geological setting of the study areas

## 2.1. Introduction

The data and the results presented in **Chapters 3-5** derive from the interpretation of a unique dataset, which is the product of a geophysical and petrophysical geohazard study performed by Shell offshore Sabah (NW Borneo). The results of **Chapter 6** are instead the product of the interpretation of 3D seismic data acquired by Shell in a frontier exploration area, the Guajira Basin, located in ultra-deep waters offshore Northern Colombia (**Figs. 2.1, 2.5**). **Chapter 7** reviews data from these two and many others well-known gas hydrate provinces. The reader is referred to the references provided in **Chapter 7** (see **Tabs. 7.1-7.3**) for details about the geological settings of these areas. Here I provide a geological and tectonic overview for the gas hydrate provinces of the NW Borneo and the Guajira basin, which will serve as a framework, regarding the structural setting, stratigraphy and hydrocarbon system, for the results presented in the following chapters. The choice of these two areas has exclusively derived from the availability of data during this PhD project. Both the NW Borneo margin and the Guajira basin represent regions dominated by compressive tectonic processes, with the development of thrust-cored anticlines, which severely impact the fluid flow system, focusing fluxes at the crest of such structures. Therefore, a limitation of this study consists in the lack of an available dataset from a passive margin dominated by extensional tectonic processes. In contrast, despite the relative similarities, in terms of tectonic structures, remarkable differences are interpreted to exist as regards the host lithology for hydrate-bearing sediments. Overall, the presented case studies highlight a wide range of possible hydrate distribution patterns in areas dominated by focused fluid fluxes in compressive settings.

## 2.2. Offshore Sabah (NW Borneo)

The present-day architecture of the continental margin offshore Sabah (**Figs. 2.1a, 2.2, 2.3**) is the result of multiple tectonic events, spanning from Early-Mid Miocene to the present-day. This region was affected by subduction processes, with the oceanic crust of the

South China Sea moving southeastward and beneath the formerly submerged NW Borneo margin. This process was halted in the Early-Mid Miocene by the interference of the Dangerous Grounds, a thinned continental crust, across the subduction zone, which led to the uplift of the accretionary complex. This event resulted in the formation of the Borneo island, accompanied by an increase in the sediment delivery along the margin (Hutchison, 2010).

Later compression along the margin, up to present-day has been driven by far-field and gravitational tectonic movements. The far-field compression (*'plate push'* mechanism) activated older weak tectonic surfaces. This compression is suggested to be associated with the subduction of the Philippine and Indo-Australian Plates beneath Sundaland and Indonesia, as well as with *'escape tectonics'* related to the Himalaya chain building. Conversely, gravity tectonic compression has been caused by the regional uplift of Borneo and the building of a deltaic system (King *et al.*, 2009 and 2010; Hesse *et al.*, 2010). Overall, this resulted in the formation of three neotectonic provinces: an inactive inverted province in the inner shelf region, an extensional province in the outer shelf region, and a compressional province along the slope and in the deepwater Delta Toe province (King *et al.*, 2009; Tingay *et al.*, 2009) (**Fig. 2.2**). The deepwater compressional province correlates with the well-explored shelf sequence and consists of a deformed low-angle clastic wedge that is Miocene to Recent in age and is dominated by thrust-related NE-SW trending anticlines, some of which prominently outcrop at the seafloor, and associated minibasins. The landward-dipping decollement surface of these trains of anticlines probably lies within the overpressured Mid Miocene-Pliocene Setap Shale (Morley *et al.*, 2003). These tectonic events have been accompanied by the deposition of several kilometres of sediments, with thicker sequences in the minibasins, thinning towards the crests of thrust-related ridges. (Morley and Leong, 2008; Morley, 2009; Hesse *et al.*, 2010) (see **Fig. 2.3a**).

The hydrocarbon exploration along this margin moved to the deepwater province in the last 15 years, with proven oil and gas reservoirs occurring in structural traps at the crests

of thrust-cored anticlines. The reservoirs are mainly siliciclastic Middle to Late Miocene sand-prone turbidites and mass-transport deposits (MTDs), sealed by hemipelagites and mud-prone MTDs. The stacking of reservoirs and seals is regulated by the combination of global-seal level fluctuations and tectonic controls (Ingram *et al.*, 2004; Jong *et al.*, 2016). Typically, the hydrocarbons in the reservoirs are of thermogenic origin, sourced by type-III coaly source rocks, most likely located immediately beneath the reservoir units (Warren *et al.*, 2010; Algar *et al.*, 2011b; Ogawa and Jong, 2016). In the region, these siliciclastic stratigraphic units, deposited from the Miocene up to Early Pliocene, are named the Kebabangan, Kinarut, Kamunsu, Pink, Yellow and Lingan (Grant, 2004; Ingram *et al.*, 2004; Jong *et al.*, 2014). The seal integrity and the presence of shallow geohazards are among the major exploration and drilling issues in this area (Ingram *et al.*, 2004; Dan-Unterseh *et al.*, 2014). Despite the occurrence of commercial hydrocarbon accumulations, the leakage of hydrocarbon fluids caused by seal failure is widely observed at the crests of the anticlines along the deepwater fold and thrust belt. The result is a complex shallow hydrocarbon plumbing system involving fluxes of thermogenic fluids (Morley, 2007; Warren *et al.*, 2010; Dan-Unterseh *et al.*, 2014) (**Fig. 2.3b, c**).

The presence of gas hydrates is well-constrained along this margin, owing to the identification of BSRs, seismic-scale indicators of vertical migration of hydrocarbons, as well as hydrate samples recovered with piston cores at the crests of anticlinal ridges. The gas hydrate system appears inevitably linked to the deeper hydrocarbon traps, providing direct evidence of vertical leakage of fluids from deep sources (Gee *et al.*, 2007; Hesse *et al.*, 2010; Warren *et al.*, 2010; Laird and Morley, 2011) (**Fig. 2.3b, c**). In 2003, Shell discovered an oil and gas accumulation (named Gumusut-Kakap) within Late Miocene turbidites (Upper Kamunsu and Pink Units), trapped at the crest of a non-cylindrical thrust-related anticline, visible at the seafloor as a dome-like ridge (named GKL Dome) **(Fig. 2.5a**). At this site, hydrates have been inferred from geophysical evidence and have been recovered from different boreholes (Hadley *et al.*, 2008).

## 2.3. Offshore Guajira Basin (Northern Colombia)

This study area is part of the outer fold belt of the offshore zone of the Guajira Basin, along the northern Colombia active margin (Ladd *et al.*, 1984; Escalona and Mann, 2011) (**Fig. 2.1b**). This outer fold belt is located at water depths of ~3500-4000 m seaward of an intensively deformed accretionary prism, the South Caribbean Deformed Belt, and a more inboard large forearc/piggy-back basin, called Tayrona or Ranchería Basin (Ladd *et al.*, 1984; Martinez *et al.*, 2015) (**Fig. 2.4a**).

A compressional and strike-slip deformation, along this portion of the margin, presumably started in the Late Cretaceous, as part of the tectonic processes resulting in the oblique subduction of the Caribbean Plate beneath South America and the subsequent formation, since the Late Paleogene, of an accretionary prism (Ladd *et al.*, 1984; Pindell *et al.*, 2005; Escalona and Mann, 2011; Londono *et al.*, 2015). In the study area, a thick Cenozoic sequence and an Upper Cretaceous condensed section overlie oceanic basalts. The Upper Cretaceous sediments, which consist of limestones, organic mudstones and volcanic ashes, predate the emplacement of the compressional regime. The Cenozoic likely includes, in the Paleocene-Eocene interval, limestones, cherts, and nannofossil chalks, whereas the Oligocene-Mid Miocene interval is characterised by siliciclastic and carbonaceous mudstones with subordinate sandstones. The more recent sediments, up to present day, postdate a major regional deformation event (Pindell *et al.*, 2005), and are likely constituted by deepwater oozes, poor in carbonate content, interlayered with a variable siliciclastic input (Edgar *et al.*, 1973; Ramirez *et al.*, 2015).

The occurrence of gas hydrates in this margin has been previously inferred by the identification of BSRs in regional seismic profiles, particularly along the deformed accretionary wedge (Shipley *et al.*, 1979; Ladd *et al.*, 1984; López and Ojeda, 2006; Ochoa, 2013) (**Fig. 2.4b, c**), similarly to other active margins worldwide (e.g. Baba and Yamada, 2004; Barnes *et al.*, 2010).

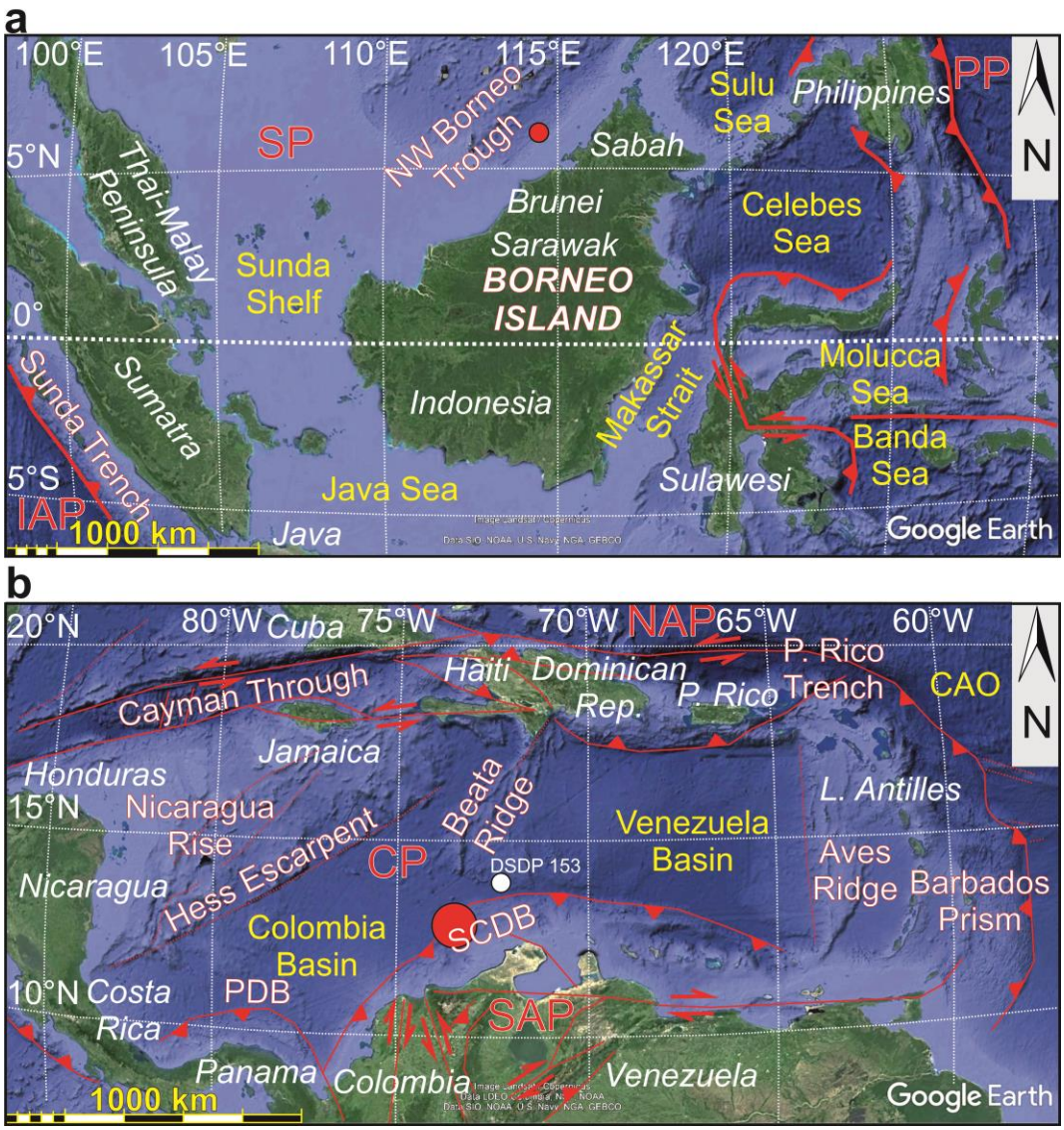



**Figure 2.1.** Modified images from Google Earth, showing the present-day plate-scale geological settings of the study areas (indicated by red circles). The major tectonic boundaries are indicated in red. **(a)** Sabah (offshore NW Borneo) (**Chapters 3-5**). SP= Sunda Plate, IAP= Indo-Australian Plate, PP= Philippine Sea Plate; **(b)** Guajira Basin (offshore Northern Colombia) (**Chapter 6**). CP= Caribbean Plate, SAP= South American Plate, NAP= North American Plate, SCDB= South Caribbean Deformed Belt, PDB= Panama Deformed Belt, CAO= Central Atlantic Ocean.

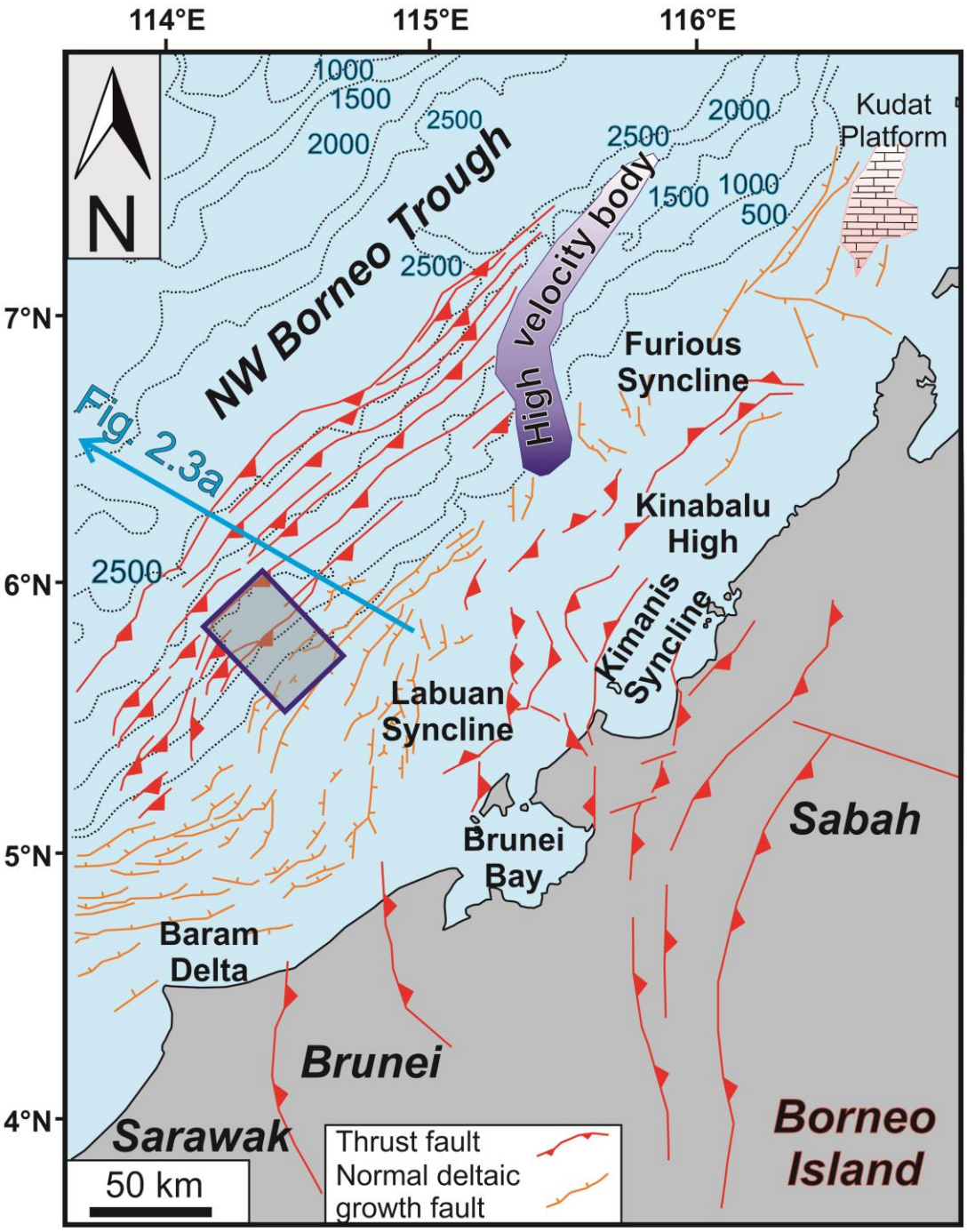



**Figure 2.2.** Detailed Tectonic map of NW Borneo (modified after Hesse *et al.*, 2010). Note the three most important neotectonic provinces of the region: an inverted inner shelf province, an extensional deltaic province and a toe-thrust compressive province in deepwaters. The study area (blue-bounded rectangle) mostly lies in the deepwater compressional domain, at water depth comprised between ~500 and ~1500 m.

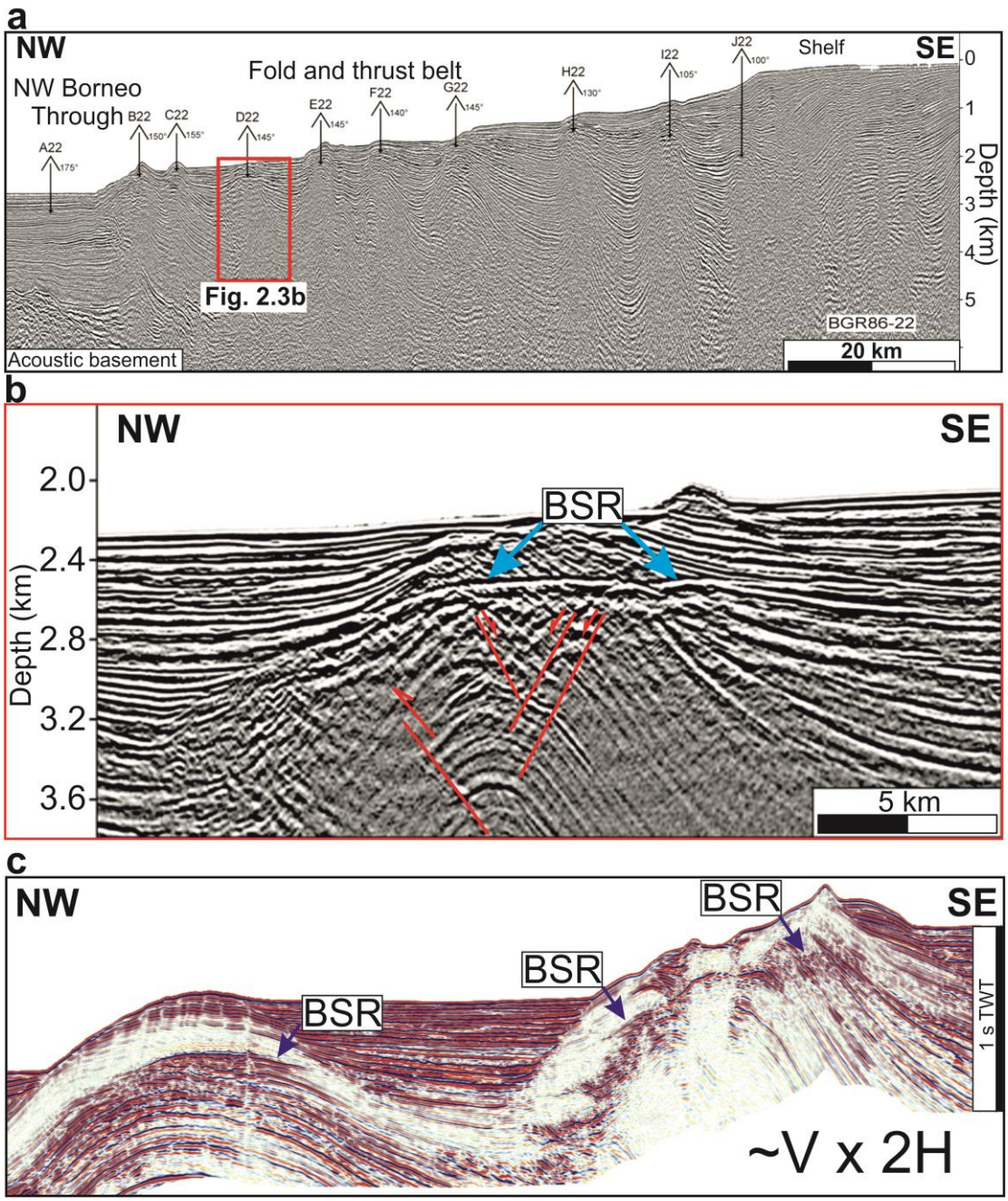



**Figure 2.3. (a)** Regional NW-SE seismic reflection line across the NW Borneo margin (modified after Hesse *et al.*, 2010, Line BGR86-22). The line has been acquired in the vicinity of the study area and displays a ~75 km long fold and thrust belt, which is the result of the interplay between gravity-driven and far-field compressive tectonic forces. **(b)** and **(c)** Examples of BSRs at the crests of the thrust-cored anticlines offshore Sabah **(b)** and in the nearby Brunei margin **(c)** (modified after Hesse *et al.*, 2010; Laird and Morley, 2011).

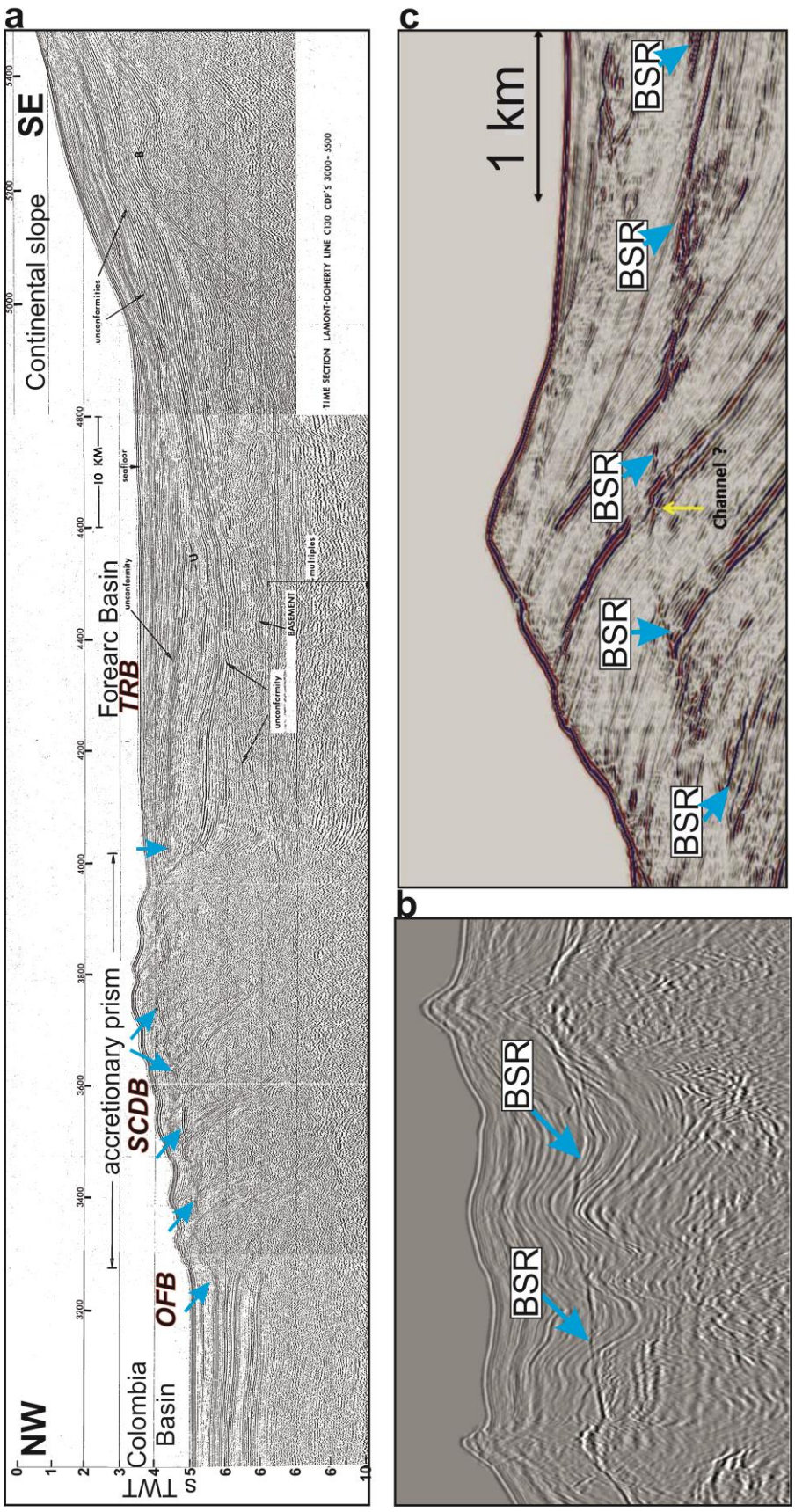



**Figure 2.4. (a)** Regional NW-SE seismic reflection line along the Guajira Basin. The BSR is indicated by blue arrows and covers large parts of the margin. TRB= Tayrona-Rancheria Basin, SCDB= South Caribbean Deformed Belt, OFB= Outer Fold Belt (modified after Ladd *et al.*, 1984, Line 130). **(b)** and **(c)** Detailed examples of BSRs along the South Caribbean Deformed Belt (modified after López and Ojeda, 2006; Ochoa, 2013)

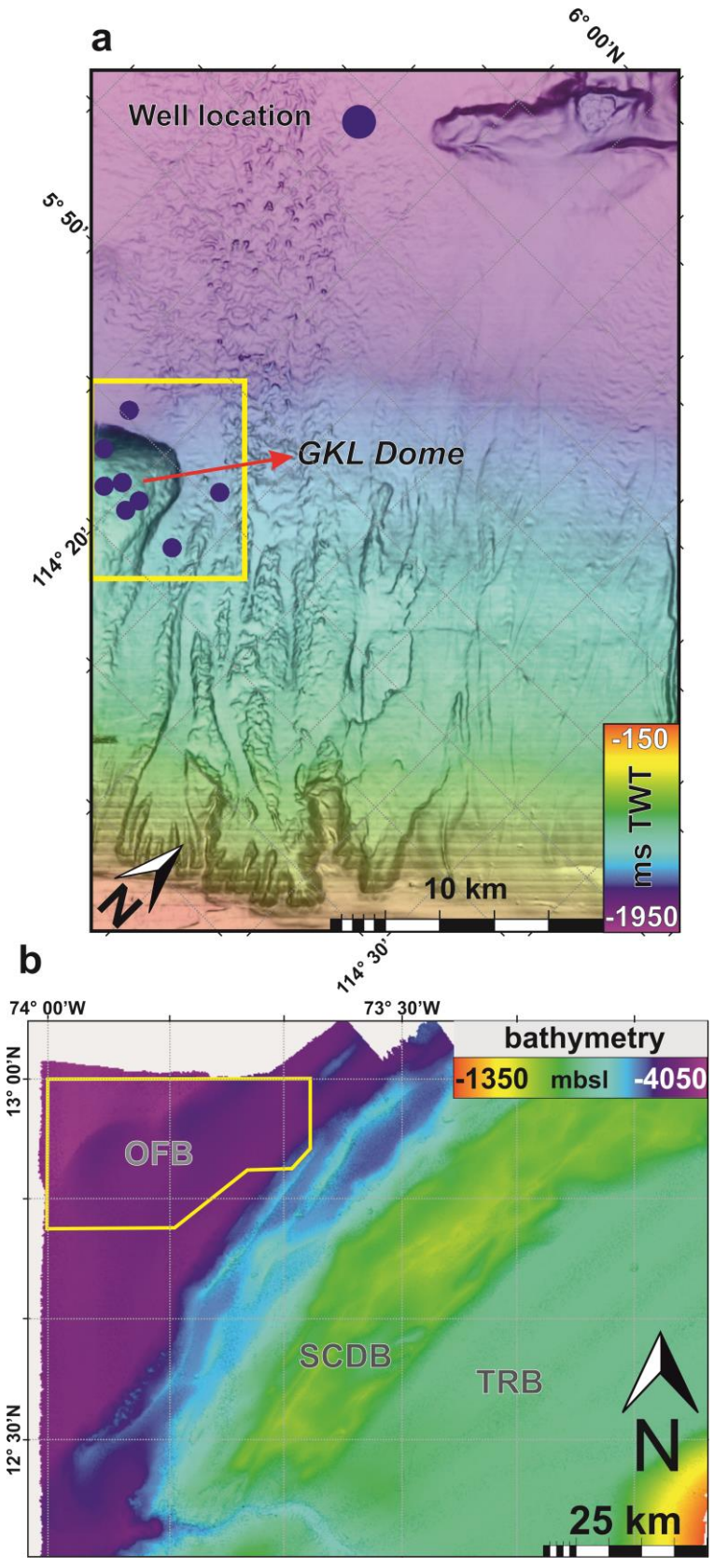



**Figure 2.5.** Bathymetric maps of the study areas. **(a)** Sabah and **(b)** Guajira Basin. The whole area in **(a)** is covered by a regional 3D seismic survey whereas the yellow rectangle indicates the coverage of a high-resolution 3D seismic survey. The blue circles indicate the location of the wells used in this thesis. The water depth varies between ~110 and ~1460 mbsl (110-1950 ms TWT below the sea level) GKL Dome is the name given to a bathymetric ridge which will be of particular focus in **Chapters 3-5**. The GKL Dome is the seafloor expression of a system of thrust-cored anticlines, one of these trapping oil and gas in the Gumusut-Kakap reservoir (see **Chapter 3**). In **(b)**, the area highlighted by the yellow polygon has been investigated with the 3D seismic survey used in this thesis. The rest of the region has been covered with 2D seismic lines. The water depth ranges between ~1350 and ~4050 mbsl.

# Chapter 3. Structure II and H gas hydrates found below the bottom-simulating reflector

This chapter is modified from ‘Paganoni, M, Cartwright, J. A., Foschi, M., Shipp, R. C., Van Rensbergen, P., 2016, Structure II gas hydrates found below the bottom-simulating reflector’, published in *Geophysical Research Letters*. Joe A. Cartwright contributed to the interpretation of seismic data. Martino Foschi contributed to the extraction of the synthetic seismogram. All the authors contributed to the revision. The seismic, well-log and core data were acquired by Shell and provided by Craig R. Shipp.

## 3.1. Introduction

The crystalline structure of gas hydrates is controlled by the composition of the feeding gas. Structure I ($S_I$) natural gas hydrates commonly include almost pure methane: this is the case for many microbially-sourced gas hydrate systems (e.g. Milkov, 2005). Structure II ($S_{II}$) and H ($S_H$) hydrates have a wider range of stability conditions compared to $S_I$ hydrates and can host a variety of gases, including methane and heavier order ($C_{2+}$) hydrocarbons. These gases are commonly thermogenic in origin and are sourced by relatively deep leaking reservoirs. (Sassen and MacDonald, 1994; Milkov, 2005; Lu *et al.*, 2007) (see also **paragraph 1.1**).

Natural gas hydrate systems associated with thermogenic hydrocarbons have been observed in several sedimentary basins worldwide (Ginsburg and Soloviev, 1994; Sassen *et al.*, 2001a, b, d; Mazurenko *et al.*, 2002; Blinova *et al.*, 2003; Kida *et al.*, 2006; Lu *et al.*, 2007; Bourry *et al.*, 2009; Pape *et al.*, 2010b and 2014; Ruffine *et al.*, 2013; Smith *et al.*, 2014b; Serié *et al.*, 2016). However, $S_{II}$ and $S_H$ gas hydrates have often been directly sampled only at or close to the seafloor, without a complete penetration and direct sampling throughout the gas hydrate stability zone (GHSZ) (Sassen *et al.*, 2001a, b, d; Pohlman *et al.*, 2005; Lu *et al.*, 2007; Bourry *et al.*, 2009; Klapp *et al.*, 2010). Thus, predicting the vertical extent of the GHSZ and the hydrate distribution in these settings can be challenging (Boswell *et al.*, 2012a; Macelloni *et al.*, 2015).

Historically, the bottom simulating reflector (BSR) is the primary seismic indicator for the presence of a gas hydrate system and it is believed to closely approximate the base of the gas hydrate stability zone (BGHSZ) (Holbrook *et al.*, 1996; Haacke *et al.*, 2007; Hornbach *et al.*, 2012). However, major concerns have been raised regarding its unequivocal use in this respect, since gas hydrates have been observed to occur in areas lacking clear and continuous BSRs (Holbrook *et al.*, 1996; Tsuji *et al.*, 2009; Boswell *et al.*, 2012a). Additionally, in some areas, multiple BSRs have further been identified, leading scientists

to suggest that they could either **(1)** represent multiple BGHSZs for different hydrate structures or **(2**) indicate paleo pressure and temperature conditions (Andreassen *et al.*, 2000; Foucher *et al.*, 2002; Bangs *et al.*, 2005; Popescu *et al.*, 2006; Pecher *et al.*, 2014) (see also **paragraph 1.7**).

The presence of gas hydrates below a BSR has been inferred in two well-known gas hydrate provinces, such as the Cascadia margin (Site U1328, IODP 311), on the basis of a temperature and chlorinity anomaly measured just beneath the BSR (Riedel *et al.*, 2009), and on the Blake Ridge, where the depth misfit between the predicted BGHSZ and the observed BSR has been explained as caused by capillary effects, ultimately provoking a zone of free gas and hydrate coexistence (Guerin *et al.*, 1999; Liu and Flemings, 2011).

This study is located on the mid-upper continental slope of Sabah (see **paragraph 2.2.** and **Fig. 2.2**). Specifically, this research is focused on the gas hydrate system overlying the Gumusut-Kakap oil and gas reservoir, discovered by Shell in 2003 (Hadley *et al.*, 2008) (**Fig. 2.5a**). The preliminary report of Hadley *et al.* (2008) was primarily aimed at a shallow geohazard study. However, these authors noted the presence of $S_{II}$ hydrates below a BSR and $S_I$ hydrates above it in a single borehole, from the analysis of core data and resistivity measurements. This study builds on their initial analyses by looking at three other wells to **(1)** further constrain the presence of gas hydrates below a BSR, **(2)** estimate their saturation, **(3)** calibrate gas hydrate indicators with stability modelling and **(4)** discuss the global implications of such unexpected hydrate distribution.

## 3.2. Data and Methods

This research integrates a 3D seismic survey with well-log and core data. The 3D seismic survey covers an area of ~37 $km^2$ (**Fig. 3.1a**), with a 6.25 m bin spacing, 1 ms sampling interval and a 25-150 Hz frequency band at -20dB for the first 1750 ms TWT. The average vertical resolution is 5.25 m (Widess, 1973). The seismic interpretation was performed on a 90° phase-shifted dataset (N. American polarity). Logging-while-drilling (LWD) data was acquired using the Halliburton downhole logging tools from four closely spaced boreholes (named DC_E, M_1, DC_F and L_2) **(Fig. 3.1a**). Conventional well-log data acquisition included gamma-ray, resistivity, density and neutron porosity measurements. In particular, resistivity, which is diagnostic to identify hydrate-bearing sediments (e.g. Cook *et al.*, 2010), was measured with the EWR®-Phase 4 multiarray propagation tool, which also allowed the acquisition of horizontal (*Rh*) and vertical (*Rv*) resistivity data. Subsequently, the borehole DC_E was re-entered with the Simultaneous Acoustic and Resistivity Imager (STAR) device, to acquire resistivity images, from ~55 to ~285 metres below the seafloor (mbsf). P- and S-wave velocities were also acquired at DC_E during the wireline acquisition with the Cross-Multipole Array Acoustic log from Baker Hughes. A synthetic seismogram was built by using the wireline velocity and LWD density logs acquired at DC_E and applying a phase-shifted Ricker wavelet, in line with the frequency of the 3D seismic data. The synthetic was used to correlate seismic and well-log observations and, in conjunction with seismic velocity information provided by Shell, to tie the well data to the seismic.

The standard techniques to recover conventional and pressure cores and analyse the gas hydrate-bearing sediments were applied at DC_E (cf. Tréhu *et al.*, 2004b; Weinberger *et al.*, 2005; Schultheiss *et al.*, 2006; Lee *et al.*, 2013; Holland and Schultheiss, 2014). A total of fourteen conventional (i.e. non-pressurised) cores, having an average length of 166.5 cm, was successfully recovered with the hydraulic percussion Fugro Corer (FC). Infra-red

(IR) images and temperature data were acquired in the FC cores to identify thermal anomalies from dissociating hydrates. Additional data was obtained using the WISON/WIP XP push sampler (cf. Hawkins and Narkus, 1998), which allowed the recovery of non-pressurised samples, using either a PVC Liner or a thin-walled Shelby tube. The Fugro Pressure Corer (FPC) and the Hyace Rotary Corer (HRC) allowed the recovery of one-metre length pressure cores under hydrate stability conditions. Once successfully recovered, the core was subjected to nondestructive measurements before being depressurised. A total of twenty pressure cores (13 FPC and 7 HRC cores) have been recovered.

The measurements of pore water chlorinity and sulphate contents have been performed, respectively by titration with silver nitrate (error = ±1%) and by barium sulphate nephelometry (error = ±2%) on samples obtained by squeezing core plug samples in a press, in order to separate the pore water. The pore water samples have been obtained from core Liners, Shelby tubes, FC cores, FPC cores and HRC cores. All the FPC cores were used for pore water chlorinity and sulphate measurements. Conversely, only the eight FPC and four HRC cores successfully recovered were used for gas geochemistry. An empirical baseline chlorinity (*Cb*) profile was built following Ussler and Paull (2001) and represents the plausible pore water conditions before freshening due to gas hydrate dissociation. Gamma density (error ±2%), P-wave velocity (error ±1%), and X-ray images (pixel resolution of ~120 μm) of successfully recovered FPC cores, measured in the Geotek Multi-Sensor Core Logger (MSCL-S) with a 0.5 cm interval, were used to study hydrate distribution in the sediment and determine the baseline parameters for the hydrate saturation predictions from methane balance.

Gas samples were taken from gas voids in FC cores and during progressive depressurisation steps in pressure cores. The composition may reflect the contribution from gas hydrates, gas previously dissolved in water and free gas. Onboard, the gas composition was calculated in percent (%) of the total amount of $C_1$-$C_4$ alkanes (cf. Heeschen *et al.*, 2007)

and was measured onboard using an Agilent MicroGC 3000A gas chromatograph. More detailed onshore analyses were carried on by CoreLab on 25 ml gas samples, with a Varian CP-3800 gas chromatograph, able to detect light hydrocarbons up to $C_{12+}$. The most significant results of these onshore analyses are shown for the first time in this study. This geochemical data will be compared with the $C_1$-$C_{6+}$ composition of the gas cap of the deep reservoir, measured with gas chromatography by Shell.

At DC_E, the seafloor temperature was obtained with a CTD probe (conductivity, temperature, depth) whereas the geothermal gradient was extrapolated from equilibrium tests and measurements with the temperature pore water sampler, accomplished with the Temperature Cone Penetration Test (TCPT) and the Fugro Pore Water Sampler (FPWS), respectively. The excess fluid pressure was measured at DC_E using a wireline-operated, EP small-diameter piezoprobe, equipped with two pressure sensors and pushed into the soil with the Fugro WISON EP system (cf. Long *et al.*, 2007).

Gas hydrate saturation (*Sh*, expressed as % of the pore space) was calculated for DC_E from **(1)** chlorinity data (cf. Malinverno *et al.*, 2008) and **(2)** excess volume computations from depressurisation experiments on the successfully recovered pressure cores (cf. Schultheiss *et al.*, 2008; Holland and Schultheiss, 2014) and, for all the four boreholes, **(3)** from resistivity data, considering the effect of hydrate-filled fractures on resistivity measurements, following the method of Lee and Collett (2012). This latter method resulted in two *Sh* profiles for each well, corresponding to a lower and an upper end-member. Further details on the methods for the estimation of *Sh* are presented in the appendix at the end of this chapter (**paragraph 3.7**).

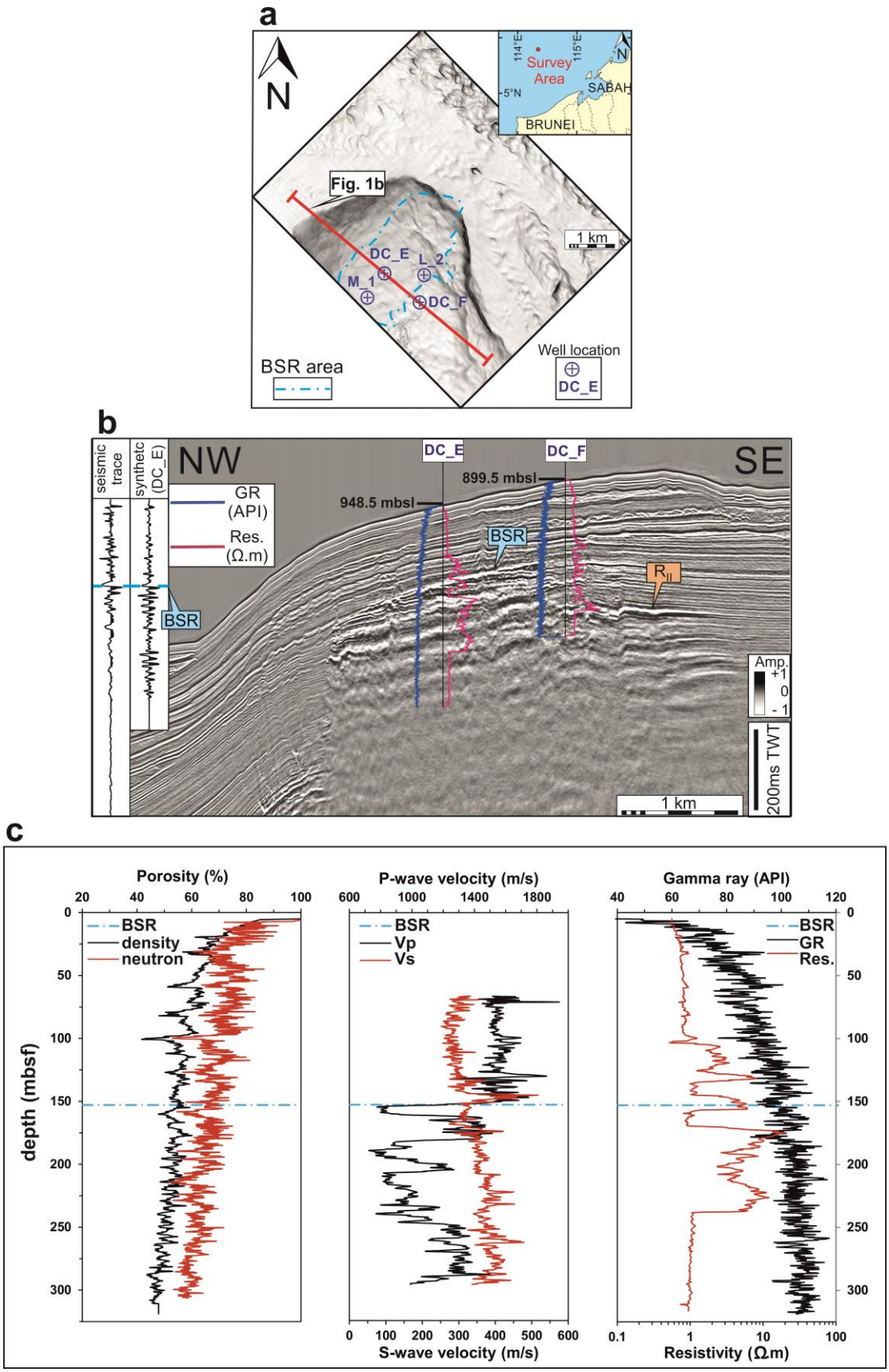



**Figure 3.1. (a)** Seafloor map (dip extraction, where darker colours represent steeper areas), with borehole locations and projection of the BSR perimeter at the crest of the bathymetric high overlying the Gumusut-Kakap hydrocarbon accumulation. **(b)** Seismic section, showing the BSR and the reflection $R_{II}$ plus the phase-shift, deep smoothed resistivity (Res.) and the gamma-ray (GR) logs along boreholes DC_E (drilled at 948.5 mbsl) and DC_F (drilled at 899.5 mbsl). A seismic trace, close to DC_E, and the synthetic seismogram are shown on the left. Both the traces are phase-shifter by 90° (N. American polarity convention) **(c)** DC_E well log data including porosity (density and neutron), velocity (P and S-wave), gamma-ray (GR) and phase-shift, deep smoothed resistivity (Res.).

## 3.3. Results

### *3.3.1. Key seismic and geological observations*

The structure of the study area (~850-1250 m water depth) is characterised by a bathymetric ridge, the seafloor expression of a system of thrust-cored NE-SW trending anticlines, deforming a slope sequence of Neogene age, consisting of alternating hemipelagites and gravity flow deposits (Lu and Shipp, 2011). A prominent reflection is mapped over the crest of this ridge. It is interpreted as a BSR on several criteria, namely, its opposite polarity with respect to that of the seafloor; its discordant relationship to the host stratigraphy; its nearly constant depth beneath the seabed (155m ±10m); and the presence of high amplitude, relatively low frequency reflections with a zone of seismic attenuation below, interpreted as evidence for a free gas zone beneath the BSR (**Figs. 3.1b, 3.2**) (cf. Holbrook *et al.*, 1996; Tréhu *et al.*, 2004b; Bünz *et al.*, 2012). A second prominent reflection (named $R_{II}$), having high amplitude and opposite polarity with respect to that of the seafloor is locally seen outside the region of seismic attenuation (**Fig. 3.1b**). Seismic attenuation and push-down effects are observed below this amplitude anomaly, which is interpreted to represent free gas-bearing sediments (cf. Løseth *et al.*, 2009).

Core and well-log data calibrate the physical properties of the sediments above and below the interpreted BSR. The X-ray images of FPC cores suggest a homogeneous lithology throughout the borehole DC_E. Additionally, the gamma-ray values are consistently higher than 80-90 API units in the four wells. Furthermore, LWD data indicate that the density porosity is generally lower than the neutron porosity. These observations (**Figs 3.1c, 3.3**) suggest a mud-prone nature for the analysed section because **(1)** high gamma-ray values are related to high K, Th and U contents in the sediments, typical of clays and **(2)** a lower density than neutron porosity is associated with high H-indexes, indicative of clay-rich sediments (Cook *et al.*, 2008).

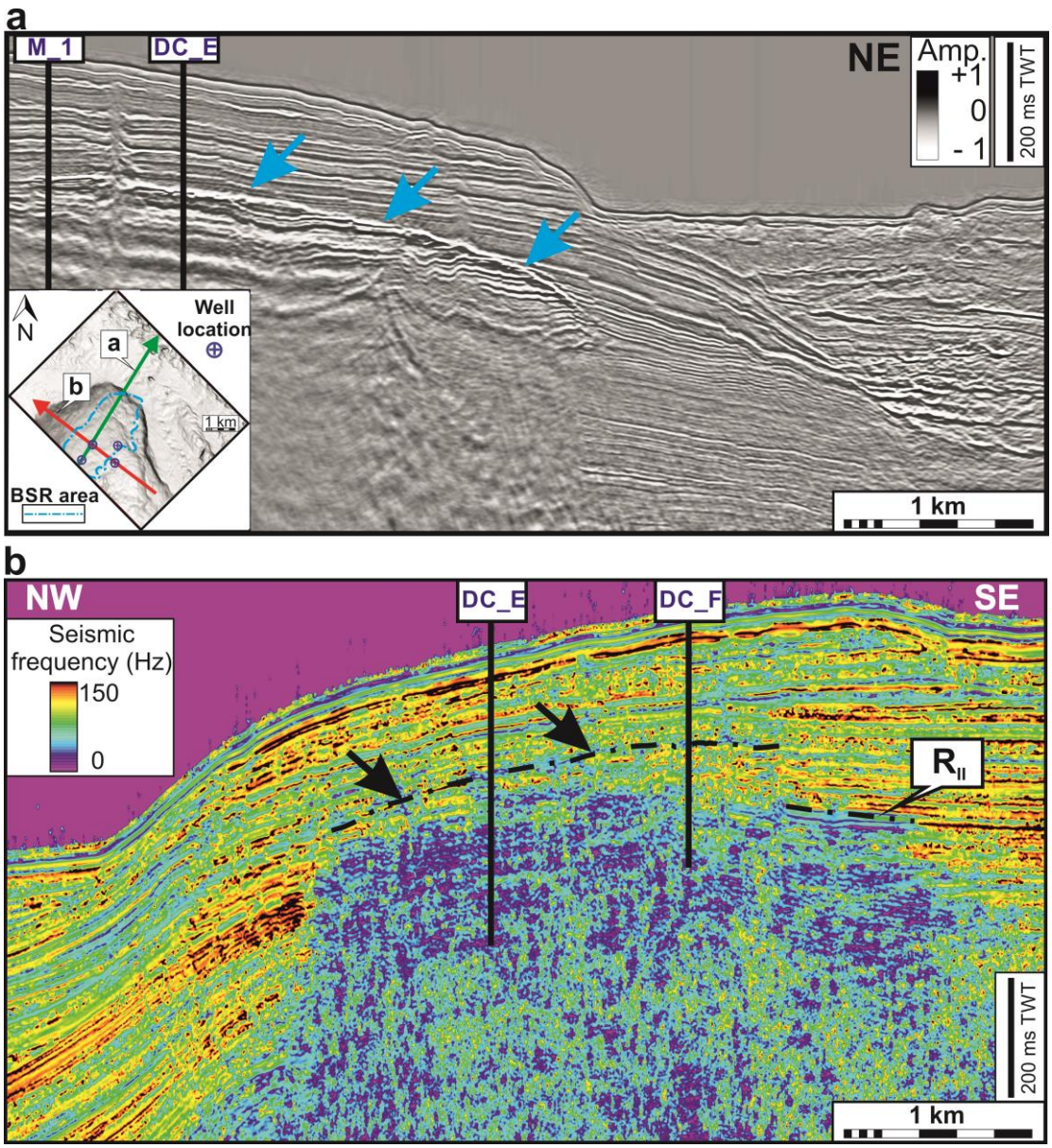



**Figure 3.2. (a)** Seismic section, showing the BSR (blue arrows) at the crest of the ridge and its cross-cutting relationship with the host stratigraphy. **(b)** Instantaneous frequency extraction along the same path of **Fig. 3.1b**. Note the strong frequency reduction below the BSR (indicated by black arrows) and below the reflection $R_{II}$. This reduction in frequency is highly diagnostic for the presence of free gas. The locations of the seismic sections are shown in the inset seafloor map in **(a)**.

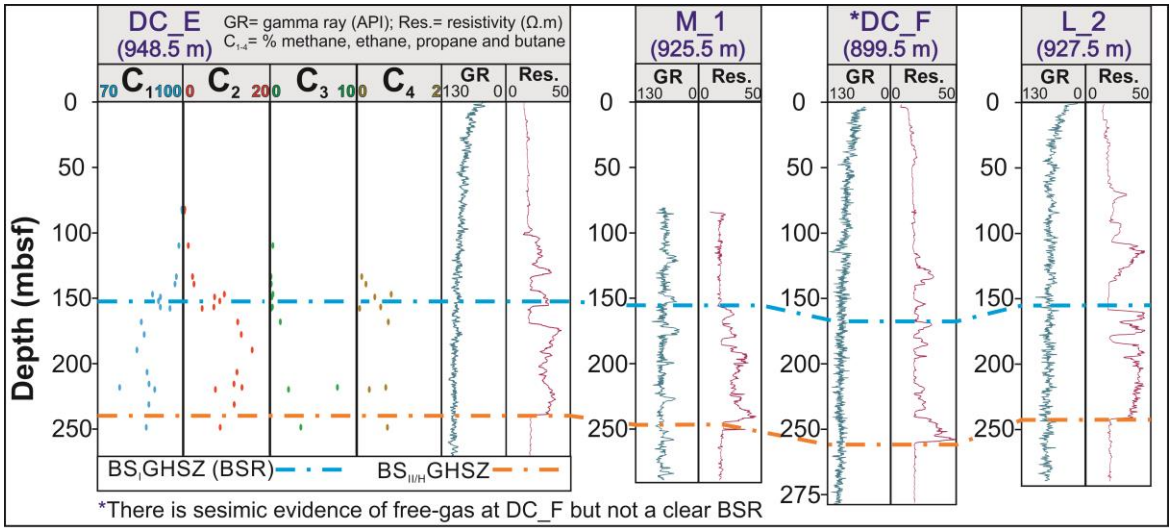


**Figure 3.3 (See the previous page).** Phase shift deep smoothed resistivity (Res.) and gamma-ray (GR) data for wells DC_E, M_1, DC_F and L_2. The water depths of the four wells are indicated in brackets. The bulk gas composition data from shipboard analyses on cores retrieved at DC_E are also included in the panels on the left. Note the increase of $C_{2+}$ hydrocarbons below the BSR (i.e. the $BS_I$GHSZ), indicated by a blue dotted line. The interpreted $BS_{II/H}$GHSZ is marked with an orange dotted line.

### *3.3.2. Evidence of gas hydrates and saturation estimates*

The cores obtained at DC_E provide unequivocal evidence that gas hydrates are present both above and below the BSR. Fracture-filling hydrates are inferred from the X-radiographs of the pressure-cores, where they display brighter colours than hydrate-free sediment **(Fig. 3.4)** (Holland and Schultheiss, 2014). It is not excluded that gas hydrates could occasionally fill the primary pore space because such occurrence is not readily observable in X-ray images (Holland *et al.*, 2008). The impact of hydrate distribution on the MSCL-S P-wave velocity measurements on FPC, frequently being discontinuous along the cores, is difficult to interpret. With one exception in the top 10 cm of FPC-E#08, the P-wave velocity does not appear to be influenced by the gas hydrates (**Fig. 3.4**).

Further compelling evidence for hydrate occurrence includes the pore water chlorinity and temperature anomalies (**Fig. 3.5a**), resulting from hydrate dissociation, which is an endothermic process that releases fresh water into the system (Tréhu *et al.*, 2004b; Weinberger *et al.*, 2005; Malinverno *et al.*, 2008). The presence of low chlorinity anomalies compared to the extrapolated *'baseline'* indicates dissociated hydrates upon core recovery. These anomalies are more pronounced below than above the BSR, with the lowest chlorinity values located between 171 and 221 mbsf (**Fig. 3.5a, b**). Gas hydrates are evident in most of the IR thermal images of FC cores below the BSR, from 180 to 233 mbsf. Below and above this depth interval, no temperature anomalies were observed. No widespread evidence of hydrates is encountered below 250 mbsf, although a relatively low chlorinity value was measured at 278 mbsf **(Fig. 3.5a, b)**. However, the other two pore water samples at this depth fit with the extrapolated *'baseline'* profile.

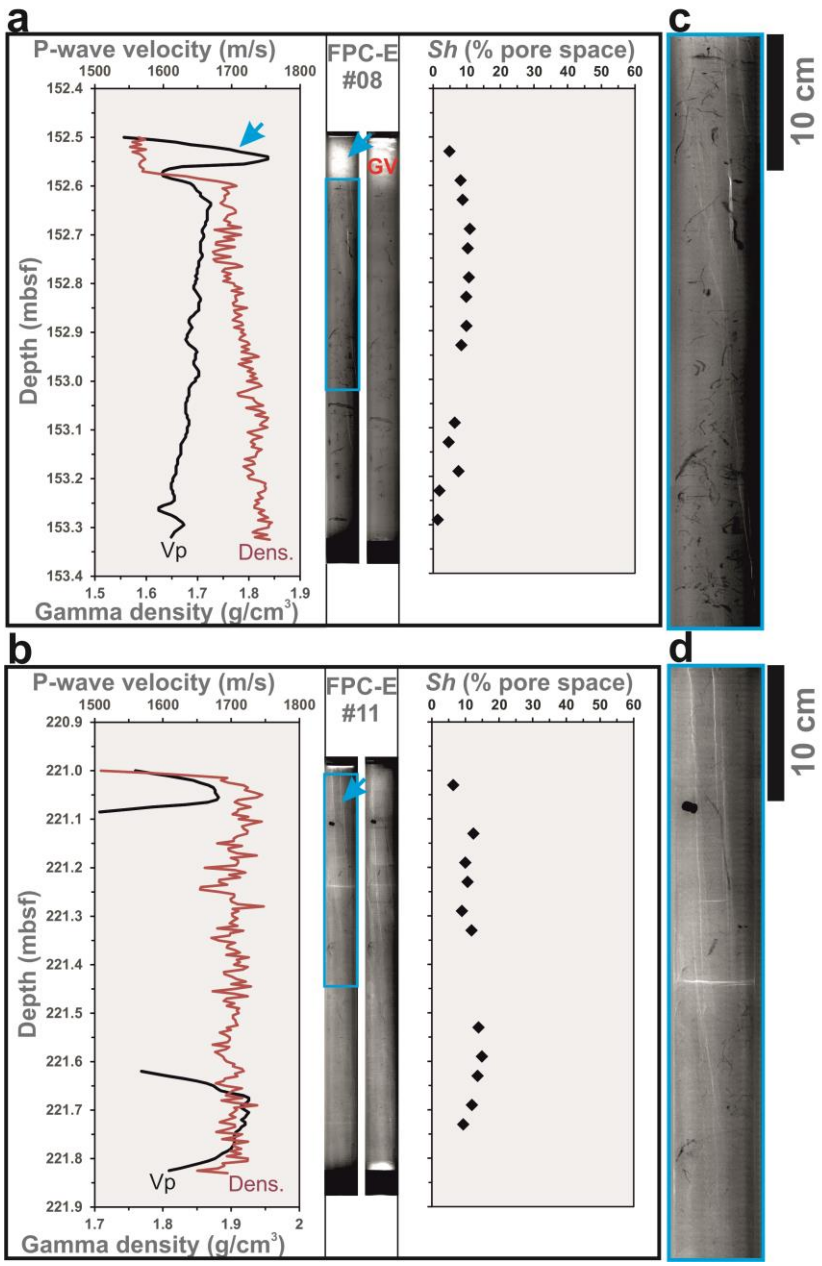



**Figure 3.4. (a)** and **(b)** X-ray images of FPC-E#08 and FPC-E#11, retrieved at 152.5 mbsf (i.e. near the BSR) and 221.0 mbsf (~70 m below the BSR), respectively. Data from MSCL-S measurements (P-wave velocity and gamma density) and the *Sh* estimates from chlorinity measurements along the cores are also included. The X-ray images on the left are of cores before depressurisation. The X-ray images on the right are of cores after depressurisation. Note the saturation profiles, having relatively low but roughly constant *Sh* values (~10%) along the entire core. A gas void (GV) can be formed after depressurisation. Vp= P-wave velocity; Dens.= gamma density. **(c)** and **(d)** Blow-ups of the portions of the cores bordered with blue rectangles in **(a)** and **(b)**, respectively, highlighting thin mm-wide hydrate-filled fractures.

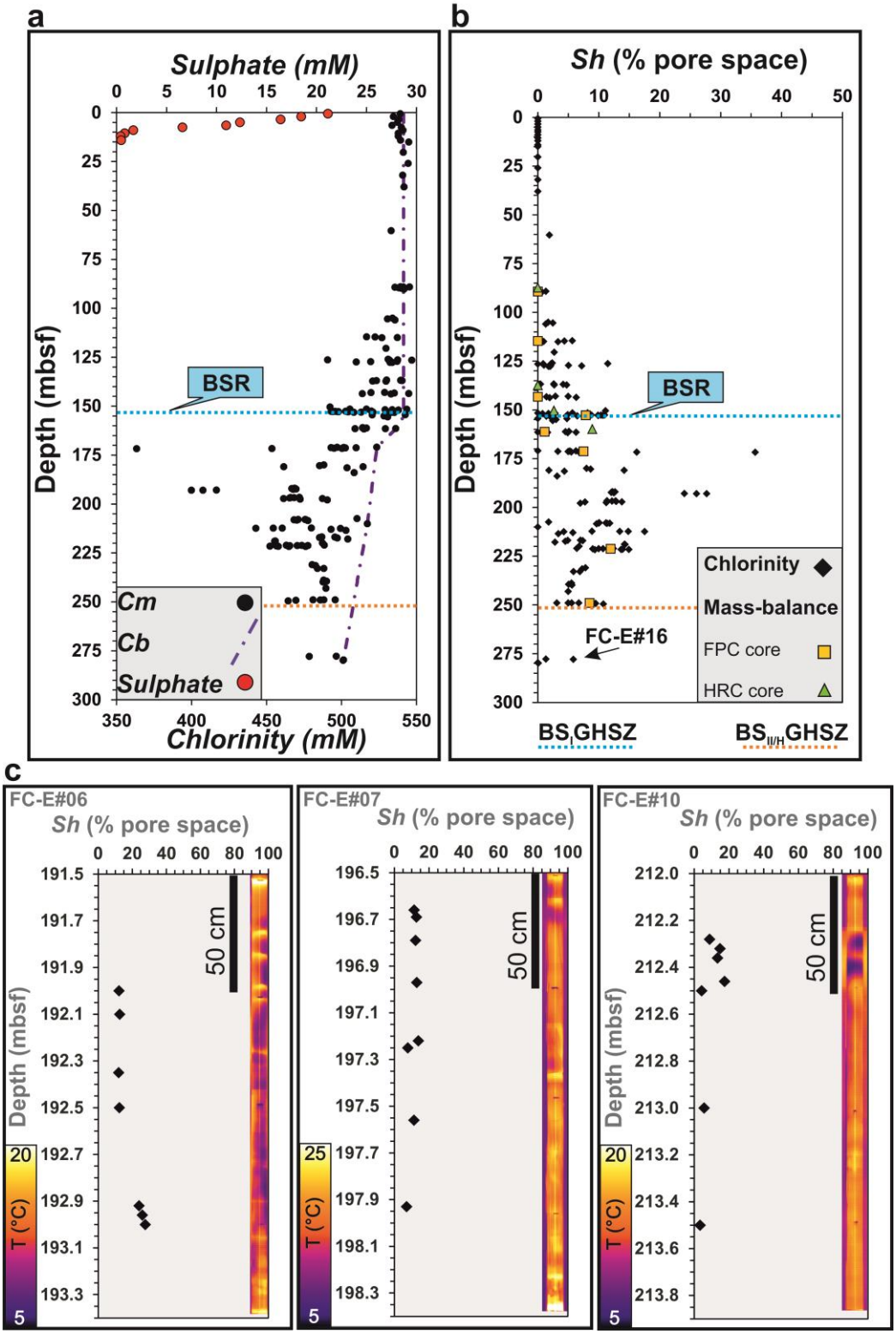



**Figure 3.5. (a)** Chlorinity and sulphate profiles at DC_E. Chlorinity anomalies extend below the BSR (i.e. the $BS_IGHSZ$), given the presence of $S_{II/H}$ hydrates. The SMTZ is at 10-12 mbsf. **(b)** Gas hydrate saturation profile. *Sh* is estimated from chlorinity anomalies and with the mass-balance approach. In **(a)** and **(b)** the depth of the interpreted $BS_IGHSZ$ and $BS_{II/H}GHSZ$ are plotted. **(c)** IR thermal image of FC cores (FC-E#06, FC-E#07 and FC-E#10, retrieved at ~191.5, 196.5 and 212.0 mbsf, respectively), displaying cold zones as a consequence of hydrate dissociation upon recovery. *Sh* is estimated from chlorinity measurements at different levels along the core.

The resistivity images acquired at DC_E support the core observations: bright colours, compared to the background, have been observed partly above but mostly below the BSR, down to 237 mbsf. This observation indicates the presence of hydrates above the BSR and, potentially, both hydrates and free gas below (**Fig. 3.6**) (cf. Riedel *et al.*, 2010a). Bright sinusoidal features, diagnostic of fracture-filling hydrates (Kim *et al.*, 2013a; Cook *et al.*, 2014), have further been observed throughout the hydrate occurrence zone. The dip of these features typically ranges between 60° and 80°. The numerous high resistivity peaks observed above and below the BSR in the four boreholes may be indicative of gas hydrates (Cook *et al.*, 2008) and are restricted to a maximum depth ranging between 237 and 260 mbsf (**Figs. 3.1c, 3.3**). The impact of gas hydrates on resistivity measurements is confirmed by the calibration with core observations. In addition, the occurrence of fracture-filling hydrates is further supported by the observation of **(1)** the separation between extra-shallow, shallow, medium and deep phase shift resistivity and **(2)** the marked difference between horizontal and vertical resistivity (**Figs. 3.7, 3.8**) (cf. Cook *et al.*, 2010).

The sulphate-methane transition zone (SMTZ) at DC_E is located at 10-12 mbsf **(Fig. 3.5a)** and, although beneath this interface hydrates could potentially occur, there is no clear evidence until 65-152 mbsf in the four boreholes (**Figs. 3.3, 3.5)**.

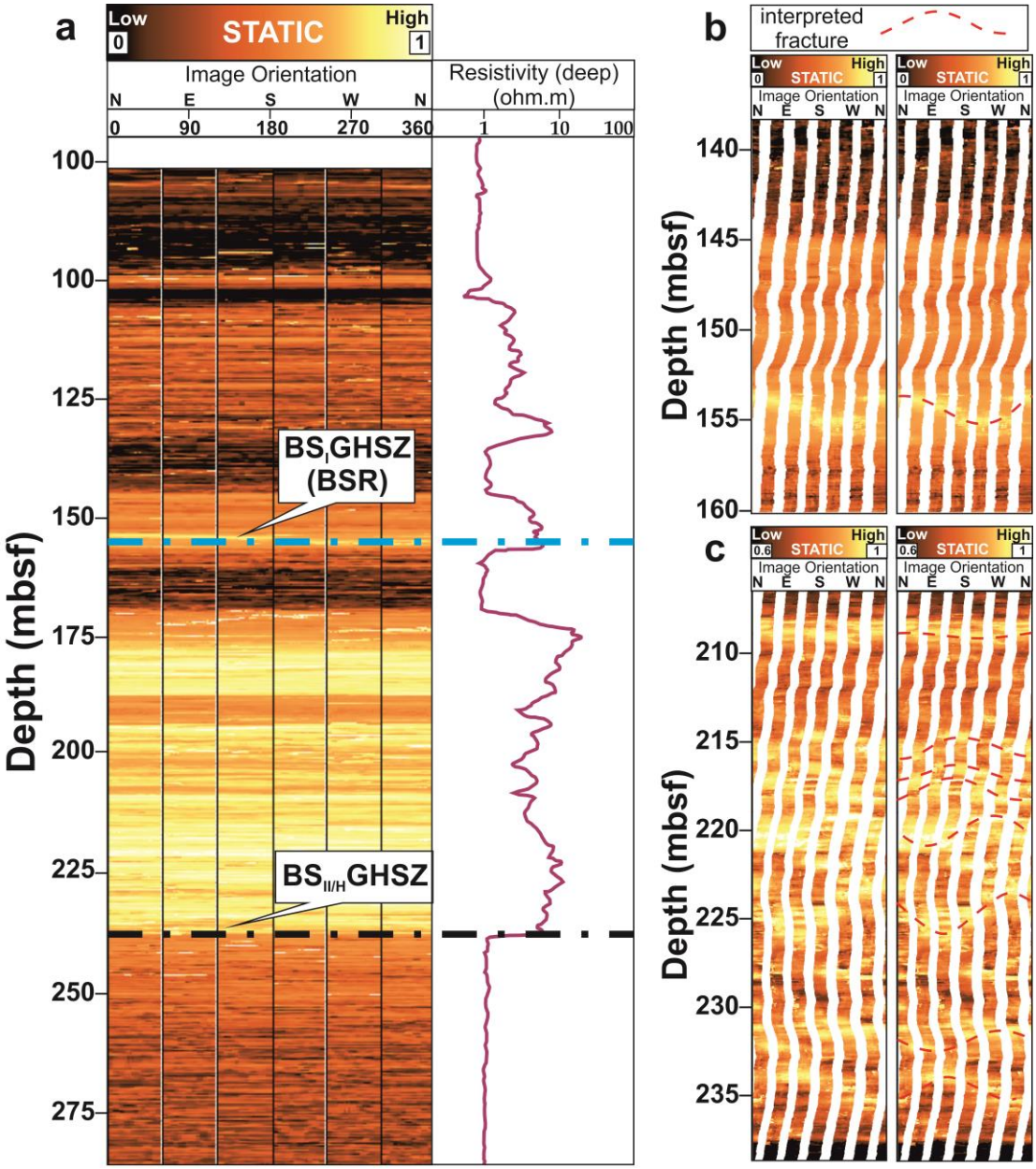



**Figure 3.6.** Resistivity images (static, i.e. fixed colour scale) at DC_E. **(a)** General view. Bright colours are related to resistive material, interpreted in this case as hydrate-bearing sediments, possibly including traces of free gas below the $BS_I$GHSZ (i.e. the BSR). The position of the interpreted $BS_I$GHSZ and $BS_{II}$GHSZ are indicated by a blue and black dotted line, respectively. The seafloor is 948.54 m deep at DC_E. **(b)** and **(c)** Detailed view of two selected intervals. Note the sinusoidal features, interpreted to represent fracture-filling hydrates approximately at the $BS_I$GHSZ (~153 mbsf) **(b)** and above the $BS_{II}$GHSZ (237-250 mbsf at DC_E) **(c)**.

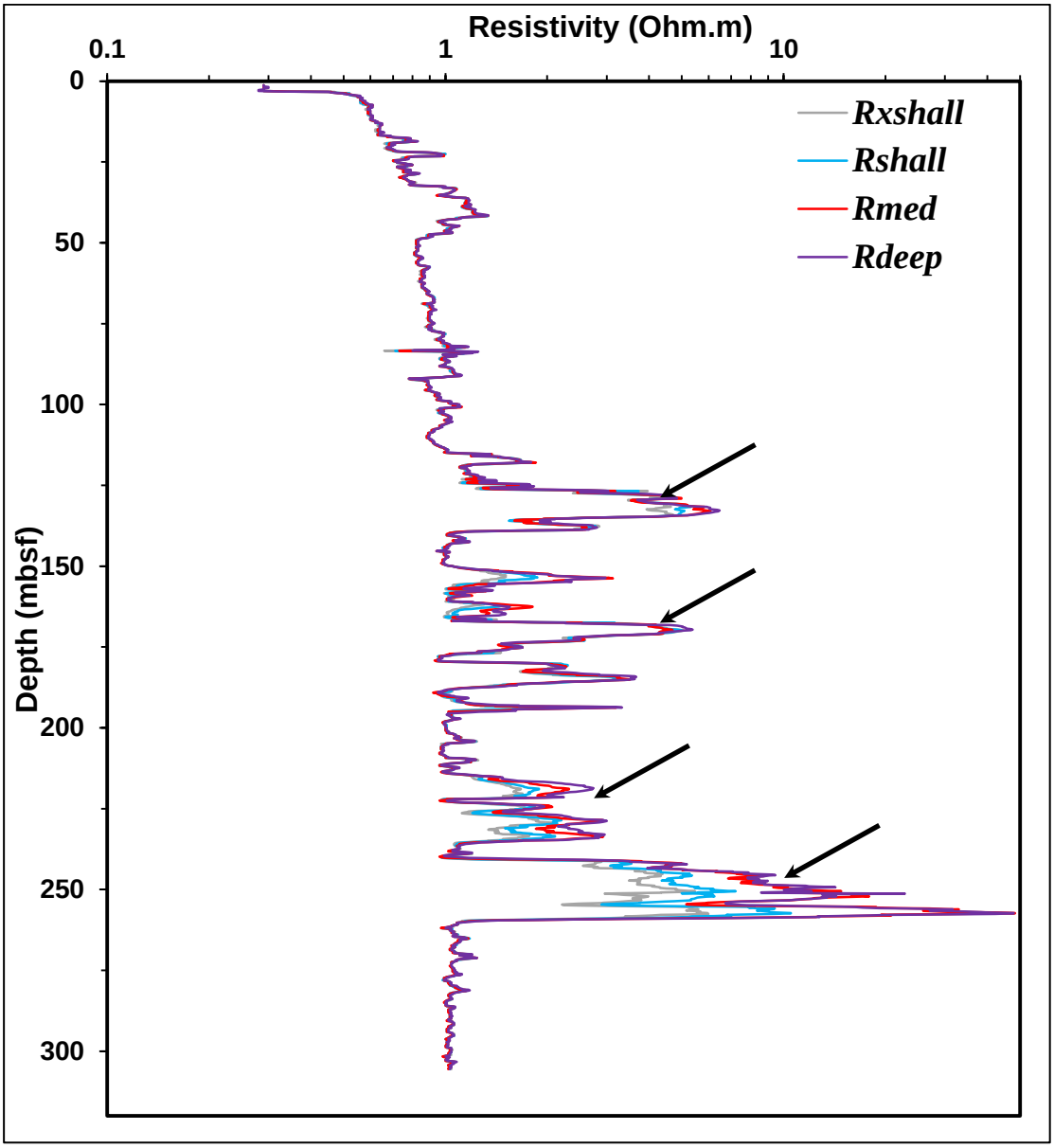



**Figure 3.7.** Resistivity *vs* depth profile at DC_F. The profile shows a separation (black arrows) between the extra-shallow (*Rxshall*), the shallow (*Rshall*), the medium (*Rmed*) and the deep (*Rdeep*) phase resistivity (different transmitter-receiver spacing), acquired with the EWR®-Phase 4 multiarray propagation tool.

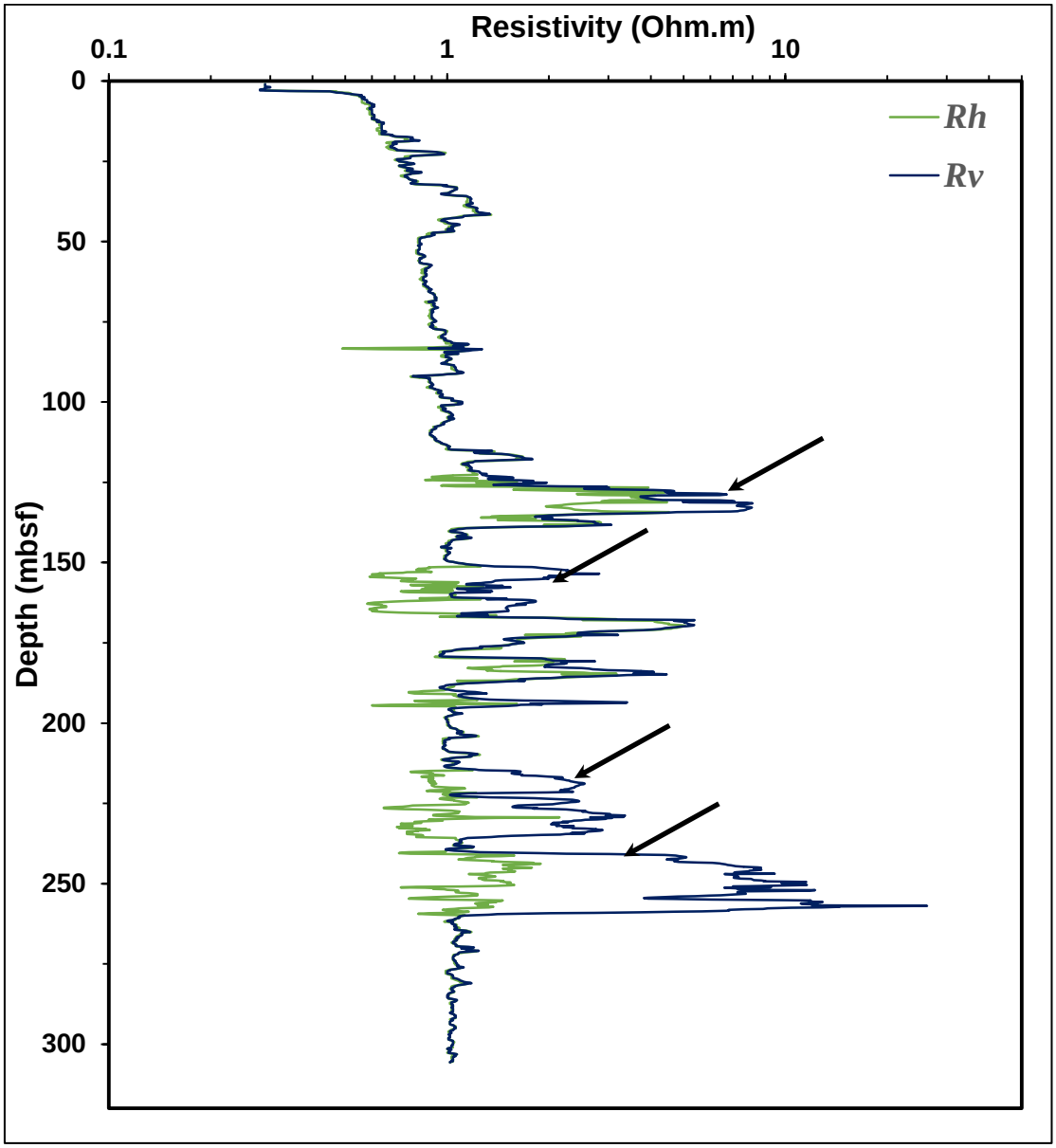
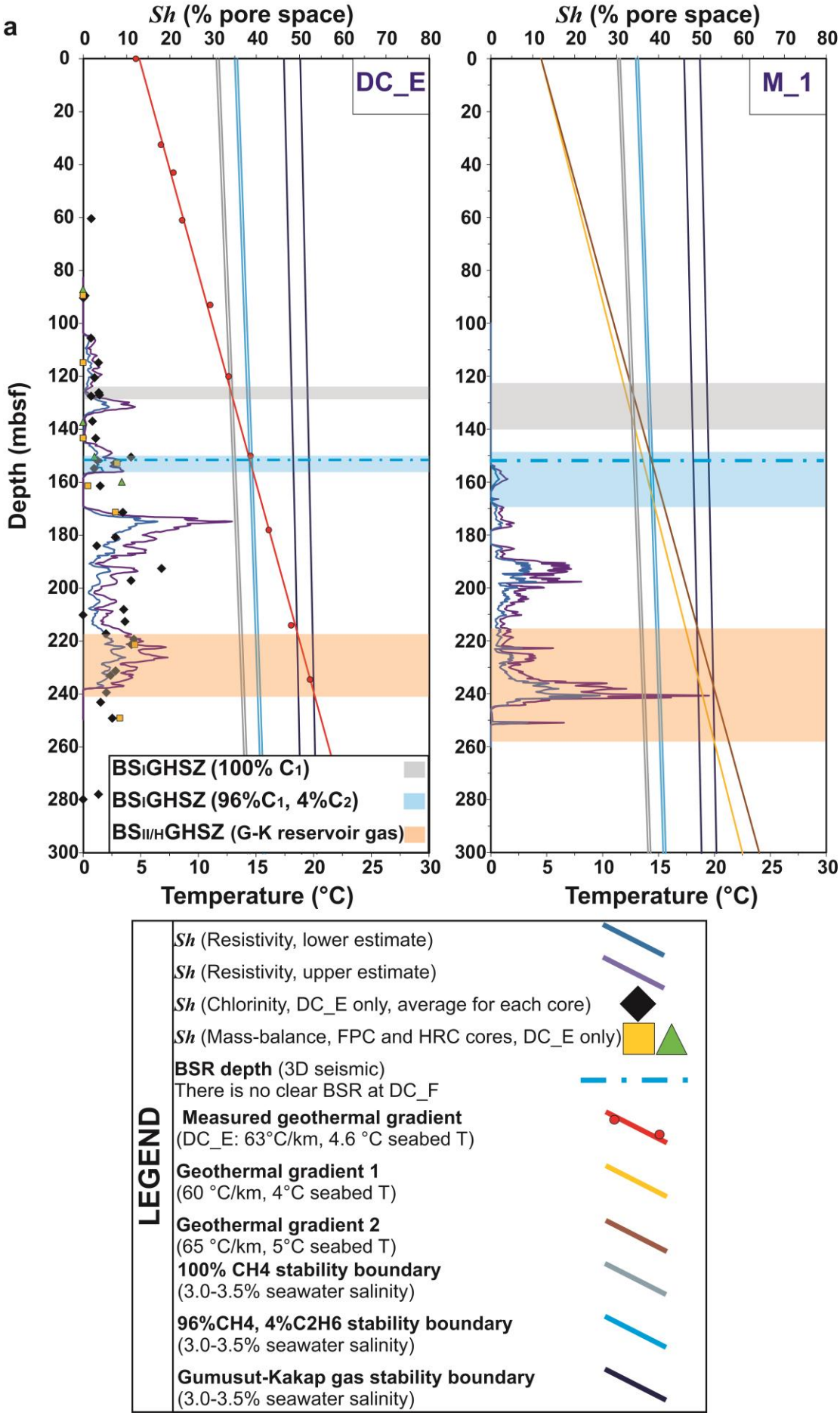



**Figure 3.8.** Horizontal (*Rh*) and vertical (*Rv*) resistivity *vs* depth profile at DC_F, acquired with the EWR®-Phase 4 multiarray propagation tool. The marked difference between *Rh* and *Rv* (black arrows), with *Rv* higher than *Rh*, suggests the presence of resistive sub-vertical features, interpreted to be filled with gas hydrates (cf. Cook *et al.*, 2010).

Along the borehole DC_E, core data indicate that the average estimated *Sh* within the zone of hydrate occurrence above the BSR (~105-155 mbsf) is 4.1%, whereas *Sh* is 9.0% in the zone of hydrate occurrence below the BSR (~153-250 mbsf). Throughout the entire zone of hydrate occurrence at DC_E (~105-250 mbsf), the average *Sh*, averaging all the values estimated from pore water freshening, is 7.1% of pore space. The maximum inferred *Sh*, considering each single measurement is 35.7% (FPC-E#10; 171 mbsf). At the core-scale, the *Sh* profiles typically show low to moderate values throughout the core (~5-15%), in both FPC and FC cores. Occasionally, there is evidence of cm-thick intervals with enhanced *Sh* (>20%) (**Figs. 3.4, 3.5b**).

At DC_E, there is no apparent correlation between the wireline velocity logs and the distribution of gas hydrates, apart from a strong positive peak in S-wave velocity just above the BSR which could link with gas hydrates that have considerably increased the sediment stiffness (Yun *et al.*, 2005; Riedel *et al.*, 2014). The saturation estimates using resistivity measurements in all the four boreholes agree with core data, indicating that *Sh* above the BSR is 1-5% of pore space, but below is 5-15% of pore space on average, with different high-saturation peaks, where *Sh* exceeds 20-30% of the pore space (**Fig. 3.9**).

Unfortunately, the seismic data below the BSR are severely attenuated, and it is not possible to confidently calibrate the abrupt resistivity reduction, occurring between 237 and 260 mbsf in the four boreholes, with any seismic reflection. An exception is represented by the resistivity reduction at DC_F (~260 mbsf), which is the only well drilled in a zone where the BSR and the underlying attenuated zone are not well developed. In this case, the base of the zone of high resistivity well correlates with $R_{II}$ **(Fig. 1b)**, suggesting a possible relationship between them.


a
Sh (% pore space)
DC_E
M_1
Depth (mbsf)
Temperature (°C)
BSIGHSZ (100% C1)
BSIGHSZ (96%C1, 4%C2)
BSII/HGHSZ (G-K reservoir gas)
LEGEND
Sh (Resistivity, lower estimate)
Sh (Resistivity, upper estimate)
Sh (Chlorinity, DC_E only, average for each core)
Sh (Mass-balance, FPC and HRC cores, DC_E only)
BSR depth (3D seismic)
There is no clear BSR at DC_F
Measured geothermal gradient
(DC_E: 63°C/km, 4.6 °C seabed T)
Geothermal gradient 1
(60 °C/km, 4°C seabed T)
Geothermal gradient 2
(65 °C/km, 5°C seabed T)
100% CH4 stability boundary
(3.0-3.5% seawater salinity)
96%CH4, 4%C2H6 stability boundary
(3.0-3.5% seawater salinity)
Gumusut-Kakap gas stability boundary
(3.0-3.5% seawater salinity)

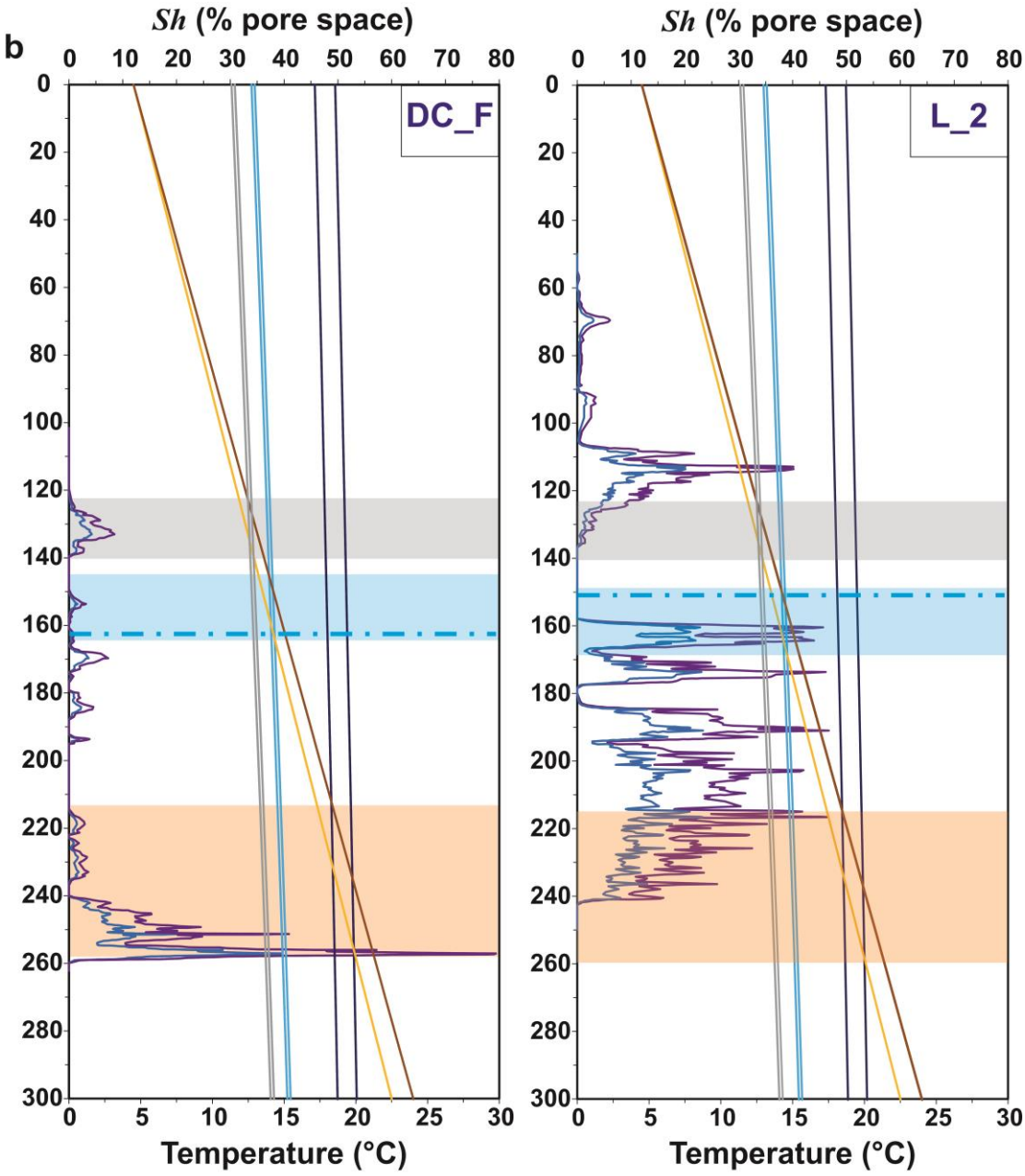



**Figure 3.9.** Gas hydrate saturation and stability modelling. The modelled $BS_{II/H}$GHSZ fits well with core and well-logs observations. The modelled $BS_{I}$GHSZ, assuming small amounts of ethane (4%) and dominant methane (96%) fits well with the observed depth of the BSR. A 100% methane composition would shift the stability boundary up to 20-30 m upward. **(a)** (See the previous page) Boreholes DC_E and M_1; **(b)** (This page) Boreholes DC_F and L_2. The legend is at the bottom of page 114.

### *3.3.3. Evidence of free gas*

Seismic observations suggest the presence of free gas below the BSR. The wireline log velocity data at DC_E confirm this interpretation. The marked P-wave velocity reduction at the BSR and below, combined with a relatively constant increase in S-wave velocity, is clear evidence of free gas within sediments (cf. Guerin *et al.*, 1999) **(Fig. 3.1c)**. Although variable, the P-wave velocity is consistently lower than average seawater velocity (~1500 m/s) below the BSR and there is no evident correlation with the high resistivity anomalies within the zone of hydrate occurrence. The P-wave velocity log indicates extremely low values, from the BSR down to approximately 250 mbsf. Deeper, the velocity is lower than that of seawater but higher than the underlying zone (**Fig. 3.1b, c**).

Despite the clear evidence of free gas on seismic and wireline velocity data, free gas was apparently absent in pressure-cores because **(1)** the MSCL-S P-wave profiles on successfully recovered FPC cores were relatively linear under in-situ conditions and **(2)** no attenuation of the 250 kHz signal was observed (**Fig. 3.4**). Furthermore, the density and neutron porosity variations with depth closely correlate with each other (**Fig. 3.1c**), suggesting small changes in the H-index with depth and possibly, only trace amounts of free gas (Cook *et al.*, 2008).

### *3.3.4. Gas geochemistry*

At DC_E, the analysed cores contained a variety of hydrocarbon gases (**Figs. 3.3, 3.10** and **Tab 3.1**). Given that free gas was not detected within FPC cores, the gas released upon depressurisation probably consists of a mixture of previously hydrate-bound gas and dissolved gas. The former likely represents the majority by volume, given the low solubility of light hydrocarbons at the typical pressure and temperature conditions of natural gas hydrate systems. However, I do not exclude the presence of small amounts of free gas within FC cores, if recovered below the BSR, where the free gas occurrence is evident from seismic images.

Almost pure methane with small amounts of ethane and less than 0.3 mol.% of heavier hydrocarbons are present above the BSR. These compositions indicate that mainly $S_I$ hydrates form above the BSR, with potentially accessory $S_{II}$ hydrates between ~150 and 155 mbsf. The geochemical data from samples shallower than ~100 mbsf (HRC-E#01 and FPC-E#02) indicate almost pure methane. The gas from these samples was most likely dissolved in the pore water, considering that all the associated saturation estimates approach or are equal to 0% (**Tab 3.6**). The $C_{2-4}$ components increase with depth, especially near and below the BSR, where the most distinct change occurs. Below the BSR, methane is often <90 and in some cases <80 mol%, whereas ethane frequently exceeds 10 mol%. Relatively high values of propane (e.g. 7.89 mol% at ~220 mbsf) and butane (e.g. 0.74 mol% at ~171 mbsf) were also detected (**Figs. 3.3, 3.10** and **Tab 3.1**).

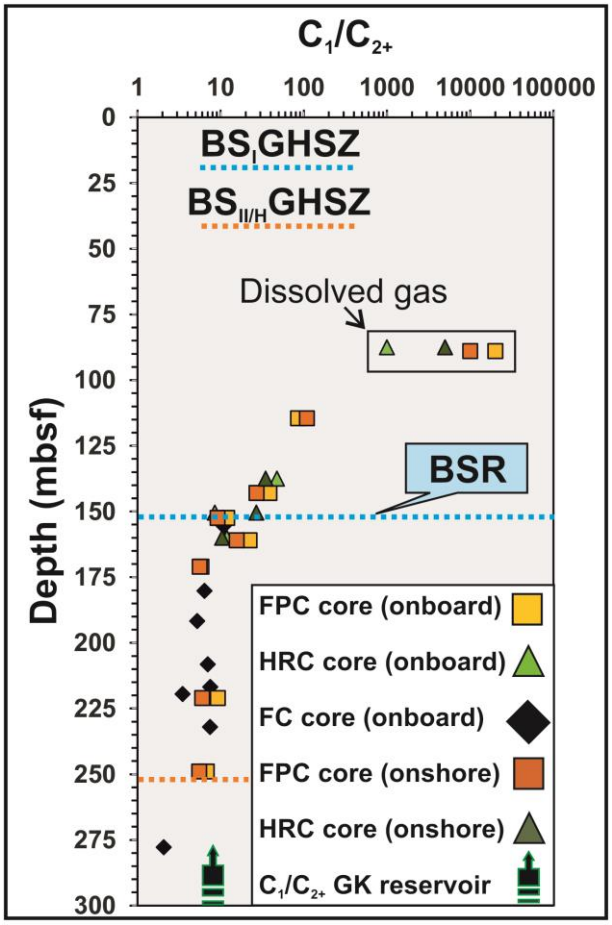



**Figure 3.10.** $C_1/C_{2+}$ ratio extrapolated from the molecular composition of gases within FC and FPC cores from onboard and onshore analyses at DC_E. Note the relative decrease of methane with depth at DC_E, which results in an $S_I$ to $S_{II/H}$ hydrate transition at approximately the depth of the BSR. The results from the onshore analyses agree well with those performed onboard. The range of $C_1/C_{2+}$ ratios of the free gas within the gas cap of the Gumusut-Kakap (GK) reservoir ($C_1/C_{2+}$ GK reservoir), varying between ~6 and ~11 is also plotted at the bottom.

The onshore geochemical analyses on samples acquired from FPC and HRC cores match well the onboard measurements and further detected small amounts of $C_5$-$C_9$ hydrocarbons (up to 0.5 mol.%) (**Fig. 3.11** and **Tab. 3.2**). Overall, the composition of the hydrocarbon gases below the BSR is consistent with $S_{II}$ and potentially $S_H$ hydrates. Contrarily to $S_{II}$, $S_H$ hydrates can incorporate even $C_{4+}$ hydrocarbon within their larger cages (cf. Sassen *et al.*, 2001a, b, d; Sassen *et al.*, 2001d; Lu *et al.*, 2007; Sloan Jr and Koh, 2007; Klapp *et al.*, 2010).

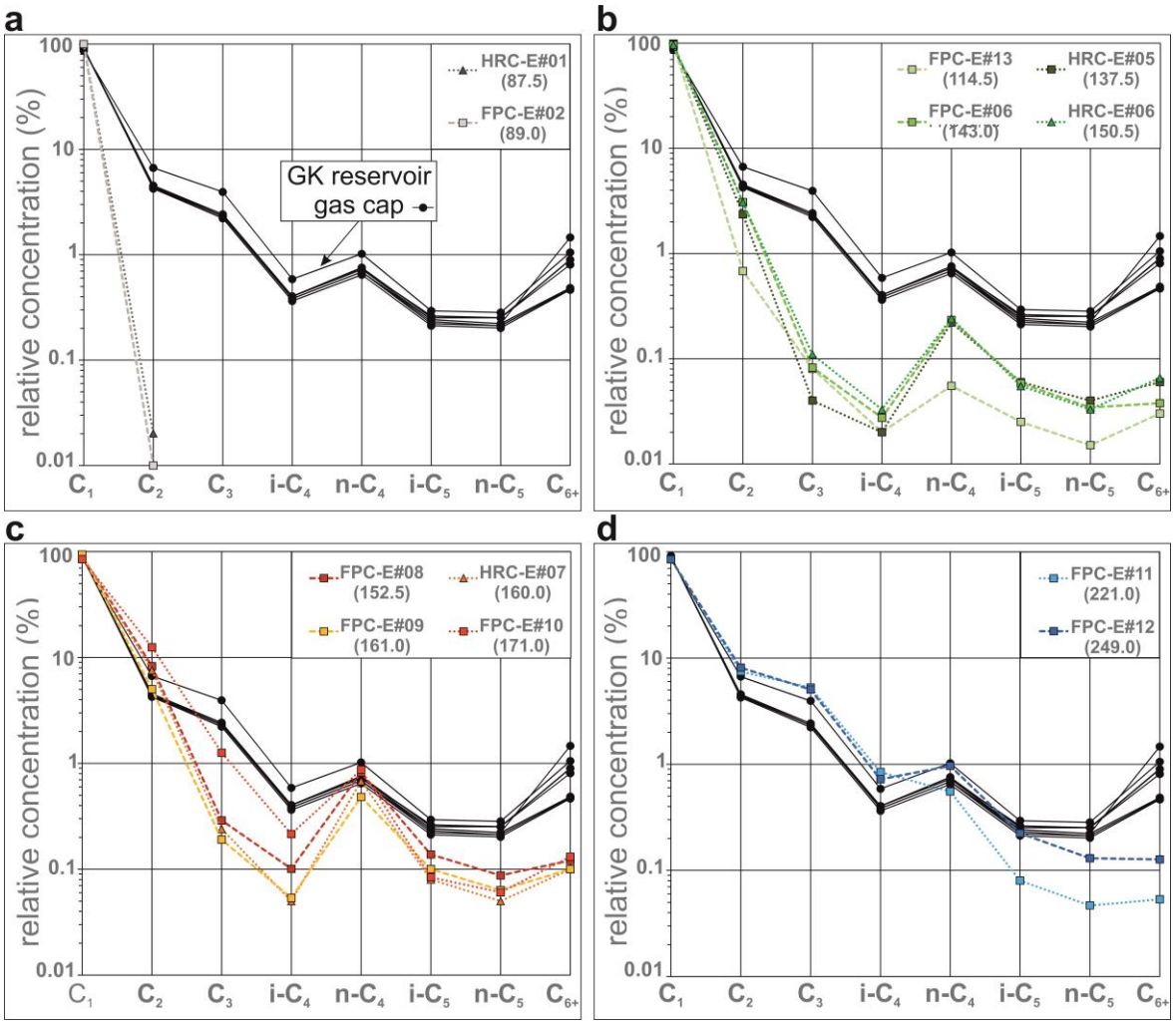



**Figure 3.11.** Onshore geochemical analyses. Relative concentrations of $C_1$-$C_{6+}$ gases collected from FPC and HRC cores at DC_E (dashed and dotted coloured lines) and of the gases present within the gas cap of the Gumusut-Kakap reservoir (GK reservoir) (continuous black lines). The values from measurements on FPC-E#06, 08, 09, 10, 11, 12 and 13 are averages from multiple measurements accomplished during progressive depressurisation steps whereas the values from the other cores reflect single measurements. Note the enrichment in $C_{2+}$ hydrocarbons with increased depth, with the molecular composition becoming more similar to that of the gas cap of the GK reservoir (e.g. see FPC-E#11 and FPC-E#12 in **(d)**). The presence of small amounts of $C_{5+}$ gases in FPC-E#11 and 12 suggests little amounts of $S_H$ hydrates. The depth of each core (mbsf) is indicated in brackets.

Importantly, the $C_1$-$C_{6+}$ concentrations of the deepest samples within the GHSZ (FPC-E#11 and FPC-E#12) and those of the gas cap of the Gumusut-Kakap reservoir (GK reservoir) are relatively similar **(Fig. 3.11d** and **Tabs. 3.1, 3.2)**. A minor difference is represented by the relative enrichment in $C_2$-$C_4$ and the relative depletion in $C_{5+}$ gases in the samples within the GHSZ compared to those from the gas cap. A progressive mismatch appears by comparing the $C_1$-$C_{6+}$ composition of the GK reservoir to that of shallower FPC cores. The gas in these samples, from the deeper to the shallower, becomes progressively and visibly more enriched in methane (**Fig. 3.11a-c**).

Finally, the geochemical measurements on FC-E#16 (277.8 mbsf) indicate a gas extremely enriched in $C_{2-4}$ components (~32.5%, see **Tab. 3.1**), even compared to the composition of the gas in the GK reservoir (**Fig. 3.12**). This non-pressurised core was recovered slightly outside the zone with of $S_{II/H}$ hydrate occurrence (core data suggest that hydrates occur until ~250 mbsf), and there is no compelling evidence of hydrates at this depth (i.e. only a single chlorinity anomaly, cf. **Fig. 3.5b**).

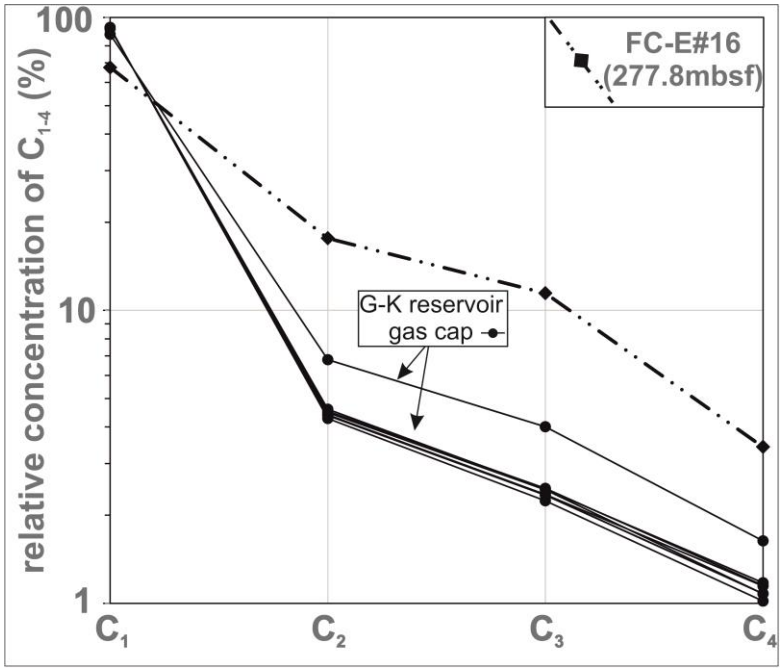



**Figure 3.12.** Relative concentrations of $C_1$-$C_4$ gases collected from FC-E#16 at DC_E (dashed- double dotted line) and of the gas of the GK reservoir (continuous black lines). The depth of the core (mbsf) is indicated in brackets.

## 3.4. Gas hydrate stability modelling

Gas hydrate stability modelling was performed using the CSMHyd software (Sloan Jr and Koh, 2007) to:

**(1)** Constrain the vertical extent of the GHSZ and, in particular, the depths of the BGHSZ for $S_I$ hydrates ($BS_IGHSZ$), as well as for $S_{II}$ and $S_H$ hydrates ($BS_{II/H}GHSZ$);

**(2)** Link the deep hydrocarbon accumulation with the shallower gas hydrate system.

The measured linear ($R^2$= 0.99) geothermal gradient is used for DC_E (63°C/km and seafloor temperature of 4.6°C). For the other three wells, the geothermal gradient has been varied between 60 and 65°C/km and the seafloor temperature between 4 to 5°C (**Fig. 3.9** and **Tab. 3.3**). The pore pressure was calibrated with the piezoprobe measurements at DC_E, as being slightly in excess of hydrostatic (**Fig. 3.13**). This excess pore pressure has been taken into account in the extrapolation of the hydrate stability boundaries. Two significant compositions from a range of geochemical measurements, performed on samples from the gas cap of the GK reservoir have been considered to constrain the extent of the $S_{II/H}GHSZ$. These compositions represent a lower and an upper end-member, in terms of $C_{2+}$ amounts (86.1-91.4% methane and 8.6-13.9% $C_{2+}$ gases). The gas in the GK reservoir is also characterised by $\delta^{13}C_{PDB}$ isotope values of methane ranging between -41.2 and -43.5‰. The modelled range of depths for the $BS_{II/H}GHSZ$ using these compositions closely matches the abrupt resistivity reduction observed in the four boreholes (**Fig. 3.9**).

The stability boundary of $S_I$ hydrates was modelled with two different compositions: **(1)** pure methane and **(2)** 96% methane plus 4% ethane. The modelling shows that the stability range with a 100% methane composition does not fit with the depth of the observed BSR, whereas a good fit exists with a composition that includes minor amounts of ethane (**Fig. 3.9**), evidence for which has been detected in bulk gas measurements near the BSR depth (**Fig. 3.3** and **Tabs. 3.1, 3.2**).

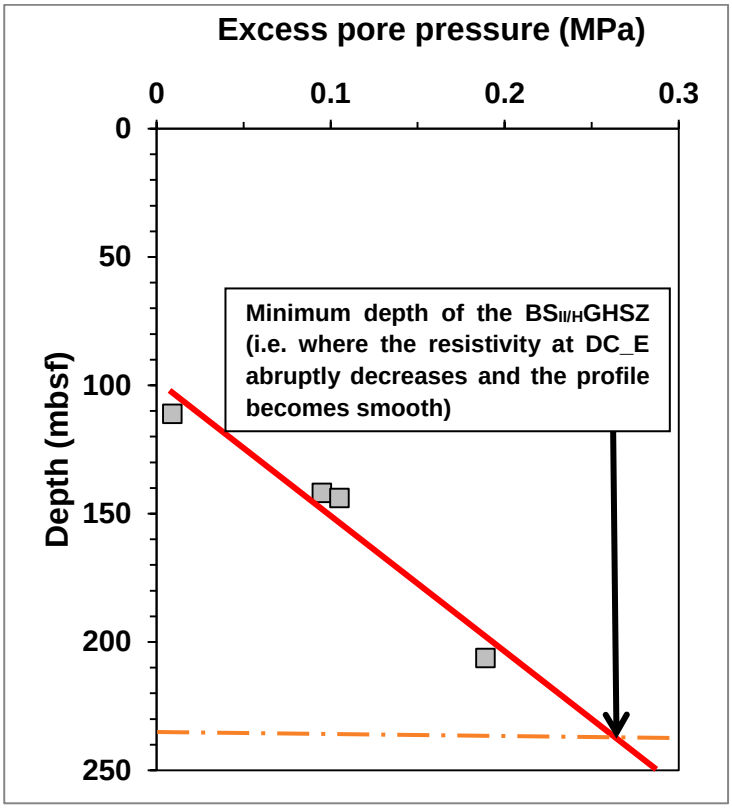



**Figure 3.13.** Excess pore pressure profile at DC_E. The pressure was measured using a wireline-operated piezoprobe equipped with two pressure sensors. Four tests have been accomplished at DC_E. For each test, the piezoprobe was pushed into the soil beyond the bottom of the borehole and pore pressure with time was recorded. The increase of excess pore pressure with depth is linear below ~100 mbsf ($R^2$= 0.94). The total pore pressure is the sum of the hydrostatic and the excess pore pressure and is assumed to control the stability of gas hydrates.

## 3.5. Discussion

### *3.5.1. Origin of gas hydrates and molecular fractionation*

The presence of $S_{II}$ and $S_H$ hydrates, in this case below the BSR, implies a thermogenic source for the hydrate-forming gas (Sassen *et al.*, 2001a, b, d; Mazurenko *et al.*, 2002; Pohlman *et al.*, 2005; Macelloni *et al.*, 2015). A thermogenic origin for the gas forming hydrates is perhaps not surprising given that the cored interval overlies a hydrocarbon accumulation (i.e. the GK reservoir) containing thermogenic hydrocarbons, as indicated by the reservoir gas compositional and isotopic data. Gas hydrates with average $\delta^{13}C_{PDB}$ of -47.65‰, similar to the $\delta^{13}C_{PDB}$ of Gumusut-Kakap reservoir gases, have been further recovered with piston cores in an adjacent area of active seepage (offshore Brunei), indicating that the leakage towards shallow depths of thermogenically-sourced gases is a widespread process in this area (Warren *et al.*, 2010).

However, the observed arrangement of gas hydrate structures (i.e. $S_I$ above the BSR and $S_{II/H}$ below) can be created either with **(1)** a combination of thermogenic and biogenic/microbial sources (cf. Malinverno and Goldberg, 2015) or **(2)** a single thermogenic source that experiences a significant compositional fractionation, from the $BS_{II}GHSZ$ up to shallower levels. I can neither exclude nor precisely assess the possibility of a minor contribution of microbial gases being involved in the formation of gas hydrates, given the relatively high $C_1/C_2$ ratio measured in the shallower (i.e. <125 mbsf) cores (**Fig. 3.10** and **Tabs. 3.1, 3.2**) and the absence of isotopic data from shallow gas and/or hydrates. However, the observed compositional trend, eventually leading to the transition from $S_{II/H}$ hydrates to $S_I$ hydrates, is interpreted as indicative of a compositional fractionation of a pure thermogenic gas. The formation itself of $S_{II/H}$ hydrates depletes the sourcing gas in heavier (i.e. $C_{2+)}$ components, which are preferentially incorporated in the hydrate cage. The ascending gas mixture is therefore progressively enriched in methane, as suggested by the onboard and onshore geochemical analyses **(Figs. 3.3, 3.10** and **Tabs. 3.1, 3.2)** (cf. Sassen *et al.*, 2001d; Smith *et al.*, 2014b; Macelloni *et al.*, 2015). Ultimately, the gas composition becomes sufficiently depleted in $C_{2+}$ components to form $S_I$ hydrates. Based on gas compositional data showing a relative $C_1$ enrichment towards shallower depths (**Figs. 3.3, 3.10**), the lowermost occurrence of $S_I$ hydrates is expected approximately the BSR depth, which is interpreted as the base of $S_I$ hydrate stability ($BS_IGHS$) (Hadley *et al.*, 2008; Boswell *et al.*, 2016).

The onboard geochemical analyses suggest that accessory $S_H$ hydrates accompany the predominant $S_{II}$ hydrates, below the BSR. These $S_H$ hydrates are interpreted to host the small detected quantities of $C_{5+}$ gases. The slightly higher amounts of $C_{2-4}$ and lower amounts of $C_{5+}$ in the samples from the deeper portions of the GHSZ (i.e. FPC-E#11 and 12, **Fig. 3.11d**), compared to the composition of the gas in the GK reservoir, could indicate a fractionation operated on a feeding gas by the process of $S_{II}$ hydrate crystallisation, which favours the inclusion in the hydrate of $C_{2-4}$ hydrocarbons over other components (cf. Sassen

*et al.*, 2001a). However, a minimal molecular fractionation during the leakage from the gas cap of the deep reservoir to the GHSZ cannot also be excluded.

The data collected so far at seafloor seeps worldwide, characterised by elevated fluid fluxes, suggest a marked difference between the composition of the feeding gas and that of the associated hydrates at the seafloor, with the latter enriched up to 15-20% in $C_{2+}$ components (Sassen *et al.*, 2001c; Pohlman *et al.*, 2005). Assuming that the vast majority of the gas evolved from the pressure cores derives from hydrates and that the sourcing gas has a composition similar to that within the GK reservoir, only a minor enrichment in the $C_{2-4}$ components has been observed in the deeper samples (**Fig. 3.11d**). This could be caused by a lack of efficient permeable pathways for a rapid leakage towards the seafloor. In this context, the gas (as a free phase and as a dissolved phase) would spend more time in the overburden, and a significant portion of it would be converted into hydrates. Thus, the molecular fractionation would become controlled by the time spent at a given depth by the sourcing free gas or dissolved gas, i.e. by the effectiveness of fluid flux. Therefore, in this scenario, hydrocarbons would effectively migrate upward only when depleted enough in heavier components, or in the presence of efficient permeable pathways.

### *3.5.2. Stacked bases of hydrate stability and occurrence of free gas*

The close match between the deepest position of positive resistivity anomalies in the four wells and the anomalies in temperature and chlorinity at DC_E indicates that in the studied natural gas hydrate system the $BS_{II/H}$GHSZ likely lies between 237 and 260 mbsf. This hypothesis has been confirmed by the hydrate stability modelling, which shows a range of depths for the $BS_{II/H}$GHSZ matching the well-log and core observations (**Figs. 3.3, 3.9**). The good fit between observations and stability modelling, performed with the gas composition of the GK reservoir, strongly supports the proposed link between the deep hydrocarbon accumulation and the gas hydrate system, where the deep leaking reservoir feeds the GHSZ with minimal compositional changes *'en-route'*. This interpretation is also supported by the similarity between the composition of the gas of the GK reservoir and the

gas in the cores retrieved near the $BS_{II/H}$GHSZ, where the effect of the molecular fractionation operated by hydrate crystallisation is less pronounced (i.e. FPC-E#11 and FPC-E#12, **Fig. 3.11d**).

The presence of small amounts of ethane in the cores above BSR and, in a minor amount, the excess fluid pressures recorded at DC_E (**Fig. 3.13**), are expected to deepen of the base of $S_I$ hydrate stability (Ballard and Sloan Jr, 2000), explaining the misfit between the BSR and the modelled $BS_I$GHSZ, assuming 100% methane (**Figure 3.9**). Alternatively, either a lower geothermal gradient (i.e. ~57°C/km) combined with a 100% methane composition or capillary effects on the free gas phase, particularly effective in fine-grained sediments with pores sizes in the order of tens of nanometres, could equally explain the observed BSR position (cf. Liu and Flemings, 2011). In this latter scenario, hydrates could occur in fractures at bulk stability conditions whereas the free gas would fill nm-scale pores, being, therefore, the only phase subject to capillary effects.

The chlorinity anomaly at FC-E#16, located beneath the $BS_{II/H}$GHSZ, suggests that small residual amounts of hydrates could at occur at ~278 mbsf, 30-50 metres below the bulk zone of $S_{II}$ and $S_H$ hydrate occurrence. The molecular composition of the gas released from this core (**Fig. 3.12**), which is more enriched in $C_{2-4}$ components than the deep thermogenic gas source, could reflect the preferential inclusion of heavier hydrocarbon in the hydrate. Some residual hydrates, particularly enriched in heavier components, could remain stable at depths greater than the vast majority of the $S_{II/H}$ hydrate reservoir, whose base is at 237-260 mbsf.

Unfortunately, the seismic attenuation below the BSR also obscures any potential reflection related to the $BS_{II}$GHSZ. Furthermore, P-wave velocity data at DC_E suggest that free gas is present from the $BS_I$GHSZ, down to depths exceeding the $BS_{II/H}$GHSZ (**Figs. 3.1, 3.2**). Such a vertically developed and seismically attenuated free gas zone could prevent the development of a clear negative acoustic impedance contrast at the $BS_{II}$GHSZ. Although a

clear and widespread BSR related to the $BS_{II}$GHSZ has not been observed, several studies conducted elsewhere proposed that such reflector could occur in the presence of different hydrate structures having different stabilities (Andreassen *et al.*, 2000; Foucher *et al.*, 2002; Bangs *et al.*, 2005; Pecher *et al.*, 2014). The findings presented here suggest that $R_{II}$, lying outside the seismically attenuated region below the BSR, could be a good candidate to locally represent the $BS_{II}$GHSZ in the seismic data, given that its position fits with the high resistivity anomaly at DC_F, and consequently the modelled $BS_{II}$GHSZ.

The fact that the very low WL P-wave velocity zone occurs within the interval of highest *Sh* indicate that free gas and hydrates preferentially occur and coexist in the same interval. The coexistence between free gas and gas hydrates is limited to the zone of $S_{II/H}$ gas hydrate occurrence (with the exception of fluid-escape pipes, **see Chapter 4**), although the free gas is suggested to be present at low saturation. Here, the $C_{2+}$ depletion associated with hydrate crystallisation can keep residual free gas outside the hydrate stability field. Immediately beneath the BSR, the free gas would be too deep to form $S_I$ hydrates and its composition too depleted in $C_{2+}$ components to form $S_{II}$ hydrates. Moreover, an ongoing hydrate recycling mechanism can feed further free gas into the system.

### *3.5.3. Reservoir characteristics of gas hydrate-bearing sediments*

The homogeneous lithology at the crest of the studied thrust-cored ridge, mainly composed of fine-grained and clay-rich mudstones, promotes the formation of hydrates within fractures (i.e. grain-displacing hydrates), frequently observed in this type of sediment (Cook *et al.*, 2008 and 2014; Holland *et al.*, 2008; Riedel *et al.*, 2010a). The generation of fractures can be promoted either through episodic fracturing, driven by overpressure pulses or through hydrate heave, a process that implies a grain displacement operated by the growth of hydrate lenses, acting against the effective confining stress (Clennell *et al.*, 1999; Daigle and Dugan, 2010b; Daigle *et al.*, 2011; Rees *et al.*, 2011).

The presence of hydrates mainly within sub-vertical thin fractures resulted, at the core-scale, in *Sh* profiles displaying low to moderate values throughout the core (**Figs. 3.4, 3.5c**). Interestingly, except for the high S-wave velocity peak observed in the WL measurements just above the $BS_IGHSZ$, little effect of gas hydrates has been observed on wireline velocity logs and the MSCL-S analyses (**Figs. 3.1c, 3.4**). This is not surprising because fracture-filling hydrates at low to moderate saturation within a clay-rich lithology are considered to exert only a minimal influence on the sediment bulk and shear modulus (Lee and Collett, 2012; Cook *et al.*, 2014). A possible reason could be that thin and low-intensity hydrate-filled fractures may not effectively influence the grain stiffness and are further not easily detected during the MSCL-S analyses. An exception is represented by the top of FPC-E#08 where, however, the precise hydrate morphology is complex to assess, and some sampling disturbance could have also occurred upon recovery **(Fig. 3.4a)**.

### *3.5.4. Thermogenic hydrate provinces: impact on carbon inventories*

A connection between deep leaky gas accumulation and overlying shallow deposits of gas hydrates has been observed in other basins before, such as in the Green Canyon (Northern Gulf of Mexico) and the Marmara Sea (Sassen *et al.*, 2001a; Bourry *et al.*, 2009). In other cases, like in the hydrate-rich pockmarks in the Niger Delta (Ruffine *et al.*, 2013; De Prunelé *et al.*, 2017), such connection is postulated on the basis of geochemical analyses on shallow hydrate samples and seismic evidence of a hydrocarbon plumbing system dominated by vertical leakage processes. However, in this study, the recovered hydrates are distributed over tens of metres in the overburden and not outcropping at the seafloor as isolated hydrate mounds or within pockmarks.

The estimated hydrate saturations suggest that at this location of focused hydrocarbon fluid flow the carbon reservoir stored within the $S_{II/H}GHSZ$ is considerably larger than that within the $S_IGHSZ$ (**Fig. 3.9**). At least in geological settings affected by thermogenic hydrocarbon fluxes, the total hydrate reservoir could be biased if based on the assumption that the base of hydrates stability is represented by the BSR. The NW Borneo margin is

characterised by numerous structures relatively similar to that described in this study (Morley, 2009; Hesse *et al.*, 2010), able to focus thermogenic hydrocarbon fluxes, possibly interacting with shallower zones of microbial methane production (Warren *et al.*, 2010). Thus, it is likely that further sub-BSR $S_{II}$ and $S_H$ hydrates could be present along this margin and in similar geological settings elsewhere. The recent discovery of $S_{II}$ gas hydrates below a BSR in the South China Sea (Liang *et al.*, 2017), in a passive margin environment, confirms that the occurrence of sub-BSR gas hydrates is not limited to the NW Borneo and could instead be widespread and relevant for exploration, geohazard and global estimates. Finally, the identification of extensive thermogenic hydrates systems in the some of the most sensitive regions for global warming (e.g. the Barents Sea and offshore western Svalbard, see Andreassen *et al.*, 2017; Plaza-Faverola *et al.*, 2017) implies that thermogenic natural gas hydrate systems could also impact the present-day and short-term climate dynamics.

## 3.6. Conclusions

This study shows evidence of structure II and probably structure H hydrates below a BSR from core and well-log resistivity data. Furthermore, the results indicate that chemical fractionation affecting the hydrate composition occurs with decreasing depth, where a thermogenic flux of $C_{2+}$-rich hydrocarbons migrates through the GHSZ. Rather than being regarded as indicative of the BGHSZ, the BSR should instead be considered, in some cases, as a transitional boundary between different hydrate structures. Finally, if the presence of sub-BSR hydrates in basins characterised by thermogenic fluid fluxes proves to be more widespread, their impact on the global carbon budget needs to be considered. Further drilling and pressure coring below the BSR in these basins are thus critical in refining our understanding of gas hydrate systems.

## 3.7. Appendix

### *3.7.1. Methods to estimate gas hydrate saturation*

The gas hydrate saturation (*Sh*, % of pore space) is calculated from chlorinity by the difference between the measured (*Cm*) and the *'baseline'* (*Cb*) chlorinity (Malinverno *et al.*, 2008) **(Tab. 3.4)**. *Sh* equals to:

$$\boldsymbol{Sh = 100(\beta(Cb - Cm)/(Cm + \beta(Cm - Cb))}$$

Where $\beta$ is a dimensionless coefficient accounting for the density change from gas hydrate to water and equals to:

$$\boldsymbol{\beta = (\rho w\ N\ V)/(nw\ mw)}$$

Where $\rho w$ is the water density (g/cc), *N* is the Avogadro's number, *V* is the volume of the hydrate elementary cell, *nw* is the number of water molecules in the hydrate elementary cell, and *mw* is the molar mass of water (**Tab. 3.5**).

*Sh* from pressure core depressurisation experiments is extrapolated from the excess moles of gas, by assuming a 100% methane composition and its solubility in the pore water (Kim *et al.*, 2013b; Lee *et al.*, 2013; Holland and Schultheiss, 2014). The errors introduced by the presence of a gas mixture instead of a pure methane phase were probably small since the *Sh* values obtained in FPC cores from chlorinity and depressurisation data produced similar results (see **Figs. 3.5b, 3.9a** and **Tab. 3.6**).

Finally, the phase shift deep smoothed resistivity (which is the measurement that better penetrates into the formation) and porosity data from density logs were used to estimate *Sh* in the four wells, taking due account of hydrate-related fractures and associated anisotropy in the sediment. A porosity *vs* depth trend extrapolated using the data at DC_E and DC_F was used for M_1 and L_2, given the lack of porosity measurements at these two sites (dashed red line in **Fig. 3.14**). Then, I followed the methodology proposed by Lee and Collett (2012), using a *'fracture porosity'* ranging from 3.5% to 5.0%, (i.e. 95.0-97.5% of the

fracture space is filled by hydrates) and a fracture dip angle of 70°, based on observations on resistivity images. These values are convenient parameters and are used to provide reliable estimates of *Sh* if calibrated with direct measurements. The calculations resulted in two continuous *Sh* profiles for each well, respectively representing a lower and an upper end-member **(Fig. 3.9)**.

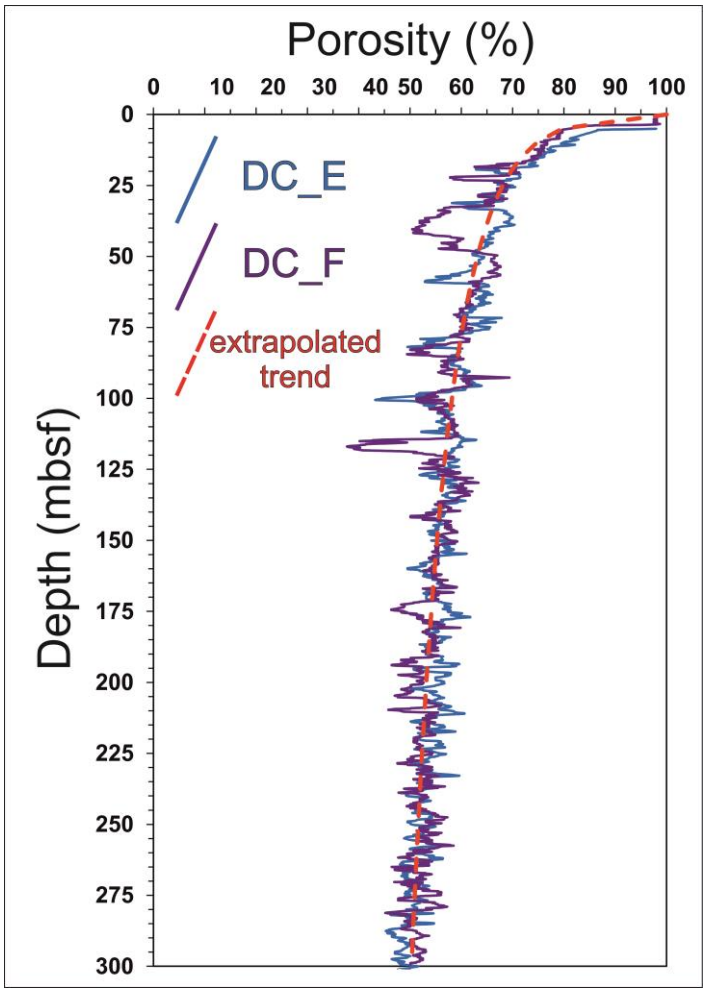



**Figure 3.14.** Porosity profiles at DC_E and DC_F. The porosity has been calculated from density logs. The neutron logs are affected by clay minerals and provide overestimated values (Cook *et al.*, 2008). Porosity values were used to estimate *Sh*. For the wells M_1 and L_2, I have obtained a porosity *vs* depth trend, by interpolating the porosities at DC_E and DC_F (dashed red line), given the little changes, in terms of stratigraphy, between these four wells.

### *3.7.2. Supplementary tables*

| **3.1** | **Depth (mbsf)** | **$C_1$** | **$C_2$** | **$C_3$** | **$C_4$** |
|---|---|---|---|---|---|
| **HRC-E#01** | 87.5 | 99.90 | 0.10 | 0.00 | 0.00 |
| **FPC-E#02** | 89.0 | 100.00 | 0.00 | 0.00 | 0.00 |
| **FPC-E#13** | 114.5 | 98.84 | 0.93 | 0.23 | 0.00 |
| **HRC-E#05** | 137.5 | 97.94 | 1.94 | 0.01 | 0.11 |
| **FPC-E#06** | 143.0 | 97.47 | 2.28 | 0.04 | 0.21 |
| **HRC-E#06** | 150.5 | 89.46 | 9.49 | 0.24 | 0.81 |
| **FPC-E#08** | 152.5 | 92.29 | 7.17 | 0.12 | 0.42 |
| **FC-E#03** | 155.5 | 91.59 | 8.41 | 0.00 | 0.00 |
| **HRC-E#07** | 160.0 | 92.26 | 7.00 | 0.18 | 0.56 |
| **FPC-E#09** | 161.0 | 95.69 | 4.22 | 0.03 | 0.06 |
| **FPC-E#10** | 171.0 | 85.48 | 12.66 | 1.12 | 0.74 |
| **FC-E#05** | 180.3 | 86.50 | 13.50 | 0.00 | 0.00 |
| **FC-E#06** | 191.8 | 83.91 | 16.09 | 0.00 | 0.00 |
| **FC-E#09** | 208.2 | 87.52 | 12.48 | 0.00 | 0.00 |
| **FC-E#11** | 216.8 | 88.23 | 11.77 | 0.00 | 0.00 |
| **FC-E#12** | 219.5 | 77.77 | 13.66 | 7.89 | 0.68 |
| **FPC-E#11** | 221.0 | 90.26 | 7.36 | 2.09 | 0.29 |
| **FC-E#13** | 232.0 | 88.17 | 11.83 | 0.00 | 0.00 |
| **FPC-E#12** | 249.0 | 87.23 | 8.50 | 3.55 | 0.72 |
| **FC-E#16** | 277.8 | 67.50 | 17.63 | 11.45 | 3.42 |

**Table 3.1.** Onboard compositional analyses on gas samples obtained from conventional and pressure cores at DC_E. $C_1$= methane; $C_2$= ethane; $C_3$= propane; $C_4$= butane (iso-butane + n-butane).

| 3.2 | Depth (mbsf) | $C_1$ | $C_2$ | $C_3$ | i-$C_4$ | n-$C_4$ | i-$C_5$ | n-$C_5$ |
|---|---|---|---|---|---|---|---|---|
| HRC-E#01 | 87.5 | 99.980 | 0.020 | 0.000 | 0.000 | 0.000 | 0.000 | 0.000 |
| FPC-E#02 | 89.0 | 99.990 | 0.010 | 0.000 | 0.000 | 0.000 | 0.000 | 0.000 |
| FPC-E#13 | 114.5 | 99.092 | 0.683 | 0.080 | 0.020 | 0.055 | 0.025 | 0.015 |
| HRC-E#05 | 137.5 | 97.200 | 2.360 | 0.040 | 0.020 | 0.220 | 0.060 | 0.040 |
| FPC-E#06 | 143.0 | 96.441 | 3.085 | 0.082 | 0.027 | 0.234 | 0.058 | 0.034 |
| HRC-E#06 | 150.5 | 96.399 | 3.063 | 0.110 | 0.033 | 0.242 | 0.055 | 0.033 |
| FPC-E#08 | 152.5 | 90.176 | 8.267 | 0.289 | 0.101 | 0.820 | 0.138 | 0.087 |
| HRC-E#07 | 160.0 | 91.240 | 7.560 | 0.240 | 0.050 | 0.680 | 0.080 | 0.050 |
| FPC-E#09 | 161.0 | 93.982 | 5.029 | 0.190 | 0.053 | 0.481 | 0.100 | 0.063 |
| FPC-E#10 | 171.0 | 84.873 | 12.504 | 1.260 | 0.215 | 0.870 | 0.084 | 0.060 |
| FPC-E#11 | 221.0 | 85.700 | 7.450 | 5.267 | 0.843 | 0.553 | 0.080 | 0.047 |
| FPC-E#12 | 249.000 | 84.683 | 8.100 | 5.050 | 0.720 | 0.963 | 0.223 | 0.130 |
| | **Depth (mbsf)** | **Neo-$C_5$** | **$C_6$** | **M-C pent.** | **Cyclo-Hex.** | **$C_7$** | **M-C Hex.** | **$C_8$** |
| HRC-E#01 | 87.5 | 0.000 | 0.000 | 0.000 | 0.000 | 0.000 | 0.000 | 0.000 |
| FPC-E#02 | 89.0 | 0.000 | 0.000 | 0.000 | 0.000 | 0.000 | 0.000 | 0.000 |
| FPC-E#13 | 114.5 | 0.000 | 0.015 | 0.005 | 0.005 | 0.005 | 0.000 | 0.000 |
| HRC-E#05 | 137.5 | 0.000 | 0.030 | 0.010 | 0.000 | 0.010 | 0.010 | 0.000 |
| FPC-E#06 | 143.0 | 0.000 | 0.024 | 0.007 | 0.000 | 0.003 | 0.003 | 0.000 |
| HRC-E#06 | 150.5 | 0.000 | 0.033 | 0.011 | 0.000 | 0.011 | 0.011 | 0.000 |
| FPC-E#08 | 152.5 | 0.000 | 0.064 | 0.024 | 0.007 | 0.017 | 0.007 | 0.003 |
| HRC-E#07 | 160.0 | 0.000 | 0.040 | 0.020 | 0.010 | 0.020 | 0.010 | 0.000 |
| FPC-E#09 | 161.0 | 0.000 | 0.050 | 0.017 | 0.003 | 0.017 | 0.010 | 0.003 |
| FPC-E#10 | 171.0 | 0.003 | 0.047 | 0.027 | 0.030 | 0.013 | 0.010 | 0.003 |
| FPC-E#11 | 221.0 | 0.007 | 0.030 | 0.007 | 0.017 | 0.000 | 0.000 | 0.000 |
| FPC-E#12 | 249.0 | 0.003 | 0.073 | 0.017 | 0.017 | 0.010 | 0.007 | 0.003 |

**Table 3.2.** Onshore compositional analyses on gas samples obtained from pressure cores at DC_E. $C_1$= methane; $C_2$= ethane; $C_3$= propane; $C_4$= butane (iso-butane + n-butane); i-$C_4$= iso-butane; n-$C_4$= n-butane; i-$C_5$= iso-pentane; n-$C_5$= n-pentane; neo-$C_5$= neo-pentane; $C_6$= hexanes; M-C pent.= methylcyclopentane; C-hex= cyclohexane; $C_7$= heptanes; M-C hex.= methylcyclohexane; $C_8$= octanes.

| Borehole | Test tool | depth (mbsf) | depth (mbsl) | T (°C) |
|---|---|---|---|---|
| DC_E | CTD | 0 | 948.5 | 4.58 |
| DC_E | PWS | 32.5 | 981.0 | 6.76 |
| DC_E | Temperature Cone | 43.0 | 1038.1 | 7.83 |
| DC_E | Temperature Cone | 61.0 | 1063.4 | 8.58 |
| DC_E | Temperature Cone | 93.0 | 1086.0 | 11.02 |
| DC_E | Temperature Cone | 120.0 | 1092.0 | 12.62 |
| DC_E | Temperature Cone | 150.0 | 1099.0 | 14.52 |
| DC_E | PWS | 178.0 | 1101.4 | 16.1 |
| DC_E | PWS | 179.0 | 1103.3 | 16.14 |
| DC_E | PWS | 214.0 | 1108.5 | 18.05 |
| DC_E | Temperature Cone | 234.0 | 1109.9 | 19.68 |

**Table 3.3.** Temperatures measured at DC_E. The derived geothermal gradient is linear ($R^2$= 0.99) for the first 234 mbsf. Details about the test tools are explained in **paragraph 3.2**.

**Table 3.4**

| Borehole DC_E | | | | | | |
|---|---|---|---|---|---|---|
| **Core** | **Depth (mbsf)** | **Depth (mbsl)** | ***Cm* (mM)** | ***Cb* (mM)** | **Sulphate (mM)** | **Drill water infiltration (%)** |
| Liner-E#01 | 0.6 | 949.2 | 539.3 | – | 22.2 | – |
| Liner-E#02 | 2.0 | 950.6 | 534.7 | – | 21.2 | – |
| Liner-E#03 | 3.5 | 952.1 | 538.4 | – | 18.5 | – |
| Liner-E#04 | 5.0 | 953.6 | 537.5 | – | 16.4 | – |
| Liner-E#05 | 6.6 | 955.1 | 533.8 | – | 12.4 | – |
| Liner-E#06 | 7.5 | 956.1 | 539.9 | – | 11.0 | – |
| Liner-E#07 | 9.0 | 957.6 | 541.1 | – | 6.6 | – |
| Shelby-E#08 | 10.6 | 959.1 | 537.9 | – | 1.7 | – |
| Shelby-E#09 | 12.1 | 960.6 | 537.9 | – | 0.8 | – |
| Shelby-E#10 | 14.2 | 962.7 | 539.4 | – | 0.4 | < 1.5 |
| Shelby-E#11 | 15.0 | 963.6 | 544.9 | – | 2.5 | 11.9 |
| Shelby-E#12 | 20.4 | 968.9 | 541.3 | – | 0.5 | < 1.5 |
| Shelby-E#13 | 26.0 | 974.5 | 544.5 | – | 0.5 | < 1.5 |
| Shelby-E#14 | 32.0 | 980.6 | 540.8 | – | 0.5 | < 1.5 |
| Shelby-E#15 | 38.0 | 986.5 | 541.7 | – | 0.4 | < 1.5 |
| Shelby-E#17 | 60.4 | 1008.9 | 533.2 | 541.4 | 1.6 | 7.6 |
| FPC-E#01 | 89.1 | 1037.6 | 539.4 | 541.4 | 0.3 | < 1.5 |
| FPC-E#01 | 89.1 | 1037.6 | 541.3 | 541.4 | 0.4 | < 1.5 |
| FPC-E#01 | 89.2 | 1037.7 | 545.4 | 541.4 | 0.3 | < 1.5 |
| FPC-E#01 | 89.2 | 1037.7 | 539.4 | 541.4 | 0.4 | < 1.5 |
| FPC-E#01 | 89.6 | 1038.1 | 538.5 | 541.4 | 0.3 | < 1.5 |
| FPC-E#01 | 89.8 | 1038.3 | 540.1 | 541.4 | 0.3 | < 1.5 |
| FPC-E#02 | 89.2 | 1037.8 | 535.7 | 541.4 | 0.3 | 535.6 |
| FPC-E#02 | 89.4 | 1037.9 | 540.1 | 541.4 | 0.3 | 539.9 |
| FPC-E#02 | 89.7 | 1038.3 | 540.1 | 541.4 | 0.3 | 539.9 |
| FPC-E#02 | 89.8 | 1038.3 | 541.4 | 541.4 | 0.3 | 541.3 |
| Shelby-E#19 | 90.2 | 1038.8 | 541.8 | 541.4 | 0.5 | < 1.5 |
| FC-E#1 | 105.1 | 1053.6 | 534.1 | 541.4 | 1.2 | 5.8 |
| FC-E#01 | 105.5 | 1054.0 | 530.7 | 541.4 | 0.5 | < 1.5 |
| FC-E#01 | 106.0 | 1054.5 | 535.7 | 541.4 | 0.4 | < 1.5 |
| FPC-E#13 | 114.6 | 1063.1 | 516.8 | 541.4 | 0.7 | 3.2 |
| FPC-E#13 | 114.7 | 1063.2 | 522.4 | 541.4 | 0.3 | < 1.5 |
| FPC-E#13 | 115.0 | 1063.5 | 537.3 | 541.4 | 0.3 | < 1.5 |
| FPC-E#13 | 115.1 | 1063.6 | 527.0 | 541.4 | 0.3 | < 1.5 |
| Shelby-E#21 | 120.5 | 1069.0 | 529.8 | 541.4 | 0.5 | < 1.5 |
| FPC-E#03 | 126.0 | 1074.6 | 531.1 | 541.4 | 0.3 | < 1.5 |
| FPC-E#03 | 126.3 | 1074.9 | 490.8 | 541.4 | 0.3 | < 1.5 |
| FPC-E#03 | 126.4 | 1075.0 | 537.6 | 541.4 | 0.4 | < 1.5 |
| FPC-E#03 | 126.5 | 1075.1 | 547.0 | 541.4 | 0.3 | < 1.5 |
| FC-E#02 | 126.5 | 1075.0 | 532.1 | 541.4 | 0.4 | < 1.5 |
| FC-E#02 | 127.0 | 1075.5 | 532.1 | 541.4 | 0.5 | < 1.5 |
| FC-E#02 | 127.5 | 1076.0 | 509.9 | 541.4 | 0.5 | < 1.5 |
| FPC-E#04 | 127.1 | 1075.7 | 537.1 | 541.4 | 0.3 | < 1.5 |
| FPC-E#04 | 127.3 | 1075.8 | 519.5 | 541.4 | 0.3 | < 1.5 |
| FPC-E#04 | 127.6 | 1076.1 | 533.4 | 541.4 | 0.3 | < 1.5 |
| FPC-E#04 | 127.7 | 1076.2 | 532.5 | 541.4 | 0.2 | < 1.5 |
| FPC-E#04 | 127.7 | 1076.3 | 533.9 | 541.4 | 0.3 | < 1.5 |
| FPC-E#05 | 136.7 | 1085.2 | 530.1 | 541.4 | 0.4 | < 1.5 |
| FPC-E#05 | 136.8 | 1085.4 | 539.5 | 541.4 | 0.3 | < 1.5 |
| FPC-E#05 | 136.9 | 1085.4 | 539.6 | 541.4 | 0.3 | < 1.5 |
| FPC-E#05 | 137.0 | 1085.5 | 540.5 | 541.4 | 0.3 | < 1.5 |
| FPC-E#05 | 137.0 | 1085.5 | 523.3 | 541.4 | 0.3 | < 1.5 |
| FPC-E#05 | 137.3 | 1085.8 | 520.8 | 541.4 | 0.4 | < 1.5 |
| FPC-E#05 | 137.3 | 1085.8 | 529.8 | 541.4 | 0.3 | < 1.5 |
| FPC-E#06 | 143.0 | 1091.6 | 528.8 | 541.4 | 0.4 | < 1.5 |
| FPC-E#06 | 143.1 | 1091.6 | 519.7 | 541.4 | 0.3 | < 1.5 |
| FPC-E#06 | 143.4 | 1091.9 | 535.3 | 541.4 | 0.4 | < 1.5 |
| FPC-E#06 | 143.6 | 1092.1 | 544.9 | 541.4 | 0.3 | < 1.5 |
| FPC-E#06 | 143.7 | 1092.2 | 513.9 | 541.4 | 0.3 | < 1.5 |
| FPC-E#06 | 143.8 | 1092.4 | 533.0 | 541.4 | 0.6 | 2.8 |
| Shelby-E#23 | 150.5 | 1099.0 | 492.4 | 541.4 | 0.5 | < 1.5 |
| FPC-E#07 | 151.5 | 1100.1 | 505.7 | 541.4 | 0.4 | < 1.5 |
| FPC-E#07 | 151.6 | 1100.1 | 516.7 | 541.4 | 0.3 | < 1.5 |
| FPC-E#07 | 151.7 | 1100.2 | 543.6 | 541.4 | 0.4 | < 1.5 |
| FPC-E#07 | 151.8 | 1100.4 | 529.1 | 541.4 | 0.3 | < 1.5 |
| FPC-E#07 | 151.9 | 1100.4 | 533.9 | 541.4 | 0.3 | < 1.5 |
| FPC-E#07 | 152.0 | 1100.5 | 538.0 | 541.4 | 0.3 | < 1.5 |
| FPC-E#08 | 152.5 | 1101.1 | 520.0 | 541.4 | 2.1 | 9.9 |
| FPC-E#08 | 152.6 | 1101.1 | 505.6 | 541.4 | 1.3 | 5.9 |
| FPC-E#08 | 152.6 | 1101.2 | 502.8 | 541.4 | 0.5 | < 1.5 |

| | | | | | | |
|---|---|---|---|---|---|---|
| FPC-E#08 | 152.7 | 1101.2 | 493.2 | 541.4 | 1.0 | 4.5 |
| FPC-E#08 | 152.7 | 1101.3 | 495.8 | 541.4 | 0.5 | 2.4 |
| FPC-E#08 | 152.8 | 1101.3 | 494.4 | 541.4 | 0.9 | 4.0 |
| FPC-E#08 | 152.8 | 1101.4 | 498.0 | 541.4 | 0.8 | 3.8 |
| FPC-E#08 | 152.9 | 1101.4 | 497.7 | 541.4 | 0.7 | 3.2 |
| FPC-E#08 | 152.9 | 1101.5 | 504.5 | 541.4 | 0.4 | < 1.5 |
| FPC-E#08 | 153.1 | 1101.6 | 513.1 | 541.4 | 0.6 | 2.7 |
| FPC-E#08 | 153.1 | 1101.7 | 521.0 | 541.4 | 0.5 | < 1.5 |
| FPC-E#08 | 153.2 | 1101.7 | 508.3 | 541.4 | 0.5 | 2.5 |
| FPC-E#08 | 153.2 | 1101.8 | 533.0 | 541.4 | 0.5 | 2.5 |
| FPC-E#08 | 153.3 | 1101.8 | 535.3 | 541.4 | 0.6 | 2.6 |
| FC-E#03 | 154.4 | 1103.0 | 529.8 | 541.4 | 0.5 | 2.5 |
| FC-E#03 | 154.4 | 1103.0 | 542.6 | 541.4 | 1.2 | 5.8 |
| FC-E#03 | 154.5 | 1103.0 | 520.6 | 541.4 | 0.5 | < 1.5 |
| FC-E#03 | 155.0 | 1103.5 | 528.4 | 541.4 | 0.6 | 3.0 |
| FC-E#03 | 155.5 | 1104.0 | 530.8 | 541.4 | 0.5 | < 1.5 |
| FPC-E#09 | 161.0 | 1109.6 | 514.2 | 536.2 | 0.3 | < 1.5 |
| FPC-E#09 | 161.1 | 1109.7 | 514.2 | 536.2 | 0.3 | < 1.5 |
| FPC-E#09 | 161.2 | 1109.8 | 516.7 | 536.2 | - | - |
| FPC-E#09 | 161.3 | 1109.9 | – | 536.2 | 0.3 | < 1.5 |
| FPC-E#09 | 161.4 | 1110.0 | 536.2 | 536.2 | 0.4 | < 1.5 |
| FPC-E#09 | 161.5 | 1110.1 | 509.1 | 536.2 | 0.7 | 3.1 |
| FPC-E#09 | 161.6 | 1110.1 | 529.3 | 536.2 | 0.4 | < 1.5 |
| FPC-E#09 | 161.7 | 1110.3 | 515.0 | 536.2 | 0.3 | < 1.5 |
| FPC-E#10 | 171.0 | 1119.5 | 523.6 | 523.6 | 1.6 | 7.6 |
| FPC-E#10 | 171.1 | 1119.6 | 497.2 | 523.6 | 0.4 | < 1.5 |
| FPC-E#10 | 171.2 | 1119.7 | 501.5 | 523.6 | 0.6 | 2.9 |
| FPC-E#10 | 171.2 | 1119.7 | 493.1 | 523.6 | 0.3 | < 1.5 |
| FPC-E#10 | 171.3 | 1119.8 | 509.8 | 523.6 | 0.4 | < 1.5 |
| FPC-E#10 | 171.4 | 1119.9 | 502.6 | 523.6 | 0.3 | < 1.5 |
| FPC-E#10 | 171.6 | 1120.1 | 495.2 | 523.6 | 0.5 | < 1.5 |
| FPC-E#10 | 171.6 | 1120.1 | 500.4 | 523.6 | 0.3 | < 1.5 |
| FPC-E#10 | 171.7 | 1120.2 | 453.6 | 523.6 | 0.4 | < 1.5 |
| FPC-E#10 | 171.8 | 1120.3 | – | 523.6 | - | - |
| FPC-E#10 | 171.8 | 1120.3 | 363.4 | 523.6 | 0.6 | 2.9 |
| FC-E#05 | 180.1 | 1128.6 | 488.2 | 514.5 | 0.5 | < 1.5 |
| FC-E#05 | 180.4 | 1129.0 | 485.4 | 514.5 | 0.5 | 2.4 |
| FC-E#05 | 181.0 | 1129.5 | 461.5 | 514.5 | 0.7 | 3.1 |
| FC-E#05 | 181.0 | 1129.5 | 514.5 | 514.5 | 0.6 | 3.0 |
| FC-E#05 | 181.5 | 1130.0 | 503.8 | 514.5 | 0.7 | 3.1 |
| Shelby-E#25 | 184.0 | 1132.6 | 508.4 | 514.0 | 3.1 | 14.7 |
| FC-E#06 | 192.0 | 1140.5 | 468.8 | 512.7 | 0.7 | 3.4 |
| FC-E#06 | 192.1 | 1140.6 | 466.9 | 512.7 | 0.5 | 2.5 |
| FC-E#06 | 192.4 | 1140.9 | 469.7 | 512.7 | 0.5 | 2.5 |
| FC-E#06 | 192.5 | 1141.0 | 467.8 | 512.7 | 0.6 | 3.0 |
| FC-E#06 | 192.9 | 1141.5 | 416.7 | 512.7 | 0.6 | 2.9 |
| FC-E#06 | 193.0 | 1141.5 | 407.6 | 512.7 | 0.5 | < 1.5 |
| FC-E#06 | 193.0 | 1141.5 | 399.9 | 512.7 | 0.6 | 3.0 |
| FC-E#07 | 196.7 | 1145.2 | 471.9 | 512.0 | 0.6 | 2.6 |
| FC-E#07 | 196.7 | 1145.2 | 466.0 | 512.0 | 0.5 | 2.5 |
| FC-E#07 | 196.8 | 1145.3 | 468.4 | 512.0 | 0.5 | < 1.5 |
| FC-E#07 | 197.0 | 1145.5 | 465.5 | 512.0 | 0.6 | 2.6 |
| FC-E#07 | 197.2 | 1145.8 | 461.4 | 512.0 | 1.6 | 7.7 |
| FC-E#07 | 197.3 | 1145.8 | 487.3 | 512.0 | 0.5 | < 1.5 |
| FC-E#07 | 197.6 | 1146.1 | 472.5 | 512.0 | 0.5 | 2.4 |
| FC-E#07 | 197.9 | 1146.5 | 490.6 | 512.0 | 0.5 | < 1.5 |
| FC-E#09 | 207.5 | 1156.0 | 510.4 | 510.4 | 0.5 | < 1.5 |
| FC-E#09 | 207.9 | 1156.5 | 475.8 | 510.4 | 0.5 | < 1.5 |
| FC-E#09 | 208.0 | 1156.5 | 471.2 | 510.4 | 0.5 | < 1.5 |
| FC-E#09 | 208.1 | 1156.6 | 476.2 | 510.4 | 0.5 | < 1.5 |
| FC-E#09 | 208.1 | 1156.7 | 468.4 | 510.4 | 0.5 | < 1.5 |
| FC-E#09 | 208.2 | 1156.8 | 470.3 | 510.4 | 0.5 | < 1.5 |
| FC-E#09 | 208.5 | 1157.0 | 477.6 | 510.4 | 0.5 | < 1.5 |
| Shelby-E#27 | 210.1 | 1158.7 | 517.3 | 510.1 | 0.5 | < 1.5 |
| 110 | 212.3 | 1160.8 | 480.0 | 509.7 | 0.5 | < 1.5 |
| FC-E#10 | 212.3 | 1160.9 | 454.6 | 509.7 | 0.5 | < 1.5 |
| FC-E#10 | 212.4 | 1160.9 | 460.6 | 509.7 | 0.5 | < 1.5 |
| FC-E#10 | 212.5 | 1161.0 | 442.9 | 509.7 | 0.5 | 2.5 |
| FC-E#10 | 212.5 | 1161.0 | 499.3 | 509.7 | 0.5 | < 1.5 |
| FC-E#10 | 213.0 | 1161.5 | 493.1 | 509.7 | 0.5 | < 1.5 |
| FC-E#10 | 213.5 | 1162.0 | 503.0 | 509.7 | 0.5 | < 1.5 |
| FC-E#11 | 216.9 | 1165.4 | 486.9 | 509.2 | 0.5 | < 1.5 |
| FC-E#11 | 216.9 | 1165.4 | 495.6 | 509.2 | 0.5 | < 1.5 |
| FC-E#11 | 217.1 | 1165.7 | 485.4 | 509.2 | 0.5 | 2.6 |
| FC-E#11 | 217.4 | 1165.9 | 497.2 | 509.2 | 0.5 | < 1.5 |
| FC-E#11 | 217.9 | 1166.4 | 504.2 | 509.2 | 0.5 | < 1.5 |
| FC-E#12 | 218.9 | 1167.5 | 455.9 | 508.9 | 0.5 | < 1.5 |
| FC-E#12 | 219.0 | 1167.6 | 455.5 | 508.9 | 0.5 | < 1.5 |
| FC-E#12 | 220.0 | 1168.5 | 487.4 | 508.9 | 0.6 | 2.8 |
| FPC-E#11 | 221.0 | 1169.6 | 488.5 | 508.7 | 0.3 | < 1.5 |

| | | | | | | |
|---|---|---|---|---|---|---|
| FPC-E#11 | 221.1 | 1169.7 | 463.3 | 508.7 | 0.3 | < 1.5 |
| FPC-E#11 | 221.2 | 1169.7 | 473.6 | 508.7 | 0.7 | 3.2 |
| FPC-E#11 | 221.2 | 1169.8 | 470.5 | 508.7 | 0.6 | 2.7 |
| FPC-E#11 | 221.3 | 1169.8 | 477.6 | 508.7 | 0.5 | < 1.5 |
| FPC-E#11 | 221.3 | 1169.9 | 465.6 | 508.7 | 0.3 | < 1.5 |
| FPC-E#11 | 221.5 | 1170.1 | 456.7 | 508.7 | 0.4 | < 1.5 |
| FPC-E#11 | 221.6 | 1170.1 | 452.4 | 508.7 | 0.5 | < 1.5 |
| FPC-E#11 | 221.6 | 1170.2 | 457.9 | 508.7 | 0.3 | < 1.5 |
| FPC-E#11 | 221.7 | 1170.2 | 465.0 | 508.7 | 0.5 | 2.6 |
| FPC-E#11 | 221.7 | 1170.3 | 476.1 | 508.7 | 0.3 | < 1.5 |
| FC-E#13 | 231.0 | 1179.6 | 480.4 | 507.4 | 0.5 | < 1.5 |
| FC-E#13 | 231.5 | 1180.1 | 482.7 | 507.4 | 0.5 | < 1.5 |
| FC-E#13 | 232.1 | 1180.6 | – | 507.4 | - | |
| FC-E#14 | 232.9 | 1181.5 | 484.0 | 507.2 | 0.6 | 2.7 |
| FC-E#14 | 233.0 | 1181.5 | 488.3 | 507.2 | 0.5 | < 1.5 |
| FC-E#15 | 238.9 | 1187.4 | 488.1 | 506.4 | 0.6 | 2.7 |
| FC-E#15 | 239.4 | 1188.0 | 490.1 | 506.4 | 0.5 | < 1.5 |
| FC-E#15 | 239.8 | 1188.4 | 487.8 | 506.4 | 0.5 | < 1.5 |
| Shelby-E#29 | 243.1 | 1191.7 | 489.6 | 505.9 | 0.5 | < 1.5 |
| FPC-E#12 | 249.0 | 1197.5 | 488.2 | 505.2 | 0.5 | < 1.5 |
| FPC-E#12 | 249.0 | 1197.5 | 481.1 | 505.2 | 3.8 | 17.7 |
| FPC-E#12 | 249.0 | 1197.5 | 495.9 | 505.2 | 3.6 | 17.1 |
| FPC-E#12 | 249.1 | 1197.6 | 486.0 | 505.2 | 2.2 | 10.5 |
| FPC-E#12 | 249.2 | 1197.7 | – | 505.2 | - | - |
| FPC-E#12 | 249.3 | 1197.8 | 469.7 | 505.2 | 0.7 | 3.5 |
| FPC-E#12 | 249.4 | 1197.9 | – | 505.2 | - | - |
| FPC-E#12 | 249.6 | 1198.1 | 464.4 | 505.2 | 1.0 | 4.7 |
| FPC-E#12 | 249.8 | 1198.3 | – | 505.2 | - | - |
| FC-E#16 | 277.8 | 1226.4 | 496.5 | 501.6 | 0.5 | < 1.5 |
| FC-E#16 | 277.9 | 1226.5 | 478.6 | 501.6 | 1.6 | 7.6 |
| Shelby-E#31 | 279.6 | 1228.2 | – | 501.4 | - | - |
| Shelby-E#31 | 279.7 | 1228.2 | 501.4 | 501.4 | 0.5 | < 1.5 |
| Shelby-E#31 | 279.8 | 1228.3 | – | 501.4 | - | - |
| Shelby-E#31 | 279.8 | 1228.4 | – | 501.4 | - | - |
| Shelby-E#31 | 279.9 | 1228.4 | 501.1 | 501.4 | 0.6 | 2.6 |

**Table 3.4.** Chloride and sulphate concentration data for DC_E. Shelby-E#= Shelby tube data; FPC-E#= Fugro Pressure Corer data; FC-E#= Fugro Corer data; *Cm* (corrected) = measured chloride concentration (chlorinity), corrected for drill water infiltration (last column on the right); *Cb*= *'baseline'* chlorinity. There is no evidence of hydrates for the first 60 mbsf. Along this interval, *Cb* is supposed to be equal to *Cm*. The % of drill water infiltration is calculated by considering a 27.4 mM sulphate content for the drill water and no sulphate in the pore water below the SMTZ (10-12 mbsf, red-coloured cells).

| **Parameter** | |
|---|---|
| *V* (structure I) | $1.728 \times 10^{-21}$ $cm^3$ |
| *nw* (structure I) | 46 |
| $\beta$ (structure I) | 1.257 |
| *V* (structure II) | $5.178 \times 10^{-21}$ $cm^3$ |
| *nw* (structure II) | 136 |
| $\beta$ (structure II) | 1.274 |

**Table 3.5.** Parameters used to calculate hydrate saturation from chlorinity. The values have been taken from Malinverno *et al.* (2008) and (Carroll, 2014). *V*= volume of the hydrate elementary cell; *nw*= number of water molecules in the hydrate elementary cell; $\beta$= dimensionless coefficient (see **sub-paragraph 3.7.1**).

| Borehole DC_E | Depth | Sh av. (%) | Sh max. (%) | *Sh* (%) |
|---|---|---|---|---|
| Core | (mbsf) | Chlorinity | Chlorinity | Mass-balance |
| Liner-E#01 | 0.6 | 0.0 | 0.0 | - |
| Liner-E#02 | 2.0 | 0.0 | 0.0 | - |
| Liner-E#03 | 3.5 | 0.0 | 0.0 | - |
| Liner-E#04 | 5.0 | 0.0 | 0.0 | - |
| Liner-E#05 | 6.6 | 0.0 | 0.0 | - |
| Liner-E#06 | 7.5 | 0.0 | 0.0 | - |
| Liner-E#07 | 9.0 | 0.0 | 0.0 | - |
| Shelby-E#08 | 10.6 | 0.0 | 0.0 | - |
| Shelby-E#09 | 12.1 | 0.0 | 0.0 | - |
| Shelby-E#10 | 14.2 | 0.0 | 0.0 | - |
| Shelby-E#11 | 15.0 | 0.0 | 0.0 | - |
| Shelby-E#12 | 20.4 | 0.0 | 0.0 | - |
| Shelby-E#13 | 26.0 | 0.0 | 0.0 | - |
| Shelby-E#14 | 32.0 | 0.0 | 0.0 | - |
| Shelby-E#15 | 38.0 | 0.0 | 0.0 | - |
| Shelby-E#17 | 60.4 | 1.9 | 1.9 | - |
| HRC-E#01 | 87.5 | - | - | - |
| FPC-E#01* | 89.1 | 0.3 | 0.7 | - |
| FPC-E#02 | 89.2 | 0.5 | 1.3 | 0.0 |
| Shelby-E#19 | 90.2 | 0.0 | 0.0 | - |
| FC-E#01 | 105.0 | 1.8 | 2.5 | - |
| HRC-E#02 | 114.5 | - | - | - |
| FPC-E#13 | 114.6 | 3.6 | 5.6 | 0.0 |
| Shelby-E#21 | 120.5 | 2.7 | 2.7 | - |
| FPC-E#03* | 126.0 | 3.7 | 11.5 | - |
| FC-E#02 | 126.0 | 3.8 | 7.2 | - |
| FPC-E#04* | 127.1 | 2.3 | 5.0 | - |
| HRC-E#03* | 128.0 | - | - | - |
| HRC-E#04* | 135.5 | - | - | - |
| FPC-E#05* | 136.7 | 2.2 | 4.7 | - |
| HRC-E#05 | 137.5 | - | - | 0.0 |
| FPC-E#06 | 143.0 | 2.9 | 6.3 | 0.0 |
| HRC-E#06 | 150.5 | - | - | 2.6 |
| Shelby-E#23 | 150.5 | 11.1 | 11.1 | - |
| FPC-E#07* | 151.5 | 3.2 | 8.2 | - |
| FPC-E#08 | 152.5 | 7.4 | 10.9 | 7.9 |
| FC-E#03 | 154.0 | 2.6 | 4.8 | - |
| HRC-E#07 | 160.0 | - | - | 8.9 |
| FPC-E#09 | 161.0 | 3.9 | 6.3 | 1.1 |
| FPC-E#10** | 171.0 | 9.1 | 35.7 | 7.5 |
| FC-E#05 | 180.0 | 7.4 | 14.2 | - |
| Shelby-E#25 | 184.0 | 3.2 | 3.2 | - |
| FC-E#06 | 191.5 | 18.2 | 27.7 | - |
| FC-E#07 | 196.5 | 11.1 | 13.8 | - |
| FC-E#09 | 207.0 | 9.4 | 11.8 | - |
| Shelby-E#27 | 210.1 | 0.0 | 0.0 | - |
| FC-E#10 | 212.0 | 9.7 | 17.5 | - |
| FC-E#11 | 216.5 | 5.3 | 7.4 | - |
| FC-E#12 | 218.5 | 11.8 | 14.3 | - |
| FPC-E#11 | 221.0 | 11.3 | 14.9 | 11.9 |
| FC-E#13 | 230.5 | 7.5 | 7.8 | - |
| FC-E#14 | 232.5 | 6.4 | 6.9 | - |
| FC-E#15 | 238.5 | 5.4 | 5.6 | - |
| Shelby-E#29 | 243.1 | 5.0 | 5.0 | - |
| FPC-E#12 | 249.0 | 6.8 | 10.8 | 8.5 |
| FC-E#16 | 277.5 | 3.6 | 5.8 | - |
| Shelby-E#31 | 279.7 | 0.0 | 0.1 | - |

**Table 3.6.** Compilation of *Sh* from all the recovered core samples at DC_E, from chlorinity measurements and mass-balance calculations. The average and maximum *Sh* has been estimated from chlorinity values along each core whereas only a single value from each FPC core has been obtained with the mass-balance approach. Av= average; - = not applicable; *= FPC unsuccessfully recovered at in-situ pressure and depressurised at atmospheric conditions; **= FPC recovered partially depressurised. The depth is referred to the top of each core with respect to the seafloor. There is little evidence of hydrates above ~105 m, and the top of the zone of hydrate occurrence is interpreted to be located at this depth.

# Chapter 4. Relationship between fluid-escape pipes and hydrate distribution in offshore Sabah (NW Borneo)

This chapter is modified from 'Paganoni, M., Cartwright, J.A., Foschi, M., Shipp, R.C. & Van Rensbergen, P. Relationship between fluid-escape pipes and hydrate distribution in offshore Sabah (NW Borneo), accepted for publication in *Marine Geology*. Joe A. Cartwright contributed to the interpretation of seismic data and the revision. Martino Foschi contributed to measure the orientation of faults and fluid-escape pipes. Pieter Van Rensbergen contributed to interpret of seismic and petrophysical data. The seismic, well-log and core data were acquired by Shell and provided by Craig R. Shipp.

## 4.1. Introduction

In fine-grained sequences, the migration of hydrocarbon-rich fluids often occurs through vertical to sub-vertical pathways which may terminate at the seafloor as pockmarks, mounds and mud-volcanoes (Hustoft *et al.*, 2007; Judd and Hovland, 2007). Fluid-escape pipes are vertical to sub-vertical elongated zones having a width ranging from a few tens to a few hundred of metres, with a seismic character disrupting an otherwise continuous stratigraphy (Cartwright and Santamarina, 2015). Similar but occasionally larger features have also been referred to as gas/fluid-escape chimneys, although there is considerable latitude in the use of these terms (Løseth *et al.*, 2009; Bertoni *et al.*, 2017).

These hydrocarbon migration phenomena, in the shallow subsurface, can be further influenced by the presence of thermobaric conditions suitable for hydrate stability (cf. Collett *et al.*, 2009, see also **paragraph 1.3**), as well as by the formation of a free gas zone (FGZ), whose upper boundary is frequently imaged in seismic data as a bottom-simulating reflector (BSR) (Holbrook *et al.*, 1996; Haacke *et al.*, 2007; Shedd *et al.*, 2012).

The analysis of seismic reflection data from various basins has revealed that hydrocarbon gases migrate throughout the gas hydrate stability zone (GHSZ) along pipe-like conduits (Gorman *et al.*, 2002; Gay *et al.*, 2006; Riedel *et al.*, 2006; Plaza-Faverola *et al.*, 2011). Geophysical models and direct sampling have shown that hydrates accumulate at extremely elevated saturations along these pipe-like conduits, in the form of pure grain-displacing lenses and veins (Westbrook *et al.*, 2008; Plaza-Faverola *et al.*, 2010; Chun *et al.*, 2011; Torres *et al.*, 2011; Attias *et al.*, 2016; Matsumoto *et al.*, 2017). Given the high concentration of hydrates potentially stored within these features, it is important to understand better their seismic expression, as well as the factors controlling their distribution and activity.

The intensity of fluid flow across the GHSZ varies at short timescales (e.g. days-years) and scales of thousands to hundreds of thousand years. In this latter case, major triggers for

fluid flow are global sea-level and temperature fluctuations, ice sheets loading and unloading, and the regional tectonic activity (e.g. Hustoft *et al.*, 2010; Andresen and Huuse, 2011; Plaza-Faverola *et al.*, 2011 and 2015; Andreassen *et al.*, 2017). These events can induce hydrate dissociation, leakage of fluids from deep reservoirs and submarine landslides along continental slopes (Vogt and Jung, 2002; Berndt *et al.*, 2012; Riboulot *et al.*, 2013).

Furthermore, in the presence of leaky thermogenic petroleum systems, hydrocarbons heavier than methane ($C_{2+}$) can be incorporated into structure II ($S_{II}$) and structure H ($S_H$) hydrates. In such cases, the thickness of the GHSZ is increased, and $S_{II}$ and $S_H$ hydrates may occur below BSRs (see **Chapter 3** and Sassen *et al.*, 2001d; Lu *et al.*, 2007; Liang *et al.*, 2017). The deepwater fold and thrust belt offshore Sabah (NW Borneo) provides an ideal location for the study of the natural gas hydrate systems fed by leaky thermogenically-sourced reservoirs (Warren *et al.*, 2010). In this study, I extend the analysis of the natural gas hydrate system at the crest of the bathymetric ridge overlying the Gumusut-Kakap hydrocarbon accumulation (cf. Hadley *et al.*, 2008 and **Chapter 3**), located in this region, with new observations and interpretations. The main objective is to characterise the seismic expression of fluid flow across the GHSZ, in order to evaluate the controls on the occurrence and on the genesis of fluid flow features interpreted as fluid-escape pipes, as well as the potential triggers for their formation and their impact on the distribution of gas hydrates.

## 4.2. Data and Methods

The seismic data shown in this research was acquired in Block K offshore Sabah by Shell and consists of a high-resolution 3D seismic post-stack dataset, covering a region of ~37 $km^2$, at water depths between ~850 and ~1250 m (**Figs. 4.1, 4.2**, see also **Fig. 3.1**). The vertical resolution of this dataset is approximately 5 m, for seismic velocities between 1500 and 1650 m/s for the first 200 ms TWT below the seafloor. The dominant frequency of these data is higher than 100 Hz in the first ~200 ms TWT below the seafloor. However, it is frequently less than ~50 Hz within zones interpreted as free gas-bearing sediments, where the vertical resolution decreases. A lower resolution dataset (45 Hz dominant frequency), having a vertical resolution of approximately 10 m and covering a broader area (~890 $km^2$) (see **Fig. 2.5a**) further provides the necessary framework for the regional structural setting and to image deeper structures. The inline and crossline spacing of the high- and low-resolution dataset are of 6.25 and 25 m, respectively. Lateral resolution is taken as being comprised between the bin spacing and the dominant wavelength, with a 6.25-20 m range for the high-resolution dataset and in a 25-50 m range for the low-resolution one (Cartwright and Huuse, 2005).

Following a North American polarity convention, both these datasets have been phase-shifted by -90° for the seismic interpretation. An increase in the acoustic impedance is termed a positive or *'hard reflection'* (e.g. the seafloor), expressed in the wiggle-traces as a trough followed by a peak and displayed in seismic cross-sections as a red-blue combination. Vice-versa, an opposite character is displayed by a decrease in the acoustic impedance, which results in a negative reflection, termed a *'soft reflection'* (e.g. the top of a free gas accumulation). The seismic data were interpreted with the Petrel E&P Software Platform, and the area of interest is located at the crest of a prominent bathymetric ridge overlying the Gumusut-Kakap hydrocarbon accumulation. Key stratigraphic horizons, as well as faults and various features indicative of fluid flow, have been mapped and interpreted (cf. Løseth

*et al.*, 2009). The extraction of specific seismic attributes, including amplitude (e.g. RMS amplitude) and dip-related (e.g. dip and variance) attributes, was performed on vertical seismic sections and specific stratigraphic horizons. Amplitude-related attributes are useful in detecting anomalies associated with gas (i.e. soft reflections), gas hydrates or authigenic carbonates (i.e. hard reflections) (cf. Roberts *et al.*, 2006; Judd and Hovland, 2007). Dip-related attributed are used to identify features with discordant or irregular geometries with respect to the background, like faults and other zones of cross-stratal fluid-flow (e.g. Ligtenberg, 2005; Plaza-Faverola *et al.*, 2012a). Depth measurements from the seismic data were based on seismic interval velocities ranging between 1500 and 1700 m/s and are accompanied by the associated TWT measurements throughout the text.

In this study, the seismic data are integrated with wireline acoustic logs acquired with the Cross-Multipole Array Acoustic log from Baker Hughes (XMAC) at the borehole location named DC_E (see **Fig. 4.2** for location). The quality of the borehole is assessed with a 6-arm caliper. This data has been previously used, in conjunction with a density log obtained while drilling with the Halliburton tool, to create a synthetic seismogram used to tie the well with the seismic data (see **paragraph 3.2** and **Fig. 3.1b**). An abrupt decrease in the wireline P-wave velocity at approximately 155 m below the seafloor (mbsf) was associated with a BSR while the presence of gas hydrates was constrained with core data at DC_E and resistivity LWD measurements at DC_E and in other three sites (M_1, DC_F and L_2, see **Fig. 4.2**). All four boreholes were drilled within an area characterised by abundant evidence of free gas, located at the crest of the bathymetric ridge overlying the Gumusut-Kakap hydrocarbon reservoir (GK reservoir). However, none of these boreholes passed through a fluid escape pipe.

The phase-shift deep smoothed resistivity measurements, acquired while drilling with the EWR®-Phase 4 multiarray propagation tool, have been used at these sites to extrapolate the gas hydrate saturation (*Sh*, % of pore space) (see **Fig. 3.9**). In this chapter, I present

averaged *Sh* profiles along these four boreholes, to provide a general view of the hydrate distribution and saturation in the area. An additional constraint on hydrate saturation and methane fluxes comes from the chlorinity anomalies measured in cores retrieved at DC_E, and from the pore water sulphate concentrations at the same location (see **paragraph 3.2** and **Tab. 3.4**). A further LWD resistivity profile, obtained at a borehole site named site M_2, drilled at the crest of the bathymetric ridge but outside areas of shallow free gas occurrence, will be shown (**Fig. 4.2**). This information is used to evaluate if hydrates, at this location, occur without any evidence of free gas.

The well-log and core data are used to evaluate the volumetric distribution of gas hydrates outside the vertical zones of cross-stratal focused fluid flow interpreted as fluid-escape pipes. The hydrate concentration within fluid-escape pipes in this study area is unknown, but drilling information and modelling of geophysical data from other gas hydrate provinces provide, by analogy, a reliable range. Therefore, it is possible to provide an estimate of the volume of hydrate present within the fluid-escape pipes *vs* outside these features. Finally, confidential information on the areal extent of the gas-oil contact (GOC) of the GK reservoir and the geochemistry of the gas in the deep reservoirs is linked to the dynamics of the shallower natural gas hydrate system.

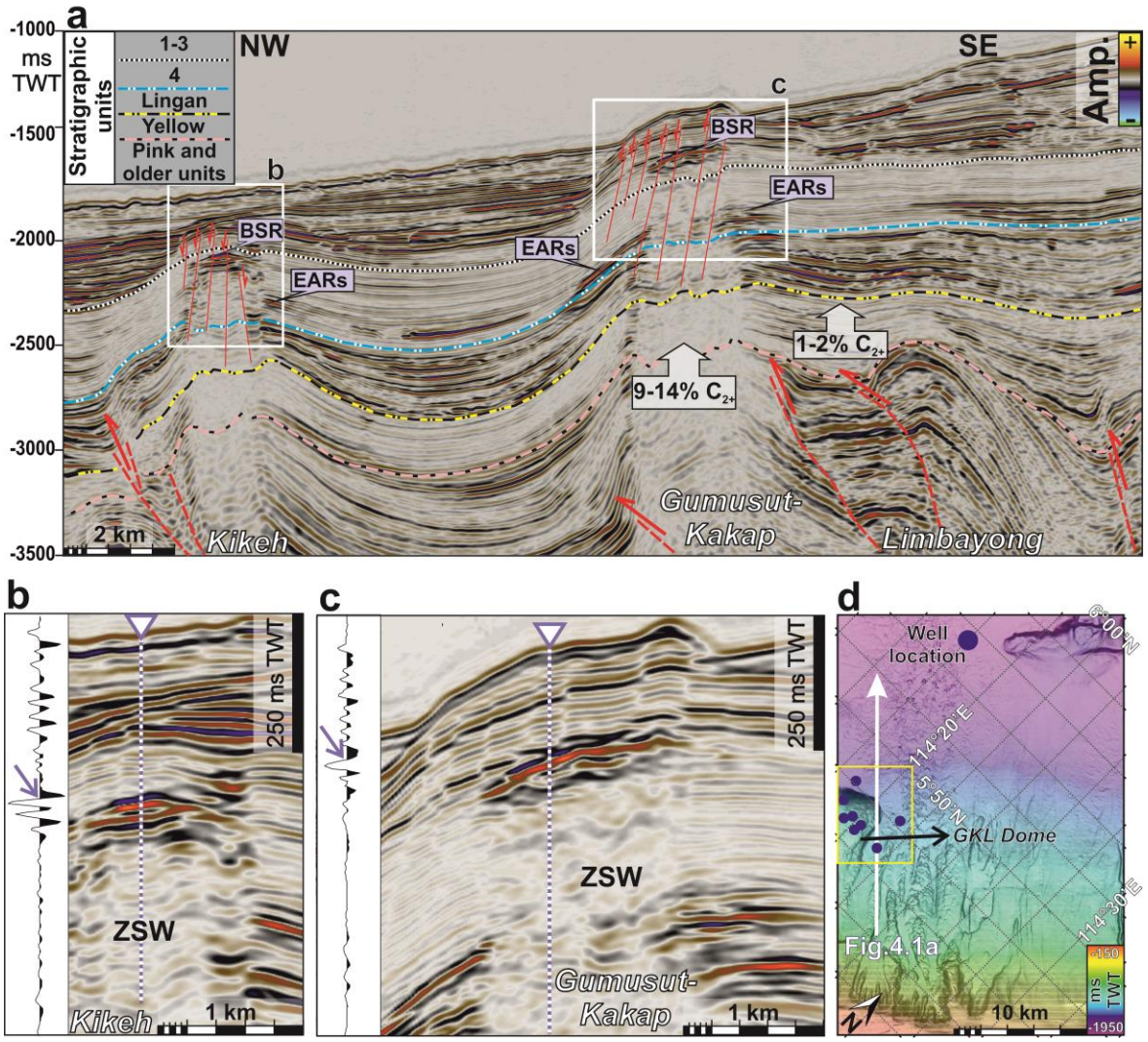



**Figure 4.1. (a)** Regional low-resolution NW-SE seismic line, showing the main tectonic features and the stratigraphic units of the study area. A simplified stratigraphic column is shown on the top left of the figure. The amounts of $C_{2+}$ hydrocarbons present in the free gas within the deep reservoirs in the Gumusut-Kakap and Limbayong structures is also indicated. **(b)** and **(c)** Blow-ups extracted from **(a)**, showing the BSRs at the crests of the Kikeh structure **(b)** and the GKL Dome **(c)**. Two significant seismic wavelets have been further extracted (location indicated by the white triangles). They indicate the polarity of the BSRs (purple arrows), enhanced amplitude reflections (EARs) beneath the BSRs and the reduced frequency within the zone of seismic wipeout (ZSW). **(d)** Blended TWT and variance seafloor map of the study area covered by the low-resolution seismic survey (same map shown in **Fig. 2.5a**). Regions with high variance appear darker and indicate areas with steep seafloor morphology. The high-resolution seismic survey is located in the area within the yellow box. The location of wells is indicated by blue circles. A white arrow indicates the trace of the seismic line shown in **(a)**.

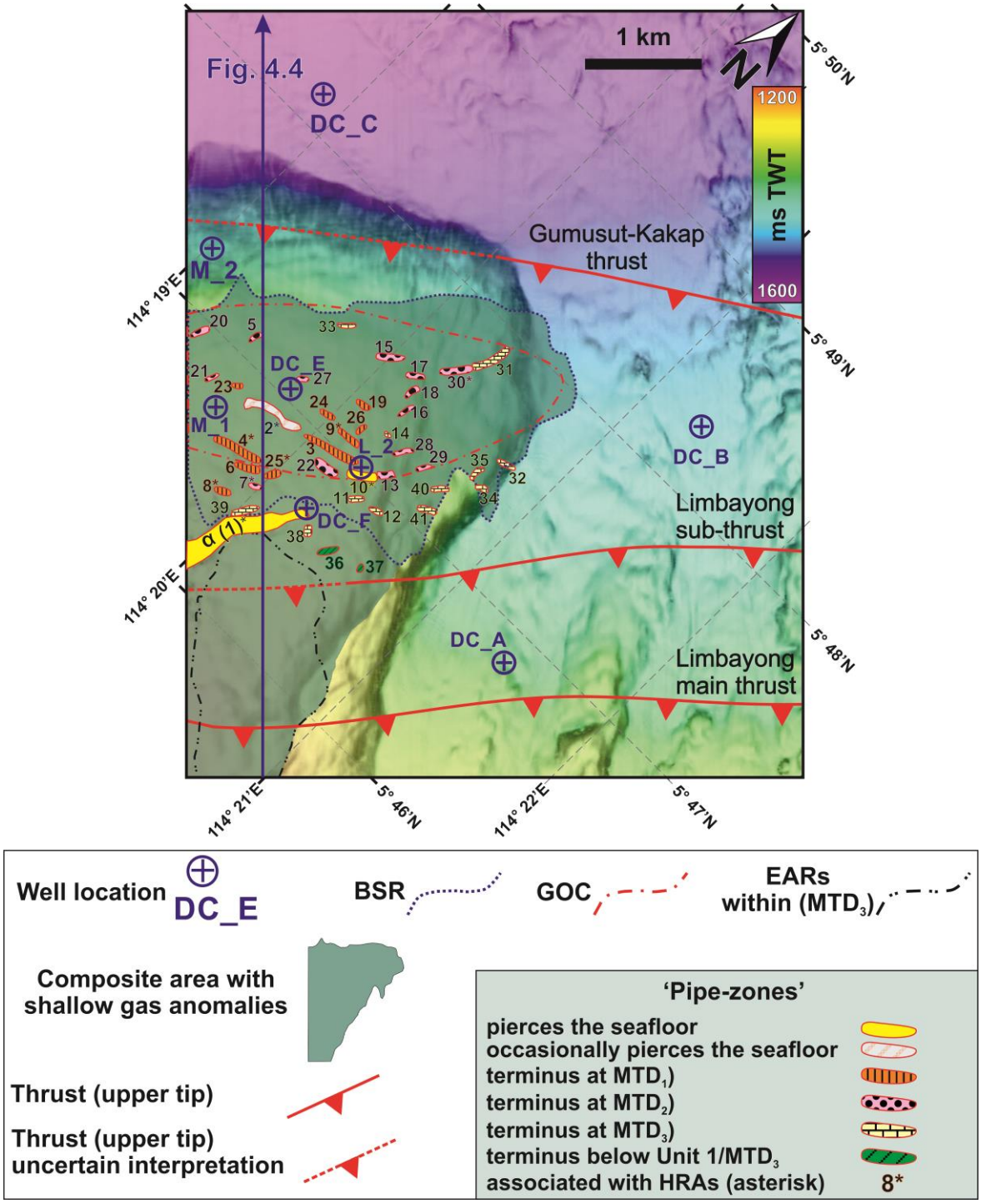



**Figure 4.2.** Blended TWT and variance seafloor map of the area investigated by the high-resolution seismic survey. The lateral extent of the BSR, the gas-oil contact (GOC) of the GK reservoir, the enhanced amplitude reflections (EARs) associated with $MTD_3$, and the well-sites are shown. The green semi-transparent area indicates the zone characterised by seismic evidence of shallow free gas. The pipe-zones are indicated by ellipses of different colours, associated with the stratigraphic position of their terminus. The number near each pipe-zone refers to **Table 4.1** (**sub-paragraph 4.7.2**, Appendix). An asterisk near the number indicates a pipe-zone overlain by a high reflectivity area at the seafloor (HRA). The blue arrow indicates the trace of the seismic line shown in **Fig. 4.4**.

## 4.3. Geological setting

### *4.3.1. Major structures of the study area*

The study area has a complex seafloor geomorphology (**Fig. 4.2**). The western and southwestern zone is dominated by a bathymetric dome-shaped ridge. This ridge, named the GKL Dome, represents the seafloor expression of a deeper system of thrust-propagation folds. These structures include the Gumusut-Kakap (GK) anticline, where the oil and gas constituting the GK reservoir are trapped, and a further system of two imbricate thrusts named the Limbayong structure (**Figs. 4.1a, 4.2, 4.12)**. In contrast, the eastern and northwestern sides of the high-resolution seismic survey are represented by structural lows, heavily influenced by erosive submarine canyons and mass-transport deposition (see Lu and Shipp, 2011). Similarly to the GK anticline, the Limbayong structure contains commercial hydrocarbons within Middle to upper Miocene reservoirs. The free gas in the GK and Limbayong reservoirs has a different $C_{2+}$ content, being higher in the former (~9-14%) than in the latter (~1-2%) (**Chapter 3**, Kelley and Bishop, 2003). Another thrust-related anticlinal structure, named Kikeh, is present seaward (**Fig. 4.1a**) and is associated with a further commercial hydrocarbon accumulation (Khan *et al.*, 2005).

The crest of the GKL Dome is pervasively affected by normal faults (**Figs. 4.1, 4.4, 4.6**). Most of these faults are divergent with respect to the core of the GK anticline and commonly extend up to the first tens of mbsf. Following Morley (2007), who described similar faults in the nearby Brunei margin, these faults are interpreted as the product of the interaction between gravity and the growth of the thrust-cored anticlines.

### *4.3.2. Stratigraphic framework*

The stratigraphy up to the Late Miocene-Early Pliocene, marked by the top of the Lingan Unit, has been characterised in previous studies (Grant, 2004; Ingram *et al.*, 2004). In this study, I define four additional more recent units, named, from the oldest to the youngest, Unit 4, 3, 2 and 1 (**Fig. 4.4a**).

At the crest of the GKL Dome, Units 2, 3 and 4 are seismically represented by thinly layered and continuous reflections having constant and relatively low amplitudes and are interpreted as a sequence of dominant hemipelagic sediments, which include minor turbidites and MTDs. In contrast, Unit 1 shows, in the southernmost part of the crest, an alternation between seismically continuous, thinly layered reflections, interpreted as hemipelagic clay-rich sediments, and MTDs, named $MTD_1$, $MTD_2$ and $MTD_3$, from the shallowest to deepest (**Fig. 4.4a**). $MTD_1$ is draped by a sequence of hemipelagic deposits and subordinate thin turbidites (cf. Lu and Shipp, 2011), whereas the base of $MTD_3$ marks the lower boundary of Unit 1, at approximately 100 mbsf (~125 ms TWT bsf).

Foraminifera, nannofossil and radiocarbon dating (Slowey, 2007; Lu and Shipp, 2011) constrained the minimum age for the deposition of $MTD_1$ at 34.5 ka BP, whereas $MTD_2$ and $MTD_3$ occurred between 75 and 500 ka BP. No seismically visible MTDs postdate the Last Glacial Maximum in the study area. Lu and Shipp (2011) associated the deposition of $MTD_1$ with a period of lowering relative sea-level predating the last glacial maximum. The draping sequence which follows $MTD_1$ (**Fig. 4.4a**) suggests a recently inactive mass-transport deposition system. A markedly different depositional system is developed in the structural lows, where Units 1-3 include major MTDs and only subordinate hemipelagic deposits (**Fig. 4.5b,** see **Chapter 5**) (Lu and Shipp, 2011).

## 4.4. Results

### *4.4.1. The bottom-simulating reflector and the free gas zone*

A BSR is prominently developed at the crest of the GKL Dome (see **Chapter 3**). This BSR has a polarity opposite to that of the seafloor and displays a clear cross-cutting relationship with stratigraphic reflections at the northern and northwestern margins of the GKL Dome (**Fig. 4.3a**). In contrast, this BSR is almost parallel to the stratigraphy in the central portions of the GKL Dome (**Fig. 4.3b**). Beneath this BSR, for 50-100 m (~75-150 ms TWT), it is possible to observe a series of reflections, characterised by high amplitudes and relatively low frequencies. These are referred to as enhanced amplitude reflections (EARs) and overlie a zone of seismic wipeout, where the seismic signal is completely disrupted (**Figs. 4.1c, 4.3b**).

The lateral extent of the gas-oil contact (GOC) of the GK reservoir matches that of the BSR, although the latter is slightly wider (**Fig. 4.2**). The extent of the GOC is also approximately matched by that of the zone of seismic wipeout developed at the crest of the GKL Dome. However, the zone of seismic wipeout locally extends further south, hiding the visualisation of the Limbayong structure (**Figs. 4.4a, 4.12**). The zone of seismic wipeout is rimmed by a halo of stacked EARs. This halo is developed from the stratigraphic intervals directly underneath the BSR, down to the Upper Miocene units but, particularly, within the Lower part of Unit 4 and the Lingan Unit (**Fig. 4.1c, 4.4a**). The BSR, the zone of seismic wipeout and the associated EARs are all diagnostic for free gas-bearing sediments, from the BSR downward (cf. Bünz and Mienert, 2004; Løseth *et al.*, 2009). This interpretation has been confirmed by **(1)** the wireline velocity log at site DC_E, showing, below the BSR, compressional velocities much lower than those typical of seawater (~1500 m/s), although with vertically variable absolute values and **(2)** the good match between the wiggle traces extracted from seismic data and that of the synthetic seismogram (cf. Bangs *et al.*, 1993; Holbrook *et al.*, 1996) (**Figs. 4.3b, 4.7a,** see also **Chapter 3**).

The BSR, in the southern part of the crest of the GKL Dome, terminates across a large sub-vertical feature interpreted as a fluid-escape pipe and named Pipe-α (**Fig. 4.4,** see **sub-paragraph 4.4.3**). Southward of Pipe-α, there is not a clear BSR, but rather a zone of stacked packages of EARs, each of them 15-35 m thick (~20-45 ms TWT). The majority of these packages extend down towards the zone of seismic wipeout overlying the Limbayong structure whereas fewer occur above the GK anticline (**Figs. 4.2, 4.4**). The polarity of these EARs is opposite to that of the seafloor (i.e. they are *'soft reflections'*) and, occasionally, a push-down effect in the seismic data is observed beneath these EARs (**Fig. 4.5a**). These elements suggest that these EARs represent free gas-bearing sediments. The uppermost and most reflective of these packages of EARs is part of $MTD_3$ and is observed between ~135 and 150 mbsf (~170-200 ms TWT bsf). This seismic character of the free gas zone, expressed as a combination of a zone of seismic wipeout overlain by EARs, and locally by a BSR, is maintained in the low-resolution seismic data and is further identified at the crest of the Kikeh structure (**Fig. 4.1a-c**).

### *4.4.2. Occurrence of gas hydrates*

At the crest of the GKL Dome gas hydrates are distributed both above and below the BSR (**Fig. 4.7**). Below the BSR, hydrates form as $S_{II}$ and possibly $S_H$, until the BGHSZ for $S_{II}$ and $S_H$ hydrates ($BS_{II/H}GHSZ$), located at approximately 250 mbsf (see **Chapter 3** for a more comprehensive interpretation). The leakage of a thermogenic gas with 9%-14% of $C_{2+}$ hydrocarbons from the gas cap of the GK reservoir and the chemical fractionation from the $BS_{II/H}GHSZ$ up to the $BS_IGHSZ$ are the most likely responsible processes for this *'layered'* hydrate structure distribution. The boreholes DC_E, M_1, DC_F and L_2 are all drilled within an area characterised by clear evidence of free gas (i.e. the BSR and/or EARs, see **Fig. 4.2**) but did not pass through the features interpreted as fluid-escape pipes, although L_2 has been drilled very close to many of these features (**Fig. 4.7d**). At these sites, hydrates fill thin mm-scale sub-vertical fractures. Therefore, the resistivity logs along these boreholes have encountered elevated values (up to 20-50 Ω·m) along an interval of ~100-150 m (see

**Fig. 3.3**). The average *Sh* in the four boreholes, along the entire gas hydrate occurrence zone (GHOZ, cf. Malinverno *et al.*, 2008), is predicted to be comprised between 3% and 7% for DC_E (GHOZ= 105-237 mbsf), 2% and 4.5% for M_1 (GHOZ= 154-252 mbsf), 1.5% and 3.5% for DC_F (GHOZ= 123-260 mbsf), and between 7% and 15% for L_2 (GHOZ= 65-242 mbsf) (**Fig. 4.7c, e-g**). Considering these saturation estimates and the porosity trend shown in **Fig. 3.14** (average of 50-55%), 2-4% of the total sediment volume from the top of the GHOZ down to the $BS_{II/H}$GHSZ is considered to be filled with hydrates. This range is the result of the average hydrate saturation, calculated in the four wells from resistivity data, with the model proposed by Lee and Collett (2012), used in **Chapter 3**. Even if the method of Lee and Collett (2012) has been tied in **Chapter 3** to the hydrate saturation profile calculated from chlorinity data at DC_E (i.e. an appropriate 'fracture porosity' range has been choosen: 3.5-5%), it is essential to list the most critical uncertainties, which are **(1)** the baseline chlorinity trend, which inevitably influence the quantification of *Sh* calculated from pore-warer freshening and, in turn, the choice of the parameters to calculate *Sh* from resistivity; **(2)** the average resistive (i.e. hydrate-filled) fracture angle measured from borehole images (70°); and **(3)** the assumption that, in the study area, the impact of free gas on resistivity is subordinate with respect to that of hydrates, from the BSR, down to the $BS_{II/H}$GHSZ. At site DC_E, the sulphate concentration decreases, with a slight *'concave-up'* profile, from a near-seafloor value of 22 mM, down to zero at the sulphate-methane transition zone (SMTZ), located between 10 and 12 mbsf (**Fig. 4.7c,** see also **Tab. 3.4**). Below this depth, hydrocarbon gases are not oxidised and can form hydrates if exceeding the saturation thresholds in the pore water (Borowski *et al.*, 1996 and 1999).

In contrast to the results from these boreholes, the resistivity profile along the borehole M_2 does not show high resistivity anomalies indicative of either gas hydrate or free gas, at least for the first 350 mbsf (LWD data was not available deeper). This well was drilled outside the BSR perimeter, and there is no evidence of shallow EARs, which are observed only from Unit 4 downwards (**Fig. 4.5b**).

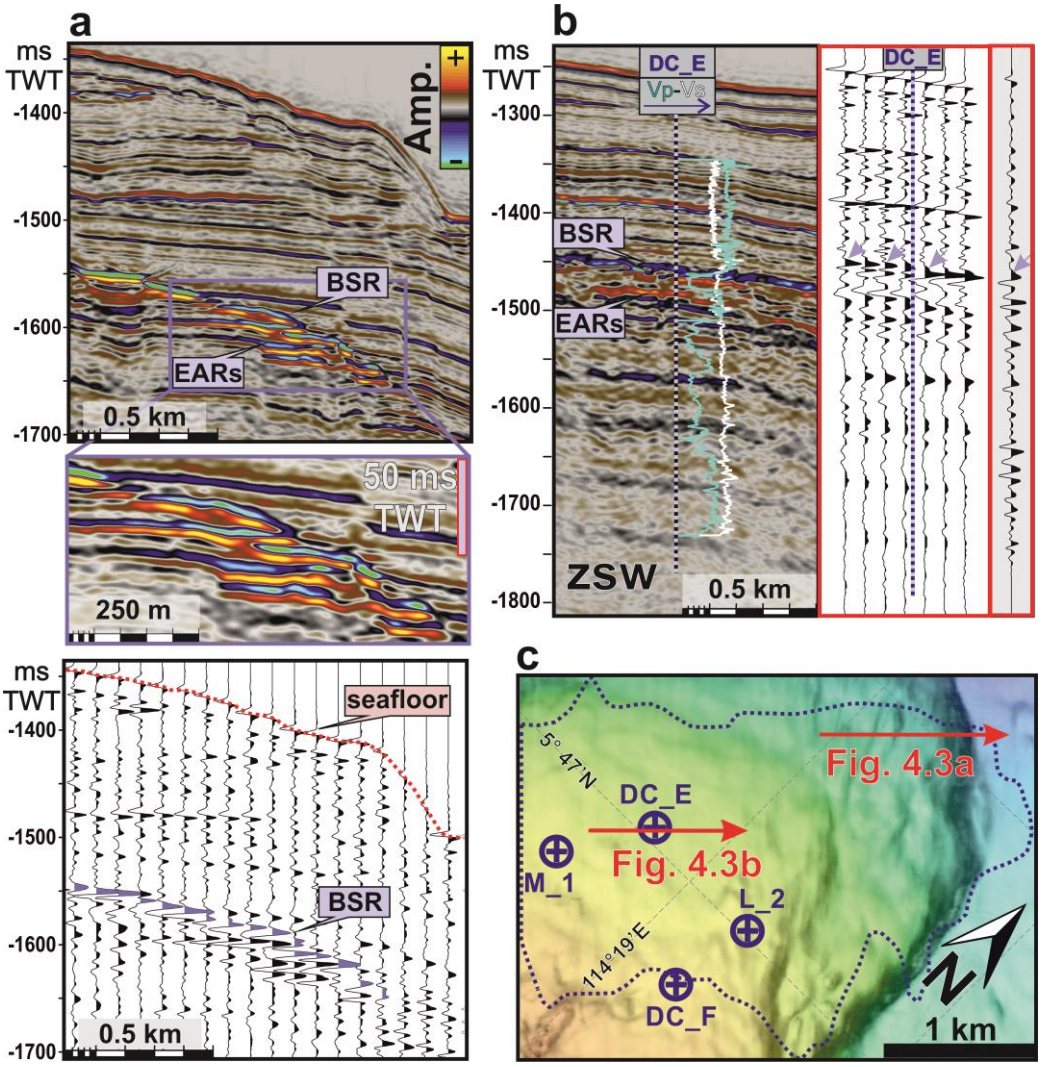
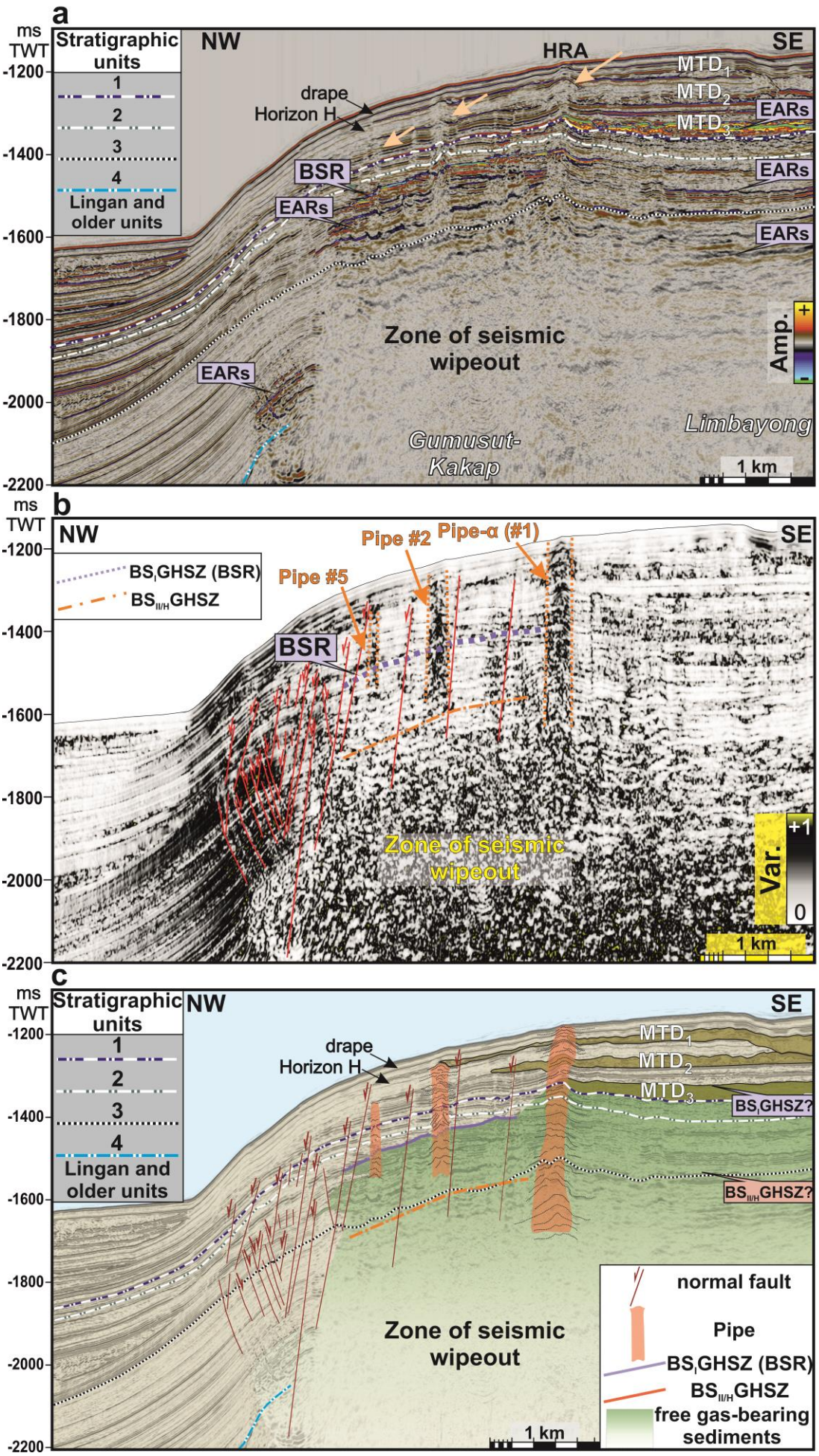



**Figure 4.3.** Detailed view of the BSR at the crest of the GKL Dome and calibration with WL velocity data. **(a)** Upper: seismic line at the northeastern margin of the GKL Dome, where the BSR displays a clear cross-cutting relation with the host stratigraphy and a series of EARs underneath; Middle: Detail of the above image (see the purple box); Lower: seismic wavelets along the same profile shown in the upper image. The BSR is characterised by a strong peak (coloured in purple) followed by a strong trough. High amplitudes are then maintained for about 50 ms TWT below the BSR (i.e. the EARs). Then, the seismic signal is attenuated (i.e. the zone of seismic wipeout); **(b)** Left: seismic expression of the BSR at site DC_E. The wireline P- (light blue) and S-wave (white) velocity log are tied to the data (see also **Fig. 4.7a**). EARs= enhanced amplitude reflections; ZSW= zone of seismic wipeout. Right: seismic wavelet extracted from the central portion of the seismic line shown in **(b)**. A vertical dotted line indicates the borehole location. The purple arrows indicate the BSR. A synthetic seismogram, extracted with the WL velocity and the LWD density logs at DC_E is shown on the right within a grey box. **(c)** Extract from the map of **Fig. 4.2**, indicating the location of the seismic lines shown in **(a)** and **(b)**.

**Figure 4.4 (See the next page).** Main stratigraphic elements and fluid flow features in the study area. **(a)** High-resolution NW-SE seismic line. Pipes are indicated by light-orange arrows. The trace of the line is indicated in **Fig. 4.2**. Note that the zone of seismic wipeout extends above both the Gumusut-Kakap and the Limbayong structures (cf. with **Fig. 4.12a**) **(b)** Variance (Var.) extraction of the line shown in **(a)**. The pipes, contoured with orange dotted lines and indicated by orange arrows (the pipe numbers refer to **Fig. 4.2** and **Tab 4.1**), are characterised by high variance (i.e. black colours). The high variance of the pipes extends below the depth of the BSR. This is particularly evident for Pipe-α (1). **(c)** Interpreted geological section. The pipes are filled with orange, and their internal stratigraphic structure is highlighted with black dotted lines. A simplified stratigraphic column is shown on the top left of **(a)** and **(c).** It is difficult to constrain the distribution of the free gas-bearing sediments within the zone of seismic wipeout, as well as the occurrence of $S_{II/H}$ hydrates in the southeastern part of the GKL Dome, above the Limbayong structure (no borehole information is available here).


a
ms TWT
-1200
-1400
-1600
-1800
-2000
-2200
Stratigraphic units
1
2
3
4
Lingan and older units
NW
SE
HRA
MTD1
MTD2
MTD3
drape
Horizon H
EARs
BSR
Zone of seismic wipeout
Amp.
+
-
Gumusut-Kakap
Limbayong
1 km
b
NW
SE
BS$_{I}$GHSZ (BSR)
BS$_{II/H}$GHSZ
Pipe #2
Pipe-α (#1)
Pipe #5
BSR
Zone of seismic wipeout
Var.
+1
0
1 km
c
NW
SE
drape
Horizon H
MTD1
MTD2
MTD3
BS$_{I}$GHSZ?
BS$_{II/H}$GHSZ?
Zone of seismic wipeout
normal fault
Pipe
BS$_{I}$GHSZ (BSR)
BS$_{II/H}$GHSZ
free gas-bearing sediments
1 km

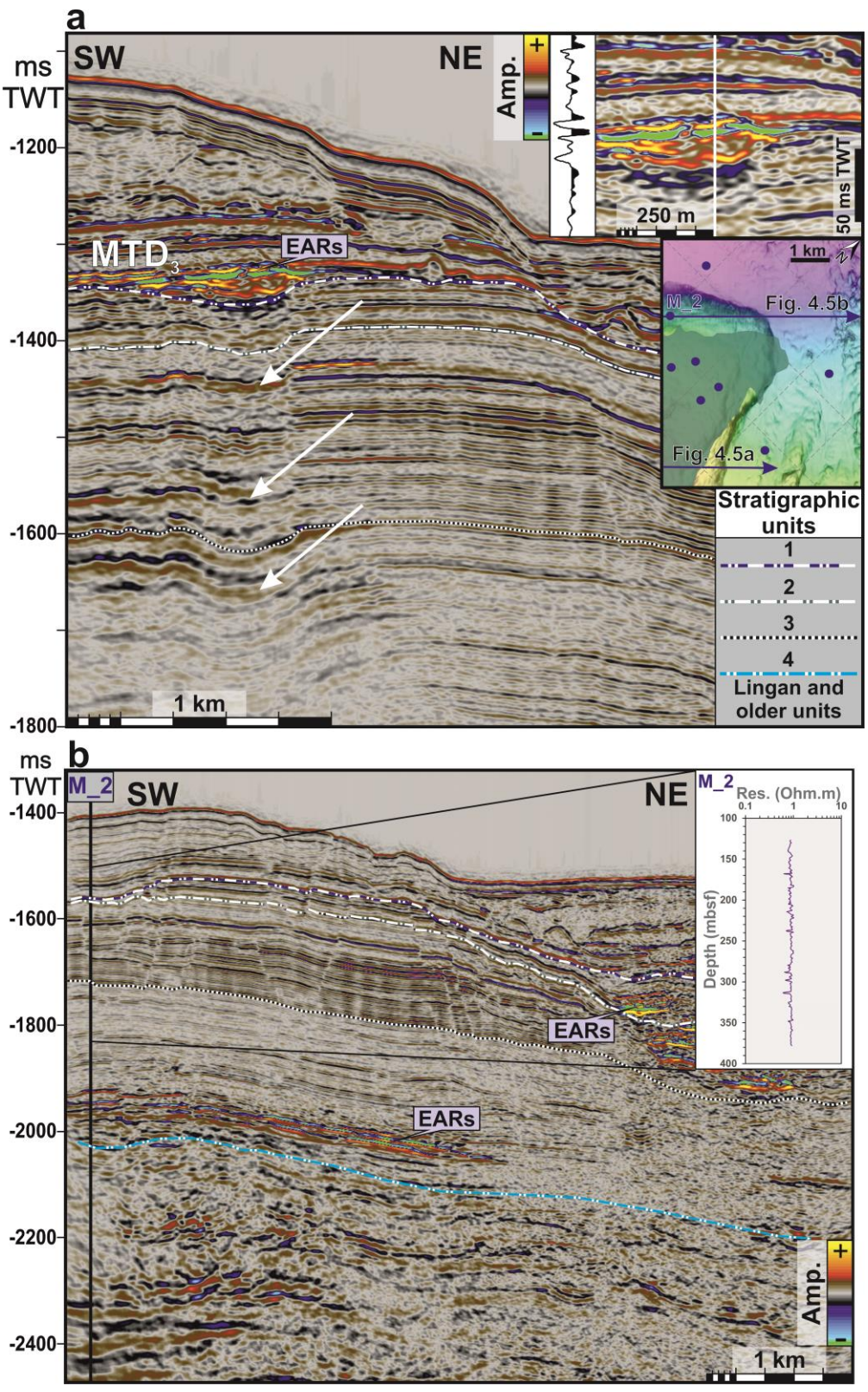



**Figure 4.5. (a)** SW-NE seismic line, showing the push-down effect (white arrows) related to the enhanced amplitude reflections (EARs) present within and below $MTD_3$. A blow-up of the EARs within $MTD_3$ is shown in the top-right portion of the figure, accompanied by a seismic wavelet extracted along the vertical white line. The top of $MTD_3$ is a soft high amplitude anomaly (peak-through) whereas the base is hard (through-peak), suggesting that $MTD_3$ contains free gas. **(b)** SW-NE seismic line, passing outside the area characterised by evidence of shallow free gas at the crest of the GKL Dome (i.e. the semi-transparent green area in the map on the right of **(a)**). At the crest, EARs are only present in the lower part of Unit 4 and below. The absence of high resistivity anomalies along the borehole M_2 suggests that hydrates are not present at this location. Note the different depositional system in the structural low in the northeastern part of the section, dominated by thick MTDs. The location of the seismic lines is shown by the blue arrows in the bathymetric map on the right of **(a)**, accompanied below by a stratigraphic column.

### *4.4.3. Fluid-escape pipes*

I have identified, within the GHSZ at the crest of the GKL Dome, 41 seismic features interpreted as fluid-escape pipes or coalesced fluid-escape pipes (cf. Cartwright and Santamarina, 2015) (**Figs. 4.4, 4.8, 4.9**). This interpretation is based primarily on the geometry and the internal seismic character of these features, which are organised as series of vertical to sub-vertical and relatively narrow zones, characterised by reflections having lower amplitude and frequency, in comparison to the surrounding stratigraphy. The stratigraphic continuity is commonly preserved along the pipes, although internally deformed and occasionally disrupted, with a complete loss of coherency. Specifically, even if there is no evidence of sediment remobilisation through these pipes, the seismic reflections are frequently and symmetrically bent upward **(Figs. 4.4, 4.8).**

These pipes are exclusively distributed within the area overlying the thrust-cored GK anticline, and most of them are located within the area where there is a clear BSR. Only four pipes are observed just outside the southern border of the BSR, in an area characterised by stacked groups of EARs (**Fig. 4.2**). One of these exceptions is Pipe-α, interpreted as the major fluid-escape pipe at the crest of the GKL Dome. The seismic continuity of the BSR is disrupted where it is cross-cut by these pipes (**Fig. 4.4a**). There are no pipes in any areas lacking shallow free gas seismic indicators. However, some areas interpreted to host free gas-bearing sediments do not contain pipes, given their absence above the Limbayong structure (**Fig. 4.2**).

In planform, the pipes are represented by elliptical to occasionally sub-circular zones with a higher variance than the surrounding sedimentary sequence (**Fig. 4.6a-c**). In some cases, each of these zones is composed of a single fluid-escape pipe. In other cases, each elliptical zone consists of an alignment, occasionally extending for more than 400-500 m, of smaller-scale sub-circular features, that are interpreted to be formerly separated pipes that have coalesced into a single feature (**Fig. 4.6c**). These individual pipes or zones with

coalesced pipes are referred to as '*pipe-zones'* or simply pipes in the following sections. The width of each single pipe-zone, measured along the minor axis, is roughly constant with depth and commonly ranges between ~20 and ~100 m, with a maximum width of ~270-280 m for Pipe-α (**Tab. 4.1**).

The pipe-zones are all located in the highly faulted area observed at the crest of the GKL Dome (**Fig. 4.6**). About 60% of the pipe-zones are close to these normal faults, near the hanging wall. There is no evidence of pipes being capable of cross-cutting the fault plane. The maximum axes of the pipe-zones are further often aligned along the main strike direction of the faults (**Fig. 4.6d**). Above the BSR, near the upper tip of the faults or adjacent to the fault planes, there are no high amplitude anomalies, potentially indicative of free gas, hydrates or authigenic carbonates.

In the first ~100 m of overburden (120-130 ms TWT), some packages of stratigraphic reflections belonging to Unit 1 either thin or more rarely truncate towards the axes of the pipes, resembling an onlap. $MTDs_{1\text{-}3}$ also are folded and occasionally thinned above pipes. This is evident for the wider pipes and, particularly, around Pipe-α (**Fig. 4.8a-c**). Along this feature, the stratigraphic thinning and truncations occur several times throughout Unit 1(**Fig. 4.8a-c**). There is a considerable upward deflection of the stratigraphic reflections along Pipe-α, from the seafloor down to its deepest seismically resolvable expression, at approximately 260-360 mbsf (~320-460 ms TWT bsf). At this depth, the reflections, although attenuated, have a geometry discordant with respect to the present-day seafloor (**Fig. 4.8a-c**).

It is challenging to differentiate between the real and the artefactual internal reflections along the smaller-scale pipes, given that in these cases the seismic wavelength could approach the pipe width, resulting in artefactual reflections (cf. Løseth *et al.*, 2011).

The upper termination of a pipe or pipe terminus is the shallowest stratigraphic position where the pipe is seismically visible. Above the terminus, the seismic reflections are continuous, without any evidence of fluid expulsion. The position of the terminus with

respect to stratigraphy can be used to date the most recent episode of high fluid flow activity along the pipe (Cartwright and Santamarina, 2015). At the crest of the GKL Dome, the termini of the pipe-zones frequently coincide with the bases (and the tops at some locations) of the three shallow MTDs, or their continuations northwestward as hemipelagic deposits (**Fig. 4.9**). In detail, 10 pipe-zones terminate at $MTD_1$, 12 at $MTD_2$ and 14 at $MTD_3$. Three pipes, including Pipe-α, pierce the seafloor. Two pipes, located in the southwestern part of the GKL Dome crest, terminate instead below these MTD and extend down to ~300 mbsf (~360 ms TWT bsf) (**Tab 4.1**).

From the better-imaged portions of the pipes, their root zones can be interpreted to lie either within or below the FGZ. By extracting the variance from the high-resolution dataset and comparing Pipe-α with other pipes in seismic cross-section, it appears that the former extends well below the entire GHOZ (i.e. below ~250 mbsf) while the other smaller pipes are rooted between the BSR and the $BS_{II/H}$GHSZ (cf. pipes 2 and 5 with Pipe-α in **Fig. 4.4b**). Nevertheless, some degree of uncertainty persists due to possible attenuation and transmission artefacts (Cartwright and Santamarina, 2015). Unfortunately, because of the loss of frequency, the push-down effects and the development a zone of seismic wipeout below the BSR, it difficult to constrain the internal morphology of the pipe-zones over their entire vertical extent and a more detailed interpretation of the root zones is not possible. Our interpretation of a deep root zone (i.e. below the $BS_{II/H}$GHSZ) for Pipe-α is confirmed by observations in the lower resolution seismic dataset (**Fig. 4.13**). Due to lateral resolution limitation, only Pipe-α is imaged at the crest of the GKL Dome in this dataset. The likelihood of a deep root zone for Pipe-α is increased by observing analogous pipes of similar size in the nearby Kikeh structure. These pipes are imaged on the low-resolution seismic data (**Fig. 4.10**). They are up to ~400 m long (~450-500 ms TWT bsf) and root within a stacked series of *'soft'* EARs (i.e. exhibiting a negative acoustic impedance contrast), suggesting that this root zone is constituted by free gas-bearing sediments, located within the Lingan Unit, up to

the lower part of Unit 4. These EARs overlie a zone of seismic wipeout which masks the deeper commercial hydrocarbon accumulation in Upper Miocene reservoirs (**Fig. 4.10**).

In summary, the fluid-escape pipes in this region exhibit a distribution that is specifically limited to areas displaying evidence of free gas-bearing sediments at the crests of the thrust-cored anticlines. The root of these features is difficult to image but most likely lies within a free gas accumulation, which can be the FGZ for small-scale pipes or deeply-rooted reservoirs for the bigger ones. The termini of the pipe-zones vary from one pipe-zone to the other. The termini are stacked at stratigraphic intervals, mostly related to the deposition of recent MTDs, although three pipes pierce the present-day seafloor.

### *4.4.4. Morphology and amplitude anomalies at and near the seafloor*

High reflectivity areas at the seafloor (HRAs) have been observed at the crest of the GKL Dome (**Fig. 4.8d**). These amplitude anomalies overlie eight pipe-zones. The lateral extent of these HRAs varies from less than 100 m up to few hundred of metres, with sub-circular, elongated or more irregular geometries in planform. In the latter case, this is likely to be the result of merging of smaller anomalies (cf. Gay *et al.*, 2007; Moss and Cartwright, 2010). Only three of the eight pipe-zones associated with HRAs pierce the seafloor whereas four others terminate at the base or within $MTD_1$ and one at $MTD_2$. The observed HRAs are associated with both mound-like features and small seafloor depressions (**Fig. 4.8a-c**). Furthermore, a hard reflection with high amplitude has been observed at ~30-40 mbsf (40-50 ms TWT bsf) within Pipe-α (**Fig. 4.8c, e**). Other zones of enhanced amplitude, although with less reflectivity, have been observed in association with smaller-scale pipes at the same stratigraphic level (named Horizon H), which is immediately beneath $MTD_1$ (**Fig. 4.8e**).

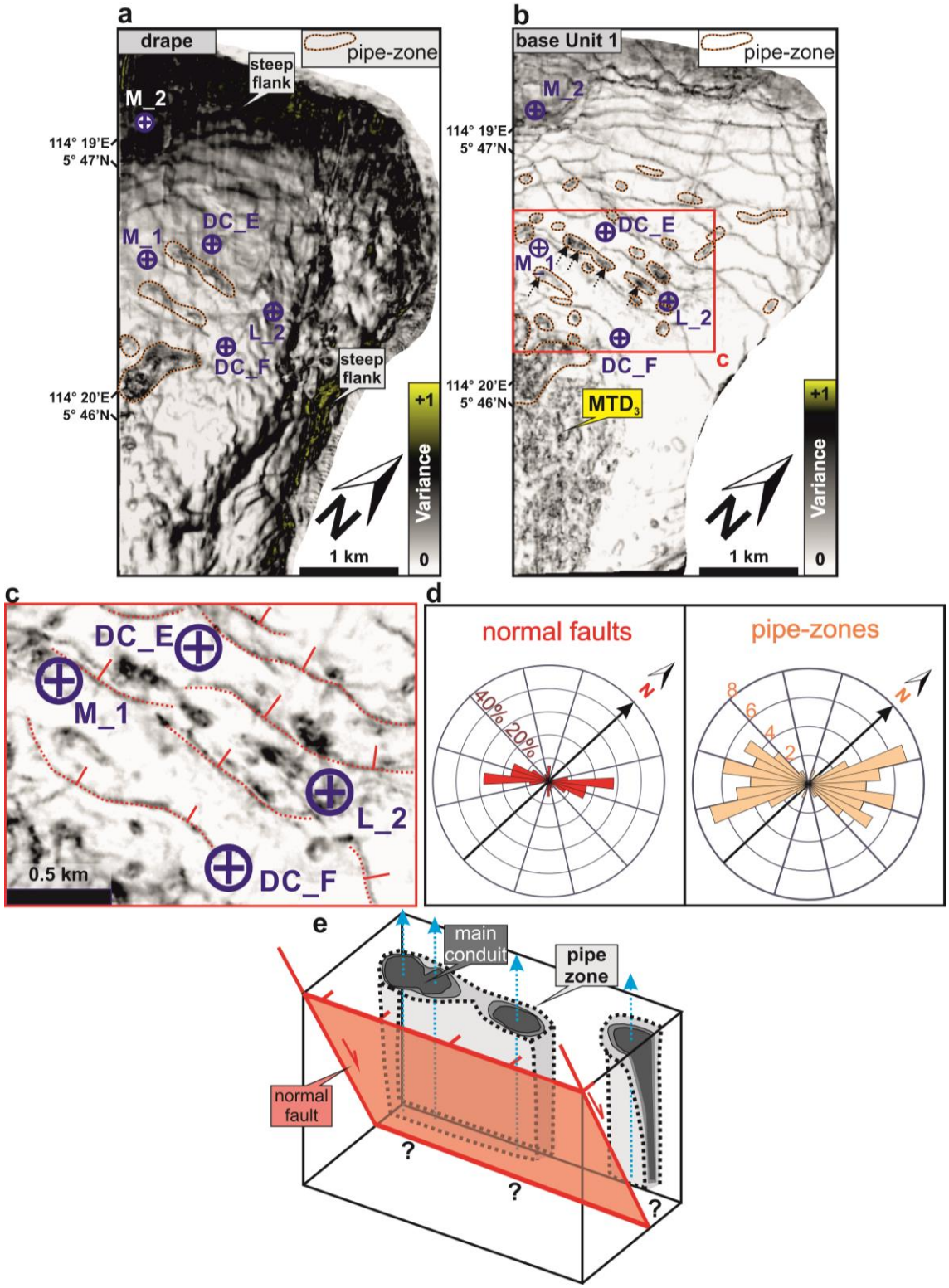



**Figure 4.6. (a, b)** Variance maps of the base of the recent drape interval **(a)** and the base of Unit 1 **(b)** at the crest of the GKL Dome (see **Fig. 4.4a** for the stratigraphic location of these horizons). The maps show the plan-view of both the normal faults and the pipe-zones, due to their impact on the seismic dip and azimuth continuity. These features are more visible at the base of Unit 1 than at the base of the recent drape. The faults show a dominant NE-SW trend, mimicked by the major axes of the pipe-zones. **(c)** Blow-up of a portion of **(b)** (see the red box), showing some pipe-zones in detail. They are characterised by sub-circular zones with an extremely high variance. These zones coalesce together and form elliptical features in planform. The trace of the normal faults is marked with red dotted lines whereas the dip direction of the fault planes is indicated by red lines on the hanging-wall sides of the faults. **(d)** Rose diagrams, showing the dominant strike directions of the normal faults (121 measurements) at the crest of the GKL Dome (left) and the maximum axis of the 41 sub-circular to elliptical pipe-zones (right). **(e)** Conceptual sketch, representing a pipe-zone, and the interpreted geometric relationship with a normal fault. The root zone is uncertain.

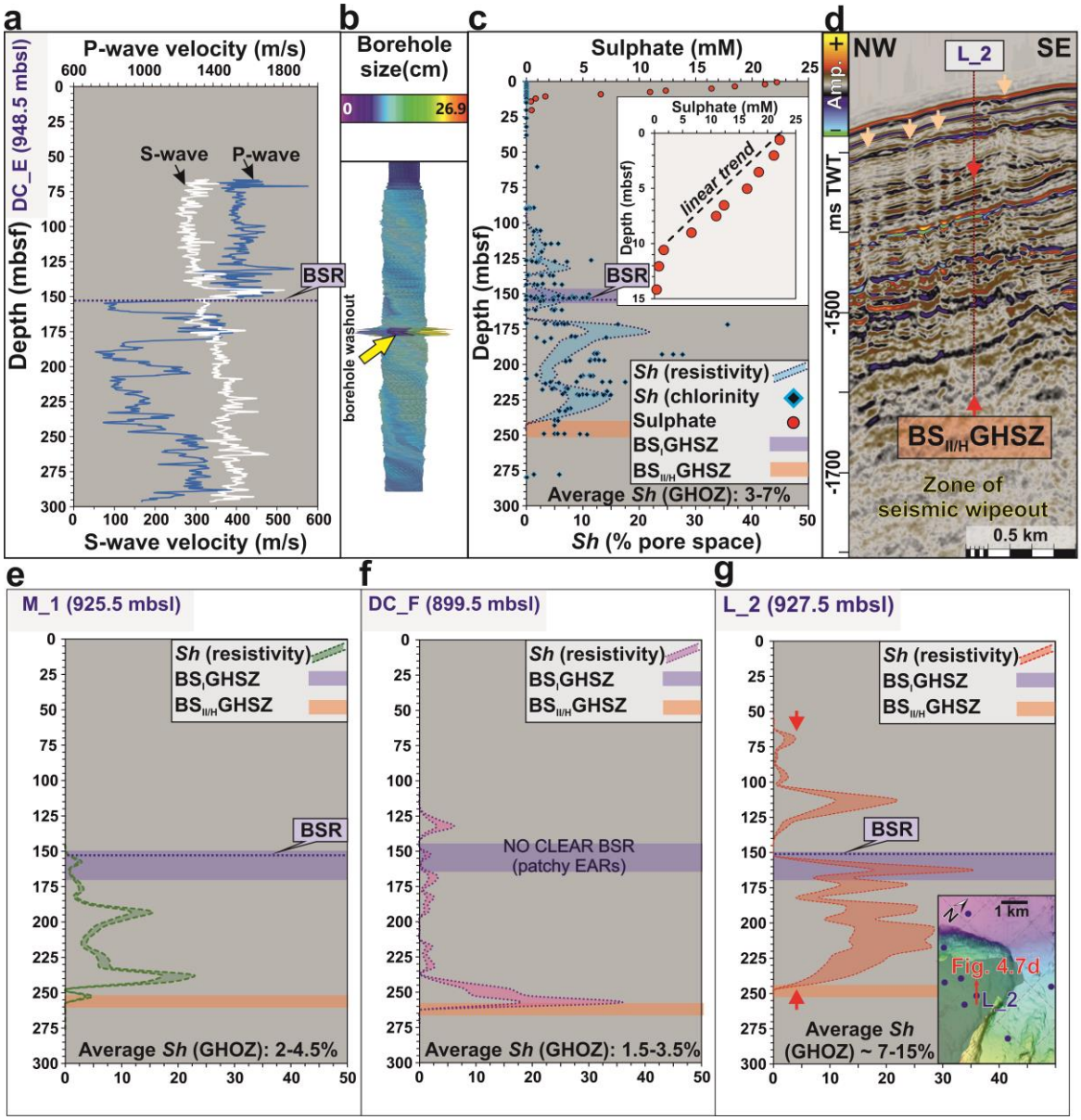



**Figure 4.7. (a)** Wireline P- and S-wave velocity logs at DC_E. Note the marked reduction in P-wave velocity at and below the BSR, indicating the presence of free gas. As expected, the S-wave velocity log does not show decreased values within the FGZ (see **Chapter 3** for a more detailed interpretation). **(b)** 3D borehole shape of borehole DC_E, extrapolated from the caliper log data. The borehole is in good condition with only a single washout at ~175 mbsf. **(c)** *Sh* and sulphate concentration profiles at DC_E. Hydrate saturation is extrapolated from resistivity and chlorinity data. A blow-up of the sulphate profile is also shown on the top-right. **(d)** NW-SE seismic section, showing the location of borehole L_2 (vertical red-black line), drilled very close to many pipe-zones. The two red arrows along the borehole projection indicate the top and the base of the GHOZ (65-242 mbsf). **(e-g)** *Sh* profiles, extrapolated from resistivity data at M_1, DC_F and L_2. In **(b, e-g)**, the *Sh* profiles from resistivity data have been smoothed, to give a more general view on the vertical trends in hydrate saturation outside the pipe-zones, and provide lower and upper end-member estimates of *Sh*. There is not a clear BSR at the location of DC_F but instead a system of patchily stacked enhanced amplitude reflections (EARs). The borehole associated with the highest hydrate concentration is L_2 (**g**) which, unsurprisingly, is located very close to numerous pipe-zones (**d**). See **Chapter 3** (**sub-paragraph 3.7.1**) for the detailed methods used to estimate *Sh*.

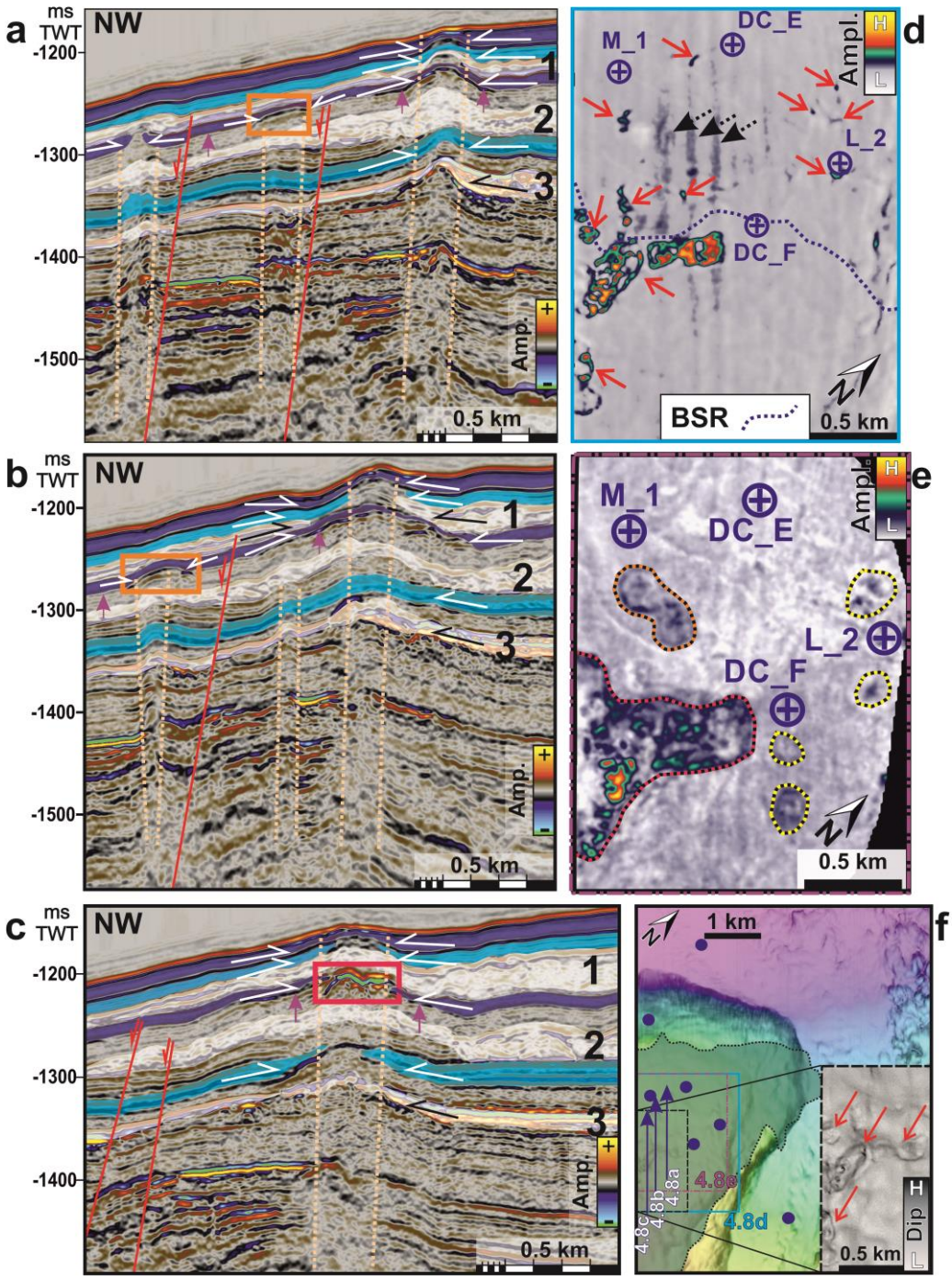



**Figure 4.8. (a-c)** Relationships between fluid-escape pipes and stratigraphy. The boundaries of the pipes are marked with light-orange dotted lines. $MTDs_{1-3}$ (indicated by numbers 1, 2 and 3) are shadowed in white. The black arrows indicate thinning of MTDs across the pipes. Other packages of horizons are shadowed in dark blue and light blue, and the zones of thinning and onlap are marked with white arrows. Horizon H is indicated by small purple arrows. **(d)** RMS amplitude map of the seafloor, showing areas with enhanced reflectivity (HRAs, red arrows). The zones with higher amplitude are red-coloured whereas those with lower amplitude are grey-coloured. The investigation spans from the seafloor to 10 ms TWT below it. The black dotted arrows indicate acquisition artefacts. **(e)** RMS amplitude map of Horizon H, which shows different zones of enhanced amplitude, highlighted by coloured lines. The colour of these lines refers to the colour of the rectangular boxes in (**a-c**), showing the best examples of these anomalies along the pipes. If the colour of these dotted lines is yellow, the pipe is not shown in seismic images. **(f)** Map of the study area, where the blue arrows indicate the traces of the sections shown in **(a-c).** The green semi-transparent area indicates the zone characterised by evidence of shallow free gas at the crest of the GKL Dome. The rectangles bounded in blue and purple indicate the areas shown in **(d)** and **(e)**, respectively. A detailed dip map of the area bounded by the dashed black rectangle is shown in the bottom-right and indicate a disrupted seafloor morphology, likely owing to the seepage of methane-rich fluids at the seafloor. In the attribute legends, H= high and L= low and refers to either amplitude **(d, e)** or dip (**f**, bottom-right).

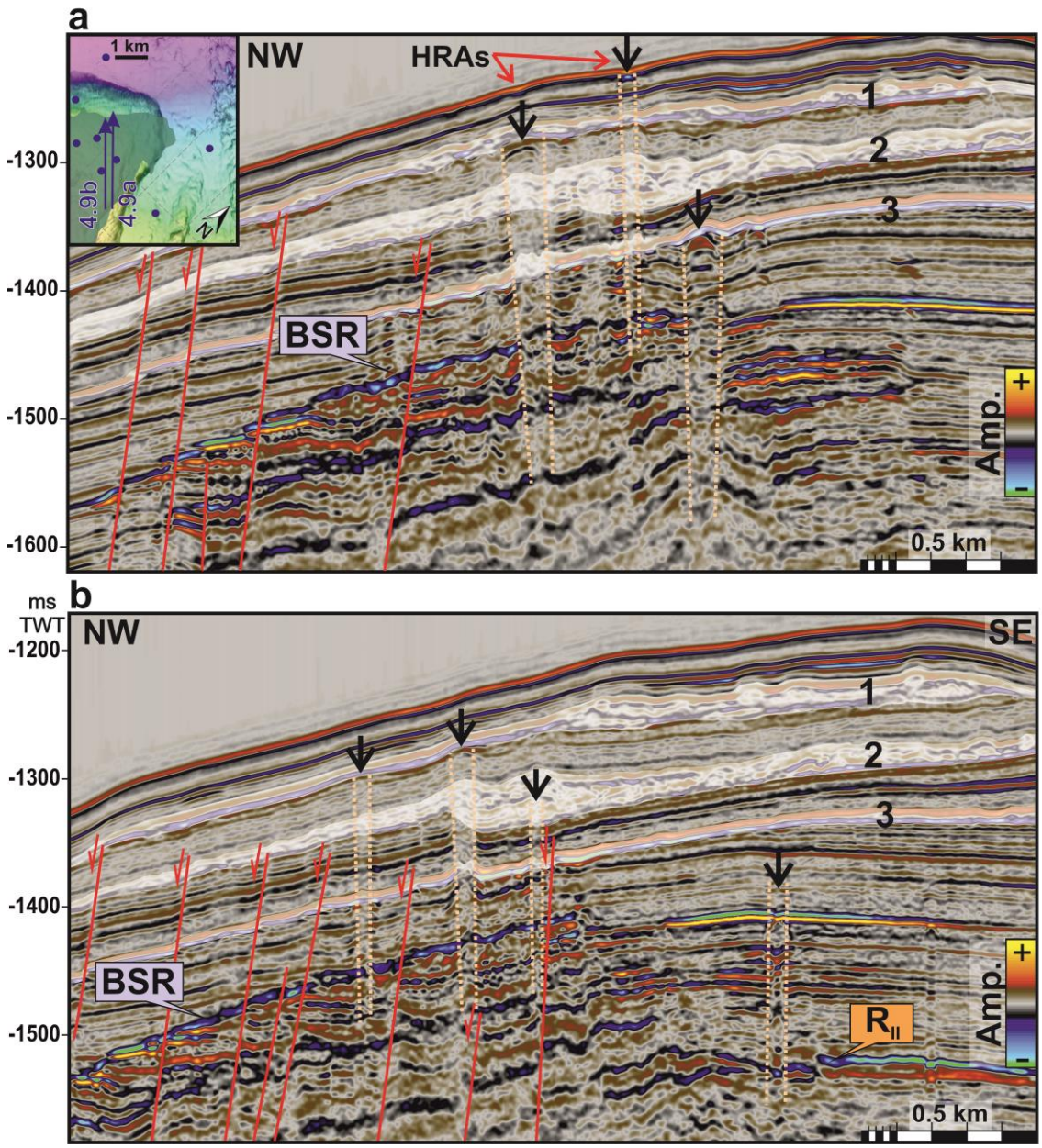



**Figure 4.9. (a, b)** NW-SE seismic sections, showing the different stratigraphic levels of the termini (black arrows) of the pipes (bordered with light-orange dotted lines). $MTDs_{1\text{-}3}$ (marked with numbers 1, 2 and 3) are shadowed in white. The termini of the pipes are typically located at the base of the MTDs or within them. More rarely, the terminus is at the seafloor or deeper than the base of $MTD_3$. The BSR, the normal faults, the HRAs and the reflection $R_{II}$ (potentially indicative of the $BS_{II/H}$GHSZ, see **Chapter 3**) are also shown. The traces of these seismic sections are indicated by the blue arrows in the bathymetric map in the top-left of **(a)**.

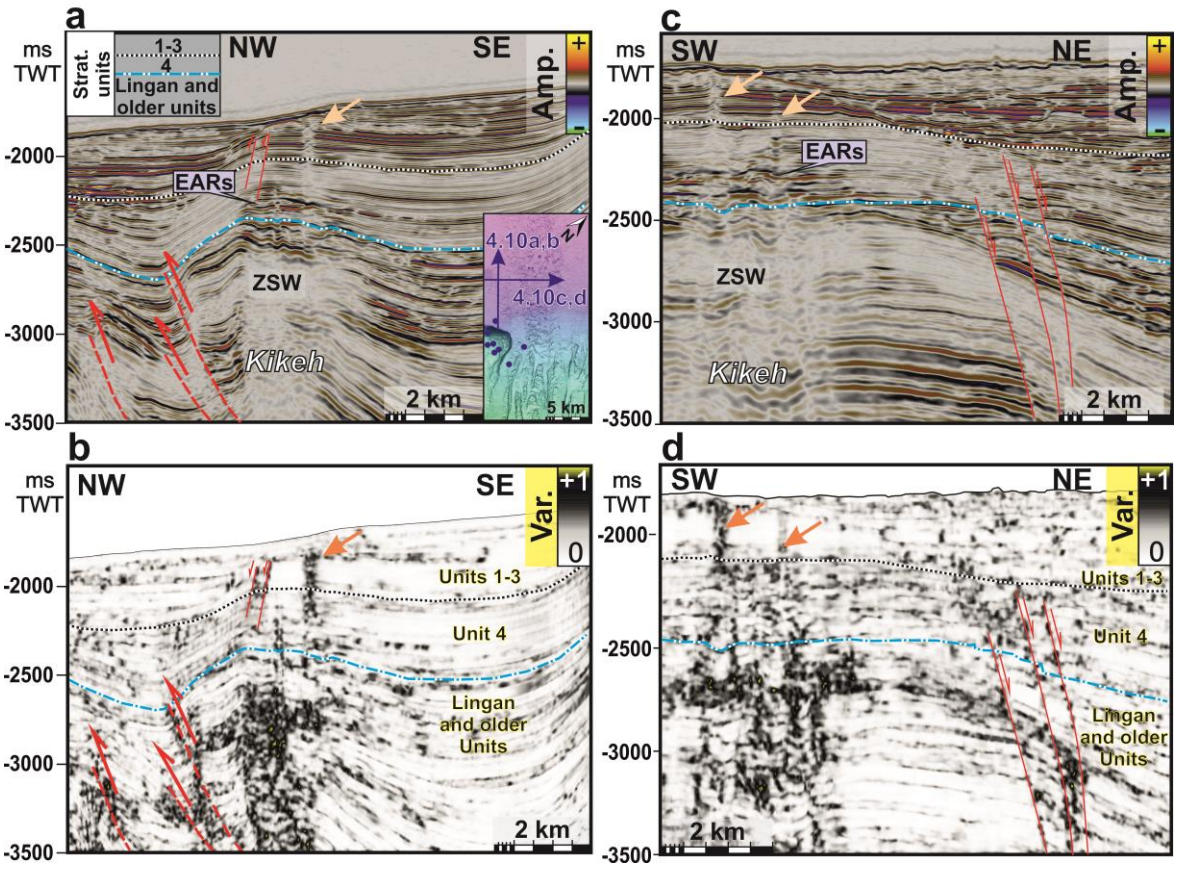



**Figure 4.10. (a, c)** NW-SE and SW-NE seismic sections, showing the crest of the Kikeh structure. (**b, d)** Variance extractions of the seismic lines shown in **(a)** and **(b)**. These images show fluid-escape pipes at the crest of the Kikeh structure. The pipes have high variance and are indicated by light-orange and orange arrows. Note the presence of enhanced amplitude reflections (EARs) within units 4 and Lingan, interpreted as the root zones of these pipes. The traces of the seismic lines are indicated on the map at the bottom-right of **(a)**.

## 4.5. Discussion

### *4.5.1. Controls on the distribution of fluid-escape pipes*

The presence of elevated overpressures at the root zone is commonly invoked to explain the genesis of fluid-escape pipes. This overpressure would trigger the migration of the fluids through sediment deformation and fracturing along a pipe-like conduit (Gay *et al.*, 2007; Hustoft *et al.*, 2007 and 2010; Cartwright and Santamarina, 2015). Given this general requirement for overpressures at depths, two questions need to be answered: **(1)** What controls the observed pipe distribution? **(2)** What is causing high pore fluid pressures at the root zones? From the preceding description of the pipes at the crest of the GKL Dome, I note that they **(1)** pass through the GHSZ, occasionally piercing the present-day seafloor, with evidence of seafloor and near seafloor amplitude anomalies; **(2)** are all located in an area characterised by free gas-bearing sediments overlying deep reservoirs, trapped within

thrust-cored anticlines; **(3)** appear influenced by the orientation of crestal normal faults and **(4)** are hosted in fine-grained sediments (cf. **Figs. 4.4, 4.6, 4.8, 4.9**).

The high amplitude anomalies at the seafloor, developed at the top of the pipes, are interpreted as an evidence of active or recent seepage of fluids. This seepage increases in the seafloor reflectivity, thanks to its *'by-products'*, including gas hydrate and authigenic mineral outcrops, as well as possible chemosynthetic communities. (cf. Roberts *et al.,* 2006; Judd and Hovland, 2007). This relationship provides good evidence that these pipes acted as pathways for free gas and methane-rich waters across the GHSZ.

The association between free gas-bearing sediments and fluid-escape pipes and their role as preferential fluid migration pathways have been suggested for many other hydrate provinces (Gorman *et al.*, 2002; Riedel *et al.*, 2002; Hustoft *et al.*, 2010; Netzeband *et al.*, 2010; Plaza-Faverola *et al.*, 2015). I hypothesise that the free gas has contributed to the formation of fluid-escape pipes in the study area, due either to its buoyancy or its high compressibility, with both of these characteristics capable of generating overpressures (Liu and Flemings, 2009). If free gas were not a critical agent in pipe genesis, then the pipes would be expected to occur even where free gas is not present, such as at the forelimb of the GKL Dome or its flanks, and this is not the case. This interpretation is further supported by the observation of a pipe root zone associated with EARs indicative of free gas-bearing sediments at the crest of the nearby Kikeh structure (**Fig. 4.10**). Although the overpressures associated with free gas buoyancy and compressibility probably played a key role in pipe formation, I do not exclude a contribution from overpressure generated by disequilibrium compaction, lateral pressure transfers and tectonic compression (Yardley and Swarbrick, 2000; Leduc *et al.,* 2013; Morley *et al.*, 2014). It is possible that the different tectonic activity associated with the GK and the Limbayong anticlines could result in a different capacity to generate and transfer overpressure. Such difference would explain the presence of pipes above the former structure *vs* their absence above the latter one (**Fig. 4.2**).

The geometric association between the areal extent of the GOC in the GK reservoir and the overlying BSR, with the zone of seismic wipeout rimmed by a halo of EARs located in between (**Figs. 4.1-4.4**), suggests that free gas has probably leaked vertically from the gas cap of this reservoir up to the GHSZ. The significant amounts of $C_{2+}$ hydrocarbons in the hydrate-bearing sediments cored near the $BS_{II/H}$GHSZ reflect such a direct connection with the underlying thermogenically-sourced reservoir and support this scenario, where thermogenic fluids have migrated vertically from through a leaky seal (see **Chapter 3**).

Many studies have suggested that BSRs represent pressure ramps and barriers for fluid flow (e.g. Gay *et al.*, 2006; Bangs *et al.*, 2011; Plaza-Faverola *et al.*, 2012a). The FGZ at the GKL Dome is characterised by gas hydrates coexisting with free gas between ~155 and ~250 mbsf and by stacked EARs interpreted as free gas-bearing intervals (**Figs. 4.3, 4.4**). The vertically variable values of P-wave velocity measured while drilling (**Fig. 4.7a**) suggest a variability in the free gas distribution below the BSR, potentially indicating stacked zones of enhanced free gas concentration, more likely to become critically overpressured and generate a pipe, compared to other intervals. Hence, there could be more than a single root zone for the pipes within the FGZ, depending on where the overpressure is preferentially accumulated. In contrast, both Pipe-α and those pipes observed at the crest of the Kikeh structure appear to be rooted in free gas reservoirs located below the FGZ and fed in turn by the leaky deeper commercial accumulations (**Figs. 4.4b, 4.10**).

Our observations indicate that fluids charging the natural gas hydrate system in the study area are focused towards the crestal regions of thrust-cored anticlines, which act as fluid-focusing structures (Morley *et al.*, 2014). This has been previously noted in this and other gas hydrate provinces (e.g. Riedel *et al.*, 2002; Netzeband *et al.*, 2010; Laird and Morley, 2011; Wenau *et al.*, 2015), although this study provides one of the few seismic evidence of leaky commercial hydrocarbon reservoirs feeding natural gas hydrate systems

(**Figs. 4.1, 4.2, 4.12**) (cf. with Inks *et al.*, 2009; Ostanin *et al.*, 2013; Simonetti *et al.*, 2013; De Prunelé *et al.*, 2017).

The alignment of the maximum axis of the pipe-zones along the main strike direction of the shallow normal faults affecting the crest of the GKL Dome (**Fig. 4.6**) suggests that the shallow state of stress impacts the distribution of the pipes. In this case, the pipes have been formed and eventually coalesced perpendicular to the least principal stress, interpreted here to be near horizontal for the first 800-1000 mbsf (Couzens-Schultz and Chan, 2010). These normal faults show no direct evidence of acting as conduits for fluid flow. Instead, the fault planes may serve as pipe nuclei, eventually governing their spatial distribution (cf. Maia *et al.*, 2016) (**Fig. 4.6e**) and potentially compartmentalising of the free gas zone.

The exact mechanism for the formation of fluid-escape pipes is debated (Cartwright and Santamarina, 2015). Typically, the onset of excess pore fluid pressure conditions in the overburden may trigger a multiphase fluid flow through hydraulic/pneumatic fracturing or capillary invasion (Cathles *et al.*, 2010; Hustoft *et al.*, 2010; Moss and Cartwright, 2010; Zhang and Wright, 2017). The clay-rich, fine-grained and low-permeability lithology at the crest of the GKL Dome suggests that fracturing is the most likely mechanism, especially by considering the shallow overburden conditions, i.e. the low effective stress contrasting the overpressures (Jain and Juanes, 2009; Choi *et al.*, 2011; Fauria and Rempel, 2011). Therefore, it is not surprising to observe that also the pipes described in other provinces (e.g. Hustoft *et al.*, 2010; Andresen and Huuse, 2011; Plaza-Faverola *et al.*, 2015) cut across fine-grained sequences, indicating that the formation of these features is favoured in such lithologies. In contrast, a stratal migration of free gas through the primary pore network is preferred in coarser-grained and more permeable sediments (e.g. Crutchley *et al.*, 2015).

The formation of these pipes implies the creation of a pathway formed by cross-stratal leakage of fluids that displace the grains, creating a positive feedback between deformation, dynamic permeability and fluid flux. After that such pathway is formed, the pressure

required to initiate further fluid flow will be governed by the effective permeability through the fracture network. The flux throughout such network, if consisting of fractures with a sufficient aperture (e.g. μm to mm-scale), would prevail over a capillary flow through the nm-scale primary pore throats that characterise fine-grained sequences (Brown, 2000; Liu and Flemings, 2011).

### *4.5.2. Episodicity and triggering events*

Fluid-escape pipes described previously have been linked either to single or multiple events of focused fluid expulsion (Cartwright and Santamarina, 2015). In the study area, it is suggested that pipes can be related to both single events of fluid expulsion and, occasionally, to more complex histories of pipe-growth. A pipe, in this latter case, once formed, can be opportunistically re-utilised by the migrating fluids a number of different times. This interpretation is supported by these observations: **(1)** The termini of the pipe-zones, which are stacked at different stratigraphic levels mostly coinciding with $MTDs_{1-3}$, and the present-day seafloor; **(2)** The high amplitude anomalies occurring along the pipe-zones both in the overburden and at the seafloor (**Figs. 4.8, 4.9**); **(3)** The stratigraphic thinning and truncations above and around the pipe-zones (**Fig. 4.8a-c**).

The association of the termini of the pipes with MTDs suggests that pipes formed prior or at the same time of mass-transport deposition. If fluid flux were constant over time, I would instead expect to see that pipes terminate over a continuous range of stratigraphic intervals. A similar observation was made in the Krishna-Godavari Basin (site NGHP-01-10), where a ~50 ka BP old fossil seep system is capped by a more recent MTD (Mazumdar *et al.*, 2009; Riedel *et al.*, 2010a). In the study area, Lu and Shipp (2011) suggested that $MTD_1$ was deposited during a period of low relative sea level predating the Last Glacial Maximum (34.5 ka BP). The period between ~30 and ~50 ka BP is characterised by rapid global sea level fluctuations (Maslin *et al.*, 1998; Lambeck and Chappell, 2001). Cyclic decreases in the relative sea level are considered one of the key factors in triggering sediment

mass failures along continental slopes at low latitudes (Maslin *et al.*, 2004). Additionally, sea-level drops can impact the pore-pressure conditions within free gas and gas hydrate-bearing sediments, resulting in a focused fluid flow. Specifically, following a sea-level drop, free gas can expand or exsolve (Riboulot *et al.*, 2013 and 2014) and hydrates can dissociate (Holtzman and Juanes, 2011; Hermanrud *et al.*, 2013), ultimately increasing the volume of free gas, facilitating the development of buoyant free gas columns. Furthermore, the presence of free gas in sediments enhances the pore fluid compressibility and reduces the relative permeability of water with respect to gas. Hence, under undrained conditions, a sea-level drop can result in the build-up of water overpressure (Liu and Flemings, 2009). Similar effects on free gas and hydrate reservoirs may also be generated by tectonic compression and uplift (Goto *et al.*, 2016), as well as by gas leakage from the deep reservoirs (Sultan *et al.*, 2011), both of them being ongoing process in the study area (Ingram *et al.*, 2004).

The more recent to present-day enhanced flux along the pipes, seismically expressed as HRAs, could be the result of this tectonic and hydrocarbon leakage activity. Alternatively, the global increase in deepwater temperature of about 2°C, following the Last Glacial Maximum (Waelbroeck *et al.*, 2002), could have provoked the dissociation of gas hydrates (Bangs *et al.*, 2005) and, therefore, the generation of adequate overpressure for fluid flux along the pipes.

The HRAs overlying those pipe-zones which lack a clear seafloor expression may indicate present-day incipient features, associated with reduced gas fluxes (cf. Liu and Flemings, 2007), capable of enhancing the reflectivity of the seabed but not effective enough to allow the pipe to clearly breach it. The slightly *'concave-up'* sulphate profile at DC_E corroborates the hypothesis of a recent to present-day increase in the fluid flux activity, even away from the pipe-zones (cf. Hensen *et al.*, 2003). Both the thinning and truncations of stratigraphic packages and the presence of high amplitude anomalies in the overburden along the pipes also suggest that they served as a pathway for fluid flow several times. This

is particularly evident for Pipe-α, where the stratigraphic thinning and truncations occur multiple times throughout Unit 1 (see **Fig. 4.8a-c**). Therefore, this feature, in contrast with the smaller pipes, has probably been more frequently active. The resulting mounded seafloor morphology, following such events of fluid flow, will then influence the sediment deposition (cf. Plaza-Faverola *et al.*, 2011; Ho *et al.*, 2012).

The interpretation of the enhanced reflections related to the smaller pipes along Horizon H is uncertain because their amplitude is indeed increased but not as much as along Pipe-α (**Fig. 4.8a-c, e**). These amplitude anomalies could just reflect an increased acoustic impedance contrast between the base of $MTD_1$ and the underlying pipes. MTDs are commonly constituted by overconsolidated and low-permeability sediments and may impact the hydraulic system (cf. Riboulot *et al.*, 2013), affecting the fluid flux along the pipes after their formation by hydraulic/pneumatic fracturing. Additionally, a constructive tuning effect associated with the thinning of stratigraphic packages at the top of the pipes would also result in enhanced amplitudes (cf. Plaza-Faverola *et al.*, 2011).

### *4.5.3. Gas hydrates along fluid-escape pipes?*

The seismic-scale internal structure of fluid-escape pipes has been associated with seismic artefacts, fracture systems, collapsed sediments, pockets of free gas, as well as authigenic minerals and hydrates (Hustoft *et al.*, 2010; Moss and Cartwright, 2010; Løseth *et al.*, 2011; Plaza-Faverola *et al.*, 2011; Ho *et al.*, 2012; Koch *et al.*, 2016). In this study, the up-bending geometry of the stratigraphic reflections at the margins and along the pipes (**Figs. 4.4, 4.8**) can suggest two possible processes, capable of modifying the original sediment structure:

**(1)** Sediment doming, due to the sole buoyancy force of free gas. However, this mechanism appears effective only in the first tens of metres below the seafloor, in the presence of overpressured gas pockets (Barry *et al.*, 2012; Koch *et al.*, 2015).

**(2)** Formation of either gas hydrates or authigenic carbonates, as a by-product of the focused flux of free gas and methane-rich waters along the pipe.

The formation of hydrates and carbonates can induce both a bulk volume increase and a pull-up effect in the seismic data (Paull *et al.*, 2008b; Plaza-Faverola *et al.*, 2010). I favour this second process as the one responsible for the observed pipe geometry considering:

**(1)** The lack of evidence of either free gas pockets (i.e. enhanced soft reflections along the pipe conduits) or push-down effects in the first tens of metres of overburden (i.e. above the free gas zone) (cf. Koch *et al.*, 2015).

**(2)** The enhanced *'hard'* reflection along Pipe-α, at 30-40 mbsf, likely representing a buried hydrate/carbonate mound (**Fig. 4.8c, e**) (cf. Chun *et al.*, 2011; Ho *et al.*, 2012).

**(3)** The extensive deformation along the pipes observed where free gas doming would be ineffective, i.e. well-below the first tens of metres of overburden (**Figs. 4.4a, 4.8a-c**). The presence of stratigraphic thinning and truncations along some of the observed pipes (**Fig. 4.8a-c**) further indicates that the internal bending of the reflections is not exclusively artefactual (i.e. not a sole pull-up effect or a transmission artefact).

**(4)** The observation of similar pipes in other provinces, associated with extensive deposits of grain-displacing hydrates, whose elevated concentrations have been constrained by quantitative geophysical analyses (Plaza-Faverola *et al.*, 2010; Attias *et al.*, 2016), and drilling (Chun *et al.*, 2011; Torres *et al.*, 2011; Kim *et al.*, 2013a; Matsumoto *et al.*, 2017). In particular, the seismic character of the fluid-escape pipes described in this study resembles that of the pipes discovered in the central Joetsu Basin (Sea of Japan), where pure hydrate nodules and lenses, interlayered with muddy sediment ($Sh$~35-85%), have been successfully recovered and inferred to occur all the way down to the BGSHZ (Matsumoto *et al.*, 2017). Elevated hydrate concentrations are also estimated for pipes in the Ulleung Basin and the Norwegian margin (Plaza-Faverola *et al.*, 2010; Kim *et al.*, 2013a).

All these observations support the interpretation that the internal deformation within the pipes is related to the presence of elevated concentrations of solid materials, most likely hydrates, capable of displacing the sediment, enhancing the bulk volume (Lee *et al.*, 2010b; Lei, 2017). A volume expansion, near and at the seafloor, would result in the formation of hydrate pingoes (Serié *et al.*, 2012; Paull *et al.*, 2015). Nevertheless, if these pipes become inactive and pore waters are no more saturated with the hydrate-forming gases, hydrates will dissolve, and pingoes may collapse, leaving only authigenic minerals as by-products (cf. Paull *et al.*, 2008b). The more elevated *Sh* along the borehole L_2, drilled very close to many pipe-zones, compared the *Sh* estimated for the other boreholes (**Fig. 4.7c-g**), reinforces the interpretation of elevated hydrate concentrations along the pipes, by indicating that *Sh* is augmented in their vicinity. The discordant geometry of the stratigraphic reflection along and around Pipe-α, at ~260-360 mbsf (**Figs. 4.4a, 4.8a-c**) could result from differential compaction, pull-up effects due to the presence of hydrates and carbonates in the overlying section and push-down effects in the free gas-bearing sediments around the pipe.

### *4.5.4. Fluid flow and gas hydrate distribution*

At the four drilled sites, there is no evidence of hydrates until 65-152 mbsf (**Fig. 4.7c, e-g)**. This relatively deep occurrence of hydrates correlates well with the depth of the SMTZ at DC_E (10-12 mbsf), which suggests a *'background'* diffusive methane flux of 1.2-1.5 mM $cm^{-2}$ $y^{-1}$, simplifying the system as one-dimensional and in steady state (Borowski *et al.*, 1996). These data indicate that, away from the pipe-zones, fluids are not sufficiently concentrated in methane to shift the SMTZ at the seafloor, allowing the formation of hydrate outcrops (cf. Borowski *et al.*, 1999; Davie and Buffett, 2003). In contrast, this could occur at the top of the presently active pipe-zones, interpreted as sites of elevated fluid flow, as suggested by the associated HRAs (cf. Luff and Wallmann, 2003; Paull *et al.*, 2005; Ruffine *et al.*, 2013) (**Fig. 4.8d**). Therefore, the SMTZ is probably very irregular in the three dimensions.

The active pipes-zones are interpreted as *'flux anomalies'* with respect to the *'background'* fluid flux and *'hydrate anomalies'* with respect to the *'background'* hydrate distribution (**Fig. 4.11**). The formation of gas hydrates along a fluid-escape pipe is thought to occur during a multiphase fluid flow throughout the GHSZ, sustained by **(1)** the increased temperature and salinity related to hydrate formation, **(2)** a kinetically effective (i.e. rapid) fluid flux and **(3)** a decreased solubility of gas in the pore water from the BGHSZ towards the seafloor (Liu and Flemings, 2007; Torres *et al.*, 2011; Smith *et al.*, 2014a).

At DC_E, geochemical data have indicated that hydrates are progressively depleted in $C_{2+}$ hydrocarbons, from the $BS_{II/H}$GHSZ up to the BSR, with only $S_I$ hydrates forming above this interface (**Chapter 3**). Chen and Cathles (2003) proposed that, within the GHSZ, the slower is the flux, then the more effective the chemical fractionation of free gas and hydrates will be (i.e. the chemical fractionation is kinetically-controlled). Hence, the *'layered'* configuration of hydrate structures observed at DC_E (i.e. $S_I$ above $S_{II/H}$ hydrates) could reflect a moderately low fluid flux of free gas. In contrast, at higher flux rates (i.e. fluxes of dissolved methane of ~$10^1$-$10^3$ mM $cm^{-2}$ $y^{-1}$, typical of cold vent systems, see Boetius and Wenzhöfer, 2013), the chemical fractionation operated by the hydrates within the GHSZ would be less efficient, and $S_{II/H}$ hydrates could occur at shallower depths, up to the seafloor, without the formation of a *'layered'* hydrate structure configuration. The fluid flux and the hydrate distribution along the active pipe-zones likely depict this latter case (**Fig. 4.11c**) and could resemble, at the seafloor, the thermogenically-sourced vents widely observed in the Northern Gulf of Mexico (e.g. Sassen *et al.*, 2001a). Overall, this natural gas hydrate system can be divided into a *'background'* system having a low to moderate fluid flux, and an additional system where the fluid flux is episodically enhanced and vertically focused. The hydrate concentration is suggested to be much higher in the zones where this second system is active (**Fig. 4.11**).

By simplifying the three-dimensional morphologies of these pipes as elliptical cylinders, it is possible to roughly estimate the hydrate volume stored in these features. To do this, I assume that only those pipes displaying HRAs allow the formation of hydrates up to the pipe terminus. For the other pipes, which lack evidence of present activity, the top of the hydrate occurrence is conservatively assumed to be at 100 mbsf, which is a depth for the top of the GHOZ in line with the borehole data away from the pipes, where the flux is set at *'background'* rates. The maximum depth of concentrated hydrate occurrence along the pipe-zones is fixed between the $BS_I$GHSZ (~155 mbsf) and the $BS_{II/H}$GHSZ (~250 mbsf), considering the uncertainty about their root zones. Given the likely grain-displacing morphology of hydrates and the possible impact of hydrate growth on sediment consolidation, the hydrate concentration is here expressed as a percentage of the total sediment volume (*Vh*) instead of a percentage of the pore space (Lei, 2017). The average *Vh* within the pipes is considered to vary between 12.5% and 25%, in agreement with results from other provinces across similar features (Plaza-Faverola *et al.*, 2010; Kim *et al.*, 2013a; Matsumoto *et al.*, 2017) **(Fig. 4.11d)**. Based on these assumptions, the gas hydrates volume within the 41 pipe-zones ranges between 1.09 and $2.80 \cdot 10^7$ $m^3$.

Similarly, the hydrate volume outside these zones can be estimated by considering that, at the crest of the GKL Dome, hydrates likely occur only in the presence of a physical connection with the underlying hydrocarbon plumbing system, expressed in seismic data as a ~8.8 $km^2$ wide area including the BSR, the pipe-zones and the adjacent shallow EARs (i.e. the semi-transparent green area in **Fig. 4.2**). By assuming an average *Vh* of 2-4% for the GHOZ, which starts in these calculations at 100 mbsf, in line with borehole data (cf. **Figs. 4.7c-g** and **4.11d)**, this volume would vary between 2.03 and $5.16 \cdot 10^7$ $m^3$. This variability mostly depends on either the presence or the absence of $S_{II/H}$ hydrates in the area of EARs overlying the Limbayong structure (see **sub-paragraph 4.7.2**, Appendix). At this location, the $BS_I$GHSZ could be approximated by the depth of the EARs within $MTD_3$, which is similar to the depth of the BSR (**Fig. 4.4**).

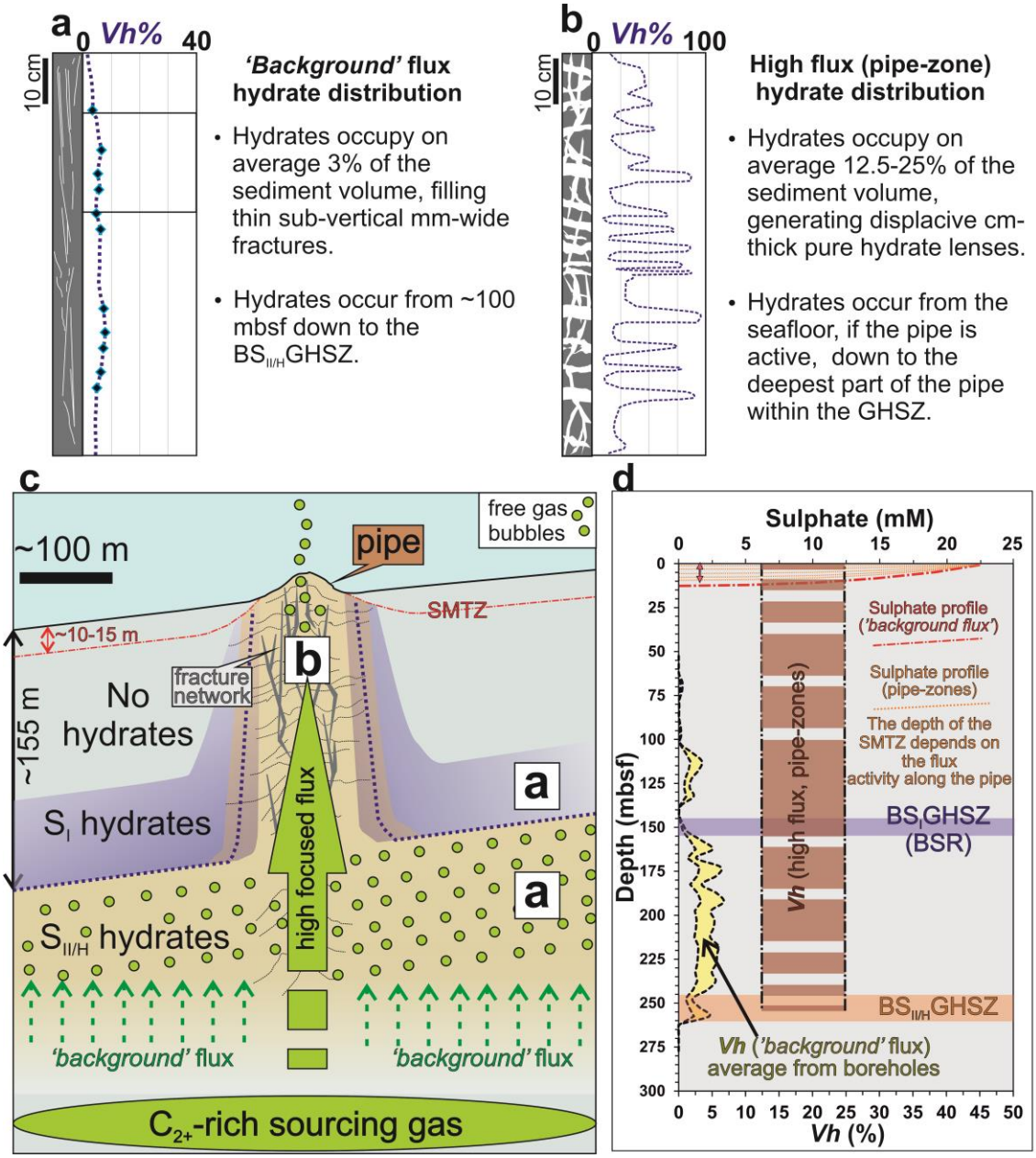



**Figure 4.11. (a, b)** Schematic representation of two gas hydrate-bearing cores (white is hydrate, grey is sediment) with their relative hydrate concentration (*Vh*, % of the total sediment volume) *vs* core length plots. These hypothetical cores depict the interpreted hydrate distribution outside **(a)** and inside **(b)** a pipe-zone, respectively (see white boxes in **c**). The core representation and the *Vh vs* length plot in **(a)** are based on chlorinity data on the pressure-core FPC#11 recovered at DC_E at 221 mbsf (see **Chapter 3, Fig. 3.4b**). The black rhombs indicate real *Vh* data, based on different chlorinity measurements along the core and a porosity trend extrapolated from the density logs at DC_E and DC_F (**Fig. 3.14**). **(c)** Schematic cartoon, representing the natural gas hydrate system at the crest of the GKL Dome. Away from pipe-zones, there is a *'background'* fluid flux, and gas hydrate crystallographic structures are *'layered'*, with $S_I$ hydrates overlying $S_{II/}$H hydrates, with a BSR marking this boundary at ~155 mbsf. Here, hydrates do not occur until approximately 100 mbsf. In contrast, within a pipe-zone, a higher fluid flux allows hydrates to occur much shallower, remaining stable if the pipe sustains an adequate flux. Theoretically, a higher flux could inhibit the molecular fractionation, and $S_{II/H}$ hydrates can crystallise within a pipe-zone up to the seafloor. The depth of the SMTZ responds to the intensity of fluid flux, piercing the seafloor above the pipe-zone and deepening down to ~10-12 m away from these areas. **(d)** *Vh vs* depth outside pipe-zone (*'background'* flux, yellow area) and within a pipe-zone (high flux, brown area). The *Vh* data from outside the pipe-zone is an average from *Sh* profiles at DC_E, M_1, DC_F and L_2. *Sh* has been converted to *Vh* using the porosity trend from the density logs at DC_E and DC_F (**Fig. 3.14**). The *Vh* within a pipe-zone is assumed to vary between 12.5% and 25%, based on estimates from drilling and geophysical models on similar pipe-like features. The depth of the SMTZ within a pipe-zone can range from the seafloor, if the pipe is active, to the depth at *'background'* flux areas, if the pipe is inactive.

If our estimates are reliable, the volume of hydrates within the pipes is of the same order of magnitude as that present in the *'background'* flux zone, although the pipes represent only 7-11%, by volume, of the zone of hydrate occurrence at the crest of the GKL Dome. Specifically, it is predicted that the system of fluid-escape pipes at this site could host between 17.5% and 58.0% of the entire hydrate volume, with the remaining hydrates dispersed at low concentrations (*Vh*= 2-4%; see **Tab. 4.2**). Globally, quantifying the volumetric amount of hydrates within pipe-like features is challenging, and such deposits constitute a largely unknown percentage of the hydrate resource pyramid (Boswell and Collett, 2006; Boswell and Collett, 2011). Our estimates suggest that in this and other areas with an elevated concentration of pipe-like features (i.e. 5-15% of the GHOZ, by volume), this type of hydrate deposit could be volumetrically significant.

## 4.6. Conclusions

This study shows that, at the crest of the GKL Dome, hydrocarbon-rich fluids, sourced from deep reservoirs, migrate across the gas hydrate stability zone through a system of fluid-escape pipes. The main conclusions are:

**(1)** The origin of fluid-escape pipes is related to the onset of critical pressure conditions, facilitated by the presence of free gas, and the consequent opening of deformable pathways. The root zones of fluid-escape pipes are located either within the free gas zone or in deeper free gas reservoirs. Fluid-escape pipes occur in this area at the crest of thrust-cored anticlines and in fine-grained sediments. The pipe geometry and distribution are influenced by shallow normal faults, which, however, do not act as conduits in the shallow part of the overburden.

**(2)** The stacked organisation of the pipe termini and the position of stratigraphic thinning and truncations suggest that fluid flow along these features was enhanced in conjunction with the deposition of MTDs. The geometrical relationship between fluid-escape pipes and MTDs of Mid-Upper Pleistocene age argues that sea level fluctuations or pulses of

tectonic activity (e.g. uplift) and hydrocarbon leakage during this period are the likely triggers for pulses of enhanced fluid flux activity along the pipes. The present-day fluid flux activity along the pipes could reflect both an ongoing tectonic uplift and hydrocarbon leakage and the temperature increase following the Last Glacial Maximum.

**(3)** The distribution of gas hydrates within fluid-escape pipes (high flux sites) and away from these features (*'background'* flux sites) can be very different. Fluid-escape pipes, if active, are capable of hosting hydrates at or near the seafloor whereas the *'background'* sites are solely characterised by a deep hydrate occurrence. These different regimes of fluid flux probably also impact the geochemistry of the gas hydrates. A layering of the hydrate structures occurs at *'background'* flux sites. Conversely, $S_{II/SH}$ hydrates can form at shallower depths along fluid-escape pipes, due to the higher fluid flux.

**(4)** The mounded internal geometry of the fluid-escape pipes in the study area is suspected to be caused by volume expansion and pull-up effects owing to the formation of gas hydrates at elevated concentrations. If this interpretation is correct, the volume of hydrates contained in these features is 17.5-58.0% of the total hydrate volume at this location, even if the pipe represent only 7-11% of the total sediment volume where hydrates can occur. In gas hydrate provinces characterised by advective fluxes of methane-rich fluids from below the BGHSZ and by the presence of pipes, methane budget estimates need to consider the volume of sediment occupied by these fluid-flow features, as they are capable of containing hydrates at elevated concentrations.

## 4.7. Appendix

### *4.7.1. Supplementary figure*

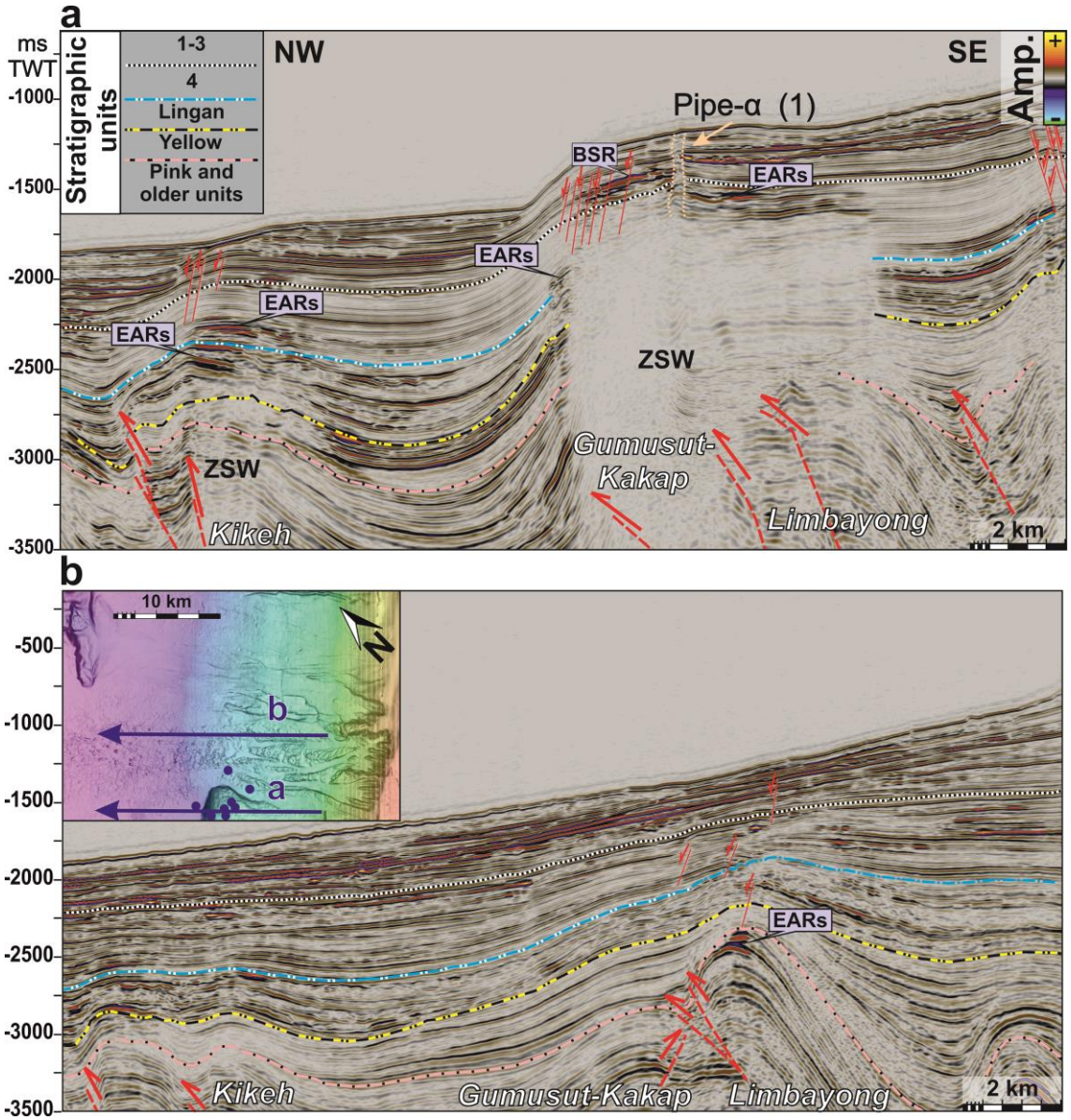



**Figure 4.12. (a)** Regional NW-SE seismic profile, showing Pipe-α at the crest of the GKL Dome. Smaller-scale pipes are not visualised in this data at the crest of the GKL Dome, likely due to lateral resolution limitations. Note also the numerous enhanced amplitude reflections (EARs) stacked within Units 4 and Lingan at the crest of the Kikeh structure. **(b)** Regional NW-SE seismic profile, showing that the studied structures become buried moving towards the northeast. The thrust at the core of the GKL Dome evolves into a back-thrust, and the Lymbayong structure shows evidence of EARs at the crest of the thrust-cored anticline. The Kikeh structure becomes buried under a ~400-450 m thick (~500 ms TWT) undeformed sediment cover. ZSW= zone of seismic wipeout.

### *4.7.2. Gas hydrate volumes within vs outside the pipe-zones*

To calculate the volume of a pipe-zone, I have assumed that its shape is approximated by an elliptical cylinder, with a volume (*Vp*) equal to:

$$\boldsymbol{Vp = \Pi(abh)}$$

Where ***a*** and ***b*** represent, respectively half of the major and half of the minor axis of the pipe-zone while ***h*** is its height.

The vertical extent of a pipe-zone interested by hydrate occurrence ranges from the terminus if the pipe is interpreted as active (i.e. it is associated with an HRA), down to the deepest portion of the pipe-zone within either the $S_I$GHSZ or the $S_{II/H}$GHSZ. If the pipe is inactive, the top of the pipe zone is considered to be at 100 mbsf. This choice is based on the fact that fluxes along an inactive pipe can be close to *'background'* values and formerly crystallised shallow hydrates could be dissolved. This assumption will make our estimates conservative because it is possible that methane fluxes along an inactive pipe can be still higher than *'background'* values if the former still has favourable permeable pathways for fluid flow. This could preserve hydrates even when pulses of high fluxes are ceased.

The depth of the root zone is the most uncertain parameter. Therefore, I considered two end-members: the $BS_I$GHSZ (155 mbsf) and the $BS_{II/H}$GHSZ (250 mbsf). The *Vh* within a pipe-zone is assumed to be comprised between 12.5 and 25%. It is possible that higher or lower values can be encountered along a hypothetical borehole throughout one of these features and that *Vh* does not abruptly decreases at the margin of a pipe-zone but rather decreases more or less gradually, as suggested by the *Sh* profile at L_2 (**Fig. 4.7g**). However, the chosen end-members provide a good range, in line with estimates from the literature. The root zone of Pipe-α clearly extends below 250 mbsf. Therefore, along this feature, hydrates can always occur down to the $BS_{II/H}$GHSZ.

A further uncertainty is related to either the presence or the absence of $S_{II/H}$ hydrates below the $BS_I$GHSZ above the Limbayong structure, given the lack of borehole data in this specific location. If fluid migration is predominantly vertical, the composition of the gas leaking from the reservoirs associated with the Limbayong structure will affect the resulting hydrate structures. The relatively low content of $C_{2+}$ hydrocarbons in the Limbayong reservoir (~1-2%) could not be enough to guarantee an efficient migration of enough of $C_{2+}$ components to form $S_{II/H}$ hydrates. In this case, the area of $S_{II/H}$ hydrate occurrence would be limited to the ~6.7 $km^2$ wide zone immediately above the GK reservoir presenting evidence of free gas anomalies. Outside this area, hydrates could be present only above the $BS_I$GHSZ, interpreted to be approximated by the depth of the EARs within $MTD_3$ (**Fig. 4.4**). Given these uncertainties, two cases have been considered (**A** and **B**). In Case **A**, $S_{II/H}$ hydrates are assumed to occur only in the area affected by vertical leakage from the GK reservoir and only $S_I$ hydrates are present in the southern part of the GKL Dome (i.e. above the Lymbayong structure). In Case **B**, $S_{II/H}$ hydrates occur down to 250 mbsf in all the area with evidence of shallow free gas anomalies, including the portion overlying the Limbayong structure (i.e. the semi-transparent green area in **Fig. 4.2**).

For both case **A** and case **B**, I have calculated the volume of hydrates associated with *'background'* fluxes, assuming *Vh*=2-4%. The top of the hydrate occurrence in this cases is fixed at 100 mbsf, and the volume of the pipe-zones is not considered. These hydrate volumes are added to that within the pipe-zone to obtain the total hydrate volume, and the percentage of this volume associated with pipe-zones is finally calculated. Tables **4.1** and **4.2** show, respectively, the geometric parameters of each pipe-zone and the results of these estimates.

| | Terminus | Terminus (mbsf) | Length-2a (m) | Width-2b (m) |
|---|---|---|---|---|
| #01* (α) | s | 0 | 1210 | 274 |
| #02* | s-$MTD_1$** | 0-24 | 514 | 76 |
| #03 | $MTD_1$ | 28 | 438 | 61 |
| #04* | $MTD_1$ | 31.5 | 466 | 101 |
| #05 | $MTD_2$ | 59 | 119 | 52 |
| #06 | $MTD_1$ | 63 | 224 | 43 |
| #07* | $MTD_2$ | 59 | 148 | 47 |
| #08* | $MTD_1$ | 24 | 140 | 49 |
| #09* | $MTD_1$ | 24 | 238 | 76 |
| #10* | s | 0 | 209 | 37 |
| #11 | $MTD_3$ | 102 | 121 | 85 |
| #12 | $MTD_3$ | 87 | 96 | 26 |
| #13 | $MTD_2$ | 63 | 143 | 46 |
| #14 | $MTD_3$ | 95 | 65 | 30 |
| #15 | $MTD_2$ | 63 | 122 | 30 |
| #16 | $MTD_2$ | 52 | 139 | 37 |
| #17 | $MTD_2$ | 52 | 146 | 29 |
| #18 | $MTD_2$ | 51 | 106 | 26 |
| #19 | $MTD_1$ | 28 | 137 | 66 |
| #20 | $MTD_2$ | 69 | 166 | 27 |
| #21 | $MTD_2$ | 57 | 116 | 35 |
| #22 | $MTD_2$ | 57 | 203 | 37 |
| #23 | $MTD_1$ | 26 | 71 | 32 |
| #24 | $MTD_1$ | 30 | 145 | 35 |
| #25* | $MTD_1$ | 24 | 111 | 35 |
| #26 | $MTD_1$ | 24 | 73 | 38 |
| #27 | $MTD_2$ | 61 | 93 | 44 |
| #28 | $MTD_3$ | 78 | 177 | 26 |
| #29 | $MTD_3$ | 52 | 135 | 29 |
| #30* | $MTD_2$ | 41 | 289 | 40 |
| #31 | $MTD_3$ | 74 | 457 | 40 |
| #32 | $MTD_3$ | 47 | 161 | 30 |
| #33 | $MTD_3$ | 95 | 67 | 32 |
| #34 | $MTD_3$ | 50 | 138 | 21 |
| #35 | $MTD_3$ | 42 | 146 | 32 |
| #36 | Below $MTD_3$ | 137 | 66 | 38 |
| #37 | Below $MTD_3$ | 140 | 152 | 43 |
| #38 | $MTD_3$ | 109 | 110 | 47 |
| #39 | $MTD_3$ | 79 | 201 | 59 |
| #40 | $MTD_3$ | 59 | 140 | 21 |
| #41 | $MTD_3$ | 59 | 163 | 21 |

**Table 4.1.** Parameters used to calculate the volume of the pipe-zones. The length of the pipe-zone (2*a*) is its major axis whereas the width (2*b*) indicates a measurement of its minor axis. s= seafloor; *= the pipe is overlain by an HRA at the seafloor; **= the pipe terminates only locally at the seafloor (I have assumed in the calculations that it terminates at the base of $MTD_1$, i.e. at 24 mbsf).

| | |
|---|---|
| **Total area with free-gas anomalies ($km^2$)** | 8.8 |
| **Area interpreted to be influenced by vertical leakage from the gas cap in the GK reservoir ($km^2$)** | 6.7 (BSR area is 5.8 $km^2$) |
| **Area with free gas anomalies overlying the Limbayong structure, interpreted as unrelated to the gas cap of the GK reservoir ($km^2$)** | 2.1 |
| **Volume of the 'high flux' GHOZ (i.e. within the pipe-zones) ($m^3$)** | $0.88\text{-}1.12\cdot10^8$ |
| **Volume of the *'background'* flux GHOZ (case A) ($m^3$)** | $1.02\text{-}1.06\cdot10^9$ |
| **Volume of the *'background'* flux GHOZ (case B) ($m^3$)** | $1.24\text{-}1.29\cdot10^9$ |
| **Gas hydrates in pipe-zones (*Vh*=12.5-25%) considering maximum and minimum vertical extensions ($m^3$)** | $1.09\text{-}2.80\cdot10^7$ |
| **Gas hydrates within Pipe-α (*Vh*=12.5-25%) assuming that hydrates occur from the seafloor down to the $BS_{II/H}$GHSZ ($m^3$)** | $0.82\text{-}1.63\cdot10^7$ |
| **Gas hydrates in the *'background'* occurrence zone (Vh=2-4%) (case A) ($m^3$)** | $2.03\text{-}4.26\cdot10^7$ |
| **Gas hydrates in the *'background'* occurrence zone (Vh=2-4%) (case B) ($m^3$)** | $2.48\text{-}5.16\cdot10^7$ |
| **% of the total hydrate volume within pipe-zones (case A; pipes extend down to the $BS_{II/H}$GHSZ with 12.5-25% *Vh;* average *'background' Vh* of 2-4%)** | 25.7-58.0 |
| **% of the total hydrate volume pipe-zones (case B; pipes extend down to the $BS_{II/H}$GHSZ with 12.5-25% *Vh;* average *'background' Vh* of 2-4%)** | 22.0-53.0 |
| **% of the total hydrate volume within pipe-zones (case A; pipes extend down to the $BS_I$GHSZ with 12.5-25% *Vh;* average *'background' Vh* of 2-4%)** | 20.4-50.7 |
| **% of the total hydrate volume within pipe-zones (case B; pipes extend down to the $BS_I$GHSZ with 12.5-25% *Vh;* average *'background' Vh* of 2-4%)** | 17.5-45.9 |
| **Total hydrate volume (cases A+B, including all the possibilities related to the hydrate volume within the pipe-zones and in the 'background' zones) ($m^3$)** | $3.22\text{-}7.77\cdot10^7$ |

**Table 4.2.** Extent of the zones interested by free gas anomalies, volumes of the GHOZ within *vs* outside the pipe-zones and hydrate volumes within *vs* outside the pipe-zones. Depending on the assumptions, the volume of hydrates within the pipe-zones varies between 17.5 and 58.0% of the total hydrate volume present in the study area. Note also that more than 50% of the hydrate volume within the pipe-zones is associated with Pipe-α, which is the major fluid-escape feature of the study area.

# Chapter 5. Investigating the impact of gas composition, migration and lithology on the distribution of gas hydrates and free gas

In this chapter, Joe A. Cartwright and Pieter Van Rensbergen contributed to the interpretation of seismic data and the revision. Martino Foschi helped in extracting the rock-physics model for gas hydrate saturation *vs* P-wave velocity. The seismic, well-log and core data were acquired by Shell and provided by Craig R. Shipp.

## 5.1. Introduction

The analysis of a natural gas hydrate system (NGHS), if integrated with a petroleum system approach, can successfully evaluate the gas hydrate stability conditions and the processes of hydrate accumulation (cf. Collett *et al.*, 2009). A multi-scale approach is required for a successful analysis of an NGHS and needs to integrate observations at the seismic, borehole and core-scales. Some significant examples are represented by the integrated expeditions across the Cascadia margin, the Indian Ocean, the South China Sea, the Ulleung Basin and the Nankai Trough, which provided invaluable information on the controls on hydrate distribution (Tréhu *et al.*, 2006; Riedel *et al.*, 2009; Ryu *et al.*, 2013; Kumar *et al.*, 2014; Wang *et al.*, 2014; Fujii *et al.*, 2015).

Importantly, the recent tectonostratigraphic setting strongly impacts the mode of accumulation and distribution of gas hydrates (Boswell *et al.*, 2012b; Plaza-Faverola *et al.*, 2014; Ito *et al.*, 2015). For example, hydrate reservoirs are frequently developed at the top of bathymetric seafloor ridges (often forming owing to thrusting), in both active and passive margins (e.g. Tréhu *et al.*, 2004b; Riedel *et al.*, 2010a; Sultan *et al.*, 2011; Bünz *et al.*, 2012; see also **Chapter 4**). These sites are characterised by lateral tectonic deformations, uplift, erosion, fluid focusing and generation of overpressures. The result is often a seepage of methane-rich fluids along cross-stratal migration pathways, up to the seafloor (Pecher *et al.*, 2005; Bangs *et al.*, 2011). The flanks of these bathymetric highs, compared to the crests, are characterised by higher accommodation spaces, frequently filled with turbidites and mass transport deposits (MTDs) (e.g. Morley and Leong, 2008). These locations are less commonly assessed in the characterisation of an NGHS.

Except for high saturation hydrate-bearing sands and massive hydrate accumulations along vertical fluid flow pathways (Boswell *et al.*, 2016), hydrates are invisible in seismic reflection data. Therefore, bottom-simulating reflectors (BSRs) represent, in some cases, the sole but not unequivocal seismic proxy for the presence of an NGHS (Holbrook *et al.*, 1996;

Tsuji *et al.*, 2009). It is thus crucial to concurrently assess the possible presence of hydrates within the GHSZ and the whole range of physical and chemical processes that can occur below the GHSZ (Plaza-Faverola *et al.*, 2011; Simonetti *et al.*, 2013; Crutchley *et al.*, 2015; De Prunelé *et al.*, 2017).

Of particular importance, is the evaluation of the processes that generate the gas for hydrate formation, which will also impact the resulting hydrate structure(s) (see **paragraph 1.3**) (e.g. Milkov, 2005). One process is represented by the primary generation of microbial methane which in marine environments mostly occur at temperatures less than ~50°C, through $CO_2$ reduction, where the $CO_2$ is the product of decarboxylation,` and methyl-conversion (Whiticar *et al.*, 1986; Stolper *et al.*, 2014). Alternatively, methane and other gases are sourced by leaky deep reservoirs, where the gas is generated during catagenesis/metagenesis and subsequent cracking processes, at temperatures higher than ~90°C (Schenk *et al.*, 1997; Sassen *et al.*, 2001a and b; Milkov, 2005). Also, methane can be generated by biodegradation processes of crude oils (Larter *et al.*, 2005).

At the scale of the borehole, the detection of gas hydrate-bearing sediments (GHBS) typically relies on their high resistivity and acoustic velocity compared to fully water-saturated sediments (Collett and Lee, 2011). However, the quantitative estimation of gas hydrate saturation (*Sh*, % of pore space) is challenged by the nonlinear impact on well-log measurements of both grain-displacing hydrates (e.g. within fractures) (Lee and Collett, 2012) and pore-filling hydrates (Spangenberg and Kulenkampff, 2006) (see **paragraph 1.5**).

The recovery of conventional (i.e. non-pressurised) and pressure cores permits a more detailed characterisation of GHBS. The endothermic dissociation of gas hydrates and the associated release of fresh water in cores at ambient pressure allow the identification of the gas hydrate-bearing intervals and an accurate core-scale estimation of *Sh* (Tréhu *et al.*, 2004b). Moreover, X-ray and Multi-sensor core-logging tools (MSCL) have been deployed for pressurised cores, to image the GHBS and measure their physical properties at in-situ

conditions (Holland *et al.*, 2008; Santamarina *et al.*, 2015). The acquisition of geochemical information on the composition and isotope ratios of the gas evolved from such cores further provides accurate insights on the origin of the hydrate-forming hydrocarbons (e.g. Milkov *et al.*, 2004b; Heeschen *et al.*, 2007). The combination of core and well-log data is thus the best approach to precisely characterise the distribution of gas hydrates at a specific site.

In the previous chapters (**3** and **4**), the interpretation was focused on the crest of the GKL Dome, a bathymetric ridge overlying a system of thermogenically-sourced and structurally-trapped oil and gas reservoirs, located offshore Sabah (NW Borneo). This system is characterised by hydrates present even below a BSR and by the presence of fluid-escape pipes, which represent seismic evidence for both cross-stratal fluid flow and probably concentrated zone of hydrate occurrence. In this study, I focus instead on the flanks of the GKL Dome, characterised by mass-transport deposits (MTDs) and no evidence of shallow vertically-focused fluid flow. I present a combination of 3D seismic, well-log and core data, to understand how the structural and stratigraphic setting and the hydrocarbon plumbing system interact and influence the gas hydrate and free gas accumulation. I will compare the vertical extent of the GHSZ at the crest *vs* at the flanks of the GKL Dome. I will further focus on the characteristics of the hydrate reservoir and the geophysical evidence of gas hydrates and free gas at the flanks.

## 5.2. Data and Methods

### *5.2.1. 3D seismic, well-log and core data*

In this study, I have interpreted the same 3D seismic data used in **Chapter 4** (see **paragraph 4.2**). The interpretation has been accomplished after shifting the seismic volumes by -90°, following a North American polarity convention. Numerous boreholes have been drilled for well-log and core data acquisition at the crest and the flanks of the GKL dome. In **Chapters 3** and **4**, I have discussed the well-log and core data from sites located at the crest (boreholes DC_E, M_1, DC_F and M_2). This study presents data from three further sites named DC_A, DC_B, and DC_C, located at approximately 1000-1200 mbsf, at the flanks of the GKL dome (**Fig. 5.1**).

Gamma-ray, resistivity, density and neutron porosity measurements were performed while drilling (LWD) with the Halliburton downhole tools (see **Chapter 3**). Wireline (WL) data included P- and S-wave velocity measurements, as well as the resistivity images and information of the borehole conditions. The velocity data were obtained with the Cross-Multipole Array Acoustic log from Baker Hughes (XMAC). Resistivity images and borehole profile information were acquired with the Simultaneous Acoustic and Resistivity Imager (STAR) device, equipped with a 6-arms caliper. The boreholes for the LWD and WL data acquisition at DC_A, DC_B and DC_C were drilled at different dedicated sites, located at maximum 30 m distance from each other, with a maximum bathymetric difference of 2 metres. There is no information on the borehole conditions for the LWD sites. In this study, the WL data are interpreted qualitatively and compared to the core and LWD information. Depending on the condition of the borehole during WL data acquisition, the quality of the resistivity images and velocity data varied from relatively poor to good. Overall, the results from the STAR device helped in interpreting the lithological framework and the hydrate distribution in the wells. The availability of confidential drilling reports

(Benting *et al.*, 2006; Gisler *et al.*, 2007) has further helped in the lithological interpretation, by indicating the location of intervals rich in sandy/silty beds along the boreholes.

DC_A and DC_B were selected for the acquisition of core data (see **Tabs. 5.4-5.7**) with the same tools described in **paragraph 3.2** (FC, WISON/WIP XP push sampler with Liner/Shelby tube, FPC and HRC). The FC non-pressurised cores were subjected to infrared thermal imaging while the FPC pressure-cores were analysed with the MSCL-S, developed by Geotek for the acquisition of X-ray images (maximum pixel resolution of ~120 μm), as well as for P-wave velocity and gamma density measurements (Schultheiss *et al.*, 2008 and 2010). The recovery pressure of the pressure cores (i.e. the pressure at which the tool autoclave sealed during ascent), was close to the hydrostatic pressure near the seafloor at both DC_A and DC_B, suggesting that the in-situ effective stress conditions were not maintained upon recovery (see Yun *et al.*, 2010). Both chlorinity and sulphate content measurements, as well as the $C_1$-$C_4$ hydrocarbon molecular composition, were measured at sites DC_A and DC-B, with the same methods described for site DC_E **(paragraph 3.2)**. Only an FC core sample, recovered at DC_A, was sent onshore for more detailed geochemical analysis with the Varian CP-3800 gas chromatograph. The geothermal gradient was also extrapolated at DC_A and DC_B, by integrating seafloor temperatures acquired with a CTD or Sonde with in-situ TCPT measurements (see **paragraph 3.2**).

### *5.2.2. Seismic interpretation and calibration of amplitude anomalies*

This research uses the seismic data to interpret the stratigraphy, as well as the evidence of focused fluid flow, hydrocarbon leakage and accumulation (cf. Andresen, 2012). One major objective is the identification of seismic proxies for the BGHSZ, taking into account that that free gas-bearing sediments can potentially occur, in the form of amplitude anomalies, at and below this boundary (e.g. Davies and Clarke, 2010; Foschi and Cartwright, 2016). At the crest of the GKL Dome, a BSR (see **Chapter 4**) represents the BGHSZ for $S_I$ hydrates ($BS_IGHSZ$) (**Chapters 3** and **4**). At the flanks of the GKL Dome, further amplitude

anomalies have been interpreted in this study. Their depth in the overburden is compared to that of a theoretical $BS_IGHSZ$, calculated with the CSMHyd software (Sloan Jr and Koh, 2007). The depth of the anomalies is extrapolated assuming a P-wave seismic velocity for the first ~200 mbsf of 1650 m/s, based on well-to-seismic tie data provided by Shell. A 100% methane hydrate stability curve, integrated with in-situ measurements of the geothermal gradients, seafloor temperatures and in-situ pore water salinities (2.0-2.5%), has been used for these calculations.

Finally, the RMS amplitude has been extracted for a few selected enhanced amplitude reflections (EARs) and two more laterally continuous stratigraphic horizons. In this latter case, the extraction of the RMS amplitude has been accomplished over an investigation window, to capture multiple anomalies over a TWT interval. The comparison of the RMS amplitude distribution with the horizon topography and variance further helps in placing these amplitude anomalies into a stratigraphic and structural framework. Overall, these attribute maps help in understanding the controls on the distribution of free gas.

### *5.2.3. Gas hydrate saturation*

*Sh* has been initially estimated from chlorinity measurements in both conventional and pressure-cores, as described in **paragraph 3.7** (see also Ussler and Paull, 2001; Malinverno *et al.*, 2008). With this method, *Sh* has been determined at different intervals along FC and FPC cores. Thus, it has been possible to compare single *Sh* measurements with the P-wave velocity recorded along FPC cores, and to associate the observed P-wave velocity *vs Sh* relationship with existing models for hydrate micro-habits in the pore space (Helgerud *et al.*, 1999; Waite *et al.*, 2009; Lee *et al.*, 2010a) (see **paragraph 1.4**). *Sh* has also been obtained from FPC cores degassing experiments with a standard methane mass-balance approach (e.g. Schultheiss *et al.*, 2010) but provides only an average value for each core, without showing the *Sh* variability at the core-scale.

I have further selected the phase shift deep smoothed resistivity ($R_{deep}$) measurements to estimate *Sh* along the boreholes at the flanks of the GKL Dome, following the Archie relationship (Archie, 1942; cf. Malinverno *et al.*, 2008):

$$\boldsymbol{Sh = 1 - Sw \; = \; 1 - (aR_w/\emptyset m R_{deep})^{1/n}}$$

Where *Sw* is water saturation (% pore space), *a* is the tortuosity factor, *m* is the cementation exponent, *n* is the saturation exponent and, *Ø* is the porosity extrapolated from density logs, and $R_w$ is the pore water resistivity. Within gas hydrate-bearing intervals, because of the high resistivity of hydrates, the measured resistivity ($R_{deep}$) is higher than the resistivity of a fully water-saturated sediment ($R_o$) (Collett and Ladd, 2000), the latter being:

$$\boldsymbol{R_o = aR_w/\emptyset^m}$$

$R_w$ has been computed considering both the in-situ water salinity, extrapolated from the *'baseline'* chlorinity profile, obtained from pore water data, and the in-situ measured geothermal gradients, following Fofonoff (1985). With this procedure, a continuous $R_w$ *vs* depth trend is obtained (**Fig. 5.17**). At DC_C, due to the lack of pore water chemistry information, I have used the $R_w$ profile obtained at DC_B, which is the closer borehole. By the use of Pickett plots, *a* and *m* are then computed, considering intervals interpreted to be hydrate-free from core data, (cf. Shankar and Riedel, 2011 and 2014; Wang *et al.*, 2014) (**Fig. 5.18**). Then, a $R_o$ *vs* depth profile is obtained and compared to the $R_{deep}$ *vs* depth profile to image the intervals with anomalously high resistivity. Finally, *Sh* is estimated, by assuming *n* comprised between 2 and 4, respectively providing an upper and a lower end-member estimate. The cementation and saturation exponents in GHBS vary depending on the hydrate habit and saturation (e.g. Spangenberg, 2001; Spangenberg and Kulenkampff, 2006; Lee and Collett, 2009). Our chosen end-members for *n* are justified by the experimental data of Spangenberg and Kulenkampff (2006), who showed that *n* approximately varies between 2 and 4, depending on *Sh*, for hydrates having a pore-filling non-cementing micro-habit, affected by capillary forces.

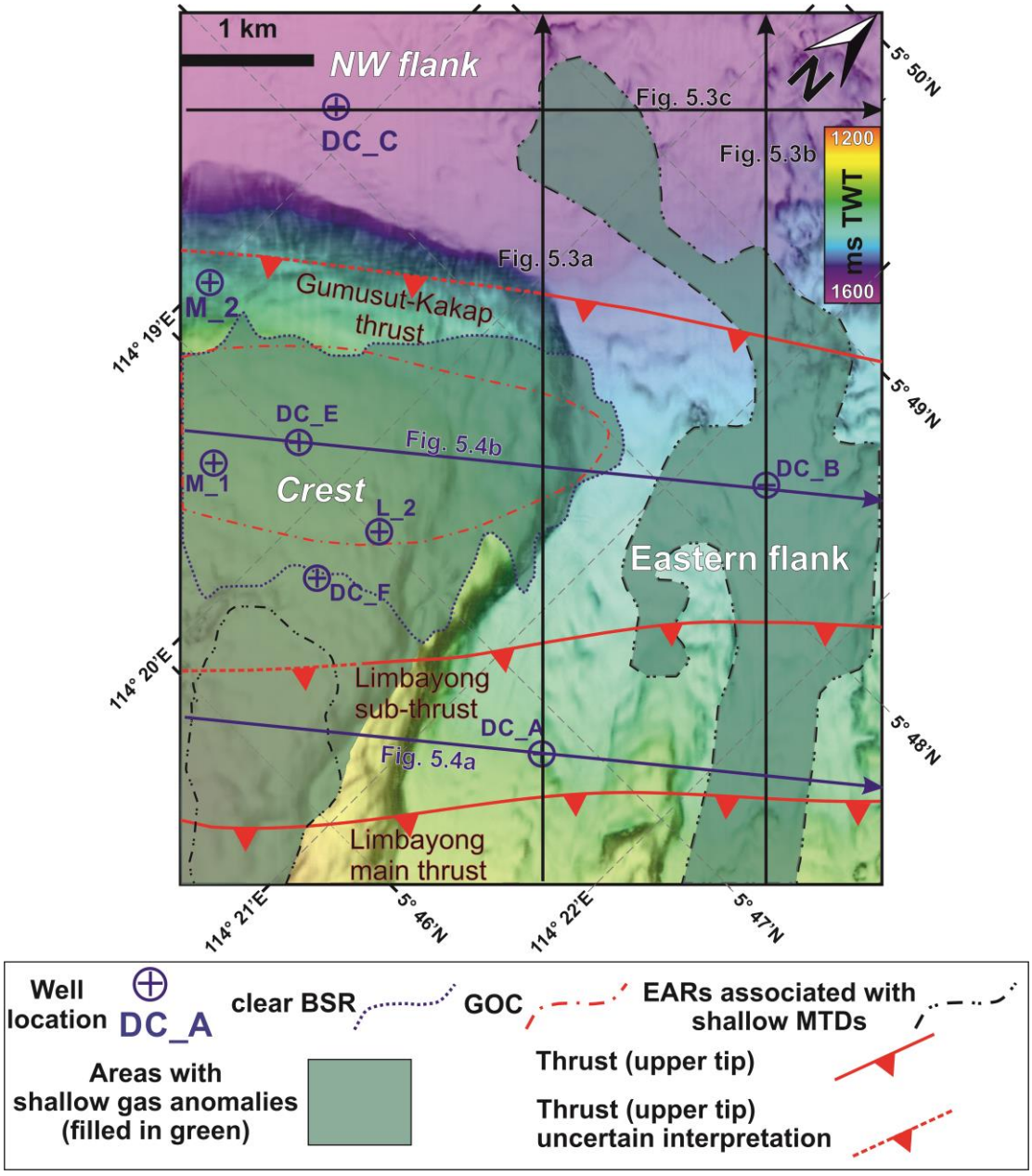



**Figure 5.1.** Blended TWT and variance bathymetric map of the study area interested by the high-resolution seismic survey. The black and blue arrows indicate, respectively, the traces of the seismic profiles in **Figs. 5.3** and **5.4**. The figure further shows the projection of the areas characterised by evidence of shallow free gas (semi-transparent green areas). The projections of the BSR at the crest of the GKL Dome, the gas-oil contact (GOC) in the GK reservoir, the enhanced amplitude reflections (EARs) associated with $MTD_1$ (at the crest of the GKL Dome), and the deep thrusts are also shown.

## 5.3. Geological setting

### *5.3.1. Seafloor geomorphology and major structures*

The study area is characterised by a complex seafloor topography, with prominent seafloor erosional canyons on the upper slope, recent mass transport deposition downslope and seafloor ridges, indicating an active fold-and-thrust belt (**Figs 5.1, 5.2**; see also **Fig. 2.5a**). On the basis of the seafloor map presented in **Fig. 5.1**, the study area is divided into three domains. The first one is the crest of the GKL Dome (see **Chapters 3 and 4**), which covers the western and southwestern part of the study area and is delimited eastward and northwestward by steep slopes. The second domain is the eastern flank of the GKL Dome, characterised by a complex seafloor, resulting from the interaction of submarine canyons and mass transport deposition. There are a few, ~600 m long, NE-SW trending shallow normal faults observed at the eastern flank of the GKL Dome, associated with the buried crest of the GK anticline. The faulting here is much less intense than over the crest (cf. **Chapter 4**). The third domain is the seaward northwestern flank of the GKL Dome, representing a classical minibasin infill, lacking any evidence of shallow faulting.

For the entire study area, I have followed the subdivision of the stratigraphic units adopted in **Chapter 4** (cf. also Ingram *et al.*, 2004; Lu and Shipp, 2011). The Upper Kamunsu and Pink Units (Late Miocene) host commercial reservoirs for oil and gas. However, the leakage of hydrocarbons from these reservoirs caused the accumulation of free gas in the more recent stratigraphic intervals which, up to the top of Unit 4, do not show lateral differences in seismic facies between the three domains described above (**Fig. 5.3**). In contrast, the more recent Units 3, 2 and 1 (Pleistocene-Holocene) show remarkable differences between the crest and the flanks of the GKL Dome, with the former dominated by clay-rich hemipelagites and subsidiary MTDs and the latter characterised by subordinate hemipelagites and thick MTDs (cf. with **Chapter 4**; see also Lu and Shipp, 2011) (**Fig. 5.4**).

### *5.3.2. The flanks of the GKL Dome: seismic stratigraphy*

The eastern flank of the GKL Dome is characterised by two partially buried canyons, evolving seaward into less confined areas (Lu and Shipp, 2011). The westernmost of these canyons is limited by the topography of the GKL Dome and is separated by a sediment ridge from the easternmost canyon. The boreholes DC_A and DC_B have been drilled in this area (**Figs. 5.1, 5.3, 5.4**).

Unit 1 and Unit 2 cover the first ~165-215 m (200-250 ms TWT) of overburden and include numerous vertically-stacked MTDs, the uppermost being up to ~75-85 m thick (~100 ms TWT). In contrast with the low amplitude and chaotic seismic facies that characterise the core of these MTDs, it is possible to recognise more continuous reflections with high amplitude at their bases and tops. Where directly stacked one above the other, the most recent MTDs frequently erode downward to cannibalise older MTDs. The degree of confinement of the MTDs with respect to the canyons diminishes both upward (i.e. in the younger sediments) and seaward. This pattern reflects a vertical and lateral change in the accommodation space and the depositional environment (Lu and Shipp, 2011). Within Unit 1, the MTDs have a more chaotic and blank internal character compared to those within Unit 2, where stratigraphic reflections are more continuous and have higher amplitudes. The canyon-filling seismic facies of Unit 2 are interpreted as a basal thalweg. The well-log data and the drilling reports (Gisler *et al.*, 2007) indicate that Unit 2 is characterised, compared to Unit 1, by an increased content of sandy and silty layers (**Figs. 5.4, 5.5a, b**).

Unit 3 shows here two main seismic facies. The upper one is represented by a homogeneously thick and internally blank package, evident landward but cannibalised by the more recent MTDs seaward. It most likely represents fine-grained clay-rich sediments, as further suggested by well-log measurements (e.g. high gamma-ray and neutron porosity) (**Figs. 5.4, 5.5a, b**). Below this blank package, the reflections are more heterogeneous and are interpreted as erosional channels and infills, embedded within hemipelagites. Seaward,

this portion of Unit 3 becomes unconfined, thicker, and characterised by more continuous and homogeneous reflections (**Figs. 5.3, 5.4**).

The MTDs on the eastern flank directly overlie the crest of the GK anticline. Immediately landward, the same MTDs overlie the structures associated with the Limbayong structure (constituted by two imbricate thrusts), whose gas in the reservoir is almost entirely composed of methane, with only 1-2% of heavier hydrocarbons (Kelley and Bishop, 2003) (**Figs. 5.1, 5.2c**).

The northwestern flank of the GKL Dome is a minibasin delimited landward by the forelimb of the GKL Dome crest and seaward by the backlimb of the Kikeh structure (**Figs. 5.1, 5.2a, 5.3c**). The borehole DC_C is drilled within this domain. Here, the most recent stratigraphy is not affected by the thrust present at the core of the Gumusut-Kakap anticline. The seismic facies present some differences compared to those at the eastern flank. The MTDs of Units 1 and 2 thin along strike, from northeast to southwest, and are equally interbedded with continuous and reflective facies, interpreted as hemipelagites. The seismic facies of Unit 3 also resemble those of Units 1 and 2 (**Figs. 5.3c** and **5.5c**). This difference between the eastern and northwestern flanks likely reflects a reduction in the accommodation space and the energy associated with mass-transport deposition.

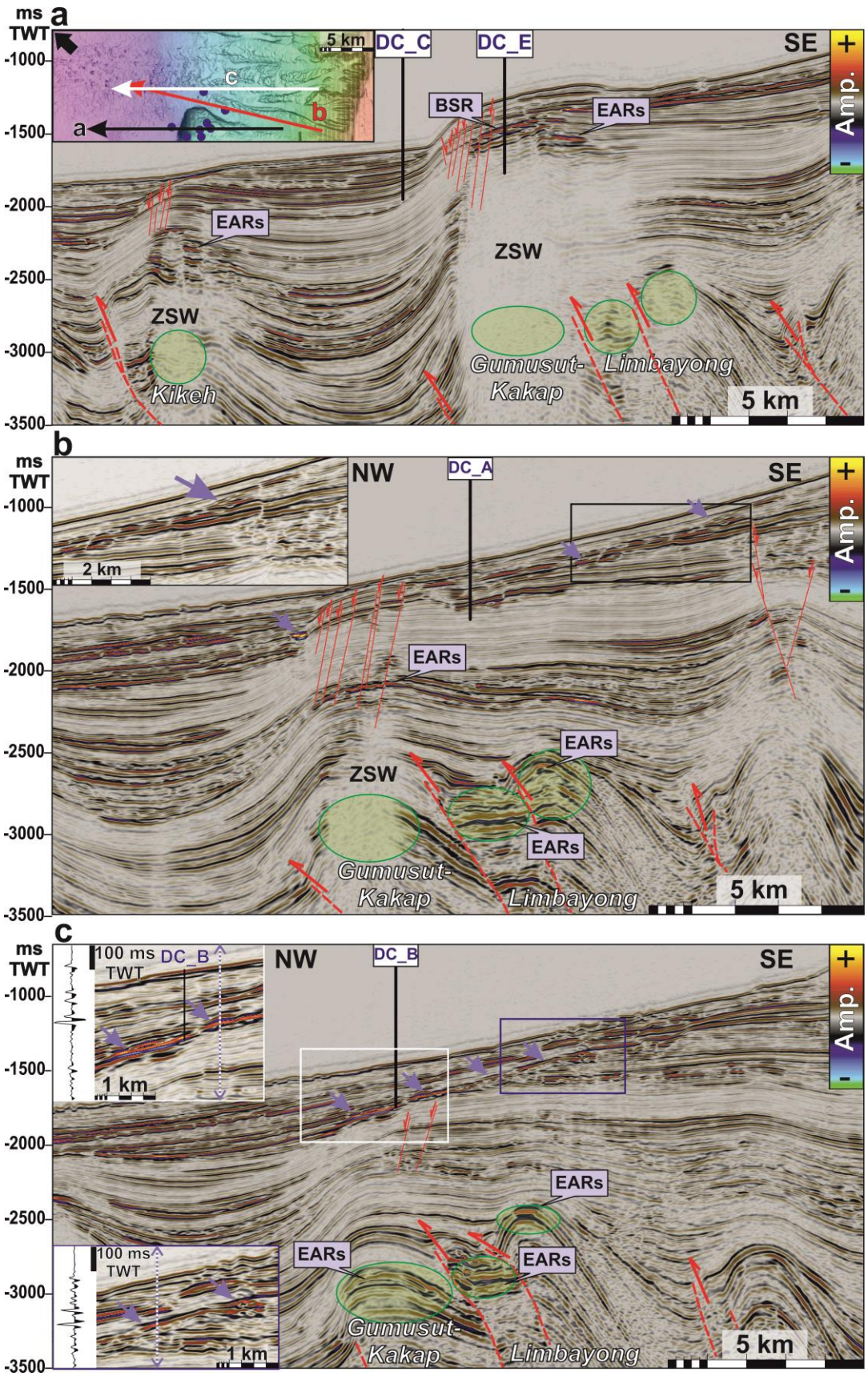



**Figure 5.2.** Regional NW-SE low-resolution seismic sections, showing the main structures and hydrocarbon reservoirs. The seafloor map in **(a)** indicates the traces of the sections. The green circles indicate the location of the deep reservoirs. The purple arrows in **(b)** and **(c)** highlight the interpreted $BS_IGHSZ$, seismically expressed as discontinuous enhanced amplitude reflections (EARs). The blow-ups in **(b)** and **(c)** are detailed views, showing a potential cross-cutting relationship between the stratigraphy and the $BS_IGHSZ$. Note also the seismic wavelets extracted from these profiles in **(c)** (location indicated by white-purple arrows). The wavelets show enhanced amplitudes and opposite polarity compared to that of the seafloor at the depths interpreted as the $BS_IGHSZ$. ZSW= zone of seismic wipeout.

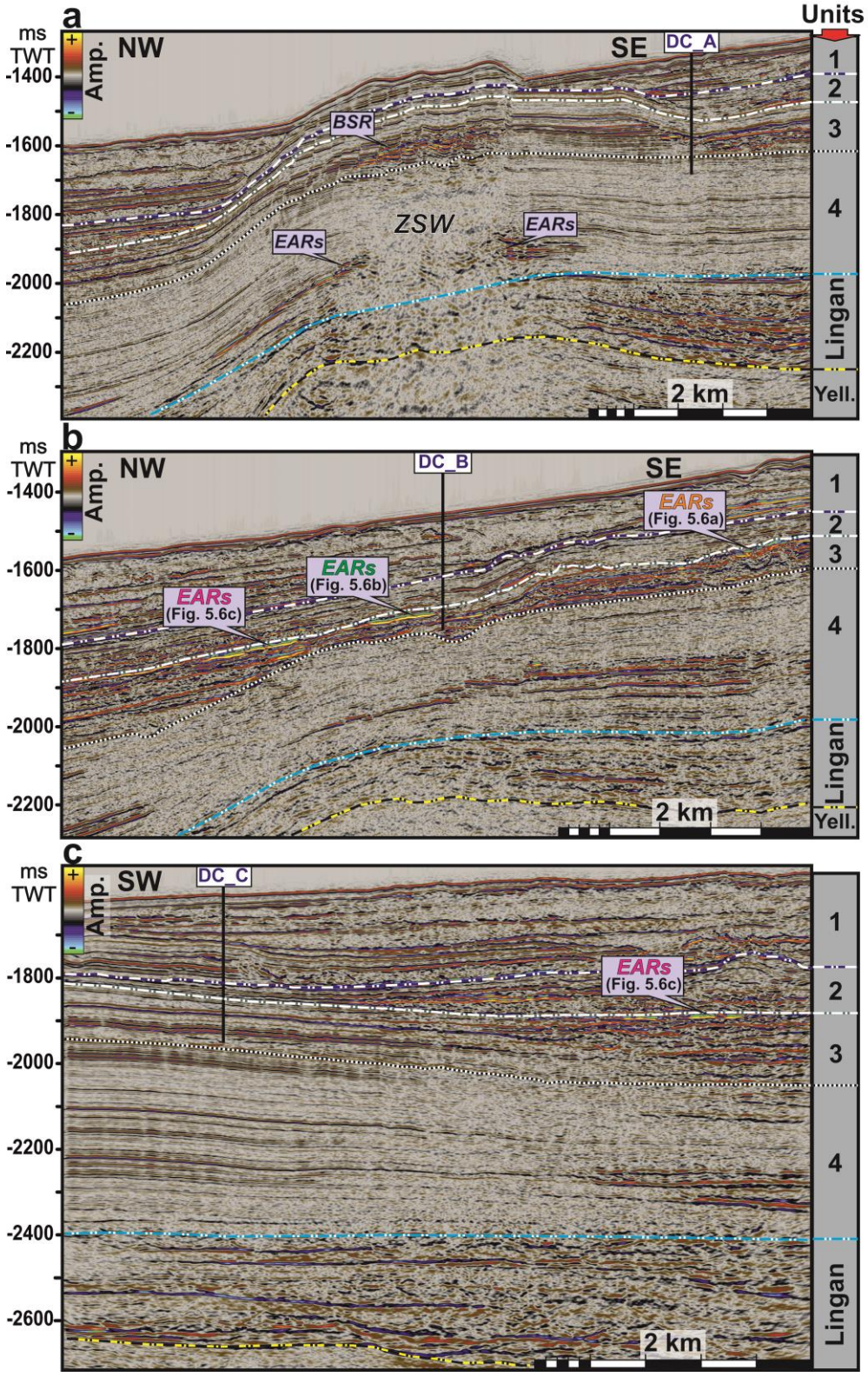



**Figure 5.3.** Representative high-resolution NW-SE **(a, b)** and SW-NE **(c)** seismic sections, covering the study area and passing through the locations of DC_A **(a)**, DC_B **(b)** and DC_C **(c)**. The boundaries of the stratigraphic units are indicated by coloured dotted, dashed-dotted and dashed-double dotted lines (see also the stratigraphic columns on the right of each section). The BSR described in the previous chapters (**3** and **4**) can be observed in **(a)**, at the crest of the GKL Dome. In contrast, in **(b)** and **(c)** it is possible to observe patchily-distributed enhanced amplitude reflections (EARs). Those EARs located at or close to the predicted $BS_fGHSZ$, and attributed to the presence of free gas, are indicated by different colours in the textbox captions (purple, green and orange). These colours refer to **Fig. 5.6**, where the gas hydrate stability boundary is modelled at in-situ pressure, temperature and salinity conditions. Finally, note the difference in seismic facies between the crest and at the flanks of the GKL Dome.

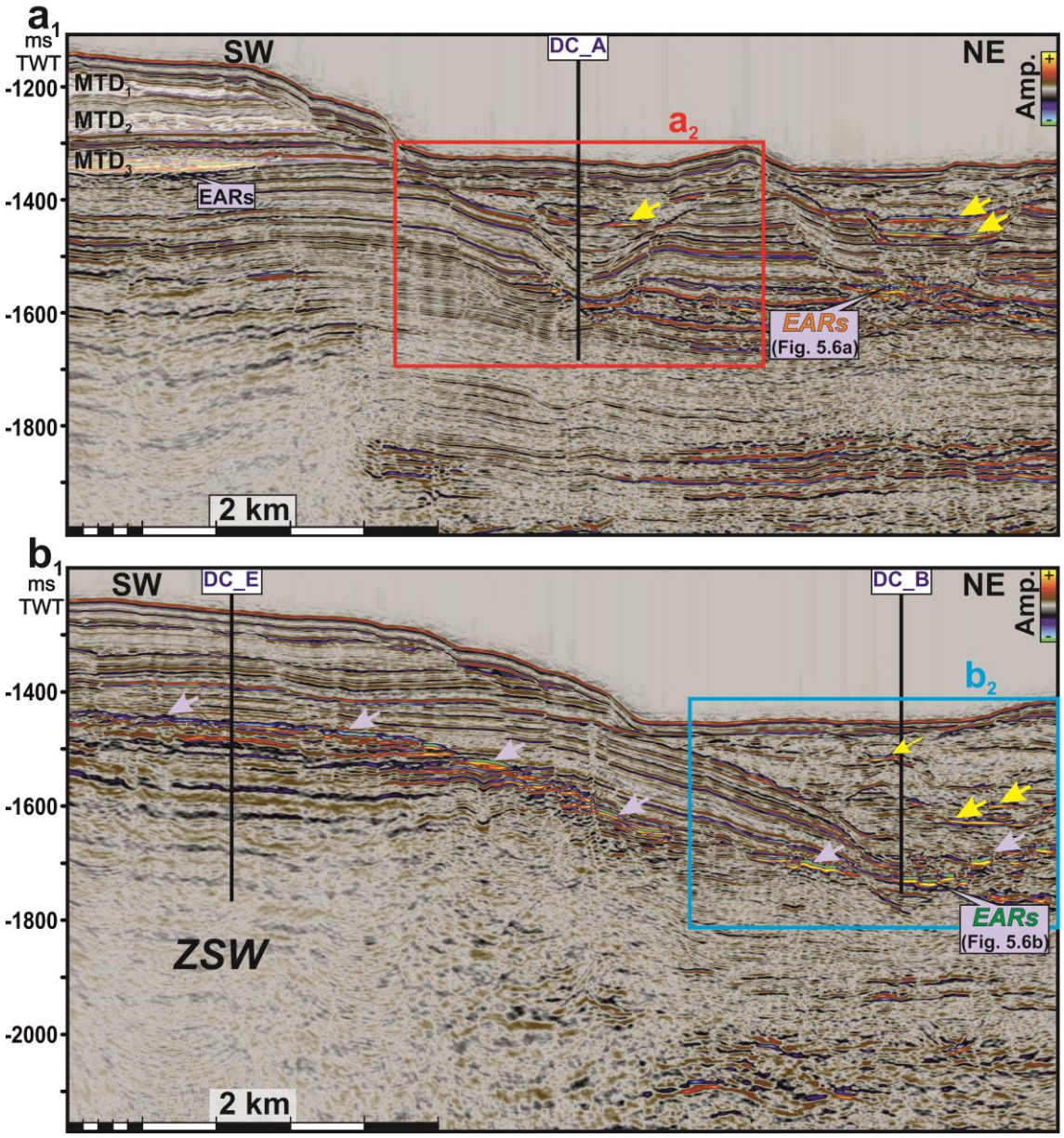



**Figure 5.4 ($a_1$ and $b_1$).** SW-NE seismic sections, passing through sites DC_E, DC_A and DC_B, showing the principal seismic characteristics of the crest and the eastern flank of the GKL Dome. See **Fig. 5.1** for the location of the seismic lines. **($a_1$)** Seismic section, located in the southern part of the study area. Note the three MTDs at the crest, within Unit 1 (see **Chapter 4**). Note the two canyons at the eastern flank. The red box indicated the close-up view shown in **($a_2$)**. **($b_1$)** Seismic section, located in the northern part of the study area. It is possible to recognise the clear BSR at the crest, as well as enhanced amplitude reflections (EARs) mimicking the seafloor morphology at the eastern flank, near DC_B. The uppermost EARs are interpreted to represent the BSlGHSZ (light-purple arrows). The blue box indicated the close-up view shown in **($b_2$)**. In **($a_1$)** and **($b_1$)** the yellow arrows indicate enhanced reflections, interpreted not to be associated with free gas but rather caused by stratigraphic heterogeneities. The EARs whose depth has been modelled in relation to the BSlGHSZ are indicated by text boxes with coloured captions. The colours used in these captions (orange, green) refer to those in **Fig. 5.6**. ZSW= zone of seismic wipeout.

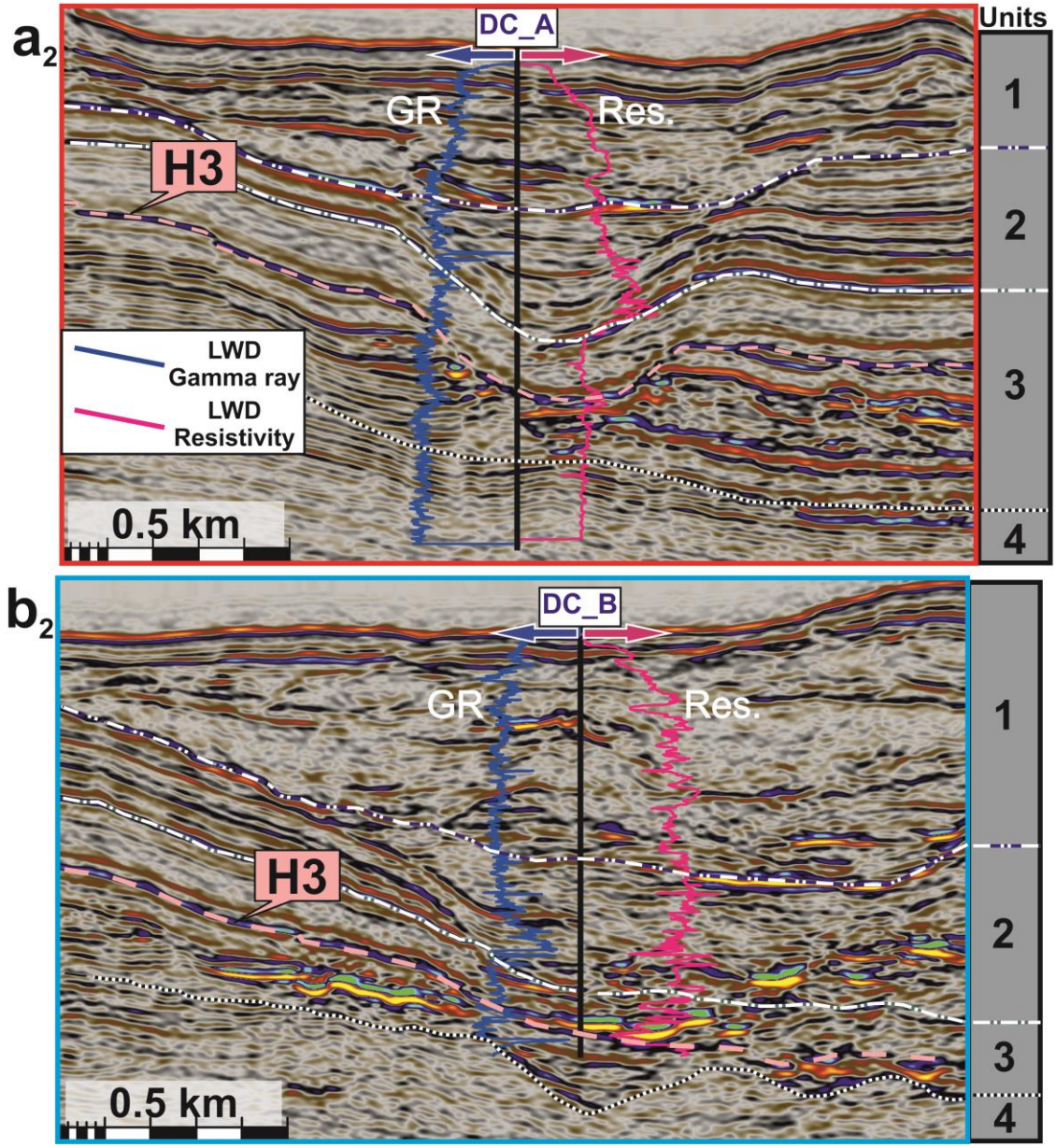



**Figure 5.4 ($a_2$ and $b_2$).** Detailed view of the seismic facies at the eastern flank of the GKL Dome. The LWD gamma-ray (GR) and deep propagation resistivity (Res.) logs at DC_A and DC_B have been tied to the seismic and shown in these figures (see **Fig. 5.5** for the complete well-log panels). Horizon 3 (H3, located within Unit 3) is indicated by a pink dashed line (see the attribute maps in **Fig. 5.8**). The well data is tied to seismic thanks to interval velocity data provided by Shell.

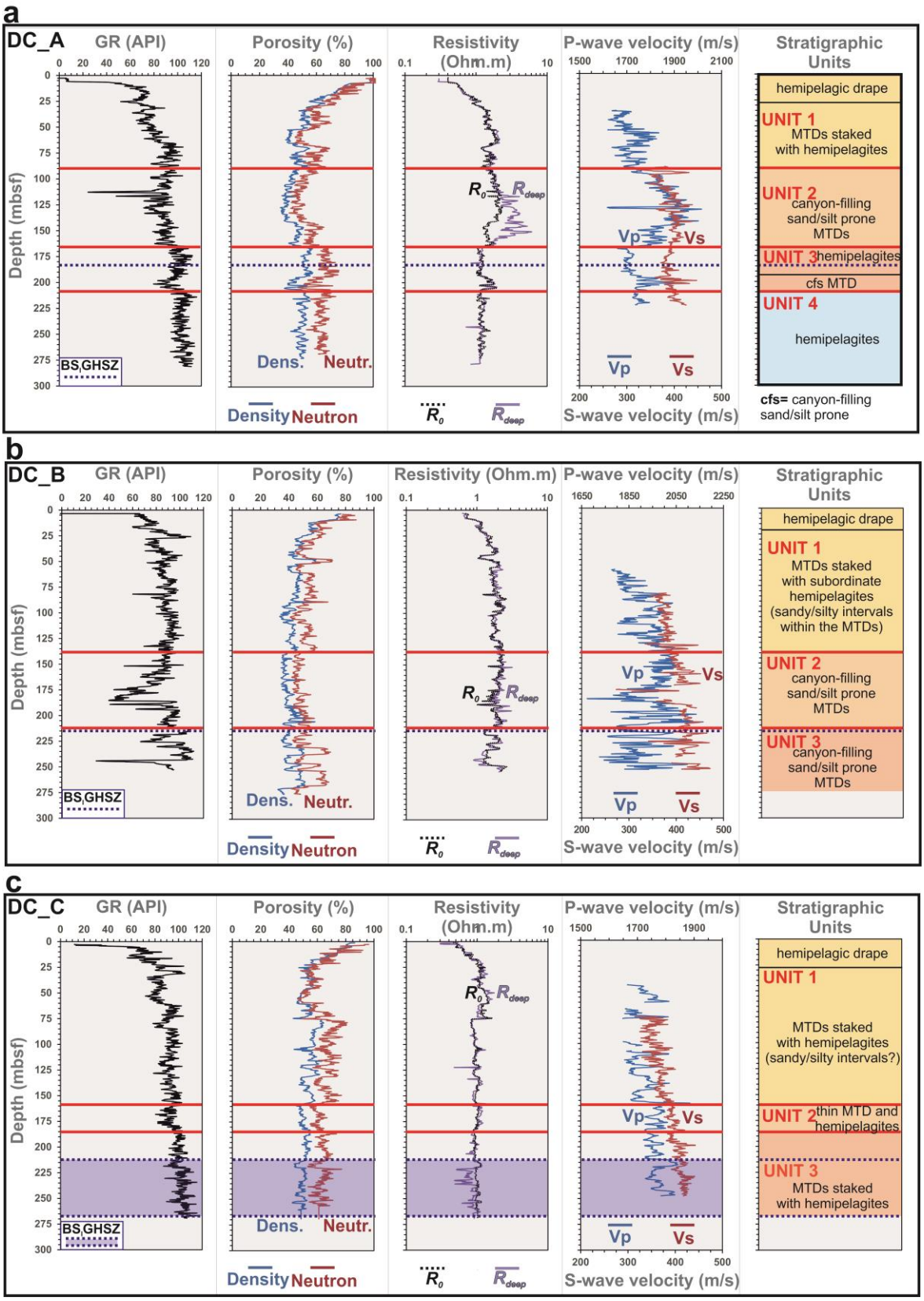



**Figure 5.5.** Gamma-ray, porosity (density and neutron), resistivity ($R_{deep}$) and velocity data, extrapolated from LWD and WL logs acquired at DC_A **(a)**, DC_B **(b)** and DC_C **(c)**. The lithological interpretation is shown in the panels on the right. The modelled $BS_IGHSZ$ is plotted for DC_A and DC_B (blue dotted line) whereas, given the uncertainties related to the geothermal gradient, the pore water salinity and the seafloor temperature, an interval where the $BS_IGHSZ$ could occur is instead shown for DC_C (semi-transparent purple areas). GR= gamma-ray; Dens.= density porosity; Neutr.= neutron porosity; $R_0$= extrapolated resistivity of a 100% water-filled sediment (see **sub-paragraph 5.2.3**); $R_{deep}$= measured resistivity (deep propagation resistivity); Vp= P-wave velocity; Vs= S-wave velocity.

## 5.4. Results

### *5.4.1. Distribution of the amplitude anomalies*

Several enhanced amplitude reflections (EARs) have been identified within Unit 3 and, locally, in the lowermost part of Unit 2. These EARs are stacked with lower amplitude reflections into ~80 m thick (~100 ms TWT) packages, and their polarity is opposite compared to that of the seafloor. These EARs are patchily distributed on the eastern flank of the GKL Dome. For instance, numerous EARs are observed in the vicinity of DC_B but are lacking around DC_A (**Figs. 5.3b, c, 5.4**). A continuous BSR is not observed at the flanks of the GKL Dome. However, the combined morphology of these EARs mimics the seafloor, although discontinuously (**Fig. 5.4b$_1$**). Assuming a 1650 m/s interval velocity, the uppermost EARs for each stacked package vary in depth from ~170 to 235 mbsf. This depth range fits with a BS$_I$GHSZ, with boundary conditions constrained by in-situ temperature and pore water salinity measurements at DC_A and DC_B (**Figs. 5.6, 5.19** and **Tabs. 5.4, 5.5**).

A few representative EARs within units 2 and 3 have been mapped in detail, and their RMS amplitude has been extracted (**Fig. 5.7**). In these maps, it is possible to distinguish narrow high amplitude zones along the canyons and lobe-shaped high amplitude zones in the unconfined areas downslope. Similar observations have been made by integrating the TWT topography, the variance and the RMS amplitude maps of two more continuous stratigraphic horizons, stratigraphically located above these EARs (i.e. the base of Unit 2 and Horizon 3, see **Fig. 5.4a$_2$, b$_2$**). By applying an investigation window of 30 ms TWT beneath the mapped horizon, multiple EARs are captured in the same image, including those underlying the BSR at the crest of the GKL Dome (**Fig. 5.8a$_2$, b$_2$,** see **Chapter 4**).

At the base and the top of the shallow MTDs, the reflections are commonly enhanced. Such enhanced reflections are shallower than the extrapolated BS$_I$GHSZ, do not mimic the seafloor and are embedded within seismically blank and chaotic MTDs (**Fig. 5.4a$_1$, b$_1$**). Their amplitude, although higher than that of the surrounding MTDs, is visually lower than

the amplitude of the EARs previously described. These shallow reflections appear purely stratigraphic and probably represent water-bearing and poorly consolidated sediments which interrupt a succession otherwise dominated by blank and chaotic seismic facies.

The lower frequency seismic data allows imaging a still patchy but relatively clear BSR at the eastern flank of the GKL Dome. This BSR overlies the buried crests of the GK anticline and the Limbayong structure, becoming shallower landward along the slope and disappears seaward, at the forelimb of the GK anticline. This BSR is constituted by the alignment of the shallowest portions of the EARs previously identified and occasionally displays a cross-cutting relationship with the host stratigraphy (**Fig. 5.2b, c**).

Deeper in the stratigraphy, above the deeper commercial reservoirs, there are other packages of EARs, exhibiting a polarity opposite to that of the seafloor (**Fig. 5.2b**), thus interpreted as free gas-bearing sediments. This interpretation is supported by the detection of gas and water flows during the drilling of industry wells (Lu *et al.*, 2005). The hydrocarbon-bearing units constituting the commercial GK and Limbayong reservoirs are further seismically visible as prominent high amplitude *'soft'* anomalies (i.e. producing a negative acoustic impedance contrast) at the top of the anticlines (**Fig. 5.2b, c**). Nevertheless, the eastern flank of the GKL Dome lacks any compelling evidence of vertically focused cross-stratal fluid flow, both at the seafloor and in the overburden. Also, the projection of the gas-oil contact (GOC) in the GK reservoir does not cover the flanks of the GKL Dome (**Fig. 5.1**). At the northwestern flank, similarly to the eastern flank, vertical fluid flow features are absent (**Fig. 5.3c**). Furthermore, there are no EARs in the first few hundred metres of overburden, with a single exception at the boundary with the eastern flank. This domain does not show any evidence of deep hydrocarbon accumulation at depth, being located seaward with respect to the GK anticline and the Lymbayong structure **(Fig. 5.1**).

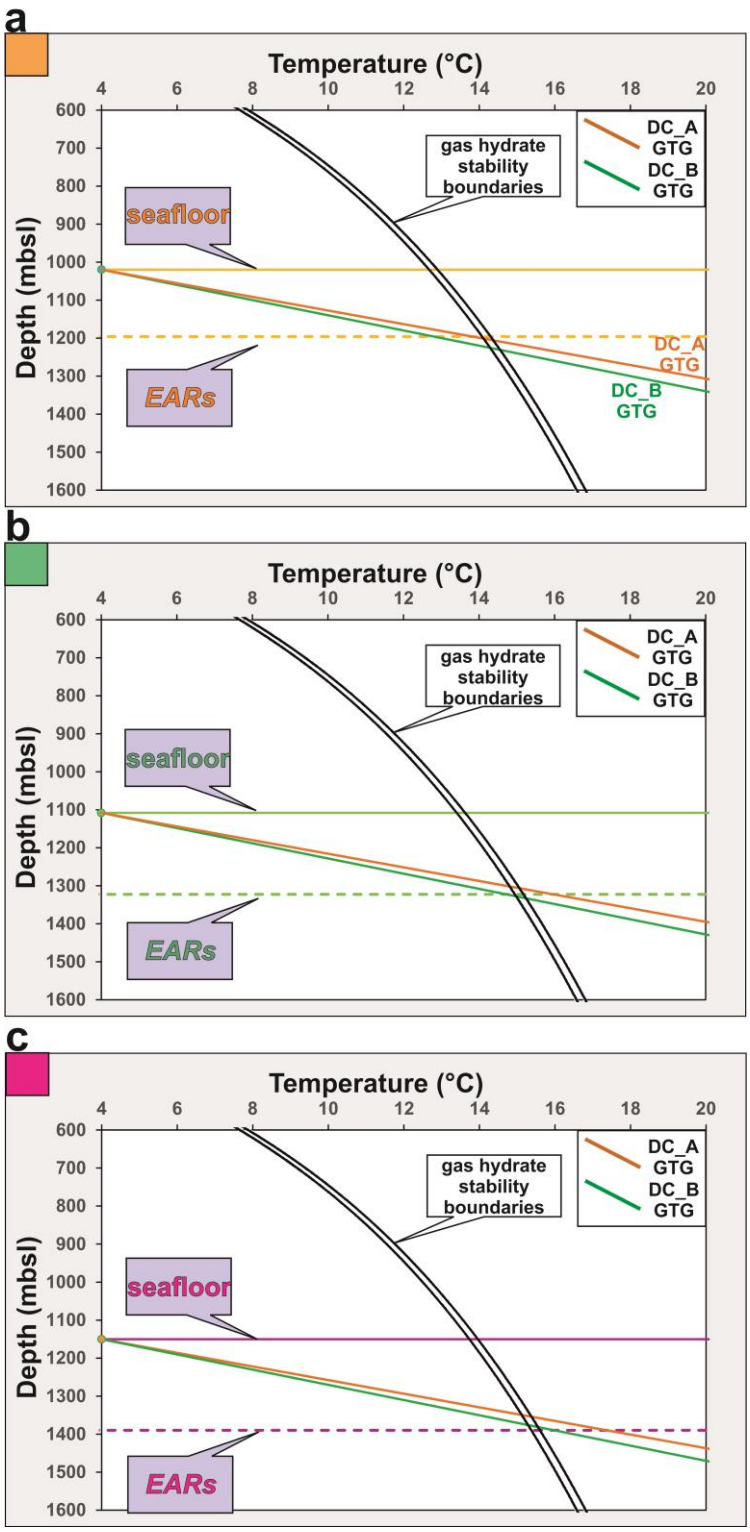



**Figure 5.6. (a-c)** Gas hydrate stability modelling in relation to the depth of three enhanced amplitude reflections (EARs) observed at different water depths along the eastern flank of the GKL Dome (see **Figs. 5.3** and **5.4**). I have extrapolated two gas hydrate stability boundaries for pure methane hydrate ($S_I$) and pore water salinities of 2.0% and 2.5%, respectively. The two plotted geothermal gradients reflect the direct measurements along the boreholes DC_A and DC_B (**Fig. 5.19**). The assumed P-wave interval velocity (i.e. from the seafloor down to the depth of the EARs) is 1650 m/s, in line with interval velocity data provided by Shell. The results show that the top of these EARs matches well with the modelled $BS_IGHSZ$. GTG= geothermal gradient.

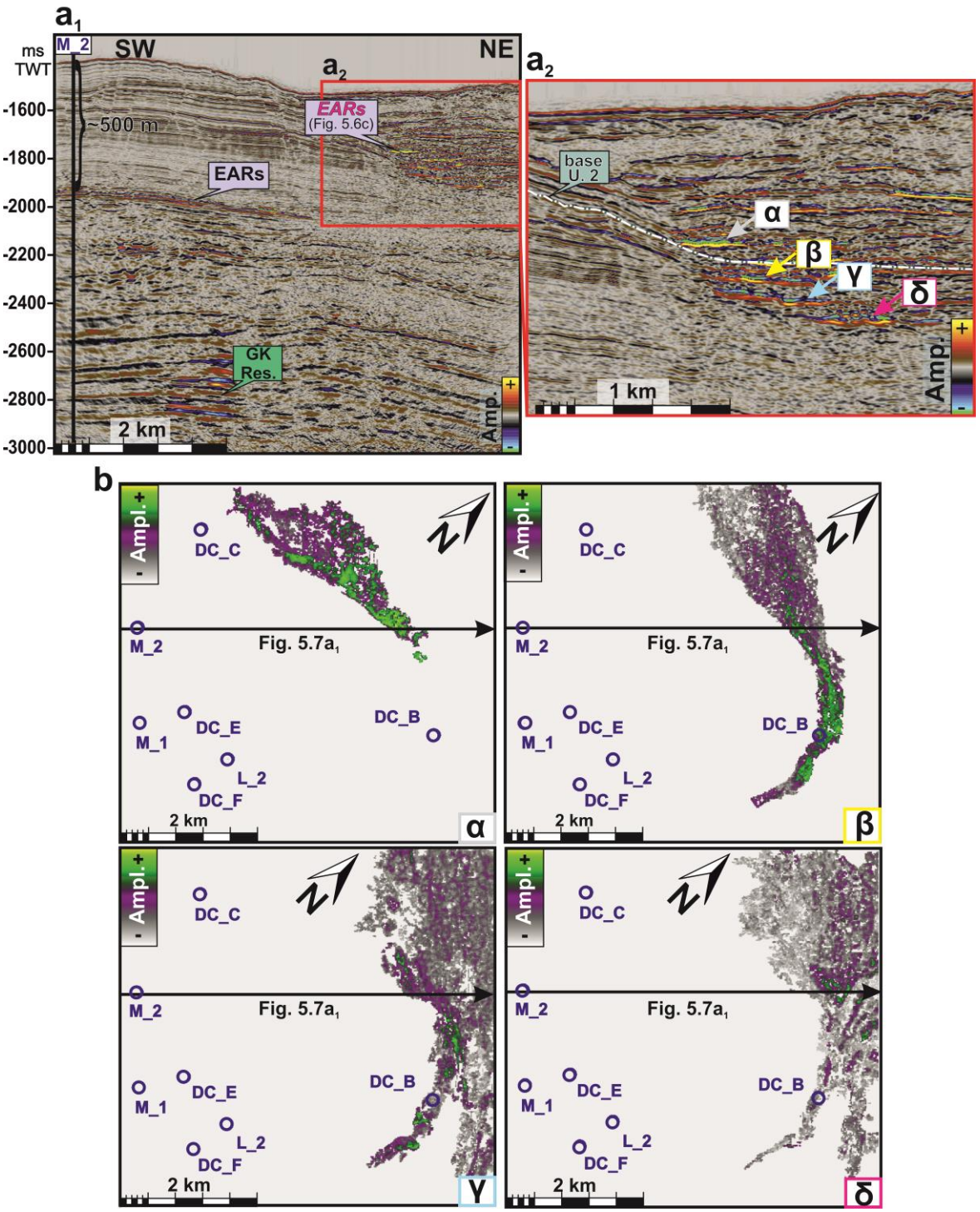



**Figure 5.7.** Amplitude characteristics of the enhanced amplitude reflections (EARs) at the eastern flank of the GKL Dome. **($a_1$)** SW-NE Seismic section passing through the borehole M_2 (no evidence of hydrates was observed in the resistivity log of this well, see **Fig. 4.5b**). Numerous shallow EARs are observed at the flank of the GKL Dome (red box) and are highlighted in the blow-up view in **($a_2$)**. Several deep EARs have also been identified in this portion of the crest, from ~500 mbsf, down to the GK reservoir (GK Res.). These EARs are too deep to represent the BGHSZ for $S_{II}$ and $S_H$ hydrates and are interpreted as stacked free gas reservoirs. **(b)** RMS amplitude maps of the EARs named α, β, γ and δ (see **($a_2$)**), showing narrow high amplitude zones in the canyons evolving into lobe-shaped high-amplitude zones downslope. The black arrows indicate the seismic trace of the section shown in **($a_1$)**.

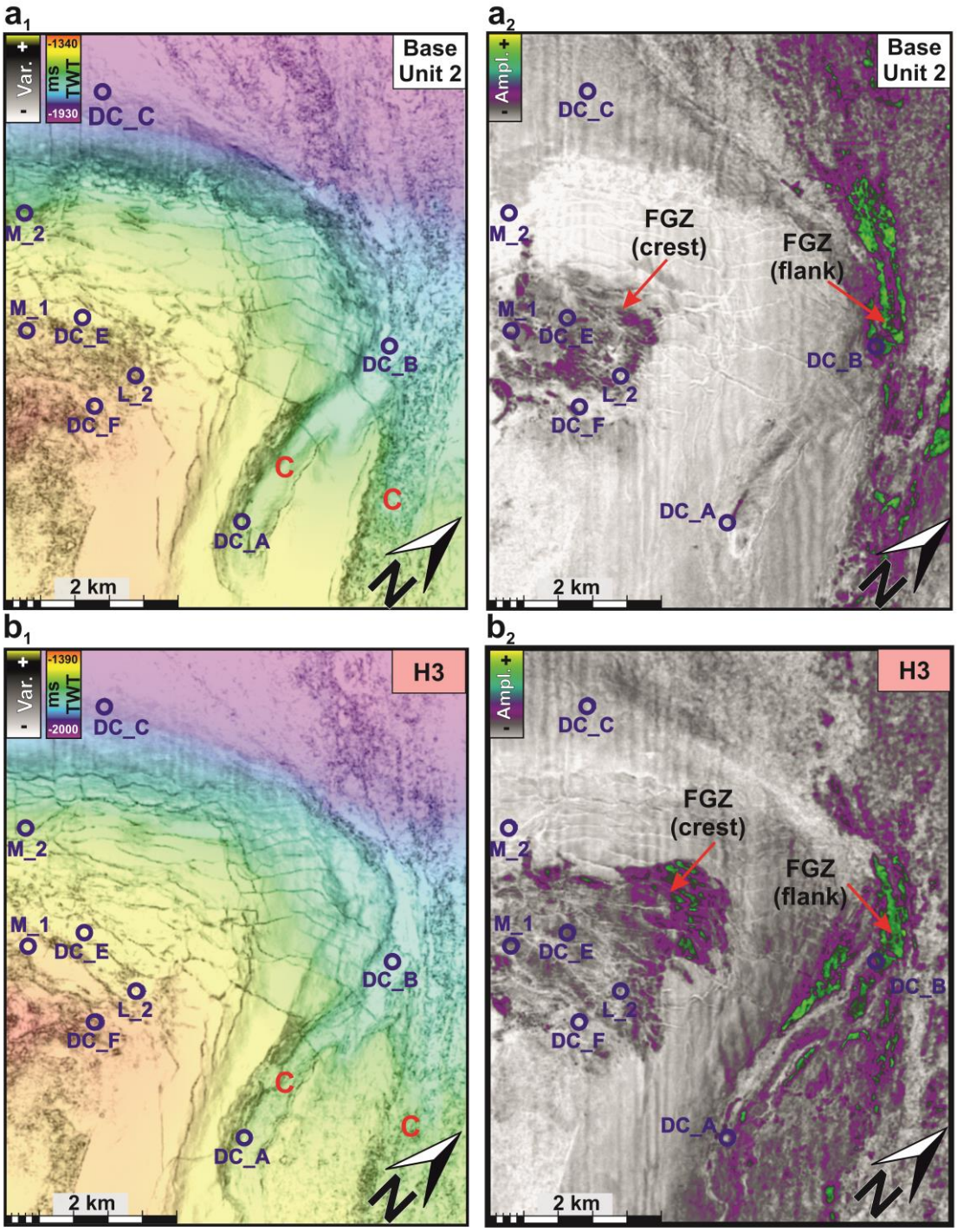



**Figure 5.8.** Attribute maps of the base of Unit 2 and Horizon 3 (H3) (See **Fig. 5.4** for the stratigraphic location of these horizons). **($a_1$, $b_1$)** Blended TWT and variance maps. Note the two canyons (C) at the eastern flank of the GKL Dome evolving into wider depositional areas downslope. Note also the intense faulting at the crest, as well as the increased variance within the free gas zone beneath the BSR (cf. with **a2** and **b2**), due to the reduced quality of seismic data. **(a2, b2)** RMS amplitude extractions with an investigation window of 30 ms TWT below the mapped horizon. High amplitude anomalies are present both at the crest and at the eastern flank of the GKL Dome (green and purple colours) and are representative of the distribution of free gas beneath the $BS_I$GHSZ.

### *5.4.2. Gas hydrate distribution at the flanks of the GKL Dome*

#### *5.4.2.1. Evidence from core data*

At DC_A, a total of 12 pressure cores (7 successful) and 32 non-pressurised cores have been recovered from a ~230 m thick interval (**Tabs. 5.4** and **5.6**). The $BS_IGHSZ$ is predicted to be at ~180 mbsf, considering the seafloor temperature (4.2 °C) and geothermal gradient (55.8 °C/km) (**Figs. 5.9a, b, 5.19** and **Tab. 5.1)**. The sulphate profile is *'kink-shaped'*, and the sulphate-methane transition zone (SMTZ) is at 14-20 mbsf (**Fig. 5.11a**).

A ~32 m thick gas hydrate-bearing interval (~128-160 mbsf) is recognised by comparing the measured (*Cm*) *vs 'baseline'* (*Cb*) chlorinity profiles (**Figs. 5.9a, b**). This interval is located at the base of Unit 2, within a canyon infill. The average *Sh* within this interval is 9.3%, with the highest values measured along two FC cores, at 134.5 mbsf (35.8%) and 150.5 mbsf (74.3%) (**Fig. 5.9c**). At the core-scale, hydrates concentrate in ~5-10 cm thick beds, with *Sh* frequently exceeding 20%. In contrast, the majority of the core has low to zero *Sh* (<5%) (**Fig. 5.9d, e**). The *Sh* extrapolated with the mass balance approach in FPC cores does not highlight these small-scale heterogeneities and provides only low average values of *Sh* for each core (**Fig. 5.9b**). The MSCL measurements on FPC cores reveal a correlation between the locations along the cores of highest *Sh* and thin zones of enhanced P-wave velocity (**Fig. 5.9d, e**). In contrast, hydrates are almost invisible in the X-ray images, as they do not produce detectable density changes. A single exception is the central portion of FPC-A#06, which in its central portion displays relatively low values of gamma density and is brighter in X-ray (**Fig. 5.9d**).

There is no evidence of either hydrates or free gas near or below the predicted $BS_IGHSZ$, given the absence of anomalous P-wave velocities, elevated methane concentrations, as well as IR and chlorinity anomalies. Beneath this interface, the *Sh* estimated from chlorinity measurements is less than 4%. These low values most likely reflect a locally slightly overestimated *Cb* (**Fig. 5.9a, b**).

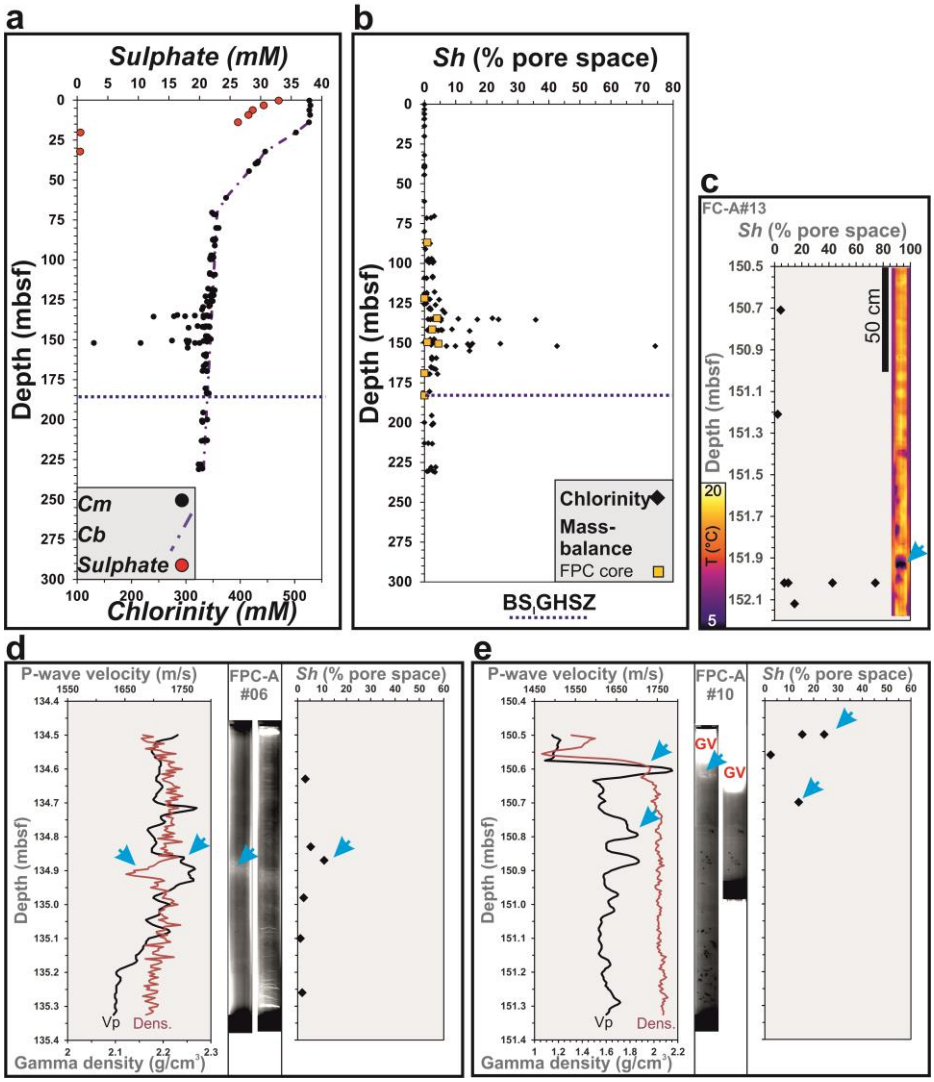



**Figure 5.9.** Core evidence of gas hydrates at DC_A. **(a)** Chlorinity and sulphate profiles. Chlorinity anomalies are localised between 128 and 160 mbsf. The SMTZ is at 14-20 mbsf (see **Fig. 5.11a**). **(b)** *Sh* profile. *Sh* is estimated from chlorinity anomalies and with the mass-balance approach. **(c)** IR thermal image of an FC core (FC-A#13), retrieved at ~150.5 mbsf, displaying evidence of cooling due to hydrate dissociation upon retrieval in the form of a clear cold spot at ~152.0 mbsf, and minor cold spots elsewhere. *Sh* is estimated from chlorinity measurements, and the highest value (74.3%) correlates with the clear cold spot at 151.9 mbsf. **(d, e)** X-ray images of FPC-A#06 and FPC-A#10, retrieved at ~134.5 mbsf and 150.5 mbsf, respectively, with MSCL measurements (P-wave velocity and gamma density) and *Sh* estimates from chlorinity measurements. The X-ray images on the left are of cores before depressurisation. The X-ray images on the right are of cores after depressurisation. Note the presence of localised intervals with enhanced P-wave velocity and *Sh* (blue arrows). The density is also slightly decreased at the centre of FPC-A#06 where *Sh* is the highest along this core. A gas void (GV) is present at the top of FPC-A#10 in both the X-ray images and results in low densities and velocities, probably due to an imperfect preservation of the hydrate stability conditions at the top of the core, upon recovery. Vp= P-wave velocity; Dens.= gamma density.

At DC_B, a total of 7 pressure cores (6 successful) and 41 non-pressurised cores have been retrieved from a ~218 m thick interval (**Tabs. 5.5 and 5.7**). The $BS_IGHSZ$ is predicted to be at ~215 mbsf, considering the seafloor temperature (3.7 °C) and the geothermal gradient (50.0 °C/km) (**Figs. 5.10a, b, 5.19** and **Tab 5.1)**. The sulphate profile appears *'S-shaped'*, with the SMTZ being at 8-10 mbsf (**Fig. 5.11b**).

The chlorinity measurements indicate that hydrates occur from 48 to 199 mbsf, with an average *Sh* of 6.4%. Within this zone, there are two main intervals with enhanced *Sh*, at 48-62 and 171-185 mbsf, respectively (**Fig. 5.10a, b**). The average *Sh* is 14.8% for the shallower interval whereas it is 11.5% for the deeper one. At the core-scale, observations are similar to those made at DC_A. Hydrates are either absent or at low *Sh* (<5%), except for ~5-10 cm thick beds, where *Sh* exceeds 20-50% (**Fig. 5.10c-f**). The maximum saturation, for the shallower and deeper intervals, is 88.6% (48 mbsf) and 71.2% (183 mbsf), respectively. These observations suggest that the pore space was almost entirely occupied by hydrates, although only along limited cm-thick portions of the cores. No clear evidence of hydrates exists above 48 and below 199 mbsf, where *Cm* approaches *Cb* (**Fig. 5.10b**). Similarly to DC_A, no hydrates occur at and beneath the modelled $BS_IGHSZ$. The MSCL measurements on FPC cores further reveal that enhanced P-wave velocities characterise the thin beds with the greatest *Sh*. However, hydrates are still invisible in X-ray, although gas voids can appear by depressurising the formerly hydrate-bearing sediments (**Fig 5.10d-f**).

It is important to remember that the sulphate profile at DC_E, located at the crest of the GKL Dome, exhibits a slightly *'concave-up'* shape, with an SMTZ located at 10-12 mbsf (**Chapters 3** and **4**) (**Fig. 5.11c**). At DC_C, coring operations were not planned. The $BS_IGHSZ$ is interpreted to be located between ~210 and 265 mbsf, on the basis of the temperature and salinity conditions at DC_A and DC_B (**Figs. 5.5c, 5.13c**).

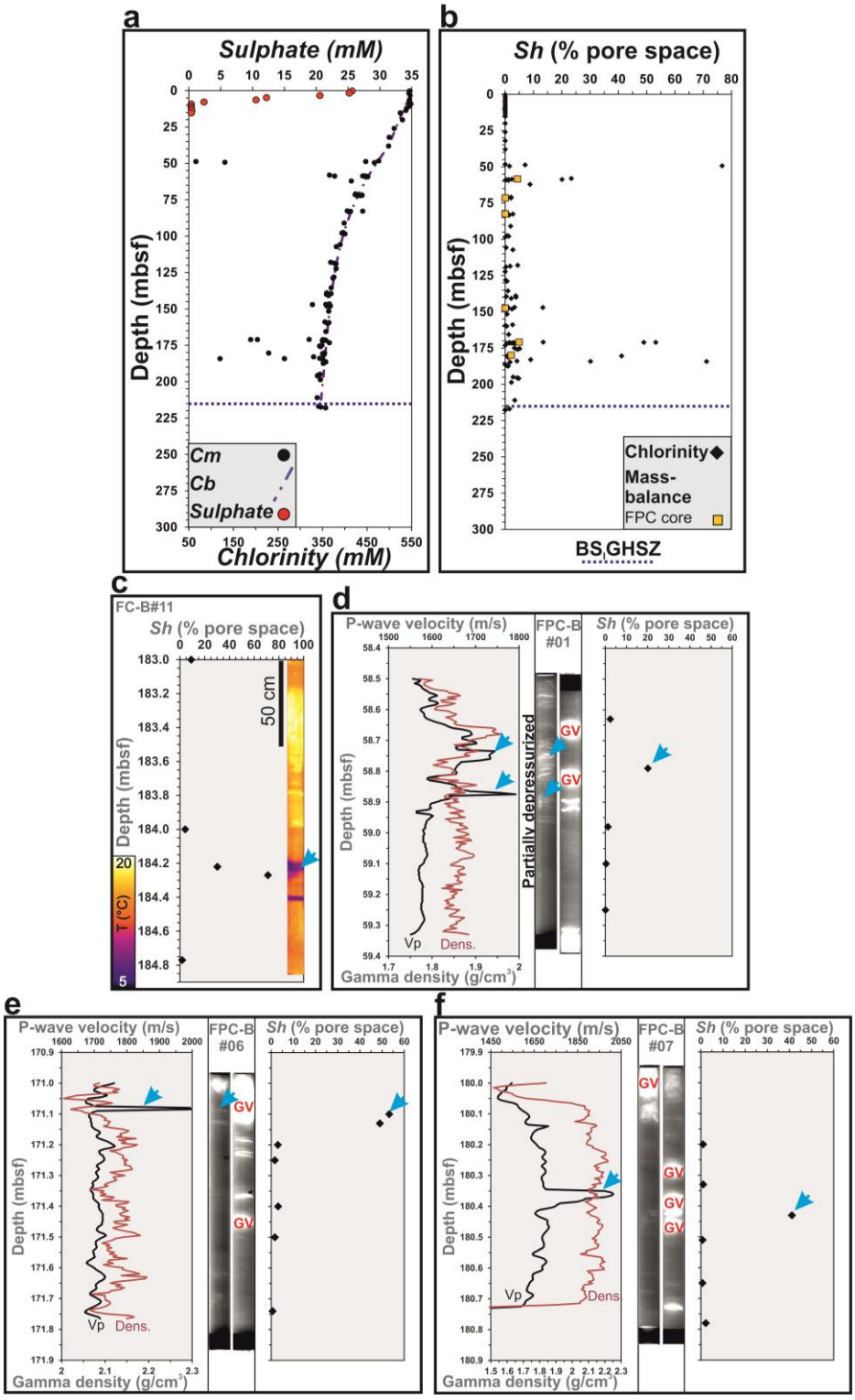



**Figure 5.10.** Core evidence of gas hydrates at DC_B. **(a)** Chlorinity and sulphate profiles. Chlorinity anomalies occur within two intervals (48-62 mbsf and 171-185 mbsf). The SMTZ is at ~8-10 mbsf (see **Fig. 5.11b**). **(b)** *Sh* profile. *Sh* is estimated from chlorinity anomalies and with the mass-balance approach. **(c)** IR thermal image of an FC core (FC-B#11) retrieved at ~183.0 mbsf, with evidence of cooling due to hydrate dissociation upon retrieval, in the form of two cold spots at 184.2 and 184.4 mbsf. *Sh* is estimated from chlorinity measurements at different levels along the core, with the highest value (71.2%) associated with the cold spots. **(d-f)** X-ray images of FPC-B#01, FPC-B#06 and FPC-B#07, retrieved at ~58.5, 171.1 and 180.0 mbsf, respectively, with MSCL measurements (P-wave velocity and gamma density) and *Sh* estimates from chlorinity measurements. The X-ray images on the left are of cores before depressurisation, except for that of FPC-B#01, taken after partial depressurisation. The X-ray images on the right are of cores after depressurisation. Note the presence of localised intervals with enhanced P-wave velocity and *Sh* (blue arrows). Gas voids (GV) appear as bright spots in X-ray images taken after depressurisation. The gas voids observed before depressurisation are likely due to an imperfect preservation of hydrate stability conditions during the core recovery. Vp= P-wave velocity; Dens.= gamma density.

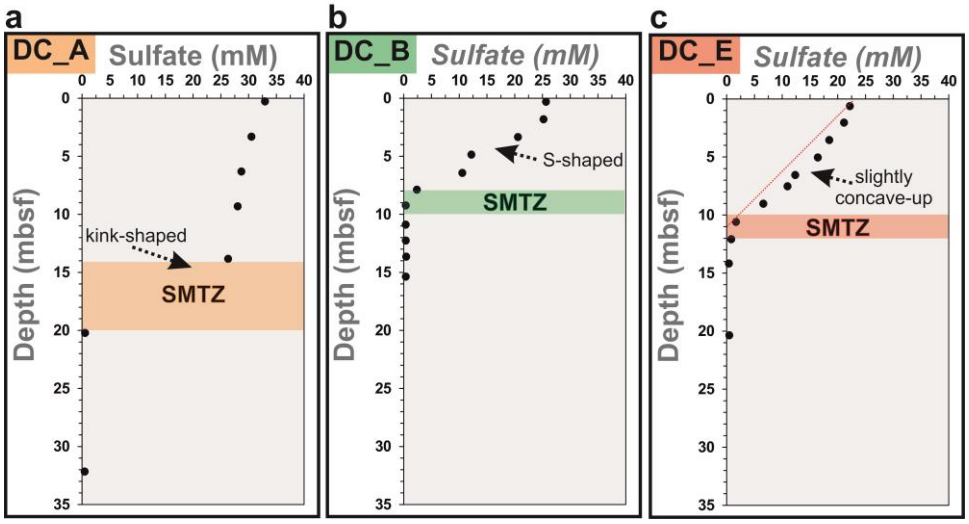



**Figure 5.11.** Sulphate profiles at DC_A **(a)**, DC_B **(b)**, and DC_E **(c)**. The sulphate-methane transition zone (SMTZ) is located at 14-20 mbsf at DC_A, at 8-10 mbsf at DC_B and at 10-12 mbsf at DC_E. The shape of the sulphate profile is *'kink-shaped'* at DC_A, *'S-shaped'* at DC_B and slightly *'concave-up'* at DC_E (note the difference between the data and an extrapolated linear trend, marked with a red line).

A P-wave velocity *vs Sh* plot has been extrapolated, by using MSCL measurements and hydrate saturation data extrapolated from chlorinity, from selected FPC cores, recovered at depth comprised between 135 and 150.5 mbsf for DC_A and between 148 and 180.5 mbsf for DC_B (**Fig. 5.12**). This choice guarantees to capture the zone where the highest *Sh* occur and the sediments have a similar porosity (~40-45%). Due to uncertainties in correlating the P-wave velocity with *Sh*, each *Sh* value is associated with a P-wave velocity value obtained from an average over a ~3-10 cm interval, considered to match the position along the core where the pore water sample was taken (the error bars in **Fig. 5.12a-d** indicate the minimum and maximum P-wave velocity measured along these intervals). This method results in a roughly linear P-wave velocity *vs Sh* trend ($R^2$=0.8). The plotted data (**Fig. 5.12a-d**) can be associated with the theoretical curves for GHBS with a pore-filling suspension and a load-bearing micro-habit. Thes curves have been calculated for four different scenarios, which illustrate the possible variations in the effective stress of the pressure cores upon recovery (~0-0.22 MPa), by using XRD-calibrated bulk modulus, shear modulus, and grain density data reported in a confidential study conducted in this area on the rock physic response of shallow gas-bearing sediments (Bryndzia *et al.*, 2005; see also Couzens-Schultz and Azbel, 2014). Nevertheless, this interpretation should be treated cautiously, considering both the lack of in-situ mineralogical and effective stress data for rock-physics model constraints.

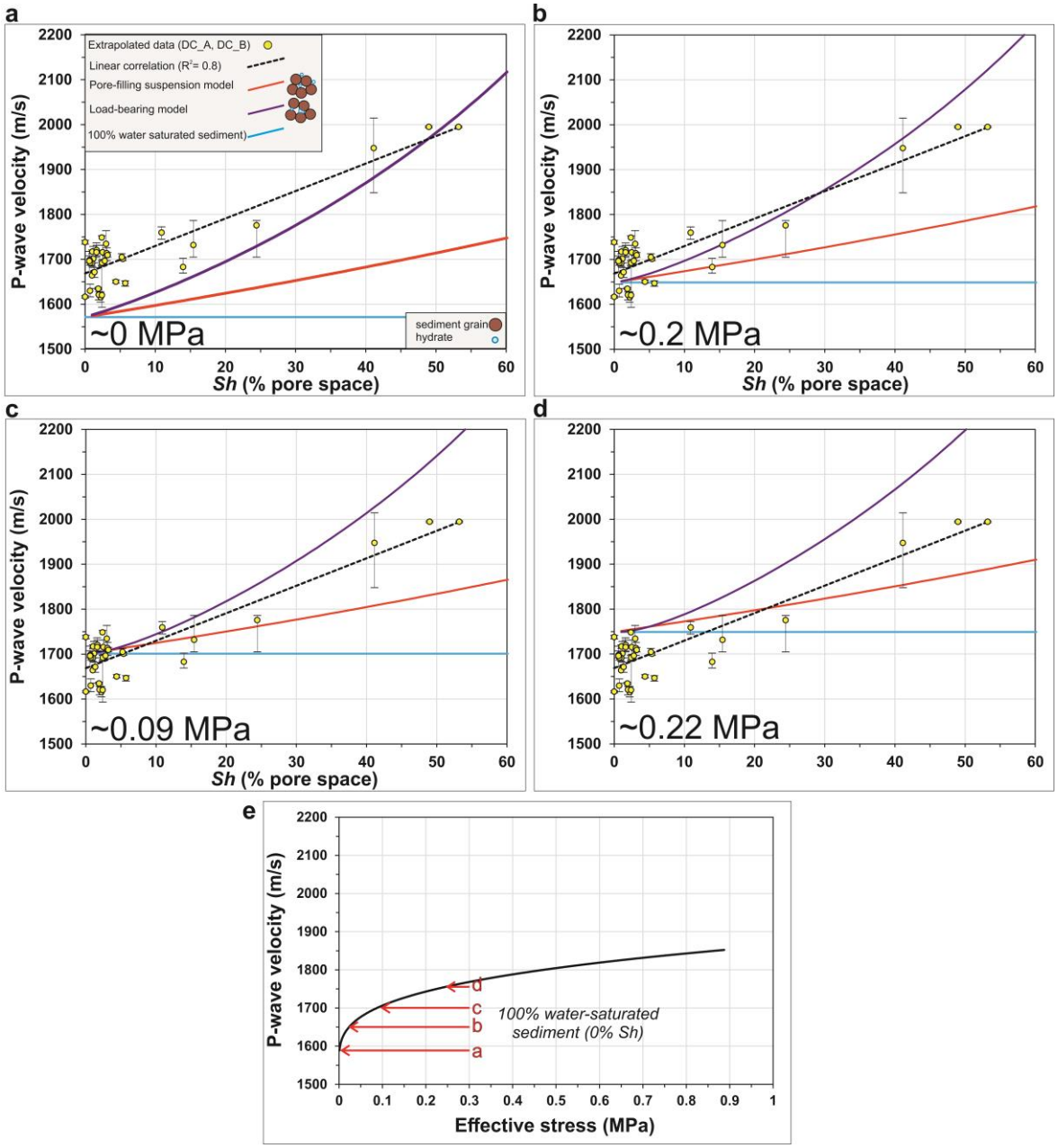



**Figure 5.12.** P-wave velocity vs hydrate saturation (*Sh*) estimated from selected MSCL and chlorinity measurements on FPC cores at DCA_ and DC_B (yellow circles). The black vertical error bars indicate the uncertainty in the correlation between P-wave velocity and *Sh*. The theoretical curves have been modelled following an effective-medium theory at different conditions of effective stress **(a-d)** (Helgerud *et al.*, 1999; Helgerud, 2001). The input parameters for the rock physics models (i.e. average bulk modulus, shear modulus, and density of the sediment grains) derive from XRD-calibrated lithological information previously used in the study area (Bryndzia *et al.*, 2005). The choice of the effective stress conditions in **(a-d)** is justified by the fact that the autoclave of the recovered pressure cores efficiently sealed at or near zero effective stress conditions (i.e. likely near the seafloor) (**Tab. 5.3**). The used effective stress conditions allow covering most of the measured P-wave velocities at 0% *Sh*. **(e)** P-wave velocity vs effective stress plot at 0% *Sh* (i.e. 100% water-saturated sediment), extrapolated using the input parameters for the sediment and water physical properties shown in **Tab. 5.3**, and following the effective-medium theory used to extrapolate the curves shown in **(a-d)**. The arrows indicate the P-wave velocity at the effective stress conditions indicated in **(a-d)**.

### *5.4.2.2. Gas geochemistry*

The shipboard analyses indicate that at DC_A methane is the dominant gas (>99.9% mol.%). The $C_1/C_2$ ratio is always higher than 1000 but irregularly decreases with depth, being relatively low within the interval where hydrates have been detected (**Fig. 5.13a**).

Ethane was detectable throughout the section, reaching a maximum value near 0.02 mol.% at 150.5 mbsf, within the hydrate-rich interval, around 30 m above the predicted $BS_I$GHSZ. Gases heavier than ethane were below detection limit in the shipboard analyses. A sample from FC-A#21 (70.0 mbsf) has been analysed more in detail onshore and detected $C_{2-6}$ gases, with ethane and propane being respectively 0.069 mol.% and 0.021 mol.%.

Methane is the dominant gas (>99.9% mol.%) at DC_B as well. Ethane was not detected (i.e. <0.002 mol.%) until 139.0 mbsf, with a single exception at 71 mbsf (0.004 mol.%). Ethane concentrations increase at ~170 mbsf, at the top of the deeper of the two inferred intervals of hydrate occurrences (**Fig. 5.13b**). Ethane increases further downward up to 0.015% near the base of the borehole (FC-B#12, 216.5 mbsf). $C_{3+}$ hydrocarbons were undetectable in all samples from this site. At DC_B, $C_1/C_2$ ratios are higher than at DC_A, being that in most of the cases ethane was below the detection limit (i.e. $C_1/C_2$ higher than 50,000). For comparison, the $C_1/C_{2+}$ ratio from geochemical analyses at DC_E is also shown in **Figure 5.13c** (see also **Fig. 3.11** and **Tabs. 3.1, 3.2**).

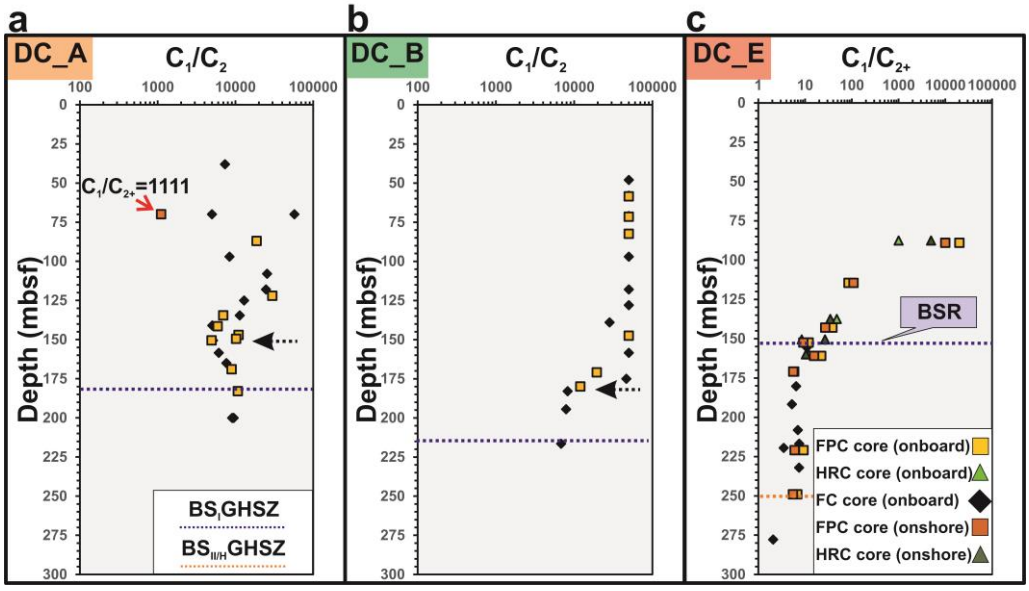



**Figure 5.13.** Molecular hydrocarbon composition of gases within FC and FPC cores from onboard and onshore analyses expressed as $C_1/C_2$, for DC_A and DC_B **(a, b)**, and as $C_1/C_{2+}$, for DC_E **(c).** At DC_A and DC_B the $C_1/C_2$ ratio is consistently higher than 1000, although it is possible to note a decrease within the deepest hydrate-rich intervals (black dotted arrows). At DC_E, the relative decrease in methane with depth results in an $S_I$ to $S_{II/H}$ hydrate transition at ~155 mbsf. The $BS_{II/H}$GHSZ is indicated by an orange dotted line (see **Chapter 3**). In all the plots, the maximum $C_1/C_2$ ratio is 50,000 (i.e. the detection limit is 0.002 mol.%).

#### *5.4.2.3. Evidence from well-log data*

At DC_A, The wireline borehole has been drilled with the wireline open face bit and is under-gauge up to ~130 mbsf while thereafter the hole is in gauge, but rugose. Between 80 and 90 mbsf the borehole is washed out due to a gas kick, possibly resulting from hydrate dissociation induced by drilling (Vaughan, 2006). Nevertheless, the measured WL sonic velocities are of good quality. The LWD data is also of good quality (**Figs. 5.5a, 5.14a**). LWD Resistivity and WL velocity data at DC_A show relatively high values between ~115 and 160 mbsf. This interval includes the hydrate-rich zone indicated by core data and is part of the lower portions of Unit 2, located in the basal part of the canyon. This zone is characterised by a higher frequency of relatively low gamma-ray and low porosity intervals, compared to the surrounding deposits (**Figs. 5.4a$_2$, 5.5a**). Numerous sandy/silty cm-thick beds and pockets were encountered in this interval during drilling (Gisler *et al.*, 2007). Thus, this zone is interpreted as characterised by muddy sediments stacked with well-consolidated sandy/silty thin layers. These observations suggest that the canyon-filling sequence at DC_A is relatively sand/silt-prone at its base. However, it is not entirely excluded that the borehole conditions have affected these measurements and my interpretation.

The extrapolated $R_o$ profile is consistently lower than measured resistivity ($R_{deep}$) in this interval (~115-160 mbsf), particularly in its lower part (**Fig. 5.5a**). The same interval also displays relatively bright colours in the resistivity images (**Fig. 5.14a**). Interestingly and in contrast to the observations in the LWD data at DC_E (cf. **Figs. 3.7, 3.8**), only minimal differences have been observed between the different propagation phase-shift resistivity measurements, suggesting the absence of sub-vertical hydrate-filled fractures (cf. Cook *et al.*, 2010). Two other intervals of moderately high resistivity and P and S-wave velocity have been observed at 50-70 m and 195-205 m, correlating with MTDs in seismic data. However, $R_o$ matches well $R_{deep}$ along these intervals. Considering the absence of clear hydrate indicators from core data and the relatively low porosity of these intervals (**Fig. 5.5a**), the observed increase in resistivity is interpreted to reflect only lithological changes

(cf. Dugan, 2012; Cook and Tost, 2014). The well-log response of these hydrate-free MTDs is thus characterised by enhanced resistivity (up to ~2 Ohm.m) and seismic velocities, as well as lower gamma-ray values and porosities, compared to the interlayered hemipelagic deposits. The resistivity increases up to ~6 Ohm.m if these deposits host gas hydrates.

Considering solely the interval where hydrates are suspected to occur from the resistivity log (~115-160 mbsf), the most conservative estimate of *Sh* (*n*=4) gives an average value of 12.6%, with a maximum value of 31.2% at 151 mbsf, matching well the estimates obtained from chlorinity data. Less conservative values are obtained with *n*=2, providing an average *Sh* of 23.1% within the interval of inferred hydrate occurrence (~115-160 mbsf) and a maximum value of 52.7% at 151 mbsf (**Fig. 5.15a**).

The wireline borehole at DC_B is rugose throughout with distinct enlarged zones (i.e. washouts) within layers interpreted to be rich in sand and silt. The WL velocity measurements are difficult to interpret because the S-wave profile is discontinuous and anomalously low P-wave velocities are observed within the deeper of the two hydrate-rich intervals (**Fig. 5.10b**). The scarce evidence of gas hydrates from velocity data is likely due to washouts within the sandy/silty layers, which represent the lithologies where hydrates preferentially occur (cf. Ostermeier *et al.*, 2002; Cook and Tost, 2014; Wang *et al.*, 2014) (**Figs. 5.5b, 5.14b**). In contrast with the observations at DC_A, at DC_B, there is no apparent effect of gas hydrates on resistivity measurements and only ambiguous values of 2-3 Ohm.m with a maximum of 3.2 Ohm.m (151-152 mbsf) are observed (**Fig. 5.5b**).

Even if the borehole profiles have not been acquired at the LWD sites, their proximity to the site of WL data acquisition suggests no significant lithological variations. It is thus likely that low-quality borehole conditions could also have affected the LWD resistivity measurements. The GR and porosity logs indicate a complex stratigraphy, in agreement with seismic observations (cf. **Figs. 5.3b, 5.4b$_1$, b$_2$** and **5.5b**). The intervals having moderately low porosity match well the MTDs identified in seismic data. Within Unit 2, between 170

and 190-195 mbsf, these low porosities correlate with a 20-25 m thick interval showing decreasing GR values. The drilling reports indicate that this interval, located at the base of the canyon and coinciding with the deeper of the two hydrate-rich intervals identified from core data, is rich in sandy/silty beds and pockets. This interval correlates with the WL borehole washouts, and it is not excluded that an enlarged borehole could have impacted the GR acquisition (**Figs. 5.5b, 5.13b**). The shallower hydrate-rich interval (~48-62 mbsf) does not induce diagnostic changes or anomalies in well-log data, although silty and organic-rich beds have been recognised during drilling operations (Gisler *et al.*, 2007).

The *Sh* profile extrapolated from resistivity data is probably affected by the interpreted borehole washouts. Nevertheless, this profile indicates two intervals, at ~45-75 and ~150-200 mbsf, respectively, characterised by moderately high peaks in Sh, mimicking the *Sh* profile obtained from core data. The shallower and the deeper intervals of hydrate occurrence have, respectively, an average *Sh* of 2.1% ($n$=4) or 4.1% ($n$=2) and 2.5% ($n$=4) or 4.8% ($n$=2). The deeper interval also shows the maximum *Sh* at 194 mbsf (15.3 with $n$=4 or 28.3% with $n$=2) (**Fig. 5.15b**). However, it is suspected that these estimates could be simply artefacts owing to an imperfect matching between $R_o$ and $R_{deep}$ (**Fig. 5.5b**).

At DC_C, the WL borehole has been drilled with the open face wireline bit and is in good conditions, being neither rugose nor undergauge, without any washout. The WL velocity data is thus of good quality, although there are intervals lacking P-wave velocity measurements in the first 100 m. Similarly, the LWD data is of good quality too, except for the first 25 mbsf, due to an excessive rate of penetration (**Figs. 5.5c, 5.14c**). This section is interpreted as an alternation of MTDs, thinner than at the eastern flank, and hemipelagic sediments (cf. **Figs. 5.3c** and **5.5c**). In contrast with DC_A and DC_B, the gamma-ray log does not seem to indicate intervals characterised by coarse-grained sediments. Thus, the high GR values, coupled with the absence of significant washouts, suggest that this section is richer in muddy sediments than sites DC_A and DC_B. A possible exception is represented

by an MTD, which is part of Unit 1 and is located at ~45-70 mbsf. This MTD exhibits lower porosity than the surrounding facies and moderate resistivity, up to 1.7 Ohm.m at ~50 mbsf, and could, therefore, host some sandy and silty overconsolidated beds (**Fig. 5.5c**). At DC_C, both the LWD resistivity and the WL velocities profiles do not show convincing anomalies indicative of hydrates. The $R_{deep}$ and $R_o$ profiles match well each other, and the obtained *Sh* rarely exceeds 5%, suggesting that GHBS could be either absent or present at very low saturations at this site. The estimated *Sh* could just reflect a slightly incorrect calculation of $R_o$ (**Fig. 5.15c**).

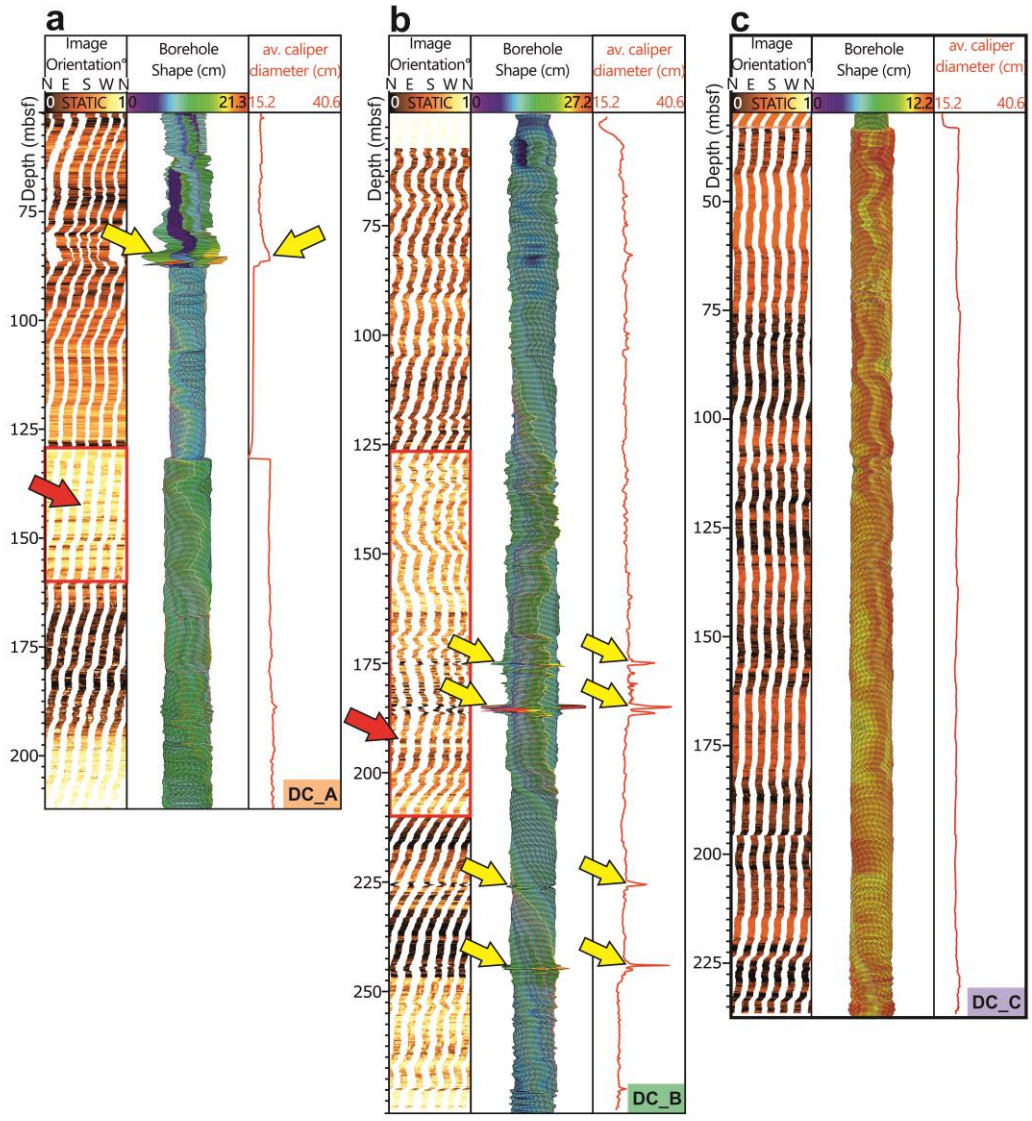



**Figure 5.14**. Resistivity images (static) (left panels), borehole 3D profiles (central panel) and average caliper log (right panels), obtained with the STAR WL device at DC_A **(a)**, DC_B **(b)** and DC_C **(c)**. The yellow arrows indicate borehole washout due to the presence of sandy/silty intervals whereas the red arrows and the red boxes at DC_A and DC_B indicate intervals of enhanced resistivity where hydrate could occur, although a high intrinsic resistivity is also typical of MTDs. The resistivity image at DC_C does not show suspect intervals for the presence of hydrates. Furthermore, the borehole profile and caliper logs are relatively monotonous with depth, with no evidence of washouts.

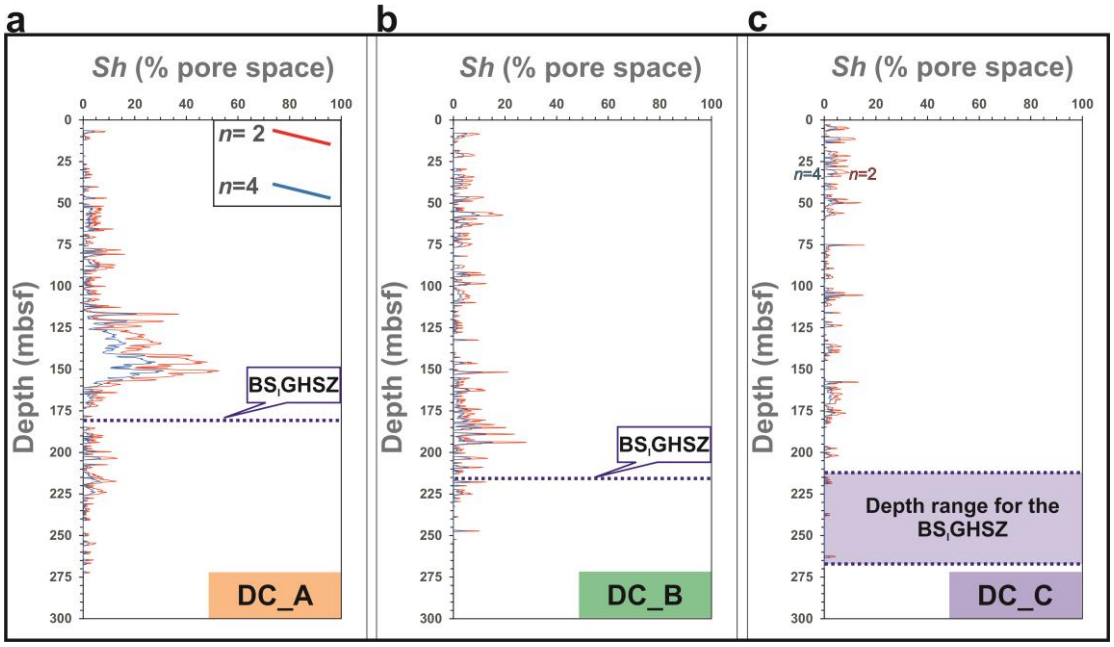



**Figure 5.15.** Gas hydrate saturation (*Sh*) estimated from LWD resistivity measurements with an Archie approach at DC_A **(a)**, DC_B **(b)** and DC_C **(c)**. The $B_ISGHSZ$ is plotted for DC_A and DC_B whereas, given the uncertainties related to the geothermal gradient, a range of depths where the $BS_IGHSZ$ could occur is plotted for DC_C (semi-transparent purple area).

| **Borehole** | **DC_A** | **DC_B** | **DC_C** | **DC_E** |
|---|---|---|---|---|
| **Domain** | Eastern Flank | Eastern Flank | Northwestern Flank | Crest |
| **Water depth (mbsl)** | 997.5 | 1096.8 | 1211.1 | 948.5 |
| **Seafloor temperature (°C)** | 4.2 | 3.7 | - | 4.6 |
| **Geothermal gradient (°C/km)** | 55.8 | 50.0 | - | 63.2 |
| **Dominant lithology** | MTDs and hemipelagites (sandy/silty intervals) | MTDs and hemipelagites (sandy/silty intervals) | MTDs and hemipelagites (sandy/silty intervals?) | Clay-rich hemipelagites |
| **Gas hydrate structure** | I | I | I? | I, II, H? |
| **Gas hydrate morphology** | Pore-filling (cm-scale intervals with high *Sh*) | Pore-filling (cm-scale intervals with high *Sh*) | - | Grain-displacing (thin sub-vertical fractures) |
| ***BGHSZ (mbsf)** | ~180 | ~215 | ~210-265 (based on $S_I$ hydrate stability) | ~250 |
| **SMTZ (mbsf)** | 14-20 | 8-10 | - | 10-12 |
| **Commercial reservoir(s) underneath (see Fig. 5.1)** | Yes (Limbayong reservoir) | Yes (oil zone of the GK reservoir) | No | Yes (gas and oil zones of the GK reservoir) |

**Table 5.1.** Summary table of the main characteristics of each borehole location, including DC_E (see **Chapters 3** and **4**). *BGHSZ refers to the BGHSZ for $S_I$ or $S_{II/H}$ hydrates, depending on the location.

## 5.5. Discussion

### *5.5.1. Controls on the thickness of the GHSZ and origin of the gas*

The primary control on the thickness of the GHSZ in the study area is the composition of the gas that sources the GHSZ. At the crest of the GKL Dome, the presence of enough of $C_{2+}$ hydrocarbons considerably thickens the GHSZ compared to its the thickness as solely inferred from the depth of the BSR (see **Chapter 3**) (**Fig. 5.13c**). Here, the sourcing gas likely resembles that entrapped in the GK reservoir and the greatest amount of molecular fractionation occurs within the GHSZ. At the eastern flank, the presence of $S_{II/H}$ hydrates is excluded because geochemical data indicate only traces of $C_{2+}$ hydrocarbons. Additionally, core and well-log observations provide no evidence of hydrates below the $BS_I$GHSZ (**Figs 5.5, 5.9, 5.10, 5.15**). Hence, in this area, the sole $S_I$ almost pure methane hydrate stability governs the thickness of the GHSZ.

It is difficult to precisely constrain how $S_{II/H}$ hydrates disappear from the crest to the eastern flank. However, by combining the results presented in this and the previous chapters, it is hypothesised that $S_{II/H}$ hydrates are limited to those zones at the crest of the GKL Dome having evidence of free gas and a direct connection with the underlying reservoirs (see **Fig. 5.1** and **Chapter 4**). The occurrence of $S_{II/H}$ hydrates likely reduces to zero towards the margins of the GKL Dome, in parallel with the lack of adequate amounts of $C_{2+}$ gases in the system. The presence of higher amounts of $C_{2+}$ hydrocarbons within *vs* outside zones of focused fluid flow is not solely restricted to this study area but has rather been recognised in a number of different basins, where fluxes of thermogenic gases are advectively focused at shallow depths (e.g. Paull *et al.*, 2005; Nuzzo *et al.*, 2009; Serié *et al.*, 2016). Some previous works have successfully modelled the impact of a focused fluid flux of thermogenic $C_{2+}$-rich fluids on hydrate stability (e.g. Paull *et al.*, 2005; Macelloni *et al.*, 2015) but this study could represent the first direct calibration, involving drilling of multiple boreholes across the GHSZ, of such an impact.

The fact that the GHSZ is several tens of metres thicker at the crest of the GKL Dome compared to the eastern flank, regardless of a higher geothermal gradient and a shallower water depth (**Tab. 5.1**), highlights the importance of the geochemistry of the gas forming hydrates on the vertical thickness of the GHSZ. The higher geothermal gradient at the crest of the structure is not surprising and confirms that bathymetric ridges associated with deeper faults are zones of increased heat flux and preferential migration of relatively warm fluids across the GHSZ (Warren *et al.*, 2010; Dewangan *et al.*, 2011; Kinoshita *et al.*, 2011). In the nearby Brunei margin, Zielinski *et al.* (2007) reported high heat flows and thermogenic hydrocarbon fluxes from seepage sites, whereas Laird and Morley (2011) extrapolated a geothermal gradient from a BSR, showing an increase from 48 °C/km, at the backlimb of a thrust-cored anticline, to 64 °C/km, at the crest. These gradients fit with those measured in this study, suggesting the presence of a fluid and heat flux system that operates at the regional-scale in a similar manner. This system is characterised by the focusing of thermogenic hydrocarbons and warm fluids at the crests of thrust-propagation folds and can be associated with fluids expelled by leaky reservoirs and by deep regional tectonic detachments (cf. Morley *et al.*, 2011).

Overall, at the eastern flank of the GKL Dome, the geochemical data is more ambiguous than at the crest, and it is hard to constrain the source of the gas forming hydrates and the possible processes resulting in the observed geochemical trends (**Fig. 5.13a, b**). The trace amounts of $C_{2+}$ hydrocarbons indicate that thermogenic gases still contribute to hydrate formation. Moreover, the decreased amounts of $C_{2+}$ hydrocarbons at DC_B, compared to DC_A, further suggests an eastward decrease of $C_{2+}$ gases in the system, i.e. moving away from the crest. However, how do we explain the occurrence of intervals still moderately rich in gas hydrates in this domain (**Figs. 5.9, 5.10**), given the evidence of a reduced flux of $C_{2+}$-rich fluids? Here I suggest two possible mechanisms that could justify these observations.

**(1)** An enhanced production rate of shallow microbial methane compared to the crest of the GKL Dome. A productive microbial methane generation could be favoured by higher sedimentation rates (cf. Mazumdar *et al.*, 2012; Johnson *et al.*, 2014), reflected in this area by the thick succession of MTDs, potentially transporting significant amounts of organic matter (cf. Algar *et al.*, 2011b). Theoretically, a microbial methane *'pool'* could justify the presence of gas hydrate-bearing intervals even without invoking a fluid flow from deep sources. However, the lack of gas hydrates at both DC_C and M_2 (**Figs. 4.5b**) suggest that a shallow zone of primary microbial methane production, if present, is either not uniformly efficient or still needs some contribution from deep sources to allow methane to exceed its solubility in the GHSZ. If this were not the case, there should be some evidence of gas hydrates even at DC_C and M_2, located in areas that lack evidence of shallow free gas and do not overlie deeper reservoirs (**Fig. 5.1**).

**(2)** A migration of a thermogenic gas from below with a different composition (i.e. consisting of almost pure methane) compared to that leaking from the gas cap of the GK reservoir (9-14% $C_{2+}$ gases) (see **Fig. 4.1**). The projection of the GOC of the GK reservoir does not overlie this area (**Fig. 5.1**) and is therefore unlikely that this $C_{2+}$-rich gas could source the hydrates at the flanks. In contrast, an almost pure methane gas can be generated by the partial degradation of the oil zone (cf. Larter *et al.*, 2005; Jones *et al.*, 2008; Milkov, 2011) and could then exsolve or diffuse upward. This second mechanism implies that enhanced rates of secondary microbial methane production are intimately associated with deeper thermogenic reservoirs, subjected to variable degrees of degradation. This hypothesis is corroborated by the recognition in a nearby area of degraded petroleum fluids, displaying evidence of molecular and isotopic diffusive fractionation (Ogawa and Jong, 2016).

Moreover, the eastern flank of the GKL Dome also overlies the Limbayong structure (**Fig. 5.2**), which in this portion of the margin hosts in deep reservoirs free gas with

maximum 1-2 mol.% of $C_{2+}$ components, i.e. more enriched in methane than the free gas within the GK reservoir. Thus, a contribution from the Limbayong reservoirs and additional molecular fractionation mechanisms (Prinzhofer *et al.*, 2000) could also result in a hydrate-sourcing fluid composed of almost pure methane. Because of the lack of shallow isotope data, I cannot discern which of these processes is the most relevant here, and I do not exclude that they could co-occur. Nevertheless, these observations highlight that *'secondary'* geochemical processes may affect the geochemistry of the hydrate-sourcing fluids during leakage, complicating a simplistic view where either purely thermogenic or microbial gases feed the GHSZ.

The impact of gas hydrates crystallisation on the composition of the gas released from the cores at the eastern flank of the GKL Dome is much less evident than at the crest (**Fig. 5.13**). The $C_1/C_2$ ratio profiles at DC_A and DC_B are difficult to interpret in these terms. A decrease in $C_1/C_2$ appears to occur with depth, consistent with observations in other gas hydrate provinces (e.g. Tréhu *et al.*, 2006; Choi *et al.*, 2013; Kida *et al.*, 2015). This trend could reflect both a gas hydrate formation from a flux of gas from below the GHSZ, with a molecular fractionation related to the preferential incorporation of ethane molecules within the $S_I$ hydrate cage, and changes in the mutual relative contribution of hydrate-bearing and dissolved gas (cf. Milkov *et al.*, 2004a; Pape *et al.*, 2010a; Choi *et al.*, 2013).

The depths of the SMTZ at DC_A, DC_B and DC_E are roughly similar (**Fig. 5.11**). These observations can be explained by either **(1)** similar fluxes of methane towards the seafloor at DC_A, DC_B and DC_E, or **(2)** a higher flux at DC_E but a more efficient coupled process of microbial organic matter degradation and anaerobic methane oxidation at DC_A and DC_B, owing to the high sedimentation rates and the possible high content in organic matter in the recent sediments at these two sites. These processes would ultimately result in a more efficient sulphate reduction (cf. Borowski *et al.*, 1999; Mazumdar *et al.*, 2012; Hong *et al.*, 2014). Site DC_E is characterised, similarly to DC_A and DC_B by the

absence of hydrates near the seafloor. However, the hydrate distribution in this borehole is not representative of that in the areas of maximum fluid flux at the crest of the GKL Dome, where the SMTZ could approach the seafloor (i.e. the fluid-escape pipes, see **Chapter 4**).

Furthermore, the pore water geochemical data from sites characterised by mass-transport activity could reflect non-steady-state situations (Hensen *et al.*, 2003; Hong *et al.*, 2014). The *'S-shaped'* sulphate profile at DC_B (**Fig. 5.11b**) supports the presence of a non-steady-state system, where the degradation of the organic matter consumes the sulphate shallower than the methane oxidation. In addition, the *'kink-shaped'* profile at DC_A indicates a recent *'rapid sedimentation'* event in the upper few metres of overburden. The resolution of the seismic data does not allow to detect thin gravity-driven depositional events within the shallow *'hemiplagic drape'*, where the sulphate reduction occurs. However, the observed anomalies in the sulphate profiles at DC_A and DC_B may indicate sub-seismic turbidites or MTDs in the most recent stratigraphy. This hypothesis is confirmed by the interpretation of site-survey data at this location (Gisler *et al.*, 2007; Lu and Shipp, 2011).

### *5.5.2. Reservoir characteristics of gas hydrate-bearing sediments*

At the eastern flank of the GKL Dome, the lithological heterogeneity inevitably impacts the distribution and the mode of occurrence of gas hydrates, from the seismic to the core-scale. The observed *Sh* profiles at DC_A and DC_B indicate the presence of metre-scale intervals which host hydrates at moderate saturation, reflecting sediments relatively abundant in silt and sand compared to the rest of the drilled section (**Figs. 5.5a, b, 5.9, 5.10**). These intervals are part of seismically-defined MTDs, confined within canyons, in the case of DC_A, and progressively less confined downslope, as in the case of DC_B (**Figs. 5.4, 5.5a, b**). The reservoir quality of MTDs in natural gas hydrate systems is poorly constrained in the literature. The heterogeneous lithology and the complex three-dimensional architecture of MTDs (Posamentier and Martinsen, 2011) make them complex elements of shallow hydrocarbon plumbing systems (Sun *et al.*, 2012; Yang *et al.*, 2013). MTDs are

further characterised by similar petrophysical characteristics compared to those of GHBS (e.g. high resistivity) (Algar *et al.*, 2011b; Dugan, 2012). Importantly, sand-rich turbidites may be embedded between stacked mud-dominated MTDs (Nelson *et al.*, 2011) and be good hydrate reservoirs (Boswell *et al.*, 2012b; Riedel *et al.*, 2012). Alternatively, sandy/silty sediments may be part of an MTD itself (Meckel III, 2011; Meckel III *et al.*, 2011), despite the majority of the MTDs are dominated by clay-rich sediments.

The proposed link between hydrate-rich intervals and coarse-grained sandy/silty sediments for sites DC_A and DC_B is not surprising. However, such association is usually found in depositional environments characterised by turbidite fans, levees and channels (e.g. Boswell *et al.*, 2012b; Wang *et al.*, 2014; Ito *et al.*, 2015). This study shows that regardless the mud-prone nature of the MTDs in this area (cf. Lu and Shipp, 2011), hydrates may occur in these deposits within subsidiary sandy/silty beds. The results of this study further suggest that the deposits at the base of the canyons in MTDs-dominated settings have the highest potential to host hydrate-bearing intervals (cf. **Figs. 5.3, 5.4, 5.9, 5.10**).

The lack of visible grain-displacing hydrates at the eastern flank of the GKL Dome and the fact that hydrate-bearing sediments, at DC_A and DC_B, are mostly invisible in X-ray images is diagnostic for a core-scale pore-filling habit (**Figs. 5.9d, e, 5.10d-f**) (Holland *et al.*, 2008). The correlation between high P-wave velocity in the MSCL measurements and the *Sh* estimates from chlorinity data indicates that hydrates concentrate at elevated saturation in 5-10 cm thick zones. A similar correlation was further observed in some IR thermal images, where the cold spots are coupled with the highest *Sh* (**Figs. 5.9c, 5.10c**). These zones of enhanced *Sh* likely represent thin cm-scale beds with coarser grains, wider pores and higher intrinsic permeability than the rest of the core (**Figs. 5.9, 5.10**). At the cm-scales, the incorporation of hydrates within coarse-grained sediments could be regulated, by capillary effects, able to create methane solubility gradients and induce diffusion-dominated fluxes of dissolved methane, from fine to coarse-grained sediments (Rempel, 2011; Cook

and Malinverno, 2013). Such hydrate distribution has been observed at the core-scale in other hydrate provinces, characterised by heterogeneous lithologies (e.g. Torres *et al.*, 2008; Lee *et al.*, 2013; Ito *et al.*, 2015). Unfortunately, the resolution of the X-ray CT scanning performed on the cores in this study is not high enough to resolve subtle mm-scale features and to better constrain the hydrate distribution.

The empirically extrapolated P-wave velocity *vs Sh* trend (**Fig. 5.12**) seems to support the interpretation of a pore-filling hydrate morphology at the eastern flank of the GKL Dome. The plotted data and the derived trend correlates with the models of hydrate micro-habits where hydrate fills the pore space either as homogeneously suspended particles without contacts with the grains (*'pore-filling suspension'* model) or as a frame supporting the mineral grains (*'load-bearing'* model) (Helgerud *et al.*, 1999; Helgerud, 2001; Lee *et al.*, 2010a). It could be possible that hydrates in natural complex pore networks exhibit a *'hybrid trend'*, which involves both suspended hydrate particles and particles in contact with the grains at fixed saturation, due to the dimensional variability of pores, particle sizes and mineral constituents. Concurrently, it is possible that the trend of data simply reflects a variation in the intrinsic reservoir quality at varying *Sh*, as well as in the effective stress of the recovered core samples. In these cases, each point could refer to slightly different sediments, in terms of mineral grains, pore network, and effective stress conditions, potentially having an enhanced reservoir quality at higher *Sh*. Although it is likely that the hydrate micro-habit in these reservoirs consists of either pore-filling suspension or load-bearing, or a mixture of the two, without more detailed analyses (e.g. further physical property measurements on pressure cores combined with studies on mineralogy and grain/pore size distribution), it is impossible to assess this issue with more confidence.

The *Sh* profiles at DC_A and DC_B indicate that intervals enriched in hydrates occur near the BGHSZ but not immediately at this interface (**Figs. 5.9b, 5.10b**). A possible explanation involves the controls of pressure, temperature and lithology on methane

solubility within the GHSZ. The methane solubility decreases at shallower depths within the GHSZ, and the size of the pores in the sediments impact the supersaturation thresholds, being lower (i.e. closer to bulk conditions) in broad pores and higher in narrow ones (Davie *et al.*, 2004; Liu and Flemings, 2007, 2011). Hence, a given flux can be undersaturated at the BGHSZ, especially if at this depth the sediments have a pore network that inhibits hydrate formation. However, such flux will exceed the thresholds at shallower depths, particularly if encounters a more favourable lithology (i.e. richer in silt/sand).

The origin the relatively shallow zone of hydrate occurrence at DC_B (48-62 mbsf) can be explained by the presence of an in-situ localised region of enhanced microbial methane production, capable of effectively sourcing these shallow hydrates. Alternatively, the rate of methane flux has changed through time. In this scenario, depending on the concentration of methane and the methane solubility thresholds, hydrates will form at deep and shallow intervals during two distinct events.

In well-log data, the *Sh* profile obtained at DC_A from resistivity data is reliable and correlates well with that obtained from chlorinity measurements (cf. **Figs 5.9b, 5.15a**). An Archie-based approach, if calibrated with in-situ information to correctly choose the value of *n*, can be valid even in these complex reservoirs. The use of values of *n* higher than 2 is physically justified by the impact of capillary effects on the bound water in the pores, at *Sh* exceeding a threshold that depends on the structure of the pore network (Spangenberg and Kulenkampff, 2006). The well-log data at DC_B (**Fig. 5.5b**) failed in identifying GHBS with confidence due to either the low quality of the resistivity data or because hydrates are not concentrated enough to be confidently detected with the well-log devices.

### *5.5.3. Significance of the seismic expression of the natural gas hydrate system*

At the flanks of the GKL Dome, the high amplitude of the observed EARs, their location at and beneath the predicted $BS_I$GHSZ and their polarity suggest that they represent free gas-bearing sediments whose accumulation is controlled by the three-phase boundary

(cf. Hustoft *et al.*, 2007; Calvès *et al.*, 2008). These EARs are patchily distributed, and their combined uppermost stratigraphic occurrence roughly mimics a BSR (**Figs. 5.2c, 5.4b$_1$**). The low-resolution seismic data, compared with the high-resolution one, has a reduced dominant seismic frequency and therefore better highlights the combined bottom-simulating character of these EARs (cf. Vanneste *et al.*, 2001) (**Fig. 5.2c**).

The *'canyon-to-lobe'* geometry of each single EAR, their location along a slope dominated by MTDs and the absence of sinuous-channel geometries suggest that they do not represent a classic turbidite system. However, these enhanced reflections are interpreted to indicate lithologies with a higher reservoir quality (i.e. a higher intrinsic permeability) than the surrounding sediments (**Fig. 5.7**). The depositional architecture of these seismic facies and, consequently, the distribution of free gas, are controlled by the physiography of the canyons and the less confined areas downslope (cf. Lu and Shipp, 2011; Meckel III *et al.*, 2011). Therefore, these seismic facies can be interpreted as the expression of a sandy/silty mass-flow (Meckel III *et al.*, 2011).

The availability of sediments with a relatively high reservoir quality and an adequate presence of gas are critical elements for the formation of these EARs. The reasons for the presence of EARs at DC_B *vs* their absence at DC_A are difficult to understand. The difference in lithology and methane solubility, rates of sedimentation *vs* erosion and rate of fluid flux of methane-rich fluids from below, between these two sites, likely represent critical controls. I favour a scenario where the fluid flux at DC_A and DC_B is similar, and the reason for the absence of EARs at DC_A would be the clay-rich and fine-grained upper portion of Unit 3. This seismic facies is present at DC_A but is instead eroded at DC_B. Within this lithology, the methane solubility would increase compared to bulk conditions. This increase in solubility prevents the formation of free gas, as well as of hydrates, near the three-phase boundary. Above (i.e. within Unit 2), the lithology changes, becoming richer in sandy/silty beds: here, bulk stability conditions and solubility thresholds dominate and

hydrates can form (cf. Liu and Flemings, 2011; Daigle and Dugan, 2014). DC_A is an excellent example of a site with hydrates in the absence of free gas. Therefore, the identification of these EARs indicates the existence of enough methane in the system to form gas hydrates. However, the distribution of such anomalies is not entirely representative of the distribution of the overlying hydrates.

At the eastern flank of the GKL Dome, a seismically-visible physical connection between deep (i.e. the GK and Limbayong reservoirs) and shallow hydrocarbon accumulations (i.e. the free gas zone and the zones of hydrate occurrence) is not as straightforward as at the crest (**Fig. 5.2**, cf. with **Chapters 3** and **4**). Thus, a less efficient migration, possibly dominated by gas in solution exceeding saturation thresholds within the GHSZ or near its base is probably the dominant fluid flow process. In this setting, the gas migration may become more or less defocused and impacted by the hydraulic connection between different stratal pathways and by possible hydraulic barriers at the BGHSZ along the slope (cf. Davies *et al.*, 2014). The absence of vertical fluid flow features within this area is attributable to a decreased fluid flux and uplift, inhibiting the generation of overpressures. At the northwestern flank, the likely absence of hydrates, shallow free gas, cross-stratal fluid flow from deeper levels and deep hydrocarbon accumulations indicates a system lacking sufficient fluxes of methane-saturated fluids, i.e. the absence of a gas charge (**Fig. 5.16**).

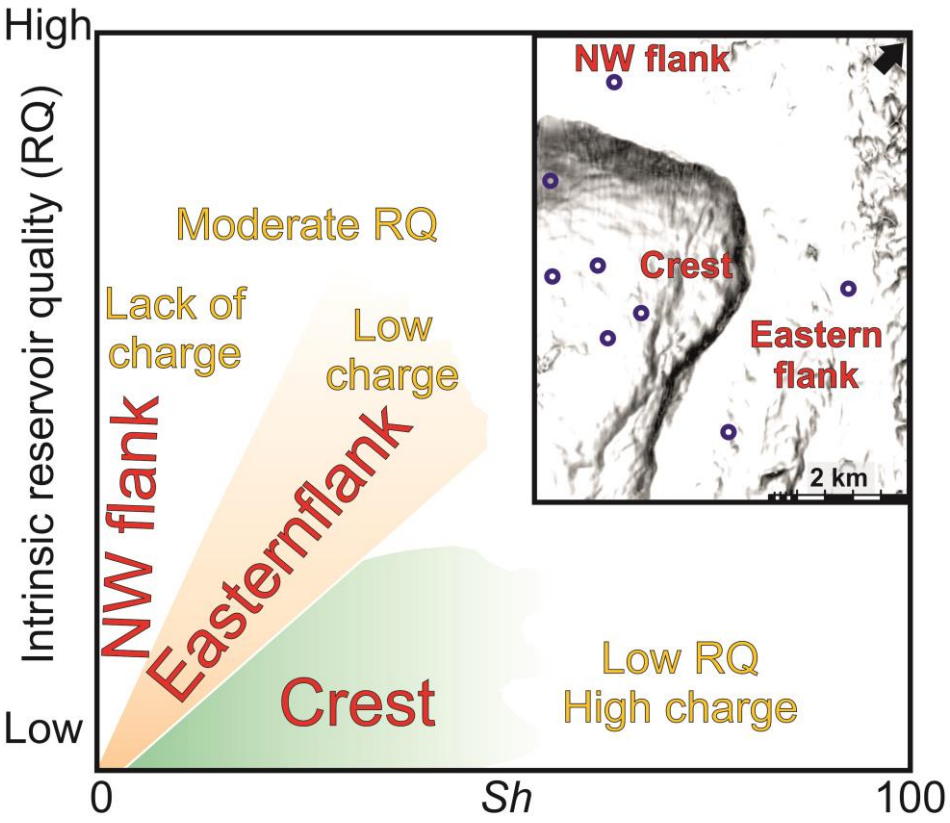



**Figure 5.16.** Schematic plot showing the relationship between the intrinsic reservoir quality of the gas hydrate reservoirs at the crest and the flanks of the GKL Dome, the observed *Sh* and the availability/supply of gas in the system (i.e. the charge) (cf. Boswell *et al.*, 2016). The crest has high charge, low intrinsic reservoir quality, enhanced only by fracture generation, and low to moderate l*Sh* (probably very high along fluid-escape pipes, see **Chapter 4**). The flanks have low (eastern flank) to zero (NW flank) charge and moderate reservoir quality (high locally, along thin sandy/silty beds). Hence, *Sh* is low to moderate at the eastern flank and zero at the northwestern flank.

## 5.6. Conclusions

3D seismic, well-log and core data from offshore Sabah (NW Borneo) have been integrated into this study to characterise and discuss the natural gas hydrate system at the flanks of the GKL Dome, and compare it to that at the crest, described in the previous chapters. The major conclusions of this study are:

**(1)** In areas dominated by thermogenic fluxes of hydrocarbons towards shallow parts of basins, the geochemistry of the feeding gas sourcing the GHSZ is an essential control to predict its vertical extension. In the presence of such hydrocarbon plumbing systems, predicting the lateral and vertical extent thickness of the GHSZ is more challenging than in provinces where hydrates are solely sourced by an almost pure methane microbial source. Where a direct link between deeply-rooted thermogenic reservoirs and the GHSZ exists, the major geochemical changes in the hydrate and feeding gas composition occur

within the GHSZ. Where this relationship is ambiguous, and the fluid flow is not intense, additional processes like secondary and primary microbial methane generation, as well as molecular fractionation during leakage, need to be considered. Thus, the identification of a thermogenic source of gas can be hidden by the mixing with a shallower microbial source or because of the alteration of the original composition by secondary processes. Sulphate profiles can provide clues on the diffusive fluid flux of methane, but in areas of relatively high sedimentation or fluid flux, the presence of non-steady-state profiles needs to be considered.

**(2)** The morphology of the gas hydrate reservoirs rapidly evolves laterally, from grain-displacing (i.e. fracture-filling hydrates) to pore-filling, moving from the crest to the eastern flank of the GKL Dome. In MTD-rich areas, hydrates concentrate in cm-thick beds with a pore-filling morphology. Interpreting the occurrence and distribution of gas hydrates in these deposits is challenging. MTDs, due to their consolidated nature and low porosity can have a high intrinsic resistivity and this needs to be considered in evaluating the distribution of hydrates along a borehole. The formation of hydrates in the pore space increases the P-wave velocity of the sediment. Despite the lack of precise mineralogical calibration for the hydrate-bearing sediments in the studied sites, the models that predict that hydrates form as a suspension in the pore space or as a load-bearing component appear the most reliable to describe the impact of hydrates on the P-wave velocity in the studied gas hydrate-bearing sediments. These micro-habits could co-occur in a complex pore network or evolve one into the other at increasing *Sh*.

**(3)** At the seismic-scale, the geophysical indicators of free gas are reliable for a first-order evaluation of a natural gas hydrate system, since they indicate the existence of oversaturated methane at shallow depths. However, hydrates have been shown to occur in the absence of geophysical indicators, even in areas characterised by deeper thermogenic reservoirs, possibly as a result of lateral heterogeneities in lithology, methane solubility and supply.

## 5.7. Appendix

### *5.7.1. Supplementary figures*

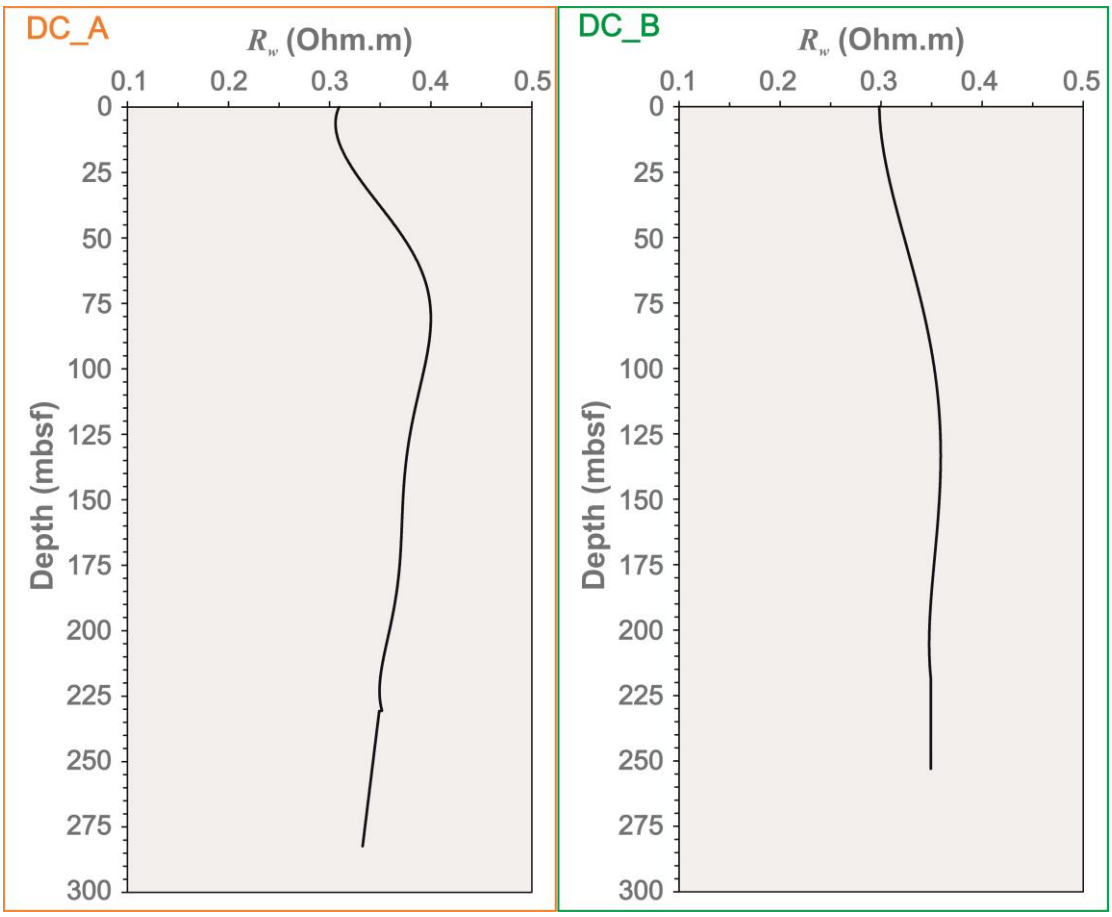



**Figure 5.17.** $R_w$ profiles for DC_A and DC_B.

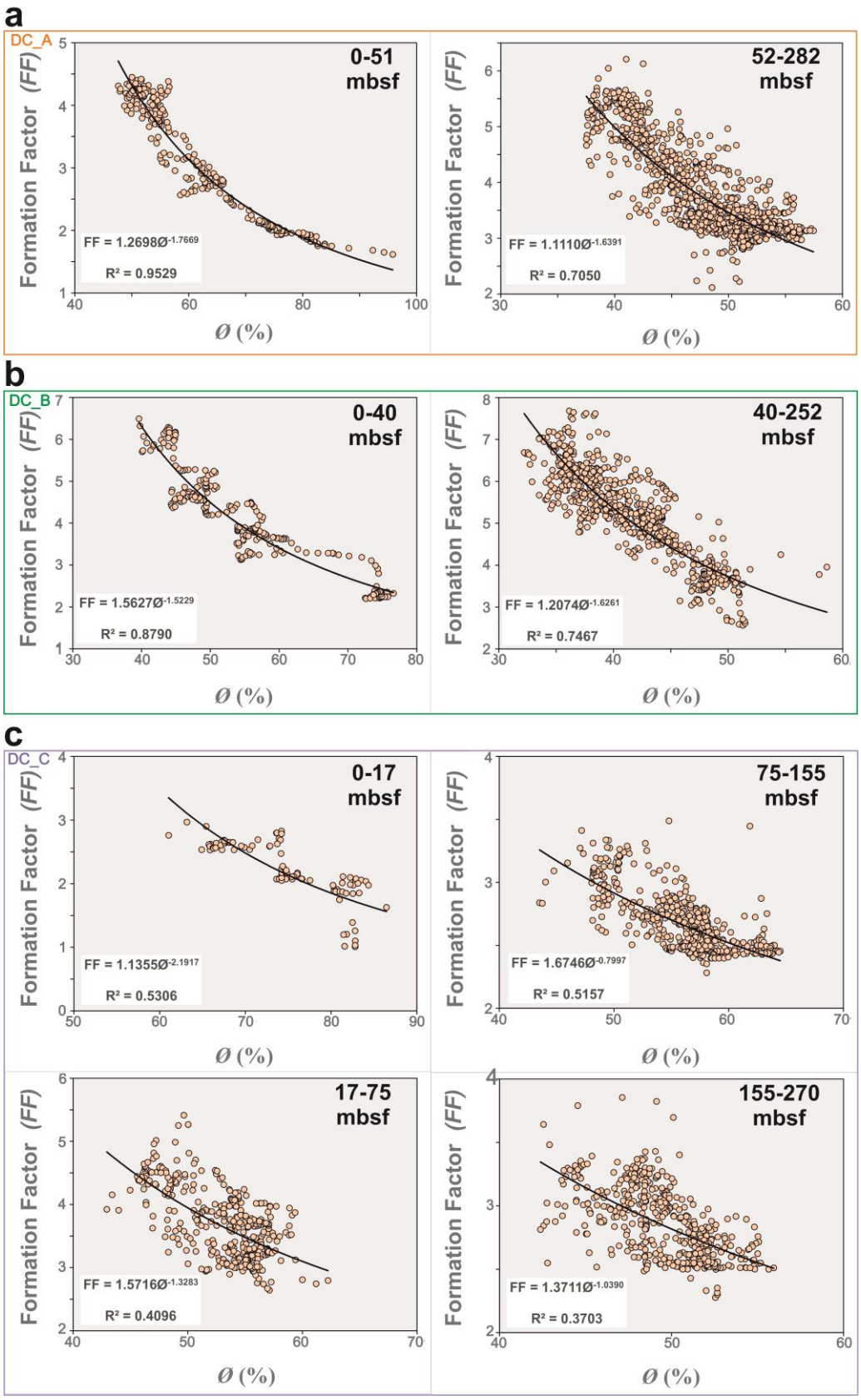



**Figure 5.18**. Pickett plots for DC_A **(a)**, DC_B **(b)** and DC_C **(c)**. The intervals interpreted to host hydrates from core data have been excluded. *FF*= Formation factor; *Ø*= porosity, extrapolated from the LWD density logs.

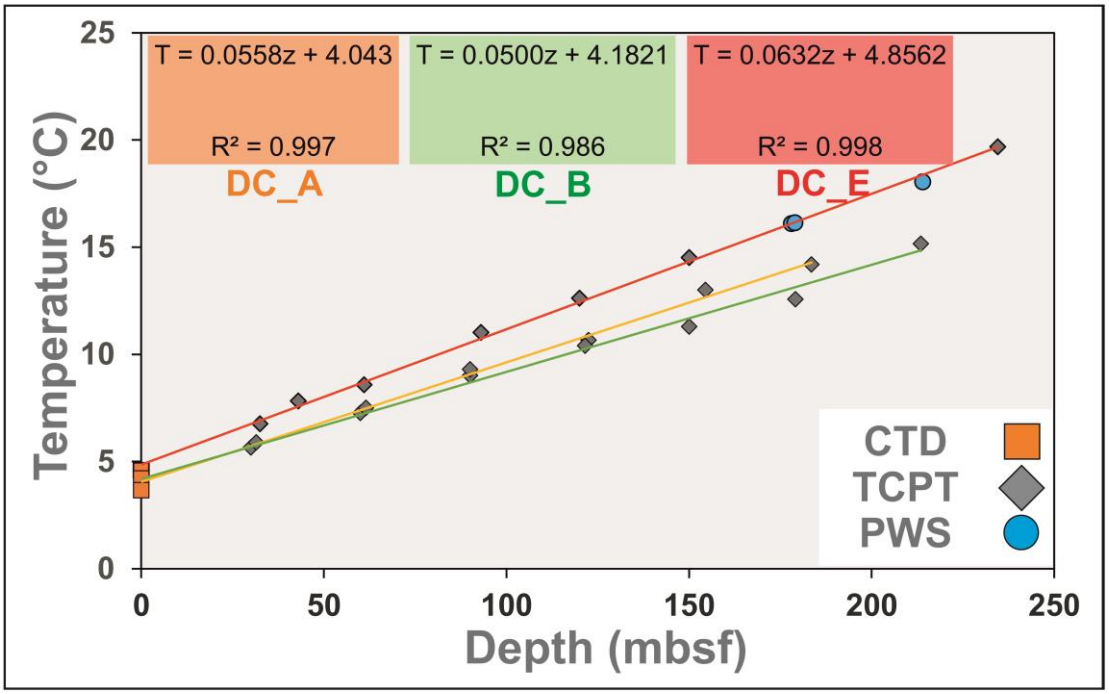



**Figure 5.19.** CTD and borehole temperature data with extrapolated geothermal gradients for DC_A (55.8 °C/km), DC_B (50.0 °C/km) and DC_E (63.2 °C/km). In the equations in the coloured panels T= temperature (°C); z= depth (mbsf). TCPT= data from the temperature cone penetration equilibrium tests; PWS= data from the pore water sampler. Note that the three geothermal gradients are almost perfectly linear ($R^2$>0.99).

### *5.7.2. Supplementary tables*

| Borehole | Test tool | depth (mbsf) | depth (mbsl) | T (°C) |
|---|---|---|---|---|
| DC_A | CTD | 0.0 | 997.5 | 4.21 |
| DC_A | Temperature Cone | 30.0 | 1027.5 | 5.66 |
| DC_A | Temperature Cone | 60.0 | 1057.5 | 7.27 |
| DC_A | Temperature Cone | 90.0 | 1087.5 | 9.02 |
| DC_A | Temperature Cone | 122.5 | 1120.0 | 10.66 |
| DC_A | Temperature Cone | 154.5 | 1152.0 | 13.01 |
| DC_A | Temperature Cone | 183.5 | 1181.0 | 14.2 |
| DC_B | CTD | 0.0 | 1096.8 | 3.67 |
| DC_B | Temperature Cone | 31.5 | 1128.3 | 5.90 |
| DC_B | Temperature Cone | 61.5 | 1158.3 | 7.50 |
| DC_B | Temperature Cone | 90.0 | 1186.8 | 9.30 |
| DC_B | Temperature Cone | 121.5 | 1218.3 | 10.40 |
| DC_B | Temperature Cone | 150.0 | 1246.8 | 11.30 |
| DC_B | Temperature Cone | 179.1 | 1275.9 | 12.57 |
| DC_B | Temperature Cone | 213.5 | 1310.3 | 15.16 |

**Table 5.2.** Temperatures measured at DC_A and DC_B. The derived geothermal gradient is linear ($R^2$~ 0.99) for the first 183.5 mbsf at DC_A and 213.5 mbsf at DC_B. See **Tab. 3.3** for the temperature measurements along DC_E.

| Parameter | Value | Parameter | Value |
|---|---|---|---|
| **Porosity** | 45% | **G sediment grains** | 6.85 GPa |
| **Critical porosity** | 50% | **G water** | 0 GPa |
| **Grain contacts** | 9 | **G gas hydrate** | 3.3 GPa |
| **K sediment grains** | 20.9 GPa | $\rho_{sediment\ grains}$ | 2580 kg/m$^3$ |
| **K water** | 2.25 GPa | $\rho_{hyd}$ | 900 kg/m$^3$ |
| **K gas hydrate** | 7.9 GPa | $\rho_{water}$ | 1020 kg/m$^3$ |
| **Model** | **Effective stress** | | |
| **#a (Fig. 5.12a)** | **~0 MPa (no effective stress)** | | |
| **#b (Fig. 5.12b)** | **0.02 MPa** | | |
| **#c (Fig. 5.12c)** | **0.09 MPa** | | |
| **#d (Fig. 5.12d)** | **0.22 MPa** | | |

**Table 5.3.** Parameters used to extrapolate the theoretical Vp *vs Sh* trends for the pore-filling and load-bearing models (**Fig. 5.12**). Models #1-#4 highlight the different effective stress conditions used to compute the curves, considering that the recovery pressure of the pressure cores was close to the hydrostatic pressure at the seafloor at DC_A and DC_B. This justifies the choice of zero to very low effective stress conditions. A proper zero effective stress condition does not allow to run the models. To simulate this case I assumed an extremely low effective stress ($9x10^{-5}$ MPa).

**Table 5.4**

| Borehole DC_A | | | | | | |
|---|---|---|---|---|---|---|
| **Core** | **Depth (mbsf)** | **Depth (mbsl)** | ***Cm* (mM)** | ***Cb* (mM)** | **Sulphate (mM)** | **Drill water infiltration (%)** |
| Liner-A#01 | 0.3 | 997.7 | 527.0 | 527.0 | 32.9 | - |
| Liner-A#03 | 3.3 | 1000.8 | 529.1 | 529.1 | 30.5 | - |
| Liner-A#05 | 6.3 | 1003.8 | 527.0 | 527.0 | 28.7 | - |
| Liner-A#07 | 9.3 | 1006.8 | 528.4 | 528.4 | 28.0 | - |
| Liner-A#10 | 13.8 | 1011.3 | 526.3 | 526.3 | 26.3 | - |
| Shelby-A#12 | 20.2 | 1017.7 | 502.5 | 502.5 | 0.5 | - |
| Shelby-A#14 | 32.2 | 1029.6 | 446.0 | 446.0 | 0.5 | < 1.5 |
| FC-A#01 | 38.4 | 1035.9 | 432.9 | 432.9 | 0.4 | < 1.5 |
| FC-A#01 | 39.0 | 1036.4 | 431.3 | 431.3 | 0.5 | < 1.5 |
| FC-A#01 | 39.4 | 1036.9 | 431.5 | 431.5 | 0.4 | < 1.5 |
| FC-A#01 | 39.8 | 1037.3 | 427.9 | 427.9 | 1.7 | 6.0 |
| Shelby-A#15 | 44.4 | 1041.9 | 416.2 | 416.2 | 0.4 | < 1.5 |
| Shelby-A#16 | 61.2 | 1058.6 | 373.7 | 373.7 | 0.5 | 2.0 |
| FC-A#21 | 70.4 | 1067.9 | 348.1 | 357.2 | 0.4 | < 1.5 |
| FC-A#21 | 71.5 | 1068.9 | 351.1 | 357.0 | 0.4 | < 1.5 |
| FC-A#21 | 71.6 | 1070.0 | 354.8 | 356.9 | 0.4 | < 1.5 |
| FC-A#03 | 80.0 | 1077.5 | 355.6 | 355.7 | 0.6 | 2.0 |
| FC-A#03 | 80.0 | 1077.5 | 357.0 | 355.7 | 0.6 | 2.0 |
| FC-A#03 | 80.0 | 1077.5 | 360.1 | 355.7 | 0.5 | < 1.5 |
| FPC-A#01 | 87.1 | 1084.5 | 351.1 | 354.7 | 0.4 | < 1.5 |
| FPC-A#01 | 87.2 | 1084.6 | 354.2 | 354.6 | 0.4 | < 1.5 |
| FPC-A#01 | 87.2 | 1084.7 | 350.0 | 354.6 | 0.5 | 1.9 |
| FPC-A#01 | 87.4 | 1084.8 | 349.7 | 354.6 | 0.5 | < 1.5 |
| FPC-A#01 | 87.6 | 1085.0 | 349.4 | 354.6 | 0.4 | < 1.5 |
| FPC-A#01 | 87.8 | 1085.2 | 351.1 | 354.5 | 0.4 | < 1.5 |
| Shelby-A#19 | 91.0 | 1088.5 | 353.2 | 354.0 | 0.5 | < 1.5 |
| FPC-A#02 | 97.1 | 1094.6 | 346.5 | 353.1 | 0.6 | 2.2 |
| FPC-A#02 | 97.3 | 1094.8 | 349.4 | 353.1 | 0.4 | < 1.5 |
| FPC-A#02 | 97.5 | 1095.0 | 346.3 | 353.1 | 0.4 | < 1.5 |
| FPC-A#02 | 97.8 | 1095.2 | 347.5 | 353.0 | 0.4 | < 1.5 |
| FC-A#04 | 97.6 | 1095.0 | 347.3 | 353.0 | 0.4 | < 1.5 |
| FC-A#04 | 98.0 | 1095.5 | 347.1 | 353.0 | 0.5 | < 1.5 |
| FC-A#04 | 98.5 | 1096.0 | 350.6 | 352.9 | 0.5 | < 1.5 |
| FPC-A#03 | 98.2 | 1095.6 | 346.6 | 353.0 | 0.4 | < 1.5 |
| FPC-A#03 | 98.3 | 1095.8 | 347.0 | 352.9 | 0.4 | < 1.5 |
| FPC-A#03 | 98.6 | 1096.1 | 345.0 | 352.9 | 0.4 | < 1.5 |
| FPC-A#03 | 98.8 | 1096.2 | 348.2 | 352.9 | 0.4 | < 1.5 |
| FPC-A#04 | 99.2 | 1096.7 | 344.6 | 352.8 | 0.4 | < 1.5 |
| FPC-A#04 | 99.4 | 1096.9 | 345.0 | 352.8 | 0.4 | < 1.5 |
| FPC-A#04 | 99.6 | 1097.0 | 348.6 | 352.7 | 0.4 | < 1.5 |
| FPC-A#04 | 99.7 | 1097.1 | 345.1 | 352.7 | 0.4 | < 1.5 |
| FC-A#05 | 108.3 | 1105.7 | 343.9 | 351.4 | 1.5 | 5.6 |
| FC-A#05 | 108.9 | 1106.3 | 343.9 | 351.3 | 0.4 | < 1.5 |
| FC-A#05 | 109.2 | 1106.6 | 353.5 | 351.3 | 0.4 | < 1.5 |
| FC-A#05 | 109.3 | 1106.8 | 349.3 | 351.2 | 0.5 | < 1.5 |
| FC-A#06 | 118.0 | 1115.5 | 340.8 | 349.9 | 0.5 | < 1.5 |
| FC-A#06 | 118.5 | 1116.0 | 347.8 | 349.8 | 0.5 | < 1.5 |
| FC-A#06 | 119.0 | 1116.5 | 352.8 | 349.8 | 0.4 | < 1.5 |
| FC-A#06 | 119.5 | 1117.0 | 347.8 | 349.7 | 0.5 | < 1.5 |
| FPC-A#05 | 122.1 | 1119.6 | 351.2 | 349.3 | 0.4 | < 1.5 |
| FPC-A#05 | 122.4 | 1119.9 | 346.1 | 349.2 | 0.5 | < 1.5 |
| FPC-A#05 | 122.6 | 1120.1 | 344.4 | 349.2 | 0.4 | < 1.5 |
| FPC-A#05 | 122.8 | 1120.3 | 336.0 | 349.2 | 0.4 | < 1.5 |
| FC-A#08 | 125.1 | 1122.6 | 347.1 | 348.8 | 0.5 | < 1.5 |
| FC-A#08 | 125.8 | 1123.2 | 349.2 | 348.7 | 0.5 | < 1.5 |
| FC-A#08 | 126.2 | 1123.6 | 338.6 | 348.7 | 0.5 | < 1.5 |
| FC-A#09 | 128.0 | 1125.5 | 343.5 | 348.4 | 0.5 | < 1.5 |
| FC-A#09 | 128.5 | 1126.0 | 344.2 | 348.3 | 0.5 | < 1.5 |
| FC-A#09 | 129.0 | 1126.5 | 342.5 | 348.2 | 0.5 | < 1.5 |
| FC-A#09 | 129.5 | 1127.0 | 331.6 | 348.1 | 0.5 | 1.8 |
| Shelby-A#21 | 131.1 | 1128.5 | 329.6 | 347.9 | 0.5 | 1.8 |
| FC-A#10 | 134.5 | 1132.0 | 284.1 | 347.4 | 0.5 | < 1.5 |
| FC-A#10 | 135.0 | 1132.5 | 337.1 | 347.3 | 0.5 | 1.9 |
| FC-A#10 | 135.3 | 1132.7 | 298.6 | 347.3 | 0.5 | < 1.5 |
| FC-A#10 | 135.3 | 1132.7 | 278.0 | 347.3 | 0.5 | < 1.5 |
| FC-A#10 | 135.5 | 1133.0 | 240.4 | 347.2 | 0.5 | < 1.5 |
| FC-A#10 | 136.0 | 1133.5 | 332.4 | 347.2 | 0.5 | < 1.5 |
| FPC-A#06 | 134.6 | 1132.1 | 338.5 | 347.4 | 0.4 | < 1.5 |
| FPC-A#06 | 134.8 | 1132.3 | 332.3 | 347.3 | 0.4 | < 1.5 |
| FPC-A#06 | 134.9 | 1132.3 | 316.5 | 347.3 | 0.4 | < 1.5 |
| FPC-A#06 | 135.0 | 1132.4 | 340.4 | 347.3 | 0.4 | < 1.5 |
| FPC-A#06 | 135.1 | 1132.6 | 344.1 | 347.3 | 0.4 | < 1.5 |

| | | | | | | |
|---|---|---|---|---|---|---|
| FPC-A#06 | 135.3 | 1132.7 | 342.0 | 347.3 | 0.4 | < 1.5 |
| FC-A#11 | 141.4 | 1138.9 | 321.4 | 346.3 | 0.5 | < 1.5 |
| FC-A#11 | 141.5 | 1139.0 | 336.6 | 346.3 | 0.5 | < 1.5 |
| FC-A#11 | 142.0 | 1139.5 | 343.5 | 346.2 | 0.5 | < 1.5 |
| FC-A#11 | 142.5 | 1140.0 | 304.9 | 346.2 | 0.8 | 2.8 |
| FPC-A#07 | 141.6 | 1139.0 | 342.6 | 346.3 | 0.4 | < 1.5 |
| FPC-A#07 | 141.6 | 1139.1 | 339.7 | 346.3 | 0.4 | < 1.5 |
| FPC-A#07 | 141.7 | 1139.2 | 338.5 | 346.3 | 0.4 | < 1.5 |
| FPC-A#07 | 141.8 | 1139.3 | 331.7 | 346.3 | 0.4 | < 1.5 |
| FPC-A#07 | 141.9 | 1139.4 | 330.3 | 346.2 | 0.4 | < 1.5 |
| FPC-A#07 | 142.2 | 1139.6 | 334.0 | 346.2 | 0.4 | < 1.5 |
| FPC-A#08 | 147.7 | 1145.1 | 336.8 | 345.4 | 0.4 | < 1.5 |
| FPC-A#08 | 147.8 | 1145.2 | 340.2 | 345.3 | 0.4 | < 1.5 |
| FPC-A#09 | 149.6 | 1147.0 | 345.9 | 345.1 | 0.4 | < 1.5 |
| FPC-A#09 | 149.6 | 1147.1 | 339.0 | 345.1 | 0.4 | < 1.5 |
| FPC-A#09 | 149.7 | 1147.1 | 339.7 | 345.1 | 0.4 | < 1.5 |
| FPC-A#10 | 150.5 | 1148.0 | 274.4 | 344.9 | 17.8 | 64.4 |
| FPC-A#10 | 150.5 | 1148.0 | 301.2 | 344.9 | 12.2 | 44.2 |
| FPC-A#10 | 150.6 | 1148.0 | 338.3 | 344.9 | 0.4 | < 1.5 |
| FPC-A#10 | 150.7 | 1148.2 | 305.5 | 344.9 | 0.4 | < 1.5 |
| FC-A#13 | 150.7 | 1148.2 | 332.4 | 344.9 | 0.5 | < 1.5 |
| FC-A#13 | 151.2 | 1148.7 | 338.8 | 344.8 | 0.3 | < 1.5 |
| FC-A#13 | 152.0 | 1149.5 | 325.1 | 344.7 | 0.3 | < 1.5 |
| FC-A#13 | 152.0 | 1149.5 | 216.5 | 344.7 | 3.3 | 11.9 |
| FC-A#13 | 152.0 | 1149.5 | 130.7 | 344.7 | - | - |
| FC-A#13 | 152.0 | 1149.5 | 316.7 | 344.7 | 1.1 | 4.0 |
| FC-A#13 | 152.1 | 1149.6 | 303.3 | 344.7 | 0.5 | < 1.5 |
| Shelby-A#23 | 155.0 | 1152.5 | 303.3 | 344.2 | 0.5 | 1.8 |
| FC-A#15 | 159.0 | 1156.5 | 337.2 | 343.6 | 0.5 | 1.9 |
| FC-A#15 | 159.5 | 1157.0 | 333.1 | 343.5 | 0.5 | 1.8 |
| FC-A#15 | 160.0 | 1157.5 | 336.6 | 343.5 | 0.5 | < 1.5 |
| FC-A#15 | 160.3 | 1157.8 | 336.7 | 343.4 | 0.5 | < 1.5 |
| FC-A#16 | 165.1 | 1162.5 | 336.9 | 342.7 | 0.9 | 3.3 |
| FC-A#16 | 165.5 | 1163.0 | 336.5 | 342.6 | 0.5 | < 1.5 |
| FC-A#16 | 166.0 | 1163.5 | 334.6 | 342.6 | 0.5 | < 1.5 |
| FC-A#16 | 166.5 | 1164.0 | 332.5 | 342.5 | 0.5 | < 1.5 |
| FPC-A#12 | 169.5 | 1167.0 | 337.3 | 342.0 | 0.4 | < 1.5 |
| FPC-A#12 | 169.6 | 1167.1 | 338.9 | 342.0 | 0.4 | < 1.5 |
| Shelby-A#24 | 169.5 | 1167.0 | 330.5 | 342.0 | 0.5 | < 1.5 |
| Shelby-A#25 | 180.5 | 1178.0 | 335.8 | 340.3 | 0.5 | 1.8 |
| FPC-A#13 | 183.2 | 1180.6 | 339.7 | 339.9 | 0.4 | < 1.5 |
| FPC-A#13 | 183.4 | 1180.8 | 338.0 | 339.9 | 0.4 | < 1.5 |
| FPC-A#13 | 183.6 | 1181.0 | 342.3 | 339.9 | 0.4 | < 1.5 |
| FPC-A#13 | 183.7 | 1181.2 | 339.2 | 339.8 | 0.4 | < 1.5 |
| Shelby-A#26 | 195.6 | 1193.0 | 331.7 | 338.0 | 0.5 | < 1.5 |
| FC-A#17 | 200.0 | 1197.5 | 339.3 | 337.3 | 0.5 | 1.8 |
| FC-A#17 | 200.5 | 1197.9 | 329.7 | 337.3 | 0.5 | < 1.5 |
| FC-A#17 | 201.0 | 1198.4 | 329.7 | 337.2 | 0.5 | < 1.5 |
| FC-A#17 | 201.5 | 1198.9 | 330.6 | 337.1 | 0.5 | < 1.5 |
| FC-A#18 | 213.0 | 1210.5 | 338.9 | 335.3 | 0.4 | < 1.5 |
| FC-A#18 | 213.0 | 1210.5 | 332.1 | 335.3 | 0.4 | < 1.5 |
| FC-A#18 | 213.3 | 1210.8 | 328.7 | 335.3 | 0.4 | < 1.5 |
| FC-A#19 | 228.0 | 1225.5 | 323.4 | 333.0 | 0.5 | < 1.5 |
| FC-A#19 | 228.1 | 1225.5 | 327.4 | 333.0 | 0.6 | 2.3 |
| FC-A#20 | 230.2 | 1227.7 | 329.1 | 332.7 | 0.5 | < 1.5 |
| FC-A#20 | 230.4 | 1227.9 | 325.5 | 332.7 | 0.5 | < 1.5 |
| FC-A#20 | 230.6 | 1228.1 | 330.4 | 332.6 | 0.5 | < 1.5 |
| FC-A#20 | 231.1 | 1228.6 | 323.6 | 332.6 | 0.5 | < 1.5 |

**Table 5.5**

| Borehole DC_B | | | | | | |
|---|---|---|---|---|---|---|
| **Core** | **Depth (mbsf)** | **Depth (mbsl)** | ***Cm* (mM)** | ***Cb* (mM)** | **Sulphate (mM)** | **Drill water infiltration (%)** |
| Liner-B#01 | 0.3 | 1097.1 | 545.1 | 549.6 | 25.7 | – |
| Liner-B#02 | 1.8 | 1098.6 | 543.9 | 547.5 | 25.2 | – |
| Liner-B#03 | 3.4 | 1100.2 | 546.7 | 545.4 | 20.6 | – |
| Liner-B#04 | 4.9 | 1101.7 | 550.2 | 543.4 | 12.2 | – |
| Liner-B#05 | 6.4 | 1103.3 | 544.9 | 541.2 | 10.6 | – |
| Liner-B#06 | 7.9 | 1104.7 | 543.7 | 539.3 | 2.4 | – |
| Liner-B#07 | 9.2 | 1106.1 | 548.4 | 537.4 | 0.4 | < 1.5 |
| Liner-B#08 | 10.9 | 1107.7 | 544.2 | 535.2 | 0.4 | < 1.5 |
| Liner-B#09 | 12.3 | 1109.1 | 538.8 | 533.3 | 0.4 | < 1.5 |
| Liner-B#10 | 13.7 | 1110.5 | 537.1 | 531.4 | 0.5 | < 1.5 |
| Shelby-B#11 | 15.4 | 1112.2 | 524.5 | 529.1 | 0.4 | < 1.5 |
| Shelby-B#12 | 20.1 | 1116.9 | 529.4 | 522.6 | 5.2 | 18.7 |
| Shelby-B#13 | 26.1 | 1122.9 | 510.8 | 514.5 | 0.4 | < 1.5 |
| Shelby-B#14 | 32.2 | 1129.0 | 499.8 | 506.2 | 0.4 | < 1.5 |
| Shelby-B#15 | 38.1 | 1134.9 | 498.3 | 498.3 | 0.4 | < 1.5 |
| FC-B#14 | 48.3 | 1145.2 | 476.2 | 474.9 | 0.4 | < 1.5 |
| FC-B#14 | 48.8 | 1145.6 | 65.7 | 473.9 | - | - |
| FC-B#14 | 48.8 | 1145.6 | 446.9 | 473.9 | 0.4 | < 1.5 |
| FC-B#14 | 49.4 | 1146.2 | 130.8 | 472.6 | 0.6 | 2.0 |
| FC-B#14 | 49.6 | 1146.4 | 466.4 | 472.1 | 0.4 | < 1.5 |
| FC-B#01 | 58.1 | 1154.9 | 365.5 | 454.2 | 0.6 | 2.1 |
| FC-B#01 | 58.7 | 1155.5 | 440.1 | 453.0 | 5.5 | 19.9 |
| FC-B#01 | 59.0 | 1155.8 | 448.4 | 452.4 | 0.6 | 2.0 |
| FC-B#01 | 59.0 | 1155.8 | 448.2 | 452.4 | 0.4 | < 1.5 |
| FC-B#01 | 59.4 | 1156.2 | 447.5 | 451.7 | 0.4 | < 1.5 |
| FPC-B#01 | 58.6 | 1155.5 | 444.7 | 453.1 | 0.5 | 1.8 |
| FPC-B#01 | 58.8 | 1155.6 | 377.3 | 452.8 | 2.4 | 8.7 |
| FPC-B#01 | 59.0 | 1155.8 | 447.8 | 452.4 | 1.1 | 3.8 |
| FPC-B#01 | 59.1 | 1155.9 | 450.8 | 452.2 | 1.2 | 4.2 |
| FPC-B#01 | 59.3 | 1156.1 | 451.6 | 451.9 | 0.8 | 3.0 |
| Shelby-B#17 | 62.2 | 1159.0 | 414.7 | 446.4 | 0.4 | < 1.5 |
| FC-B#02 | 71.0 | 1167.8 | 424.1 | 431.3 | 0.5 | < 1.5 |
| FC-B#02 | 71.6 | 1168.4 | 427.8 | 430.4 | 0.4 | < 1.5 |
| FC-B#02 | 72.1 | 1168.9 | 428.4 | 429.7 | 0.4 | < 1.5 |
| FPC-B#02 | 71.6 | 1168.4 | 423.3 | 430.4 | 0.4 | < 1.5 |
| FPC-B#02 | 71.8 | 1168.6 | 438.7 | 430.1 | 0.5 | < 1.5 |
| FPC-B#02 | 72.0 | 1168.9 | 438.8 | 429.7 | 0.4 | < 1.5 |
| FPC-B#02 | 72.2 | 1169.0 | 434.9 | 429.4 | 2.2 | 7.7 |
| Shelby-B#18 | 75.6 | 1172.4 | 423.5 | 424.3 | 0.5 | < 1.5 |
| FPC-B#03 | 82.7 | 1179.5 | 405.6 | 414.7 | 0.4 | < 1.5 |
| FPC-B#03 | 82.9 | 1179.7 | 440.0 | 414.4 | 0.5 | 1.9 |
| FPC-B#03 | 83.0 | 1179.9 | 413.0 | 414.2 | 0.5 | < 1.5 |
| FPC-B#03 | 83.2 | 1180.1 | 409.1 | 414.0 | 0.5 | < 1.5 |
| Shelby-B#19 | 91.1 | 1187.9 | 398.5 | 404.8 | 0.4 | < 1.5 |
| FC-B#04 | 97.5 | 1194.3 | 396.0 | 398.2 | 0.4 | < 1.5 |
| FC-B#04 | 98.0 | 1194.8 | 393.7 | 397.7 | 0.4 | < 1.5 |
| FC-B#04 | 98.5 | 1195.3 | 400.5 | 397.2 | 0.4 | < 1.5 |
| Shelby-B#20 | 105.8 | 1202.7 | 389.7 | 390.7 | 0.4 | < 1.5 |
| Shelby-B#21 | 107.3 | 1204.1 | 381.0 | 389.5 | 2.0 | 7.1 |
| FC-B#05 | 118.0 | 1214.8 | 368.3 | 381.8 | 0.5 | 1.8 |
| FC-B#05 | 118.6 | 1215.4 | 376.1 | 381.4 | 0.4 | < 1.5 |
| FC-B#05 | 119.1 | 1215.9 | 380.3 | 381.1 | 0.4 | < 1.5 |
| Shelby-B#22 | 122.4 | 1219.2 | 380.5 | 379.1 | 0.5 | < 1.5 |
| Shelby-B#22 | 122.4 | 1219.2 | 380.6 | 379.1 | 0.4 | < 1.5 |
| FC-B#16 | 128.2 | 1225.0 | 375.4 | 375.9 | 0.5 | < 1.5 |
| FC-B#16 | 128.6 | 1225.4 | 374.5 | 375.6 | 2.6 | 9.3 |
| FC-B#16 | 128.9 | 1225.7 | 373.5 | 375.5 | 0.4 | < 1.5 |
| Shelby-B#23 | 135.6 | 1232.4 | 369.3 | 372.1 | 0.4 | < 1.5 |
| FC-B#06 | 139.0 | 1235.8 | 359.6 | 370.6 | 0.4 | < 1.5 |
| FC-B#06 | 139.5 | 1236.3 | 369.2 | 370.4 | 0.4 | < 1.5 |
| FC-B#06 | 140.0 | 1236.8 | 358.8 | 370.2 | 0.4 | < 1.5 |
| FC-B#06 | 140.8 | 1237.6 | 363.6 | 369.8 | 0.4 | < 1.5 |
| FPC-B#04 | 146.7 | 1243.5 | 364.9 | 367.5 | 0.5 | < 1.5 |
| FPC-B#04 | 146.8 | 1243.7 | 364.9 | 367.4 | 0.4 | < 1.5 |
| FPC-B#04 | 146.9 | 1243.8 | 357.6 | 367.4 | 0.5 | < 1.5 |
| FPC-B#04 | 147.1 | 1243.9 | 327.4 | 367.3 | 0.4 | < 1.5 |
| FPC-B#05 | 147.6 | 1244.4 | 365.2 | 367.1 | 0.4 | < 1.5 |
| FPC-B#05 | 147.8 | 1244.6 | 364.0 | 367.1 | 0.4 | < 1.5 |
| FPC-B#05 | 148.0 | 1244.8 | 367.7 | 367.0 | 0.4 | < 1.5 |
| FPC-B#05 | 148.2 | 1245.0 | 359.9 | 366.9 | 0.4 | < 1.5 |
| Shelby-B#24 | 151.7 | 1248.5 | 363.7 | 365.6 | 0.5 | < 1.5 |

| | | | | | | |
|---|---|---|---|---|---|---|
| FC-B#07 | 159.0 | 1255.8 | 355.6 | 363.1 | 0.4 | < 1.5 |
| FC-B#07 | 159.5 | 1256.3 | 364.2 | 362.9 | 0.5 | < 1.5 |
| FC-B#07 | 160.0 | 1256.8 | 361.2 | 362.8 | 0.4 | < 1.5 |
| Shelby-B#25 | 165.7 | 1262.5 | 357.4 | 361.0 | 0.4 | < 1.5 |
| FC-B#08 | 171.0 | 1267.8 | 319.8 | 359.3 | 0.6 | 2.1 |
| FC-B#08 | 171.5 | 1268.4 | 355.3 | 359.2 | 3.1 | 11.1 |
| FC-B#08 | 171.7 | 1268.6 | 352.3 | 359.1 | 0.6 | 2.1 |
| FC-B#08 | 171.9 | 1268.8 | 349.6 | 359.1 | 0.9 | 3.3 |
| FC-B#08 | 173.3 | 1270.1 | 365.4 | 358.7 | 0.4 | < 1.5 |
| FPC-B#06 | 171.1 | 1267.9 | 188.6 | 359.3 | 6.4 | 23.0 |
| FPC-B#06 | 171.1 | 1268.0 | 203.7 | 359.3 | 3.9 | 14.1 |
| FPC-B#06 | 171.2 | 1268.0 | 350.7 | 359.3 | 0.4 | < 1.5 |
| FPC-B#06 | 171.3 | 1268.1 | 354.6 | 359.3 | 1.0 | 3.6 |
| FPC-B#06 | 171.4 | 1268.2 | 350.3 | 359.2 | 0.4 | < 1.5 |
| FPC-B#06 | 171.5 | 1268.3 | 354.6 | 359.2 | 0.4 | < 1.5 |
| FPC-B#06 | 171.7 | 1268.6 | 357.4 | 359.1 | 0.4 | < 1.5 |
| FC-B#10 | 175.0 | 1271.8 | 348.8 | 358.2 | 0.5 | < 1.5 |
| FC-B#10 | 175.5 | 1272.3 | 343.4 | 358.0 | 0.4 | < 1.5 |
| FC-B#10 | 176.0 | 1272.8 | 345.5 | 357.9 | 0.4 | < 1.5 |
| FPC-B#07 | 180.2 | 1277.0 | 353.8 | 356.7 | 0.4 | < 1.5 |
| FPC-B#07 | 180.3 | 1277.2 | 353.8 | 356.6 | 0.4 | < 1.5 |
| FPC-B#07 | 180.4 | 1277.3 | 229.2 | 356.6 | 0.4 | < 1.5 |
| FPC-B#07 | 180.5 | 1277.3 | 354.5 | 356.6 | 0.4 | < 1.5 |
| FPC-B#07 | 180.7 | 1277.5 | 354.5 | 356.5 | 0.4 | < 1.5 |
| FPC-B#07 | 180.8 | 1277.6 | 350.3 | 356.5 | 1.4 | 5.1 |
| Shelby-B#26 | 181.6 | 1278.4 | 353.2 | 356.3 | 0.4 | < 1.5 |
| FC-B#11 | 183.0 | 1279.8 | 329.8 | 355.8 | 2.0 | 7.0 |
| FC-B#11 | 184.0 | 1280.8 | 343.7 | 355.6 | 0.4 | < 1.5 |
| FC-B#11 | 184.2 | 1281.0 | 264.6 | 355.5 | 0.4 | < 1.5 |
| FC-B#11 | 184.3 | 1281.1 | 120.0 | 355.5 | 0.4 | < 1.5 |
| FC-B#11 | 184.8 | 1281.6 | 350.4 | 355.3 | 0.4 | < 1.5 |
| FC-B#17 | 186.3 | 1283.1 | 356.8 | 354.9 | 0.4 | < 1.5 |
| FC-B#17 | 186.5 | 1283.3 | 357.2 | 354.8 | 0.5 | < 1.5 |
| FC-B#17 | 186.8 | 1283.6 | 354.0 | 354.8 | 0.4 | < 1.5 |
| FC-B#17 | 187.0 | 1283.8 | 352.8 | 354.7 | 0.4 | < 1.5 |
| FC-B#17 | 187.3 | 1284.1 | 352.7 | 354.6 | 0.4 | < 1.5 |
| FC-B#17 | 187.5 | 1284.3 | 351.6 | 354.5 | 0.4 | < 1.5 |
| FC-B#12 | 195.0 | 1291.8 | 344.4 | 352.3 | 0.4 | < 1.5 |
| FC-B#12 | 195.5 | 1292.3 | 340.2 | 352.2 | 0.4 | < 1.5 |
| FC-B#12 | 195.7 | 1292.5 | 340.2 | 352.2 | 0.4 | < 1.5 |
| FC-B#12 | 196.0 | 1292.8 | 338.4 | 352.0 | 0.4 | < 1.5 |
| Shelby-B#28 | 198.7 | 1295.5 | 345.1 | 351.2 | 0.4 | < 1.5 |
| Shelby-B#29 | 211.0 | 1307.9 | 337.9 | 347.4 | 0.4 | < 1.5 |
| FC-B#13 | 217.0 | 1313.8 | 341.1 | 345.4 | 0.5 | < 1.5 |
| FC-B#13 | 217.5 | 1314.3 | 346.4 | 345.2 | 0.4 | < 1.5 |
| FC-B#13 | 218.0 | 1314.8 | 357.0 | 345.0 | 0.4 | < 1.5 |

**Tables 5.4 (pages 230, 231) and 5.5 (pages 232, 233).** Chloride and sulphate concentration data for DC_A **(Tab 5.4)** and DC_B **(Tab 5.5)**. Shelby-A/B#= Shelby tube data; FPC-A/B#= Fugro Pressure Corer data; FC-A/B#= Fugro Corer data; *Cm* (corrected) = measured Chloride concentration (chlorinity), corrected for drill water infiltration (last column on the right); *Cb*= baseline chlorinity. There is no evidence of hydrates for the first 128 mbsf at DC_A and 48 mbsf at DC_B. From the seafloor until these depths, *Cb* approximates *Cm*. The % of drill water infiltration is calculated by considering a 27.4 mM sulphate content for the drill water and no sulphate in the pore water below the SMTZ (red-coloured cells).

**Table 5.6**

| Borehole DC_A | Depth | Sh av. (%) | Sh max. (%) | *Sh* (%) |
|---|---|---|---|---|
| Core | (mbsf) | Chlorinity | Chlorinity | Mass-balance |
| Liner-A#01 | 0.3 | 0.0 | 0.0 | - |
| Liner-A#03 | 3.3 | 0.0 | 0.0 | - |
| Liner-A#05 | 6.3 | 0.0 | 0.0 | - |
| Liner-A#07 | 9.3 | 0.0 | 0.0 | - |
| Liner-A#10 | 13.8 | 0.0 | 0.0 | - |
| Shelby-A#12 | 20.2 | 0.0 | 0.0 | - |
| Shelby-A#14 | 32.2 | 0.0 | 0.0 | - |
| FC-A#01 | 38.0 | 0.0 | 0.0 | - |
| Shelby-A#15 | 44.4 | 0 | 0.0 | - |
| Shelby-A#16 | 61.2 | 0 | 0.0 | - |
| FC-A#21 | 70.0 | 2.0 | 3.2 | - |
| FC-A#03 | 79.0 | 0.0 | 0.0 | - |
| FPC-A#01 | 87.0 | 1.3 | 1.8 | 0.9 |
| Shelby-A#19 | 91.0 | 0.3 | 0.3 | - |
| FC-A#04 | 97.0 | 1.6 | 2.1 | - |
| FPC-A#02* | 97.0 | 2.0 | 2.4 | - |
| FPC-A#03* | 98.0 | 2.2 | 2.8 | - |
| FPC-A#04* | 99.0 | 2.5 | 2.9 | - |
| FC-A#05 | 108.0 | 1.5 | 2.7 | - |
| FC-A#06 | 118.0 | 1.2 | 3.3 | - |
| FPC-A#05 | 122.0 | 1.9 | 4.7 | 0.0 |
| FC-A#08 | 125.0 | 1.4 | 3.6 | - |
| FC-A#09 | 128.0 | 2.8 | 5.9 | - |
| Shelby-A#21 | 131.1 | 6.5 | 6.5 | - |
| FC-A#10 | 134.5 | 17.9 | 35.8 | - |
| FPC-A#06 | 134.5 | 4.2 | 10.9 | 4.1 |
| FC-A#11 | 141.0 | 7.0 | 14.5 | - |
| FPC-A#07 | 141.5 | 3.6 | 5.7 | 2.5 |
| FPC-A#08* | 147.0 | 2.5 | 3.1 | - |
| FPC-A#09 | 149.5 | 1.4 | 2.2 | 0.9 |
| FC-A#13 | 150.5 | 22.2 | 74.3 | - |
| FPC-A#10** | 150.5 | 14.1 | 24.4 | 4.5 |
| Shelby-A#23 | 155.0 | 14.5 | 14.5 | - |
| FC-A#15 | 159.0 | 2.8 | 3.8 | - |
| FC-A#16 | 165.0 | 2.7 | 3.6 | - |
| FPC-A#12 | 169.0 | 1.4 | 1.7 | 0.0 |
| Shelby-A#24 | 169.5 | 4.2 | 4.2 | - |
| Shelby-A#25 | 180.5 | 1.7 | 1.7 | - |
| FPC-A#13 | 183.0 | 0.3 | 0.7 | 0.0 |
| Shelby-A#26 | 195.6 | 2.3 | 2.3 | - |
| FC-A#17 | 200.0 | 2.0 | 2.8 | - |
| FC-A#18 | 212.0 | 1.2 | 2.5 | - |
| FC-A#19 | 228.0 | 2.9 | 3.6 | - |
| FC-A#20 | 230.0 | 2.1 | 3.4 | - |

**Table 5.7**

| Borehole DC_B | Depth | Sh av. (%) | Sh max. (%) | *Sh* (%) |
|---|---|---|---|---|
| **Core** | **(mbsf)** | **Chlorinity** | **Chlorinity** | **Mass-balance** |
| Liner-B#01 | 0.3 | 0.0 | 0.0 | - |
| Liner-B#02 | 1.8 | 0.0 | 0.0 | - |
| Liner-B#03 | 3.4 | 0.0 | 0.0 | - |
| Liner-B#04 | 4.9 | 0.0 | 0.0 | - |
| Liner-B#05 | 6.4 | 0.0 | 0.0 | - |
| Liner-B#06 | 7.9 | 0.0 | 0.0 | - |
| Liner-B#07 | 9.2 | 0.0 | 0.0 | - |
| Liner-B#08 | 10.9 | 0.0 | 0.0 | - |
| Liner-B#09 | 12.3 | 0.0 | 0.0 | - |
| Liner-B#10 | 13.7 | 0.0 | 0.0 | - |
| Shelby-B#11 | 15.4 | 0.0 | 0.0 | - |
| Shelby-B#12 | 20.1 | 0.0 | 0.0 | - |
| Shelby-B#13 | 26.1 | 0.0 | 0.0 | - |
| Shelby-B#14 | 32.2 | 0.0 | 0.0 | - |
| Shelby-B#15 | 38.1 | 0.0 | 0.0 | - |
| FC-B#14 | 48.0 | 34.8 | 88.6 | - |
| FC-B#01 | 58.0 | 6.1 | 23.4 | - |
| FPC-B#01 | 58.5 | 4.8 | 20.1 | 4.3 |
| Shelby-B#17 | 62.2 | 8.8 | 8.8 | - |
| FC-B#02 | 71.0 | 1.1 | 2.1 | - |
| FPC-B#02 | 71.5 | 0.5 | 2.1 | 0.0 |
| Shelby-B#18 | 75.6 | 0.2 | 0.2 | - |
| FPC-B#03 | 82.5 | 1.2 | 2.7 | 0.0 |
| Shelby-B#19 | 91.1 | 1.9 | 1.9 | - |
| FC-B#04 | 97.0 | 0.6 | 1.2 | - |
| Shelby-B#20 | 105.8 | 0.3 | 0.3 | - |
| Shelby-B#21 | 107.3 | 2.7 | 2.7 | - |
| FC-B#05 | 118.0 | 2.2 | 4.4 | - |
| Shelby-B#22 | 122.4 | 0.0 | 0.0 | - |
| FC-B#16 | 128.0 | 0.4 | 0.6 | - |
| Shelby-B#23 | 135.6 | 1.0 | 1.0 | - |
| FC-B#06 | 139.0 | 2.5 | 3.8 | - |
| FPC-B#04* | 146.5 | 4.6 | 13.3 | - |
| FPC-B#05 | 147.5 | 1.0 | 2.4 | 0.0 |
| Shelby-B#24 | 151.7 | 0.6 | 0.6 | - |
| FC-B#07 | 158.0 | 1.0 | 2.6 | - |
| Shelby-B#25 | 165.7 | 1.2 | 1.2 | - |
| FC-B#08 | 171.0 | 4.1 | 13.4 | - |
| FPC-B#06 | 171.0 | 16.0 | 53.2 | 4.9 |
| FC-B#10 | 175.0 | 4.2 | 5.1 | - |
| FPC-B#07 | 180.0 | 7.8 | 41.1 | 2.1 |
| Shelby-B#26 | 181.6 | 1.1 | 1.1 | - |
| FC-B#11 | 183.0 | 23.2 | 71.2 | - |
| FC-B#17 | 186.0 | 0.4 | 1.0 | - |
| FC-B#12 | 194.5 | 4.0 | 4.8 | - |
| Shelby-B#28 | 198.7 | 2.2 | 2.2 | - |
| Shelby-B#29 | 211.0 | 3.4 | 3.4 | - |
| FC-B#13 | 217.0 | 0.5 | 1.5 | - |

**Tables 5.6 (See the previous page) and 5.7 (This page).** Compilation of *Sh* from all the recovered core samples, from chlorinity measurements and mass-balance calculations at DC_A and DC_B. The average and maximum *Sh* has been estimated from chlorinity values along each core whereas only a single value from each FPC core has been obtained with the mass-balance approach. Av= average; - = not applicable; *= FPC unsuccessfully recovered at in-situ pressure and depressurised at atmospheric conditions; **= FPC recovered partially depressurised. The depth is referred to the top of each core with respect to the seafloor.

# Chapter 6. Three-dimensional seismic evidence of extensive gas hydrate deposits linked with large free gas columns suggests long-range advection mechanisms

This chapter is modified from 'Paganoni, M., Cartwright, J.A. & Van Rensbergen, P. Three-dimensional seismic evidence of extensive gas hydrate deposits linked with large free gas columns suggests long-range advection mechanisms, accepted for publication in *Marine and Petroleum Geology*. Joe A. Cartwright and Pieter Van Rensbergen contributed to the interpretation of seismic data and the revision. The seismic and well-log data were acquired by Shell and provided by Pieter Van Rensbergen.

## 6.1. Introduction

Deepwater marine sediments host the largest portion of natural gas hydrates and represent an efficient methane sink which, contrarily to natural gas hydrate systems on the upper continental slopes and in shallow Arctic shelves, is relatively insensitive to climate change dynamics (Ruppel and Kessler, 2017). Among the different types of gas hydrate deposits in the deepwater realm, those characterised by coarse-grained sediments represent one of the most critical components of the gas hydrate resource pyramid, having the greatest future commercial potential (Collett *et al.*, 2009; Boswell *et al.*, 2016). The host sediments of such deposits further represent preferred pathways for the migration of methane-rich fluids below and across the gas hydrate stability zone (GHSZ) (Tréhu *et al.*, 2004a; Crutchley *et al.*, 2015). The mechanisms promoting the formation of gas hydrates at elevated concentrations in this type of sediments may be either diffusion- or advection-dominated (Crutchley *et al.*, 2015; Malinverno and Goldberg, 2015; Nole *et al.*, 2017). Understanding the relative importance of these processes and the scales at which they act is crucial to predicting hydrate distribution in natural systems.

Rock physics models, coupled with seismic observations, suggest that the presence of hydrates in the sediment pore space enhances the amplitude of stratigraphic reflections at saturation (*Sh*, % of the pore space) higher than ~50%, while at lower *Sh* or within pipe-like structures blanking effects prevail (Lee, 2004; Riedel *et al.*, 2006; Saeki *et al.*, 2008; Lee *et al.*, 2009; Davies *et al.*, 2014; Boswell *et al.*, 2016) (**Fig. 6.1**). In contrast, free gas impacts the amplitude response of the host sediments even at low concentrations (i.e. <5% of the pore space) (Carcione and Tinivella, 2000; Lee, 2004; Boswell *et al.*, 2016) (see **Fig. 1.24b**). Importantly, other factors may affect the amplitude of seismic reflections. For instance, tuning effects result from either the constructive or the destructive interference of seismic waves, and are intimately associated with the seismic resolution and, therefore, the spacing between adjacent reflections (Yilmaz, 2001; Brown, 2011; Hillman *et al.*, 2017a). Moreover,

the lateral and vertical changes in lithology inevitably impact the resulting seismic amplitude too. Hence, it is critical to consider that the modifications of seismic amplitude owing to either hydrates or free gas superimpose over a lithologically heterogeneous background (cf. Noguchi *et al.*, 2011; Boswell *et al.*, 2012a; Cook and Tost, 2014; Crutchley *et al.*, 2016).

Many researchers have further suggested that the formation of hydrates could impact methane fluxes by trapping buoyant free gas columns at the base of the GHSZ (BGHSZ), eventually released if overpressure reaches critical levels (cf. Grauls, 2001; Flemings *et al.*, 2003; Hornbach *et al.*, 2004; Bangs *et al.*, 2011; Daigle *et al.*, 2011). However, the efficiency of these hydrate seals in controlling free gas fluxes remains poorly constrained and hard to assess with seismic data. In some circumstances, the analysis of three-dimensional (3D) seismic data can help in visualising the distribution of hydrate deposits and in gaining a better understanding of their genetic processes at the km-scale. Previous studies have successfully imaged in 3D the seismic amplitude patterns of free gas migration and gas hydrate accumulation (e.g. Hustoft *et al.*, 2007; Boswell *et al.*, 2012b; Davies *et al.*, 2014; Wang *et al.*, 2016). However, likely due to lithological complexities, a paucity of coarse-grained sediments and inadequate hydrate concentrations, they did not fully capture the possible processes fostering hydrate formation in coarse-grained sediments.

This study aims to improve our understanding of the distribution and genesis of coarse-grained gas hydrate-bearing sediments (C-GHBS) at high concentrations and their relationship with the free gas zone (FGZ). I integrate, by the use of 3D seismic data acquired in offshore Northern Colombia (**Fig. 6.2**), observations of seismic cross-sections with attribute maps of the bottom-simulating reflector (BSR), which is interpreted as the BGHSZ, and key seismic horizons passing through this interface. Given the relatively simple structural and stratigraphic setting that characterises the study area, this data is ideal to provide a clear visualisation of the impact on the seismic amplitude of gas hydrates *vs* free gas, and therefore to confidently hypothesise the most likely controls on their distribution.

## 6.2. Data and Methods

The seismic interpretation was performed with the Petrel E & P Software Platform at 0° phase (N. American polarity), on a post-stack 3D seismic data acquired by Shell in the Guajira Basin (offshore Northern Colombia), in both time-migrated and depth-converted forms, using a standard stacking velocity inversion (**Fig. 6.3**). The seismic data has inline (E-W) and crossline (N-S) spacing of 25 and 12.5 m, respectively, 4 ms sampling interval and a coverage area of 815 $km^2$. The seismic interval velocities of 1900-2000 m/s for the first km below the seafloor and the 45-50 Hz dominant frequency yield a vertical resolution of ~10 m while the lateral resolution likely ranges between ~12.5 and ~45 m, taken as intermediate between the bin spacing and the dominant wavelength (Cartwright and Huuse, 2005). Regional 2D seismic lines, with similar resolution, were also used to place our interpretation in a broader geological context.

The analysis of seismic data included the detection of amplitude anomalies potentially related to both gas hydrates and free gas and their interpretation, facilitated by extracting seismic wavelet from selected portions of seismic profiles. This was followed by a line-by-line mapping of an interpreted BSR and key stratigraphic reflections, in order to generate amplitude (root-mean-square and mean amplitude) and variance maps, which are crucial to better constrain the free gas and hydrate distribution, as well as to visualise the major structural elements in the area of interest (cf. Boswell *et al.*, 2012b; Plaza-Faverola *et al.*, 2012a; Davies *et al.*, 2014). These maps have been converted to depth by the use of the stacking velocity data (**Fig. 6.3**). The interpretation of the BSR has further been constrained by plotting its depth versus 100% methane hydrate stability conditions along this margin, using the CSMHyd software (Sloan Jr and Koh, 2007) at variable geothermal gradients, seafloor temperature and salinity conditions (**Fig. 6.4**). For confidentiality reasons, the seismic intervals older than the Late Miocene are not shown in detail in the figures.

## 6.3. Geological Setting

The 3D seismic dataset investigates a system of frontal anticlines in the Guajira Basin (offshore Northern Colombia). These anticlines are located seaward with respect to the Southern Caribbean Deformed Belt (Ladd *et al.*, 1984; Escalona and Mann, 2011; see **paragraph 2.3**), at water depths of 3500-4000 m (**Fig. 6.2**). The occurrence of bottom-simulating reflectors (BSRs) along this margin is well documented (Ladd *et al.*, 1984; López and Ojeda, 2006; Ochoa, 2013, see also **Fig. 2.4**). These BSRs are extensively distributed along the entire accretionary prism, as well as in the less deformed frontal anticlines (**Fig. 6.2c**), similarly to what observed in other convergent margins (e.g. Baba and Yamada, 2004; Barnes *et al.*, 2010). The study area is dominated by two NE-SW trending asymmetric thrust-propagation folds that deform the seafloor, creating pronounced bathymetric reliefs. This work focuses on these two anticlines (named $A_1$ and $A_2$). Three other minor anticlines ($A_3$-$A_5$), geometrically symmetrical and lacking a bathymetric relief, as well as the southwestern margin of a further asymmetric anticline ($A_6$) and the deepest and most seaward portion of the accretionary prism (i.e. the South Caribbean deformed Belt), have been observed in the 3D seismic data (**Fig. 6.2d**).

The investigated zones of free gas and hydrate occurrence are developed within Plio-Pleistocene sediments. The absence of borehole calibration in the study area, apart from a relatively far DSDP borehole (Leg 15, site 153) (Edgar *et al.*, 1973; Hopkins, 1973; Moore and Fahlquist, 1976) (**Fig. 6.2a**), makes the stratigraphic interpretation somewhat uncertain. Nevertheless, the available published studies of the Guajira Basin and the nearby Magdalena Fan area (e.g. Ercilla *et al.*, 2002; Romero Otero, 2009; Cadena *et al.*, 2015; Ramirez *et al.*, 2015; Leslie and Mann, 2016) let me interpret this shallow sequence as represented by an alternation between deepwater oozes and siliciclastic sediments, including a mass-transport deposit (MTD) and sheet-like turbidites. Part of these deposits likely constitute the most distal portions of the Magdalena Fan, and could further incorporate sediments transported

along nearby deepwater canyons (Romero Otero, 2009; see also the canyon in the lower-left portion of **Fig. 6.2b**). The seismic facies in this Plio-Pleistocene sequence appear laterally and vertically homogeneous at least for the first ~1000 m of overburden, indicating no substantial lateral variations in the depositional system. The continuity and the homogeneity of the observed Plio-Pleistocene stratigraphic reflections allow the interpretation of the high amplitude anomalies as being almost exclusively due to the impact of free gas *vs* hydrates on the sediment acoustic properties, superimposed over *'background'* acoustic impedance contrasts owing to lithology (cf. Crutchley *et al.*, 2016; Hillman *et al.*, 2017a). Nevertheless, the tectonic deformation that affects the study area has influenced the thickness of the most recent stratigraphic packages (i.e. the first 500-750 ms TWT of overburden, equal to ~500-750 m), which thin towards the crests of the anticlines (**Figs. 6.5-6.9**).

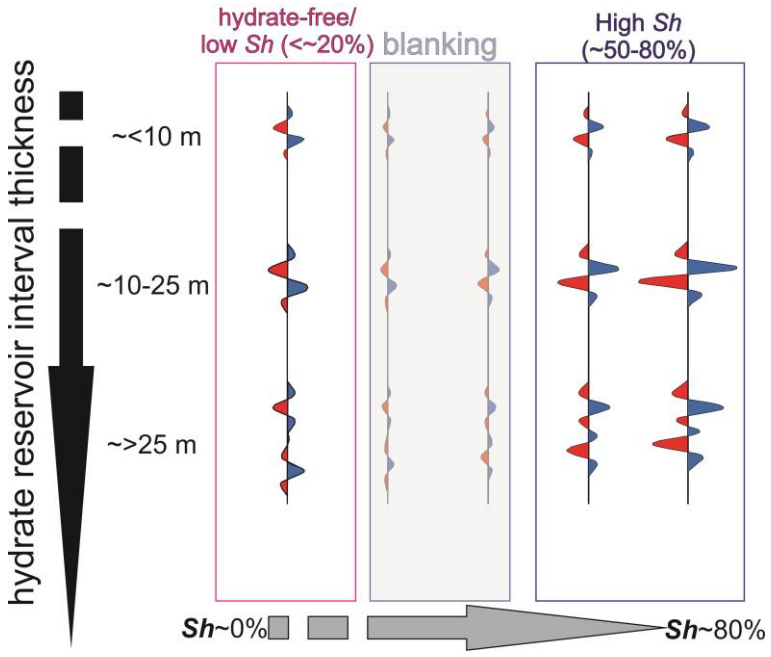



**Figure 6.1.** Seismic-trace conceptual model (modified after Lee *et al.*, 2009) for gas hydrate-bearing sediments with variable saturation (*Sh*, % of the pore space) and reservoir interval thickness, assuming a Ricker wavelet as input. The model of Lee *et al.* (2009) assumed a clean sand reservoir with 38% porosity and used a modified Biot-Gassmann rock physics theory (see the paper for further details). The seismic response in relation to the reservoir thickness changes, depending on seismic frequency and amplitude. The ranges of thickness shown in the figure could be valid for standard 3D seismic surveys frequencies (40-60 Hz) and should be taken as approximate values. Note how the seismic amplitude decreases at intermediate *Sh*, due to blanking. In contrast, at high *Sh* (e.g. 50-80%), the seismic amplitude of GHBS increases. Depending on the thickness of the reservoir, the seismic response can be more or less complex. For thick reservoirs, it is possible to observe a series of peak-trough combinations. In contrast, for relatively thin reservoirs, which approach the tuning thickness (which depends on seismic frequency and velocity), the amplitude response is represented by a single and amplified peak-trough combination. Finally, a change in polarity may occur at high *Sh*, depending on the initial acoustic impedance contrast between the hydrate reservoir and the overlying sediments.

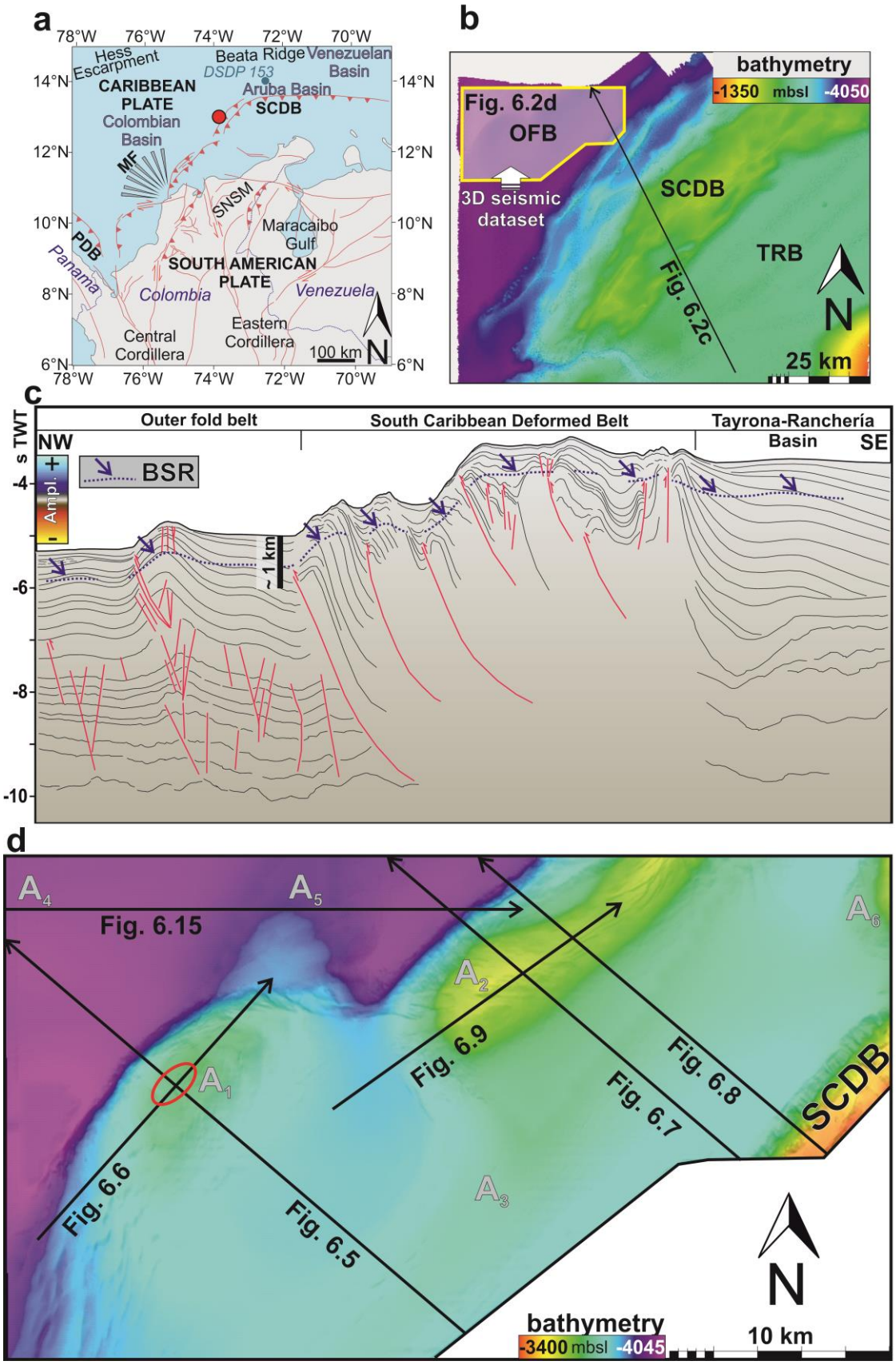



**Figure 6.2. (a)** Schematic map of the Northern South America. The red circle indicates the location of the study area. SCDB= South Caribbean Deformed Belt. **(b)** Bathymetric map of the offshore Guajira Basin. The shaded polygon highlights the study area, which has been covered by a 3D seismic survey. The black arrow indicates the trace of the seismic section shown in **(c)**. OFB= Outer fold belt; TRB= Tayrona-Ranchería Basin. **(c)** Line drawing of a 2D regional seismic line, showing the tectonic domains of the Guajira Basin. An extensive BSR is identified in the region (white dotted line). The study area is located in the Outer fold belt. **(d)** Detailed depth-converted bathymetric map of the study area. $A_1$, $A_2$, $A_3$, $A_4$, $A_5$, $A_6$= anticlines 1-6. The red ellipse indicates the location of the seafloor depression interpreted as a pockmark. The black arrows show the traces of the seismic sections in **Figs. 6.5-6.9** and **6.15**. Mbsl= metres below sea level.

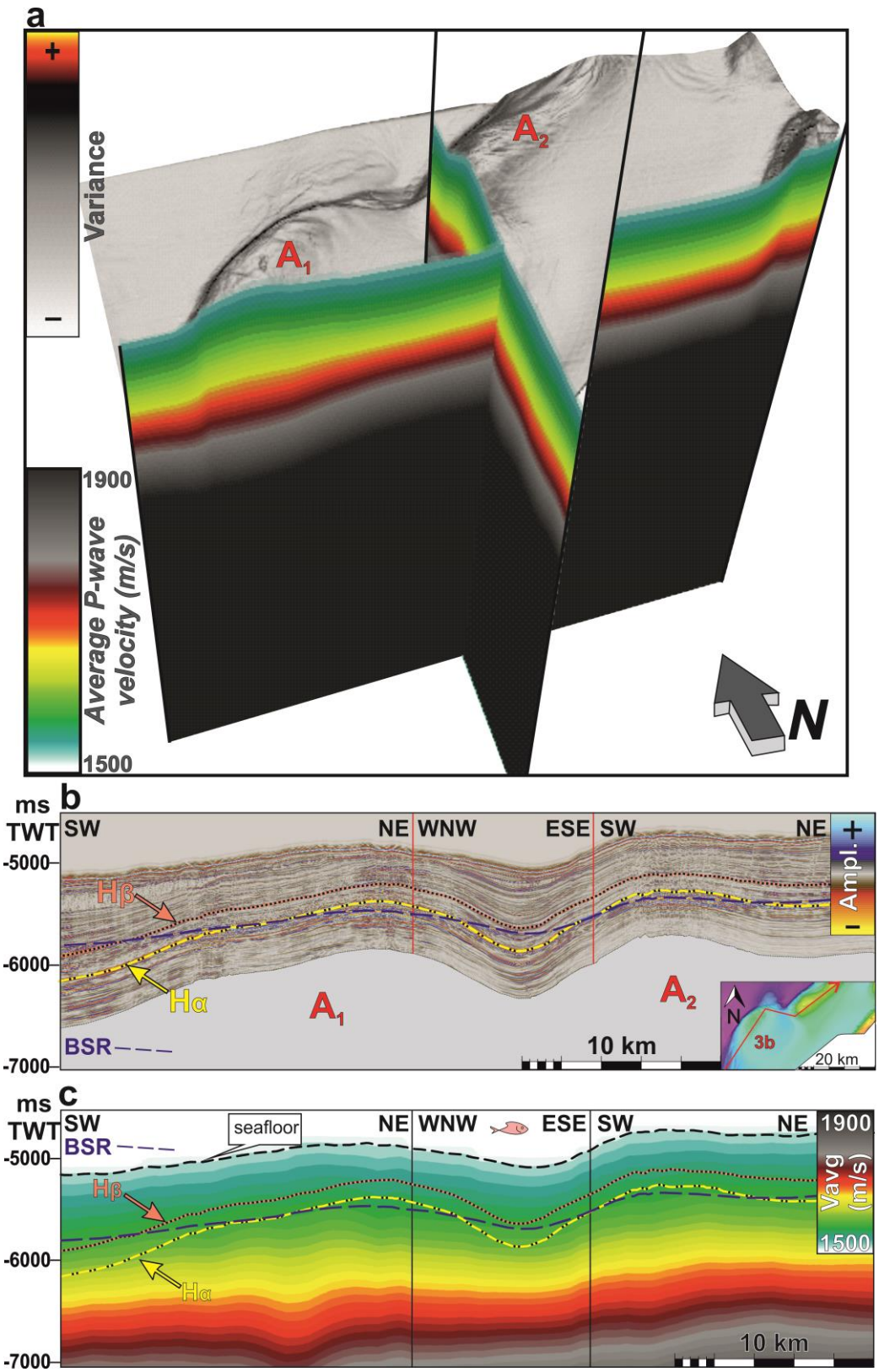



**Figure 6.3. (a)** 3D view of the seafloor of the study area (with a variance extraction), superimposed on the velocity model used to convert the TWT data into depth in the maps shown in **Figs. 6.12-6.14**. Note that the velocity scale refers to the average P-wave velocity (**Vavg**), therefore accounting for both the water column and the overburden at each TWT interval. **(b)** and **(c)** are, respectively, a composite seismic line passing across the two main anticlines of the study area ($A_1$ and $A_2$) and the average P-wave velocity along the same path. Both the BSR and the two seismic horizons interpreted in detail in this study (Hα and Hβ) are shown in these sections.

## 6.4. Results: seismic observations and interpretations

### *6.4.1. Seismic evidence of gas hydrates and free gas*

A clear BSR is identified at the limbs and at the crests of the anticlines that characterise the study area, between 550 and 700 metres below the seafloor (mbsf) (**Figs. 6.4-6.9**). This BSR exhibits all the diagnostic seismic characteristics to make it interpretable as the BGHSZ (Holbrook *et al.*, 1996; Baba and Yamada, 2004) (**Figs. 6.5-6.9**). The depth range of this BSR is in line with previous basin-scale predictions and suggests geothermal gradients of ~34-40°C/km, assuming 100% methane hydrate stability conditions, seawater salinity (3.0-3.5%) and a seafloor temperature of 2.0-2.5 °C (Ladd *et al.*, 1984; López and Ojeda, 2006; Ochoa, 2013) (**Fig. 6.4b, c**).

The stratigraphic reflections are cross-cut by the BSR (**Figs. 6.5-6.9**). These reflections further exhibit enhanced amplitudes along segments of variable length and vertical extent, both immediately above and below the BSR (**Figs. 6.5-6.9**). The polarity of these enhanced reflections, above the BSR, indicates an increase in the acoustic impedance contrast, given that the uppermost reflection has the same polarity of the seafloor. Thus, these reflections are associated with seismic wavelets exhibiting either a strong peak-trough combination, if the reflective interval is relatively thin (~15-25 ms TWT, ~15-25 m), or in more numerous leading peaks and troughs, if the reflective interval is relatively thick (~35-65 ms TWT, ~35-65 m) (**Fig. 6.10**). At or near the interpreted BGHSZ, the polarity of these enhanced reflections is reversed and, below this interface, becomes opposite to that of the seafloor, with the response in the seismic wavelet dominated by leading troughs (**Fig. 6.11)**.

The enhanced reflections above the BGHSZ are interpreted as C-GHBS at elevated *Sh*, as highlighted by **(1)** their high amplitude, **(2)** their polarity, **(3)** their direct connection to the BGHSZ and **(4)** their deep location within the GHSZ (**Figs. 6.5-6.10**) (cf. Boswell *et al.*, 2012b and 2016; Crutchley *et al.*, 2015). These observations also indicate that these amplitude anomalies are unlikely to be a response to either shallow water-bearing sands

surrounded by high-porosity muds or methanogenic carbonates, given that both would be expected to occur in the shallower portions of the overburden, with methanogenic carbonates spatially limited to areas of vertically-focused fluid flow (cf. Roberts *et al.*, 2006; Boswell *et al.*, 2012b and 2016; Cook and Tost, 2014; Crutchley *et al.*, 2015). In contrast, I interpret the enhanced reflections below the BGHSZ as free gas-bearing sediments, given their enhanced amplitude and opposite polarity response, compared to that of the overlying C-GHBS. The base of the FGZ is expressed as strong amplitude shut-offs along stratigraphic reflections (**Figs. 6.5-6.10**) (Calvès *et al.*, 2008; Foschi and Cartwright, 2016; Wang *et al.*, 2017a). The vertical seismic resolution (~10 m) does not permit us to resolve the real thickness of the beds richest in either hydrates or free gas. Hence, it is likely that these packages of enhanced reflections represent intervals consisting of thin beds with variable sand content and *Sh*, but overall consistently higher than in the surrounding sequence (cf. Fujii *et al.*, 2015; Hillman *et al.*, 2017a).

A polarity reversal, which indicates the BGHSZ, is observed along those horizons characterised by the most evident and extensive amplitude anomalies. This polarity reversal is particularly evident at the backlimb of $A_2$ (**Fig. 6.11b, c**). In contrast, at the backlimb of $A_1$, it appears ~20-60 ms TWT (~20-60 m) deeper than the depth of the interpreted BSR in the surrounding stratigraphy (**Fig. 6.11a**). This anomaly could reflect a broad spectrum of phenomena, such as **(1)** wavelet tuning effects (Yilmaz, 2001): it is observed that stratigraphic packages slightly thin from the backlimbs to the crests of the anticline (i.e. in an up-dip direction) and is therefore possible that the amplitude response of the same stratigraphic package varies laterally (cf. Lee *et al.*, 2009), complicating a clear recognition of polarity reversals; **(2)** localised overpressures, which would be capable of deepening the BGHSZ (Tinivella and Giustiniani, 2013); **(3)** capillary effects on the free gas phase, which would similarly deepen the three-phase boundary if hydrates fill the largest pores at the BGHSZ (Liu and Flemings, 2011); **(4)** the presence of $C_{2+}$ gases along the packages where

these anomalies are observed (cf. Milkov *et al.*, 2005), which could lead to the localised formation of methane-ethane structure I, or structure II hydrates, having a wider range of stability conditions than pure methane structure I hydrates (see **paragraph 1.1**). Without the current availability of borehole and geochemical data, it is complex to favour an interpretation for the observed localised shift of the polarity reversal, and I do not exclude that the observed anomaly is the result of a combination between geophysical artefact and real physical phenomena.

### *6.4.2. Distribution of gas hydrates and free gas*

The interpretation of seismic cross-sections, in conjunction with the extraction of seismic attribute maps from interpreted surfaces, has been used to characterise the distribution of both gas hydrates and free gas. The enhanced stratigraphic reflections interpreted to be associated with C-GHBS at elevated *Sh* are spatially limited to the crests of the anticlines. In contrast, those enhanced reflections related to free gas extend, beneath the interpreted BGHSZ, down the limbs of the anticlines, as well as at the cores of these structures, where they are organised into vertically stacked packages, up to several hundreds of ms TWT thick (see anticlines $A_{1\text{-}5}$ in **Figs. 6.5-6.9** and **6.15**).

The root-mean-square (RMS) amplitude map of the BSR indicates variable amplitudes across its areal extent (**Fig. 6.12a**). In this map, the zones characterised by high amplitudes are organised in elongated curvilinear bands, which follow the structural architecture of the study area and correlate in cross-sections with those segments of dipping stratigraphic reflections having enhanced amplitudes (cf. **Figs 6.5-6.9** with **Fig. 6.12a**). Thus, the amplitude of the BSR (**Fig. 6.10**) reflects the interaction between the BGHSZ and packages of stratigraphic reflections with different amplitude, a interpreted to reflect changes in gas hydrate and free gas concentration, as well as in lithology (cf. Boswell *et al.*, 2012b; Davies *et al.*, 2014; Wang *et al.*, 2016; Hillman *et al.*, 2017b). By applying an investigation window

restricted to the stratigraphy either above or below the BSR (**Fig. 6.12b, c**), it is further possible to visualise the extent of the high amplitude anomalies either immediately above or below this interface, respectively associated with C-GHBS at high concentrations and free gas-bearing sediments (cf. **Figs 6.5-6.9** with **Fig. 6.12b, c**).

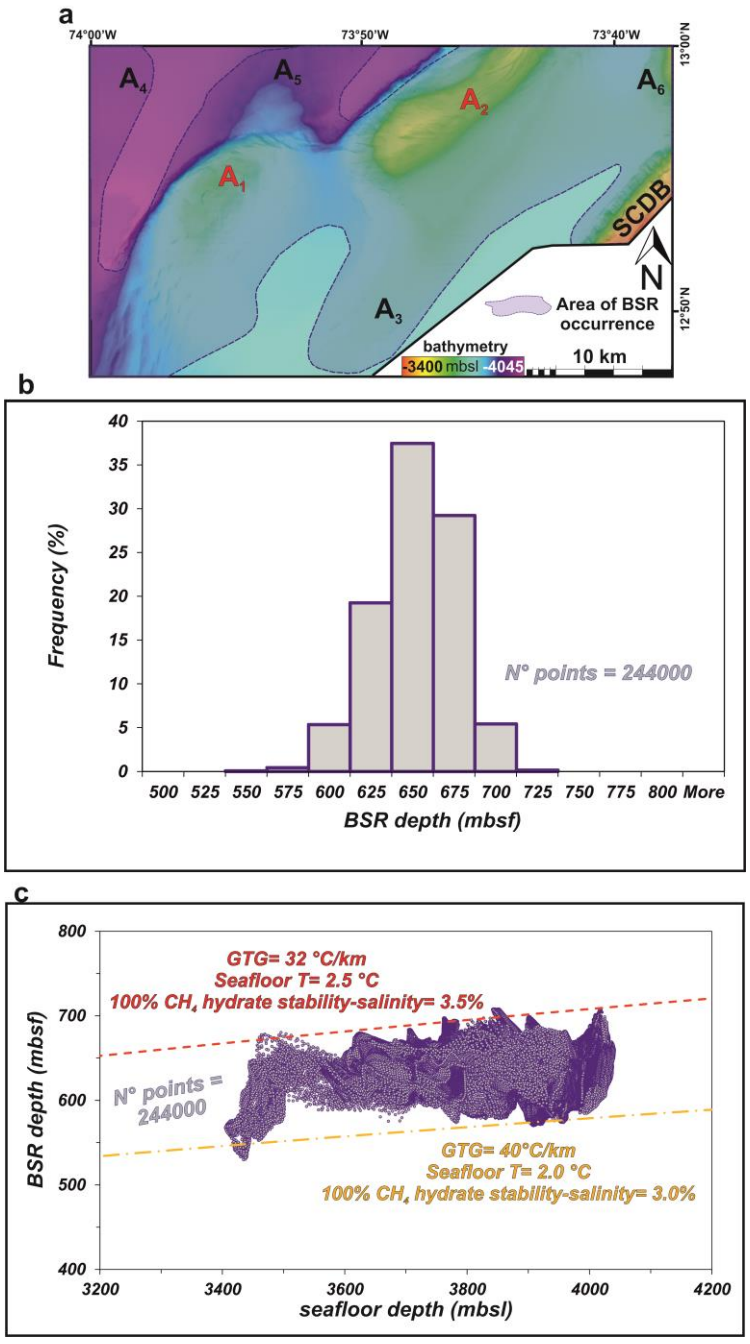



**Figure 6.4. (a)** Detailed depth-converted bathymetric map of the study area, showing the areal occurrence of the BSR (semi-transparent light-blue area). $A_1$, $A_2$, $A_3$, $A_4$, $A_5$, $A_6$= anticlines 1-6. **(b)** Frequency histogram showing the range of depths below the seafloor of the BSR. **(c)** BSR depth in metres below the seafloor (mbsf) *vs* seafloor depth above the BSR, expressed in metres below the sea level (mbsl). The red and light-orange lines represent the 100% methane hydrate stability conditions, where the geothermal gradient (GTG) varies between 34 and 40 °C/km, the salinity varies between 3.0 and 3.5% and the seafloor temperature ranges between 2.0 and 2.5 °C. The vast majority of the points plot within this range, in agreement with previous basin-scale models of the depth of the BGHSZ (e.g. Ochoa, 2013).

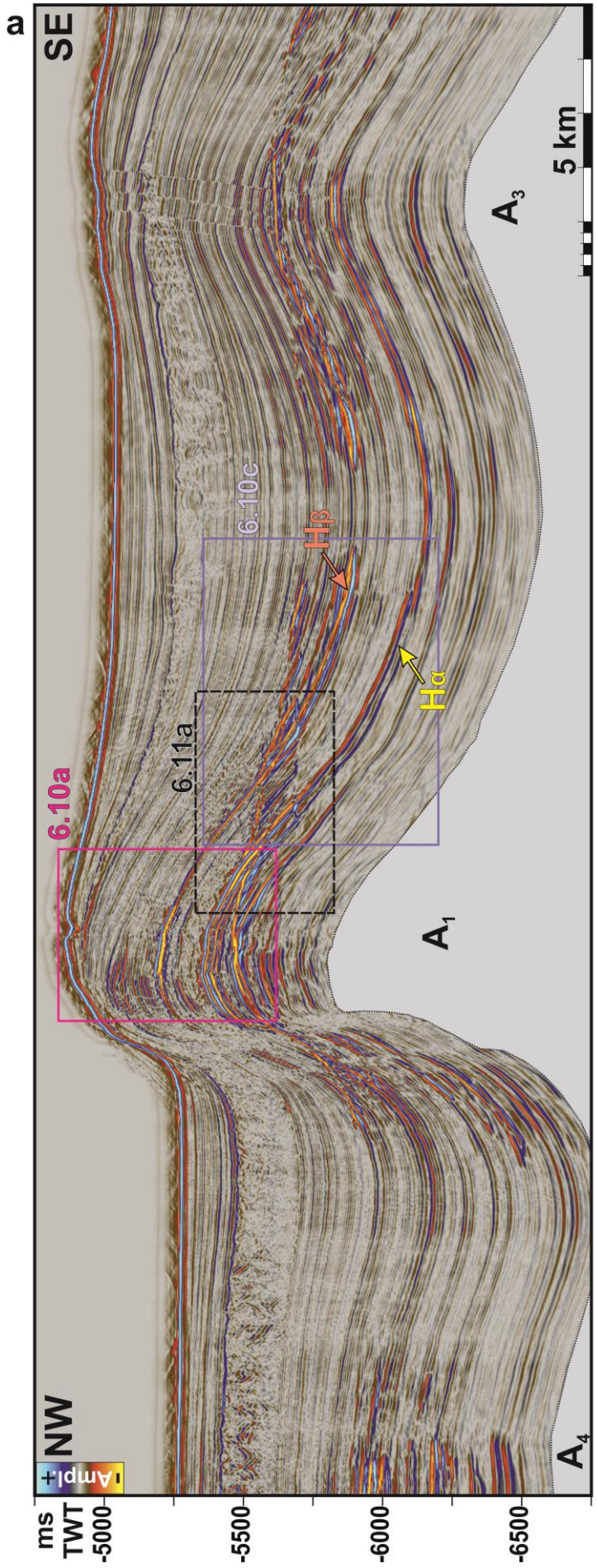



**Figure 6.5. (a)** NW-SE seismic section, passing through $A_4$, $A_1$ and $A_3$. The rectangular boxes refer to portions of this section shown in **Figs. 6.10** and **6.11**. See **Fig. 6.5b** for the interpreted version of this section.

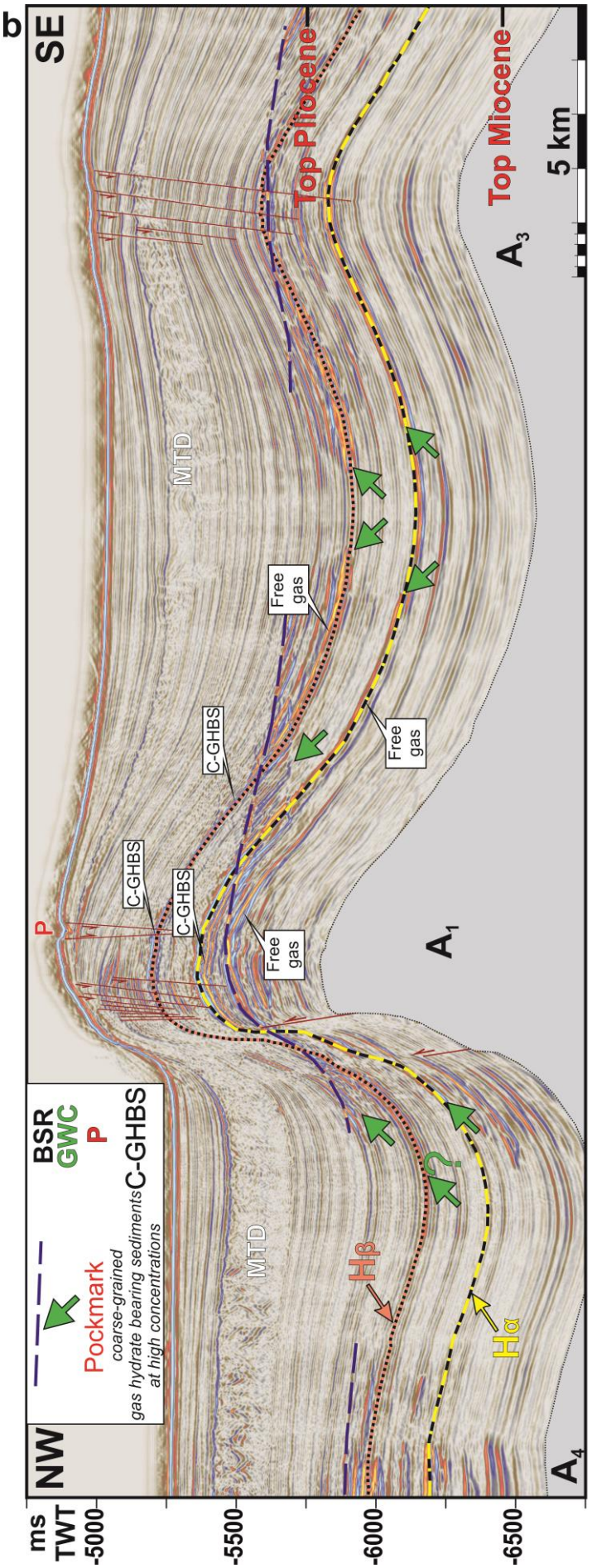



**Figure 6.5. (b)** NW-SE seismic section, passing through $A_4$, $A_1$ and $A_3$ (interpreted section). The stratigraphic reflections with enhanced amplitudes above the BSR (blue dashed line) are interpreted as coarse-grained gas hydrate-bearing sediments (C-GHBS) at high concentrations whereas the enhanced reflections beneath the BSR are interpreted as free gas-bearing sediments. The green arrows indicate the base of the free gas zone, expressed as a gas-water contact (GWC) which varies in depth along different horizons. Hα (yellow-black dashed-dotted line) and Hβ (orange-black dotted line) pass through the BSR (i.e. the BGHSZ). Note the dense array of faults at the crest of $A_1$. The approximate stratigraphic marker (uncalibrated) for the Top Miocene and Top Pliocene are also indicated on the right.

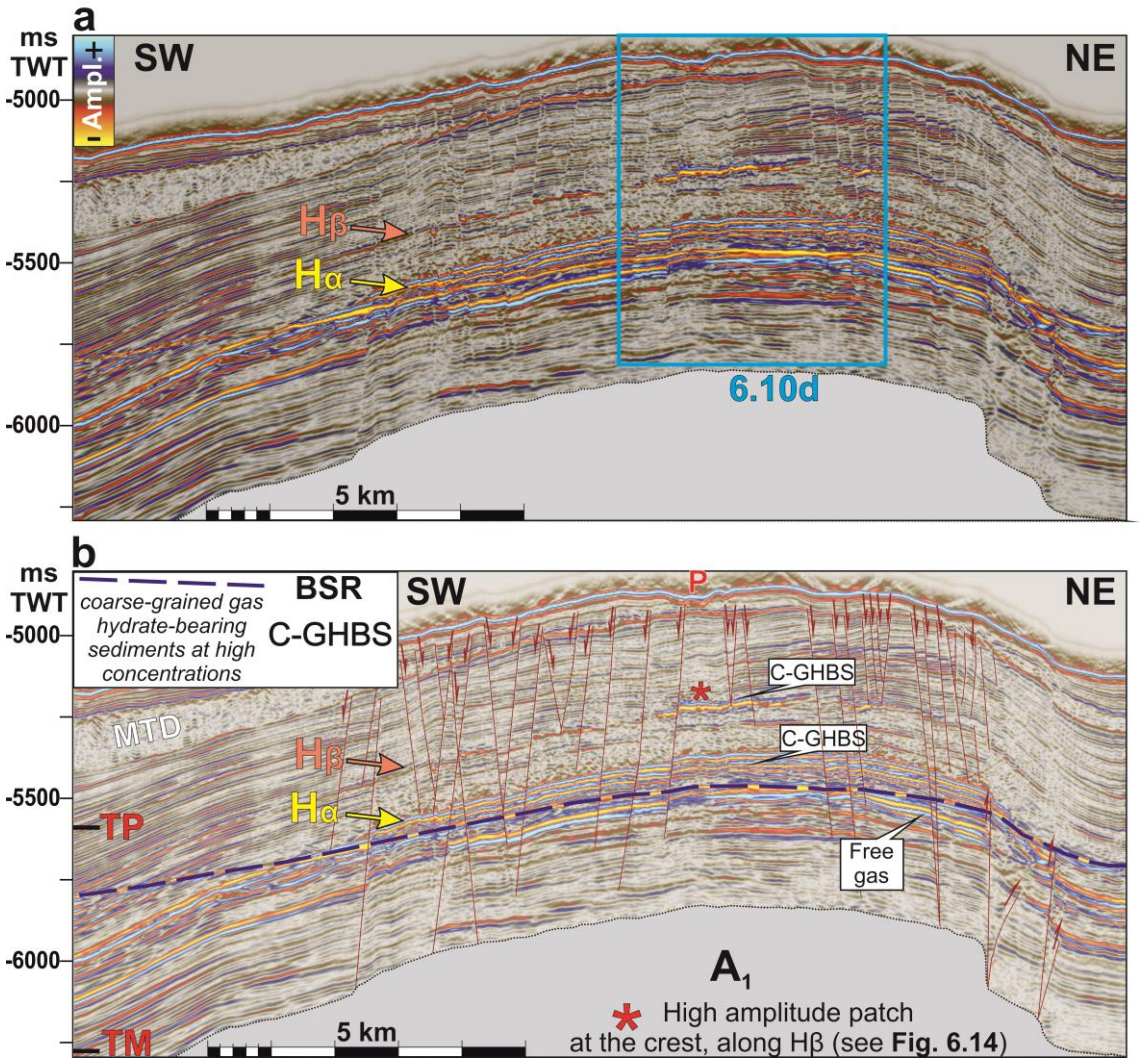



**Figure 6.6.** SW-NE seismic section, showing the crest of $A_1$. **(a)** Uninterpreted version; **(b)** Interpreted version. The rectangular box in **(a)** refers to a portion of the section shown in **Fig. 6.10**. The stratigraphic reflections with enhanced amplitudes above the BSR (blue dashed line) are interpreted as coarse-grained gas hydrate-bearing sediments (C-GHBS) at high concentrations whereas the enhanced reflections beneath the BSR are interpreted as free gas-bearing sediments. Hα and Hβ are indicated with a yellow and an orange arrow, respectively. Note the dense array of faults at the crest of $A_1$, possibly linked with a pockmark at the seafloor (P). The high amplitude patch at the crest of the $A_1$, along Hβ, is indicated by an asterisk. The approximate stratigraphic marker (uncalibrated) for the Top Miocene (TM) and Top Pliocene (TP) are also indicated on the left.

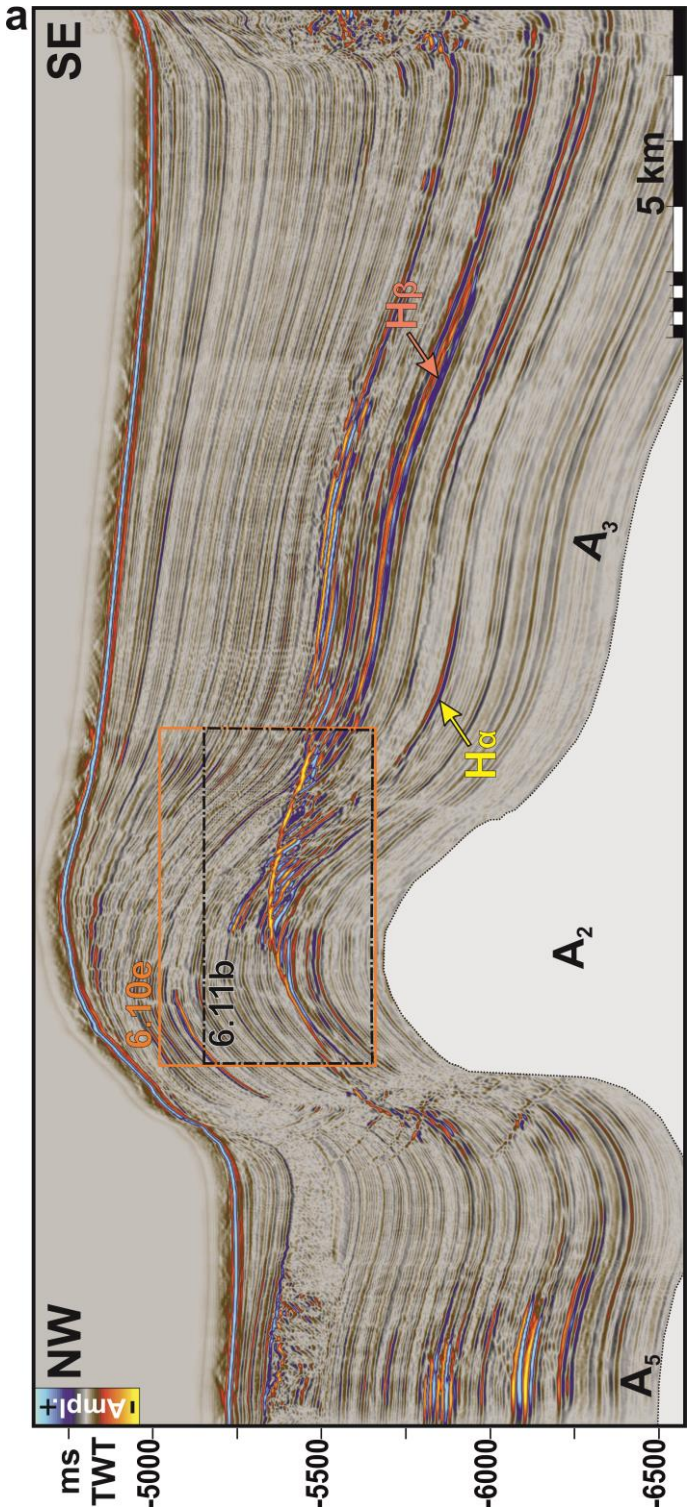



**Figure 6.7. (a)** NW-SE seismic section, passing through $A_5$, $A_2$, $A_3$ and the seaward front of the South Caribbean Deformed Belt (SCDB). The rectangular boxes refer to portions of this section shown in **Figs. 6.10** and **6.11**. See **Fig. 6.7b** for the interpreted version of this section.

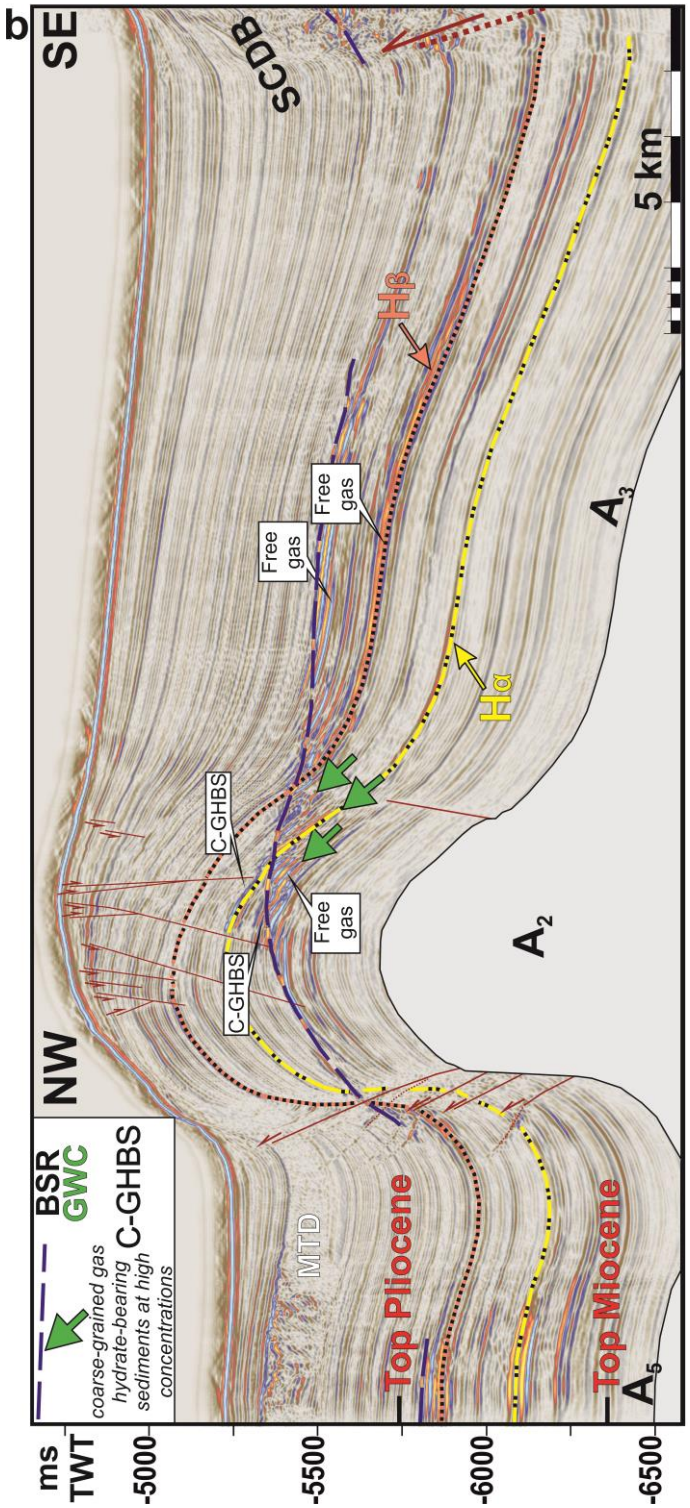



**Figure 6.7. (b)** NW-SE seismic section, passing through $A_5$, $A_2$, $A_3$ and the most seaward portion of the South Caribbean Deformed Belt (SCDB) (interpreted section). The stratigraphic reflections with enhanced amplitudes above the BSR (blue dashed line) are interpreted as coarse-grained gas hydrate-bearing sediments (C-GHBS) at high concentrations whereas the enhanced reflections beneath the BSR are interpreted as free gas-bearing sediments. The green arrows indicate the base of the free gas zone, expressed as a gas-water contact (GWC) which varies in depth along different horizons. Hα (yellow-black dashed-dotted line) and Hβ (orange-black dotted line) pass through the BSR (i.e. the BGHSZ). The base of the FGZ is unclear along Hβ, despite the evidence of free gas (cf. with **Fig. 6.14**). Note the dense array of faults at the crest of $A_2$. The approximate stratigraphic marker (uncalibrated) for the Top Miocene and Top Pliocene are also indicated on the left.

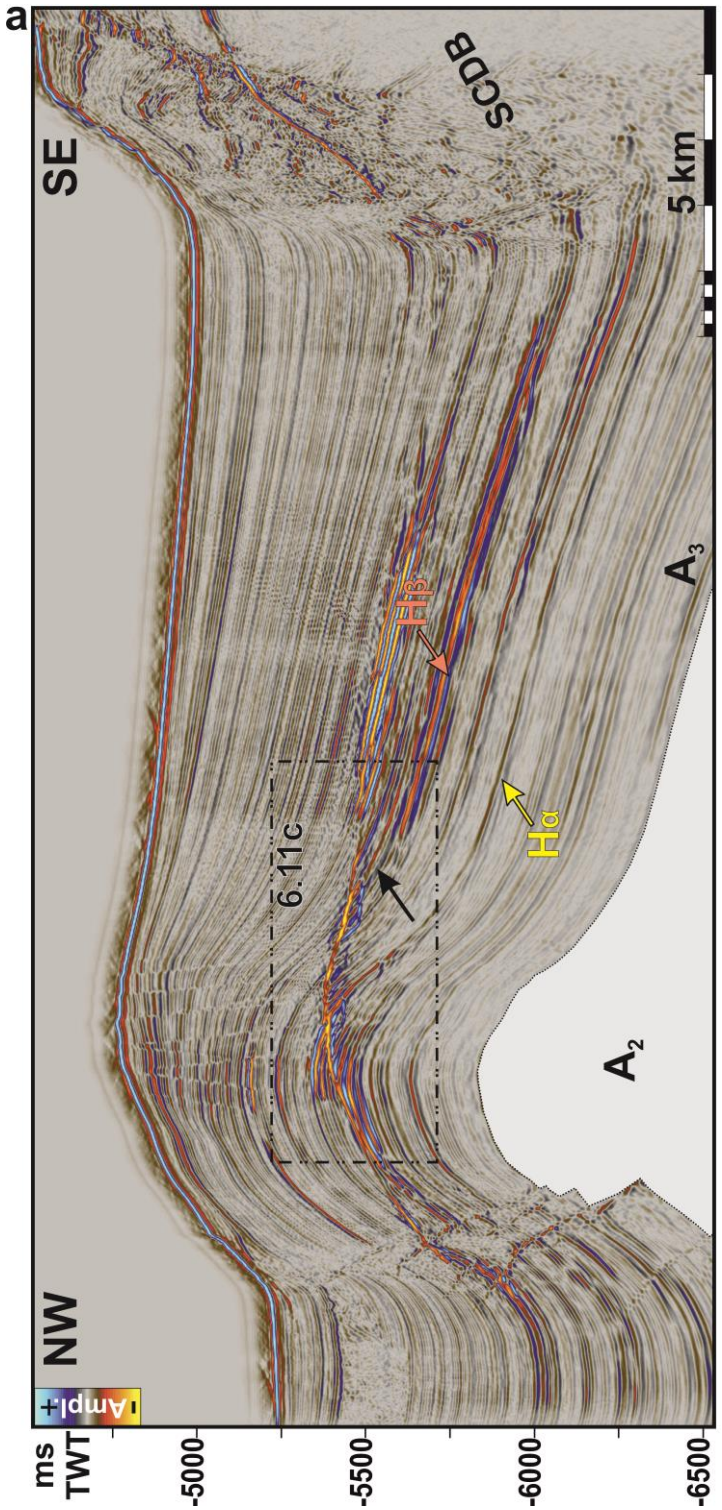



**Figure 6.8. (a)** NW-SE seismic section, passing through $A_2$, $A_3$ and the seaward front of the South Caribbean Deformed Belt (SCDB). The rectangular box refers to a portion of this section shown in **Fig. 6.11**. See **Fig. 6.8b** for the interpreted version of this section. The black arrow indicates a zone of low amplitude along Hβ, separating zones of enhanced amplitudes. This observation suggests that the free gas zone along Hβ is not continuously developed at the backlimb of $A_2$ (cf. with **Fig. 6.14**), possibly due to the interference of other structures (e.g. $A_3$ and $A_6$).

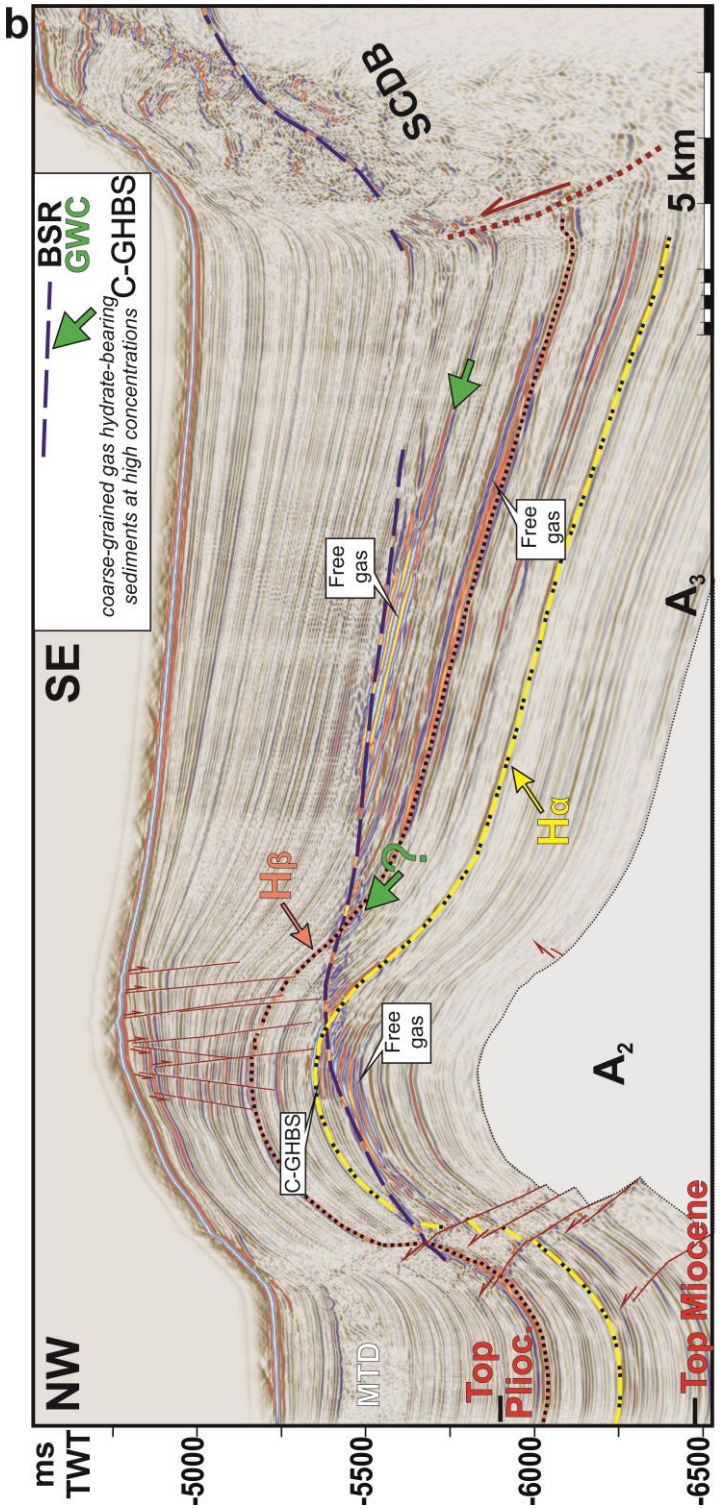



**Figure 6.8. (b)** NW-SE seismic section, passing through $A_2$, $A_3$ and the most seaward portion of the South Caribbean Deformed Belt (SCDB) (interpreted section). The stratigraphic reflections with enhanced amplitudes above the BSR (blue dashed line) are interpreted as coarse-grained gas hydrate-bearing sediments (C-GHBS) at high concentrations whereas the enhanced reflections beneath the BSR are interpreted as free gas-bearing sediments. The green arrows indicate the base of the free gas zone, expressed as a gas-water contact (GWC) which varies in depth along different horizons. Hα (yellow-black dashed-dotted line) and Hβ (orange-black dotted line) pass through the BSR (i.e. the BGHSZ). The base of the FGZ is unclear along Hβ, despite the evidence of free gas (cf. with **Fig. 6.14**). Note the dense array of faults at the crest of $A_2$. The approximate stratigraphic marker (uncalibrated) for the Top Miocene and Top Pliocene are also indicated on the left.

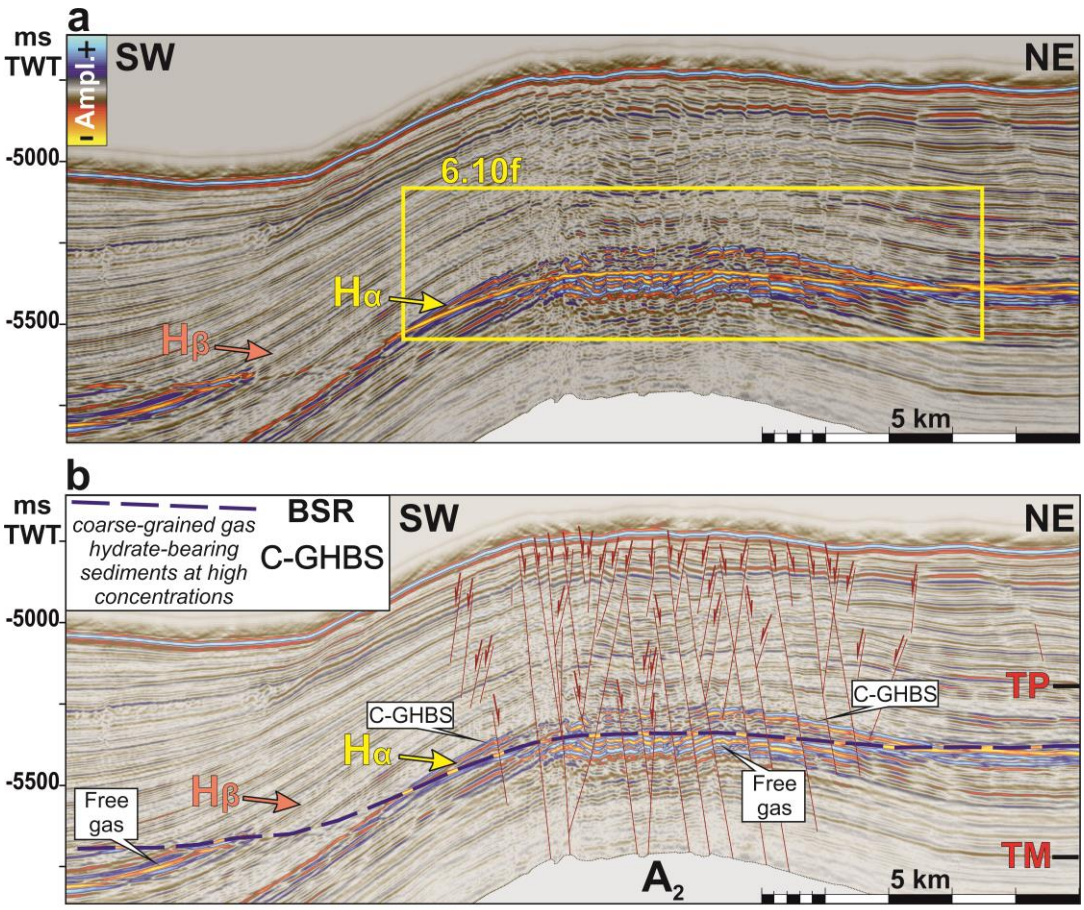



**Figure 6.9.** SW-NE seismic section, showing the crest of $A_2$. **(a)** Uninterpreted version; **(b)** Interpreted version. The rectangular box in **(a)** refers to a portion of the section shown in **Fig. 6.10**. The stratigraphic reflections with enhanced amplitudes above the BSR (blue dashed line) are interpreted as coarse-grained gas hydrate-bearing sediments (C-GHBS) at high concentrations whereas the enhanced reflections beneath the BSR are interpreted as free gas-bearing sediments. Hα and Hβ are indicated with a yellow and an orange arrow, respectively. Note the dense array of faults at the crest of the anticline. The approximate stratigraphic marker (uncalibrated) for the Top Miocene (TM) and Top Pliocene (TP) are also indicated on the right.

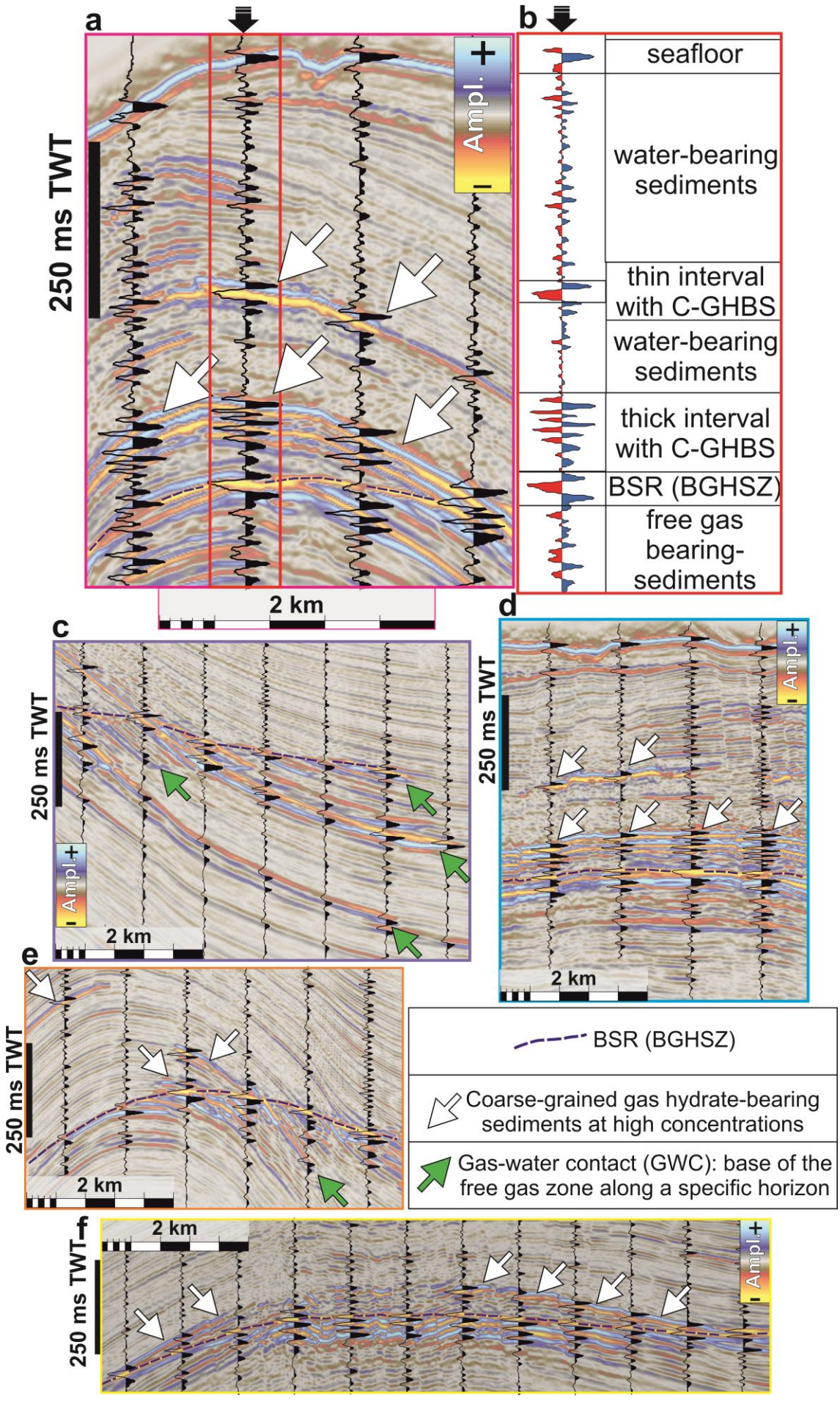

a
b
250 ms TWT
Ampl.
+
-
seafloor
water-bearing sediments
thin interval with C-GHBS
water-bearing sediments
thick interval with C-GHBS
BSR (BGHSZ)
free gas bearing-sediments
2 km
c
d
e
f
BSR (BGHSZ)
Coarse-grained gas hydrate-bearing sediments at high concentrations
Gas-water contact (GWC): base of the free gas zone along a specific horizon

**Figure 6.10 (See the previous page).** Seismic wavelet extraction from selected portions of seismic sections (see **Figs. 6.5-6.9** for the location), and interpretation of the high amplitude anomalies as due to either gas hydrates or free gas. The seismic profiles and wavelets are at zero-phase (North American polarity convention). The seismic wavelet, where indicating coarse-grained gas hydrate-bearing sediments (C-GHBS) at high concentrations, exhibits either a strong peak-trough combination, if the reflective interval is relatively thin (~15-25 ms TWT, ~15-25 m), or more numerous leading peaks and troughs if the reflective interval is relatively thick (~35-65 ms TWT, ~35-65 m). In contrast, a strong leading trough characterises the BSR. The underlying FGZ displays a more complex combination of enhanced amplitudes, dominated by leading troughs. **(a)** Crest of $A_1$ (NW-SE, see **Fig. 6.5a**). **(b)** Interpretation of the seismic wavelet bounded with a red rectangle in **(a)**, which captures intervals with C-GHBS of various thickness, the BSR and free gas-bearing sediments. **(c)** Backlimb of $A_1$ (NW-SE, see **Fig. 6.5a**). **(d)** Crest of $A_1$ (SW-NE, see **Fig. 6.6a**). **(e)** Crest and limbs of $A_2$ (NW-SE, see **Fig. 6.7a**). **(f)** Crest of $A_2$ (SW-NE, see **Fig. 6.9a**).

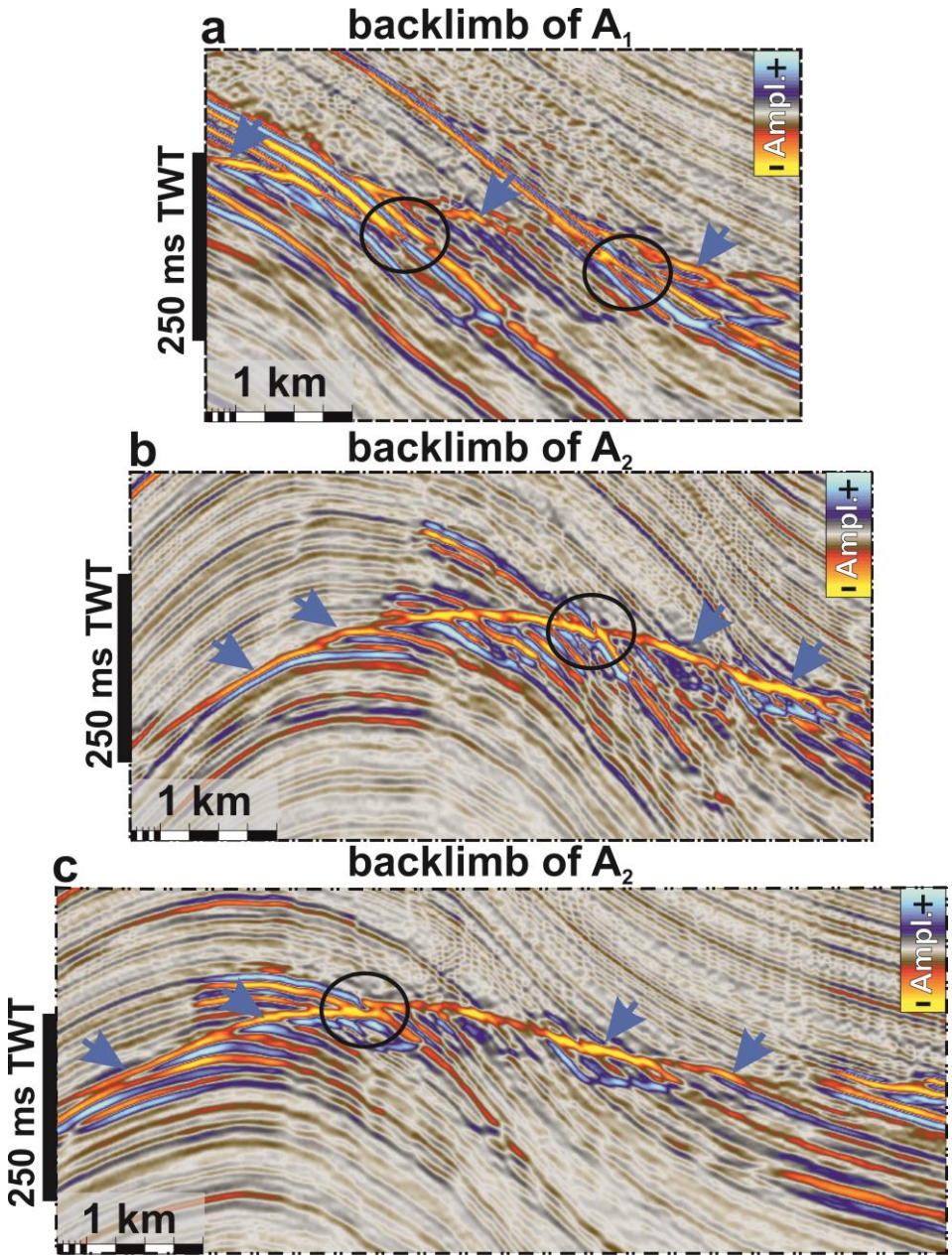



**Figure 6.11.** Portions of the seismic sections shown in **Figs. 6.5, 6.7** and **6.8**, showing possible polarity reversals (black circles) near and at the interpreted BGHSZ (i.e. the BSR), at the backlimb of $A_1$ **(a)** and $A_2$ **(b, c)**. The reversal is more evident at the backlimb of $A_2$ than at the backlimb of $A_1$. In this latter anticline, the reversal seems to occur slightly deeper than the interpreted position of the BGHSZ (blue arrows).

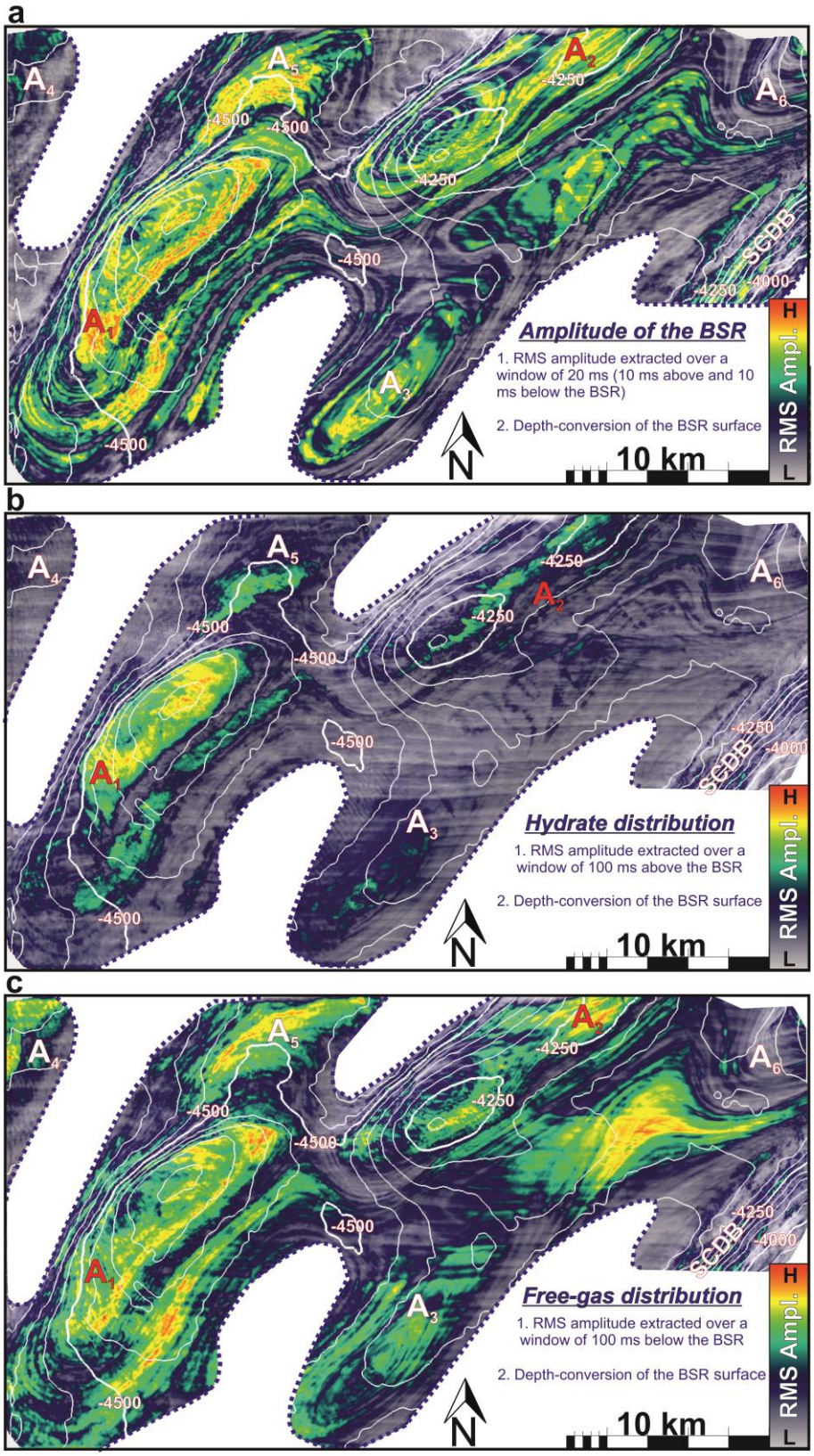



**Figure 6.12.** RMS amplitude maps of the area of BSR occurrence. Points 1 and 2 describe the procedure used to extract and depth-convert these attribute maps. In all the maps, the RMS amplitude has been firstly extracted from the time-migrated seismic data and then depth-converted, by applying the velocity model shown in **Fig. 6.3**. In **(a)**, the investigation window is of 20 ms TWT (10 ms TWT above the BSR and 10 ms TWT below the BSR). In **(b)**, the investigation window is of 100 ms TWT above the BSR. In **(c)**, the investigation window is of 100 ms TWT below the BSR. Therefore, the map shown in **(a)** captures the amplitude of the BSR and the immediately nearby reflections. In contrast, the maps in **(b)** and **(c)**, permit to visualise the amplitude anomalies respectively associated with gas hydrates and free gas.

I have extracted the mean amplitude from two significant stratigraphic reflections, named Horizon-α (Hα) and Horizon-β (Hβ) (**Figs. 6.13a, 6.14a**), being part of two separate 20-50 m thick packages of enhanced reflections, exhibiting the seismic characteristics described earlier (**Figs. 6.5-6.11**). This attribute extraction allows us to discriminate between high amplitude anomalies with opposite and equal polarities with respect to that of the seafloor. In these attribute maps, the zones of high amplitude associated with a positive acoustic impedance contrast are coloured in white and, in line with our interpretation of the seismic cross-sections (see **sub-paragraph 6.4.1**), are considered indicative of C-GHBS at high concentrations. By contrast, the zones of high amplitude related to a negative acoustic impedance contrast are coloured in bright green and are interpreted to indicate free gas-bearing sediments (**Figs. 6.13a, 6.14a**). The variance renderings of the same horizons accompany the amplitude extractions, to provide a view of the structural framework. Notably, these maps show that the crests of $A_1$ and $A_2$ are affected by dense arrays of normal faults (**Figs. 6.13b, 6.14b**).

The package of reflections containing Hα is older, closer to the cores of the anticlines and steeper at the limbs than that containing Hβ (**Figs. 6.5-6.9**). The portion of Hα that overlies the BGHSZ at the crest and the limbs of $A_1$ is entirely characterised by enhanced amplitudes, indicating an extensive accumulation of gas hydrates. In contrast, these amplitude anomalies are only observed at the backlimb of $A_2$, extending throughout the GHSZ for a maximum of 1 km far from the three-phase boundary (cf. **Fig. 6.13a** with **Figs. 6.5, 6.6, 6.10a, d**). At the backlimb of $A_2$, the geometry of the termination of the amplitude anomalies related to hydrates exhibits *'finger-shaped'* high-amplitude patches in the southwestern portion of the anticline, where the faults are oriented approximately perpendicular to the fold axis. In the northeastern portion of $A_2$, where the faults strike almost parallel to the fold axis, the high-amplitude anomalies become more homogeneous than in the southwestern portion of this thrust-cored fold. Here, the upper termination of such

anomalies is abrupt and appears to terminate across a fault surface (cf. **Fig. 6.13a, b** with **Figs. 6.3a** and **6.7a, b**). Along, Hβ, at the limbs of $A_1$, the high-amplitude anomalies indicative of C-GHBS at high concentrations are not as homogeneously distributed as along Hα, being instead constituted of *'finger-shaped'* high-amplitude patches, departing upward from the BGHSZ. These zones of high amplitude are separated by *'recession zones'* with a *'background'* amplitude (i.e. coloured in black in the amplitude map), whose location overlaps in some places with the NW-SE oriented normal faults **(Fig. 6.14a, b**). The high-amplitude anomalies within the GHSZ are only locally developed at the forelimb and the crest of $A_2$, whereas, at the backlimb of this structure, they are limited to areas close to the BGHSZ (**Fig. 6.14a**). An irregular patch having high amplitude has been further observed at the crest of $A_1$ (cf. **Figs. 6.6** and **6.14a**) and can be interpreted as a localised hydrate accumulation. Similar high-amplitude anomalies are only locally developed at the forelimb and the crest of $A_2$, whereas at the backlimb of this structure these anomalies are limited to areas close to the BGHSZ (F**ig. 6.14a**). The normal faults observed at the crest of $A_1$ and $A_2$ (**Figs. 6.6, 6.9)** occasionally pierce the seabed and further extend below the BSR. **6.13b, 6.14b**). Therefore, these faults intersect numerous enhanced reflections, both below and above the interpreted BGHSZ, including the high-amplitude patch observed along Hβ (cf. **Figs. 6.6** and **6.9**). Above this zone of enhanced amplitude, I have identified a pockmark-like depression at the seafloor, which constitutes the termination of some of these faults (**Fig. 6.6**).

The mean amplitude extractions along Hα and Hβ further show extensive zones of high amplitude as a result of a negative acoustic impedance contrast, and therefore indicative of free gas-bearing sediments (see **sub-paragraph 6.4.**1). These high-amplitude anomalies are more extensively developed along the limbs of $A_1$ than at those of $A_2$ (**Figs. 6.13, 6.14**). This difference is clear for Hα, which shows almost no evidence of free gas at the limbs of $A_2$, except for the first ~100 m below the BGHSZ. Along Hβ, the high-amplitude anomalies

indicative of free gas are clearly recognised between $A_1$ and $A_3$. These anomalies persist, although with a lower amplitude, between the backlimb of $A_2$ and the front of the South Caribbean Deformed Belt. In this latter area, such zones of enhanced amplitude do not appear directly connected to the BGHSZ at the backlimb of $A_2$ (see the black arrow in **Fig. 6.8a**), possibly owing to the topographic interference of anticlines $A_3$ and $A_6$ (see **Fig. 6.14a**). At the backlimb of $A_1$, the free gas column along Hα is larger (at least 570 m thick) compared to that along Hβ (at least 265 m thick). The bases of these free gas accumulations are sharp and conform to the structure, indicating a gas-water contact (GWC) in the amplitude maps (**Fig. 6.13a, 6.14a**). These observations suggest that these free gas columns are internally connected and exert a buoyancy pressure at the BGHSZ (cf. Grauls, 2001; Bangs *et al.*, 2011; Boswell *et al.*, 2012b).

These observations indicate that the largest and probably buoyant free gas accumulations developed beneath the BGHSZ correlate with the most extensive and seismically-visible deposits of C-GHBS. This coupling between free gas and hydrate-bearing sediments is validated by comparing the different structures ($A_1$ *vs* $A_2$) and different stratigraphic intervals characterised by packages of enhanced reflections (Hα *vs* Hβ) (cf. **Figs. 6.13**, **6.14**). Much thinner free gas columns (max. 100 m thick) have been observed in association with other packages of stratigraphic reflections, whose amplitude is further not particularly enhanced above the BGHSZ (**Figs. 6.5-6.9**). This latter observation suggests that in these intervals hydrates are either absent or present at low to moderate concentrations.

At the forelimb of $A_1$, the GWC along Hα appears a few tens of metres deeper than at its backlimb (cf. the GWC *vs* the 5000 m contour in **Fig. 6.13a**). A similar observation has been made for a nearby symmetrical anticline ($A_5$), where there is a difference of more than ~100 ms TWT (~100 m) between the bases of stacked enhanced reflections, interpreted as free gas-bearing sediments (**Fig. 6.15**). Among these free gas traps, the shallowest is cross-cut, and therefore hydraulically impacted, by the BGHSZ (see the blue dashed line in **Fig.**

**6.15b**) Such differences between the depths of the GWCs at different limbs of anticlines, in conjunction with the lack of evidence of a fault-controlled reservoir compartmentalisation, may indicate the presence of water overpressure in the system. Two likely causes for this overpressure include the existence of a hydrodynamic system linked to fluids expelled from inboard thrusts (Carson and Screaton, 1998; Muggeridge and Mahmode, 2012), and perched water conditions in the minibasins (Rolfsvåg and Danielsen, 2016). Alternatively, a presently active and directional gas supply to the shallow reservoir along carrier beds, or the occurrence of permeability changes within the same reservoir could further help in explaining these observations (e.g. England *et al.*, 1987; Wang *et al.*, 2017b). Differences in the amounts of lateral pressure transfer owing to tilting (Yardley and Swarbrick, 2000) at different limbs of the anticlines would result in a GWC shallower at the steep forelimb of $A_1$ rather than at the gentle backlimb, which is opposite to what is observed.

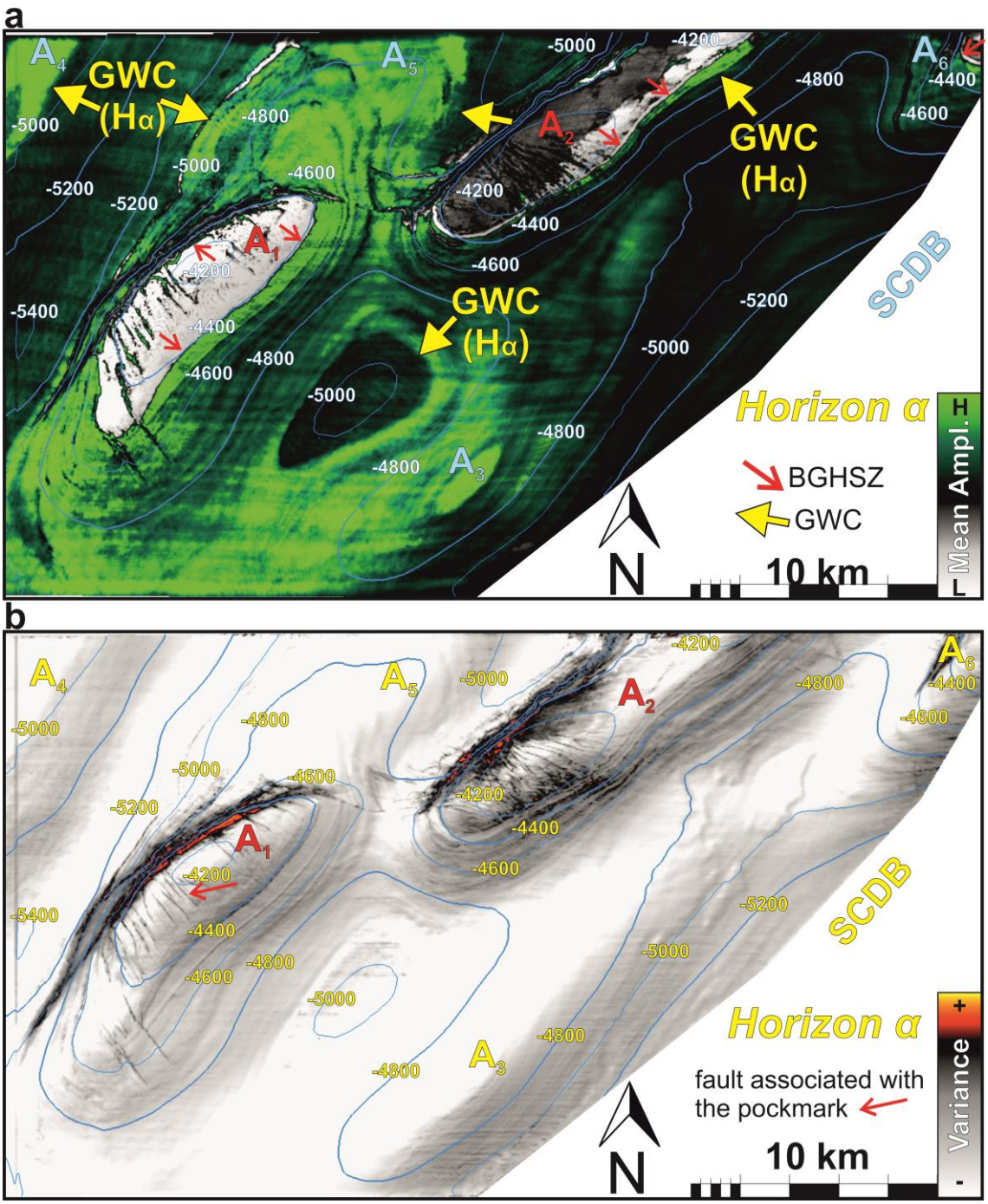



**Figure 6.13.** Attribute maps of Hα. These maps have been depth-converted, and the depth is in metres below the sea level (mbsl). **(a)** Mean amplitude map of Hα. The map shows the areas of enhanced amplitude. If the high amplitude anomaly is associated with a positive acoustic impedance contrast, it is coloured in white and is interpreted to indicate coarse-grained gas hydrate-bearing sediments (C-GHBS) at high concentrations. In contrast, if the high amplitude anomaly reflects a negative acoustic impedance contrast, it is coloured in bright green and is interpreted to indicate free gas-bearing sediments. Note the clear GWC at the limbs of $A_1$. A GWC is also observed at the backlimb of $A_2$. The amplitude anomalies at the crest and the limbs of $A_1$ are much more widespread, compared to $A_2$. The red arrows indicate the BGHSZ along this horizon. The GWC is further slightly deeper at the forelimb than at the backlimb of $A_1$ (compare the GWC with the 5000 mbsl contour). **(b)** Variance map of Hα. Note the numerous NW-SE trending faults at the crests of $A_1$ and $A_2$, as well as the high variance zones at the forelimbs of these folds, indicating thrust zones. The red arrow indicates a crestal normal fault that connects the pockmark to the overburden.

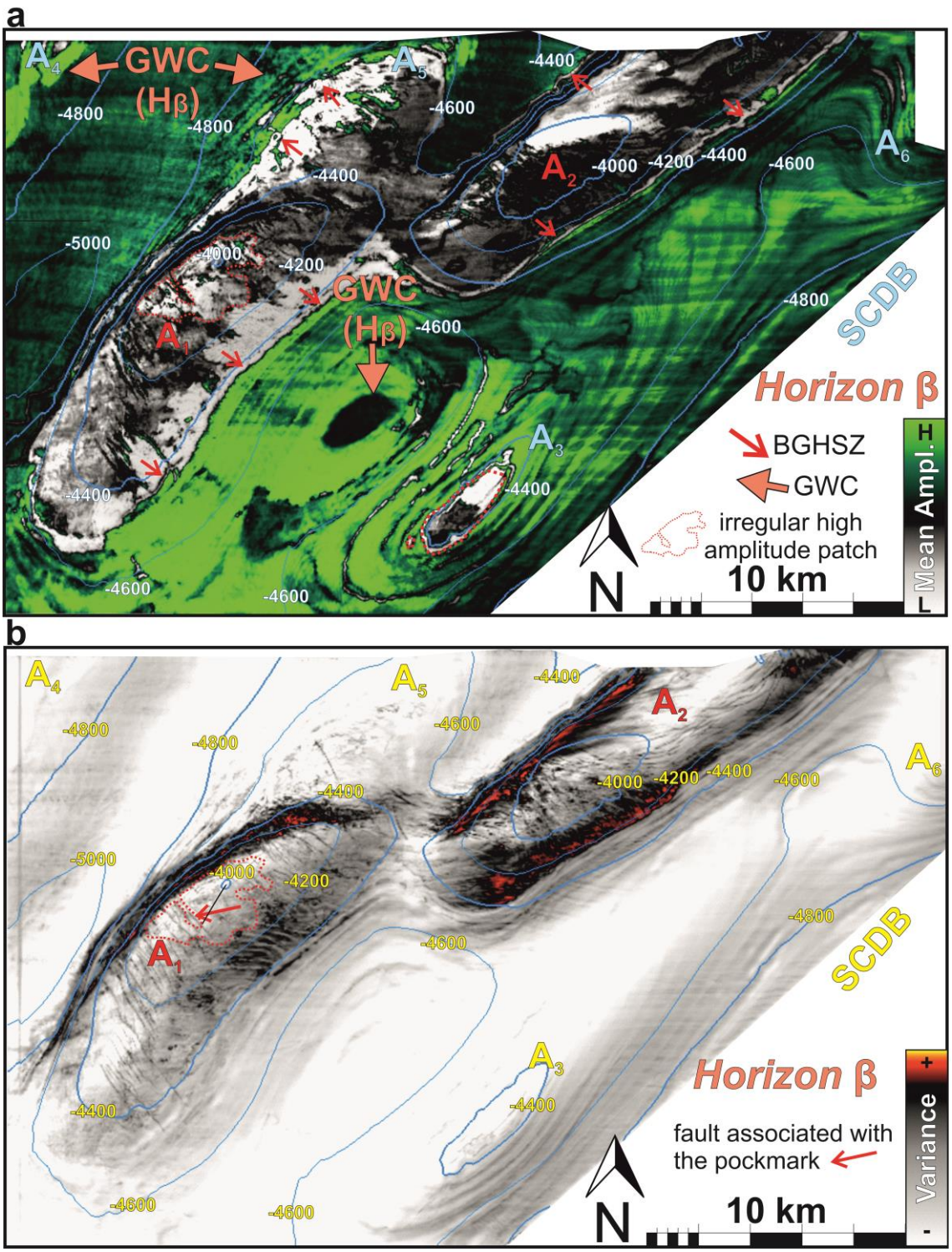



**Figure 6.14.** Attribute maps of Hβ. These maps have been depth-converted, and the depth is in metres below the sea level (mbsl). **(a)** Mean amplitude map of Hβ. The map shows the areas of enhanced amplitude. If the high amplitude anomaly is associated with a positive acoustic impedance contrast, it is coloured in white and is interpreted to indicate coarse-grained gas hydrate-bearing sediments (C-GHBS) at high concentrations. In contrast, if the high amplitude anomaly reflects a negative acoustic impedance contrast, it is coloured in bright green and is interpreted to indicate free gas-bearing sediments. Note the clear GWC at the backlimb of $A_1$, as well as the more widespread extent of amplitude anomalies at the crest and the limbs of $A_1$, compared to $A_2$. The irregular high amplitude patch at the crest of $A_1$ is contoured with a red dotted line. The red arrows indicate the BGHSZ along this horizon. Between the backlimb of $A_2$ and the South Caribbean Deformed Belt (SCDB), the high amplitude anomalies indicative of free gas are patchily distributed. **(b)** Variance map of Hβ. Note the numerous NW-SE trending faults at the crests of $A_1$ and $A_2$ and the high variance zones at the forelimbs of these folds, indicating thrust zones. The red arrow indicates a crestal normal fault that connects the pockmark to the overburden.

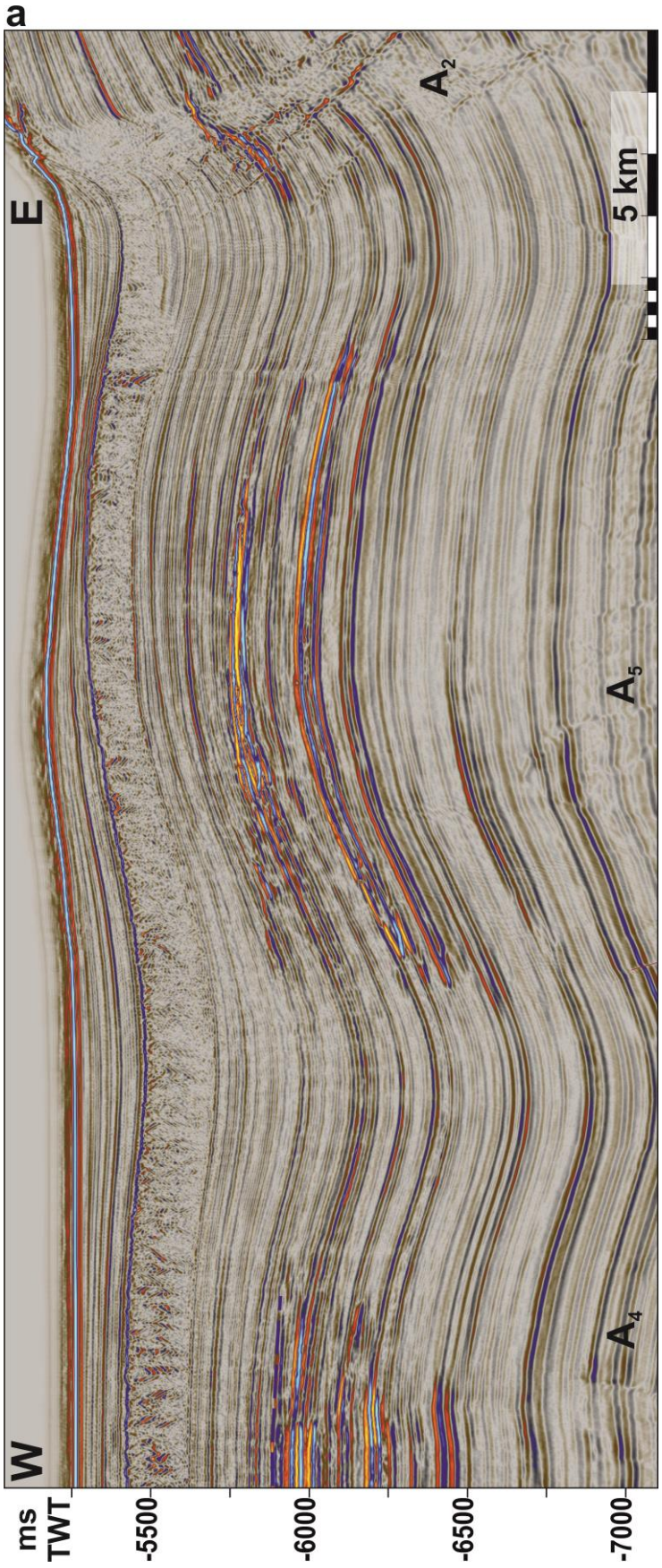



**Figure 6.15. (a)** W-E seismic section, passing through $A_4$, $A_5$ and $A_2$. See **Fig. 6.15b** for the interpreted version.

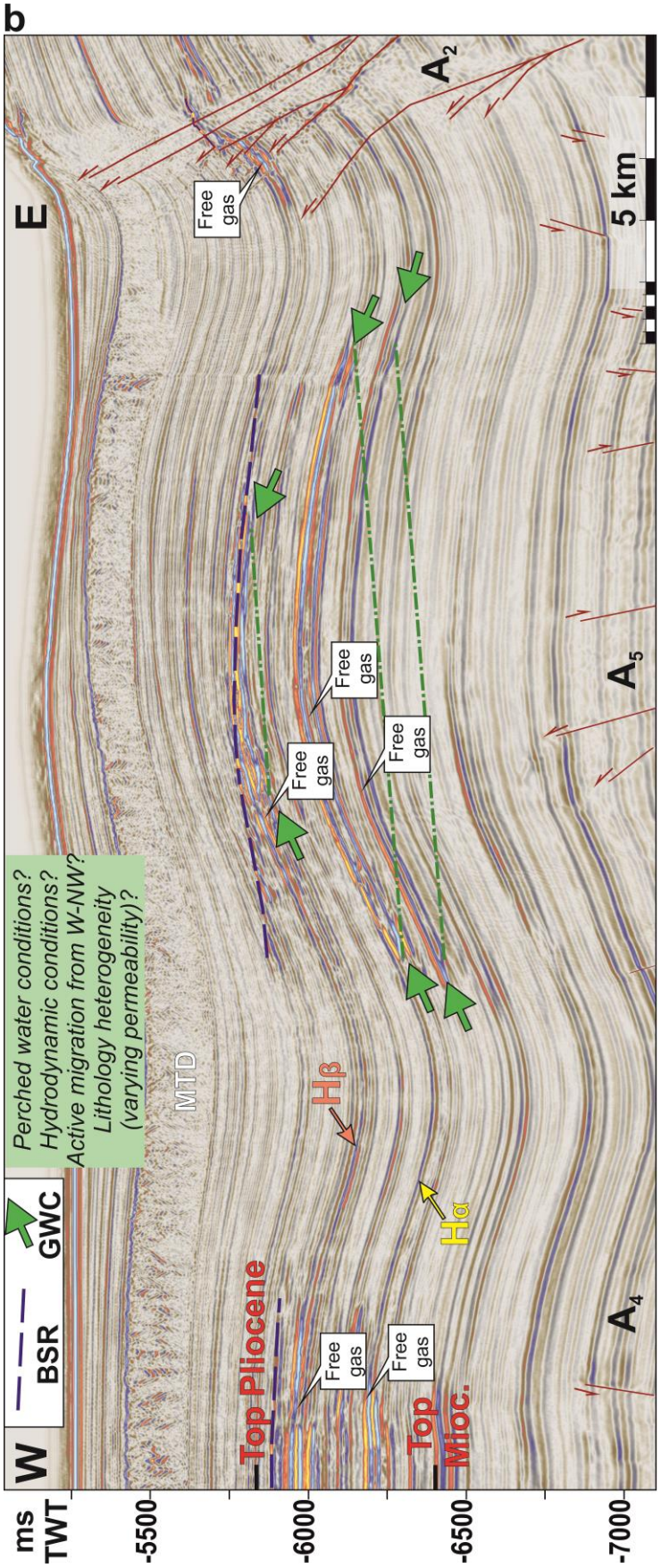



**Figure 6.15. (b)** Interpreted W-E seismic section, passing through $A_4$, $A_5$ and $A_2$. The BSR (i.e. the BGHSZ) is represented by a blue dashed line. The enhanced reflections beneath the BSR are interpreted as free gas-bearing sediments. The green arrows indicate the base of stacked free gas reservoirs at the crest of $A_5$, expressed as gas-water contacts (GWC). Note how the depths of the GWCs along the same stratigraphic reflections vary from the Western to the Eastern limb of $A_5$ (see the dip of the green dashed-dotted lines). The uppermost of these free gas accumulation is the free gas zone directly underneath the BGSHZ. The green box indicates possible explanations for this observation. The stratigraphic position of Hα and Hβ are shown by a yellow and an orange arrow, respectively. The approximate stratigraphic marker (uncalibrated) for the Top Miocene and Top Pliocene are also indicated on the left.

## 6.5. Discussion

### *6.5.1. Long-range advection feeding hydrate formation*

In the pre-drill analysis of a natural gas hydrate system, it is fundamental to constrain, in the best possible way, the most likely mechanisms that provide methane within the GHSZ and promote hydrate accumulation (Collett *et al.*, 2009). In this study, four sets of observations strongly support the existence of a system where methane-charged fluids, dominated by free gas, are transported towards the BGHSZ by long-range advection, controlled by stratal pathways in the FGZ, and potentially normal faults at the anticlines cores (**Fig. 6.16**):

**(1)** The concentration of gas hydrates at the crests and the limbs of anticline structures, with free gas present underneath the phase boundary, in conjunction with the lack of seismic evidence of hydrates in the syncline areas (**Figs. 6.5-6.10, 6.13a, 6.14a**). This observation points out the critical role played by structural highs in focusing methane-rich fluids from underlying sources and accords with theoretical models and observations in other hydrate provinces (Frederick and Buffett, 2011; Laird and Morley, 2011; Wenau *et al.*, 2015; Wang *et al.*, 2017a). The identification of vertically stacked enhanced reflections indicative of free gas-bearing sediments (see e.g. the crest of $A_4$ in **Figs 6.5** and **6.15**) has further been recently argued as evidence of a vertically-focused advective fluid flow (Bertoni *et al.*, 2017; Foschi *et al.*, 2017). Such free gas accumulations have been observed in several other hydrate provinces characterised by fluid advection from sources deeper than the BGHSZ (Scholl *et al.*, 2009; Andresen and Huuse, 2011; Bünz *et al.*, 2012; Plaza-Faverola *et al.*, 2012b; Ostanin *et al.*, 2013; see also **Chapter 4**).

**(2)** The markedly different extension of amplitude anomalies related to free gas and C-GHBS at the crest and the limbs of different anticlines ($A_1$ *vs* $A_2$) (**Figs. 6.5-6.9, 6.13, 6.14**). This observation suggests that, in this area, advection mechanisms foster free

gas accumulation and hydrate formation more efficiently at the crest and the limbs of $A_1$, in comparison to those of $A_2$.

**(3)** The possible impact of the geometry and orientation of the normal faults at the crest of the anticlines on the resulting hydrate distribution. The geometry of the high-amplitude anomalies related to C-GHBS along Hα and Hβ, with respect to the faults orientation (**Figs. 6.13a, 6.14a**), suggest that, in some cases, faults can compartmentalise the distribution of gas hydrates. Concurrently, the pockmark-like depression located at the upper tip of some of the crestal faults and the underneath high-amplitude irregular patch observed along Hβ at the crest of $A_1$ (**Figs. 6.5, 6.6, 6.14a**) suggest that, at the core of the studied anticlines, faults **(Figs. 6.6, 6.9**) could promote a cross-stratal fluid migration and seepage at the seafloor, as well as the formation of hydrates (cf. Riedel *et al.*, 2010a; Crutchley *et al.*, 2013; Plaza-Faverola *et al.*, 2014; Haines *et al.*, 2017). Therefore, it is arguable that faults control the fluid flux of methane-rich fluids, by favouring an upward migration along the fault surfaces but possibly hindering the flux across such surfaces.

**(4)** The occurrence of amplitude anomalies related to gas hydrates and free gas along the same stratigraphic intervals (**Figs. 6.5-6.9, 6.12-6.14**). The consistent impact of stratigraphy on the amplitude patterns of the BSR (**Fig. 6.12**) highlights how free gas and gas hydrates at high saturation are preferentially concentrated along specific intervals. Within such a system, the lateral extent of the hydrate and free gas amplitude anomalies are further correlated. For example, at the crest and the limbs of $A_1$, the more extensive free gas and gas hydrate amplitude anomalies along Hα compared to Hβ are interpreted as being caused by the vicinity of the former horizon to deep sourcing fluids (**Figs. 6.5, 6.13, 6.14**). The occurrence of gas hydrate and free gas-bearing sediments along the same stratigraphic intervals has been considered diagnostic for advection-dominated natural gas hydrate systems in other convergent margins (Crutchley *et al.*, 2015; Wang *et al.*, 2017a), as well as in different geological

settings (Laird and Morley, 2011; Boswell *et al.*, 2012a). Recent results of numerical models of free gas and hydrate accumulation owing to advection along dipping layers also highlight the critical role played by focused fluid flow along permeable pathways in enhancing hydrate and free gas concentrations (Chatterjee *et al.*, 2014), supporting the observations and interpretations presented here.

In the study area the lack of lateral variations in seismic facies, the consistent depth of the BSR relative to the seafloor (i.e. similar temperature conditions in the first hundreds metres), and the structural similarity between $A_1$ and $A_2$ suggest no abrupt lateral changes in the conditions favouring or disfavouring an in-situ microbial generation of methane and accumulation as hydrate over time (cf. Davie and Buffett, 2001; Wallmann *et al.*, 2006a; Frye, 2008; Pohlman *et al.*, 2009b; Yoshioka *et al.*, 2010). Consequently, if in-situ methane generation were dominant at the km-scale, it would result in **(1)** a homogeneous hydrate distribution in $A_1$ *vs* $A_2$, **(2)** a hydrate distribution not affected by faulting, given that methane would be generated in the sediments immediately surrounding the hydrate reservoir and not transported over larger distances, and **(3)** some seismic evidence of hydrates in the syncline areas adjacent to the anticlines, contrary to what is observed (e.g. **Figs. 6.5-6.10, 6.13a, 6.14a**). In addition, the character of the seismic facies in the study area suggests no substantial vertical changes in the depositional and stratigraphic trends, from the seafloor down to the BGHSZ, with the exception of a single MTD (**Figs. 6.5-6.9**). Thus, in a diffusion-dominated system where methane is generated in-situ, we would expect an opposite scenario than that observed because the decrease in methane solubility towards the seafloor (Davie *et al.*, 2004) would facilitate hydrate accumulation in shallower rather than deeper stratigraphic intervals (cf. Nole *et al.*, 2017).

The presented arguments let us infer that the primary and decisive factor controlling hydrate distribution is the presence of a free gas source beneath the BGHSZ. However, the lack of a direct lithological control in the study area constitutes a critical uncertainty.

Growing folds, which create irregularities in the seafloor topography, represent significant controls on the depositional patterns in deepwater compressional settings (e.g. Corredor *et al.*, 2005; Morley and Leong, 2008). Thus, we do not exclude that an upward decrease in the intrinsic reservoir quality of the sediments within the GHSZ could occur at the crest of growing structures, eventually contributing in concentrating hydrates at high concentrations near the BGSHZ, within sediments deposited in a less deformed setting. Importantly, in an advection-dominated system, diffusion may still be relevant at the metre-scale, by activating concentration gradients capable of enhancing *Sh* within the coarser-grained intervals. In this case, the sandy hydrate-bearing beds are sourced not only through advective methane transport from the underlying FGZ but also from the confining fine-grained units, thanks to favourable concentration gradients (e.g. Rempel, 2011).

### *6.5.2. Overpressure-driven migration through hydrate seals*

The association between free-gas and gas hydrates along the same stratigraphic intervals suggests a genetic link between free gas and hydrate accumulation. What is the most likely physical process to explain the observed amplitude anomalies within the GHSZ? I hypothesise that a process of capillary invasion of free gas within the pore space above the BGHSZ is the most plausible mechanism. Capillary invasion, which occurs preferentially over hydraulic fracturing in coarse-grained sediments, is controlled by the interfacial tension between the fluid phases, their contact angle with the solid, the pore throats radii and their geometries (Bakke and Øren, 1997; Jain and Juanes, 2009). This process could occur by free gas invasion pulses throughout the GHSZ, regulated by the interplay between overpressure and sealing effectiveness of the C-GHBS at the three-phase boundary (**Fig. 6.17**). Where the free gas can penetrate into the GHSZ, new hydrates can form at the boundary between free gas and the pore water (see Chen *et al.*, 2017). The preservation of three-phases into the GHSZ could be then promoted by a combination of mechanical, thermodynamic and geochemical processes (Ginsburg and Soloviev, 1997; Torres *et al.*,

2004; Liu and Flemings, 2007; Smith *et al.*, 2014a), including limited water availability owing to elevated free gas saturation at the BGHSZ (Claypool *et al.*, 2006).

Our seismic observations suggest that the free gas columns along Horizons α and β are internally connected and buoyant (**Figs. 6.10c, 6,13a, 6.14a**). Based on this interpretation, the free gas is efficiently sealed at the BGHSZ only if the capillary entry pressure at this interface equals the buoyancy of the free gas columns (cf. Fauria and Rempel, 2011). At the backlimb of $A_1$, this would only happen if the pore-throat entry radius for free gas at the BGHSZ is less than ~50 nm, considering the free gas buoyancy as the sole source of overpressure (for more details, see the Appendix B, **paragraph 6.7**). Therefore, if the host sediments of these gas hydrate accumulations are rich in sand and silt, we infer that hydrates inhibit a continuous free gas invasion, by occluding the μm-scale throats that characterise these sediments prior to hydrate formation (Kleinberg *et al.*, 2003; Nelson, 2009) (**Figs. 6.17, 6.18**). Ostwald-ripening phenomena will then contribute to reducing permeability to free gas, by promoting hydrate growth in the larger *vs* the smaller pores (Klapp *et al.*, 2007; Jung and Santamarina, 2012). If free gas migration is inhibited, hydrates can still form by both advective flow of methane-rich pore waters (the system is water-wet) and molecular diffusion of methane from the BGHSZ, and from adjacent fine-grained layers (**Figs. 6.17, 6.18**). Nevertheless, the pore water advection is inevitably hindered by the permeability reduction at the BGHSZ (cf. Daigle and Dugan, 2011).

Further free gas injection into the GHSZ can occur by increasing free gas column heights, therefore enhancing the buoyancy pressure beneath the BGHSZ. Also, by increasing its concentration, free gas would increase its mobility with respect to water (Tréhu *et al.*, 2004a). These factors promote a more effective gas injection into the GHSZ and subsequent hydrate formation. In such view, the gas hydrate-bearing sediments at the BGHSZ act as a dynamic membrane seal (**Fig. 6.18**). At the crest of $A_1$, along Hα and in the immediately nearby enhanced reflections, the advection-dominated methane supply has probably been so

effective as to result in a hydrate accumulation that mimics a conventional four-way closure trap (**Figs. 6.6** and **6.13a**). In this scenario of fluid flow and advective methane supply to the GHSZ, each package of enhanced reflections represents a free gas and hydrate compartment, stratigraphically adjacent to zones with lower-permeability sediments, where the free gas and hydrates only form in the vicinity of the BGHSZ, probably sustained by recycling processes and lower advection rates (**Fig. 6.18**).

It is hard to constrain if water overpressures are present or not in the system and many options could explain the observed tilted gas-water contacts (**Fig. 6.15**). If such overpressures are present, they can reduce the free gas column height required to invade the GHSZ (cf. Flemings *et al.*, 2003), and promote the efficient injection of methane-rich aqueous fluids into the GHSZ, which are then potentially converted into hydrate if allowed by the supersaturation thresholds (cf. Davie *et al.*, 2004). It is predicted that, at the BGHSZ, C-GHBS seal the free gas at fluid pressures (buoyancy of the free gas plus the hydrostatic pressure from the seafloor) equal to 88% and 70% of the lithostatic stress, for Hα and Hβ, respectively (for more details, see Appendix, **paragraph 6.7**). These fluid pressure values could be close to those required to initiate fracturing (Flemings *et al.*, 2003; Tréhu *et al.*, 2004a; Daigle *et al.*, 2011), although the absence of seismic indicators of fracturing and cross-stratal fluid flow at the backlimb of the anticlines (e.g. fluid-escape pipes), suggests that overpressures are released through capillary invasion prior to reaching such critical conditions. It is not excluded that the presence of hydrates at elevated saturations at the BGSHZ could prevent the onset of fractures, by increasing the strength of the host sediment (Yun *et al.*, 2005 and 2007; Jung and Santamarina, 2011; Yoneda *et al.*, 2015 and 2017). A final degree of complexity is added to this system at the faulted crests of the anticlines, where the stratal fluid flow competes with cross-stratal advection along fault planes.

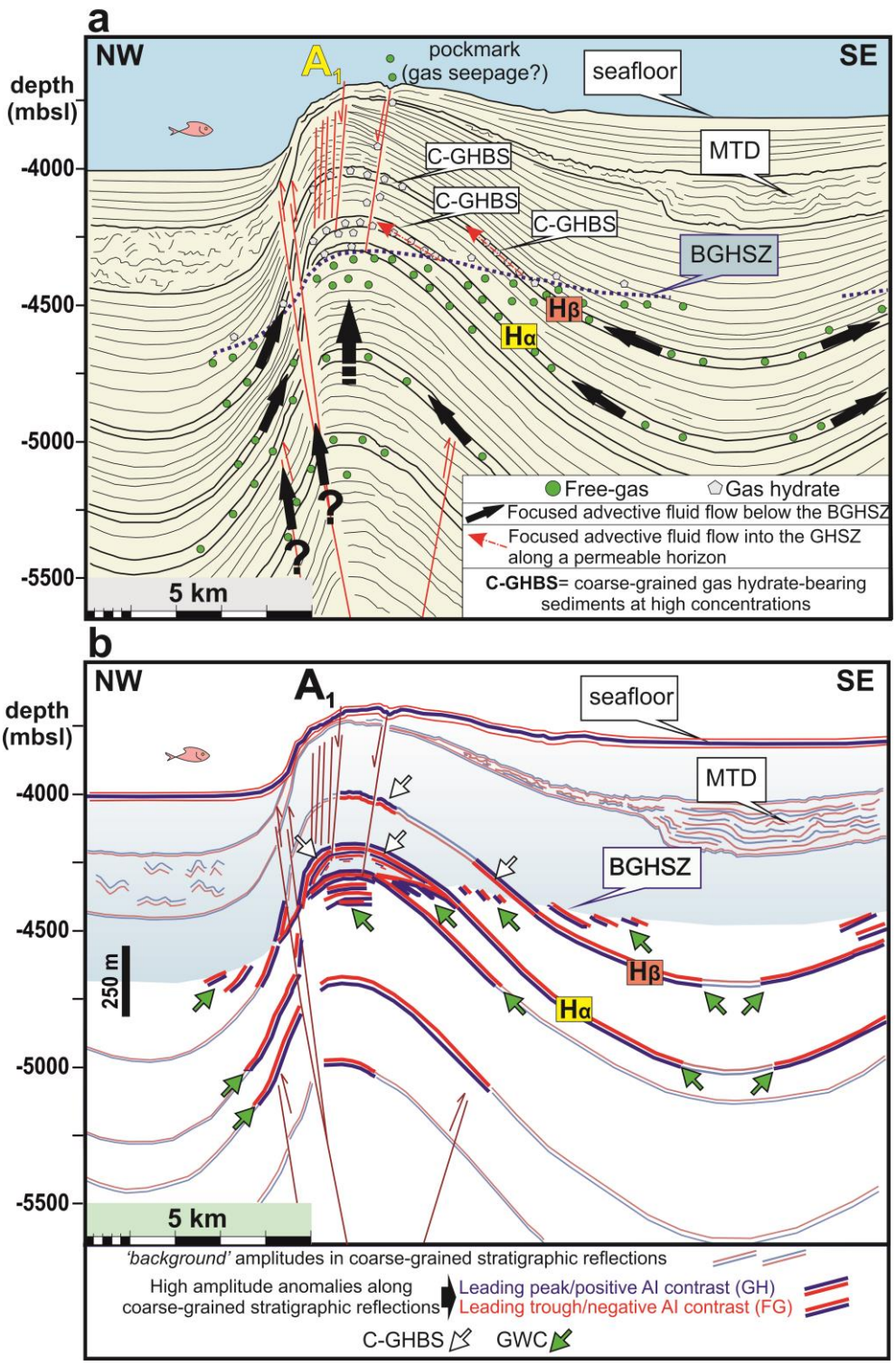



**Figure 6.16. (a)** Sketch of the natural gas hydrate system in the study area. Fluid flow below the BGHSZ is focused along permeable stratal and possibly cross-stratal pathways. In the backlimb, hydrate formation is favoured along stratal pathways, which also show evidence of hundreds of metres thick free gas columns. C-GHBS= coarse-grained gas hydrate-bearing sediments at high concentrations Mbsl= metres below sea level. **(b)** Schematic view of the geophysical character (i.e. the seismic amplitude expression) of the gas hydrate-bearing sediments and the free gas zone in the study area, assuming a standard 0° phase North American polarity (cf. Boswell *et al.*, 2016). AI= acoustic impedance; GH= gas hydrates; FG= free gas. Note that a polarity reversal could also be identifiable at the base of the free gas zone.

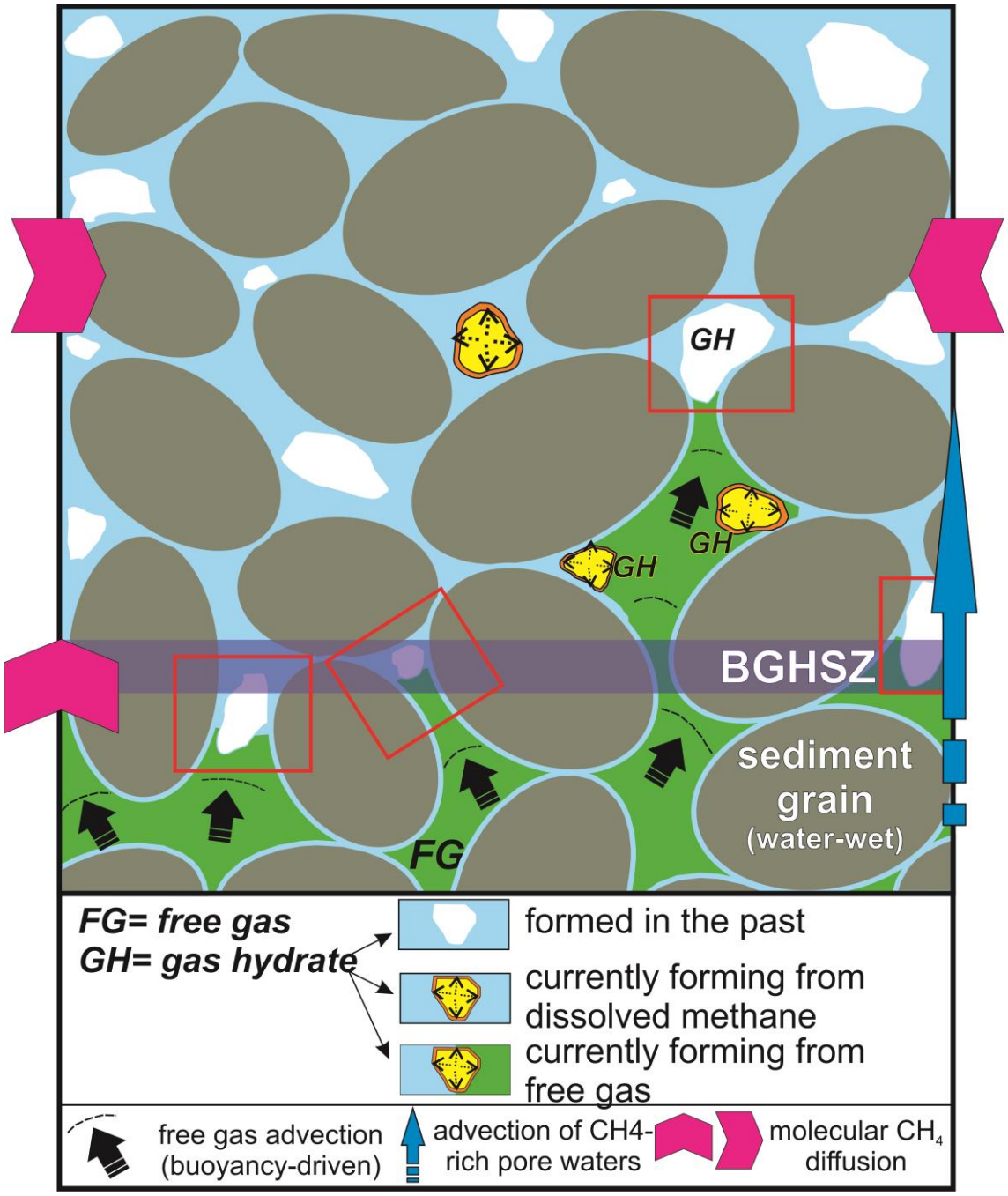



**Figure 6.17.** Schematic representation, showing the process of capillary invasion of free gas, inhibited by gas hydrates at the BGHSZ (modified after Jain and Juanes, 2009). The red rectangles indicate pore throats reduced in size by hydrates. Within the GHSZ, hydrates can form at the boundary between migrating free gas and the pore water, as well as by advective flow of methane-rich pore waters and molecular diffusion.

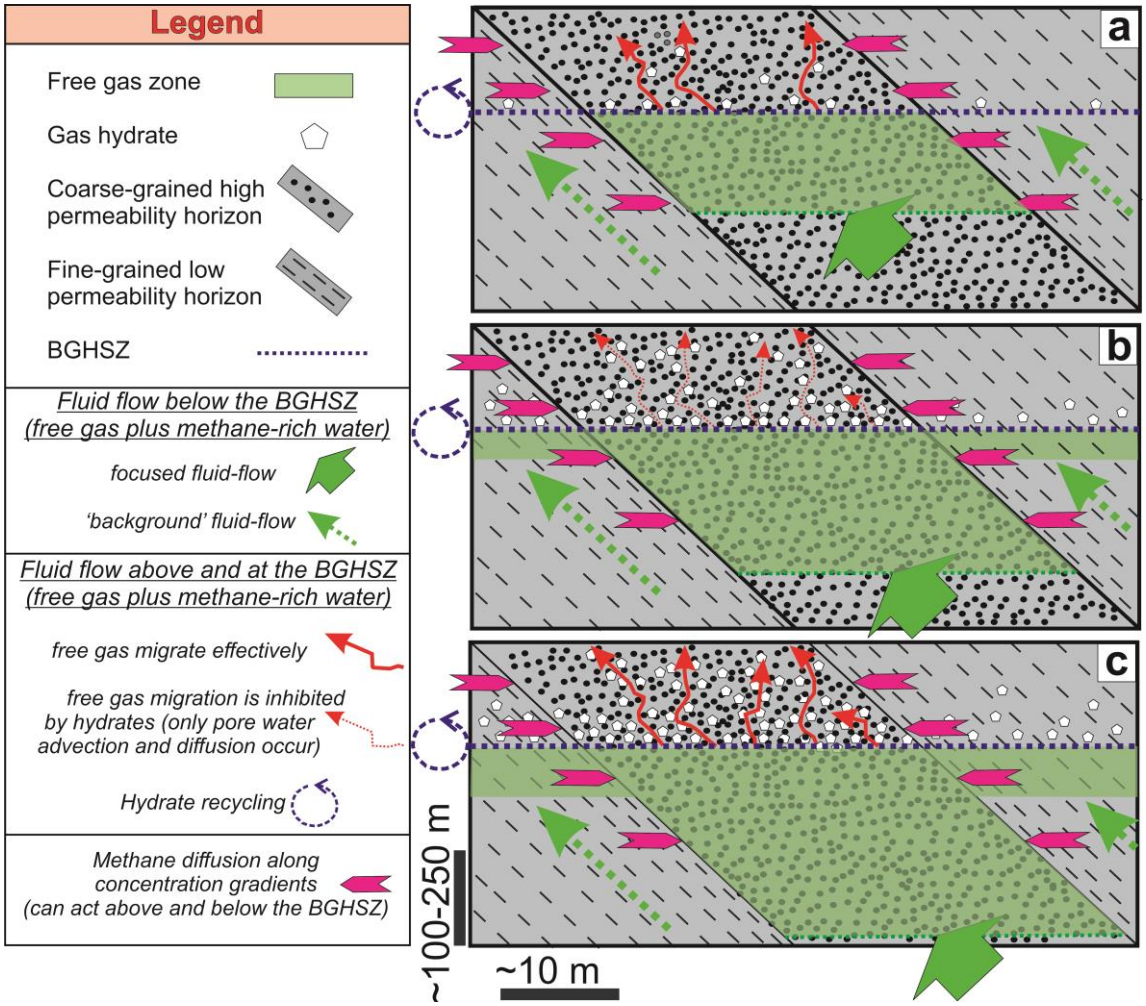



**Figure 6.18.** Conceptual model describing the processes of fluid flow from the free gas zone towards and throughout the GHSZ in the study area. **(a)** Fluid flow, dominated by free gas advection by buoyancy, is favoured along a dipping coarse-grained and high permeability horizon (e.g. Hα). Gas hydrates start to form within the GHSZ along this horizon, fostered by an effective process of capillary invasion. **(b)** Gas hydrates continue to form and, eventually, inhibit further free gas invasion within the GHSZ. Gas hydrate-bearing sediments act as a membrane seal and trap a buoyant column of free gas, which starts to grow. In the meanwhile, a background fluid flow and hydrate recycling processes can lead to the formation of a thin free gas column in the adjacent low permeability horizons. **(c)** The column of free gas grows further, and the buoyancy pressure of the free gas increases enough to promote further free gas invasion and hydrate formation. Importantly, hydrate recycling at the BGHSZ, advection of methane-rich pore waters and molecular diffusion processes are always active throughout these stages, although the pore water advection is hindered by the permeability reduction at the BGHSZ.

### *6.5.3. Global implications*

Natural gas hydrates within coarse-grained sediments represent the most prospective class of hydrate deposits. Remarkable examples in marine settings are the deposits in the Kumano Forearc Basin (Eastern Nankai Trough, e.g. Saeki *et al.*, 2008; Fujii *et al.*, 2015; Taladay *et al.*, 2017) and the Terrebonne Basin, in the Northern Gulf of Mexico (Boswell *et al.*, 2012b; Frye *et al.*, 2012), where borehole results indicate hydrate saturation exceeding 50-60% of the pore space, along coarse-grained layers. Onshore, the most studied systems are those in the Canadian and Alaskan permafrost, where gas hydrate deposits in sand-rich units overlie conventional free gas and oil accumulations, in a system governed by thermogenic sources and fault-controlled hydrocarbon migration (Inks *et al.*, 2009; Collett *et al.*, 2011). The results of this study reveal that C-GHBS at elevated concentrations can also occur in the deepwater frontal anticlines of compressive margins. An analogous system could be the Hikurangi Margin (cf. Plaza-Faverola *et al.*, 2012b), where a recent petroleum system model indicates that fluid flow and focusing are sustained by the ongoing tectonic deformation while methane is supplied by deep microbial and thermogenic methane generation processes (Kroeger *et al.*, 2015).

The coupling between hydrate and free gas accumulations appears a diagnostic character of long-range advective systems (cf. Crutchley *et al.*, 2015; Wang *et al.*, 2017a). Our three-dimensional analysis of seismic amplitude further indicates that the efficiency of the advective methane supply towards the GHSZ can dramatically change at the km-scale, i.e. from an anticline to the adjacent one. This variability indicates a complex hydrocarbon plumbing system and results in greater uncertainty in the regional evaluation of gas hydrate systems, in the absence of three-dimensional seismic data. Finally, the overpressure associated with hundreds of metres of buoyant columns of free gas trapped beneath the BGHSZ, as well as the potential occurrence of water overpressures must be considered in evaluating geohazards related to advection-dominated natural gas hydrate systems (cf. McConnell *et al.*, 2012).

## 6.6. Conclusions

This research shows three-dimensional evidence of extensive accumulations of coarse-grained gas hydrate- and free gas-bearing sediments in a natural gas hydrate system interpreted to be dominated by long-range advection processes. The major conclusions of this study are:

**(1)** Coarse-grained gas hydrate-bearing sediments are seismically characterised by reflections with high amplitude anomalies, opposite in amplitude to those observed in the underlying FGZ.

**(2)** The three-dimensional extent of *'hydrate and free gas anomalies'* is correlated. The most extensive gas hydrate deposits are directly linked to the underlying FGZ and therefore occur in the vicinity of the three-phase boundary. The extent of hydrate and free gas amplitude anomalies further varies along different stratigraphic horizons and in different anticlines, despite the absence of substantial lateral variations in seismic facies. These characteristics, in conjunction with the occurrence of hydrate deposits only in the anticline areas and the possible impact of fault on the resulting hydrate distribution, are interpreted as seismic evidence for a system dominated by a long-range advection of free gas and methane-rich aqueous fluids.

**(3)** Gas hydrate and free gas mutually and dynamically influence each other in long-range advective systems. Coarse-grained gas hydrate-bearing sediments are hypothesised to act as a dynamic membrane seal, where the free gas injection into the gas hydrate stability zone is interpreted to occur in overpressure-controlled pulses.

## 6.7. Appendix: capillary invasion and free gas buoyancy at the BGHSZ

The mechanism of capillary invasion can be treated with the simplified form of the Young-Laplace equation, valid for cylindrical tubes (e.g. Underschultz, 2007):

$$\boldsymbol{Pc = (2\gamma_{gw}\cos\varphi)/a} \quad \textbf{(1)}$$

Where ***Pc*** represents the capillary entry pressure, $\gamma_{gw}$ is the interfacial tension between the fluid phases (i.e. between methane as free-gas and water, cf. Schmidt *et al.*, 2007), $\varphi$ is their contact angle against the solid, assumed to be 180°, given that water is considered completely wetting (**Tab. 6.1**), and ***a*** is the pore throats radius. For a more general system of pore throats (Bakke and Øren, 1997), ***Pc*** is:

$$\boldsymbol{Pc = \gamma_{gw}(1 + 2\sqrt{\pi G})/a} \quad \textbf{(2)}$$

Where ***G*** is a shape factor relating the area to the square of the pore perimeter and for a pore shape resembling an equilateral triangle is 0.0481. **Equation 2** reduces to **Equation 1** if the pore throat is circular. The same ***Pc*** is sustained by slightly smaller values of ***a*** in the case of a triangular-shaped pore throat, compared to a circle-shaped one. The pore throat radii necessary to trap the buoyant free gas columns along Hα and Hβ are calculated by reversing the previous equations and assuming that the gas column developed along Hα and Hβ exercises a ***Pg*** equal to ***Pc***, where the former equals to:

$$\boldsymbol{Pg = \Delta\rho_{(w-g)} g Th_{FGZ}} \quad \textbf{(3)}$$

Where $\Delta\boldsymbol{\rho_{(w\text{-}g)}}$ is the density difference between the pore water and the free gas, $\boldsymbol{g}$ is the gravity acceleration, and $\boldsymbol{Th_{FGZ}}$ is the thickness of the buoyant free gas column. By considering reasonable values of $\gamma_{gw}$, water density ($\rho_w$) and free gas density ($\rho_g$) (**Tab. 6.1**), the free gas columns along Hα and Hβ would be trapped by a capillary seal with pore throat radii of ~20-50 nm (**Fig. 6.19**).

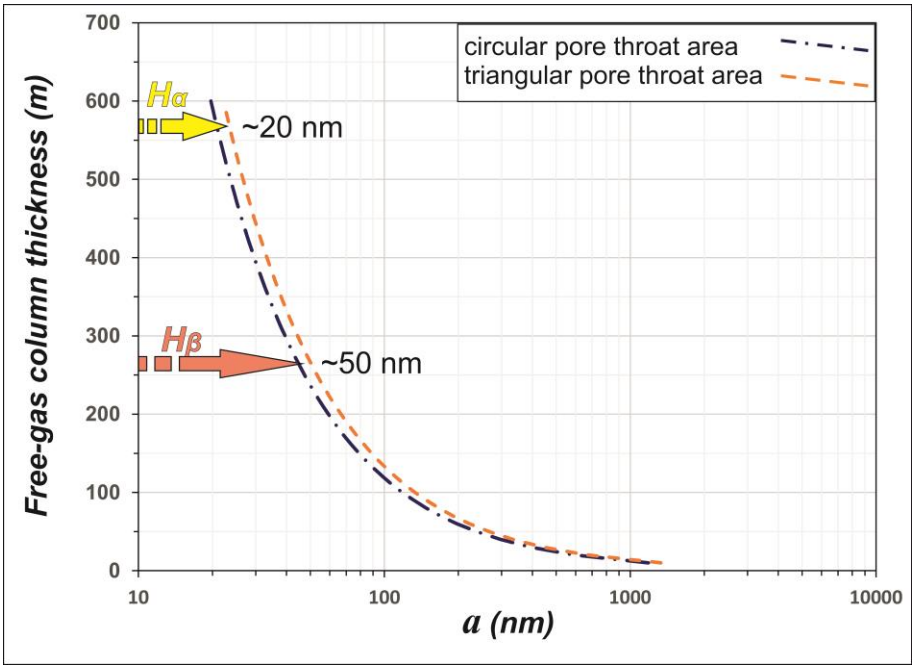



**Figure 6.19.** Thickness of the free gas column *vs* pore throat radius (***a***). The curves indicate the size of the pore throats capable of sustaining a given column of free gas, which exercises a buoyancy pressure. Smaller throats (e.g. due to extensive hydrate formation at the BGHSZ) allow sealing higher columns. The yellow and orange arrows indicate the free gas column height in the free gas zone at the backlimb of $A_1$, for Hα and Hβ, respectively. Slightly different values further result from diverse pore throat geometries.

The buoyancy pressure exerted by a free gas column (***Pg***) is added to the hydrostatic pressure from the seafloor to the BGHSZ (***Pw***), to compute the fluid pressure (***Pf***):

$$\boldsymbol{Pf = Pw + Pg} \quad \textbf{(4)}$$

Where ***Pw*** is:

$$\boldsymbol{Pw = \rho_w g h} \quad \textbf{(5)}$$

Where ***h*** represents the interval from the seafloor to the BGHSZ. The following relationship gives instead the overburden stress (i.e. the lithostatic pressure, ***Pv***):

$$\boldsymbol{Pv = \rho_b g h} \quad \textbf{(5)}$$

Where $\boldsymbol{\rho_b}$ is the average sediment bulk density along the considered interval. Consequently, considering the values expressed in **Table 6.1** for $\boldsymbol{\rho_b}$, $\boldsymbol{\rho_w}$ and $\boldsymbol{\rho_g}$, the ***Pf*** for Hα and Hβ equals to ~11.1 MPa (88% of ***Pv***) and ~8.6 MPa (70% of ***Pv***), respectively (**Fig. 6.20**). These values are calculated assuming that the BGHSZ, along Hα and Hβ, lies where the polarity reversal is observed in seismic data (i.e. slightly deeper than the interpreted BSR, **Fig. 6.11a**). Higher

values of ***Pg*** are expected if the position of that reversal is the result of a geophysical artefact and the BGHSZ occurs instead at shallower levels (i.e. the free gas columns are larger).

The pressure required to initiate hydraulic/pneumatic fracturing is most commonly taken as between ~70 and 100% of the overburden pressure, depending on the Poisson ratio, the degree of anisotropy of the shallow state of stress and the presence of poroelastic effects driven by overpressures (Engelder and Fischer, 1994; Osborne and Swarbrick, 1997; Hillis, 2000; Flemings *et al.*, 2003; Mourgues *et al.*, 2011). Eventually, fracturing occurs if the fluid pressure exceeds the least principal stress plus the rock tensile strength, with the latter parameter that can be significantly influenced by the presence of hydrates in the sediment (Yun *et al.*, 2005 and 2007; Jung and Santamarina, 2011; Yoneda *et al.*, 2015 and 2017). The seismic observation presented in this study support a view where C-GHBS serve as a dynamic membrane seal, where free gas is injected across the GHSZ through capillary invasion before that the conditions required to fracture the sediment are met.

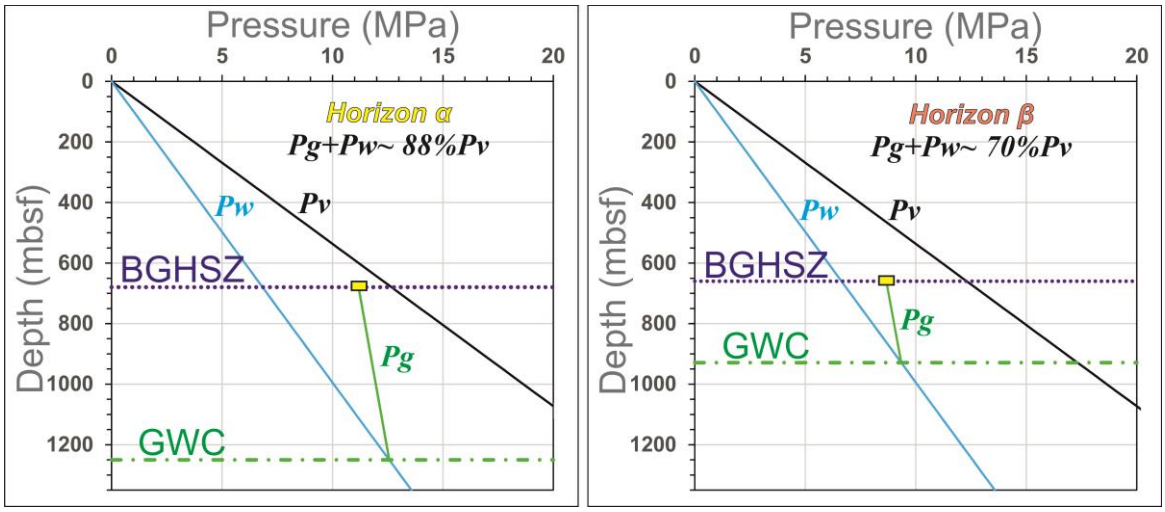



**Figure 6.20**. Plots of hydrostatic (***Pw***), overburden (***Pv***) and free gas buoyancy pressures (***Pg***), in relation to the free gas zone developed beneath the BGHSZ along Hα (left) and Hβ (right), at the backlimb of $A_1$. The pressures in the plots are measured from the seafloor (mbsf= metres below the seafloor)

| Parameter | Value |
|---|---|
| $\rho_g$ | 255 kg/m$^3$ |
| $\rho_w$ | 1025 kg/m$^3$ |
| $\rho_b$ | 1900 kg/m$^3$ |
| $\gamma_{gw}$ | 0.05 J/m$^2$ |
| $\varphi$ | 180° |

**Table 6.1.** Parameters used to compute the free gas buoyancy pressure (***Pg***), the hydrostatic pressure (***Pw***), the lithostatic pressure (***Pv***) and the capillary pressure (***Pc***).

# Chapter 7. A review of the critical state and the fluid flow processes associated with free gas zones beneath hydrate stability

In this chapter, Martino Foschi contributed to the calculation of the methane solubility gradients. Joe A. Cartwright and Pieter Van Rensbergen helped in the revision. The seismic data from NW Borneo and offshore Colombia has been provided by Shell. The seismic data from the South Falkland Basin has been provided by Borders & Southern Petroleum plc. The seismic data from the Hikurangi margin has been provided by New Zealand Petroleum & Minerals. The other seismic lines, as well as the core and well-log density data shown in this Chapter, have been taken from published literature and available databases, which has been properly cited throughout the text.

## 7.1. Introduction

In natural gas hydrate systems (NGHSs), the free gas zone (FGZ) is that volume of sediment, which directly underlies the gas hydrate stability zone (GHSZ), whose pore space contains a certain amount of free gas. The formation of an FGZ requires that methane, or a mixture of gases, exceed the supersaturation thresholds in the pore waters at in-situ conditions (Xu and Ruppel, 1999). Under particular circumstances, free gas and gas hydrate-bearing sediments coexist within the FGZ (cf. **Chapter 3** and Liu and Flemings, 2011). The origin of the FGZ has been attributed to three processes, namely **(1)** The advection of hydrocarbon-rich fluids from deeper portions of the basin which overcome supersaturation thresholds below the base of the GHSZ (BGHSZ); **(2)** The recycling of gas hydrates at the three-phase boundary owing to e.g. uplift or sedimentation and **(3)** The solubility curvature mechanism (Hyndman and Davis, 1992; Von Huene and Pecher, 1999; Baba and Yamada, 2004; Haacke *et al.*, 2008; Crutchley *et al.*, 2015) (**Fig. 7.1**.).

In different gas hydrate provinces, it has been argued that the pore fluid pressure at the top of the FGZ (i.e. the BGHSZ) is critical for either hydraulic/pneumatic fracturing or fault reactivation (Flemings *et al.*, 2003; Hornbach *et al.*, 2004; Tréhu *et al.*, 2004a). The observation of cross-stratal vertical fluid flow pathways in seismic reflection data suggests a present-day or recent focused and overpressured fluid flux system, rooted either within the FGZ or deeper in the sedimentary section (see **Chapter 4**; Gorman *et al.*, 2002; Moss and Cartwright, 2010; Plaza-Faverola *et al.*, 2012a; Cartwright and Santamarina, 2015). Possible mechanisms responsible for the generation of such overpressures and the focused fluid flow of free gas and pore waters include the buoyancy of free gas, disequilibrium compaction and lateral pressure transfer (Yardley and Swarbrick, 2000; Flemings *et al.*, 2003; Tréhu *et al.*, 2004a; Leduc *et al.*, 2013).

The regional tectonic setting of a sedimentary basin has been postulated to influence the thickness of an FGZ. According to this view, the FGZs in compressional margins are

relatively thin (i.e. up to ~50 m thick), are generated by hydrate recycling mechanisms, and cover large portions of the basin. The recycling would counterbalance advective fluxes of undersaturated and overpressured fluids, further capable of limiting the maximum possible thickness of a buoyant FGZ. In contrast, extensional margins would be characterised by low methane fluxes but up to few hundred of metres of either mobile or immobile FGZs. (Hornbach *et al.*, 2004; Haacke *et al.*, 2007 and 2008). Haacke *et al.* (2007 and 2008) have further suggested that a downward diffusion of methane, owing to highly curved solubility gradients beneath BSRs, and limited upwardly directed fluid fluxes of undersaturated fluids interplay to generate thick FGZs in passive margins. This diffusion-driven flux, theoretically more efficient at higher geothermal gradients, would be controlled by a continuously saturated hydrate stability zone, capable of diffusing methane towards the sediment beneath the three-phase boundary. The methane concentration within these sediments would then exceed saturation thresholds for the free gas formation and further contribute to this downward diffusion process. Overall, these views are primarily based on a limited number of regional-scale observations and on the assumptions that methane fluxes in compressive margins are widespread over large portions of the basins and are characterised by a dominant transport of methane as a soluble phase.

A given column of free gas, to be interconnected and exert an adequate buoyancy pressure, needs to reach a percolation threshold, i.e. a critical free gas saturation (*Sg*, % of pore space) allowing the formation of an interconnected free gas phase. The exact value of this critical *Sg* is not well constrained, being suggested to vary between 0.5% and 20%. In this context, the pore network of the host lithology, as well as the sizes of free gas bubbles and their formation rates, represent critical but difficult parameters to constrain (Schowalter, 1979; Henry *et al.*, 1999; Flemings *et al.*, 2003; Liu and Flemings, 2007; Haacke *et al.*, 2008). Therefore, it is complex to evaluate whether or not an FGZ exerts a buoyancy pressure at the BGHSZ. Unfortunately, little is known about the distribution of free gas beneath the BGHSZ.

The estimates based on the quantitative analysis of seismic data suggest that, within FGZs, the free gas fills only small percentages of the pore space (e.g. Singh *et al.*, 1993; Holbrook *et al.*, 1996; Andreassen *et al.*, 1997; Ecker *et al.*, 1998; Sain *et al.*, 2000; Flemings *et al.*, 2003; Bünz *et al.*, 2005; Zillmer *et al.*, 2005; Plaza-Faverola *et al.*, 2010; Fohrmann and Pecher, 2012). Similarly, well-log data suggest that *Sg* in FGZs is overall less than 5-10% (Bangs *et al.*, 1993; Holbrook *et al.*, 1996; Lee and Collett, 2006; Shankar *et al.*, 2013). Importantly, these indirect methods need to consider the uncertainty related to the mode of free gas distribution in the pore space, which can be homogeneous, patchy or even fracture-filling (Dvorkin and Nur, 1998). The direct measurements on cores, to date, are relatively rare: for example, at Blake Ridge, the upper portion of the FGZ is considered to contain free gas at *Sg*= 12% (Dickens *et al.*, 1997). Above FGZs, the gas hydrate-bearing sediments exhibit significantly variable saturation (*Sh*, % of pore space) and morphology. Eventually, the effective permeability and the fluid flow across the GHSZ can be severely affected by hydrate formation (Kleinberg *et al.*, 2003; Dai and Seol, 2014; Kang *et al.*, 2016).

Considering such background information and taking into account the existing uncertainties, the objectives of this study are: **(1)** Understanding whether or not, and in which geological context, FGZs can be considered at a critical status for a buoyancy-driven free gas migration; **(2)** Reviewing the mechanisms of fluid migration within the FGZ and throughout the GHSZ and the triggers for these phenomena and **(3)** Defining the controlling factors on the seismic expression and thickness of the FGZ and provide a classification of FGZs based on such factors, with a focus on the prospectivity for hydrate resources, geohazards and climate impacts.

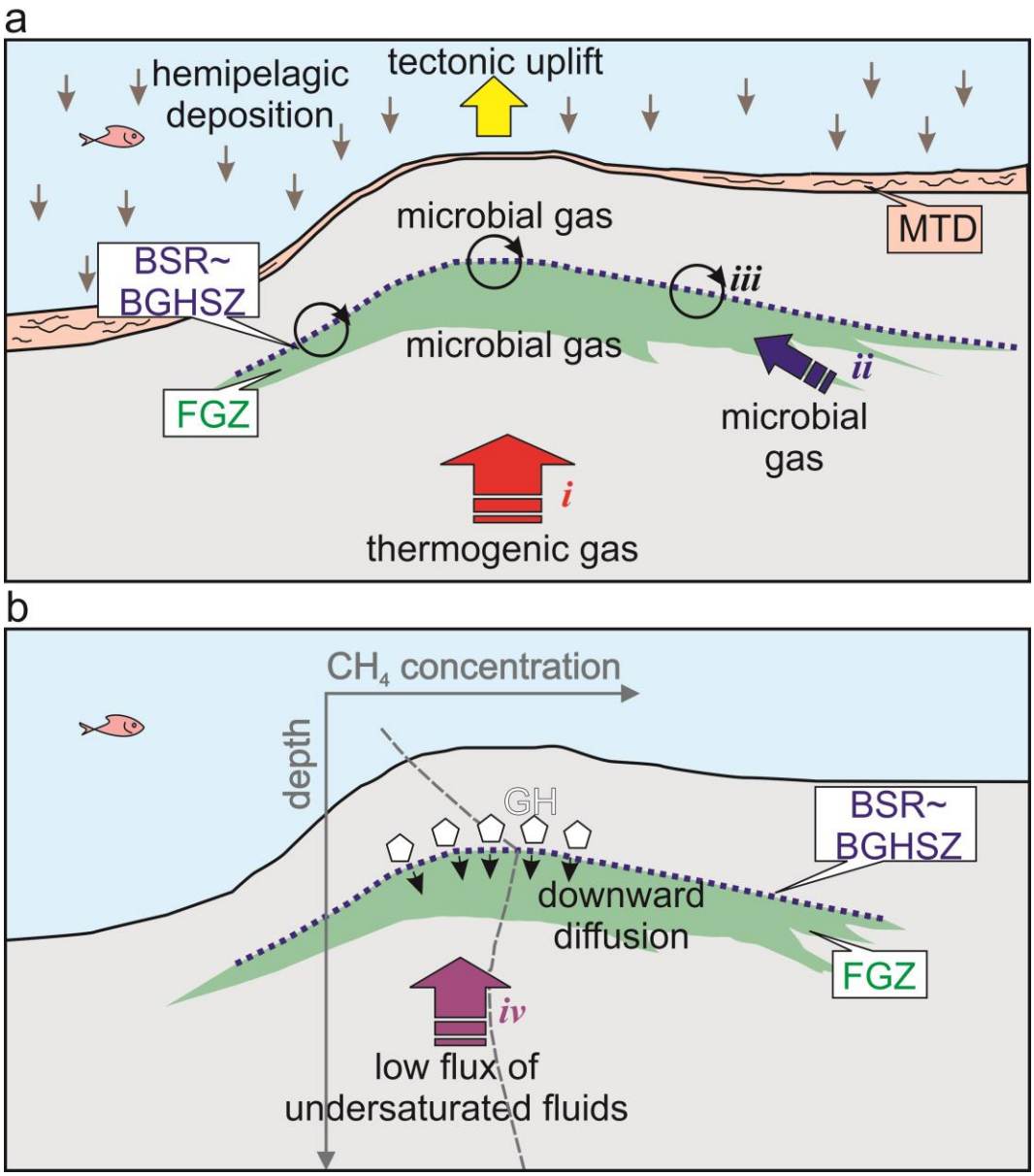



**Figure 7.1.** Schematic representations, displaying the possible origins of a free gas zone in a natural gas hydrate system. **(a)** Upward advective migration of methane-rich (***i***) thermogenic or (***ii***) microbial gas as a free-phase or dissolved in water; (***iii***) Recycling of gas hydrates at the BGHSZ owing to uplift or sediment deposition. **(b)** Solubility-curvature mechanism: the free gas is sourced by a downward diffusion of methane from the GHSZ, coupled with (***iv***) a low flux of undersaturated fluids from below of any origin. The concentration gradient (grey dashed line) refers to methane solubility (e.g. methane os oversaturated on the right and undersaturated on the left).

## 7.2. Seismic expression of the free gas zone

In most of the marine and lacustrine gas hydrate provinces, free gas is observed to be present, continuously or discontinuously, at or near the BGHSZ, which is expressed as a bottom-simulating reflector (BSR) in seismic reflection data (see **paragraph 1.7**).

In some cases, the FGZ is so thin (e.g. around 10-30 m) that the seismic character of the stratigraphic reflections is not impacted beneath BSRs (e.g. Pecher *et al.*, 2001; Mosher, 2011). In other cases, FGZs are thicker. Therefore, below BSRs, it is possible to encounter either enhanced amplitude reflections (EARs) or zones of seismic wipeout, the latter characterised by reduced amplitude and frequency. A combination of EARs and zones of seismic wipeout is further possible. While EARs provoke an amplitude variation, which is concordant to the stratigraphy, the zones of seismic wipeout are discordant. The zones of seismic wipeout are further either volumetrically limited to narrow fluid flow pathways or cover a wider area below a BSR. In the latter case, a clear visualisation of the stratigraphy beneath the BSR is compromised (see **Chapters 3, 4**). The origin of both the EARs and zones of seismic wipeout is attributed to the presence of free gas in the sediment. However, most of the vertical extent of a zone of seismic wipeout can result from the attenuation and energy absorption of the overlying reflections (Løseth *et al.*, 2009; Andresen, 2012; Plaza-Faverola *et al.*, 2012b). Therefore, the lower boundary of an FGZ can be complicated to interpret.

Occasionally, the base of the FGZ is visible. It can be represented by a clear gas-water contact (GWC), resulting from the positive acoustic impedance contrast between free gas-bearing sediments and 100% water-saturated sediment. This GWC can be flat along a single or several dipping stratigraphic horizons. The observation of GWCs at the base of FGZs suggests the existence of a zone of buoyant free gas, exerting an overpressure at the BGHSZ. In this case, the free gas is in hydraulic communication between individual layers or along a single dipping layer. In the presence of several free gas-bearing dipping layers cross-

cutting the BGHSZ and separated by low-permeability *'sealing units'*, the vertical extent of the FGZ can be laterally variable (cf. **Chapter 6**; Sain *et al.*, 2000; Grauls, 2001; Bangs *et al.*, 2011; Boswell *et al.*, 2012b; Lin *et al.*, 2014; Fraser *et al.*, 2016). In rare occasions, the base of the FGZ was found to be represented by a reflection with polarity equal to that of the seafloor and sub-parallel to the BSR over vast distances (Lodolo *et al.*, 2002). In other circumstances (e.g. Site 994 along the Blake Ridge), the formation of a BSR is inhibited, and free gas-bearing layers only occur tens of metres below the BGHSZ (Holbrook, 2001). In these cases, the mass of methane in the system decreases upward toward the BGHSZ, i.e. the free gas is not able to migrate towards the BGHSZ. Alternatively, assuming a constant mass of methane in the system but with the methane solubility increasing near the BGHSZ, the free gas can evanesce towards the BGHSZ.

## 7.3. Data and methods

To achieve the objectives of this review, FGZs from 37 gas hydrate provinces have been characterised. The database used in this study is primarily based on the existing literature and covers a wide range of geological settings (**Tab. 7.1**). However, new observations and measurements have been performed in 3D and 2D datasets from offshore Sabah (NW Borneo), the Guajira Basin (northern Colombia), the Pegasus Basin (southern Hikurangi margin) and the South Falkland/Malvinas Basin. For each gas hydrate province, I have considered only those locations where the FGZ has been studied in previous works, or it is easily identifiable in published 2D and 3D seismic data. Thus, this review does not consider those areas characterised by either faint BSRs or hydrates without BSRs.

| Location | Geological Setting | References |
|---|---|---|
| (1) Hydrate Ridge, central Cascadia margin | Accretionary prism | Tréhu *et al.* (2004a); Milkov *et al.* (2005); Bangs *et al.* (2011) |
| (2) Northern Cascadia margin and Winona Basin | Accretionary prism and frontal anticlines | Davis *et al.* (1990); Singh *et al.* (1993); Kastner *et al.* (1995); Ganguly *et al.* (2000); Riedel and Rohr (2012) |
| (3) Chile Triple Junction | Accretionary prism | Bangs *et al.* (1991); Brown and Bangs (1991); Bangs *et al.* (1993); Bangs and Brown (1995); Froelich *et al.* (1995) |
| (4) Peruvian margin | Accretionary prism | Miller *et al.* (1991); Pecher *et al.* (1996); Pecher *et al.* (2001) |
| (5) South Shetland margin | Accretionary prism | Tinivella *et al.* (1998); Lodolo *et al.* (2002); Tinivella *et al.* (2002); Loreto *et al.* (2010) |
| (6) Offshore Western Colombia | Accretionary prism | Minshull *et al.* (1994) |
| (7) South America margin (exact location is unknown) | Accretionary prism (uncertain) | Grauls (2001) |
| (8) Nankai Trough | Accretionary prism and forearc basin | Matsumoto *et al.* (2004); Kinoshita *et al.* (2009); Tsuji *et al.* (2009); Bangs *et al.* (2010); Daigle and Dugan (2014); Taladay (2015) |
| (9) Makran accretionary prism | Accretionary prism and frontal anticlines | Minshull and White (1989); Grevemeyer *et al.* (2000); Sain *et al.* (2000) |
| (10) Offshore Taiwan | Accretionary prism and frontal anticlines | Chen *et al.* (2014); Lin *et al.* (2014); Klaucke *et al.* (2016) |
| (11) Guajira Basin, offshore northeast Colombia | Accretionary prism, forearc basin, frontal anticlines and foreland basin/abyssal plan | **This study** (see also **Chapter 6**); López and Ojeda (2006); Ochoa (2013) |
| (12) South Falkland Basin | Accretionary prism, frontal anticlines and foreland basin/abyssal plan | **This study**; Foschi (2014); Foschi and Cartwright (2016) |
| (13) Hikurangi margin | Accretionary prism, frontal anticlines and foreland basin/abyssal plan | **This study**; Fohrmann and Pecher (2012); Krabbenhoeft *et al.* (2013); Crutchley *et al.* (2015); Fraser *et al.* (2016); Koch *et al.* (2016) |
| (14) Sea of Japan, Joetsu Basin | Fold and thrust belt with incipient subduction processes | Freire *et al.* (2011) |
| (15) NW Borneo Through, offshore Sabah and Brunei | Fold and thrust belt related to gravity and far-field tectonics | **This study** (see also **Chapters 3-5**); Laird and Morley (2011) |
| (16) Offshore Nigeria | Passive margin with shale/gravity tectonics | Hovland *et al.* (1997); Sultan *et al.* (2011) |
| (17) Krishna-Godavari Basin | Passive margin with shale/gravity tectonics | Riedel *et al.* (2010a); Dewangan *et al.* (2011); Kumar *et al.* (2014) |
| (18) Blake Ridge crest and Blake Ridge Diapir, offshore South Carolina | Passive margin with salt tectonics | Holbrook *et al.* (1996); Ruppel (1997); Taylor *et al.* (2000); Holbrook (2001); Flemings *et al.* (2003) |
| (19) Canadian atlantic margin, offshore Labrador Sea and Scotian Sea, Makkovik | Passive margin with salt tectonics | Mosher (2011) |
| (20) Walker Ridge, Terrebonne Basin, Gulf of Mexico | Passive margin with salt tectonics | Frye (2008); Boswell *et al.* (2012b); Frye *et al.* (2012) |
| (21) Green Canyon, Gulf of Mexico | Passive margin with salt tectonics | Frye (2008); Boswell *et al.* (2012b); Zhang *et al.* (2012); Haines *et al.* (2017) |
| (22) Lower Congo Basin | Passive margin with salt tectonics | Gay *et al.* (2007); Andresen and Huuse (2011); Wenau *et al.* (2015) |
| (23) Kwanza Basin, Offshore Angola | Passive margin with salt tectonics | Serié *et al.* (2016) |
| (24) Andaman Sea | Back-arc basin with compressional structures | Shankar and Riedel (2013); Kumar *et al.* (2014) |
| (25) Ulleung Basin | Back-arc basin | Horozal *et al.* (2009); Kim *et al.* (2013a); Yoo *et al.* (2013) |
| (26) Black Sea, Danube Fan and Dnepr Canyon | Back-arc basin | Zillmer *et al.* (2005); Popescu *et al.* (2006) |
| (27) Sea of Okhotsk, northern Sakhalin continental margin | Back-arc basin | Lüdmann and Wong (2003) |
| (28) Baikal Lake, South Basin | Lacustrine basin with active rifting | Vanneste *et al.* (2001, 2003); Van Rensbergen *et al.* (2002) |
| (29) Barents Sea | Epicontinental sea with extensional minibasins | Ostanin *et al.* (2013); Vadakkepuliyambatta *et al.* (2015) |
| (30) Norway margin, near Storegga Slide | Passive margin | Bünz *et al.* (2005); Hustoft *et al.* (2007); Plaza-Faverola *et al.* (2012a) |
| (31) Vestnesa Ridge | Passive margin | Hustoft *et al.* (2009); Bünz *et al.* (2012); Smith *et al.* (2014b); Plaza-Faverola *et al.* (2015) |
| (32) Offshore Mauritania | Passive margin | Davies and Clarke (2010); Li *et al.* (2016) |
| (33) Offshore Cameroon, slope setting | Passive margin | Le *et al.* (2015) |
| (34) Offshore Namibia | Passive margin | Moss (2010); Moss and Cartwright (2010) |
| (35) Mahanadi Basin | Passive margin | Kumar *et al.* (2014); Shankar and Riedel (2014) |
| (36) South China Sea, Shenhu area | Passive margin | Wang *et al.* (2011); Qian *et al.* (2014); Wang *et al.* (2014); Li *et al.* (2015); Sha *et al.* (2015) |
| (37) Beaufort Sea | Passive margin | Andreassen *et al.* (1995) |

**Table 7.1.** Location, geological settings and references for each gas hydrate province considered in this study. The FGZs in the provinces highlighted in pale yellow are discussed in detail in **sub-paragraph 7.4.2**.

### *7.3.1. Critical status of the free gas zone and fluid flow mechanisms*

In this review, I have collected data on **(1)** the thickness of the overburden, from the seafloor up to the BSR ($\boldsymbol{D_{BSR}}$) (i.e. top of the FGZ) and on **(2**) the thickness of the FGZ ($\boldsymbol{Th_{FGZ}}$). Where provided, I have used literature data from quantitative measurements of the depth of the BSR, the water depth and the thickness of the FGZ. In other cases, such information has been extrapolated from the interpretation of seismic sections, seismic attribute maps, and available literature information on seismic velocity. The objective is relating $\boldsymbol{D_{BSR}}$ to $\boldsymbol{Th_{FGZ}}$ (cf. Hornbach *et al.*, 2004), to discuss and contextualise the existence of overpressure at the BGHSZ. For certain locations, $\boldsymbol{D_{BSR}}$ and $\boldsymbol{Th_{FGZ}}$ have been characterised with a range of depths and thicknesses rather than with single values, given **(1)** the uncertainties of the time to depth conversion and of seismic interpretation, and **(2)** the variability of $\boldsymbol{Th_{FG}}$ along different adjacent stratigraphic horizons. Importantly, until the FGZ exceeds a thickness of 1/8 to 1/4 of the wavelength of the seismic source signal (~5-15 m in conventional 3D seismic data) it may not be possible to measure its thickness in seismic sections confidently (Widess, 1973; Miller *et al.*, 1991) (**Tab. 7.3** and **Figs. 7.4-7.12**). The most critical sources of errors in these measurements are represented by the use of constant velocity values for the determination of $\boldsymbol{D_{BSR}}$ and $\boldsymbol{Th_{FGZ}}$, particularly considering the impact of gas hydrates and free gas on the P-wave velocity of shallow marine sediments (Helgerud, 2001; Chand *et al.*, 2004; Lee, 2004).

To understand the stress that may counteract overpressures at the BGHSZ is crucial to calculate the lithostatic or overburden stress ($\boldsymbol{Pv}$). Therefore, I have computed a series of empirical curves that reflect the increase with depth of $\boldsymbol{Pv}$ (**Fig. 7.2a**). These curves originate from a compilation of bulk densities from core data recovered offshore in various ODP/IODP cruises (http://iodp.tamu.edu/database/), as well during the Shell geohazard study at the crest and the flanks of the GKL Dome (Benting *et al.*, 2006). Further density measurements have been obtained from open access LWD data, acquired during the Northern Gulf of Mexico Gas Hydrate Joint Industry Project (Collett *et al.*, 2012) (**Tab. 7.2**

and **Fig. 7.22**). The vertical hydrostatic effective stress (***P'v***) has been then calculated from these curves, according to the Terzaghi's principle (Terzaghi, 1943), assuming a constant pore water density of 1025 kg/m$^3$.

Two free gas densities (50 and 275 kg/m$^3$), which represent end-members for marine NGHSs, have been used to relate the buoyancy pressure exerted by free gas (***Pg***) to the thickness of a free gas column (**Fig. 7.2b**) (e.g. Clennell *et al.*, 2000b). Finally, the gas column thickness ($\boldsymbol{Th_{FGZ}}$) capable of being equal to ***P'v*** at the top of an FGZ ($\boldsymbol{D_{BSR}}$) was extrapolated, for each trend of lithostatic stress *vs* depth and each end-member gas density (**Fig.7.3**). These relations define a range of critical conditions, where the buoyancy exerted by an interconnected free gas column equals the effective stress of the overlying overburden (i.e. ***P'v***). Such conditions are considered to approximate a boundary for the initiation of fracturing phenomena.

For simplicity, hydraulic fracturing (driven by a liquid) and pneumatic fracturing (driven by gas) are included in this study under the widely used term hydraulic fracturing, although a more correct and generic term would be *'fluid-driven'* fracturing. Hydraulic fractures are predicted to initiate when the overpressure equals the minimum effective stress (horizontal in the absence of lateral compression) plus the sediment tensile strength. Here, I hypothesise that hydraulic fractures can initiate when the overpressure approaches the effective vertical stress.

Firstly, at those depths where hydrates and shallow free gas are observed, the state of stress can be roughly isotropic, due to the poorly consolidated and relatively soft nature of the sediments (Flemings *et al.*, 2003; Tréhu *et al.*, 2004a). Secondly, gas hydrates can severely impact the resulting strength of the sediment. Major controls on such effect are represented by the hydrate saturation, the confining stress (which influences the interparticle frictional forces) and, inevitably, the hydrate morphology (Yun *et al.*, 2005 and 2007; Jung and Santamarina, 2011; Yoneda *et al.*, 2015 and 2017). The presence of a free gas phase

during hydrate formation can result in an even more pronounced increase of strength of the sediment, given that hydrates could grow as a cementing phase under such conditions (Waite *et al.*, 2004; Hyodo *et al.*, 2013). Therefore, the overpressure required to initiate fractures at the BGHSZ can easily exceed the minimum effective stress and the hydrate-free sediment tensile strength. Thirdly, an overpressure would lead to an increase in the minimum horizontal stress (***Ph***), because of pore pressure/stress coupling due to poroelastic effects. This increase is proportional to the amount of overpressure and the size of the overpressured zone relative to the overburden (Engelder and Fischer, 1994; Hillis, 2000; Tingay *et al.*, 2003; Mourgues *et al.*, 2011). This theory, based on poroelasticity, also predicts a more likely occurrence of tensile rather than shear fractures under overpressure conditions and would justify the observation, on 3D seismic data, of deformable cross-stratal pathways for fluid flow, commonly associated with overpressure conditions and fracturing genetic mechanisms (see **Chapter 4**).

A simple description of the variation in the minimum horizontal stress with pore pressure is presented in the Appendix (**sub-paragraph 7.7.1**). It is shown that, under typical conditions for the shallow parts of sedimentary basins, the minimum horizontal stress increases up to values close to lithostatic before hydraulic fracturing could occur (ignoring the effect of tensile strength). Thus, the assumption of hydraulic fracture initiation where overpressure exceeds the effective vertical overburden stress is a valid approximation. Notwithstanding these uncertainties, the different trends of ***P'v*** *vs* depth considered here, as well as the end-member gas densities, likely allow encompassing most of the conditions required for hydraulic fracturing in the shallow parts of many sedimentary basins. Moreover, I have considered the conditions to reactivate normal fault slip, following the method of Hornbach *et al.* (2004) (see Appendix**, sub-paragraph 7.7.2**).

I have further accounting for the mechanism of capillary invasion. This process does not require the creation of new pathways for fluid flow or the reactivation of faults. Capillary

invasion is instead controlled by the interfacial relationships between the immiscible phases (i.e. water and gas), expressed as wettability and interfacial tension ($\gamma$), and by the three-dimensional structure of the porous media, expressed as the pore throat entry radius ($a$). The simplified form of the Young-Laplace equation, which approximates the pore network to a system of capillary cylindrical tubes, has been used to compute the free gas column required to invade a water-saturated sediment, at different values of $a$, which depends on lithology, and $\gamma$, which depends on pressure and temperature (Watts, 1987; Kleinberg *et al.*, 2003; Schmidt *et al.*, 2007; Jain and Juanes, 2009). In the presence of a fracture-dominated pore network, which can be approximated by parallel plates of aperture= $2l$, the pressure required to cause invasion is half of that in the cylindrical tube model, in the presence of a wetting water phase (Brown, 2000). Overall, I will interpret real data from various hydrate provinces by taking into account for key physical processes of fluid flow and sediment failure.

### *7.3.2. Impact of the gas solubility and geothermal gradient*

The solubility of methane or a mixture of gases is controlled by temperature, pressure and pore water salinity (Duan *et al.*, 1992; Tishchenko *et al.*, 2005). Haacke *et al.* (2007) investigated the role of the methane solubility profiles in the overburden. These authors plotted the geothermal gradients of different hydrate provinces against the pressure at $D_{BSR}$ and implemented on this diagram a series of isolines of equal solubility curvature as a function of varying geothermal gradients and pressures. Here, by the use of new data (**Tab. 7.3**), the role of methane solubility in favouring the formation of FGZs is re-appraised.

The geothermal gradient (***GTG***) in the analysed gas hydrate provinces has been estimated in the exact locations where $Th_{FGZ}$ has been measured. The gas hydrate stability boundary has been computed, from 0 to 30 °C with the CSMHyd software (Sloan Jr and Koh, 2007), assuming, in most of the cases, a water salinity ranging from 3.0 to 3.5%, a pure methane composition for the feeding gas and ignoring capillary effects on hydrate stability. For a few hydrate provinces (e.g. the Lake Baikal, the Black Sea, the NW Borneo, the region

offshore Svalbard and the Barents Sea,), either the salinity or the feeding gas composition have been modified, to consider low-salinity to fresh waters settings and $C_{2+}$ hydrocarbons in the system. Subsequently, I have extrapolated the ***GTG***, dividing the temperature difference between the BSR and the seafloor by $\boldsymbol{D_{BSR}}$ (see Grevemeyer and Villinger, 2001). Information on the temperature at the seafloor, for most of the study areas, has been found in the literature database summarised in **Tab. 7.1**. The extrapolated ***GTGs*** (**Tab. 7.3**) match with those found in the literature. The presence of overpressures at the BSR has been considered to not significantly impact its position (Bhatnagar, 2008), whereas other authors highlighted, under particular scenarios, its importance in influencing the depth of BSRs (Tinivella and Giustiniani, 2013). Therefore, the assumption of hydrostatic pore pressures at the BSR, even if could not cause substantial errors in estimating approximate GTGs, undoubtedly constitutes a source of errors.

In order to investigate the impact of methane solubility on $\boldsymbol{Th_{FGZ}}$ the solubility profiles related to the analysed locations have been extracted by the use of the calculations of Tishchenko *et al.* (2005), for pure methane structure I hydrates (**Fig. 7.23**). The solubility gradient observed for the first ~100 m below the BGHSZ is linear and is directly correlated with the ***GTG***. The steeper solubility gradients (i.e. greater solubility variation in a short depth interval) are associated with the higher thermal gradients, and vice-versa. This simple correlation (**Fig. 7.24a**) suggests that the temperature gradients within the FGZ could somehow influence its vertical extent. The solubility gradient is expressed as the angular coefficient ($\boldsymbol{\Delta_{SOL}}$, expressed in $10^{-5}$ mol. $CH_4 \cdot kg^{-1} \cdot m^{-1}$) of the solubility variation observed for the first ~100 m below the BGHSZ. The value of this gradient should be treated with caution if $C_{2+}$-rich gases are present in the system, if free gas coexist with hydrates within the FGZ and in the presence of capillary effects on methane solubility (e.g. Liu and Flemings, 2011; Ostanin *et al.*, 2013; Daigle and Dugan, 2014; Smith *et al.*, 2014b).

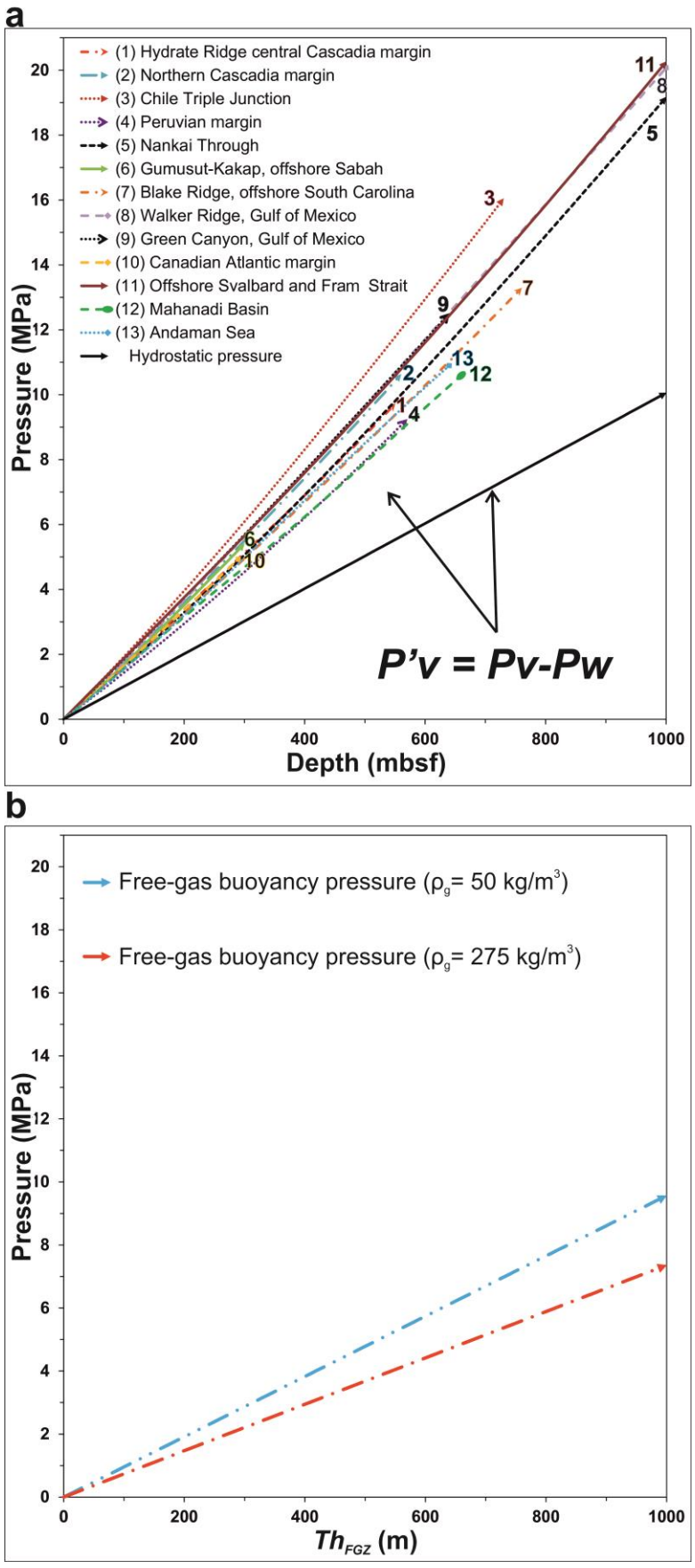



**Figure 7.2. (a)** Variation of the lithostatic pressure (***Pv***) with depth in the 13 analysed locations (see **Tab. 7.2**). The hydrostatic pressure (***Pw***, measured from the sea/lake bottom) is also plotted as a continuous black line. The number near each line refers to the legend in the top-left of the figure. **(b)** Variation of the gas pressure (***Pg***) *vs* the thickness of the free gas column, here referred to as the thickness of the FGZ (***Th$_{FGZ}$***). Two end-member gas densities (50 and 275 kg/m$^3$) have been chosen for these calculations.

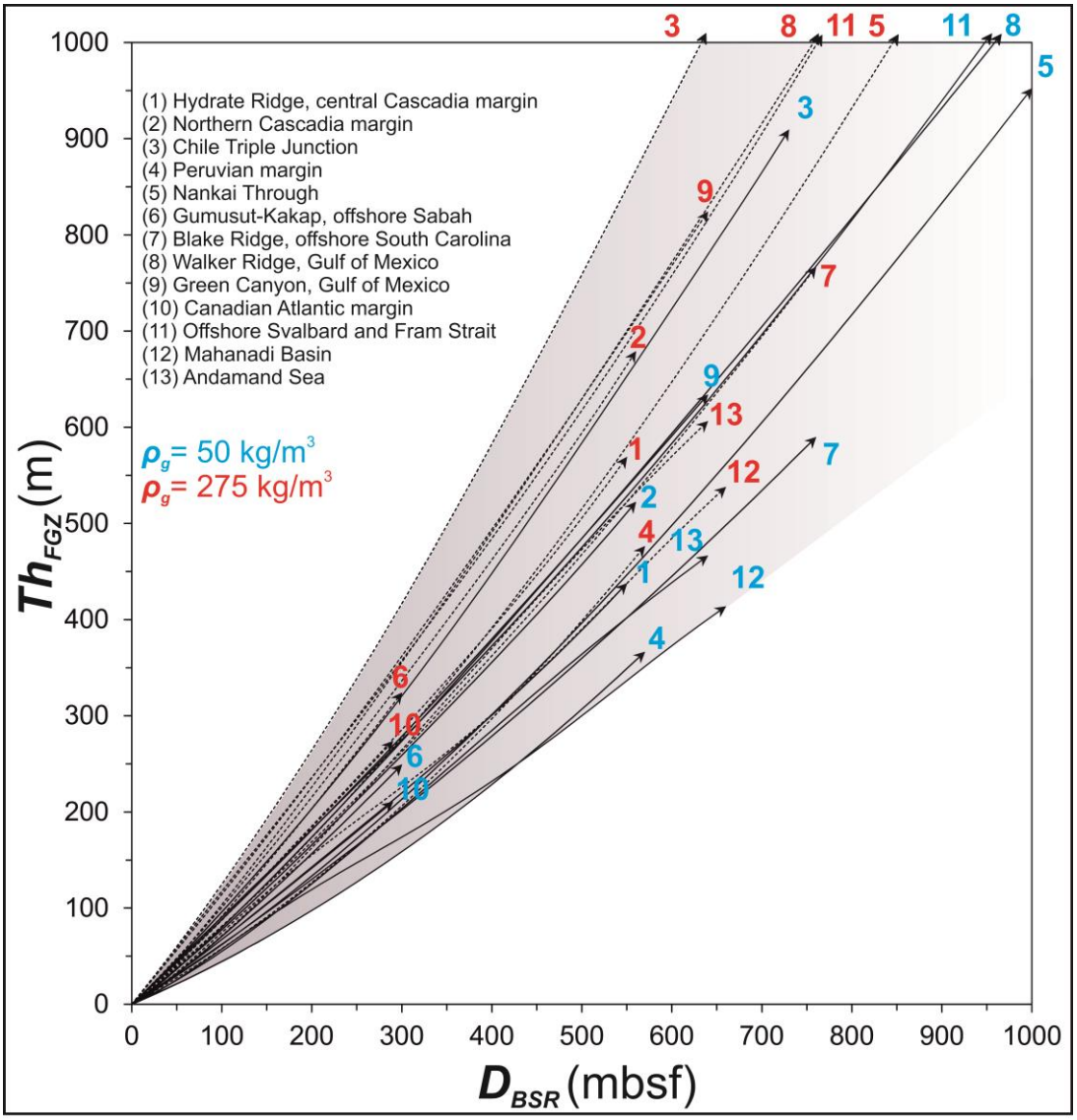



**Figure 7.3.** Variation of the critical $Th_{FGZ}$ required to initiate hydraulic fracturing in relation to the thickness of the overburden expressed as the depth of the BSR ($D_{BSR}$). The difference in the variation of ***Pv*** with depth and the possible different free gas density leads to the construction of an envelope instead of a single curve.

| Location | Sites | Data |
|---|---|---|
| Hydrate Ridge, central Cascadia margin | ODP Leg 204, sites 1244-1252 | Bulk density measurements on cores |
| Northern Cascadia margin | ODP Leg, 146, sites 888-892; IODP Leg 311, sites 1325-1329 | Bulk density measurements on cores |
| Chile Triple Junction | ODP Leg 141, sites 859-863 | Bulk density measurements on cores |
| Peruvian margin | ODP Leg 112, sites 679-688; ODP Leg 201, sites 1227-1230 | Bulk density measurements on cores |
| Nankai Trough | ODP Leg 190, sites 1173-1178; ODP Leg 196, site 1173 | Bulk density measurements on cores |
| Gumusut-Kakap, offshore Sabah | Shell Geohazard evaluation-this study | Bulk density measurements on cores |
| Blake Ridge, offshore South Carolina | ODP Leg 164, sites 991-997; ODP Leg 172, site 1061 | Bulk density measurements on cores |
| Walker Ridge, Gulf of Mexico | Gas Hydrate Joint Industry Project Leg II, holes WR313 G and H | LWD density log |
| Green Canyon, Gulf of Mexico | Gas Hydrate Joint Industry Project Leg II, holes GC955 H, I and Q | LWD density log |
| Canadian Atlantic margin, Orphan Knoll and Erik Drift | IODP Leg 303, sites 1302, 1303, 1305, 1306 and 1307 | Bulk density measurements on cores |
| Offshore Svalbard and Fram Strait | ODP Leg 151, sites 909 and 909; ODP Leg 162, sites 986 and 987 | Bulk density measurements on cores |
| Mahanadi Basin | IODP Leg 353, sites U1445 and U1446 | Bulk density measurements on cores |
| Andaman Sea | IODP Leg 353, sites U1447 and 1448 | Bulk density measurements on cores |

**Table 7.2.** Location, sites and data used to extrapolate the ***Pv*** *vs* depth functions used in this study.

## 7.4. Results

### *7.4.1. Thickness of free gas zones in sedimentary basins*

The measured $\boldsymbol{D_{BSR}}$ and $\boldsymbol{Th_{FGZ}}$ have been implemented with the extrapolated criteria for hydraulic fracturing and fault reactivation. Each location has been classified considering the regional geological setting and margin type (**Tab. 7.3**). **Figures 7.4-7.12** show some examples of FGZs in various gas hydrate provinces. $D_{BSR}$ and $Th_{FGZ}$ are plotted in **Fig. 7.13**, together with the extrapolated criteria for hydraulic fracturing and fault reactivation. It is possible to observe that thick FGZs, i.e. exceeding ~150-200 m in thickness, occur in many different geological settings. Each gas hydrate province in **Tab. 7.3** is associated with a number, which allows its recognition in **Fig. 7.13**.

#### *7.4.1.1. Convergent margins*

In different zones along convergent margins, from the deformed accretionary prisms to the abyssal plains, the majority of the measured FGZs are within the sub-critical zone of the plot (**Fig. 7.13a**). However, a good number of locations are close to or within the conditions required for hydraulic fracturing and fault reactivation and have extremely thick FGZs. These areas include some of the largest FGZs ever observed to date, located in the frontal anticlines of the Guajira Basin, offshore NE Colombia (**Figs. 7.4a, g, h**). FGZs of similar thickness have also been observed along the accretionary prism of the Hikurangi margin (Crutchley *et al.*, 2015) (**Fig. 7.10e**).

Given the relatively low ***GTGs*** and the deep waters of these regions, the overburden above such FGZs exceeds 500 m of thickness. Such a thick overburden will often provide the adequate lithostatic stress to compete against free gas buoyancy. These thick free gas columns are seismically expressed by dipping stratigraphic reflections with enhanced amplitudes and have been interpreted to form in the presence advective fluxes of gas-charged fluids along permeable dipping strata (see **Chapter 6**). These FGZs are extremely

variable in thickness, and a critical or nearly critical FGZ is only observed along certain stratigraphic horizons. The lateral permeability contrasts between nearby strata and, consequently, the lateral differences in the flux of hydrocarbon gases, probably represent the key controls on the vertical extent of FGZs (cf. Chatterjee *et al.*, 2014).

Another gas hydrate province with extremely thick FGZs compared to $\boldsymbol{D_{BSR}}$ is the abyssal plain and foreland sector of the South Falkland Basin. Here, the FGZ is characterised by a combination of dipping stratigraphic horizons with enhanced reflections that extend down to maximum ~200-250 m below a BSR. These FGZs are frequently by-passed by fluid-escape pipes, linked to deeper normal faults (Foschi and Cartwright, 2016) (**Fig. 7.7c, d**). Depending on the hydraulic properties of the free gas-bearing sediments within the FGZ, there could be either a single interconnected FZG or multiple compartmentalised reservoirs. Further examples of thick FGZs developed along tectonically compressive margins include those in the accretionary prisms and frontal anticlines of the Makran (**Fig. 7.10d**) and Taiwan margins (Sain *et al.*, 2000; Chen *et al.*, 2014). Overall, the frontal anticlines and the adjacent abyssal plains, located more seaward than the accretionary prisms, seem to represent favourable locations for the development of thick FGZs.

The FGZs along the accretionary prism and the forearc of the Guajira basin (**Fig. 7.4b-f**), are overlain by a thick overburden (~400-500 m), and their thickness is sub-critical for hydraulic fracturing, solely considering the possible buoyancy of the present-day free gas as a source for overpressure. Nonetheless, these gas hydrate systems display numerous cross-stratal fluid flow pathways, including normal faults, pipes and mud volcanoes (cf. **Figs. 7.4b-f, 7.13a**). Therefore, additional sources of overpressure, other mechanical failure criteria (e.g. the reactivation of pre-existing faults) or migration along pre-existing fracture networks need to be invoked to justify the presence of these features. Alternatively, the observed $\boldsymbol{Th_{FGZ}}$ has been depleted compared to an original greater thickness at the time of hydraulic fracturing and vertical gas leakage (see the discussion in **sub-paragraph 7.5.2**).

In addition, the BSR is shifted upward around mud volcanoes and pipes in the forearc basin of the Guajira basin (**Fig. 7.4e, f**), likely due thermal perturbations around the conduits. Such perturbation creates a *'four-way closure trap'* for free gas, whose geometry is regulated by the uplifted three-phase boundary. This mechanism of free gas trapping is expected to be common around mud volcanoes and other sites of high-flux seepage in other compressional (Baba and Yamada, 2004; Crutchley *et al.*, 2014; Pape *et al.*, 2014), and actively extensional settings (Van Rensbergen *et al.*, 2002; Vanneste *et al.*, 2003) (**Fig. 7.12b**).

#### *7.4.1.2. Continental margins with gravity, shale, salt and far-field tectonics*

In the presence of compression driven by gravity, shale, salt and far-field tectonics, fold and thrust belts may form along continental margins away from plate boundaries (Morley *et al.*, 2011). The resulting NGHSs in these margins are somehow similar to those observed along accretionary prisms, although the BSRs, FGZs and fluid-escape phenomena at the seafloor, are patchier and frequently related to the flux of hydrocarbons from deeper reservoirs (Cunningham and Lindholm, 2000; Gay *et al.*, 2007; Warren *et al.*, 2010; Andresen and Huuse, 2011; Serié *et al.*, 2016). In many cases, the FGZs in these settings are characterised by enhanced reflections along dipping stratigraphic pathways at the backlimb of anticlines, and normal faults and fluid-escape pipes at their crests (Hovland *et al.*, 1997; Riedel *et al.*, 2010a; Laird and Morley, 2011; Sultan *et al.*, 2011; Wenau *et al.*, 2015) (**Figs. 7.9, 7.11**). Occasionally, thick FGZs have also been observed in flat areas, characterised by horizontal and faulted stratal reflections with enhanced amplitudes (**Figs. 7.11e**, **7.13b, c**). The data collected in this review indicate that the FGZs in these setting can be critically pressured (**Fig. 7.13b, c**).

One of the thickest FGZs is observed at the crest of the Blake Ridge Diapir (offshore South Carolina, near the ODP site 996, Leg 164), located along a passive margin with salt diapirism. Here, the FGZ is up to ~380 ms TWT thick (~280-300 m) (Taylor *et al.*, 2000) (see **Fig. 1.8a**). The heat-flow and salinity perturbations, induced by the presence of the

diapir, determine a shallower BSR above the diapir crest and, thus, a thicker FGZ than at the flanks, similarly to what observed for the mud volcanoes in the Guajira basin. FGZs thicker than ~200 m have also been observed in the Terrebonne Basin (Gulf of Mexico), within sand-rich horizons at the backlimb of a salt-related ridge (Boswell *et al.*, 2012b) (**Figs. 7.11c**, **7.13c**). However, the great depth of the BGHSZ (~850-950 mbsf), owing to the low geothermal gradient of this region (18-20 °C/km), prevents the formation of critical FGZs.

#### *7.4.1.3. Passive and actively extensional margins*

Extremely thick FGZs, confined to thin stratigraphic pathways, exist along the continental slopes in the western portion of the Ulleung Basin and offshore Mauritania. These FGZs form below a BGHSZ that progressively pinches out at shallower depths along the slope and cross-cuts the stratigraphic reflections. The base of these FGZs appears as a sharp reduction in acoustic amplitude (Davies and Clarke, 2010; Yoo *et al.*, 2013) (**Figs. 7.12a, 7.13d, e**).

Where the tectonic compression and the stratal dip do not play a dominant role in the accumulation of free gas, the distribution of the high-permeability *vs* that of the low-permeability facies become a dominant control on the distribution of free gas. The result is an FGZ characterised by packages of sub-horizontal enhanced reflections, occasionally thicker than ~200 m. Such FGZs are controlled in the three dimensions by the original depositional patterns of channel/canyon, levee and contourite systems, in these cases scarcely influenced by tectonic deformation. Notable examples include the Green Canyon (Gulf of Mexico), the Danube Fan (Black Sea), the Mahanadi Basin (offshore East India) and the Pearl River Mouth Basin (South China Sea) (Popescu *et al.*, 2006; Zhang *et al.*, 2012; Shankar and Riedel, 2014; Wang *et al.*, 2014) (**Figs. 7.12e, f, 7.13d, e**).

#### *7.4.1.4. General observations*

Along convergent margins, the maximum thickness reached by the FGZs is often greater than in other tectonic contexts (**Fig. 7.13**). The main reason is the water depth and the ***GTGs*** of these provinces, which are, respectively, higher and lower compared to other settings. In this study, the average water depths of the analysed NGHSs is ~2000-2100 m for convergent margins and ~1300-1400 m for other settings, whereas the extrapolated ***GTGs*** are on average 40-45 °C/km along convergent margins and about 50-55 °C/km elsewhere. Nevertheless, there are remarkable exceptions, such as the Chilean triple Junction, the Joetsu basin (having extremely high ***GTGs***) and the Northern Gulf of Mexico (having extremely low ***GTGs***) (**Tab. 7.3**).

It has been finally observed that the FGZs which fall inside the critical zone for hydraulic fracturing exhibit one or more of the following characteristics: **(1)** Evidence of cross-stratal fluid migration and active seepage at the seafloor; **(2)** Presence of dipping stratigraphic reflections at the flanks of anticlines displaying segments with enhanced reflectivity and **(3)** BSRs that pinch out at the seafloor along the slope and cross-cut the stratigraphy (cf. **Tab. 7.3, Figs. 7.4-7.12** and **Fig. 7.13**). However, there are no points that plot to the left of the hydraulic fracturing envelope, with one single exception (cf. **Fig. 7.8b, 7.13a**), still very close to the left side of the envelope. Therefore, the hydraulic fracturing criteria defined in this study could approximate an upper boundary for the total vertical extent of an FGZ.

**Tab. 7.3**

| **Gas hydrate province, location and reference** | ***Geologic Setting*** | **Water depth (mbsl)** | ***$D_{BSR}$* (mbsf)** | ***$Th_{FGZ}$* (m)** | ***GTG* (°C/km)** | ***TWT to depth constrain*** | ***Faults at $D_{BSR}$*** | ***Def. paths*** | ***FGZ*** |
|---|---|---|---|---|---|---|---|---|---|
| **(1)** Hydrate Ridge. Tréhu *et al.* (2004a), *Fig. 1* (**Fig.7.10a**) | Accretionary prism | 800 | 150 | 100-110 | 55 | Well-logs and drilling | Yes | Yes | $A_1$; $C_1$ |
| **(2)** Northern Cascadia, profile 89-08. Singh *et al.* (1993), *Fig. 2.* | Accretionary prism | 1300 | 240 | 30 | 55 | Waveform inversion | No | No | $D_2$ |
| **(2)** Winona Basin, line 85-04, fold crest. Riedel and Rohr (2012), *Fig. 10.* | Frontal anticline | 1900 | 270 | 40-60 | 61.5 | Depth converted profile | Yes | No | $D_2$ |
| **(2)** Winona Basin, line 85-04, gentle buried folds. Riedel and Rohr (2012), *Fig. 11.* | Accretionary prism | 1750 | 250 | 130-140 | 65 | Depth converted profile | No | No | $B_1$ |
| **(3)** Chile Triple Junction, near site ODP Leg 141, 859. Bangs *et al.* (1993), *Figs. 2, 3* (**Fig. 7.10b**) | Accretionary prism | 2741 | 97 | 7 | 177.3-191.8 (non-linear ***GTG***) | Well-logs, waveform and AVO modelling | likely | No | $D_1$ |
| **(3)** Chile Triple Junction, near site ODP Leg 141, 860. Bangs *et al.* (1993), *Fig. 2* (**Fig. 7.10b**). | Forearc basin | 2146 | 200 | 12 | 86.5 | Well-logs, waveform and AVO modelling | unlikely | No | $D_2$ |
| **(4)** Peruvian margin, Peru line 1018, CMP 1126 near site 688. Pecher *et al.* (1996), *Fig. 2.* | Accretionary prism | 4000 | 600 | 6-18 | 39.2 | Full waveform inversion | unlikely | No | $D_2$ |
| **(5)** South Shetland margin, MCS lie IT9043. Tinivella *et al.* (1998), *Fig. 6.* | Accretionary prism | 1400-2300 (1950) | 640 | 50 av. (70 max) | 32.5-40 | Seismic tomography inversion | likely | No | $D_2$ |
| **(5)** South Shetland margin, line I97213. Tinivella *et al.* (2002), *Figs. 3, 9.* | Accretionary prism | 1600-1800 (1700) | 500-700 (600) | 100 av. (200 max) | 32.5-40 | Travel time inversion | likely | No | $D_2$ |
| **(6)** Offshore Western Colombia, Minshull *et al.* (1994), *Figs. 2, 3.* | Accretionary prism | 1500 | 500 | 30 | 30.4 (*Tsf* =3°C) | Full waveform inversion | unlikely | No | $D_2$ |
| **(7)** South America margin, Grauls *et al.* (2001), *Figs. 2, 3.* | Accretionary prism | 2000 | 570 | 200-330 | 31.2 (*Tsf*=2.5°C) | Depth converted profile | No | No | $B_1$ |
| **(8)** Kumano forearc, site C002. Bangs *et al.* (2010), *Fig. 2*; Daigle *et al.* (2014), *Figs. 1, 2;* Taladay (2015) (**Fig. 7.10c**) | Forearc basin | 1900-2000 (1936) | 320-400 | 70-200 | 40 | Depth converted seismic data and well-logs | No | No | $B_1$ |
| **(8)** Nankai Trough, MITI wells location. Tsuji *et al.* (2009), *Fig. 15.* | Accretionary prism | 945 | 295 | 85-90 | 36.3-43.0 | Seismic and well constrain. | No | No | $B_1$ |
| **(9)** Makran accretionary prism; Sain *et al.* (2000), CDP 4375-43400 along line in *Fig 2* (**Fig. 7.10d**) | Accretionary prism | 1700 | 500 | 200-350 | 29.5 | Full waveform inversion | No | No | $B_1$ |
| **(9)** Makran accretionary prism Line 9707, Grevemeyer *et al.* (2000), *Figs. 2, 5.* | Accretionary prism | 2500 | 700 | 200 | 28.5 | Inversion of wide angle and refraction data | No | No | $B_1$ |
| **(9)** Makran margin, frontal anticline. Minshull and White (1989), *Fig. 5.* | Frontal anticline | 1710 | 550 | 130-300 | 27.4 | Velocity structure derived from stacking velocities | No | No | $B_1$ |
| **(9)** Makran margin, frontal anticline. Minshull and White (1989), *Fig. 6.* | Frontal anticline | 2210 | 350 | 160-165 | 50.6 | Velocity structure derived from stacking velocities | No | No | $B_1$ |
| **(10)** Four-way Closure Ridge, Klaucke *et al.* (2016), *Fig. 6.* | Accretionary prism | 1350 | 320-360 | 98-110 | 40.6 (*Tsf* assumed 3 °C) | Assumed to vary between 1.7 and 1.9 km/s. | Yes | Yes | $A_1$; $B_1$ |
| **(10)** Yung-An Ridge, Chen *et al.* (2014), *Fig. 6.* | Accretionary prism | 1365 | 240-250 | 115-170 | 50.7 | Depth converted data. | Yes | Yes | $A_1$; $B_1$ |
| **(10)** Frontal anticline, profile MCS716-02. Lin *et al.* (2013), *Fig. 9.* | Frontal anticline | 2370 | 400 | 225 | 44.5 | 1.8 km/s suggested from nearby ODP wells. | No | No | $B_2$ |
| **(11)** Guajira Basin, frontal anticline $A_1$. Horizons at the backlimb Hα, Hβ, intra α-β, (**Fig. 7.4a**). | Frontal anticline | 3728-Hα<br>3785-Hβ<br>3763<br>intra α-β | 680<br>660<br>269<br>622 | 570<br>269<br>133 | 33.5<br>34.5<br>36.6 | Depth converted | Yes | Yes | $A_1$; $B_1$ |
| **(11)** Guajira Basin, frontal anticline A2. (**Fig 6.7, 6.8**). | Frontal anticline | 3600.0 | 620 | 83-179 | 36.3 | Depth converted | Yes | No | $A_1$; $B_1$ |
| **(11)** Guajira Basin, accretionary prism, section 1 (**Fig. 7.4b**). | Accretionary prism | 2112.5 | 435-460 | 185-195 | 41.9 | 1.7-1.8 km/s | Yes | Yes | $A_1$; $B_1$ |
| **(11)** Guajira Basin, accretionary prism, section 2. | Accretionary prism | 2369.0 | 392-415 | 106-112 | 46.6 | 1.7-1.8 km/s | Yes | Yes | $A_1$; $B_1$ |
| **(11)** Guajira Basin, accretionary prism, section 3. | Accretionary prism | 2216.0 | 451-478 | 100-106 | 40.4 | 1.7-1.8 km/s | Yes | No | $B_1$ |
| **(11)** Guajira Basin, accretionary prism, section 4 (**Fig. 7.4c**). | Accretionary prism | 2337.0 | 422-447 | 247-262 | 43.3 | 1.7-1.8 km/s | No | Yes | $A_1$; $B_1$ |
| **(11)** Guajira Basin, accretionary prism, section 5 (**Fig.7.4d**). | Accretionary prism | 2175.0 | 447-473 | 121-129 | 40.8 | 1.7-1.8 km/s | Yes | Yes | $A_1$; $B_1$ |
| **(11)** Guajira Basin, forearc basin, mud volcano section 6 (**Fig. 7.4e**). | Forearc basin | 2682.0 | 468-496 | 73-77 | 40.5 | 1.7-1.8 km/s | Yes | Yes | $C_1$ |
| **(11)** Guajira Basin, forearc basin, pipe/mud diapir section 7 (**Fig. 7.4f**). | Forearc basin | 2687.0 | 463-490 | 58-61 | 40.9 | 1.7-1.8 km/s | Yes | Yes | $C_1$ |
| **(11)** Guajira Basin, frontal anticline, section 3 (**Fig. 7.4g**). | Frontal anticline | 3479.0 | 525-590 | 80-490 | 37.2 | 1.8-1.9 km/s | Yes | No | $A_1$; $B_1$ |

| | | | | | | | | | |
|---|---|---|---|---|---|---|---|---|---|
| **(11)** Guajira Basin, frontal anticline, section 4 (**Fig. 7.4h**). | Frontal anticline | 3532.0 | 503-570 | 80-316 | 41.1 | 1.8-1.9 km/s | Yes | No | $A_1$; $B_1$ |
| **(11)** Guajira Basin, frontal anticline, section 5 (**Fig. 7.5a**). | Frontal anticline | 3830.0 | 644-680 | 95-492 | 34.7 | 1.8-1.9 km/s | No | No | $A_2$ |
| **(11)** Guajira Basin, abyssal plan, cluster of sub-horizontal enhanced reflections A, section 8 (**Fig. 7.5b**). | Abyssal plan/ Foreland basin | 3926.0 | 551-582 | 200-210 | 40.6 | 1.8-1.9 km/s | No | No | $A_2$ |
| **(11)** Guajira Basin, abyssal plan, cluster of sub-horizontal enhanced reflections B, section 8 (**Fig. 7.5b**). | Abyssal plan/ Foreland basin | 3960.0 | 591-623 | 190-200 | 38.1 | 1.8-1.9 km/s | No | No | $A_2$ |
| **(11)** Guajira Basin, abyssal plan, cluster of sub-horizontal enhanced reflections C, section 9 (**Fig. 7.5c**). | Abyssal plan/ Foreland basin | 4120.0 | 403-425 | 57-61 | 55.6 | 1.8-1.9 km/s | Yes | No | $C_1$; $D_1$ |
| **(12)** South Falkland Basin, accretionary prism, BSR zone 1 (**Fig. 7.6a**). | Accretionary prism | 1170 | 356-375 | 70-150 | 34.8 | 1.9-2.0 km/s suggested by well calibration | No | No | $B_1$ |
| **(12)** South Falkland Basin, accretionary prism, BSR zone 2 (**Fig. 7.6b**). | Accretionary prism | 1200 | 310-330 | 45-60 | 39.6 | 1.9-2.0 km/s suggested by well calibration | No | No | $B_1$ |
| **(12)** South Falkland Basin, accretionary prism, BSR zone 3 (**Fig. 7.6c**). | Accretionary prism | 1485 | 330-350 | 45-50 | 42.9 | 1.9-2.0 km/s suggested by well calibration | Yes | No | $B_1$ |
| **(12)** South Falkland Basin, accretionary prism, BSR zone 4 (**Fig. 7.6e**). | Accretionary prism | 1878 | 396-417 | 40-60 | 40.9 | 1.9-2.0 km/s suggested by well calibration | No | No | $D_2$ |
| **(12)** South Falkland Basin, accretionary prism, BSR zone 5 (**Fig. 7.6e**). | Accretionary prism | 1909 | 447-470 | 30-45 | 37.0 | 1.9-2.0 km/s suggested by well calibration | No | No | $D_2$ |
| **(12)** South Falkland Basin, accretionary prism, BSR zone 6 (**Fig. 7.6e**). | Accretionary prism | 1920 | 464-488 | 10-20 | 35.8 | 1.9-2.0 km/s suggested by well calibration | No | No | $D_2$ |
| **(12)** South Falkland Basin, accretionary prism, BSR zone 7 (**Fig. 7.6d**). | Abyssal plan/ Foreland basin | 1945 | 420-470 | 25-30 | 38.3 | 1.8 km/s | No | No | $D_2$ |
| **(12)** South Falkland Basin, frontal anticline line 105, backlimb (b) and forelimb (f) (**Fig. 7.7a**). | Frontal anticline | 735 (b)<br>983 (f) | 223<br>278 | 63<br>76 | 35.2<br>38.5 | 1.77 km/s | No | No | $B_1$ |
| **(12)** South Falkland Basin, frontal anticline, line 4067 (**Fig. 7.7b**). | Frontal anticline | 1585 | 419 | 157 | 36.8 | 1.77 km/s | No | No | $B_1$ |
| **(12)** South Falkland Basin, foreland basin, line 4077 (**Fig. 7.7c**). | Abyssal plan/ Foreland basin | 1245 | 203-255 | 85-297 | 59.6 | 1.77 km/s | Yes | Yes | $A_1$; $B_1$; $C_1$ |
| **(12)** South Falkland Basin, foreland basin, line 4081 (**Fig. 7.7d**). | Abyssal plan/ Foreland basin | 1090 | 205 | 185 | 54.1 | 1.77 km/s | Yes | Yes | $A_1$; $B_1$; $C_1$ |
| **(12)** South Falkland Basin, foreland basin line 4081 (**Fig. 7.7d**). | Abyssal plan/ Foreland basin | 1090 | 230 | 160-205 | 49.1 | 1.77 km/s | Yes | Yes | $A_1$; $B_1$; $C_1$ |
| **(13)** Hikurangi margin, Pegasus Basin, line PEG04, anticline W (**Fig. 7.8a**). | Accretionary prism | 2350 | 580 | 152 | 33.1 | 1.7 km/s | No | No | $B_1$ |
| **(13)** Hikurangi margin, Pegasus Basin, line PEG04, anticline E (**Fig. 7.8a**). | Accretionary prism | 2520 | 578 | 65 | 34.4 | 1.7 km/s | No | No | $B_1$ |
| **(13)** Hikurangi margin, Pegasus Basin, line PEG05, anticline N (**Fig. 7.8b**). | Accretionary prism | 840 | 164 | 240 | 39.8 | 1.7 km/s | No | Yes | $A_1$; $B_1$ |
| **(13)** Hikurangi margin, accretionary prism, West Uruti Ridge, Crutchley *et al.* (2015), *Fig. 7.* | Accretionary prism | 1090 | 400 | 270 | 28.1 | Velocity analysis | No | Yes | $A_1$; $B_1$ |
| **(13)** Hikurangi margin, accretionary prism, East Uruti Ridge, Crutchley *et al.* (2015), *Fig. 8* (**Fig. 7.10e**) | Accretionary prism | 1390 | 520 | 450 | 27.4 | Velocity analysis | Yes | Yes | $A_1$; $B_1$ |
| **(13)** Hikurangi margin, accretionary prism, line BR05-002, Fohrmann and Pecher (2012), *Figs. 3, 8.* | Accretionary prism | 1680 | 580 | 80-100 | 28.1 | Velocity analysis | No | No | $B_1$ |
| **(13)** Hikurangi margin, accretionary prism, Opouawe Bank, Koch *et al.* (2016), *Figs. 2, 3.* | Accretionary prism | 1090 | 360 | 90-180 | 30.5 | Velocity analysis | Yes | Yes | $A_1$ |
| **(13)** Hikurangi margin, Pegasus Basin, line PEG02, chimney site (**Fig.7.8c**). | Frontal anticline | 1955 | 548 | 130-170 | 31.9 | 1.7 km/s | No | Yes | $A_1$ |
| **(13)** Hikurangi margin, Pegasus Basin, line PEG02, EARs site (**Fig. 7.8d**). | Frontal anticline | 2160 | 550 | 263 | 33.5 | 1.7 km/s | No | No | $B_1$ |
| **(13)** Hikurangi margin, Pegasus Basin, line PEG09, frontal anticline, (**Fig. 7.8e**). | Frontal anticline | 1850 | 410 | 130 | 40.4 | 1.7 km/s | Yes | No | $A_2$ |
| **(13)** Hikurangi margin, Pegasus Basin, line PEG06, cluster of sub-horizontal enhanced reflections (**Fig. 7.8f**). | Abyssal plan/ Foreland basin | 2768 | 677 | 105-365 | 30.9 | 1.7 km/s | No | No | $A_2$ |
| **(13)** Hikurangi margin, Pegasus Basin, line PEG06, Hikurangi channel (**Fig. 7.8g**). | Abyssal plan/ Foreland basin | 2513 | 589 | 112 | 33.7 | 1.7 km/s | No | No | $B_2$ |
| **(14)** Crest and backlimb of the Umitaka Spur, Joetsu Basin, Freire *et al.* (2011), *Figs. 5,6.* | Accretionary prism | 960 | 130 | 50 at the backlimb, uncertain at the crest | 98.5 | Assumed 1.4 km/s based on calibration with well-logs. | Yes | Yes | $A_1$; $B_1$ |

| | | | | | | | | | |
|---|---|---|---|---|---|---|---|---|---|
| **(15)** NW Borneo Through, offshore Sabah, fold and thrust belt, crest of the GKL Dome (**Fig. 7.9a**). | Fold and thrust belt (gravity and far-field tectonics) | 950 | 150-155 | 100-120 (minimum) | 63 | Seismic data calibrated with well-logs | Yes | Yes | $A_1$ |
| **(15)** NW Borneo Through, offshore Sabah, fold and thrust belt, crest of the Kikeh structure (**Fig. 7.9b**). | Fold and thrust belt (gravity and far-field tectonics) | 1345 | 230-240 | 80-90 (minimum) | 63.8 | Assumed 1.6 km/s based on Gumusut-Kakap well-logs | Yes | Yes | $A_1$ |
| **(15)** NW Borneo Through, offshore Sabah, fold and thrust belt, backlimb of the Petai structure, 2 measurements along different horizons (**Fig. 7.9c, d**). | Fold and thrust belt (gravity and far-field tectonics) | 1300<br>1300 | 220-230<br>215-225 | 130-140<br>180-250 | 62.7<br>63.1 | Assumed 1.6 km/s based on Gumusut-Kakap well-logs | No | Yes | $A_1$; $B_1$ |
| **(15)** NW Borneo, Trough, offshore Brunei, anticline VII, Laird and Morley (2011), *Figs. 2, 8.* | Fold and thrust belt (gravity and far-field tectonics) | 2060 | 215-265 | 250 | 64 | 1.55-1.85 km/s | Yes | Yes | $A_1$; $B_1$ |
| **(16)** Offshore Nigeria, Niger Delta front, Hovland *et al.* (1997), *Fig. 3.* | Fold and thrust belt (gravity and shale tectonics | 1315-1320 | 320-330 | 50 av. (110-115 max.) | 44.5 | Assumed 1.7 km/s | unlikely | Yes | $A_1$; $B_1$ |
| **(16)** Offshore Nigeria, eastern Niger Delta, shale-cored anticline, Sultan *et al.* (2011), *Fig. 8.* (**Fig. 7.11a**) | Fold and thrust belt (gravity and shale tectonics | 732.5 | 75-80 | 70 | 62.6 | Assumed 1.5 km/s | Yes | Yes | $A_1$; $B_1$ |
| **(17)** Krishna-Godavari Basin, near site NGHP-01-10, e.g. Dewangan *et al.* (2011), *Figs. 2, 3.* | Fold and thrust belt (gravity and shale tectonics | 1038 | 160 | 80-100 | 38.1 | Seismic data calibrated with well-logs | Yes | Yes | $A_1$ |
| **(17)** Krishna-Godavari Basin, near site NGHP-01-11, Kumar *et al.* (2014), *Fig. 20.* | Fold and thrust belt (gravity and shale tectonics | 1026 | 150 | 100-150 | 45 | Seismic data calibrated with well-logs | No | No | $B_1$ |
| **(18)** Blake Ridge crest, sites 995 and 997, e.g. Holbrook *et al.* (1996), *Fig. 2.* (**Fig. 7.11b**). | Passive margin with salt tectonics | 2778 (995)<br>2770 (997) | 440 (995)<br>464 (997) | 200-250 (29 m interconnected) | 32.7 (995)<br>36.9 (997) | VSP and well-log calibration | Yes | Yes* | $A_2$ |
| **(18)** Blake Ridge Diapir, near site 996, Taylor *et al.* (2000), *Fig. 3.* | Passive margin with salt tectonics | 2181 | 290-300 | 280-300 | 52.5 | Assumed 1.6 km/s | Yes | Yes | $C_1$ |
| **(19)** Offshore Labrador Sea and Scotian Sea, Makkovik, Mosher (2011), *Fig. 3.* | Passive margin with salt tectonics | 825 | 450 | 10-30 | 26.9 | 2.0 km/s, calibrated with OBS velocity data | No | No | $C_2$ |
| **(19)** Offshore Labrador Sea and Scotian Sea, Hamilton Spur, Mosher (2011), *Fig. 4.* | Passive margin with salt tectonics | 1313 | 437.5 | 10-30 | 33.7 | 1.75 km/s, calibrated with OBS velocity data | No | No | $D_2$ |
| **(19)** Offshore Labrador Sea and Scotian Sea, Orphan Spur, Mosher (2011), *Fig. 5.* | Passive margin with salt tectonics | 900 | 251 | 10-30 | 39.0 | 1.75 km/s, calibrated with OBS velocity data | Yes | No | $D_2$ |
| **(19)** Offshore Labrador Sea and Scotian Sea, Sackville Spur, Mosher (2011), *Fig. 6.* | Passive margin with salt tectonics | 1005 | 235 | 60-80 m | 44.5 | 1.75 km/s, calibrated with OBS velocity data | No | No | $B_1$ |
| **(19)** Offshore Labrador Sea and Scotian Sea, Haddock channel, Mosher (2011), *Fig. 7.* | Passive margin with salt tectonics | 1740 | 375 | 30 max. (80-90 m from OBS) | 38.4 | 1.7 km/s, calibrated with OBS velocity data | Yes | No | $D_2$ |
| **(19)** Offshore Labrador Sea and Scotian Sea, Mohican channel, Mosher (2011), *Fig. 10.* | Passive margin with salt tectonics | 1545 | 345 | 55-60 | 38.7 | 1.6 km/s, calibrated with OBS velocity data | Yes | Yes | $A_1$ |
| **(19)** Offshore Labrador Sea and Scotian Sea, Barrington, Mosher (2011), *Fig. 11.* | Passive margin with salt tectonics | 2475 | 378 | 10-30 | 44.2 | 1.6 km/s, calibrated with OBS velocity data | No | No | $D_2$ |
| **(20)** Walker Ridge, Terrebonne Basin, Gulf of Mexico, *Blue (B), Orange (O)* and *Green (G)* units, Boswell *et al.* (2012b), *Figs. 2, 5, 7, 9, 10* (**Fig. 7.11c**) | Passive margin with salt tectonics | 1910 (*B*)<br>1950 (*O*)<br>1987 (*G*) | 850<br>900<br>949 | 280<br>280<br>230 | 17.9<br>18.5<br>19.2 | Seismic data calibrated with well-logs | No | No | $B_1$ |
| **(21)** Green Canyon, Gulf of Mexico, near site GC955-Q, Zhang *et al.* (2012), *Figs. 2, 13.* | Passive margin with salt tectonics | 1975-2025 | 450-460 | 70-100 | 33.8 | Seismic data calibrated with well-logs | Yes | Yes | $A_1$; $B_2$ |
| **(22)** Lower Congo Basin, Southern Seep site (backlimb (b), crest (c) and forelimb (f)), Wenau *et al.* (2015), *Fig. 3.* | Passive margin with salt tectonics | 2663 (b)<br>2625 (c)<br>2795 (f) | 375<br>323<br>200 | 70<br>130<br>100 | 49.2 56.3<br>92.1 | Assumed 1.5 km/s | Yes | Yes | $A_1$; $B_1$ |
| **(22)** Lower Congo Basin, Northern Seep site (backlimb, crest and forelimb), Wenau *et al.* (2015), *Fig. 4* (**Fig. 7.11d**). | Passive margin with salt tectonics | 2738 (b)<br>2700 (c)<br>2869 (f) | 292<br>292<br>217 | 95<br>140<br>95 | 63.3<br>62.9<br>86.2 | Assumed 1.5 km/s | Yes | Yes | $A_1$; $B_1$ |
| **(22)** Lower Congo Basin, Zaire Canyon, area 6, Gay *et al.* (2007), *Figs. 4, 11.* | Passive margin with salt tectonics | 1400 | 175-198 | 62-71 | 63.7 | Assumed to vary between 1.5 and 1.7 km/s | Yes | Yes | $A_1$; $B_2$ |
| **(22)** Lower Congo Basin, Zaire Canyon, area 8, Gay *et al.* (2007), *Figs. 4, 13.* | Passive margin with salt tectonics | 1650 | 262-297 | 119-135 | 50.6 | Assumed to vary between 1.5 and 1.7 km/s | Yes | Yes | $A_1$ |
| **(22)** Lower Congo Basin, Zaire Canyon, Andresen and Huuse (2011), *Fig. 9* (**Fig. 7.11e**) | Passive margin with salt tectonics | 1400-1420 | 210-215 | 140-145 | 57.0 | Assumed 1.55 | Yes | Yes | $A_1$ |
| **(23)** Kwanza Basin, Offshore Angola, BSR 5, Serié *et al.* (2016), *Fig. 10.* | Passive margin with salt tectonics | ~1300 | 285-290 | 180 | 40.8 | Assumed 1.8 km/s | No | No | $C_2$ |

| | | | | | | | | | |
|---|---|---|---|---|---|---|---|---|---|
| **(23)** Kwanza Basin, Offshore Angola, BSR 6, Serié *et al.* (2016), *Fig.10.* | Passive margin with salt tectonics | ~1300 | 90 | 15 | 118.2 | Assumed 1.7 km/s | Yes | Yes | $D_1$ |
| **(23)** Kwanza Basin, Offshore Angola, BSR 13, Serié *et al.* (2016), *Fig. 10.* | Passive margin with salt tectonics | ~1100 | 100 | 20 | 88.5 | Assumed 1.7 km/s | Yes | No | $D_1$ |
| **(23)** Kwanza Basin, Offshore Angola, BSR 14, Serié *et al.* (2016), *Fig. 10.* | Passive margin with salt tectonics | ~1100 | 230 | 115-120 | 42.4 | Assumed 1.8 km/s | No | No | $B_1$ |
| **(23)** Kwanza Basin, Offshore Angola, BSR 15, Serié *et al.* (2016), *Fig. 10.* | Passive margin with salt tectonics | ~1300 | 102 | 10-15 | 104.8 | Assumed 1.7 km/s | Yes | Yes | $D_1$ |
| **(23)** Kwanza Basin, Offshore Angola, BSR 16, Serié *et al.* (2012), *Fig. 3* (**Fig. 7.11f**). | Passive margin with salt tectonics | ~950 | 70 | 25-30 | 107.8 | Assumed 1.7 km/s | Yes | Yes | $D_1$ |
| **24)** Crest of the anticline near site NGHP-01-17, e.g. Kumar *et al.* (2014), *Fig. 44.* $\boldsymbol{Th_{FGZ}}$ from Shankar and Riedel (2013). | Backarc Basin | 1344 | 608 | 100 max. | 20 | Assumed 1.6 km/s based on calibration with well-logs. | No | No | $B_1$ |
| **(25)** Slope of the western margin of the Ulleung Basin, Yoo *et al.* (2013), *Fig. 5* (**Fig. 7.12a**). | Backarc Basin | 1450 | 180-190 | 170-180 max | 85.4 | Assumed 1.6 km/s based on calibration with well-logs. | No | No | $C_2$ |
| **(25)** Basinal flat area of the Ulleung Basin, Horozal *et al.* (2009), *Fig. 4.* | Backarc Basin | 2188 | 160 | 60-65 m max | 117.1 | Assumed 1.6 km/s based on calibration with well-logs. | Yes | Yes | $A_1$; $B_2$ |
| **(25)** Basinal flat area of the Ulleung Basin, Kim *et al.* (2013a), *Fig. 4.* | Backarc Basin | 2158 | 154 | 45 | 120.8 | Assumed 1.6 km/s based on calibration with well-logs. | Yes | Yes | $A_1$; $B_2$ |
| **(26)** Black Sea, Danube Fan, Popescu *et al.* (2006), *Fig. 2.* | Backarc Basin | 1380 | 320-360 | 230-360 | 26.5 | Assumed comprised between 1.6 and 1.8 km/s. | No | No | $B_2$ |
| **(26)** Black Sea, near Dnepr Canyon, Zillmer *et al.* (2005), *Fig. 3.* | Backarc Basin | 1135-1185 | 205-270 | 100-150 | 27-30 | Depth converted OBS data. | No | No | $B_2$ |
| **(27)** Sea of Okhotsk, northern Sakhalin continental margin, profile 8 (INESSA), Lüdmann and Wong (2003), *Fig. 3.* | Backarc Basin | 565 | 105-110 | 60-65 | 59.1 | Assumed 1.7 km/s | Yes | Yes | $A_1$; $C_2$ |
| **(28)** Baikal Lake, South Basin, line GAHY017, 2 measurements, Vanneste *et al.* (2001), *Fig. 4.* | Young rifted basin | 1515<br>1510 | 265-280<br>255-270 | 75-85<br>40-45 | 55.0<br>57.0 | Assumed to vary between 1.7 and 1.8 km/s | No | No | $B_1$ |
| **(28)** Baikal Lake, South Basin, near Malenki mud volcano, Van Rensbergen *et al.* (2002), *Fig. 4*; Vanneste *et al.* (2003), *Fig. 5* (**Fig. 7.12b**). | Young rifted basin | 1315 | 182-193 | 76-81 | 76.2 | Assumed to vary between 1.7 and 1.8 km/s | Yes | Yes | $C_1$ |
| **(29)** Barents Sea, Hammerfest basin, Ostanin *et al.* (2013), *Fig. 9.* | Epicontinental extensional basin | 320 | 300 | 120-130 | 31 | Inferred 2.0 km/s | Yes | Yes | $A_1$; $B_1$ |
| **(29)** Barents Sea, near Loppa High, Vadakkepuliyambatta *et al.* (2015), *Fig. 3.* | Epicontinental extensional basin | 320 | 150 | 120-130 | 35 | Extrapolated velocity function | Yes | Yes | $A_1$ |
| **(30**) Norway margin, near Storegga Slide, OBS JM517, 523 and 524, Bünz *et al.* (2005), *Figs. 2, 10* (**Fig. 7.12c**). | Old rifted passive margin (with later compression) | 919 (JM524)<br>921 (JM523)<br>945 (JM517) | 280 | 80 av. (90 max) | 50.7<br>50.7<br>51.3 | Velocity inversion | Yes | Yes | $A_1$; $C_2$ |
| **(30**) Norway margin, near Storegga Slide, Plaza-Faverola *et al.* (2012), *Fig. 2.* | Old rifted passive margin (with later compression) | 730 | 245 | 80 | 50.4 | Tomographic analysis | Yes | Yes | $A_1$ |
| **(31)** Western side of the Vestnesa Ridge, Petersen *et al.* (2010), *Fig. 7.* | Old rifted passive margin | 1291 | 160-170 | 35 | 98.8 | Calibration from OBS data | Yes | Yes | $A_1$ |
| **(31)** Eastern side of the Vestnesa Ridge, Smith *et al.* (2014), *Fig. 3*; Plaza-Faverola *et al.* (2015), *Fig. 3.* | Old rifted passive margin | 1200 | 162 | 60-100 | 97.5 | Assumed 1.62 km/s | Yes | Yes | $A_1$ |
| **(32)** Offshore Mauritania, amplitude anomalies B and E, Davies and Clarke (2010), *Fig. 4.* | Old rifted passive margin | 905 (B)<br>1400 (E) | 220 (B)<br>270 (E) | 310-320<br>125-130 | 30.5<br>34.8 | Assumed 1.7 km/s | No | Yes | $A_1$; $C_2$ |
| **(32)** Offshore Mauritania, base of failure anomaly, Li *et al.* (2016), *Fig. 7.* | Old rifted passive margin | 1100 | 220-230 | 263 | 33.3 | Assumed 1.8 km/s | No | No | $C_2$ |
| **(33)** Offshore Cameroon, Low gradient slope, Le *et al.* (2015), *Fig. 4.* | Old rifted passive margin | 1550 | 220 | 120 max. | 55.9 | Assumed 1.8 km/s | No | No | $B_2$ |
| **(34)** Offshore Namibia, pipe 7, see Moss (2010). | Old rifted passive margin | 1004 | 268 | 108 | 36.2 | Assumed 1.6 km/s | Yes | Yes | $A_1$ |
| **(34)** Offshore Namibia, pipe 10, see Moss (2010). | Old rifted passive margin | 1030 | 261 | 107 | 37.5 | Assumed 1.6 km/s | Yes | Yes | $A_1$ |
| **(34)** Offshore Namibia hydrate cross-section 7, see Moss (2010). | Old rifted passive margin | 959 | 257 | 172 | 36.1 | Assumed 1.6 km/s | Yes | Yes | $A_1$ |
| **(34)** Offshore Namibia hydrate cross-section 10, see Moss (2010) (**Fig. 7.12d**). | Old rifted passive margin | 1307 | 210 | 73 | 52.9 | Assumed 1.6 km/s | Yes | Yes | $A_1$; $B_1$ |

| | | | | | | | | | |
|---|---|---|---|---|---|---|---|---|---|
| **(35)** Mahanadi Basin, near site NGHP-01-08, Shankar and Riedel (2014), *Fig. 4.* | Old rifted passive margin | 1675 | 257 | 50-140 | 50.6 | Assumed 1.6 km/s based on calibration with well-logs. | No | No | $B_2$ |
| **(35)** Mahanadi Basin, near site NGHP-01-09, Shankar and Riedel (2014), *Fig. 5.* | Old rifted passive margin | 2025 | 290 | 50-140 | 50.3 | Assumed 1.6 km/s based on calibration with well-logs. | Yes | No | $A_2$; $B_2$ |
| **(35)** Mahanadi Basin, near site NGHP-01-18, Kumar *et al.* (2014), *Fig. 38.* | Old rifted passive margin | 1374 | 210 | 70-180 | 50.2 | Assumed 1.6 km/s based on calibration with well-logs. | Yes | Yes | $A_1$; $B_2$ |
| **(35)** Mahanadi Basin, near site NGHP-01-19, Kumar *et al.* (2014), *Fig. 40* (**Fig. 7.12e**). | Old rifted passive margin | 1425 | 205 | 100-120 | 52 | Assumed 1.6 km/s based on calibration with well-logs. | No | No | $B_2$ |
| **(36)** Pearl River Mouth Basin, Shenhu area, near site SH2, Qian *et al.* (2014), *Figs. 1, 10.* | Old rifted passive margin | 1140 | 195 | 105-140 | 46.8 | Assumed 1.6 km/s based on calibration with well-logs. | No | No | $B_2$ |
| **(36)** Pearl River Mouth Basin, Shenhu area, near site SH4, Wang *et al.* (2014), *Figs. 11, 12* (**Fig. 7.12f**). | Old rifted passive margin | 1289 | 175 | 95 | 56.1 | Assumed 1.6 km/s based on calibration with well-logs. | No | No | $A_2$; $B_2$ |
| **(36)** Pearl River Mouth Basin, Shenhu area, near site SH7, Wang *et al.* (2014), *Figs. 11, 12.* | Old rifted passive margin | 1065 | 190 | 150-155 | 40.1 | Assumed 1.6 km/s based on calibration with well-logs. | No | No | $A_2$; $B_2$ |
| **(36)** Pearl River Mouth Basin, Shenhu area, Site 5, Sha *et al.* (2015), *Fig. 4.* | Old rifted passive margin | 1127 | 200 | 70-120 | 51.7 | Assumed 1.6 km/s based on calibration with well-logs. | No | No | $B_2$ |
| **(36**) Pearl River Mouth Basin, Shenhu area, Site 16, Sha *et al.* (2015), *Fig. 6.* | Old rifted passive margin | 871 | 200 | 100-320 | 38.4 | Assumed 1.6 km/s based on calibration with well-logs. | No | Yes | $A_1$; $B_2$ |
| **(36)** Pearl River Mouth Basin, Shenhu area, site 8, Sha *et al.* (2015), *Fig. 8.* | Old rifted passive margin | 805 | 118 | 70 | 50.6 | Assumed 1.6 km/s based on calibration with well-logs. | Yes | Yes | $A_1$; $B_2$ |
| **(37)** Beaufort Sea, seismic line 769, Andreassen *et al.* (1995), *Fig. 2.* | Old rifted passive margin | 1500 | 435-505 | 11-16** | 35.6-40.7 | Assumed 2.15 km/s from AVO analysis | No | No | $D_2$ |

**Table 7.3.** Detailed dataset used for this study. This table includes information on the reference to the figures in the literature database (*italic*), the geological setting, the water depth, the range of values for $\boldsymbol{D_{BSR}}$, $\boldsymbol{Th_{FGZ}}$, ***GTG***, the methods used to accomplish the measurements of $\boldsymbol{D_{BSR}}$ and $\boldsymbol{Th_{FGZ}}$, the presence of faults and deformable pathways (Def. paths, i.e. cross-stratal fluid-escape conduits such as pipe-like features), and the classification of FGZs (**sub-paragraph 7.5.4**). The numbers **1-37**, in brackets before each location, relate to those used in **Figs. 7.13, 7.15** and in **Tab. 7.1**. *= at Blake Ridge there is evidence of pipe-like features (Gorman *et al.*, 2002). However, the termini of these pipes do not pierce the present-day seafloor, suggesting a fossil system and reduced fluxes at present-day. **= at this site in the Beaufort Sea, the FGZ could be up to 50 m thick if ***Sg*** gradually decreases with depth from the BSR. Where the temperature at the seafloor (*Tsf*) is specified in the table, it has been assumed considering the water depth, the latitude and the *Tsf* in nearby gas hydrate provinces.

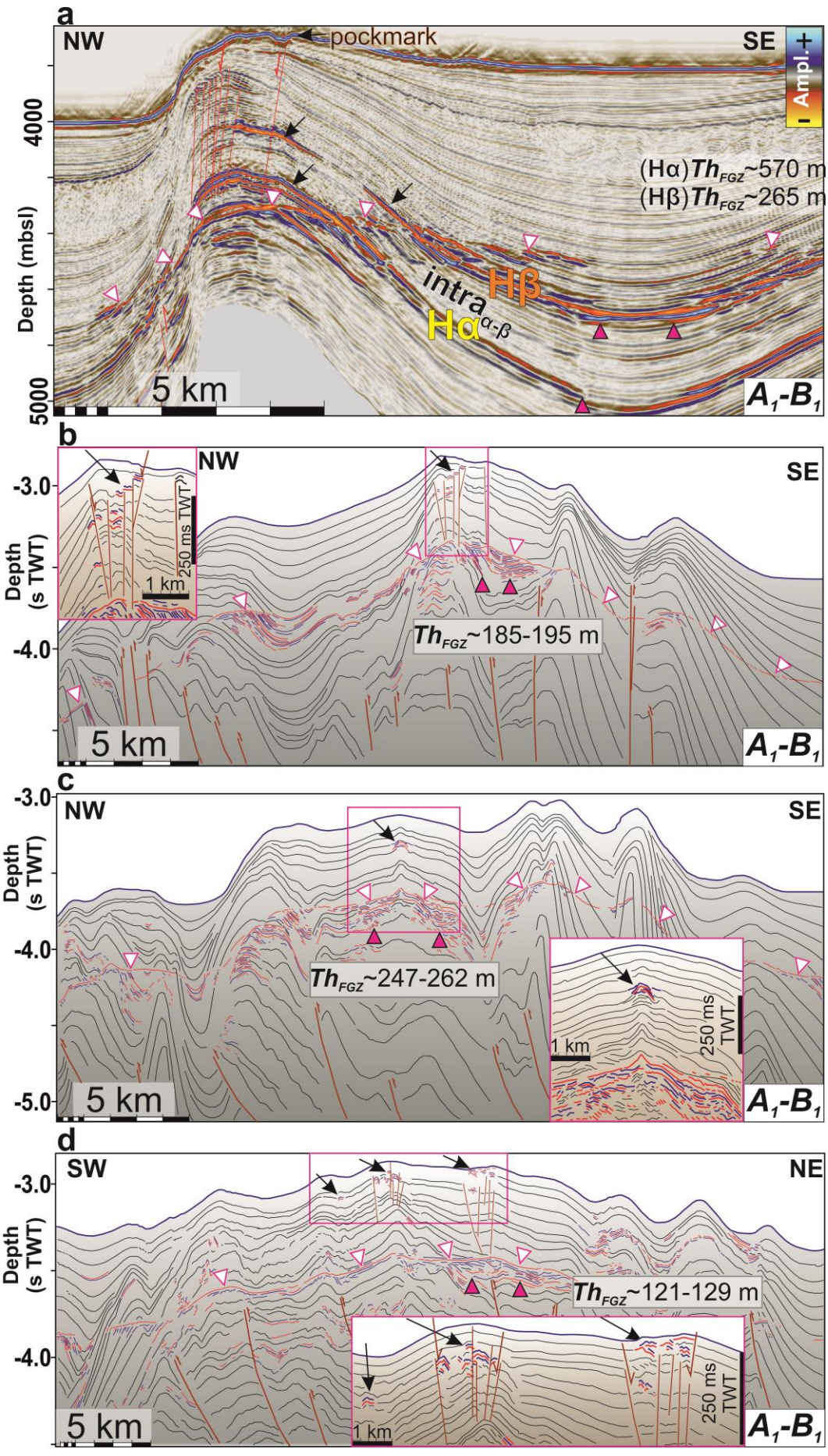

a
NW
pockmark
SE
+ Ampl. -
4000
5000
Depth (mbsl)
(Hα)Th_FGZ~570 m
(Hβ)Th_FGZ~265 m
intra α-β
Hβ
Hα
5 km
A1-B1
b
NW
SE
-3.0
-4.0
Depth (s TWT)
250 ms TWT
1 km
Th_FGZ~185-195 m
5 km
A1-B1
c
NW
SE
-3.0
-4.0
-5.0
Depth (s TWT)
Th_FGZ~247-262 m
1 km
250 ms TWT
5 km
A1-B1
d
SW
NE
-3.0
-4.0
Depth (s TWT)
Th_FGZ~121-129 m
1 km
250 ms TWT
5 km
A1-B1

**Fig. 7.4a-d**

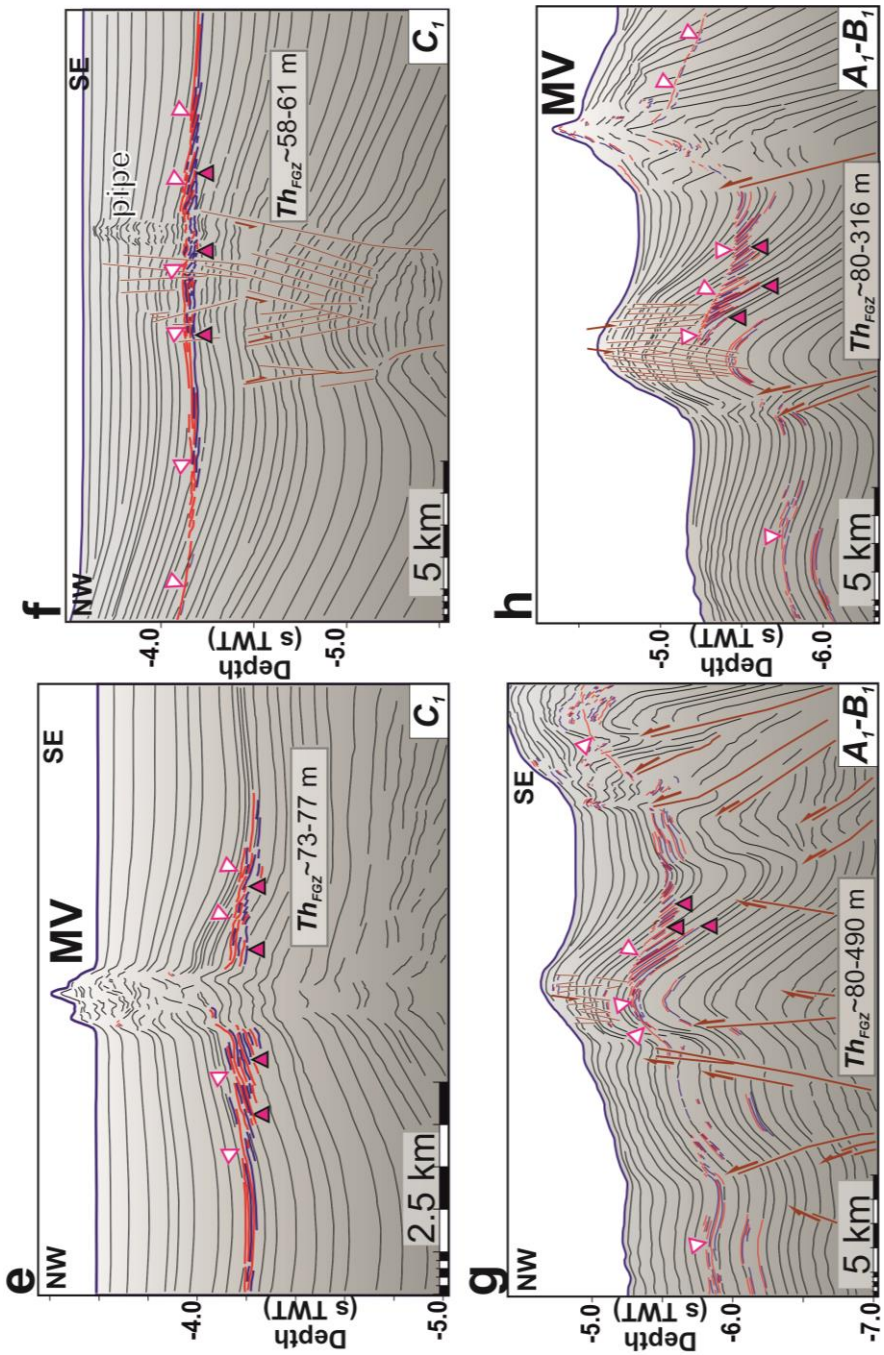



**Figure 7.4 (See the previous page for a-d).** Examples of FGZs in the Guajira Basin. The white triangles indicate the BSR; the purple triangles indicate the bases of the measured FGZs (cf. with **Tab. 7.3**). The letters at the bottom-right of each image indicate the interpreted type of FGZ (see **paragraph 7.5.4**). **(a, g, h)** FGZs along the frontal anticlines of the margin. **(b-d)** FGZs along the accretionary prism. **(e, f)** FGZs in the forearc basin of the margin. The black arrows indicate either seismic evidence of high saturation hydrates along stratigraphic horizons (**a**) or massive outcropping/buried hydrate/authigenic carbonate deposits, formed due to cross-stratal focused fluxes of methane-rich fluids (See the blow-ups in (**b-d**)). MV= mud volcano. Seismic data is 0° Phase (North American polarity convention) in (**a**). The seismic lines in **b-h** have been sketched, and the significant amplitude changes (e.g. the seafloor, the BSR, the EARs in the FGZ) are represented by blue and red lines, mimicking a 0° Phase seismic image.

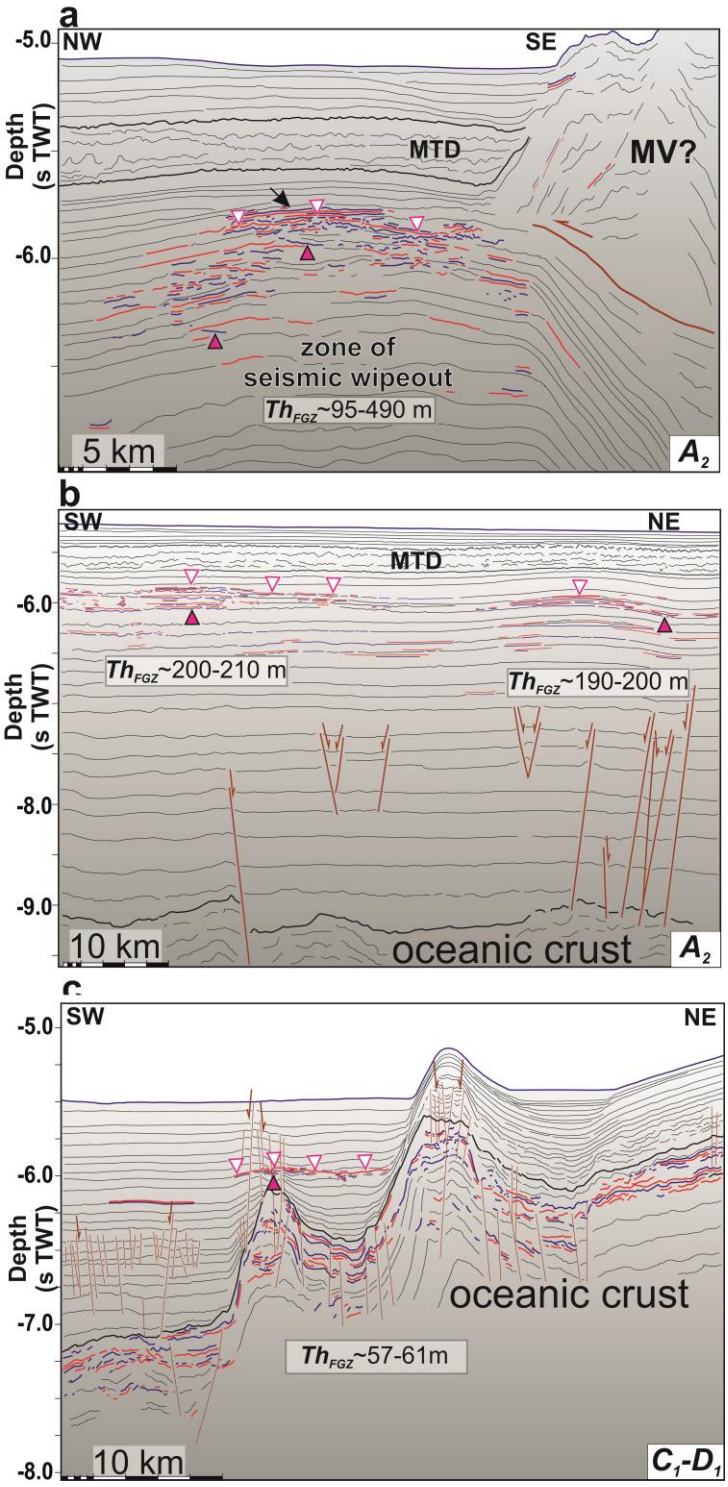



**Figure 7.5.** Examples of FGZs in the Guajira Basin. The white triangles indicate the BSR; the purple triangles indicate the bases of the measured FGZs (cf. with **Tab. 7.3**). The letters at the bottom-right of each image indicate the interpreted type of FGZ (see **paragraph 7.5.4**). The black arrow in **(a)** indicates possible high saturation hydrates just above the BSR. **(a)** FGZs at the crest of a frontal anticline. The base of the FGZ is of difficult interpretation, due to the presence of a ZSW (the two purple triangles show the location of two possible bases of the FGZ, i.e. an upper and a lower end-member). **(b, c)** FGZs along the abyssal plan formed above deep structural highs in the oceanic crust. Note that the BGHSZ does not properly mimic the seafloor, likely owing to the influence of the oceanic crust. The seismic lines have been sketched, and the significant amplitude changes (e.g. the seafloor, the BSR, the EARs in the FGZ, as well as enhanced reflections due to lithology in the oceanic crust) are represented by blue and red lines, mimicking a 0° Phase seismic image. (North American polarity convention).

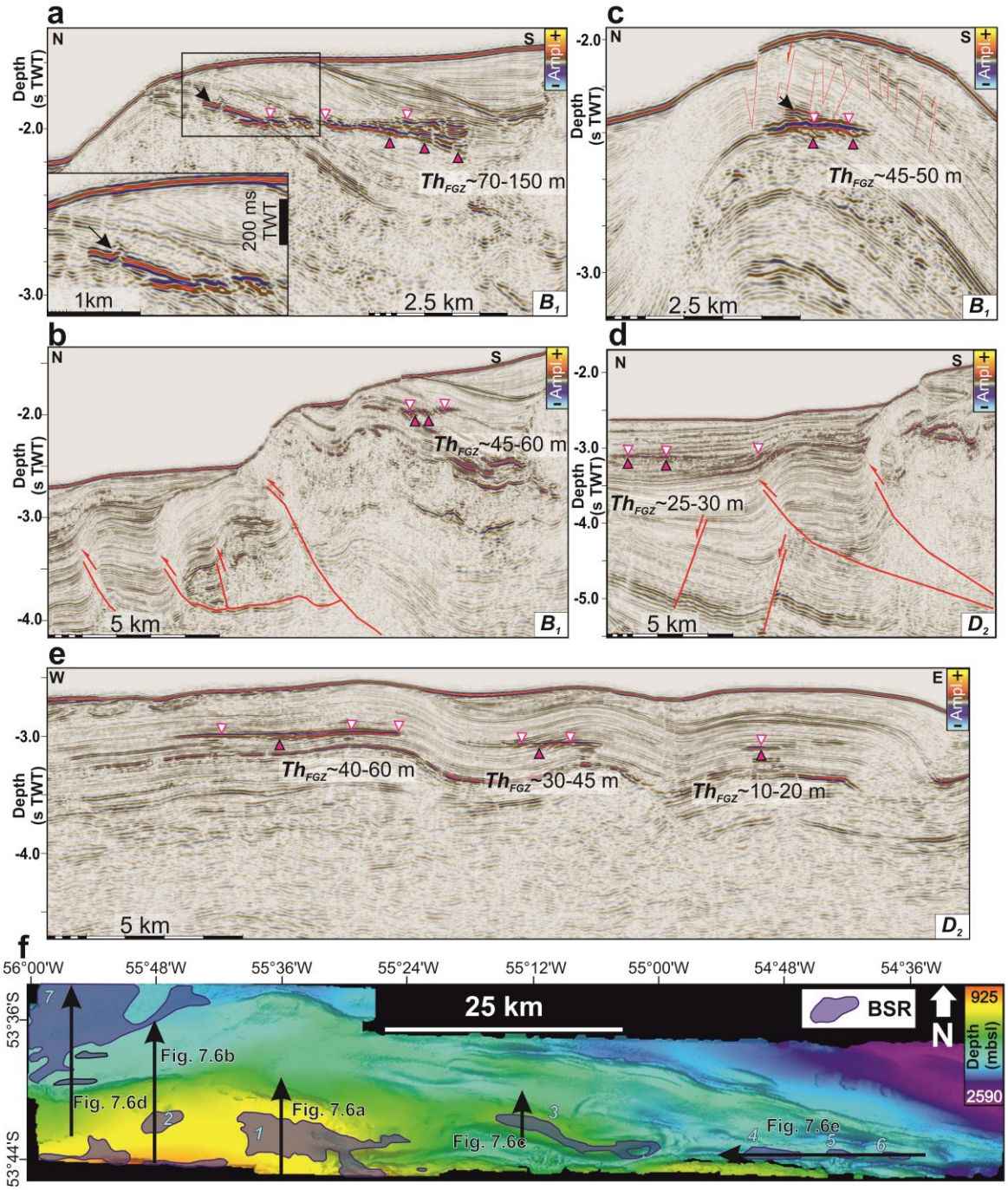



**Figure 7.6.** Examples of FGZs in the South Falkland Basin. The white triangles indicate the BSR; the purple triangles indicate the bases of the measured FGZs (cf. with **Tab. 7.3**). The letters at the bottom-right of each image indicate the interpreted type of FGZ (see **paragraph 7.5.4**).The pale blue numbers (1-7) indicate seven areas of BSR occurrence (named *'BSR zones'* in **Tab. 7.3**), where ***Th*$_{FGZ}$** has been measured. **(a-c, e)** FGZs along the accretionary prism. **(d)** FGZ along the foreland basin within an MTD. The black arrows in **(a)** and **(c)** indicate possible gas hydrate-bearing sediments at high saturation along stratigraphic reflections (See the blow-ups in (**a**)). **(f)** Seafloor map of the study area with location of the seismic sections in **Figs 7.6a-e**. The blue areas indicate the areas of BSR occurrence. Seismic data is 0° Phase (European polarity convention).

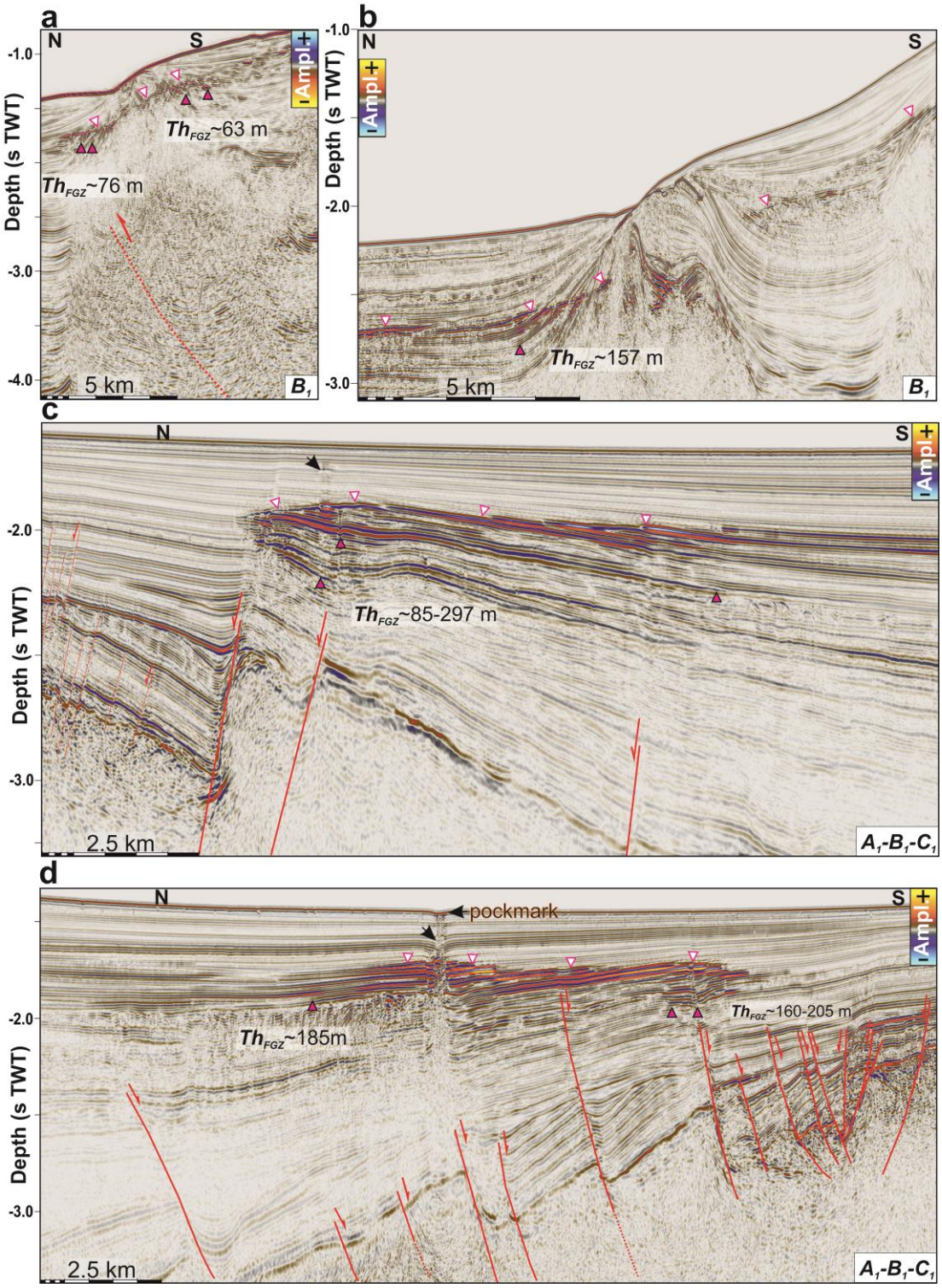



**Figure 7.7.** Examples of FGZs in the South Falkland Basin. The white triangles indicate the BSR; the purple triangles indicate the bases of the measured FGZs (cf. with **Tab. 7.3**). The letters at the bottom-right of each image indicate the interpreted type of FGZ (see **paragraph 7.5.4**). **(a, b)** FGZs at the frontal anticlines of the accretionary prism. **(c, d)** FGZs in the foreland basin. The black arrows indicate vertical fluid flow pathways throughout the GHSZ. Note that the BGHSZ does not mimic the seafloor and could be influenced by the migration of relatively warm fluids along the faults (The seismic images are modified after Foschi, 2014; Foschi and Cartwright, 2016). Seismic data is 0° Phase (North American polarity convention in **(a)** and European polarity convention in **(b-d)**).

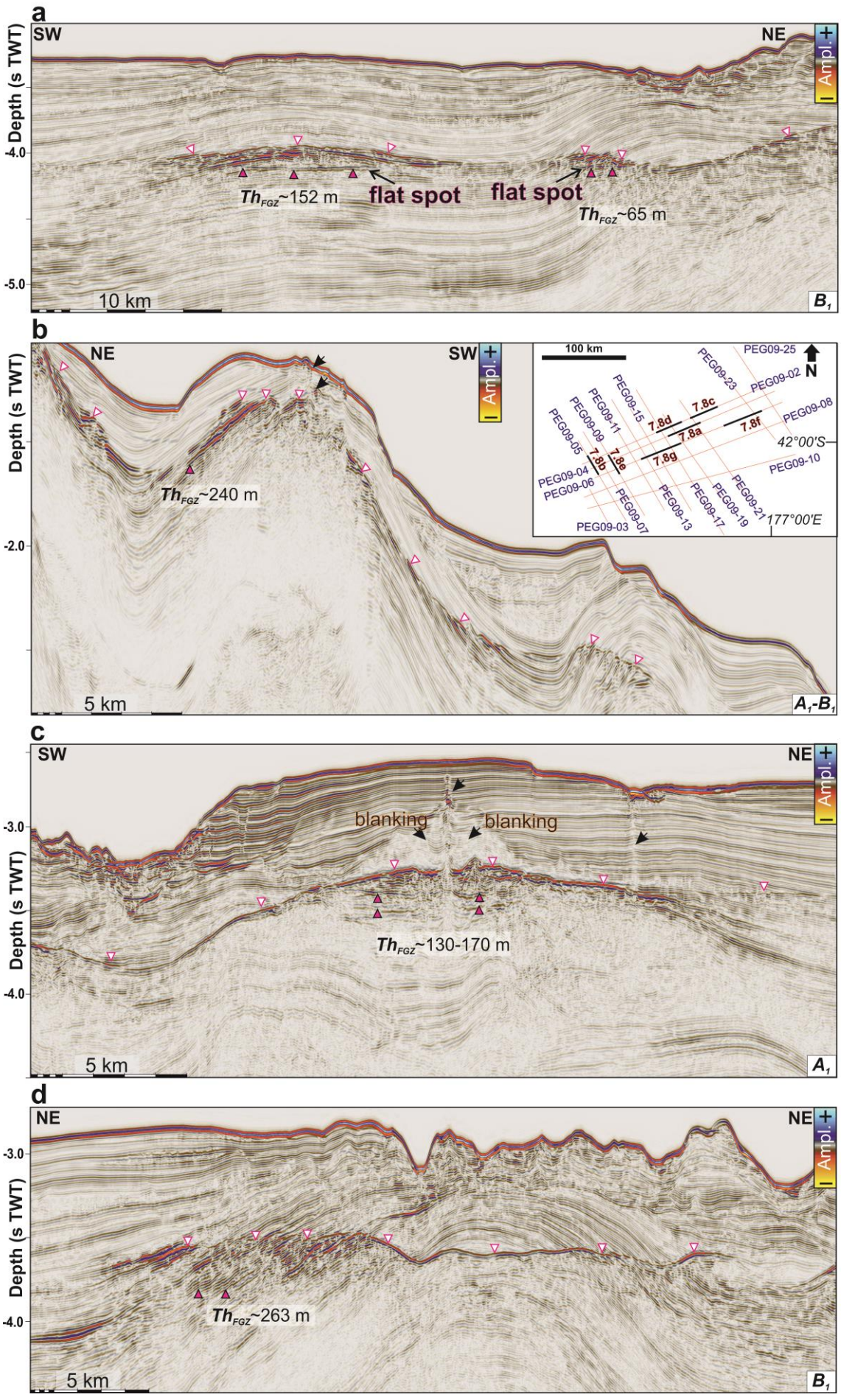

a
SW
NE
Depth (s TWT)
-4.0
-5.0
Ampl.
Th_FGZ~152 m
flat spot
flat spot
Th_FGZ~65 m
10 km
B1
b
NE
SW
Depth (s TWT)
-2.0
Th_FGZ~240 m
5 km
A1-B1
100 km
PEG09-25
PEG09-23
PEG09-02
N
PEG09-15
PEG09-11
PEG09-09
PEG09-05
PEG09-04
PEG09-06
PEG09-03
PEG09-07
PEG09-13
PEG09-17
PEG09-19
PEG09-21
PEG09-08
PEG09-10
7.8a
7.8b
7.8c
7.8d
7.8e
7.8f
7.8g
42°00'S
177°00'E
c
SW
NE
Depth (s TWT)
-3.0
-4.0
blanking
blanking
Th_FGZ~130-170 m
5 km
A1
d
NE
NE
Depth (s TWT)
-3.0
-4.0
Th_FGZ~263 m
5 km
B1

**Fig. 7.8a-d**

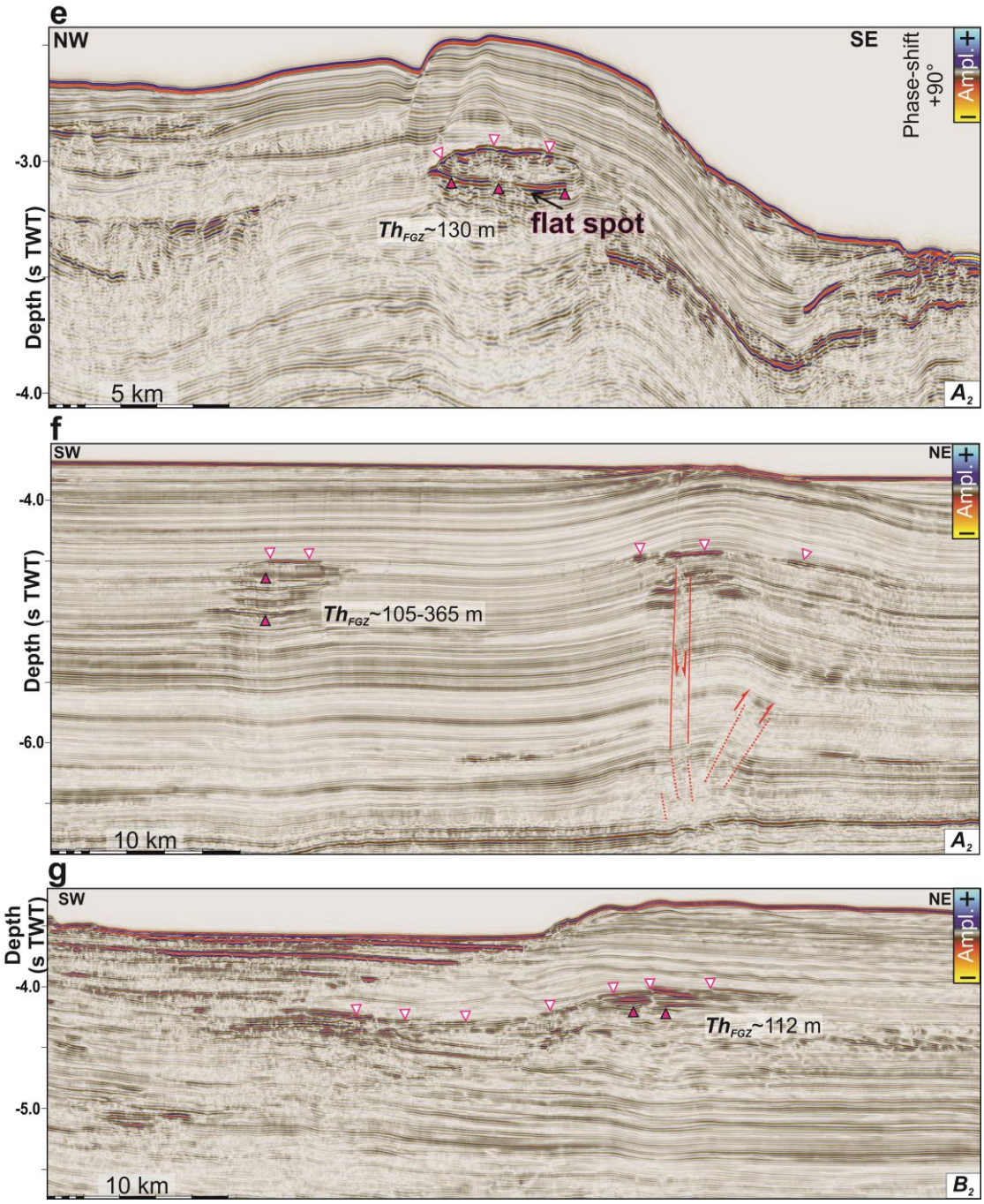



**Figure 7.8 (See the previous page for a-d).** Examples of FGZs from the Pegasus Basin (Hikurangi margin). The white triangles indicate the BSR; the purple triangles indicate the bases of the measured FGZs (cf. with **Tab. 7.3**). The letters at the bottom-right of each image indicate the interpreted type of FGZ (see **paragraph 7.5.4**). (**a, b)** FGZs along the accretionary prism. **(c-e)** FGZs at the frontal anticlines. Note in **(e)** a possible flat spot that indicates the base of the FGZ. **(f, g)** FGZs along the foreland basin. In **(f**), although there is evidence of free gas-bearing sediments for more than ~300 m below the BGHSZ, the existence of a mobile free gas phase is uncertain because the stacked enhanced reflections are horizontal and this geometry, particularly in the presence of low-permeability sediments separating the free gas-bearing units, may preclude an internal connection of the free gas phase. Where not specified, the black arrows indicate vertical fluid flow pathways throughout the GHSZ (**b** and **c**). The inset map in **(b)** indicates the location of the seismic profiles (see also Fraser *et al.*, 2016). Seismic data is 0° Phase (North American polarity convention), except for **(e)**, where seismic data is shifted by 90° (North American polarity convention).

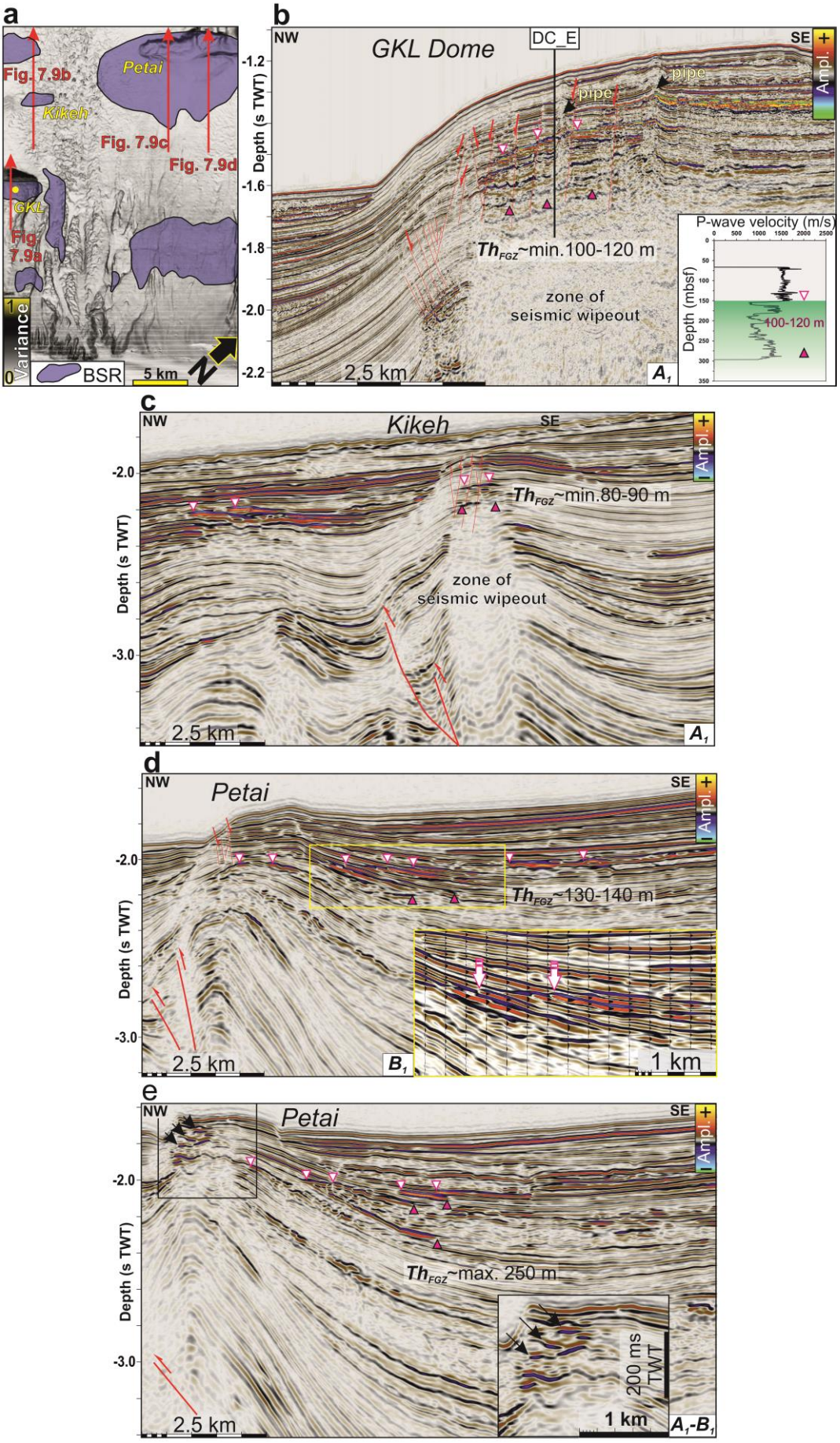

a
Fig. 7.9b
Petai
Kikeh
Fig. 7.9c
Fig. 7.9d
GKL
Fig. 7.9a
Variance
BSR
5 km
b
NW
GKL Dome
DC_E
SE
Ampl.
pipe
pipe
Depth (s TWT)
-1.2
-1.6
-1.8
-2.0
-2.2
Th_FGZ~min.100-120 m
zone of
seismic wipeout
P-wave velocity (m/s)
Depth (mbsf)
100-120 m
2.5 km
A1
c
NW
Kikeh
SE
Ampl.
-2.0
-3.0
Depth (s TWT)
Th_FGZ~min.80-90 m
zone of
seismic wipeout
2.5 km
A1
d
NW
Petai
SE
Ampl.
-2.0
-3.0
Depth (s TWT)
Th_FGZ~130-140 m
2.5 km
B1
1 km
e
NW
Petai
SE
Ampl.
-2.0
-3.0
Depth (s TWT)
Th_FGZ~max. 250 m
200 ms
TWT
2.5 km
1 km
A1-B1

**Fig. 7.9**

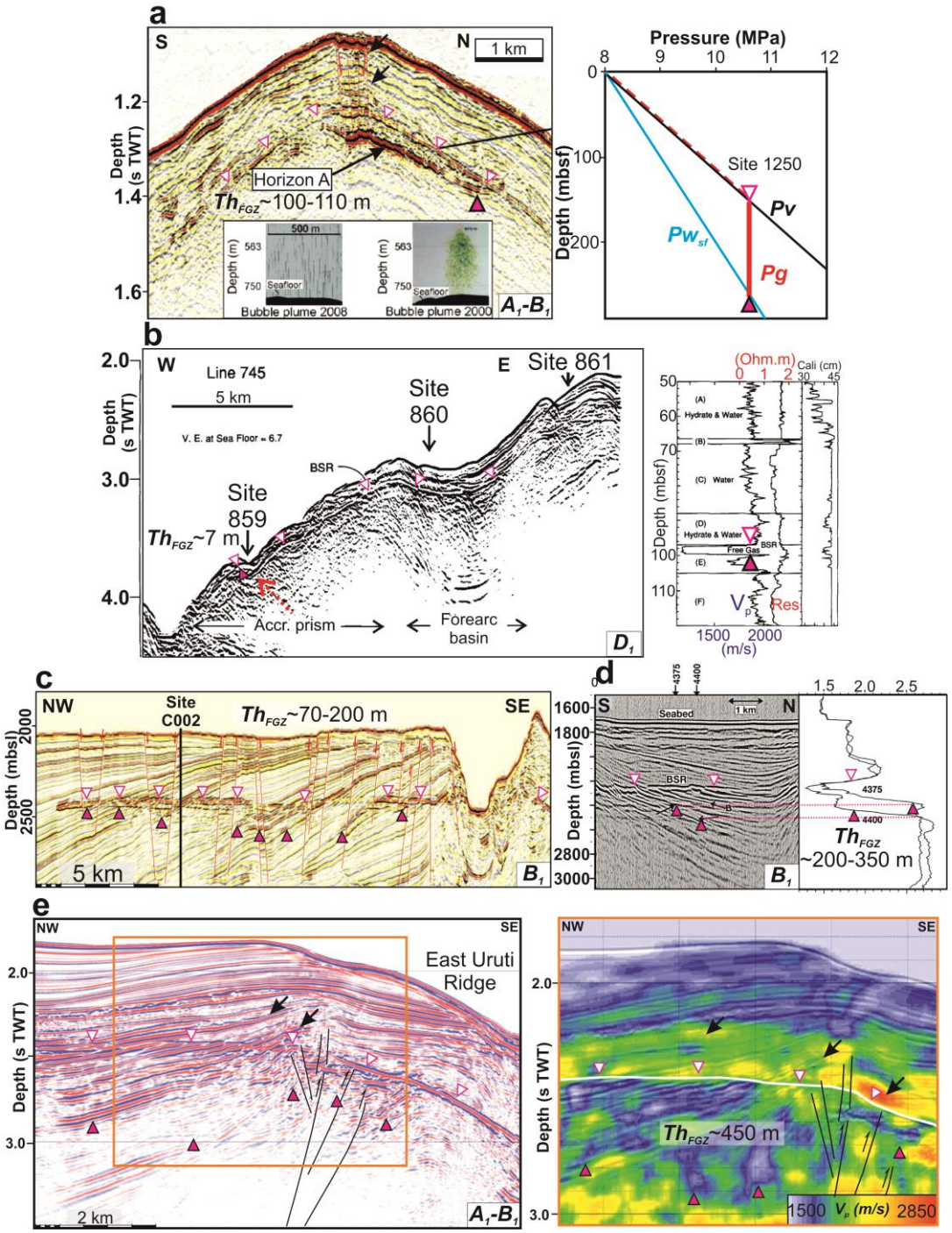

a
S
N
1 km
Depth (s TWT)
1.2
1.4
1.6
Horizon A
Th_FGZ~100-110 m
500 m
Depth (m)
563
750
Seafloor
Bubble plume 2008
Bubble plume 2000
A1-B1
Pressure (MPa)
8
9
10
11
12
0
100
200
Depth (mbsf)
Site 1250
Pv
Pwsf
Pg
b
W
E
Line 745
5 km
V. E. at Sea Floor = 6.7
Site 861
Site 860
Site 859
BSR
Th_FGZ~7 m
Accr. prism
Forearc basin
D1
2.0
3.0
4.0
(Ohm.m)
0 1 2
Cali (cm)
30 45
50
60
70
100
110
(A)
Hydrate & Water
(B)
(C) Water
(D)
Hydrate & Water
Free Gas
BSR
(E)
(F)
Vp
Res
1500 2000
(m/s)
c
NW
SE
Site C002
Th_FGZ~70-200 m
Depth (mbsl)
2000
2500
5 km
B1
d
S
N
Seabed
1 km
BSR
1600
1800
2800
3000
1.5 2.0 2.5
4375
4400
Th_FGZ ~200-350 m
e
NW
SE
East Uruti Ridge
Depth (s TWT)
2.0
3.0
2 km
A1-B1
Th_FGZ~450 m
1500 Vp (m/s) 2850

**Fig. 7.10**

**Figure 7.9 (See page 313).** Examples of FGZs from the fold and thrust belt offshore Sabah (NW Borneo). The white triangles indicate the BSR; the purple triangles indicate the bases of the measured FGZs (cf. with **Tab. 7.3**). The letters at the bottom-right of each image indicate the interpreted type of FGZ (see **paragraph 7.5.4**). **(a)** Variance extraction of the seafloor highlighting the locations of the seismic sections shown in **b-e**. The purple areas indicate the distribution of BSRs. **(b-c)** FGZs at the crest of the Gumusut-Kakap and Kikeh anticlines. Note the presence of EARs beneath the BSR, overlying zones of seismic wipeout. **(d, e)** FGZ at the bakclimb of the Petai anticline. The BSR is scarcely recognised at the crest of the structure. In contrast, it is possible to observe possible accumulations of high saturation hydrates (expressed as an enhanced reflection with positive acoustic impedance contrast) related to crestal normal faults **(e)**. The base of the FGZ is located at different depths along adjacent stratigraphic horizons **(d, e)**. The seismic data in **(b)** is -90° Phase-shifted (North American polarity convention), while is at 0° Phase in **(c-e)** (European polarity convention).

**Figure 7.10 (See the previous page).** Examples of FGZs from different convergent margins. The white triangles indicate the BSR; the purple triangles indicate the bases of the measured FGZs (cf. with **Tab. 7.3**). The letters at the bottom-right of each image indicate the interpreted type of FGZ (see **paragraph 7.5.4**). **(a-left)** Seismic reflection profile from Southern Hydrate Ridge. The black arrows indicate possible fracture/fault-driven fluid escape routes leading to seepage at the seafloor. Note the highly reflective Horizon A (HA), interpreted as the main carrier beds for free gas. The small insets at the bottom of the image highlight the episodicity in seafloor seepage, with an absence of bubble plums in 2008 and the presence of a bubble plume in 2000 (modified after Bangs *et al.*, 2011). **(a-right)** Plot of lithostatic pressure (***Pv***), hydrostatic pressure (***Pw***) and free gas buoyancy pressure (**Pg**, related to Horizon A) at Southern Hydrate Ridge (**a-left**) (Site 1250). Note that the total fluid pressure (***Pg+Pw***) equals ***Pv***, leading to possible free gas migration throughout the GHSZ (modified after Trehu *et al.*, 2004a). **(b)** Regional seismic section (left) and well-log data at site 859 along the Chile Triple Junction. The P=wave velocity log on the right indicates a that the BGHSZ is at ~97 mbsf and the FGZ is only ~7 m thick at this site. This shallow BGHSZ, considering the water depth of 2741 mbsl and the non-linear temperature profile at this site (Brown and Bangs, 1991), suggest an advection of warm fluids from below the FGZ (modified after Bangs *et al.*, 1993). **(c)** Regional seismic reflection profile, passing through site C002 in the Kumano forearc basin, in the Nankai Trough (modified after Bangs *et al.*, 2010). Note the clear base of the FGZ, indicated as a strong amplitude reduction along numerous dipping stratigraphic horizon, cross-cutting a sub-horizontal BSR. The depth of the BSR at site C002 (~360 mbsf) appears shallower than its predicted position owing to capillary effects (Daigle and Dugan, 2014). **(d)** Detailed seismic reflection profile (left) and waveform inversion results (right) from the accretionary prism of the Makran margin (modified after Sain *et al.*, 2000). The FGZ is interpreted to be thicker than 200 m at this site. **(e)** Seismic reflection profile and interval velocities overlaid on seismic reflection data from the East Uruti Ridge (accretionary prism of the Hikurangi margin). The FGZ is interpreted to be ~450 m thick and is associated with dipping stratigraphic horizons, interpreted as potential carrier beds for methane-rich fluids directed towards the GHSZ. The black arrows indicate potential high saturation hydrates along these horizons, interpreted to have a high intrinsic permeability (modified after Crutchley *et al.*, 2015). Seismic data appears at 0° Phase (North American polarity convention), except **(e)** (0° Phase, European polarity convention).

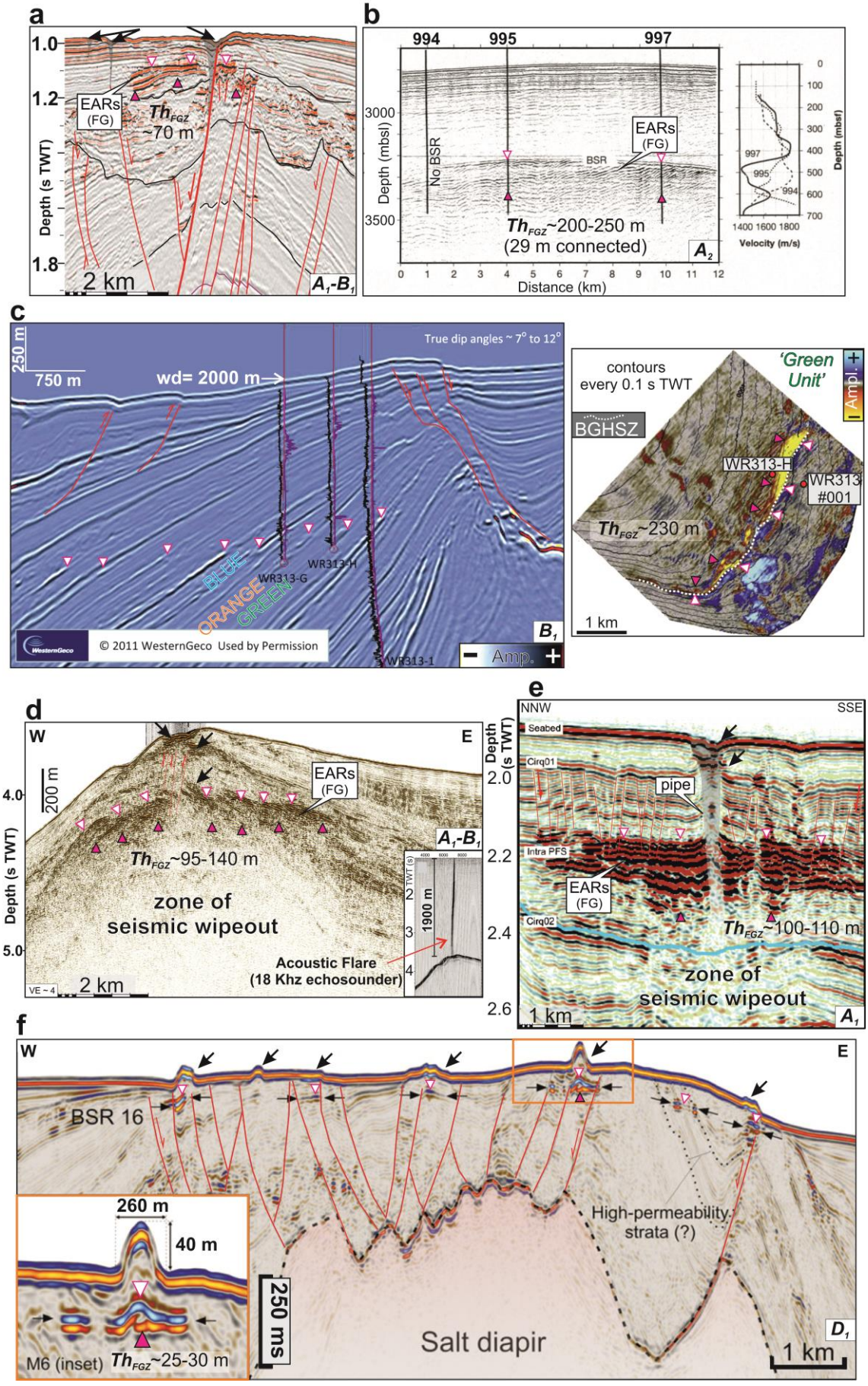

a
1.0
1.2
1.8
Depth (s TWT)
EARs (FG)
Th_FGZ ~70 m
2 km
A1-B1
b
994
995
997
3000
3500
Depth (mbsl)
No BSR
BSR
EARs (FG)
Th_FGZ~200-250 m
(29 m connected)
A2
0 1 2 3 4 5 6 7 8 9 10 11 12
Distance (km)
1400 1600 1800
Velocity (m/s)
Depth (mbsf)
c
250 m
750 m
wd= 2000 m
True dip angles ~ 7° to 12°
BLUE
ORANGE
GREEN
WR313-G
WR313-H
WR313-1
© 2011 WesternGeco Used by Permission
B1
Amp.
contours
every 0.1 s TWT
'Green Unit'
Ampl.
BGHSZ
WR313-H
WR313 #001
Th_FGZ~230 m
1 km
d
W
E
4.0
5.0
Depth (s TWT)
200 m
EARs (FG)
A1-B1
Th_FGZ~95-140 m
zone of
seismic wipeout
Acoustic Flare
(18 Khz echosounder)
1900 m
VE ~ 4
2 km
e
NNW
SSE
Depth (s TWT)
2.0
2.2
2.4
2.6
Seabed
Cirq01
pipe
Intra PFS
EARs (FG)
Cirq02
Th_FGZ~100-110 m
zone of
seismic wipeout
1 km
A1
f
W
E
BSR 16
260 m
40 m
M6 (inset)
Th_FGZ~25-30 m
250 ms
High-permeability
strata (?)
Salt diapir
D1
1 km

**Fig. 7.11**

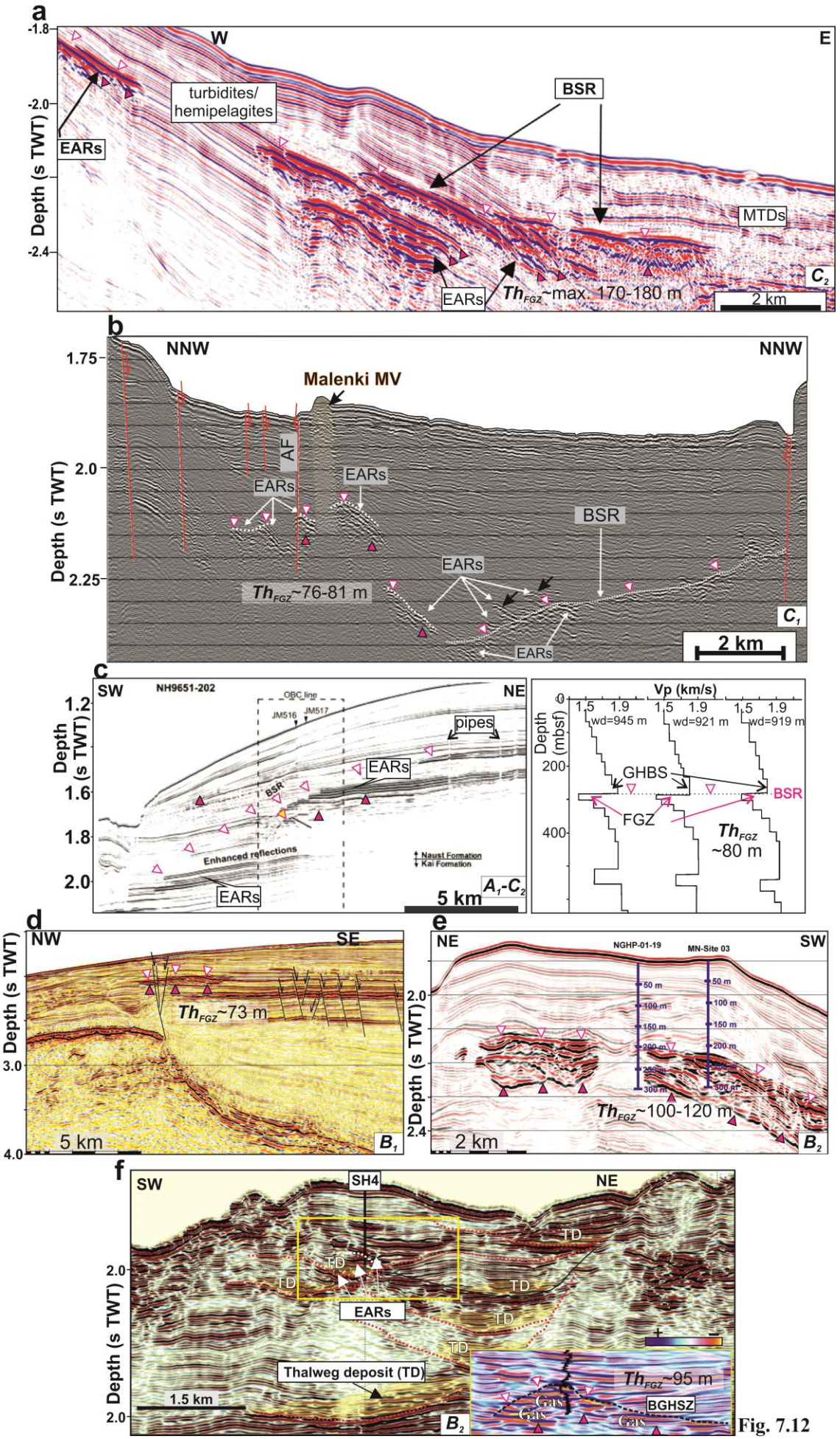

a
W
E
turbidites/
hemipelagites
BSR
EARs
MTDs
Depth (s TWT)
-1.8
-2.0
-2.4
EARs
Th_FGZ~max. 170-180 m
2 km
C_2
b
NNW
NNW
Malenki MV
AF
EARs
EARs
BSR
EARs
Th_FGZ~76-81 m
EARs
Depth (s TWT)
1.75
2.0
2.25
C_1
2 km
c
SW
NE
NH9651-202
OBC_line
JM516
JM517
pipes
EARs
BSR
Enhanced reflections
Naust Formation
Kai Formation
EARs
A_1-C_2
5 km
Depth (s TWT)
1.2
1.6
1.8
2.0
Vp (km/s)
1.5 1.9 1.5 1.9 1.5 1.9
wd=945 m
wd=921 m
wd=919 m
Depth (mbsf)
200
400
GHBS
BSR
FGZ
Th_FGZ
~80 m
d
NW
SE
Th_FGZ~73 m
5 km
B_1
Depth (s TWT)
3.0
4.0
e
NE
SW
NGHP-01-19
MN-Site 03
50 m
100 m
150 m
200 m
300 m
Th_FGZ~100-120 m
2 km
B_2
Depth (s TWT)
2.0
2.4
f
SW
NE
SH4
TD
TD
TD
TD
TD
TD
EARs
Thalweg deposit (TD)
1.5 km
B_2
Th_FGZ~95 m
BGHSZ
Gas
Gas
Gas
Depth (s TWT)
2.0
2.0

Fig. 7.12

**Figure 7.11 (See page 316).** Examples of FGZs from continental margins dominated by shale/gravity **(a)** or salt **(b-e)** tectonics. The white triangles indicate the BSR; the purple triangles indicate the bases of the measured FGZs (cf. with **Tab. 7.3**). The letters at the bottom-right of each image indicate the interpreted type of FGZ (see **paragraph 7.5.4**). **(a)** High-resolution seismic reflection profile of a shale-cored anticline from deepwater Nigeria, showing a ~70 m thick FGZ. The numerous faults are interpreted as the conduits for methane-rich fluids. Seepage at the seafloor is indicated by a system of pipes and pockmarks (black arrows) (modified after Sultan *et al.*, 2011). **(b)** Single-channel depth-converted seismic line along the Blake Ridge (left) and traveltime inversion results from vertical seismic profiles (right) (modified after Holbrook *et al.*, 1996). The data indicate a ~200-250 m thick FGZ below the BGHSZ which, probably due to capillary effects, is shallower than its theoretical position (Ruppel *et al.*, 1997). **(c-left)** Seismic reflection profile along the Walker Ridge (Terrebonne Basin) in the Northern Gulf of Mexico, combined with WL resistivity (purple) and gamma-ray (black) data from three wells (modified after Frye *et al.*, 2012). Blue, Orange and Green are the names of the sand-rich units with characterised by hydrates at high saturation. The BSR is discontinuous, and it is recognisable only along specific horizons (cf. Hillman *et al.*, 2017b). **(c-right)** RMS amplitude map of the '*Green Unit'*, highlighting the amplitude characteristics of the FGZ (yellow in the amplitude map) and of gas hydrate-bearing sediments (blue in the amplitude map). Note the polarity reversal at the BGHSZ (white dotted line). The FGZ appears to be up to ~230 m thick along this horizon (modified after Boswell *et al.*, 2012b). **(d)** Seismic reflection profile across the Northern Seep site in the Lower Congo Basin. The FGZ is interpreted to be ~95-140 m thick, and it is observed from the backlimb to the forelimb of the anticline. This FGZ is underlain by a zone of seismic wipeout. At the crest of the anticline, there is evidence of free gas migration throughout the GHSZ (note the faults and the enhanced reflections near the seafloor), confirmed by the detection of a gas flare (bottom-right). The black arrows indicate possible zones of accumulation of hydrates at high saturation, both immediately above the BGHSZ and near the seafloor (modified after Wenau *et al.*, 2015). **(e)** Seismic reflection profile from a flat area on the flank of a salt-related anticline in the Lower Congo Basin, indicating a ~100-110 m thick FGZ in polygonally-faulted intervals. Note the presence of a fluid-escape pipe and a pockmark, indicating seepage at the seafloor. The black arrows highlight potential accumulation of high saturation hydrates or free gas pockets along the pipe (modified after Andresen and Huuse, 2011). **(f)** Seismic reflection profile across a salt-related anticline in the Kwanza Basin (offshore Angola), indicating a relatively shallow and patchily distributed BSR, underlying by a thin FGZ (max 25-30 m thick, bottom-left). The free gas accumulation appears connected with the migration of fluids along faults and is overlain by gas hydrate pingoes (black arrows) (modified after Serié *et al.* 2012). Seismic data appears at 0° Phase (European polarity convention for **(a, e, f)** and North American polarity convention for **(b-d)**).

**Figure 7.12 (See the previous page).** Examples of FGZs from active extensional basins **(a, b)** and old rifted passive margins **(c-f)**. The white triangles indicate the BSR; the purple triangles indicate the bases of the measured FGZs (cf. with **Tab. 7.3**). The letters at the bottom-right of each image indicate the interpreted type of FGZ (see **paragraph 7.5.4**). **(a)** Seismic reflection profile along the western continental slope of the Ulleung Basin. Note the widely developed enhanced reflections below the BGHSZ, within a lithology dominated by turbidites and hemipelagites. The BGHSZ is scarcely recognisable within the MTDs that dominated the easternmost part of the profiles. The FGZ could be up to 170-180 m thick. However, it is complex to predict if the free gas phase interconnected over this entire interval (modified after Yoo *et al.*, 2013). **(b)** Seismic reflection profile along the Southern Basin of the Lake Baikal (modified after Vanneste *et al.*, 2001). Note that the BGHSZ is greatly influenced by heat flow fault-controlled anomalies. Furthermore, active seepage occurs in the form of mud volcanoes. The maximum thickness of the FGZ around the Malenki mud volcano (MV) is ~76-81 m (see Van Rensbergen *et al.*, 2002). **(c)** Seismic reflection profile (left) and OBS P-wave velocity profiles from the Norway margin, in the vicinity of the Storegga Slide (modified after Bünz *et al.*, 2005). The FGZ is ~80 m thick. Note the presence of a multiple/double BSR beneath the present-day BGHSZ (black triangle). **(d)** Seismic reflection profile from the Namibe Basin along the West African margin. The FGZ (~73 m thick) is formed above a possible fluid conduit at the margin of a structural high (modified after Moss, 2010). **(e)** Seismic reflection profile from the Mahanadi Basin, crossing site NGHP-01-19. The FGZ is ~100-120 m thick and is expressed as free gas pockets associated with a turbidite channel system (modified after Kumar *et al.*, 2014). **(f)** Seismic profile from the Shenhu area of the South China Sea, across site SH4. Free gas-bearing sediments are patchily distributed and appear controlled by a migrating canyon system, resulting in the deposition of thalweg deposits (TD) with high reservoir quality (modified after Wang *et al.*, 2014). Seismic data appears at 0° Phase (European polarity convention for **(a, b, d, f)** and North American polarity convention for **(c, e)**).

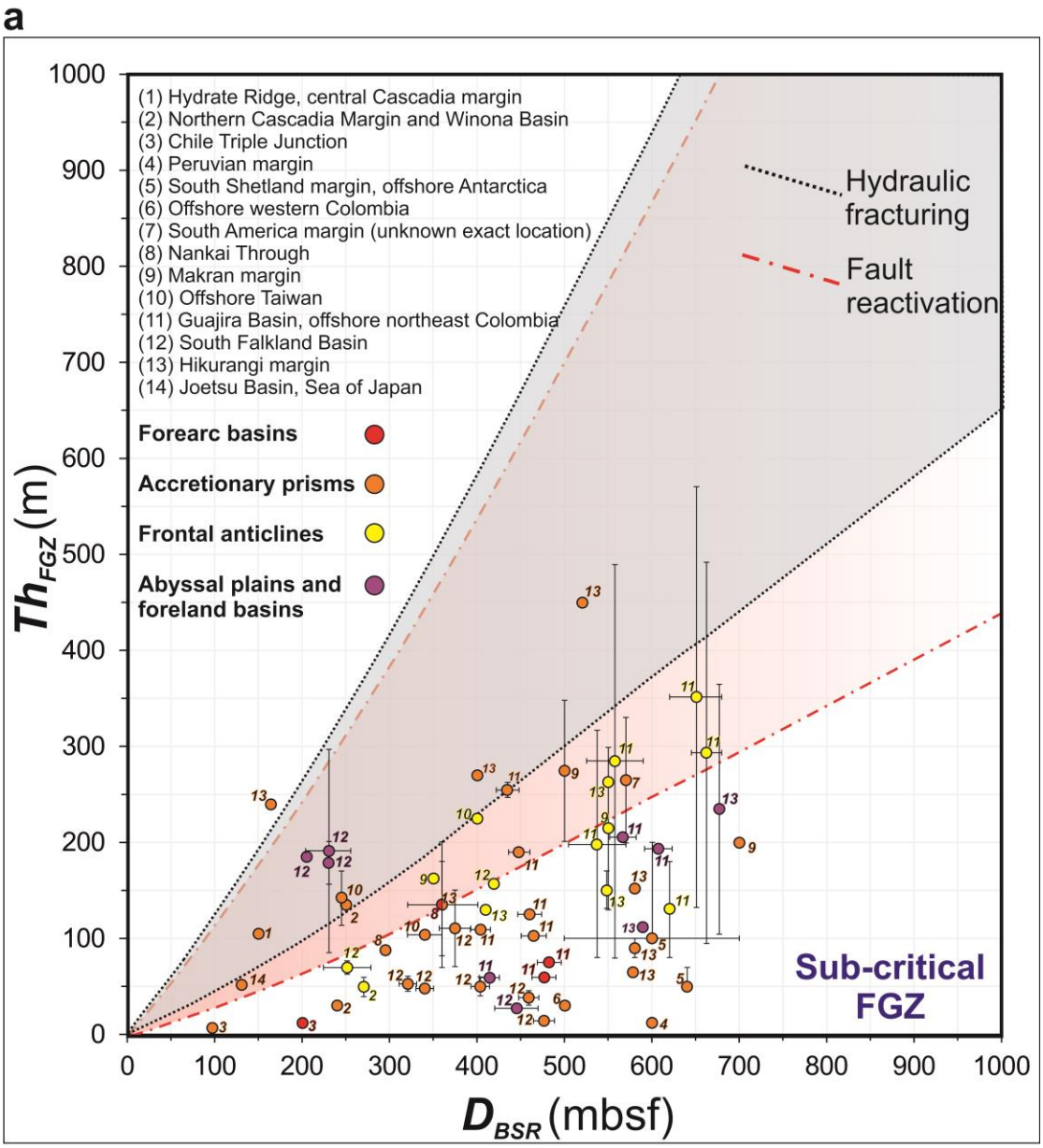

a
(1) Hydrate Ridge, central Cascadia margin
(2) Northern Cascadia Margin and Winona Basin
(3) Chile Triple Junction
(4) Peruvian margin
(5) South Shetland margin, offshore Antarctica
(6) Offshore western Colombia
(7) South America margin (unknown exact location)
(8) Nankai Through
(9) Makran margin
(10) Offshore Taiwan
(11) Guajira Basin, offshore northeast Colombia
(12) South Falkland Basin
(13) Hikurangi margin
(14) Joetsu Basin, Sea of Japan
Forearc basins
Accretionary prisms
Frontal anticlines
Abyssal plains and foreland basins
Hydraulic fracturing
Fault reactivation
Sub-critical FGZ
$Th_{FGZ}$ (m)
$D_{BSR}$ (mbsf)
0
100
200
300
400
500
600
700
800
900
1000

**Fig. 7.13a**

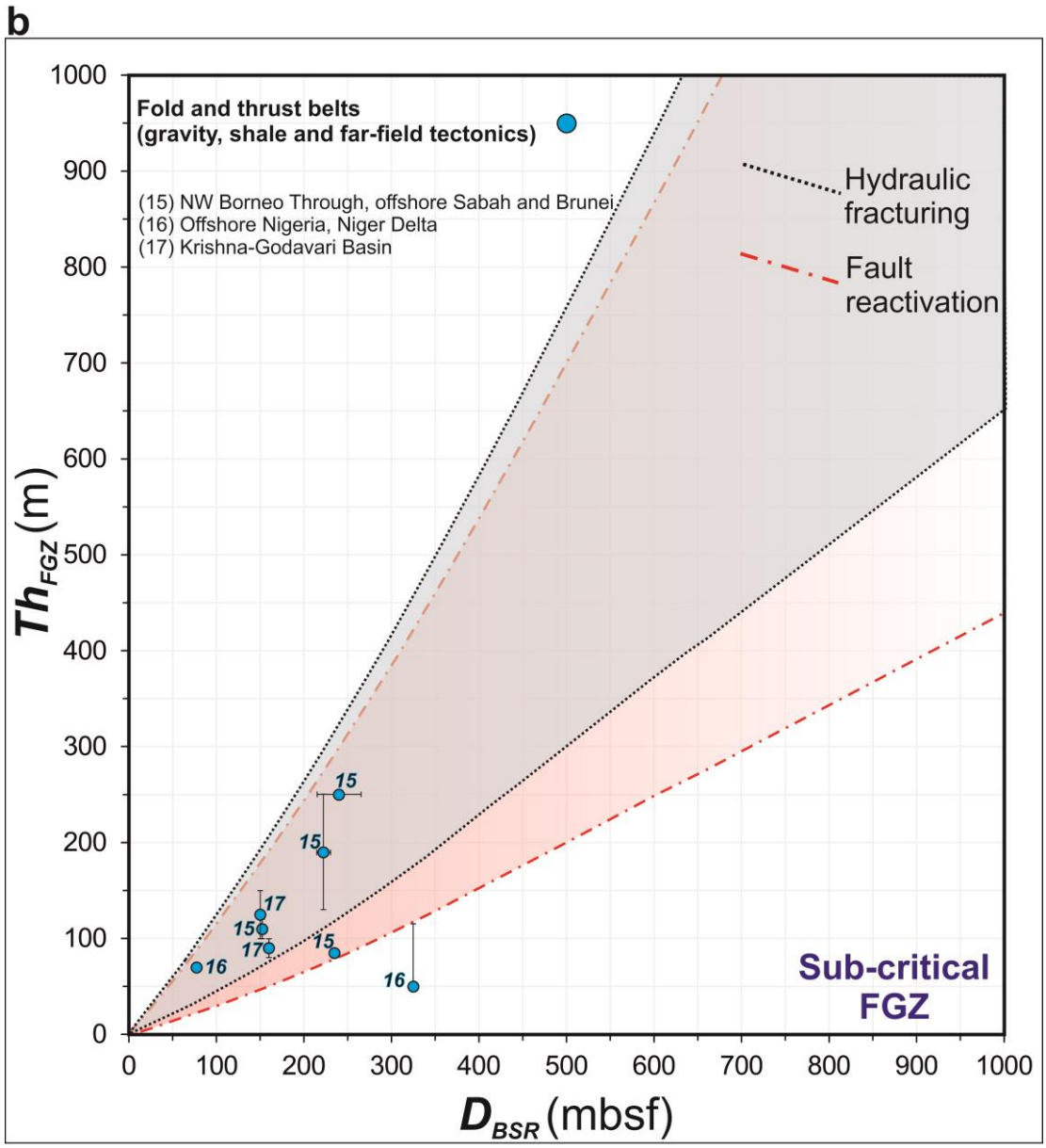

b
Fold and thrust belts
(gravity, shale and far-field tectonics)
(15) NW Borneo Through, offshore Sabah and Brunei
(16) Offshore Nigeria, Niger Delta
(17) Krishna-Godavari Basin
Hydraulic fracturing
Fault reactivation
Sub-critical FGZ
Th_FGZ (m)
D_BSR (mbsf)
0
100
200
300
400
500
600
700
800
900
1000
15
15
17
15
17
15
16
16

**Fig. 7.13b**

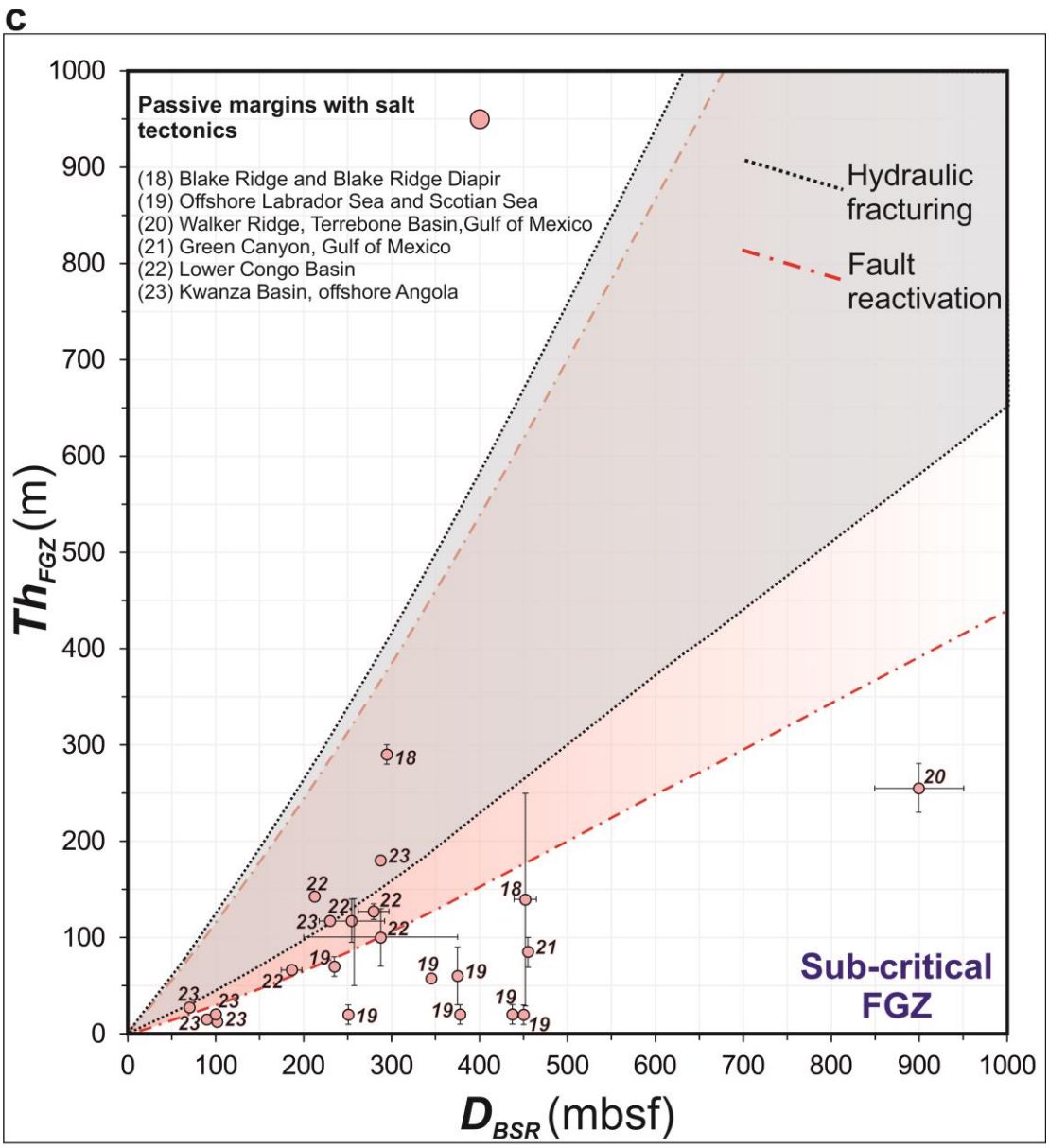

c
Passive margins with salt tectonics
(18) Blake Ridge and Blake Ridge Diapir
(19) Offshore Labrador Sea and Scotian Sea
(20) Walker Ridge, Terrebone Basin,Gulf of Mexico
(21) Green Canyon, Gulf of Mexico
(22) Lower Congo Basin
(23) Kwanza Basin, offshore Angola
Hydraulic fracturing
Fault reactivation
Sub-critical FGZ
Th_FGZ (m)
D_BSR (mbsf)
0
100
200
300
400
500
600
700
800
900
1000

**Fig. 7.13c**

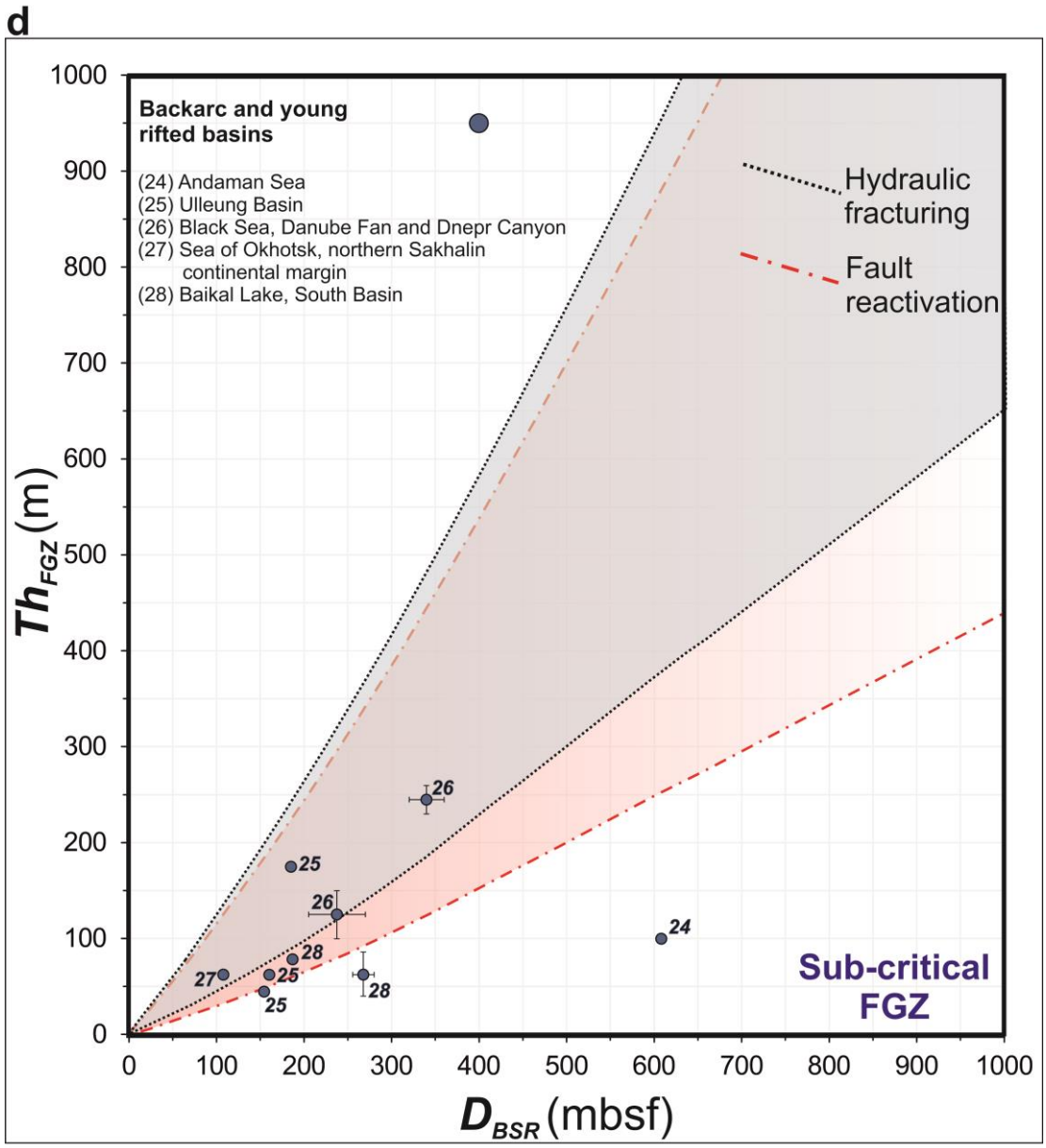

d
Backarc and young rifted basins
(24) Andaman Sea
(25) Ulleung Basin
(26) Black Sea, Danube Fan and Dnepr Canyon
(27) Sea of Okhotsk, northern Sakhalin continental margin
(28) Baikal Lake, South Basin
Hydraulic fracturing
Fault reactivation
Sub-critical FGZ
$Th_{FGZ}$ (m)
$D_{BSR}$ (mbsf)
0
100
200
300
400
500
600
700
800
900
1000

**Fig. 7.13d**

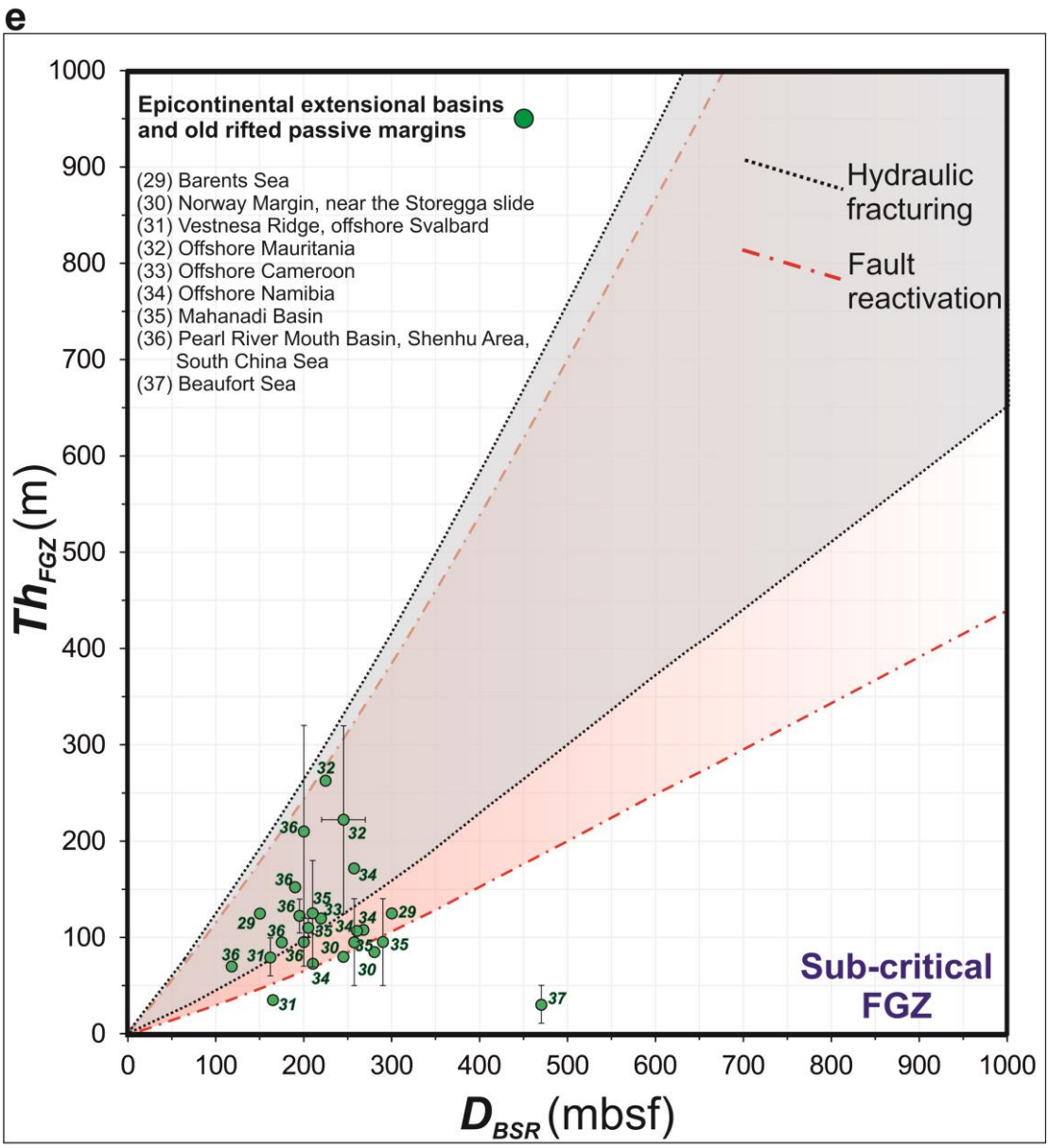



**Figure 7.13.** ***Th*$_{FGZ}$** *vs* ***D*$_{BSR}$** for convergent margins **(a)** and other geological settings **(b-e)**. The number near each point refers to the locations indicated in the legend in the left part of the plot. See also **Tab. 7.3** for more detailed references. The colour of the points in **Fig. 7.13a** allows distinguishing between different parts of a tectonically-active margin.

### *7.4.2. Mechanisms of free gas migration: significant examples*

Here, I compare the observed thickness of the FGZ with the theoretical thresholds required to activate free gas leakage at the BGHSZ via **(1)** hydraulic fracturing, **(2)** fault reactivation and **(3)** capillary invasion through the pore space and along pre-existent fractures. **Figure 7.14** displays examples of FGZs from six different gas hydrate provinces. Except for the Guajira Basin, the sediment properties are calibrated with core and well-log data (**Tab. 7.2**) and the effective lithostatic stress can be estimated precisely.

#### *7.4.2.1. Hydrate Ridge (Cascadia margin)*

**Figure 7.14a** refers to the Hydrate Ridge, located along the Cascadia accretionary prism (Tréhu *et al.*, 2006) (**Fig. 7.10a**). Here, the FGZ is up to ~100-110 m thick (**Tab. 7.3**) along a sand-rich permeable layer, named Horizon A. Tréhu *et al.* (2004a) and Bangs *et al.* (2011) interpreted the FGZ as interconnected and therefore buoyant. If this is the case, this FGZ is at critical conditions for hydraulic fracturing and fault reactivation. Hence, the presence of a widespread fracture and fault network at the crest of the Hydrate Ridge could reflect these failure mechanisms (Crutchley *et al.*, 2013).

However, free gas could theoretically be injected within the GHSZ at lower buoyancy pressure by capillary invasion through the primary pore network. The nominal (i.e. the most frequent) pore radius of the host stratigraphy at Hydrate Ridge is ~ 200 nm whereas the maximum pore radius is ~635 nm, from the analysis of a core at 127 mbsf (Site 1248, ODP Leg 204) (Liu and Flemings, 2011). Therefore, the capillary pressure required for invasion is modelled for entry pore throat radii of 100, 200, 300 and 600 nm. With the largest pore throat radii (200-600 nm), a shorter gas column is required to inject free gas within the GHSZ than that observed during the ODP 204 expedition. However, if the entry radius is ~100 nm, the FGZ will grow until either hydraulic fracturing or fault reactivation occur before a critical capillary pressure is reached.

Initially, it is possible that free gas migrates along Horizon A via capillary invasion, driven by relatively low buoyancy pressures ($\boldsymbol{Th_{FGZ}}$ < 50-80 m). However, the formation of gas hydrates at the BGHSZ could reduce the capillary entry radius and thicken the FGZ, until critical conditions for hydraulic fracturing or fault reactivation are met. This hypothesis would explain the seismic observations. The dissociation or dissolution of hydrates at the BGHSZ could result in the re-opening of larger pore throats and the reactivation of capillary invasion. Also, once fractures and faults are formed, further hydraulic fracturing or fault reactivation is probably inhibited by the invasion along the fracture walls at lower amounts of overpressure, even if the fracture aperture (***2l***) is microscopic (i.e. higher than ~ 200 nm).

#### *7.4.2.2. Blake Ridge (offshore south Carolina)*

**Figure 7.14b** refers to the FGZ at Blake Ridge, offshore South Carolina. The low-velocity zone associated with free gas-bearing sediments extends down to ~250 m below the BSR (**Fig. 7.11b**). However, free gas is postulated to be interconnected only for the first 29 m below the BGHSZ (Flemings *et al.*, 2003). The nominal pore radius at Blake Ridge is ~75 nm (Liu and Flemings, 2011), while the percolation threshold radius is ~100 nm (Henry *et al.*, 1999). Therefore, capillary invasion into the GHSZ can only occur if a connected FGZ of 130-190 m exists. However, water overpressure (~70% of the lithostatic stress at this site, see Flemings *et al.*, 2003), can combine with a thinner free gas buoyant phase to reach a critical overpressure without such a thick interconnected FGZ (**Fig. 7.14b**). Smaller entry radii (~30-40 nm), would instead facilitate, in the presence of adequate sources of overpressure, hydraulic fracturing or fault reactivation, which could have occurred at this site as well (Gorman *et al.*, 2002).

#### *7.4.2.3. GKL Dome (offshore Sabah, NW Borneo)*

At the crest of this bathymetric ridge (see **Chapters 3, 4**), LWD data indicates that sediments are clay-rich and fine-grained. Piezocone tests further indicated a permeability in the order of $10^{-18}$ $m^2$ (Gisler *et al.*, 2007). Therefore, the presence of pore throat radii larger

than 100 nm is unlikely (cf. Clennell *et al.*, 2000a; Hildenbrand *et al.*, 2002; Liu and Flemings, 2011). The FGZ is at least 100-120 m thick, based on the thickness of the interval with the lowest P-wave velocity values, according to wireline data (**Figs. 7.9a, 7.14c**).

This FGZ is suggested to host free gas at small *Sg*, and the pore pressure appears only slightly in excess compared to hydrostatic below the BSR (see **Chapter 3**). However, some mechanisms can transiently contribute to the formation of a buoyant free gas column. These include the migration of free gas from underlying reservoirs, the dissociation of gas hydrates (including the $S_{II/H}$ hydrates coexisting with the free gas), the exsolution of free gas and the generation of water overpressures (e.g. following pressure drops) (see **Chapter 4**). A 100-120 m thick free gas buoyant phase would generate an overpressure close to that required for fault reactivation or hydraulic fracturing. Conversely, to activate a capillary invasion through pore radii of 50-100 nm, larger columns are required. The observation of fluid-escape pipes further suggests that hydraulic fracturing is the favoured mechanism for free gas migration across the GHSZ. A cyclic build-up of overpressure could trigger multiple episodes of hydraulic fracturing. Nevertheless, if fractures maintain adequate apertures available for fluid flow (more than ~100 nm), without being completely clogged by hydrates, migration occurs along these features instead of forming new pathways. The preservation of favourable fracture conduits along the pipes would also explain why the same pipes have been used for fluid flow multiple times (see **Chapter 4**).

#### *7.4.2.4. Vestnesa Ridge (Fram Strait)*

The Vestnesa Ridge is a sediment drift located at arctic latitudes, offshore western Svalbard. The presence of active fluid-escape pipes, rooted in the FGZ, is limited to the crest of the ridge and a 35 to 100 m thick FGZ is observed (Petersen *et al.*, 2010; Plaza-Faverola *et al.*, 2015) (**Fig. 7.14d,** see also **Fig. 1.27c**). The buoyancy of this FGZ does not seem enough to form hydraulic fractures or reactivate faults unless other sources of overpressure are present in the region. Capillary invasion can occur within primary pore throats with radii

bigger than 200 nm or within pre-existing fractures with at least the same aperture, assuming a free gas buoyancy exerted by a 65-70 m thick FGZ. The present-day evidence of active seepage at the seafloor (Smith *et al.*, 2014b) suggests that conditions critical for fluid flow are somehow satisfied. It is possible that, in the presence of fine-grained sediments, free gas migrates towards the seafloor by re-utilising the pre-existence fractures along the numerous pipe-like conduits in this region.

#### *7.4.2.5. Walker Ridge (Terrebonne Basin, Gulf of Mexico)*

The Walker Ridge is an asymmetric anticline generated as a consequence of salt tectonism in the Terrebonne Basin (Frye *et al.*, 2012). At the backlimb of this anticline, at ~850-950 mbsf, a discontinuous BSR is observed and reflects the presence of dipping sand-rich and gas-charged horizons. Above the BGHSZ, high values of *Sh*, occasionally greater than 80% are inferred for these horizons from LWD data (Boswell *et al.*, 2012b). As mentioned earlier, the depth of the BGHSZ at this site prevents the onset of critical conditions. The FGZ is organised into separated sand-rich horizons. The amplitude maps of these FGZs suggest the existence of isolated columns thicker than ~200 m (Boswell *et al.*, 2012b) (**Figs. 7.11c, 7.14e**). If buoyant, these columns can only be sealed at the BGHSZ by pore throats with radii smaller than ~50 nm. This radius is typical of clayey sediments but at least one order of magnitude smaller than that expected in sandy/silty layers (Nelson, 2009). However, considering the elevated *Sh* estimated from LWD data, it is possible that hydrates occlude most of the pore space at the BGHSZ. Faults or fractures are not observed at the BGSHZ along these coarse-grained horizons suggesting that, if occurring, free gas migration operates via capillary invasion along the primary pore space.

#### *7.4.2.6. Frontal anticlines of the Guajira Basin (Colombian margin)*

**Figure 7.14f** combines all the measurements made for the frontal anticlines of the Guajira Basin (Colombian margin). Given the lack of in-situ density data, the hydraulic fracture and fault reactivation criteria are extrapolated using the density data from the

Nankai Trough (a relatively similar convergent margin) and the Walker Ridge (a region of deepwater sediment deposition). Each green rhomb represents the average $\boldsymbol{Th_{FGZ}}$ in each anticline, and the vertical bars show the variability in $\boldsymbol{Th_{FGZ}}$ along adjacent horizons. The largest FGZs can exceed 400-500 m in thickness and are interpreted to be interconnected and generate buoyancy pressures (see **Chapter 6**). These pressures are nearly critical for hydraulic fracturing and probably within the range of pressures required to reactivate a fault. It is possible that free gas overpressures have triggered some fault displacements at the crests of these anticlines (see **Fig. 7.4a, g, h**). Active free gas migration could also occur at lower overpressures if the faults and fractures are wide enough to act as preferential conduits. The presence of permeable faults and fractures would inhibit the formation of large free gas columns. Such scenario could also explain why, for some anticlines, a BSR is not observed in the most intensively faulted zones (**Fig. 7.4g, h**). Finally, similarly to the Walker Ridge, the thickest FGZs could be sustained only in the presence of small pore throats, with radii less than ~50 nm wide, suggesting that hydrates at elevated *Sh* reduce the porosity available for fluid flow at the BGHSZ (see **Chapter 6**).

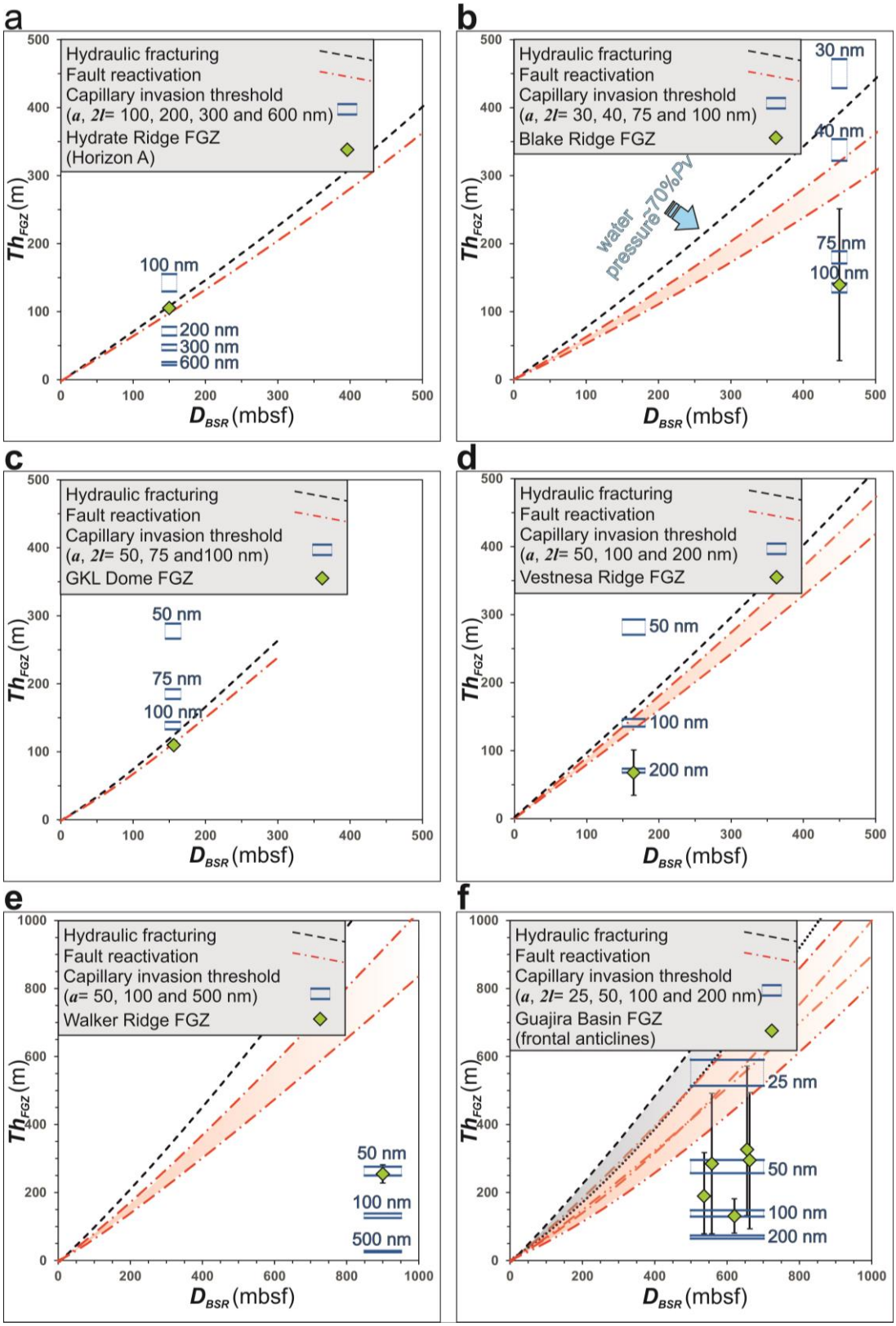



**Figure 7.14.** FGZs plotted with the hydraulic fracturing, fault reactivation and capillary invasion thresholds, calibrated with in-situ information and reasonable ranges for the Poisson ratio ($\nu$), the gas density ($\rho_g$), and the interfacial tension ($\gamma$). $\rho_g$ and $\gamma$ are consistent with the P, T conditions at each location. The water density is 1025 kg/m$^3$. The conditions for capillary invasion for specific values of $a$ and $2l$ are indicated by blue bars. **(a)** Hydrate Ridge (***Pv*** curve n°1-**Fig. 7.2a**; $\rho_g$= 79 kg/m3; $\nu$= 0.475; $\gamma$= 0.06-0.072 J/m$^2$); **(b)** Blake Ridge (***Pv*** curve n°7-**Fig. 7.2a**; $\rho_g$= 232.5 kg/m$^3$; $\nu$= 0.41-0.45; $\gamma$= 0.05-0.055 J/m$^2$); **(c)** GKL Dome (***Pv*** curve n°6-**Fig. 7.2a**; $\rho_g$= 105 kg/m$^3$; $\nu$= 0.475; $\gamma$= 0.06-0.065 J/m$^2$); **(d)** Vestnesa Ridge (***Pv*** curve n°11-**Fig. 7.2a**; $\rho_g$= 120.5 kg/m$^3$; $\nu$= 0.45-0.48; $\gamma$= 0.06-0.065 J/m$^2$); **(e)** Walker Ridge (***Pv*** curve n°8-**Fig. 7.2a**; $\rho_g$= 211 kg/m$^3$; $\nu$= 0.40-0.45; $\gamma$= 0.05-0.055 J/m$^2$); **(f)** Guajira Basin (frontal anticlines) (***Pv*** curve n°5 and 8-**Fig. 7.2a**; $\rho_g$= 265 kg/m$^3$; $\nu$= 0.4-0.45; $\gamma$= 0.05-0.055 J/m$^2$).

### *7.4.3. Impact of methane solubility on the formation of a free gas zone*

The data presented in **Figure 7.15a** indicate that, along convergent margins, the pore fluid pressures at the BSR (i.e. the top of the FGZ) are distributed over a wider interval, from ~10 to ~45 MPa whereas the observed ***GTGs*** are commonly between ~30 and ~55 °C/km. There are, however, a few locations where these values are exceeded, like along the Triple Chile Junction (~80-190 °C/km) or in the Joetsu Basin (~100 °C/km) (**Tab. 7.3**). As a result of this diversity in pressure and geothermal gradients, the methane solubility curvature is highly variable too. Similarly, the FGZs in other tectonic settings are developed over a broad range of solubility curvature conditions (**Figs. 7.15b-e**). In these cases, the ***GTGs*** vary between ~20 and ~100 °C/km, with a tendency to cluster between ~35 and ~65 °C/km. Conversely, the pressures at the BSR are limited between ~10 and ~30 MPa.

By plotting either the ***GTG*** or $\Delta_{SOL}$ against $Th_{FGZ}$, it emerges that the locations characterised by high ***GTGs*** and therefore steeper solubility gradients below the BSR, display thinner FGZs than the locations with by lower ***GTGs***, where the methane solubility changes less abruptly below the BSR (**Figs. 7.16**). In the latter case, there is a broad range of thicknesses of FGZs. This observation suggests that the formation of thick FGZs is somehow inhibited in areas with high ***GTGs***, contrasting with the model proposed by Haacke *et al.* (2008). This effect does not appear to be related, on a first-order, to the depth of the BSR (i.e. to the lithostatic stress) (**Fig. 7.24b**).

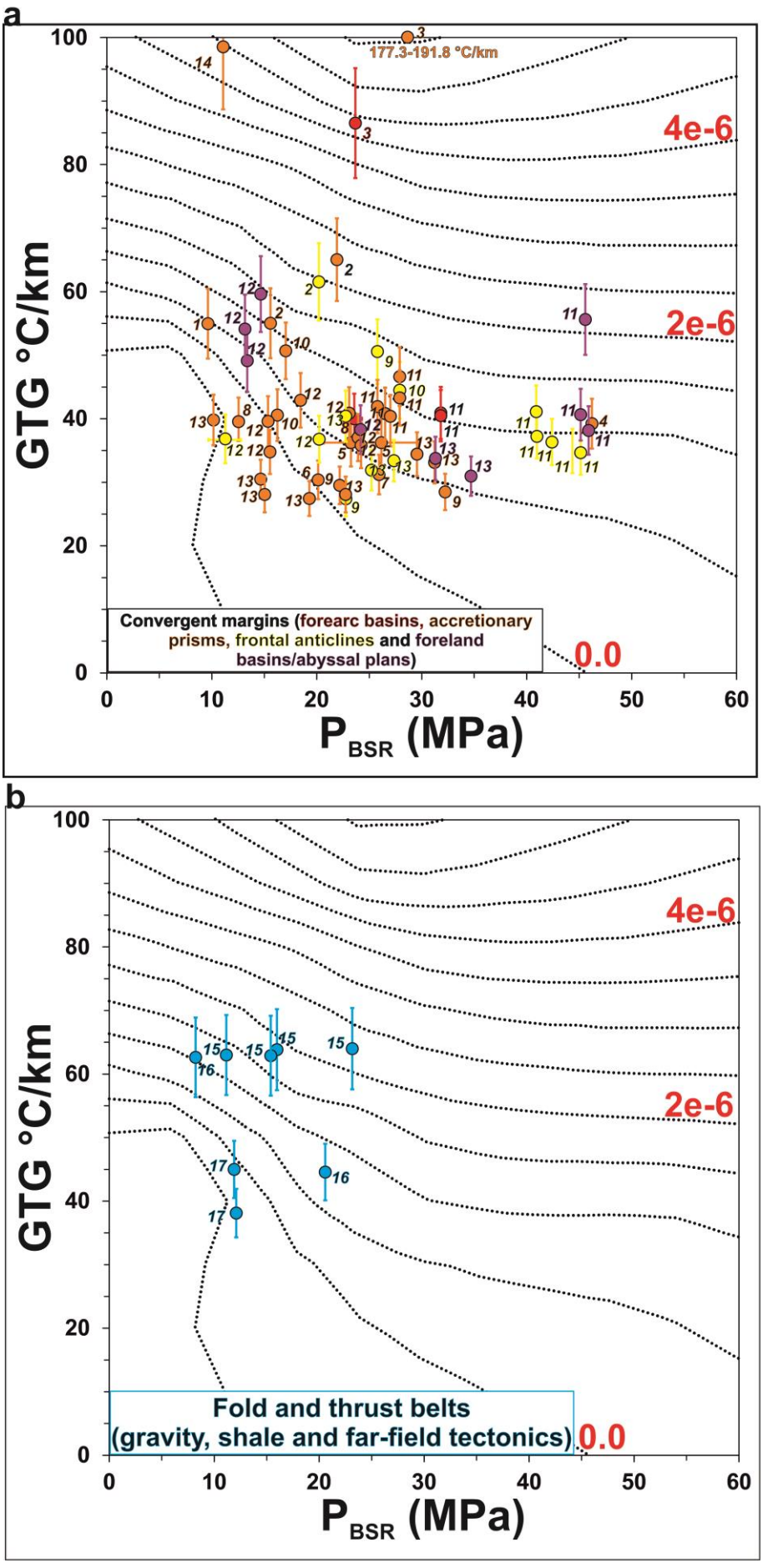

a
177.3-191.8 °C/km
4e-6
2e-6
0.0
Convergent margins (forearc basins, accretionary prisms, frontal anticlines and foreland basins/abyssal plans)
GTG °C/km
P BSR (MPa)
b
4e-6
2e-6
0.0
Fold and thrust belts
(gravity, shale and far-field tectonics)
GTG °C/km
P BSR (MPa)

**Fig. 7.15a, b**

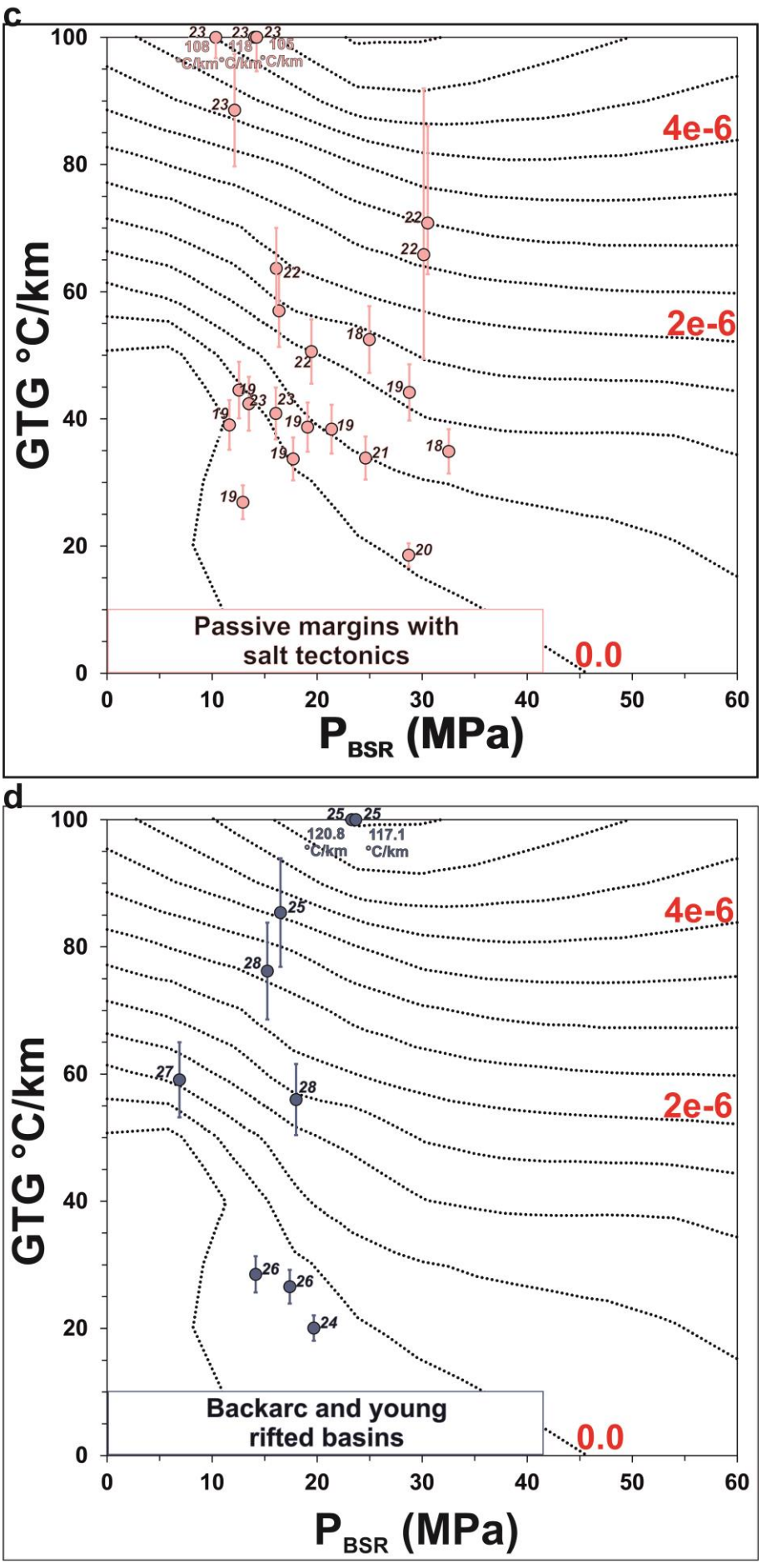

c
GTG °C/km
P BSR (MPa)
4e-6
2e-6
0.0
Passive margins with
salt tectonics
23 23 23
108 118 105
°C/km °C/km °C/km
d
GTG °C/km
P BSR (MPa)
4e-6
2e-6
0.0
Backarc and young
rifted basins
25 25
120.8 117.1
°C/km °C/km

**Fig. 7.15c, d**

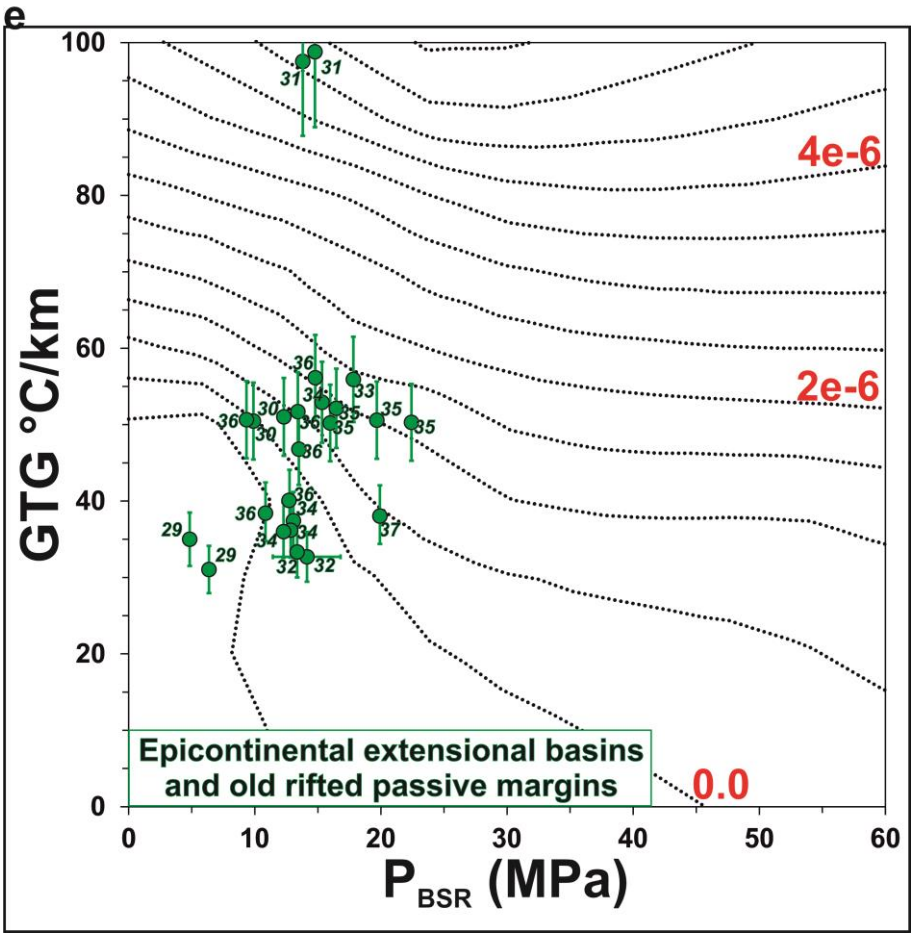



**Figure 7.15.** ***GTG vs $P_{BSR}$*** for convergent **(a)** and other geological settings **(b-e)**. The colour and the number of each point refer to a specific geologic setting and geographic location (see legends of **Fig. 7.13** and **Tabs. 7.1, 7.3**). There is an error bar for each point that accounts for a 10% error in the estimated GTG. The curvature of the methane solubility right beneath the BGHSZ is derived from Haacke *et al.* (2007) and is indicated by red-coloured numbers on the right of each plot. The interval separation between each contour is 0.5 x $10^{-6}$ kg/$m^5$. The solubility curvature for those locations characterised by a gas hydrate stability impacted by $C_{2+}$ hydrocarbons would be higher than that indicated on the plot. Such locations include the South Shetland margin (5), the NW Borneo (15), the Barents Sea (29) and the Vestnesa Ridge (31). It is not excluded that $C_{2+}$ hydrocarbons could impact the solubility curvature in other systems, particularly in petroleum-rich basins (e.g. the Niger Delta and offshore Angola).

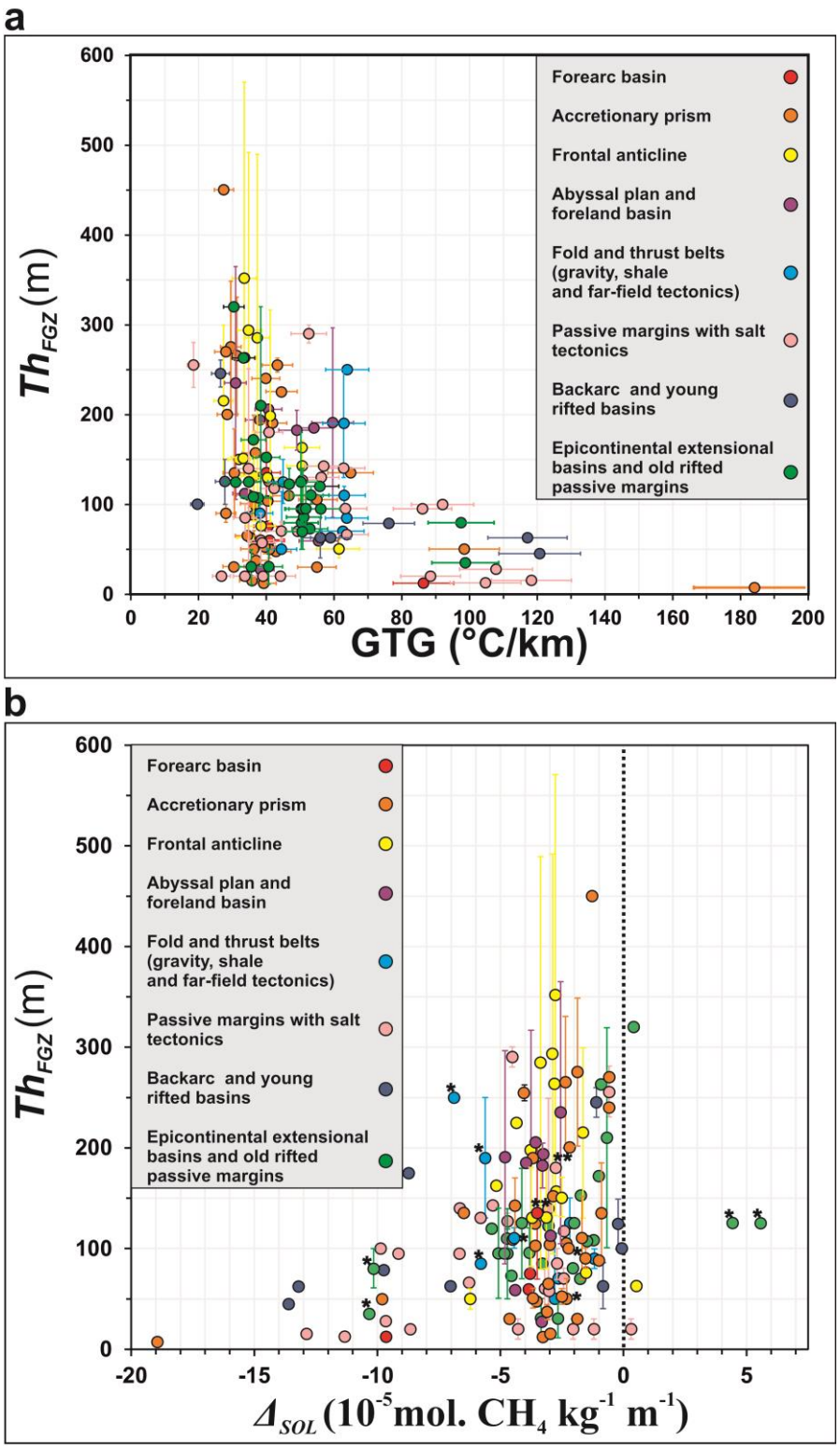



**Figure 7.16. (a)** ***Th**FGZ vs GTG* (°C/km) and **(b)** ***Th**FGZ vs Δ**SOL*** ($10^{-5}$ mol. $CH_4$ $kg^{-1}$ $m^{-1}$). There is an error bar for each point that accounts for a 10% error in the estimated GTG. The colour of each point refers to a specific geologic setting (see legends). *= locations whose BGHSZ is influenced by $C_{2+}$ hydrocarbons. For NW Borneo, the BGHSZ for structure I hydrates with 4%$C_2$ and 96%$C_1$ was considered (i.e. the position of the BSR; see **Chapter 3**). However, structure II hydrates can occur beneath BSRs and may severely impact the solubility variations. $C_{2+}$ hydrocarbons could further impact the solubility gradients in other systems, particularly in petroleum-rich basins (e.g. the Niger Delta and offshore Angola). **= locations where the BGHSZ is observed to be shifted upward due to capillary effects (The Blake Ridge and the Kumano Basin). The values of $\Delta_{SOL}$ are mostly negative since they refer to an increase in depth (i.e. 100 m below the BGHSZ), which leads to a decrease in solubility.

## 7.5. Discussion

### *7.5.1. Critically pressured free gas zones: controlling factors*

The data presented in this review suggest that critical conditions for hydraulic fracturing or fault reactivation can exist due to the buoyancy of a free gas zone (FGZ) in natural gas hydrate systems (NGHSs). The occurrence of these critical conditions appears independent of the tectonic setting, and the existence of a critical FGZ seems instead governed by the dynamics of the NGHS at the km-scale. However, it is recognised that larger free gas columns form in convergent margins than in other geological settings, owing to the greater water depths and the lower ***GTGs*** of the NGHSs in these regions (**Fig. 7.13**).

The extrapolated criteria for hydraulic fracturing and fault reactivation cover a broad range of conditions, but more restrictive parameters can be adopted in analysing specific systems (**sub-paragraph 7.4.2**). The lithostatic stress, which depends on the bulk density, the Poisson ratio, which is controlled by lithology and porosity, and the free gas density (see **paragraph 7.7**) represent primary controls on the maximum thickness of a buoyant free gas zone. Once a critical pressure has been reached, the free gas will migrate throughout the GHSZ and escape at the seafloor, if not converted into hydrates, dissolved or oxidised '*en-route'* (Torres *et al.*, 2004; Tréhu *et al.*, 2004a; Liu and Flemings, 2007).

The presence of structural highs of any origin promotes the accumulation of free gas and the generation of overpressures (Weinberger and Brown, 2006; Frederick and Buffett, 2011; Krabbenhoeft *et al.*, 2013). These locations are often affected by shallow gravitational and tectonic extensional stresses, resulting in the formation of normal faults and vertical fluid-escape features which, if permeable, may facilitate leakage processes (**Figs. 7.4-7.12,** see **sub-paragraph 7.4.2**).

The absence of in-situ calibration on *Sg*, free gas distribution and percolation thresholds is the major uncertainty of this study. The amount of free gas required to form a connected and mobile phase (i.e. the critical gas saturation) is of complex assessment but is

probably influenced by **(1)** the host lithology and the effective stress, which together determine the pore network geometry, as well as **(2)** the mechanism by which the mobile free gas phase is generated (e.g. continuous advection from below *vs* exsolution *vs* hydrate recycling) (cf. Du and Yortsos, 1999; Tsimpanogiannis and Yortsos, 2004). The mode of formation of the free gas phase into the FGZ and the host lithology are probably critical factors that govern the presence of a patchy *vs* homogeneous distribution of free gas. Conceptually, a homogeneous distribution seems more likely to occur if free gas advectively migrates by buoyancy along a permeable and well-sorted carrier bed, and accumulates below the BGHSZ, independently from solubility thresholds. In contrast, if methane exsolves only within the FGZ, its distribution would be controlled by the solubility thresholds in the pore space (Liu and Flemings, 2011). Similarly, if free gas is generated by hydrate recycling, its distribution would depend on the former *Sh* and hydrate morphology, which is still controlled (at the metre- to cm-scales) by the pore network and methane solubility (Torres *et al.*, 2008; Nole *et al.*, 2017).

Some authors suggested that FGZs can be characterised by an upper buoyant portion, and a lower portion, where immobile and isolated free gas bubbles are trapped by capillary forces (Flemings *et al.*, 2003; Haacke *et al.*, 2008). In this case, the base of an FGZ represents the depth where the methane content is just high enough to allow the nucleation of free gas bubbles. In such conditions, the vertical extent of the FGZ would solely reflect the interaction between the rate of methane supply and its solubility in pore waters. Assuming a constant methane supply, geothermal gradient and solubility conditions, the base of the FGZ would be an isotherm roughly parallel to the BSR. This could constitute a valid interpretation only if fluid contacts or sharp amplitude reductions, conform to the structure, are not observed in seismic data. These observations indicate instead the presence of an equal buoyancy pressure over a relatively large area. In these cases, this overpressure can be approximately quantified, and the base of the FGZ is instead controlled by the *'sealing efficiency'* of the BGHSZ (**Figs. 7.4a, 7.10a, 7.11c**).

The lack of data in the regions above the hydraulic fracturing envelope indicates that the accumulation of hundreds of metres of immobile free gas beneath a BSR (i.e. an apparently *'super-critical'* column) is very rare and not favoured in natural systems. The presence of hundreds of metres thick zones of immobile free gas in FGZs should be seen as a transient phenomenon unless there is a fluid flux high enough in methane to prevent the evanescence of these immobile bubbles over time, but low enough to avoid the formation of buoyant columns. In some locations, the observation of extensive zones of seismic wipeout could suggest that free gas-bearing sediments continuously occur for hundreds of metres (e.g. **Figs. 7.5a, 7.9b, c**). However, it is most likely that free gas accumulates into stacked reservoirs, separated by 100% water-bearing sediments but such configuration is masked by attenuation artefacts, resulting in a zone of seismic wipeout. The identification of high-amplitude *'halos'* surrounding these attenuated zones is critical for a correct interpretation of free gas distribution (Løseth *et al.*, 2009; see also **Chapter 4**).

The presence of layers of water-bearing sediments can further compromise the formation of elevated overpressures in an FGZ, particularly in horizontally-layered sequences. In such cases, it is hard to relate the whole thickness of an FGZ to its overpressure at the BGHSZ (see e.g. **Figs. 7.5b, 7.8f, g**). Eventually, free gas can spread laterally along distinct carrier beds, with an effectiveness that depends on the carrier bed reservoir quality (see Foschi *et al.*, 2017). In the absence of fractures, the upward migration of methane across the local seals could occur as a dissolved phase, with methane exsolving as a free gas phase only within the reservoir units. In contrast, where a stratigraphic package is tilted, the potential to generate a continuous and therefore buoyant FGZ is higher. This geometry favours the accumulation of water overpressures and a major focusing effect of the vertical component of fluid flow (Flemings *et al.*, 2002; Chatterjee *et al.*, 2014). It is not surprising that the thickest FGZs observed in this study are associated with dipping reflections, which represent in many cases the more permeable layers at the backlimbs of anticlines (e.g. **Figs. 7.4a, 7.7c-7.11**).

The increase in hydrate stability due to the presence of a buoyant free gas column, which induces an increase in the total pore fluid pressure, is minimal (Bhatnagar, 2008). Thus, the fact that the vast majority of the BSRs worldwide are close or near the bulk stability conditions at hydrostatic pressures, even in the presence of considerable free gas columns, cannot be used as evidence for the absence of a connected free gas zone. It is not surprising that the thickest FGZ measured so far is the only one that shows a possible (but still uncertain) evidence of a downward shift of gas hydrate stability due to free gas buoyancy (see **Chapter 6, Fig. 6.11a**). Other effects, such as capillary controls and presence of $C_{2+}$ hydrocarbons seem to provoke more frequent and seismically detectable shifts in the depth of the BGHSZ (cf. **Chapter 3** and Ruppel, 1997; Liu and Flemings, 2011; Daigle and Dugan, 2014; Plaza-Faverola *et al.*, 2017).

### *7.5.2. Fluid migration processes*

#### *7.5.2.1. Free gas advection: hydraulic fracturing vs capillary invasion*

At given overpressure conditions, the onset of either hydraulic fracturing or capillary invasion is, to a first-order, controlled by the interplay between lithology and effective stress. Specifically, the migration of gas across the BGHSZ through hydraulic fracturing will be favoured over capillary invasion in fine-grained sediments and at low burial depths. (Judd and Hovland, 2007; Jain and Juanes, 2009; Shin and Santamarina, 2010; Holtzman *et al.*, 2012). Therefore, it might be expected to see seismic evidence of conduits created by hydraulic fracturing in NGHSs in such conditions. This expectation is satisfied by the fact that the FGZs characterised by fluid-escape conduits mostly occur (70% of the cases; see **Tab. 7.3**) in fine-grained sediments at shallow depths below the seafloor (typically less than ~300 m). In the presence of a higher effective stress and large pore throats (i.e. in permeable and coarse-grained sediments), we would instead expect that free gas moves throughout the sediment via capillary invasion, which is not influenced by the effective stress (**Fig. 7.17a**).

If pre-existent fracture networks constitute efficient permeable pathways, free gas can migrate without the creation of new conduits. Hydrate-filled fractures appear to have sub-millimetre to millimetre-scale widths (Cook *et al.*, 2008; Rees *et al.*, 2011). Thus, fluid flow through the primary pores of fine-grained sediments (tens to hundreds nm wide) is prevented if these fractures are even partially open. Hence, at a given effective stress condition and lithology, hydraulic fracturing could be initially favoured but, once fractures are formed, further migration might occur by advective flow along such fractures, at a lower overpressure than that which predates fracture formation, given that the permeability of the media has been enhanced. The persistence in the system of discontinuities in the vertical permeability would result over time in a focusing of subsequent fluid flow events along pre-existent pathways. The fact that fluid flow tends to re-utilise the same routes for migration has been confirmed by the observation in 3D-seismic data of multiple episodes of leakage along vertical pathways (cf. **Chapter 4** and Davy *et al.*, 2010; Plaza-Faverola *et al.*, 2011; Ho *et al.*, 2012). Therefore, those FGZs which are not at a critical state for hydraulic fracturing or fault reactivation at present-day but display evidence of deformable pathways and methane seepage on seismic data could reflect a system where such pathways efficiently serve as pressure valves and permeable conduits (**Fig. 7.4b-d**).

In a different scenario, during the same event of migration, a transition from capillary invasion to hydraulic fracturing can also occur, given that the overpressured fluid moves upward towards conditions of lower effective stress (Fauria and Rempel, 2011). By combining into the same plot the theoretical criteria for hydraulic fracturing and capillary invasion, it is possible to discern which mechanism is the most likely, taking into account the effective stress (i.e. the overburden), the pore throat radius and $\boldsymbol{Th_{FGZ}}$ (**Fig. 7.17b**).

However, two further factors can complicate this simple buoyancy-driven system**: (1)** The presence of overpressures other than free gas buoyancy and **(2)** The reduction in permeability at the BGHSZ because of hydrate formation. The existence of overpressure

conditions in the first few hundred metres of overburden results from undercompaction, lateral and vertical pressure transfers, the formation of *'perched water'* aquifers and, in some cases, from diagenetic dehydration reactions (e.g. opal-A to -CT) (cf. **Chapter 6** and Moore and Vrolijk, 1992; Osborne and Swarbrick, 1997; Carson and Screaton, 1998; Dugan and Flemings, 2000; Flemings *et al.*, 2002; Davies *et al.*, 2006; Tingay *et al.*, 2007; Rolfsvåg and Danielsen, 2016). These conditions can be estimated petrophysically (Flemings *et al.*, 2003) and occasionally be inferred from seismic observations (Leduc *et al.*, 2013 and **Chapter 6**). The existence of water overpressures at the BGHSZ will reduce the required thickness of FGZs to be at a critical state for free gas migration (Flemings *et al.*, 2003; Hornbach *et al.*, 2004). This condition may be likely along the most deformed parts of accretionary prisms (e.g. the Colombian and Hikurangi margins, **Figs. 7.4b-d**, **7.8c**), where the pore waters are expelled upward and seaward by tectonic processes.

The presence of gas hydrates at and above the three-phase boundary reduces the pore space available for fluid flow (Kleinberg *et al.*, 2003; Nimblett and Ruppel, 2003) and increases the sediment strength and stiffness (Yun *et al.*, 2007; Miyazaki *et al.*, 2011). Consequently, it is expected that an additional overpressure is needed to induce a flux of free gas throughout the GHSZ. Dai and Seol (2014) and Santamarina *et al.* (2015), among others, described the dependency between relative permeability, hydrate micro-habits and *Sh*. These studies show that hydrates preferentially grow in the centre of the pore in sandy coarse-grained sediments. This morphology would decrease the permeability more dramatically, compared to simpler configurations, with hydrates forming at the walls of a capillary tube. In complex pore networks, hydrate formation can be further controlled by the Gibbs-Thomson effect, with only the larger pores capable of hosting gas hydrates (Liu and Flemings, 2011). This preferential hydrate formation in the larger pores can be further enhanced by pore-scale Ostwald-ripening phenomena (Jung and Santamarina, 2012). The occlusion of the larger pores can compromise the effectiveness of capillary invasion of free gas within the GHSZ (see **Chapter 6**).

Therefore, if hydrates occupy an adequate fraction of the pore space, the thickness of an FGZ will increase, in parallel with the sealing efficiency of the BGHSZ. This process helps to explain the occurrence of buoyant FGZ, thicker than ~100 m, within deepwater sandy sediments, having maximum pore radii in the range of ~0.2-50 μm (see **Figs. 7.4a, 7.10a, 7.11c** and **sub-paragraph 7.4.2**). Overall, natural gas hydrate systems can auto-regulate through time and alternate periods of free gas accumulation and periods of leakage throughout the GHSZ, as predicted to occur at the Hydrate Ridge, Blake Ridge, GKL Dome, Vestnesa Ridge and the frontal anticlines of the Guajira Basin (cf. also Bangs *et al.*, 2011; Crutchley *et al.*, 2013 and **Chapter 6**).

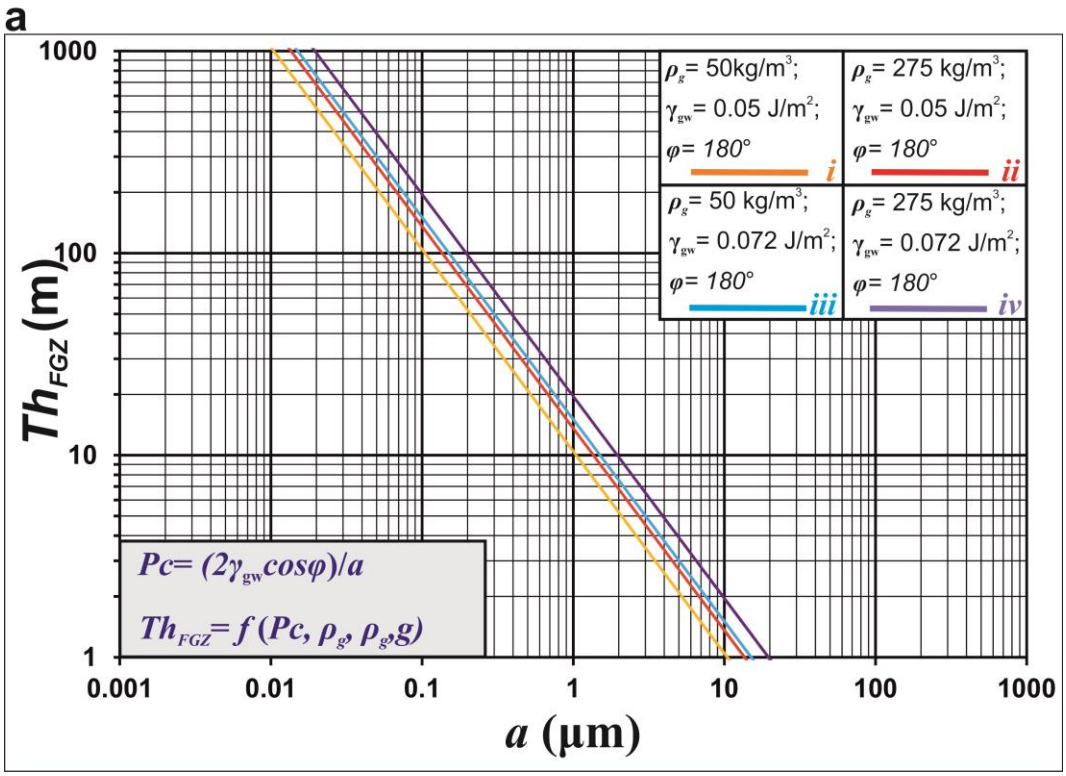



**Figure 7.17. (a)** Variation of $Th_{FGZ}$ *vs* that of the pore throat size (***a***), required to initiate a capillary invasion of free gas in a water-bearing sediment. The Young-Laplace equation (bottom-left) is used to calculate the capillary entry pressure (***Pc***) and therefore the $Th_{FGZ}$ required to activate capillary invasion throughout pore throats equal to ***a***. The smaller the pore throat is, the higher the free gas column will be. Two end-member interfacial tensions ($\gamma$= 0.05 and 0.072 J/m$^2$, cf. Schmidt *et al.*, 2007) and free gas densities ($\rho_g$= 50 and 275 kg/m$^3$) are used to compute ***Pc*** and define four different scenarios (***i, ii, iii, iv***).

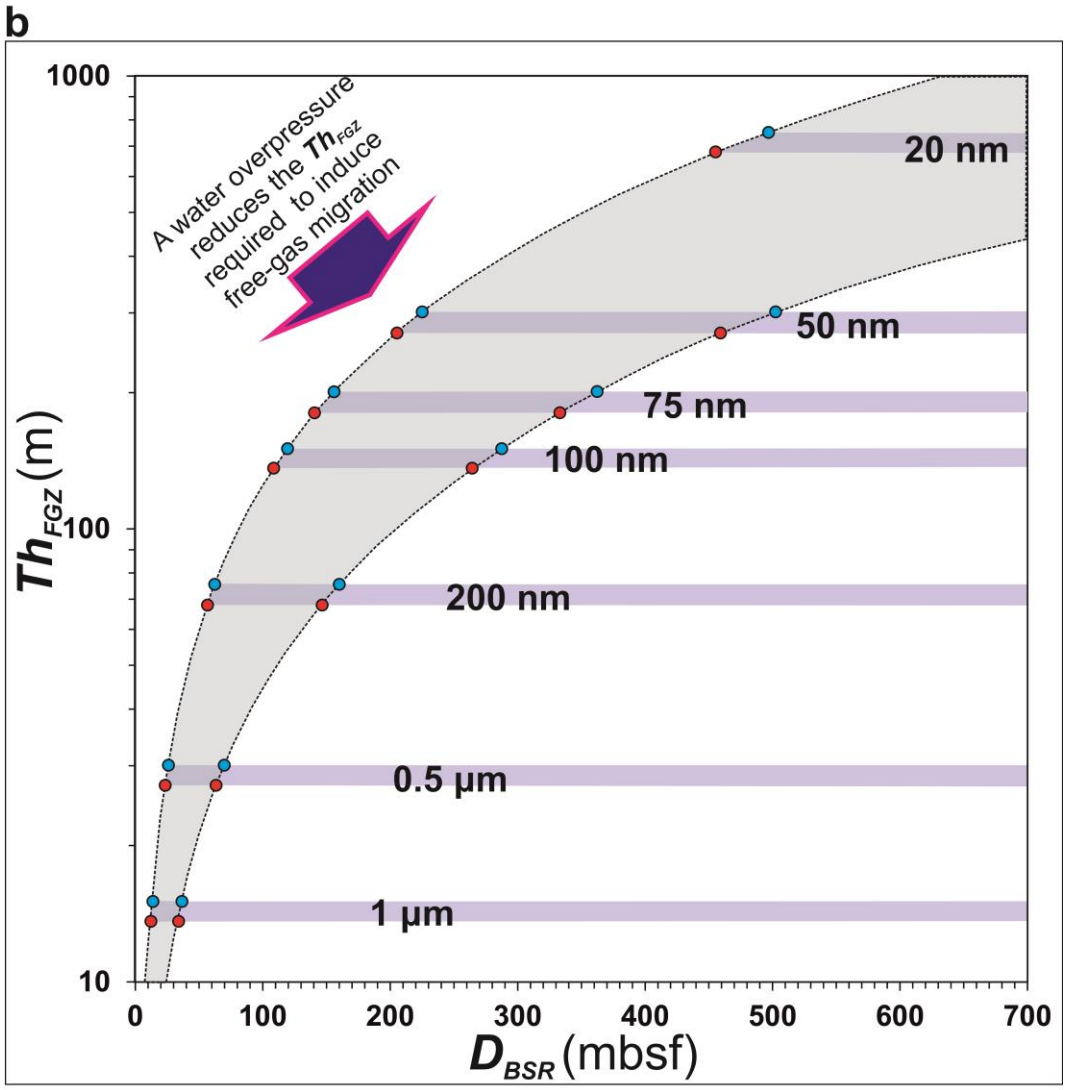



**Figure 7.17. (b)** Variation of $Th_{FGZ}$ at varying $D_{BSR}$, required to initiate hydraulic fracturing (grey-filled envelope), plus ranges of $Th_{FGZ}$ required to reach the capillary entry pressure (***Pc***), and initiate capillary invasion, at discrete values of ***a*** (1 µm, 0.5 µm, 200 nm, 100 nm, 75 nm, 50 nm and 20 nm). The vertical extent of these rectangles is derived considering the combinations (***ii***) and (***iii***) shown in **(a)**. These combinations represent two possible end-members in natural systems because $\gamma$ decreases with increasing pressure whereas $\rho_g$ increases with increasing pressure. With values of ***a*** typical of fine-grained sediments (0.01-0.1 µm= 10-100 nm), buoyant FGZs thicker than ~100 m may form before invasion occurs. However, in these lithologies, hydraulic fracturing is achieved at lower overpressures, especially at shallow overburden. For example, at $D_{BSR}$ of ~100 m in a clay-rich sediment with ***a***~ 50 nm, gas invasion occurs by hydraulic fracturing with $Th_{FGZ}$ equal to ~40-100 m. In contrast, to activate capillary invasion in this sediment, $Th_{FGZ}$ needs to be ~300 m thick. In this case, only at $D_{BSR}$ greater than ~500 m, invasion will be favoured over hydraulic fracturing. Conversely, for micron-sized pore throats (typical of sands and silts), capillary invasion happens even with very thin FGZs (less than ~20 m). The values of ***a*** shown in these figures can also be seen as values of ***2l*** (fracture aperture) if the invasion occurs along plate-like fracture conduits. Thus, fractures wider than 1 µm can allow free gas invasion with very thin (<20 m) buoyant FGZs.

#### *7.5.2.2. Advection of methane-rich water*

The movement of methane-rich fluids throughout the FGZ and the GHSZ is not solely restricted to the free gas phase. Gas hydrates are thought to form, in many cases, from an aqueous solution that achieves supersaturation thresholds within the GHSZ, due to the rapid decrease in methane solubility (Davie *et al.*, 2004). The advection of methane-rich waters ascending from deeper portions of the basin is not completely impeded by the occlusion of the pore space by hydrates because the water, being the wetting phase, is interconnected and probably forms thin films around mineral grains even where hydrate crystals occupy most of the pore space (Tohidi *et al.*, 2001). Hydrate formation would solely decrease the permeability of the medium by increasing the tortuosity of the pore network. Eventually, if hydrates considerably reduce the permeability at the BGHSZ, water overpressures may arise (Daigle and Dugan, 2011). Following Darcy's Law, in the presence of a constant aqueous flux towards the BGHSZ, the existence of a low-permeability layer of gas hydrate-bearing sediments would result in fluid pressure increase proportional to the rate of permeability reduction by hydrate saturation.

#### *7.5.2.3. Diffusion processes and methane solubility near the base of hydrate stability*

Within the GHSZ, at the metre- to cm-scale, physical models and observations indicate that the molecular diffusion driven by solubility gradients between fine and coarse-grained sediments is a critical process, capable of concentrating hydrates in coarse-grained sediments (Malinverno, 2010; Rempel, 2011; Nole *et al.*, 2017).

In the shallow overburden, The zone of highest methane solubility coincides with the BGHSZ (Davie *et al.*, 2004). With few exceptions, methane solubility decreases downward, towards the base of the FGZ and upward, towards the seafloor, with this latter gradient being steeper than that below the BGHSZ (Davie *et al.*, 2004; Haacke *et al.*, 2007). With these imposed conditions and in the presence of free gas at the BGHSZ, a molecular diffusion,

driven by a concentration gradient could represent an auxiliary mechanism for the migration of methane from the BGHSZ upward.

Similarly, within the FGZ, the variability in the methane solubility gradient ($\Delta_{SOL}$) could be considered as a first-order proxy for the effectiveness of large-scale methane diffusion processes beneath the BGHSZ. Our results indicate that thick FGZs form with solubility gradients comprised between ~-7 and ~$0 \cdot 10^{-5}$ mol.$CH_4$ $kg^{-1}$ $m^{-1}$ (***GTG***~25-60 °C/km). FGZs which are consistently thinner than ~50-100 m have been observed in geological settings with more abrupt solubility changes and therefore higher ***GTGs*** (**Fig. 7.16**). It is hypothesised that these latter FGZs are relatively thin because:

**(1)** If an upward advective fluid flow of free gas or methane-rich aqueous fluids encounters a rapid increase in the methane solubility towards the BGHSZ, the formation of an efficiently migrating buoyant phase could be inhibited, and free gas bubbles will evanesce. The FGZ, in such cases, could just be associated with hydrate recycling at the BSR. In this view, a gentle solubility gradient would instead favour the persistence of free gas during an upward migration. This hypothesis accords well with the fact that the thickest FGZs occur in locations where the solubility does not change or slightly decrease with depth. The vast spectrum of $Th_{FGZ}$ observed at gradients between ~-5 and ~0·10-5 mol. CH4 $kg^{-1}$ $m^{-1}$ might, therefore, reflect different rates of methane availability and supply in various geological settings.

For the few locations where a steep solubility gradient (i.e. a high ***GTG***) is associated with thick FGZs, high rates of single and multi-phase advection should be expected. Otherwise, a very thin FGZ would exist. Remarkable examples include the Blake Ridge Diapir, the crest of the anticlines offshore NW Borneo and the Lower Congo Basin. These settings are characterised by relatively high ***GTGs*** (greater than ~50°C/km) and thick FGZs because an efficient advective leakage of gas-rich fluids makes diffusion processes of second-order importance (**Figs. 1.8a, 7.9, 7.11d**).

**(2)** The presence of relatively high geothermal gradients also implies steep solubility gradients within the GHSZ, determining a faster upwardly directed loss of methane from the three-phase boundary by diffusion (Brown *et al.*, 1996; Davie *et al.*, 2004). If diffusion effectively drives methane towards the colder regions, from the BGHSZ upward, it will act in a direction opposite to that postulated for the solubility-curvature mechanism (Haacke *et al.*, 2007). In this case, the diffusion mechanism would be highly directional (cf. Soloviev and Ginsburg, 1997) and could compromise, in high ***GTG*** systems, the presence of thick FGZs beneath the three-phase boundary.

#### *7.5.2.4. Colloidal flow of isolated free gas bubbles*

A final mechanism that deserves some attention for the migration of methane in NGHSs is the flow of isolated free gas bubbles as a colloidal flow (Saunders *et al.*, 1999). This mechanism is considered less effective than a buoyancy-driven flow of a continuous and connected free gas phase, and it is limited by the sizes of the pore and fracture network (Brown, 2000). However, it can be important along permeable systems of fractures, wide enough to favour the ascent of separate bubbles. Boudreau (2012) reviewed the physics beyond free gas bubbles formation and movement in shallow sediments (0-100 mbsf) and highlighted the key role played by fractures in promoting bubble migration.

A quantitative analysis of the competition between the pore network (primary pores and fractures) and the buoyancy of the bubbles dispersed in the sediments (Algar and Boudreau, 2010; Algar *et al.*, 2011a) at P-T conditions typical of FGZs (e.g. ***Pv***~1-5 MPa and T~10-25 °C) is the key to understand the effectiveness of such mechanism. At such depths, the colloidal flow of gas bubbles could be limited by the small pore sizes, the high stress and the absence of large fractures. In contrast, the observation of bubble streams emanating from seep sites in different hydrate provinces, coupled with the evidence of seafloor doming (Barry *et al.*, 2012) suggest that this process may occur in the first tens of metres of sediment at sites of active seepage and near the *'hydrate-wedge'*, where the BGHSZ is located at low effective stress conditions.

### *7.5.3. Triggering events*

The accumulation of free gas in an FGZ and its migration into the GHSZ are controlled, respectively, by the availability of methane in the system and by the onset of critical pressure gradients which compete with the local state of stress and the pore network. The triggers for this fluid migration are associated with a variety of geological processes that affect the pressure and thermal state of the system, as well as its lithological skeleton. These processes include e.g. **(1)** a tectonic event (e.g. compression, uplift, fault displacement), **(2)** a sea-level fall, **(3)** a temperature increase; **(4)** a removal of the overburden owing to submarine landslides and **(5)** leakage of free gas from deep reservoir towards the FGZ (cf. Xu and Germanovich, 2006; Liu and Flemings, 2009; Holtzman and Juanes, 2011; Sultan *et al.*, 2011; Hermanrud *et al.*, 2013; Ostanin *et al.*, 2013; Imbert *et al.*, 2014; Goto *et al.*, 2016; see also **Chapter 4**). As discussed earlier (**sub-paragraph 7.4.2.** and in **Chapter 4**), these events can facilitate the onset of overpressure conditions, as well as the generation of faults and other cross-stratal conduits for fluid flow.

In particular, the onset of water overpressures owing to the poroelastic effects (Liu and Flemings, 2009) may be relevant for those FGZs in fine-grained lithologies (i.e. under undrained conditions), even if immobile and characterised by small *Sg*, which are subjected to either an uplift or a sea level fall. The presence of a low *Sg* (e.g. 1-10%) is enough to increase the compressibility of the media. The amount of water overpressure generated after an uplift or a sea level fall will be a function of the reduction in the water column, of the free gas saturation and its compressibility at in situ conditions. This mechanism can explain episodic events of fluid flow of free gas throughout the GHSZ, even if the FGZ is apparently sub-critical or immobile (**Fig. 7.18a**).

The movement of fluids throughout the GHSZ can be associated with regional tectonic events. For example, earthquakes along the convergent margins offshore Pakistan and Costa Rica have been shown to trigger seepage of free gas across the GHSZ (Mau *et al.*, 2007;

Fischer *et al.*, 2013). In a different setting such as the Vestnesa Ridge, which is a region of active extension and strike-slip deformation, the changes in the tectonic stress and the glacial cycles have been associated with the episodic release of free gas throughout the GHSZ across sub-vertical faults and fractures (Plaza-Faverola *et al.*, 2015).

A further destabilising factor for gas hydrate stability is an increase in the temperature at the BGHSZ. The observation of multiple BSRs at different sites worldwide (see **Fig. 1.31**) has been associated with the rapid temperature increase following the Last Glacial Maximum, which has shifted the BGHS upward (Foucher *et al.*, 2002; Bangs *et al.*, 2005). A combined temperature and pressure perturbation on hydrate stability will also follow episodes of ice sheets formation/loading and retreat/unloading. Recently, blow-out craters and mounds, accompanied by acoustic flares in the water column, have been observed in the Barents Sea and offshore Svalbard (Andreassen *et al.*, 2017; Serov *et al.*, 2017). The authors suggested that these observations are evidence that the BGHSZ re-equilibrated at shallower depths, after glacial unloading and temperature warming, and methane leakage from the hydrate reservoir (due to dissociation) and the underlying FGZ (due to leakage) has continuously occurred since the retreat of the ice sheets. Similarly, Plaza-Faverola *et al.* (2011) observed that a cross-stratal fluid flow in the form of pipe-like features occurred episodically, in response to overpressure buildups in free gas reservoirs, triggered by sea-level cycles and the accumulation of thick glacigenic debris.

Shorter timescales, governed by decadal to seasonal warming, may impact hydrate stability along continental slopes, by modifying the depth of the *'hydrate-wedge'* and increase the seepage of methane in the water column (Westbrook *et al.*, 2009; Brothers *et al.*, 2014; Skarke *et al.*, 2014). Furthermore, the role of tides in controlling the migration of free gas seepage in hydrate provinces has been recently hypothesised by Krabbenhoeft *et al.* (2013) and Römer *et al.* (2016). The primary factor responsible for such fluid flux is the hydrostatic pressure drop following falling tides, with a propagation effectiveness in the

overburden proportional to its permeability (Wang and Davis, 1996; Tryon *et al.*, 2002). Such pressure drops could cause the internal gas pressure of a shallow free gas pocket to meet sediment failure criteria and generate or re-open fractures (Scandella *et al.*, 2011; Boudreau, 2012). However, it is possible that the accumulation of water overpressure due to poroelasticity could be substantial too, under undrained conditions. For example, a free gas pocket close to the seabed could be sealed by low-permeability sediments or surrounded by pure hydrate. Assuming tidal excursions in the order of ~5 m, the water overpressure exerted by a shallow gas pocket with ~10-50% *Sg* would be relatively similar to the buoyancy of a ~2.5-5 m thick internally-connected gas pocket, especially at shallow water depths (**Fig. 7.18b**).

The impact of the dissociation of gas hydrates on overpressure generation has been subject to several studies. Large overpressures, up to tens of MPa, were predicted to form by Xu and Germanovich (2006). However, the fact that the onset of overpressures would, theoretically, induce the self-preservation of hydrate stability, has somehow downsized the importance of such mechanism. Hydrate dissociation would become relevant only at kinetic rates higher than those of pressure drainage (Holtzman and Juanes, 2011). In fine-grained sediments, gas hydrates typically occur with a fracture-filling morphology. Their dissociation would result in the presence of gas and water filled cracks, with a capacity to propagate upward that is balanced by the competition between the fracture toughness and the stress intensity of the fracture at its upper tip (Jin *et al.*, 2015). Overall, various triggers may regulate the fluid flow from the BGHSZ to the seafloor. Their relative importance depends on local internal and external factors.

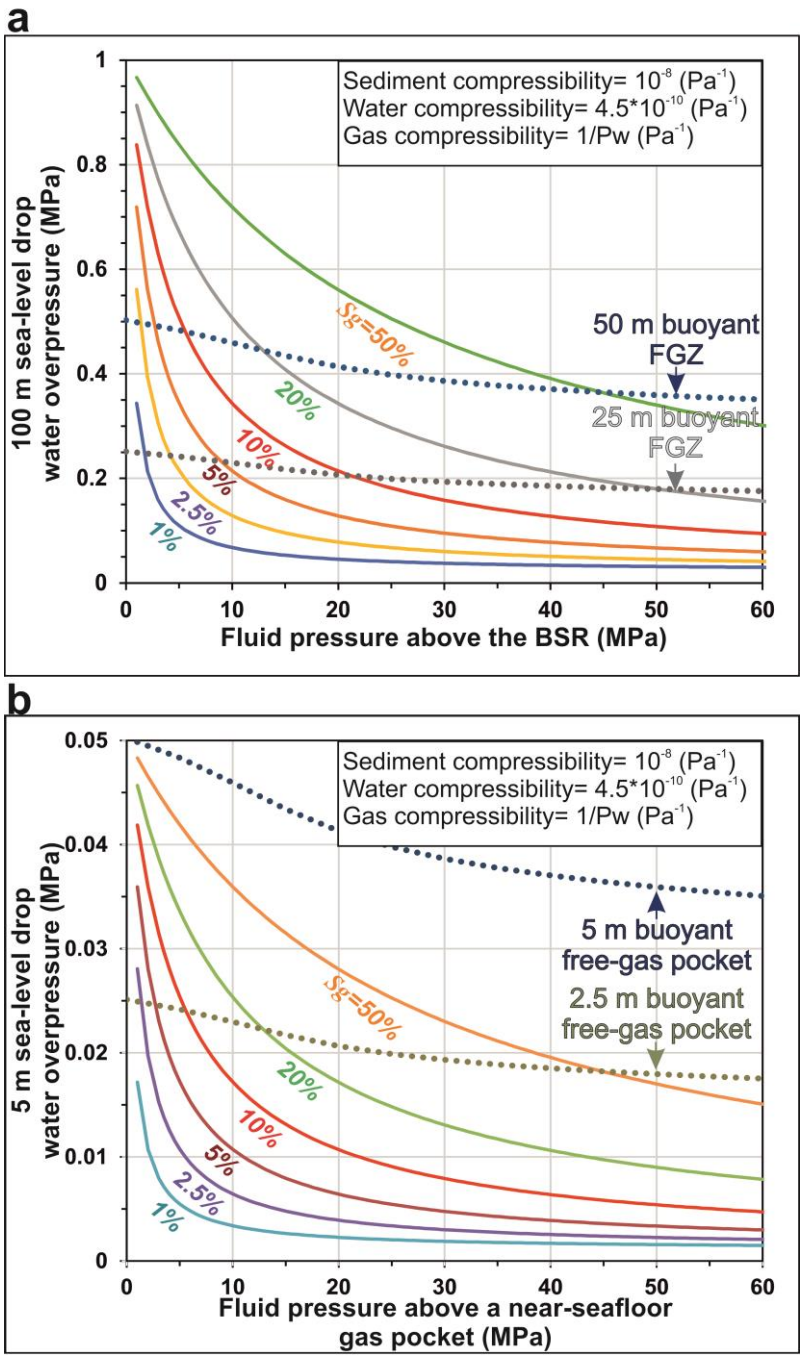



**Figure 7.18.** Water overpressure generated by **(a)** a sea level drop of 100 m and **(b)** a tidal excursion of 5 m, at various *Sg* (1-50%) and hydrostatic pressures above a given free gas accumulation (considering a water density of 1025 kg/m$^3$). The sediment, water and gas compressibility, as well as the resulting water overpressure, have been calculated following Liu and Flemings (2009). This water overpressure is effective only under undrained conditions. Note how the water overpressure increases at low hydrostatic pressures (i.e. at shallow waters and low effective stress). For reference, the overpressures generated by buoyant FGZ of 25 and 50 m thickness are shown with dotted lines in **(a)**. Similarly, the overpressures related to a 2.5 and a 5 m thick buoyant free gas pocket are shown in **(b)**.

### *7.5.4. Classification of free gas zones*

The observation and the interpretation of free gas zones from many different gas hydrate provinces performed in this review allow identifying five criteria which form the basis for a classification of free gas zones (**Figs. 7.19** and **Tabs. 7.4, 7.5**). These criteria are: (**1)** The fluid flux, which can be vertically-focused, controlled by stratigraphy etc.; **(2)** The stratigraphic heterogeneity (i.e. high-permeability *vs* low-permeability sediments); **(3)** The dip of stratigraphic reflections; **(4)** The shape of the BSR with respect to pressure (i.e. the water depth), temperature (i.e. the geothermal gradient and the seabottom temperature) and salinity anomalies; **(5)** The geothermal gradient, which can influence, in particular circumstances, the thickness of an FGZ.

The relative importance of these parameters defines eight classes of FGZ, characterised by different levels of **(1**) prospectivity of the overlying gas hydrate reservoir, **(2)** geohazard and **(3)** Climate sensitivity, related to the feasibility of free gas migration from the FGZ towards the water column (**Tab. 7.4, Fig. 7.19**). Hence, assessing the selected five criteria could help in evaluating the prospectivity, the geohazard and the climate sensitivity of a gas hydrate province, or a particular prospect. Importantly, certain FGZs may change laterally from one class into another, following the variations of the controlling parameters. Finally, over geological times, the structural evolution of a certain area will inevitably impact the NGHS. Consequently, an FGZ can evolve from one class into another one.

#### *7.5.4.1. Type-A free gas zones (FGZs-A)*

FGZs-A are hosted within homogeneous fine-grained sediments with low to zero stratigraphic dip angles. It is possible to distinguish a high-flux (named $A_1$) and a low-flux (named $A_2$) end-member. FGZs-$A_1$ are characterised by a BSR disrupted by vertical fluid flow pathways and faults. The three-phase boundary is vertically and transiently extended along these pathways, and seepage at the seafloor is the natural consequence, with an effective methane escape in the water column at fluid flux velocities able to exceed ~1 m/y

(Luff and Wallmann, 2003; Wallmann *et al.*, 2006b). At the seafloor, it is possible to recognise pockmarks, hydrate pingoes and carbonate mounds. In the overburden, along the vertical fluid flow pathways, hydrates, free gas pockets or buried carbonate mounds can occur and be seismically identifiable (e.g. **Chapter 4** and Ho *et al.*, 2012; Serié *et al.*, 2012; Koch *et al.*, 2016). FGZs-$A_1$ have been recognised in those portions of sedimentary basins with vigorous fluid fluxes at the crests of anticlines. Less commonly, these FGZs develop in the flat portions of minibasins, separating structural highs (**Figs. 7.4, 7.7, 7.8, 7.9-7.11**). This FGZ is typical but not exclusive of those basins characterised by the migration of thermogenically-sourced fluids towards the GHSZ (e.g. NW Borneo, offshore Nigeria, Lower Congo Basin, Gulf of Mexico, see also **Tab. 7.3**).

The distribution of gas hydrates is controlled by a *'background'* low-intensity advection methane-rich fluids (fluid fluxes of ~$10^{-3}$ m/y) and a localised free gas migration along fluid flow pathways (highly variable fluid fluxes in the order of ~$10^{-2}$ to $10^{1}$ m/y). Along these pathways, it is possible to encounter columnar zones of extremely high hydrate saturation (>50%) (cf. **Chapter 4** and Sultan *et al.*, 2007; Riedel *et al.*, 2010a; Torres *et al.*, 2011; Matsumoto *et al.*, 2017). Such deposits could be a prospective target in these gas hydrate systems, although nowadays not economically recoverable (Boswell *et al.*, 2016).

The fact that FGZs-$A_1$ are associated with fine-grained sediments makes the cross-stratal migration through hydraulic fracturing the favourite mechanism for fluid flux. The thickness of these FGZs is often difficult to constrain (Wood *et al.*, 2002; Koch *et al.*, 2016) but can approach that required to generate critical buoyancy pressures (**Fig. 7.14a, c**). The triggering events discussed earlier control the processes of free gas leakage across the GHSZ. The geohazard potential of FGZs-$A_1$ is mostly related to the presence of overpressured free gas and aqueous fluids at the BGHSZ and along fluid flow conduits.

FGZs-$A_2$ are observed at the crest of gentle folds or in relatively flat areas of sedimentary basins. The FGZ is characterised by a cluster of segments of enhanced

amplitudes beneath a BSR, with the base of the FGZ occasionally displaying a flat spot, i.e. a gas-water contact. The internal connection between different free gas-bearing layers may be compromised by the interbedding of low permeability layers. FGZs-$A_2$ have been observed along tens km-sized ridges (e.g. the Blake Ridge) (Holbrook *et al.*, 1996; Holbrook, 2001) (**Fig. 7.11b**), polygonally-faulted intervals in passive margins (e.g. the Norwegian margin), as well as the abyssal plains and foreland basins (e.g. the outer portion of the Guajira Basin and the Pegasus Basin, **Figs. 7.5a, b, 7.8e, f**). Here, without cross-stratal pathways for fluid flow, the hydrate distribution is controlled by the advection of methane-rich aqueous fluids (in the order of ~$10^{-4}$ to $10^{-3}$ m/y) and by diffusion processes. Being a low-flux analogue of FGZs-$A_1$, FGZs-$A_2$ are characterised by minor geohazards, less capacity to leak free gas towards the seafloor and a reduced prospectivity.

#### *7.5.4.2. Type-B free gas zones (FGZs-B)*

The presence of lithological heterogeneities and marked permeability contrasts are the primary characteristic of these FGZs. The three-dimensional changes in permeability control the flux of methane-rich fluids and the accumulation of free gas beneath the BGHSZ and hydrates above. Depending on the dip of stratigraphic horizons with respect to the BGHSZ, FGZs-B are divided into two classes, named $B_1$ (high dip angles) and $B_2$ (low dip angles).

FGZs-B1 are characterised by **(1)** cross-cutting relationships between the BSR and the host stratigraphy, which dips at angles of ~5-15° and **(2)** depositional elements (commonly deepwater turbidites) with a relatively high intrinsic permeability. The free gas-bearing horizons below the BGHSZ display enhanced amplitudes for a variable vertical extent in seismic sections. FGZs-$B_1$ generate the thickest free gas columns (**Figs. 7.4a, 7.10e, 7.11c**) observed in this study, although they are only occasionally at critical conditions for hydraulic fracturing (e.g. **Fig. 7.14e, f**).

In some circumstances, enhanced reflections with positive acoustic impedance contrast are observed within the GHSZ, indicating pore-filling hydrates at high saturation

(>40-50%) (Boswell *et al.*, 2016) (**Fig. 7.4a,** see **Chapter 6**). Therefore, FGZs-$B_1$ are associated with the most prospective gas hydrate reservoirs and have been identified in a variety of geological settings (e.g. the Guajira Basin, the region offshore NW Borneo, the Terrebonne Basin, the Cascadia margin, the Hikurangi margin, the Nankai Trough and the Lower Congo Basin, see also **Tab. 7.3**).

These FGZs typically form at the flanks of anticlines (generally at the backlimbs if the anticline is asymmetric) (e.g. **Figs. 7.4g, h, 7.9d, e**). The geohazard of these FGZs depends on the overpressures developed below the BGHSZ. The free gas can be delivered to the oceans only in the presence of fluid fluxes elevated enough to channelise free gas throughout the GHSZ up to the seafloor, without forming hydrates. However, these FGZ appear, in many cases, not directly associated with evidence of seafloor gas seepage and methane fluxes, and would instead favour the accumulation of gas hydrates. Nevertheless, if vertical pathways intersect these dipping and coarse-grained sediments, the methane-flux can be efficiently and vertically redirected towards the seabed (Tréhu *et al.*, 2004a; Bangs *et al.*, 2011) (**Figs. 7.4a, g, h, 7.10a**).

In contrast, the characteristics of FGZs-$B_2$ are mostly controlled by the primary stratigraphic architecture of the system, given the nearly horizontal dipping angle of stratigraphic reflections. This FGZ occurs in geological settings dominated by turbidites, mass-transport deposits, canyons and contourite drifts. These elements interrupt an otherwise monotonous hemipelagic sedimentation pattern and define the three-dimensional distribution of the coarse-grained facies, where free gas and hydrates preferentially occur. The interplay between the sand-rich facies and the BSR dictate the three-dimensional distribution of free gas, in the presence of an adequate supply (**Fig. 7.12e, f**).

Gas hydrates at elevated saturation are confined to the sand-rich facies. In some cases, the same channel or levee complex, if cross-cut by the BGHSZ, can host both gas hydrates and free gas (Zhang *et al.*, 2012) (**Fig. 7.12f**). FGZs-$B_2$ have been observed in a variety of

geological settings and represent an important class of FGZ in three gas hydrate provinces of increasing scientific and economic importance, i.e. the Danube Fan, the Shenhu Area (South China Sea) and the Mahanadi Basin (Shankar and Riedel, 2014; Wang *et al.*, 2014; Zander *et al.*, 2017). The geohazard related to these FGZs depends primarily on the recent burial and sedimentation history, which may have or not favoured the creation of water overpressures. Similarly to FGZs-$A_2$, even if the total thickness of these FGZs may fall into the criteria for buoyancy-driven hydraulic fracturing, the presence of low-permeability intervals can inhibit the formation of thick and buoyant FGZs. If the FGZ is adequately sourced by deeply-rooted structural conduits, a combination of FGZs $A_1$ and $B_2$ can occur, as observed in the Green Canyon (Gulf of Mexico) (Haines *et al.*, 2017).

#### *7.5.4.3. Type-C free gas zones (FGZs-C)*

The key characteristic of these FGZs is that the BGHSZ is discordant with respect to the seafloor, mainly in response to changes in pressure and temperature in the system. For this reason, FGZs-C are divided into $C_1$ (temperature dependent) and $C_2$ (pressure dependent). FGZs-$C_1$ are influenced by perturbations in the thermal field and may exhibit *'dome-shaped'* three-phase boundaries, capable of trapping free gas below. Typical examples are related to anomalous heat flows associated with e.g. salt diapirs, faults and mud volcanoes, with a secondary effect played by pore water salinity variations (Taylor *et al.*, 2000; Van Rensbergen *et al.*, 2002; Crutchley *et al.*, 2014) (**Figs. 7.4e, f, 7.7c, d, 7.12b**).

Two well-known regions where such FGZs can occur are the Lake Baikal, where extraordinary km-scale changes in the thermal field determine an incredibly irregular BGHSZ (Vanneste *et al.*, 2003) and the Gulf of Mexico, where the presence of thermogenically-sourced gases further complicates the prediction of the depth of the BGHSZ (Macelloni *et al.*, 2015). Less extreme examples of a BGHSZ influenced by thermal advection have been recognised in the Krishna-Godavari Basin (Dewangan *et al.*, 2011) and in the southern Hikurangi margin (Pecher *et al.*, 2010), where fluid fluxes estimated from

thermal anomalies are in the order of $10^{-4}$ to $10^{-2}$ m/y. However, in the presence of proper mud volcanoes, the fluid flux associated with these FGZs can exceed that characterising seeps in FGZs-$A_1$, even during dormant phases (Milkov *et al.*, 2003). The gas hydrate deposits associated with mud-volcanoes are likely subjected to cycles of formation and decomposition, depending on the episodes of eruption (Pape *et al.*, 2014). The hydrates and the free gas stored in such system are probably among the most dynamic (Milkov *et al.*, 2003). However, similarly to gas hydrates associated fluid escape pipes, the prospectivity of gas hydrates accumulated in mud-volcano systems is low at present day.

FGZs-$C_2$ are encountered along continental slopes, where the water depth changes relatively rapidly. Even if the dip of the stratigraphic horizons is consistent with that of the seafloor, a cross-cutting relationship occurs along the *'hydrate-wedge'* (Rajan *et al.*, 2012; Davies *et al.*, 2015) (**Fig. 1.29a**). These FGZs can be exceptionally thick (≥100-200 m) along thin stratigraphic reflections (Davies and Clarke, 2010; Yoo *et al.*, 2013) (**Fig. 7.12a**). The accumulation of high-quality gas hydrate reservoirs could be not favoured by the paucity of sandy facies, given that these areas are mainly sediment by-pass settings, where submarine erosion dominates (Davies *et al.*, 2012) and the deposition is mostly hemipelagic.

The geohazard related to these FGZs is principally focused to the possible overpressures and fluid expulsion near and at the pinch-out between the BGHSZ and the seafloor. Being that the overburden is vertically-limited at such locations, thin accumulations of free gas can be enough to promote sediment failure and free gas venting. It is probable that fluid flux at these shallow depths operates with more frequency than in deeper parts of the basins because the overpressure required for free gas leakage can be achieved even by short-term processes (e.g. tides, currents and decade-scale warming) For this reason, FGZs-$C_1$ are the most sensitive to global warming and may be associated with either seasonal or permanent hydrate destabilisation (Phrampus and Hornbach, 2012; Phrampus *et al.*, 2014; Ruppel and Kessler, 2017).

#### *7.5.4.4. Type-D free gas zones (FGZs-D)*

FGZs-D are very thin, less than ~50 m and are seismically represented either by solely a BSR or by a BSR plus few enhanced reflections underneath it. The BSR can be either continuous over large distances or patchy, depending on local variations in lithology and fluid flux. This FGZ is observed in both active and passive margins (Brown *et al.*, 1996; Mosher, 2011; Bai *et al.*, 2016).

These thin FGZs could result from either a homogeneous in-situ generation of methane and subsequent hydrate recycling or fluxes from below the BGHSZ of pore waters dominantly undersaturated in methane. Gas hydrates are expected to be distributed at low saturation (e.g. less than 5%). *Sg* is probably at low saturation too, with the free gas distributed solely in the bigger pores (Bai *et al.*, 2016). However, along tectonically complex settings, the observation of such thin BSRs is not a guarantee for low fluid fluxes. These BSRs could instead be related to either elevated solubility gradients beneath and above the BGHSZ (i.e. elevated ***GTGs***), which would not favour the migration of methane as a free-phase, or to elevated fluxes of aqueous and potentially overpressured fluids. Therefore, it is possible to split FGZs-D into two classes, named $D_1$ (high fluid flux, in the order of ~$10^{-3}$ to $10^{-2}$ m/y, and potentially high ***GTG*** , i.e. more than ~60°C/km) and $D_2$ (low fluid flux, in the order of ~$10^{-4}$ m/y). Only FGZs-$D_1$ can be a geohazard and a source of methane-rich fluids for the oceans.

| *7.4a* | ***Lithology*** | ***Stratigraphic dip*** | ***Fluid flux*** | ***Does the BGHSZ mimic the seafloor?*** | ***Geothermal gradient*** |
|---|---|---|---|---|---|
| ***$A_1$*** | Homogeneous and fine-grained | Near horizontal | High | Locally not (focused fluid flux) | Constant at the km-scale |
| ***$A_2$*** | Homogeneous and fine-grained | Near horizontal | Low | Yes | Constant at the km-scale |
| ***$B_1$*** | Presence of sand-rich facies | Dipping (5-15°) | Variable | Yes | Constant at the km-scale |
| ***$B_2$*** | Presence of sand-rich facies | Near horizontal | Variable | Yes | Constant at the km-scale |
| ***$C_1$*** | Variable | Variable | Typically high | No (thermal and salinity perturbations) | Extremely variable at the km-scale |
| ***$C_2$*** | Variable | Variable | Variable | No (the hydrostatic pressure changes along the slope) | Constant at the km-scale |
| ***$D_1$*** | Variable | Variable | *High | Locally not (focused fluid flux) | Potentially High |
| ***$D_2$*** | Variable | Variable | Low | Yes | Variable |

| *7.4b* | **Climate sensitivity** | **Geohazard** | **Hydrate prospectivity** |
|---|---|---|---|
| ***$A_1$*** | Moderate (related to fluid flux activity, water depth, latitude) | High (related to fluid flux activity, presence and magnitude of overpressure) | Low (pipe-like conduits are not currently prospective) |
| ***$A_2$*** | Low (hydrates and free gas are far from the seafloor) | Moderate (related to the presence and magnitude of overpressure) | Low |
| ***$B_1$*** | Low (hydrates and free gas are far from the seafloor) | Moderate/High (related to fluid flux activity, presence and magnitude of overpressure) | High (the dip of the layering is ideal to focus methane fluxes into the GHSZ) |
| ***$B_2$*** | Low (hydrates and free gas are far from the seafloor) | Moderate/High (related to fluid flux activity, presence and magnitude of overpressure) | Moderate (in the presence of elevated fluxes of methane these systems can become highly prospective) |
| ***$C_1$*** | Moderate (related to fluid flux activity, water depth, latitude) | High (related to fluid flux activity, presence and magnitude of overpressure) | Low (unless associated with sand-rich deposits) |
| ***$C_2$*** | High (related to temperature perturbations at the *'hydrate-wedge'*, fluid flux activity, latitude) | High (related to fluid flux activity, presence and magnitude of overpressure) | Low (unless associated with sand-rich deposits) |
| ***$D_1$*** | Moderate (related to fluid flux activity, water depth, latitude) | High (related to fluid flux activity, presence and magnitude of overpressure) | Low (methane supply is limited, despite the high fluid fluxes) |
| ***$D_2$*** | Low (hydrates and free gas are far from the seafloor) | Low (fluid flux and overpressure are limited) | Low (methane supply is limited) |

**Table 7.4. (a)** Characteristics of each type of FGZ, based on the five main factors considered in the discussion (fluid flux, lithology, stratigraphic dip, shape of the BSR, geothermal gradient). *The fluid flux is high but dominated by aqueous fluids, undersaturated in methane. **(b)** Climate sensitivity, geohazard and Prospectivity for gas hydrates related to each class of FGZ.

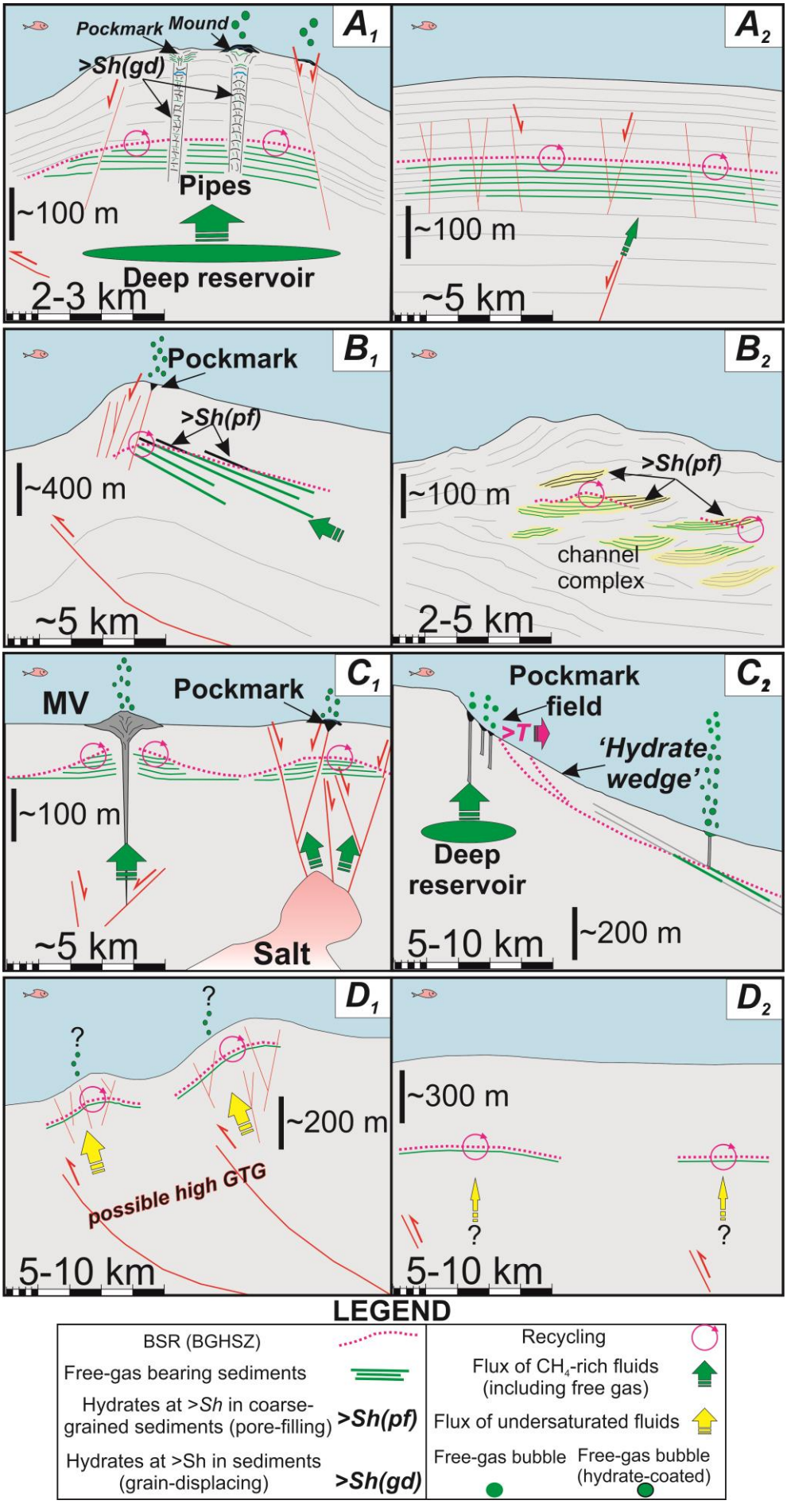



**Figure 7.19.** Schematic sketches, showing the principal characteristics of each class of FGZ.

## 7.6. Conclusions

This study has analysed and reviewed the potential overpressures associated with free gas zone and the processes of fluid flow in natural gas hydrate systems. The major findings are:

**(1)** The conditions for hydraulic fracturing or fault reactivation represent constitute the upper mechanical boundaries for the thickness of an FGZ. The data collected in this study indicates both potentially critical and sub-critical FGZs in diverse geological settings. The view that thin FGZs solely characterise tectonically compressive margins oversimplifies the natural gas hydrate systems in such complex contexts, which can instead be locally associated with hundreds of metres of free gas columns, potentially buoyant. Importantly, the presence of sources of overpressure other than buoyancy, the possible existence of an immobile free gas zone and the lack of connection between stacked free gas-bearing layers should always be considered in evaluating an FGZ.

**(2)** The thickest and potentially critical FGZs are seismically characterised by the presence of vertical pathways for fluid flow, dipping stratigraphic reflections and a BGHSZ (i.e. the BSR) close enough to the seafloor (i.e. a relatively low overburden stress counteracting the overpressure).

**(3)** Free gas migrates across the GHSZ by both capillary invasion and hydraulic fracturing, with the latter phenomenon favoured at shallow burial depths in fine-grained sediments. However, the two mechanisms can also occur in the same evolving system. The presence of hydrates at high saturation can enhance the maximum thickness that an FGZ can reach. In contrast, the presence of a permeable fracture network facilitates fluid flow at lower degrees of overpressure.

**(4)** The formation of thick FGZs could be inhibited in the presence of high geothermal gradients, which impact the methane solubility gradients and, potentially, diffusion processes, within and below the BGHSZ.

**(5)** The likely triggers for free gas migration across the GHSZ are related to episodic and cyclic tectonic or climatic events. Such events facilitate the onset of critical conditions, by increasing the mobility of the free gas phase and by producing water overpressures.

**(6)** The most climate-sensitive free gas zones are located along continental slopes, where the BGHSZ pinches-out at the seafloor. Conversely, the free gas zones related to the most prospective hydrate deposits are associated with dipping and heterogeneous stratigraphic successions, where the flux of methane is preferentially focused along permeable pathways.

**(7)** The biggest unknowns in evaluating an FGZ are associated with the determination of the critical free gas saturation for the generation of a mobile phase, the understanding of the mode of distribution of free gas in shallow and relatively unconsolidated sediments and the state of stress conditions near the BGHSZ.

**(8)** At this stage, this chapter represents a work in progress, given the presence of a number of critical uncertainties and approximations, the most important being the assumption of constant P-wave velocities for the determination of $\boldsymbol{D_{BSR}}$ and $\boldsymbol{Th_{FGZ}}$, the neglection of overpressures and capillary effects for the calculation of ***GTGs***, as well as the assumed fracture criteria. This latter element certainly needs to consider the tensile strength associated with sediment-hosted gas hydrates, which likely results in additional overpressure required for fracture initiation. Concurrently, the occurrence of poroelastic effects on the horizontal stress, in the presence of overpressures (see Appendix**, sub-paragraph 7.7.1**), still to be directly evaluated on the shallow sediments that characterise natural gas hydrate systems.

## 7.7. Appendix

### *7.7.1. Hydraulic fracturing*

In this review, a simple hydraulic fracture generation criterion has been adopted, where a critical stress is reached if overpressure (i.e. the pore fluid pressure in excess of hydrostatic, e.g. generated by the buoyancy of a gas column) equals the effective overburden stress. This criterion has been used in many previous publications reporting, discussing and modelling the fluid flow in NGHSs (Flemings *et al.*, 2003; Tréhu *et al.*, 2004a; Daigle and Dugan, 2010a; Daigle *et al.*, 2011). Other studies suggested a model where hydraulic fractures generate if the excess pore fluid pressure exceeds the minimum effective stress at hydrostatic conditions plus the rock tensile strength, frequently assumed to be close to zero in shallow sediments (Daigle and Dugan, 2010b). However, this latter assumption does not consider the poroelastic effects, induced by pore pressure increases, on the minimum stress, assumed to be horizontal (Engelder and Fischer, 1994) and defined by the following equation (assuming hydrostatic conditions):

$$\boldsymbol{Ph = kPv + \alpha(1 - k)Pw_{sf}} \quad \textbf{(1)}$$

Where ***Ph*** is the minimum horizontal stress, ***Pv*** is the vertical (overburden) stress, $\boldsymbol{Pw_{sf}}$ is the hydrostatic pressure (measured from the sea/lakefloor), $\boldsymbol{\alpha}$ is the Biot's coefficient of effective stress, which approaches unity at porosities typical of gas hydrate systems (Lee, 2002), and ***k*** is a function of the Poisson ratio (***ν***), according to:

$$\mathbf{k = \nu/(1 - \nu)} \quad \textbf{(2)}$$

Considering **Equation 2**, ***Ph*** under overpressure conditions becomes:

$$\boldsymbol{Ph = kPv + \alpha(1 - k)(Pw_{sf} + \theta OP)} \quad \textbf{(3)}$$

Where ***OP*** is the fluid pressure in excess of hydrostatic, for example, due to the buoyancy of a gas column (***Pg***). Hence, the total fluid pressure in the sediment column (***Pf***) is:

$$\boldsymbol{Pf = (Pw_{sf} + OP)} \quad \textbf{(4)}$$

Following the arguments Mourgues *et al.* (2011), the variation of the minimum stress in relation to overpressure depends on $\boldsymbol{v}$, $\boldsymbol{\alpha}$ and the width of the source of fluid overpressure, here expressed with an arbitrary parameter ($\boldsymbol{\theta}$), assumed to be 1 in uniaxial models (widespread *'basin-scale'* overpressure) and 0.5 if the ratio between the width of the overpressure source and the overburden tends to zero (i.e. with a *'localised'* overpressure). The variation of ***Ph*** related to an increase in ***Pf*** can thus be expressed by this equation:

$$\boldsymbol{\Delta Ph/\Delta Pf = \theta\alpha(1-k)} \quad \textbf{(5)}$$

Therefore, it is possible to quantify the increase in ***Ph*** with respect to the overburden stress (***Pv***), under overpressure conditions, before that the total fluid pressure exceeds ***Ph***, assuming here the range of conditions defined in **Tab. 7.5**.

According to **Equation 1** and the parameters defined in **Tab. 7.5**, at hydrostatic conditions, ***Ph/Pv*** varies between approximately 0.85 and 0.97, with ***Pf/Ph*** ranging from 0.57 to 0.65, mostly depending on ***v*** (related to the lithology and degree of sediment consolidation), which has been varied between 0.40 and 0.48 (**Fig. 7.20**) (Hamilton, 1979; Hornbach *et al.*, 2004; Lee *et al.*, 2010a).

In the presence of overpressures, the total fluid pressure (***Pf***) becomes progressively higher. Concurrently, the ratio between ***Ph*** and ***Pv*** approaches one. Hence, ***Pf*** equals ***Ph*** only where ***Ph*** is higher than ~0.9-0.95***Pv*** (i.e. 90-95% of lithostatic, **Fig. 7.20**). Ratios very close to one are obtained at higher ***v*** (i.e. with softer and more unconsolidated sediments). Importantly, by varying the bulk density of the sediment between 1700 and 2000 kg/m$^3$, only minimal changes in these ratios have been observed (not shown here).

If ***Pf*** equals ***Pv*** (***OP=Pv'***), ***Ph*** equals ***Pv*** in the uniaxial models (**θ=1)**, with a hypothetical Mohr circle becoming a point, independently of the input parameters. A localised overpressure, however, would keep ***Ph*** lower than ***Pv***, preventing the onset of

liquefaction phenomena or the generation of horizontal fractures and rather favouring the formation of tensile vertical fractures. In the case of an extremely localised overpressure (**θ** =0.5), ***ΔPv*** and ***ΔPf*** would become coupled as well (Mourgues *et al.*, 2011).

If the sediment overlying the source of overpressure is cohesive or if its strength is enhanced by the presence of gas hydrates, we would expect higher ***Pf/Ph*** ratio before that hydraulic fractures could form (Yun *et al.*, 2007; Waite *et al.*, 2009; Daigle and Dugan, 2010a). The cohesion of an unconsolidated sediment is in the order of ~0.5 MPa and can increase up to ~1.5 MPa in the presence of hydrates. These values become progressively more relevant if the overpressured zones are at shallow depths. In the presence of significant amounts of hydrates in the sediments, ***v*** is predicted to decrease, and a decrease of ***v*** is expected in free gas-bearing sediments too (Tinivella and Accaino, 2000; Lee *et al.*, 2010a). Therefore, the presence of gas hydrates in sediments would decrease the poroelastic effect on ***Ph***, but the enhanced cohesion could counterbalance such effect by adding further strength to the sediment.

Following this discussion, it is suggested that vertical hydraulic fractures occur when the total fluid pressure is close to lithostatic conditions (from ~90% to 100% of ***Pv***), depending on the distribution of overpressure, the sediment physical properties and the presence of hydrates. In low-cohesion, low-*Sh* unconsolidated sediments, hydraulic fractures probably occur where ***Pf*** is 95 to 100% of ***Pv***.

| Parameter | Value |
|---|---|
| Biot's coefficient (***α***) | 1 |
| Poisson ratio (***v***) | 0.4-0.48 |
| ***θ*** | 0.5-1 |
| Bulk sediment density (kg/m3) | 1850 |
| Water density (kg/m3) | 1025 |
| Gravity ($m/s^2$) | 9.81 |

**Table 7.5.** Parameters used to calculate ***Pf/Ph***, ***Pf/Pv*** and ***Ph/Pv*** in **Fig. 7.20**.

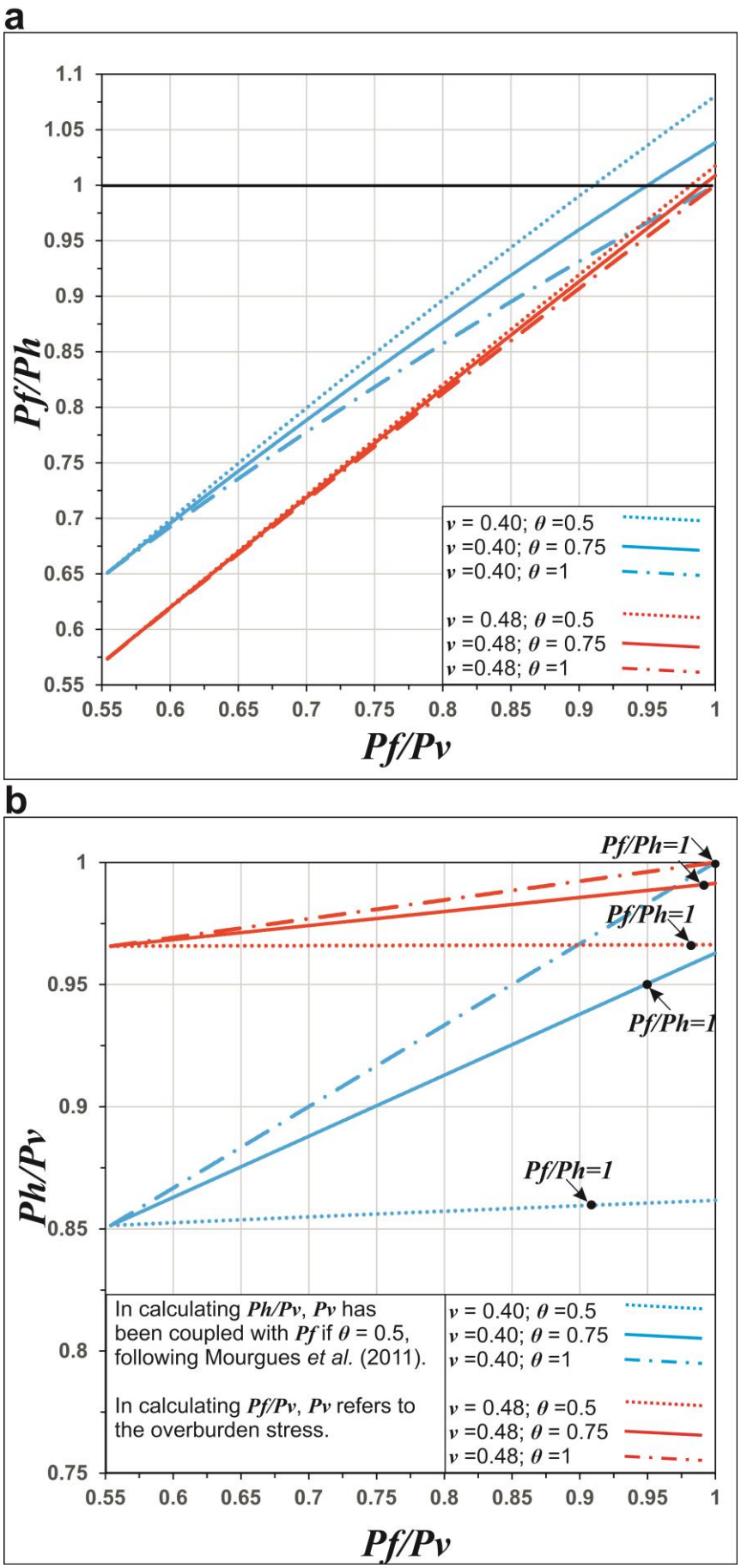



**Figure 7.20. (a)** Relationship between ***Pf/Ph*** and ***Pf/Pv***. A horizontal black line indicates ***Pf/Ph***= 1. **(b)** Relationship between ***Ph/Pv*** and ***Pf/Pv*.** Hydrostatic conditions (***Pf/Pv***~0.55) are represented on the left of the plot whereas the ***Pf/Ph*** and ***Ph/Pv*** ratios progressively increase at higher overpressures. The black arrows show when ***Pf/Pv*** equals 1 along the different trends.

### *7.7.2. Fault reactivation*

To extrapolate suitable conditions for fault reactivation, I have considered the method used by Hornbach *et al.* (2004). The maximum principal stress (***Pv***) is considered vertical and equal to the overburden stress. ***Pv*** has been extrapolated by the use of density data from core and LWD measurements (see **paragraph 7.3**). The minimum horizontal stress (***Ph***) has been calculated taking into account poroelasticity under hydrostatic and uniaxial conditions, using **Equation 1**, with $\boldsymbol{\alpha}$ equal to 1 (Lee, 2002) and $\boldsymbol{\nu}$ comprised between 0.40 and 0.48 (Hamilton, 1979; Lee *et al.*, 2010a). Under such conditions, the overpressure required to reactivate a fault ($\boldsymbol{P_{fault}}$) is:

$$\boldsymbol{P_{fault}} = [(\boldsymbol{Pv} + \boldsymbol{Ph})] + [(\boldsymbol{Pv} - \boldsymbol{Ph})/2](1 + \cos 2\boldsymbol{\beta} - \sin 2\boldsymbol{\beta}/\boldsymbol{\mu}) + \boldsymbol{C}/\boldsymbol{\mu} - \boldsymbol{Pw_{sf}} \quad \textbf{(6)}$$

Where $\boldsymbol{\beta}$ is the dip angle of the fault, considered here to be 60°, ***C*** is the cohesion along the fault (assumed to be 0), and $\boldsymbol{\mu}$ is the sliding friction coefficient, equal to:

$$\boldsymbol{\mu} = tan(2\boldsymbol{\beta} - 90) \sim 0.58 \quad \textbf{(7)}$$

Given this criterion, $\boldsymbol{P_{fault}}$ has been calculated using the *'end-member'* lithostatic stress trends as input (Chile Triple Junction, Peruvian margin and Mahanadi Basin, **Fig. 7.2a**). Then, the corresponding buoyant gas column capable of equalling that pressure has been estimated for the two free gas density end-members used to compute the hydraulic fracturing criterion ($\boldsymbol{\rho_g}$= 50 and 275 kg/m$^3$). This calculation does not consider the impact of overpressure on ***Ph***. Theoretically, in the presence of an overpressure, ***Ph*** is increased due to poroelasticity. Therefore, the ***Ph***/***Pv*** ratio could in turn increase of a degree that can depend on the structure of the overpressured zone (Mourgues *et al.*, 2011). At higher ***Ph/Pv***, due to high values of $\boldsymbol{\nu}$ or to the presence of an overpressure, a higher $\boldsymbol{P_{fault}}$ (i.e. a higher $\boldsymbol{Th_{FGZ}}$) is required to reactivate a fault (**Fig. 7.21**). A similar result is also expected if the fault plane has some cohesion.

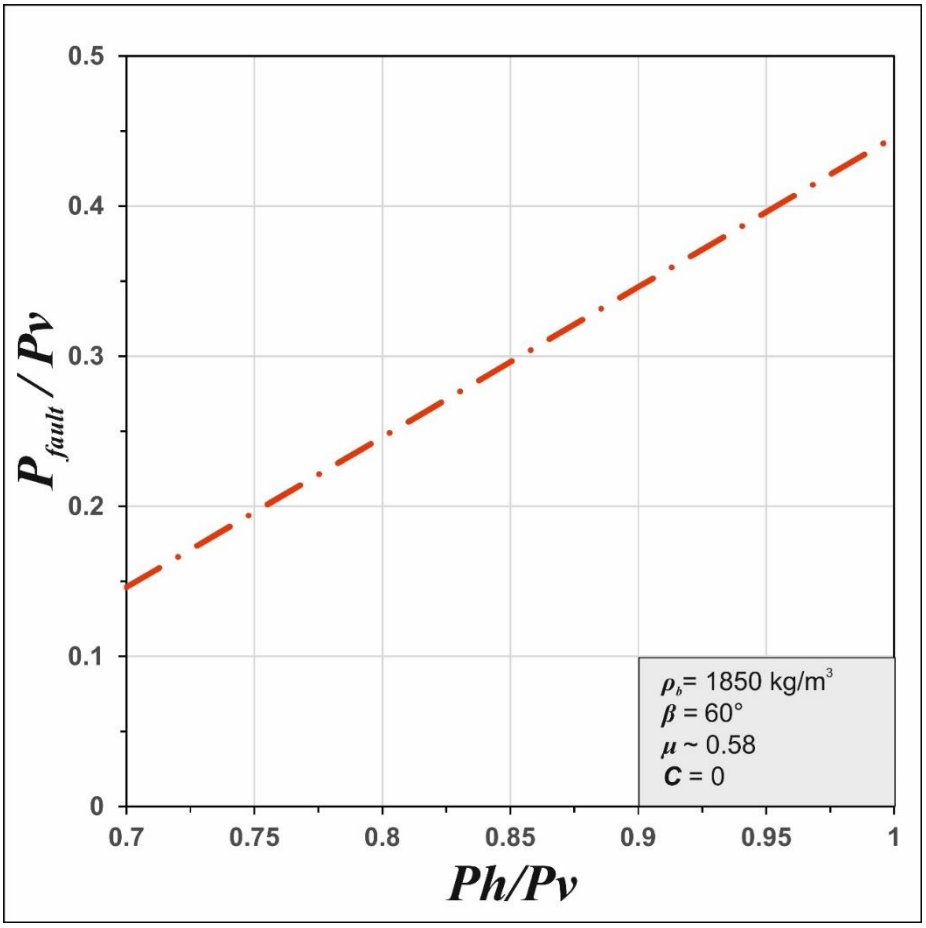



**Figure 7.21.** Effect of the increase in ***Ph***, expressed as ***Ph/Pv***, on the increase in ***Pfault***, expressed as $P_{fault}/Pv$, for $\beta$= 60°; $\mu$~0.58; ***C***= 0 and a constant sediment bulk density ($\rho_b$= 1850 kg/m$^3$). In the studied natural systems, ***Ph/Pv*** under hydrostatic conditions is higher than ~0.8-0.85.

### *7.7.3. Supplementary figures*

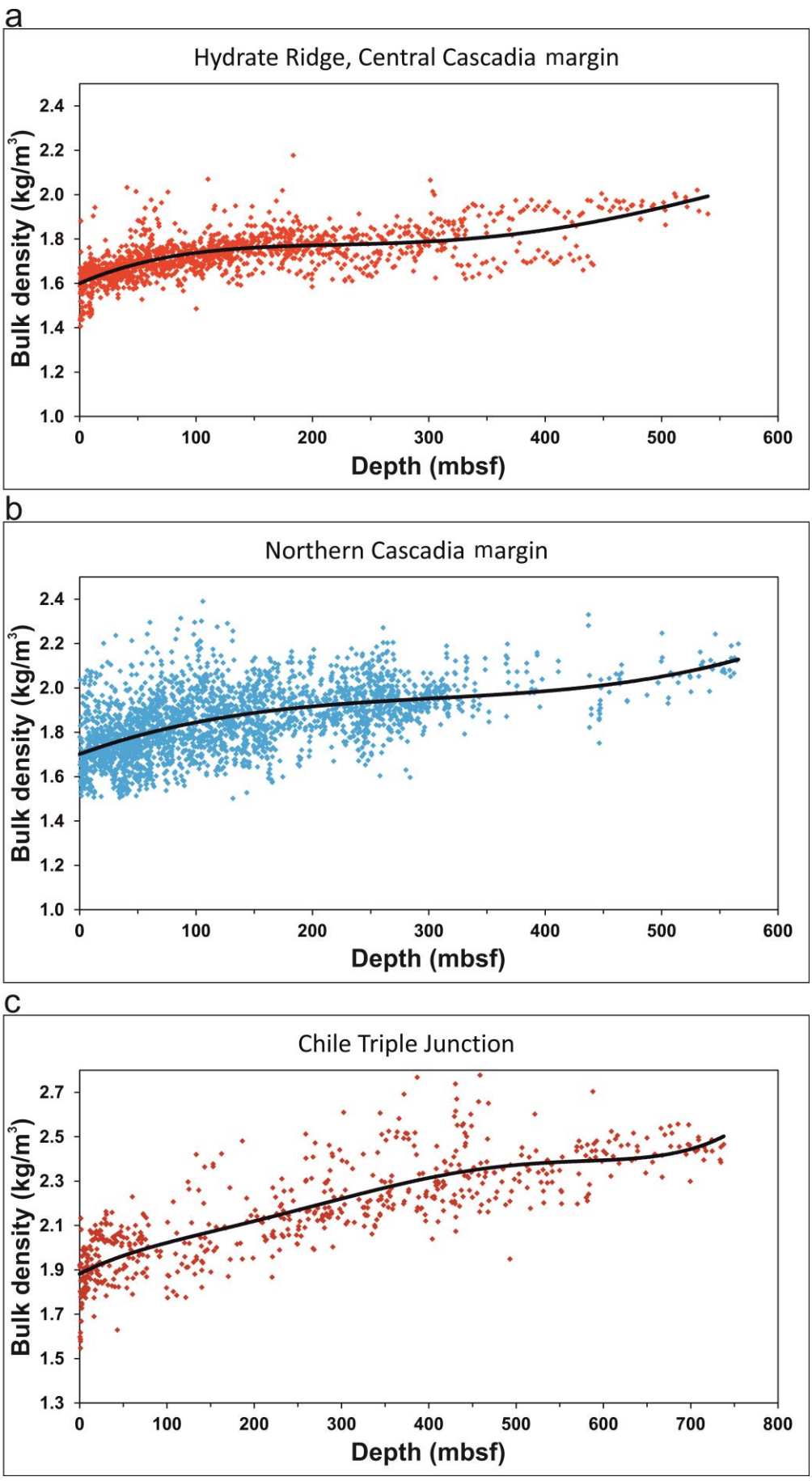



**Fig. 7.22 a-c**

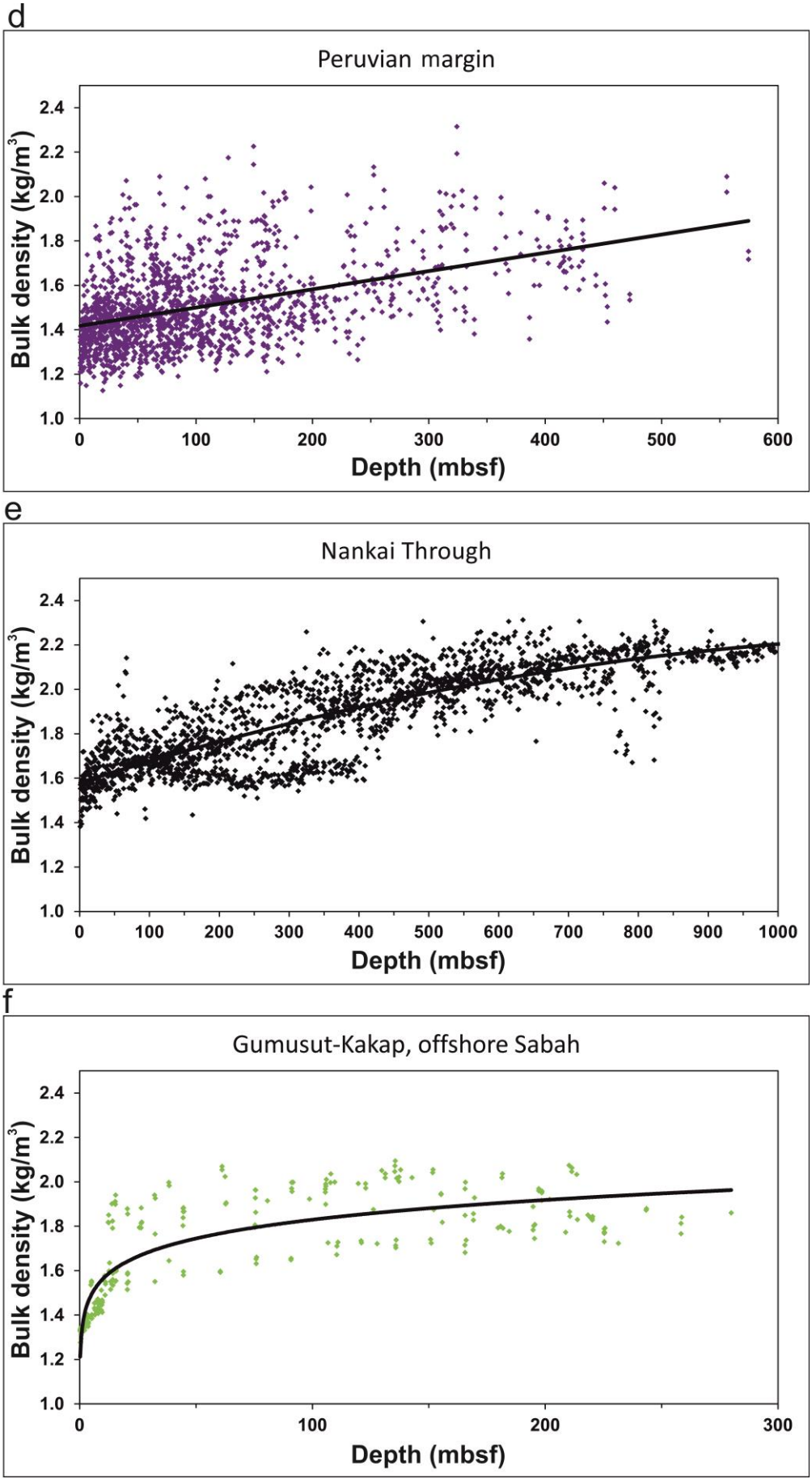
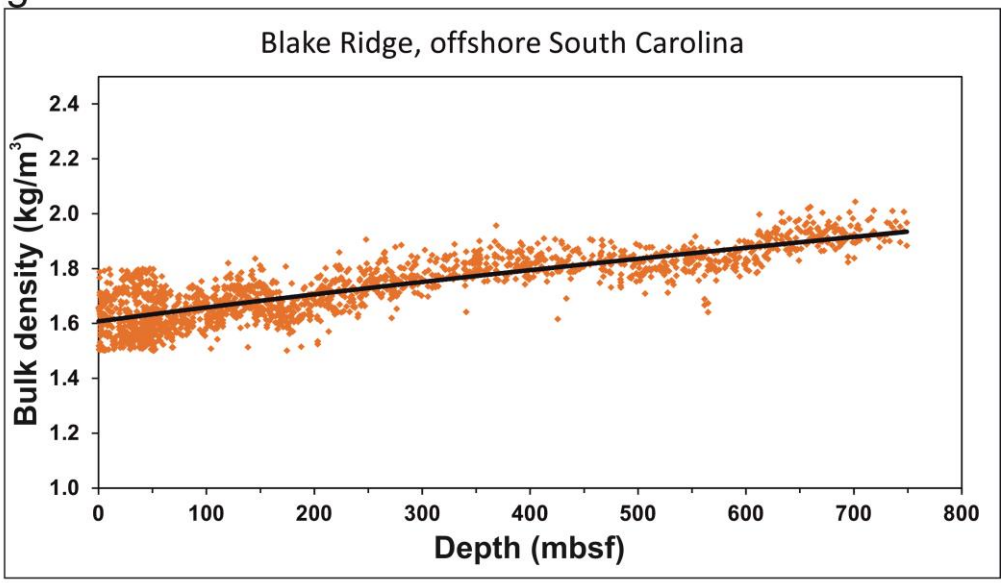
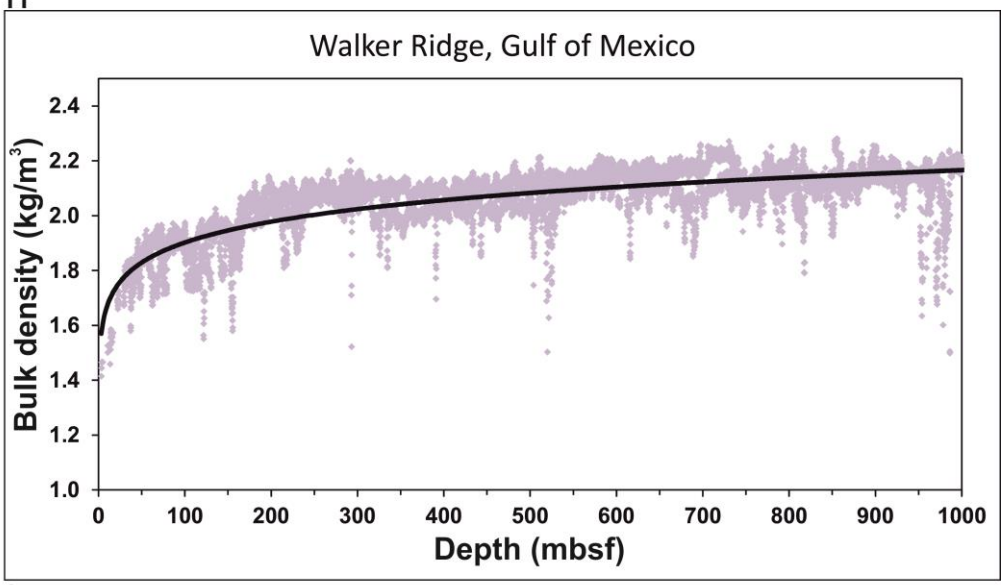

d
Peruvian margin
Bulk density (kg/m3)
Depth (mbsf)
e
Nankai Through
Bulk density (kg/m3)
Depth (mbsf)
f
Gumusut-Kakap, offshore Sabah
Bulk density (kg/m3)
Depth (mbsf)

**Fig. 7.22 d-f**

g




h




i

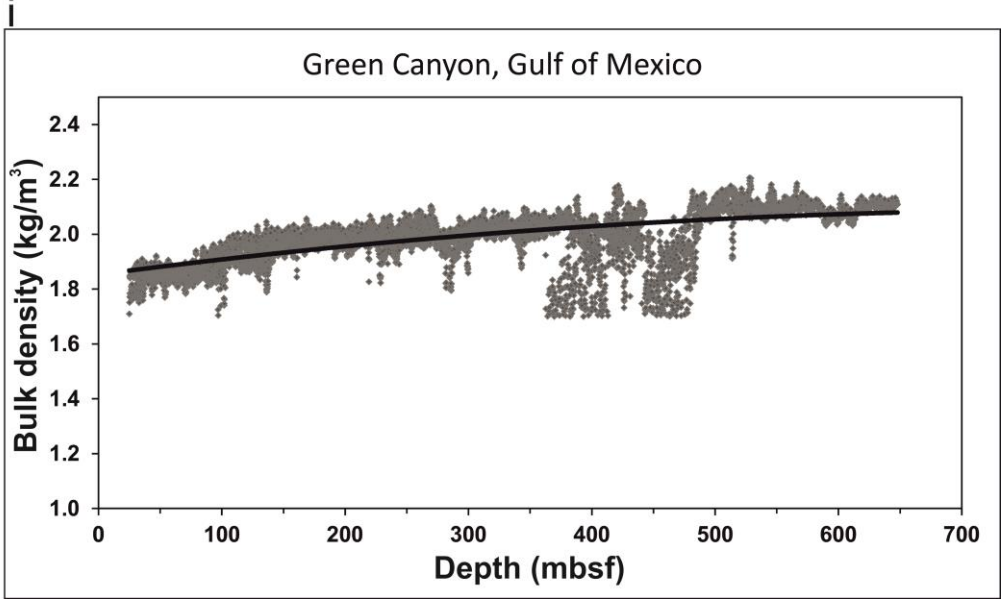



**Fig. 7.22 g-i**

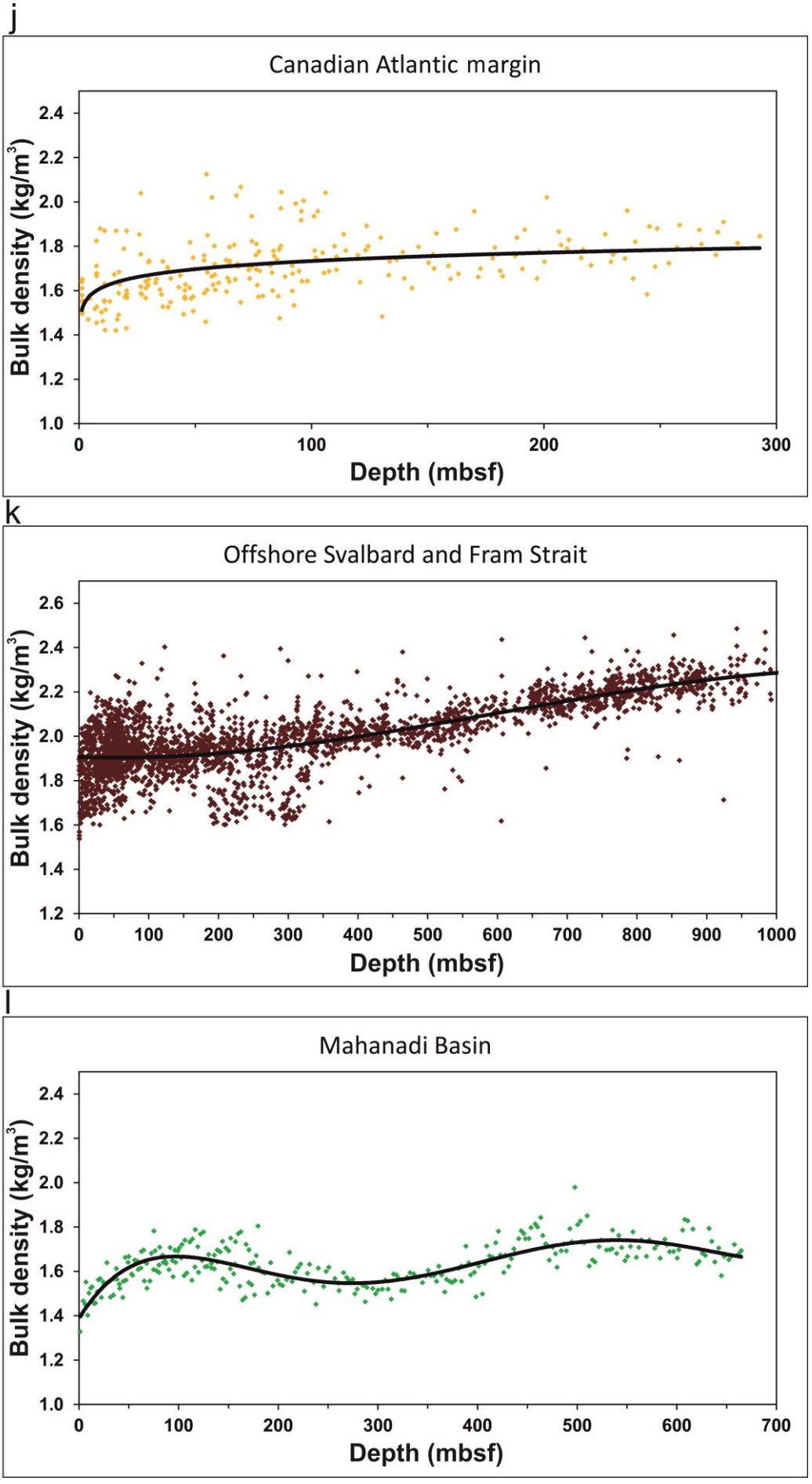

j
Canadian Atlantic margin
Bulk density (kg/m3)
Depth (mbsf)
k
Offshore Svalbard and Fram Strait
Bulk density (kg/m3)
Depth (mbsf)
l
Mahanadi Basin
Bulk density (kg/m3)
Depth (mbsf)

**Fig. 7.22j-l**

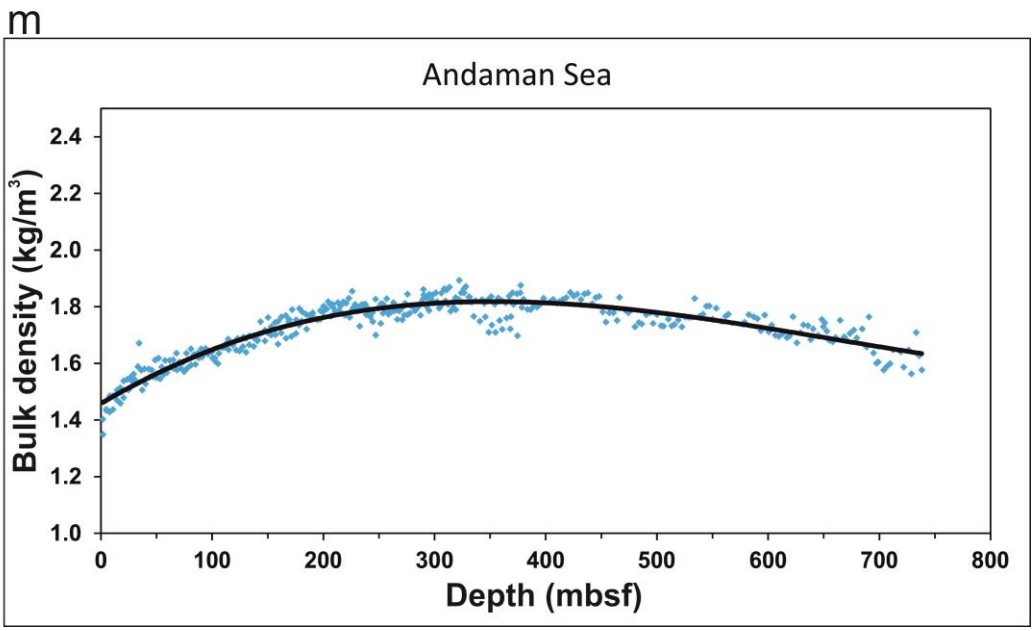



**Figure 7.22.** Density plots from core and LWD data from different locations worldwide where the presence of natural gas hydrates is proven or inferred (see **Tab. 7.2**). The black lines represent the functions that approximate the observed trends with the best possible fit. These functions have been used to extrapolate ***Pv*** (**Fig. 7.2a**). **(a)** = Hydrate Ridge, central Cascadia margin; **(b)** = Northern Cascadia margin; **(c)** = Chile Triple Junction; **(d)** Peruvian margin; **(e)** Nankai Trough; **(f)** Gumusut-Kakap, offshore Sabah; **(g)** Blake Ridge, offshore South Carolina; **(h)** Walker Ridge, Gulf of Mexico; **(i)** Green Canyon, Gulf of Mexico; **(j)** Canadian Atlantic margin, Orphan Knoll and Erik Drift; **(k)** Offshore Svalbard and Fram Strait; **(l)** Mahanadi Basin **(m)** Andaman Sea. Some density values **(c)** (Chile Triple Junction) reach density of pure mineral constituents (i.e. 0% porosity) and are most likely artefacts.

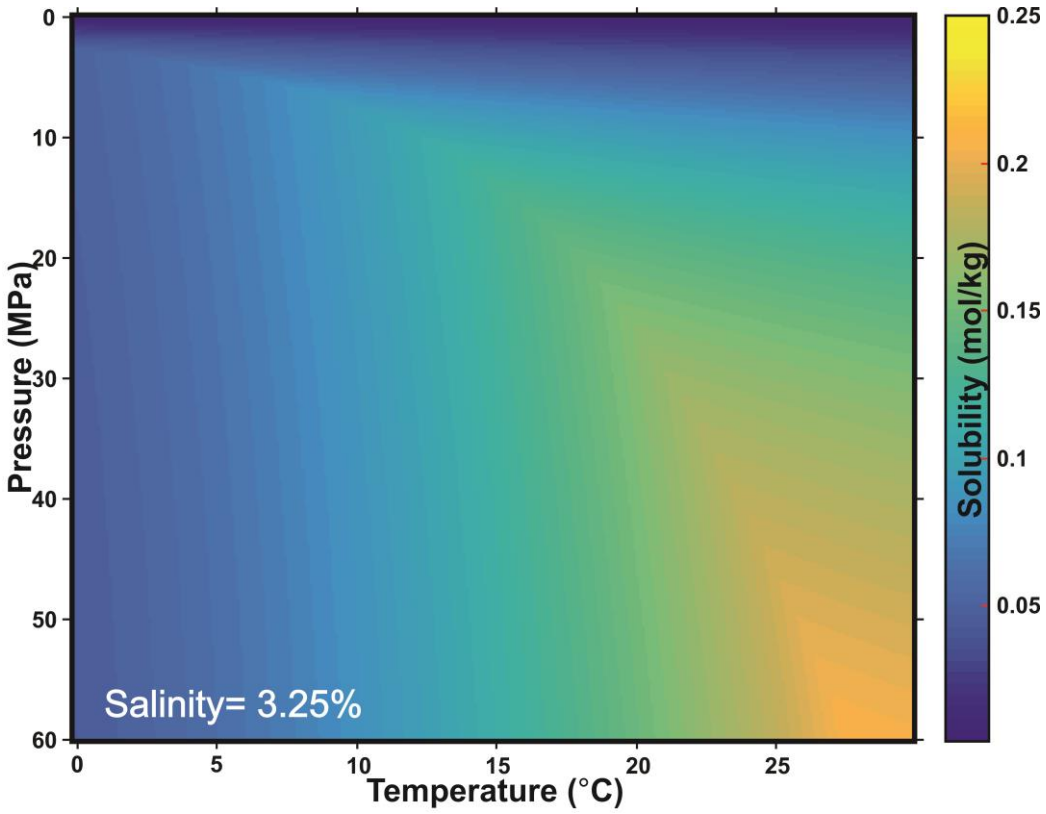



**Figure 7.23.** Solubility of methane (mol/kg), at varying temperature (0-30 °C) and pressure (0-60 MPa). In this case, the solubility is calculated with a fixed water salinity of 3.25% following Tishchenko *et al.* (2005).

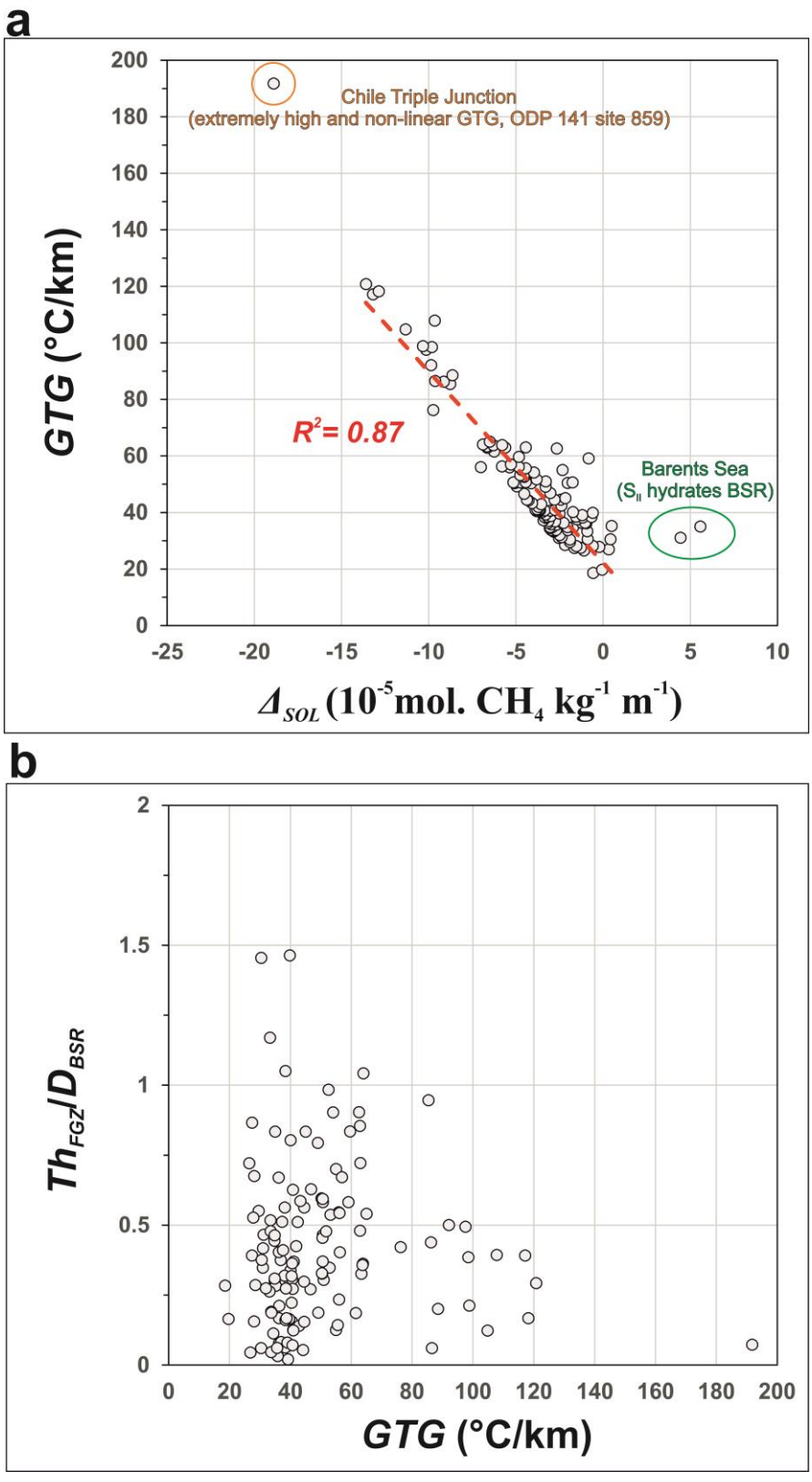



**Figure 7.24. (a)** Relationship (almost linear) between ***GTG*** and $\Delta_{SOL}$. **(b)** Relationship between the $Th_{FGZ}/D_{BSR}$ ratio and ***GTG*** for the analysed FGZs. The average values of $Th_{FGZ}$, $D_{BSR}$ and ***GTG*** have been used for this plot, which shows that the impact of high ***GTGs*** (>60°C/km) on $Th_{FGZ}$ is still visible, even taking into account $D_{BSR}$, which can be seen as an approximation of the effective stress above the BGHSZ.

# Chapter 8. Final discussion and conclusions

## 8.1. Multi-scale controls on hydrate distribution

The Seismic, well-log and core data from marine sedimentary basins worldwide (cf. **Chapters 3-6**; Tréhu *et al.*, 2004b; Sultan *et al.*, 2011; Boswell *et al.*, 2012b; Lee and Collett, 2012; Lee *et al.*, 2013; Wang *et al.*, 2014; Ito *et al.*, 2015), as well as the results from theoretical models (e.g. Bhatnagar *et al.*, 2007; Liu and Flemings, 2007; Daigle and Dugan, 2010a, 2011; Chatterjee *et al.*, 2014; Nole *et al.*, 2017), indicate the existence of two sets of controls on hydrate distribution at multiple scales:

**(1)** *Geological and fluid flow controls* (i.e. the *'plumbing system'*);

**(2)** *Gas hydrate stability controls*.

The *geological and fluid flow controls* include the stratigraphic and depositional architecture of a basin, a prospect (i.e. the km-scale structure hosting gas hydrates), or part of it. These controls also comprise the mechanisms of gas generation and supply, as well as the geometrical organisation of fluid flow pathways and the geological structures where hydrates occur. In contrast, the *gas hydrate stability controls* delimit the vertical extent of the GHSZ and are thus represented by the in-situ temperature, pore fluid pressure, composition of the feeding gas and pore water salinity. Finally, the temporal variability of all these factors, in the context of the natural geological evolution of an area, further complicates the analysed system (**Fig. 8.1** and **Tab. 8.1**). Ultimately, the interplay between these controls results in a patchy, although not randomly organised, hydrate distribution. The same controlling factors repeat at different scales and geological settings. Below, as a final discussion for this thesis, I shortly highlight and discuss some of the critical processes that affect hydrate distribution, from the pore-scale to the basin-scale.

### *8.1.1. Controls from the pore- to the core-scale*

At the pore- and the core-scales, the host lithology is the primary factor controlling hydrate distribution and morphology. Most of the observations to date show grain-displacing and pore-filling morphologies, respectively in fine-grained and coarse-grained sediments (**Chapters 3** and **5**; see also Holland *et al.*, 2008; Rees *et al.*, 2011; Konno *et al.*, 2015).

In the most prospective hydrate provinces, the host lithologies for pore-filling hydrates are constituted by silty to sandy sediments, deposited in turbidite systems, including channel, lobe and levee facies (Boswell *et al.*, 2012b; Wang *et al.*, 2014; Ito *et al.*, 2015). The results presented in this work further show that pore-filling hydrate morphologies occur in complex depositional elements like MTDs, where hydrates concentrate in cm-thick sandy layers, embedded in a mud-prone *'matrix'* (**Chapter 5**). The molecular diffusion of methane along concentration gradients, at the centimetre- to metre-scale, likely contribute to enhancing the hydrate saturation differences between sand-rich *vs* mud-rich zones.

In the case of fracture-hosted gas hydrate deposits, the initial reservoir quality of the sediment is low, given the small primary pore throats and the limited permeability of such sediments (~$10^{-17}$-$10^{-19}$ $m^2$). These conditions limit hydrate formation by enhancing methane solubility and reducing fluid fluxes (Clennell *et al.*, 1999; Cook *et al.*, 2008). However, hydrate could still form within pre-existing tectonic or self-generating fractures in these sediments (Cook *et al.*, 2008; Daigle and Dugan, 2010b; Rees *et al.*, 2011). Self-generating fractures originate from dilation of the sediments related to **(1)** hydraulic/pneumatic fracturing and subsequent hydrate precipitation (e.g. Rees *et al.*, 2011) and **(2)** hydrate-induced heave, a mechanism similar to that leading to the formation of ice lenses in permafrost soils (Clennell *et al.*, 1999; Rempel, 2007).

Hydraulic/pneumatic fractures form as a consequence of fluid-driven overpressures, whose critical thresholds may vary from region to region (see **Chapter 7**) (Flemings *et al.*, 2003; Hornbach *et al.*, 2004; Daigle *et al.*, 2011; Sultan *et al.*, 2011).

In contrast, the occurrence of fracture-filling hydrates in the absence of elevated fluid fluxes and far from potential sources of overpressures (e.g. Cook *et al.*, 2014) can be explained by pre-existing discontinuities in the host sediment or by hydrate-induced heave. In the latter mechanism, hydrate crystals grow in the small pores of fine-grained sediments, if not inhibited by the Gibbs-Thomson effect (Clennell *et al.*, 1999; Anderson *et al.*, 2009), which causes a temperature depression of the phase boundary. Once hydrate formation is no longer inhibited, the pressure exerted by a segregated hydrate crystal will be related to its interfacial tension with water and the pore size (Torres *et al.*, 2004). A displacive hydrate lens can therefore grow and support suction phenomena, eventually increasing the sediment bulk volume (Lee *et al.*, 2010b).

Within the GHSZ and in the absence of free gas, considering the interfacial tension at the hydrate-water interface, which is similar to that of ice lenses (~0.025-0.030 $J \cdot m^{-2}$) (Anderson *et al.*, 2003), the maximum depth at which hydrate can crystallise by displacing the sediment will be given by the competition between capillary and mechanical (i.e. the minimum effective stress) forces (Dai *et al.*, 2012). Therefore, the growth of hydrate lenses could be inhibited at high effective stress conditions, even within the GHSZ. Such a relationship could explain why, in certain low-flux locations, there are intervals with fracture-filling hydrates located well above the BGHSZ, apparently without any connection with the underlying hydrocarbon plumbing system (cf. Cook *et al.*, 2014).

### *8.1.2. Controls at the prospect-scale*

This thesis provides significant results on the distribution of gas hydrates at the prospect-scale, thanks to the use 3D seismic data, integrated with petrophysical and geochemical information.

The geochemistry of the hydrate-forming gases has been shown to be a crucial control on hydrate distribution (see **Chapters 3** and **5**). Local variations in the geothermal gradients due to fluid flux of warm fluids, presence of salt bodies in the subsurface and mud volcanoes

can impact the distribution and the stability of hydrates as well (**Chapter 5**; see also Taylor *et al.*, 2000; Dewangan *et al.*, 2011; Wei *et al.*, 2015). Our results indicate that lateral variations in the geothermal gradient, if not extreme, are less important than the geochemistry of the feeding gas in defining the thickness of the GHSZ. The pore pressure is another key control on hydrate distribution, and the most dramatic evidence of the pore pressure influence on hydrate stability is observed in the upper portions of continental slopes, at the *'hydrate wedge'* (Davies *et al.*, 2015).

Methane supply is a further critical factor, severely impacting the distribution of hydrates. Regions with a high charge of methane-rich fluids commonly result in the formation of concentrated hydrate deposits (e.g. the crest of the GKL Dome or the anticline $A_1$ in the Guajira Basin, see **Chapters 4** and **6**). In dominantly long-range advective systems, the distribution of hydrates can correlate with that of the sourcing fluids beneath the three-phase boundary (e.g. the FGZ, see **Chapter 6**), and is inevitably influenced by the distribution of stratal and cross-stratal pathways for fluid flow across the GHSZ (cf. **Chapters 4 and 6**). Processes like sedimentation, erosion, tectonic uplift and hydrocarbon leakage can be either continuous or episodic, and control the lifetime of gas hydrate prospects. The possible generation of adequate amounts of in-situ microbial methane could inevitably complicate this simple view, by promoting the formation of hydrates, without any relationship with the underlying plumbing system.

### *8.1.3. Controls at the basin-scale*

In evaluating a basin for the presence of natural gas hydrate systems, several elements need to be assessed. The stratigraphic framework and its interaction with the tectonic evolution of a basin can play a crucial role in favouring the development over time of a methane-rich environment. The availability of organic matter, of coarse-grained *vs* fine-grained sediments, the sedimentation *vs* subsidence *vs* erosion rates and the presence of

basin-wide current patterns (e.g. turbidity and contour currents) are key elements that certainly influence the resulting hydrate distribution.

For instance, both the sediment supply and tectonic evolution control the basin-scale thermal state and hence, its methane generation potential. Tectonic processes can activate sedimentation, subsidence and erosion processes which impact the prospectivity of the km-scale structures where hydrates can accumulate (Kroeger *et al.*, 2015; Dumke *et al.*, 2016; Burwicz *et al.*, 2017). Moreover, the thermal state of the basin impacts the vertical extent of the GHSZ. The thermal regime in the shallow section also influences the methane solubility gradient, activating diffusion processes within and below the BGSHZ (see **Chapter 7**).

Many convergent margins (e.g. the Nankai Trough, the Cascadia margin and the Hikurangi margin) present ideal conditions for the formation of gas hydrates, thanks to the widespread presence of fluid-focusing and permeable pathways, as well as recently deposited and rapidly subsiding terrigenous sediments. The result is the presence of gas hydrates and free gas along many portions of the basin and more local factors (e.g. the depositional environment at the prospect-scale) will determine the distribution of concentrated deposits (Ashi *et al.*, 2002; Tréhu *et al.*, 2006; Riedel *et al.*, 2009; Tsuji *et al.*, 2009; Barnes *et al.*, 2010; Plaza-Faverola *et al.*, 2012b). In fold and thrust belt associated with gravity and shale tectonics, as well as in the regions of salt tectonism, the distribution of natural gas hydrates often links with deeper and actively working deeper petroleum systems. Many parts of the West African margin, the Northern Gulf of Mexico, as well as the NW Borneo, represent excellent examples of such natural gas hydrate systems (e.g. Cunningham and Lindholm, 2000; Sassen *et al.*, 2001b; Warren *et al.*, 2010). The findings of this research suggest that these settings may also be characterised by hydrates distributed below BSRs and coexisting with free gas (**Chapters 3**). In tectonically-active extensional settings (e.g. the Svalbard margin, the Ulleung Basin and the Lake Baikal), but also in older passive margins, it is frequently observed that hydrates are associated with active or paleo

seeps, underlain by faults or fluid-escape pipes (Van Rensbergen *et al.*, 2002; Hustoft *et al.*, 2007; Horozal *et al.*, 2009; Davies and Clarke, 2010; Smith *et al.*, 2014b).

Overall, the major controls on the distribution of gas hydrates repeat at different scales (**Fig. 8.1** and **Tab. 8.1**). The distribution of natural gas hydrates displays a multi-scale patchiness, which results from various heterogeneities that occur from the pore-scale to the basin-scale. In the analysis of a natural gas hydrate system, a basin-scale approach will firstly constrain the physical and chemical controls on hydrate stability and the methane generation potential. Then, depending on the aim, a study can focus on more local and detailed processes, always taking into account the interplay between stability factors, geological heterogeneities and fluid flow.

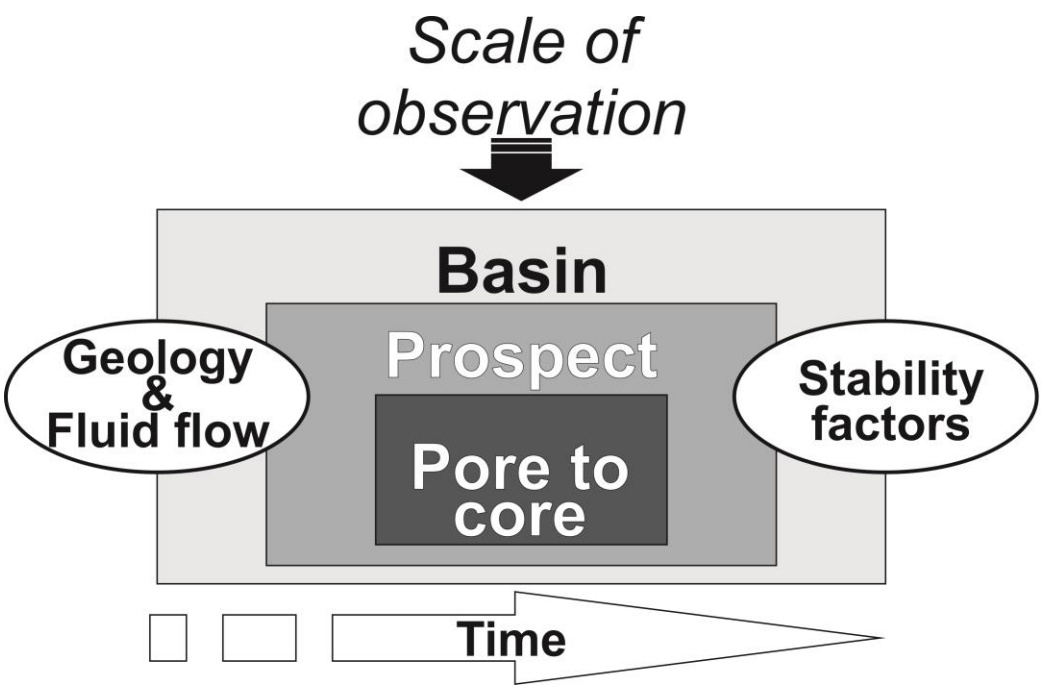



**Figure 8.1.** Schematic representation of the major controls on hydrate distribution (geology and fluid flow plus stability factors through time) at different scales. Time is an *'across-the-board'* factor, given that the geological and fluid flow framework, as well as the stability factors, will inevitably evolve temporally.

| CONTROLS | | SCALE OF OBSERVATION | | |
|---|---|---|---|---|
| | | ***Pore to Core*** | ***Prospect*** | ***Basin*** |
| ***Geological & fluid flow system*** | *Lithology* | * Grain size and mineralogy<br>* Pore size distribution and pore shape | * Facies architecture and depositional system<br>* Stratigraphic position within the GHSZ | * Sediment supply from the shelf<br>* Currents<br>* Slope instability and resedimentation<br>* Interaction with tectonics |
| | *Structure* | * Fracture shape, size, intensity and distribution<br>* Fracture origin (pre-existent, hydraulic fracturing, heave)<br>* Proximity to seismically-visible structures | * Folding<br>* Faulting and large-scale fracturing<br>* Dipping stratigraphic layering<br>* State of stress | * Plate tectonic regime<br>* Gravity and far-field stress<br>* Salt and shale tectonic<br>* Km-scale changes of the state of stress |
| | *Fluid flow* | * Capillary effects on hydrate nucleation, solubility variations and diffusion gradients<br>* Hydrate micro-habits and Ostwald-ripening<br>* Free gas distribution (patchy *vs* homogeneous)<br>* Advective multi-phase Fluid flow through the primary pore space and along fractures (capillary invasion *vs* hydraulic fracturing)<br>* Permeability changes due to hydrate crystallisation (seal efficiency at the BGHSZ) | * Distribution of cross-stratal and stratal fluid flow pathways<br>* Distribution, saturation and buoyancy of the FGZ<br>* Water overpressure distribution (disequilibrium compaction, lateral pressure transfer, perched water aquifers, hydrate dissociation and dissolution)<br>* Diffusion mechanisms<br>* Fluid flow at and around the *'hydrate-wedge'* | * Distribution of regional tectonic and stratal pathways for fluid flow (e.g. major tectonic faults, high permeability units)<br>* Distribution and quality of biogenic and thermogenic sources of free gas<br>* Variability in the location of the *'hydrate wedge'* along the slope |
| ***Stability factors*** | *Temperature* | * Hydrate formation and dissociation at three-phase boundaries<br>* Coexistence of three phases within the GHSZ<br>* Depression of the temperature of the three-phase boundary owing to Gibbs-Thomson effect | * Vertical extent of the GHSZ (relation to bathymetry and GTG variability)<br>* Impact of focused fluid flow, salt tectonic and mud-volcanism on the GTG<br>* Impact of the GTG on diffusion mechanisms | * Seafloor temperature<br>* Regional geothermal gradient (GHSZ) |
| | *Pressure* | * Hydrate formation and dissociation at three-phase boundaries | * Vertical extent of the GHSZ (relation to bathymetry and pore fluid pressure variability)<br>* Overpressure generation due to hydrate dissociation and dissolution | * Vertical extent of the GHSZ (in relation to the bathymetry) |
| | *Gas composition* | * Gas hydrate structure and stability<br>* Molecular fractionation (variation of the $C_1/C_{2+}$ ratio)<br>* Coexistence of hydrate and free gas | * Vertical extent of the GHSZ and distribution of microbial *vs* thermogenic fluids<br>* Molecular fractionation and lateral variability due to fluid flow<br>* Mixing of microbial and thermogenic fluids | * Vertical extent of the GHSZ and distribution of microbial *vs* thermogenic fluids<br>* Basin-scale generation of microbial and thermogenic fluids, including secondary methane generation |
| | *Water salinity* | * Hydrate formation and dissociation<br>* Coexistence of three phases within the GHSZ | * Vertical extent of the GHSZ<br>* Lateral variability in relation to fluid flow and salt tectonics | * Vertical extent of the GHSZ<br>* Lateral variability in relation to latitude, ocean circulation, regional fluid flow and salt tectonics |
| ***Time*** | | * Compaction (mechanical diagenesis)<br>* Cementation (chemical diagenesis; e.g. authigenic minerals)<br>* Fluctuations of the BGHSZ<br>* Hydrocarbon generation, free gas dissolution and exsolution | * Sedimentation and erosion<br>* Uplift and subsidence<br>* Fluctuations of the BGHSZ<br>* Hydrocarbon generation, leakage from below, free gas dissolution and exsolution<br>* Variability of charge of methane-rich fluids through time | * Sea-level fluctuations<br>* Cooling and warming events<br>* Tectonic events<br>* Regional evolution of currents, sediment supply, tidal forces<br>* Earthquakes |

**Table 8.1**. Detailed list of the controls of gas hydrate distribution at different scales.

## 8.2. Final conclusions

### *8.2.1. Summary of the results*

This thesis has focused on the analysis of natural gas hydrate systems, by the use of three-dimensional seismic, well-log and core data. The aim of the project was to improve our understanding of the controls on the distribution of gas hydrates in sedimentary basins, as well as the mechanisms of fluid flow below and across the GHSZ (see **paragraph 1.10**). In the literature review (**Chapter 1**), I have provided a background framework for the interpretation of a natural gas hydrate system, and I have stated some major unknowns in this field. In **Chapters 3-6**, I have presented the results from single case studies, although the most significant findings of this work are not solely limited to a particular study area. Finally, in **Chapter 7**, I have reviewed the processes associated with the formation of the free gas zone and its relationships with hydrate accumulations and overpressure. Here, I summarise the principal findings of this PhD research.

***Chapter 3***. Structure II and H gas hydrates found below the bottom-simulating reflector

This study highlights the existence of gas hydrates below a BSR in the deepwater region offshore Sabah (NW Borneo), by integrating three-dimensional seismic data with well-log and core observations. The zone of gas hydrate occurrence below the BSR is characterised by $S_{II}$ and potentially $S_H$ hydrates, capable of hosting $C_{2+}$ hydrocarbons. These hydrocarbons are sourced by an underlying conventional oil and gas accumulation (the Gumusut-Kakap reservoir), located at the core of a thrust-propagation fold.

Within the zone of $S_{II}$ and $S_H$ hydrates occurrence, I have recognised a process of geochemical molecular fractionation, eventually leading to almost pure methane hydrates above a BSR. Thus, the BSR should be considered, in some cases, as the boundary between different hydrate structures.

In the studied natural gas hydrate system (i.e. the crest of the GKL Dome), the petrophysical and well-log data indicate that the amounts of hydrates stored within the zone

of $S_{II}$ and $S_H$ hydrate occurrence are significantly higher than that stored above the BSR, i.e. in the zone of $S_I$ hydrate occurrence. Thus, it is important to assess the possible presence of sub-BSR hydrates in those basins characterised by the generation of hydrocarbons by thermogenic processes, to have better estimates of the global amount of carbon stored within natural gas hydrates and to improve our understanding of the fluid-flow phenomena in the shallow overburden.

***Chapter 4***. Relationship between fluid-escape pipes and hydrate distribution in offshore Sabah (NW Borneo)

This research is a continuation of the study presented in **Chapter 3** and analyses, mainly by the use of seismic data, the hydrocarbon plumbing system at the crest of the GKL Dome (offshore Sabah, NW Borneo). This shallow plumbing system is characterised by the migration of fluids along cross-stratal pathways, expressed as fluid-escape pipes.

The origin of fluid-escape pipes is attributed to the onset of hydraulic/pneumatic fracturing, a phenomenon facilitated by the presence of free gas in the system. The pipes are interpreted to be rooted both in the free gas zone and in deeper reservoirs, the latter stacked at intermediate depths between the GHSZ and the deep conventional accumulations of oil and gas. The spatial distribution of the fluid-escape pipes is influenced by the shallow state of stress. The pipes appear as features exclusively forming in fine-grained sediments, where the presence of overpressures results in the creation of new deformable pathways.

The stacked organisation of the upper termination of the pipes and the observation of stratigraphic thinning and truncations at multiple stratigraphic levels along the biggest pipes of the study area suggest that fluid flow in this system acted in pulses of enhanced activity, possibly in conjunction with mass-transport deposition. Evaluating the triggers for fluid flow is hard. However, the geometrical relationship between fluid-escape pipes and MTDs of Mid-Upper Pleistocene age argues that sea level fluctuations, pulses of tectonic activity (e.g. uplift) and hydrocarbon leakage during this period are the possible triggers. The most recent

fluid flux along the pipes could reflect an ongoing tectonic uplift and leakage, or the temperature increase following the Last Glacial Maximum.

The distribution of gas hydrates within fluid-escape pipes, which are sites of high fluid flux, and away from these features, in regions of *'background'* fluid flux, is probably very different. Seismic observations, well-log data and literature analogues suggest that the hydrate concentration increases towards the pipes and is likely to be extremely elevated inside these features. In contrast, away from the pipes (see **Chapter 3**), most of the hydrates occur in the deeper portions of the GHSZ, at only moderate to low concentrations. It is likely that a configuration with layered hydrate structures occurs at *'background'* fluid fluxes ($CH_4$ flux of ~1-2 mM $cm^{-2}$ $y^{-1}$) whereas $S_{II}$ and $S_H$ hydrates can be present up to the seafloor at higher fluxes ($CH_4$ flux of ~$10^1$-$10^3$ mM $cm^{-2}$ $y^{-1}$).

The volume of hydrates contained within fluid escape pipes at the crest of the GKL Dome is extrapolated to be of the same order of magnitude of that stored in the more extensive zone of *'background'* fluid flux. Therefore, in those areas characterised by advective fluxes of methane-rich fluids, the hydrate reservoir within fluid-escape pipes can be volumetrically significant. Hence, constraining the distribution of fluid-escape features in the preliminary assessment of a natural gas hydrate system is critical.

***Chapter 5***. Investigating the impact of gas composition, migration and lithology on the distribution of gas hydrates and free gas

In this work, I have integrated three-dimensional seismic data with core and petrophysical information, to characterise and discuss the natural gas hydrate system at the flanks of the GKL Dome (offshore Sabah, NW Borneo), and compare it to that at the crest, analysed in detail in **Chapters 3** and **4**.

The results indicate that it is extremely challenging to assess the distribution of gas hydrates with solely seismic data, particularly in those setting characterised by fluxes of

thermogenic fluids, where the vertical extent of the GHSZ can suddenly change. The results of **Chapter 3** show that, in areas of focused fluxes of thermogenic fluids, the major geochemical modification to the composition of the sourcing gas occur within the GHSZ. In contrast, moving far from these areas, it is possible that additional processes like secondary and primary microbial methane generation, as well as molecular fractionation during leakage, become relevant and impact the resulting vertical extent of the GHSZ. In areas dominated by mass-transport deposition, the high sedimentation rate can provide a mean to preserve the organic matter and furnish primary microbial methane to the system.

The morphology of the gas hydrate-bearing sediments is highly dependent on the host lithology and rapidly evolves laterally, being fracture-filling in homogeneously fine-grained sediments (the crest of the GKL Dome) and pore-filling, in more heterogeneous sequences (the eastern flank of the GKL Dome). Specifically, even in areas dominated by mud-prone MTDs, gas hydrates concentrate within the pore space of cm-thick sandy/silty beds. The petrophysical nature of mass-transport deposits should be further taken into account in quantifying hydrate saturation. The formation of hydrates in the pore space increases the P-wave velocity of the sediment, as revealed by comparing the Multi-Sensor Core Logging measurements on pressure cores and the gas hydrate saturation estimates from pore water chlorinity measurements. The theoretical models that predict that hydrates form as a suspension in the pore space or as a load-bearing component appear the most reliable to describe the impact of pore-filling hydrates on the P-wave velocity in the studied lithologies.

Gas hydrate can occur in the absence of BSRs, owing to limited methane fluxes and the impact of lithology on gas solubility. Therefore, the identification of free gas beneath the three-phase boundary is only a first-order evaluation tool in the analysis of a natural gas hydrate system. However, integrating geophysical observations in the shallow overburden with a more comprehensive understanding of the structures and the petroleum system of an area can help in reducing the uncertainties.

***Chapter 6.*** *Three-dimensional seismic evidence of extensive gas hydrate deposits linked with large free gas columns suggests long-range advection mechanisms*

In this work, seismic data from the outer fold belt of the Guajira Basin (offshore Northern Colombia) are used to image the three-dimensional seismic expression of coarse-grained gas hydrate-bearing sediments and discuss the control on their distribution. The study area shows diagnostic evidence of extensive accumulations of coarse-grained gas hydrate and free gas-bearing sediments in a natural gas hydrate systems interpreted to be dominated by long-range advection processes. The stratigraphic sequence is laterally homogeneous but vertically characterised by the presence of intervals interpreted to be relatively porous and permeable, likely representing deepwater terrigenous sediments.

The gas hydrate accumulations are seismically expressed in cross-sections as segments of enhanced amplitude, reflecting a positive acoustic impedance contrast at their upper interface. This seismic character indicates high-quality gas hydrate reservoirs, given that gas hydrate-bearing sediments induce an increase in the seismic amplitudes only at saturation higher than ~50% of the pore space. These gas hydrate deposits represent the primary target for gas hydrate exploration. The data presented here further represent the first seismic evidence of such hydrate deposits in the outer fold belt of a convergent margin.

A clear correlation between the distribution of the free gas and that of sediment-hosted gas hydrate at elevated concentration has been observed. The most extensive gas hydrate deposits occur close to the three-phase boundary and along those stratigraphic intervals displaying evidence of large and buoyant free gas columns. A change in the distribution of hydrates and free gas is further observed between different but structurally similar structures. This observation has provided evidence of a critical role played by long-range advective processes in sourcing, with a different efficiency, lithologically and structurally identical prospects. Identifying a mutual influence between free gas and hydrates in three-dimensional seismic data is key to distinguish long-range advection systems.

The observation of large and buoyant free gas accumulations underlying coarse-grained gas hydrate-bearing sediments suggest that the free gas is dynamically trapped beneath the three-phase boundary. The gas hydrate-bearing sediments are interpreted to behave as a dynamic membrane seal, where the interplay between the overpressure and capillary seal efficiency causes free gas injection pulses into the GHSZ.

***Chapter 7.*** A review of the critical state and the fluid flow processes associated with free gas zones beneath hydrate stability

This study has examined the controlling parameters on the critical status of a free gas zone, i.e. the existence of overpressures at the three-phase boundary, as well as the fluid migration processes below and throughout the GHSZ. This study integrates new seismic observations in different basins (i.e. NW Borneo, the Guajira Basin, the South Falkland Basin and the Hikurangi margin) with seismic and petrophysical data from the literature. One of the primary objectives has been to understand the relationship between the thickness of free gas zones and the mechanical mechanisms of failure and fluid flow, by fracturing, fault reactivation and capillary invasion. The collected data from different gas hydrate provinces have been integrated with simple theoretical models for fluid-driven fracturing and fault reactivation. These failure criteria represent upper boundaries for the vertical thickness of a free gas zone.

Sub-critical and critical free gas zones can occur in a variety of geological settings. The regional tectonic framework appears of secondary importance compared to more local factors in determining the critical status of a free gas zone. The presence of cross-stratal vertical pathways for fluid flow and dipping stratigraphic horizons charged with free gas could be diagnostic for those natural gas hydrate systems characterised by critical overpressure conditions. These conditions are more easily met at shallower water depths, due to the progressive decrease in the overburden stress above the base of hydrate stability. The view that convergent margins are uniquely characterised by thin free gas zones largely

oversimplifies the natural gas hydrate systems in these settings, where hundreds of metres of buoyant free gas columns can form.

Free gas migration across the GHSZ occur by both capillary invasion and fracturing. The state of stress and lithology are the most critical parameters controlling the occurrence of such mechanisms. I have discussed a few significant examples, by plotting the observed thickness of the free gas zone in a diagram that considers both these processes. The presence of pre-existent fractures can reduce the overpressure to activate fluid flow. In contrast, the presence of hydrates at the three-phase boundary will increase this overpressure. The migration of free gas throughout the GHSZ happens in response to tectonic events and climate cycles, capable of increasing the overpressures near the three-phase boundary. Importantly, there are various sources of overpressures other than buoyancy (e.g. the water overpressure). In addition, free gas zones can be immobile, unable to exert overpressures. These possibilities need to be taken into account in the study of fluid migration mechanisms in natural gas hydrate systems. The sole use of seismic data often does not allow to precisely understand how the free gas is distributed within the free gas zone and if a buoyancy-driven overpressure is effectively present.

The geothermal gradient of a natural gas hydrate system impacts the solubility gradients below and above the three-phase boundary. In this review, I hypothesise that the development of a thick free gas zone could be inhibited in areas of high geothermal gradients (i.e. >60-70 °C/km). Nevertheless, a high methane supply (i.e. driven by an efficient long-range advection of methane) could counterbalance this effect.

I have suggested a classification of free gas zones, by integrating information on the lithology, the stratigraphic dip, the rates of fluid flux, the three-dimensional shape of the three-phase boundary and the geothermal gradient. Assessing these parameters is important to evaluate a natural gas hydrate system in terms of sensitivity to climate changes, prospectivity and geohazard.

### *8.2.2. Contribution to the understanding of natural gas hydrate systems*

Some of the results of this PhD thesis have helped in improving our understanding of the key topics stated in the introductory chapter (see **paragraph. 1.10**), as summarised here:

**(1)** The vertical distribution of gas hydrates

Gas hydrates can occur below BSRs owing to thermogenic fluxes. Global estimates of hydrate volumes should consider the role played by thermogenic sources in feeding natural gas hydrate systems (see **Chapter 3**). In the presence of homogeneous sequences of fine-grained lithologies and vertically-focused fluxes, gas hydrates can concentrate along fluid-escape pipes (see **Chapter 4**). The lithology plays a primary role in concentrating hydrates within particular intervals inside their stability zone (see **Chapters 5** and **6**). The vertical distribution of gas hydrates in systems dominated by long-range advection can be further controlled by the distribution of the underlying free gas zone (see **Chapter 6**).

**(2)** The coexistence between gas hydrates and free gas

Free gas can coexist at equilibrium with $S_{II}$ and $S_H$ hydrates (**Chapter 3**). Free gas and gas hydrates can also coexist, locally and transiently (i.e. during episodes of fluid flow), along fluid-escape pipes and similar features (**Chapter 4**). In long-range advective systems, free gas can be injected along stratal pathways into the GHSZ, through a multi-phase process of capillary invasion, where three phases can transiently coexist too (**Chapter 6**)

**(3)** The Geochemical changes in hydrates and free gas within the GHSZ

Thermogenic fluxes across the GHSZ undergo a process of molecular fractionation. Eventually, this can results in the presence of a *'layered'* hydrate structure configuration, where $S_{II}$ and $S_H$ hydrates underlie $S_I$ hydrates (**Chapter 3**). However, at high fluid fluxes, the stratification of $S_I$ hydrates above $S_{II}$ and $S_H$ hydrates could not occur (**Chapter 4**). The molecular composition of the hydrate-forming gases can abruptly change laterally, reflecting a variation in the efficiency of leakage from the underlying hydrocarbon plumbing system, as well as in the origin and composition of the sourcing fluids (**Chapter 5**).

**(4)** The impact of focused fluid flow on hydrate distribution and the triggering events

The regions with elevated fluid fluxes are more likely characterised by zones of concentrated hydrates. The methane supply is probably the most critical factor controlling the distribution of hydrates at the km-scale (see **Chapters 4** and **6**). The triggers for fluid flow in natural gas hydrate systems induce a perturbation in the gas hydrate stability field and include sea-level drops, tectonic uplifts, temperature changes, earthquakes and tidal excursions (see **Chapters 4** and **7**). Unfortunately, with the data avalilable in this project, it has been impossible, in the study areas, to unquestionably discern between such processes.

**(5)** The physical mechanisms of hydrocarbon migration

Both vertically focused cross-stratal and stratal fluid migration pathways are essential controls on gas hydrate distribution (**Chapters 4** and **6**). The advection of free gas across the GHSZ can occur through fracturing or capillary invasion. These processes are controlled by the state of stress, the lithology and the amount and nature of overpressure. The efficiency of diffusion processes in natural gas hydrate systems is impacted by lithology and, possibly, by the geothermal gradient, both influencing methane solubility gradients (**Chapter 7**).

**(6)** The role of free gas in influencing gas hydrate distribution and the sealing capacity of gas hydrate-bearing sediments

Gas hydrate and free gas dynamically influence their reciprocal distribution. Buoyant columns of free gas can be trapped beneath gas hydrate-bearing sediments at the three-phase boundary (**Chapter 6**). Free gas can be injected through the GHSZ once that the overpressure at the BGHSZ equals the mechanical thresholds (**Chapters 6** and **7**). The evaluation of a free gas zone as critically trapped beneath the three-phase boundary should consider the effective interconnection of the free gas phase, as well as the occurrence of additional sources of overpressure. Local factors control the formation of critically-pressured free gas zones, which can occur in different geological settings (**Chapter 7**).

### *8.2.3. Guidelines for future research*

Nowadays, the amount of research on natural gas hydrate systems is vast and is growing exponentially. Nevertheless, some topics still need a better understanding. In this last paragraph, I provide some suggestions for future works on natural gas hydrates.

- An increment of seismic acquisition and sampling in thermogenically-sourced natural gas hydrate systems would be beneficial to understand their importance in the global carbon budget. In these provinces, the successful sampling of gas hydrates across the entire stability zone in these provinces will significantly help in refining the existing theories of molecular fractionation owing to hydrate crystallisation. Importantly, the rate of fluid flux could be a key parameter impacting the geochemistry of gas hydrates. Once that an adequate amount of data has been acquired, it will be possible to confidently construct hydrocarbon migration models that take into account for the whole ranges of geochemical processes within the GHSZ.
- What is the internal structure of vertical fluid-flow features? In this work, it is suggested that gas hydrates occur at high concentrations along pipe-like structures. Drilling results from a few gas hydrate provinces confirm this interpretation. However, the number of undisturbed samples acquired from such features is still limited. To better understand the process of multi-phase fluid flow along these pathways, it is essential to comprehend how hydrate form and how they temporally and spatially evolve within these zones, in response to fluctuation in the methane supply. The combination between geochemical (e.g. dating methods on authigenic minerals and molecular, as well as isotope analyses on hydrate samples recovered at multiple depths) and petrophysical tools (e.g. standard LWD and CPTu analyses throughout the gas hydrate stability zone) could be the key to gain further insights on the nature of these vertical fluid-escape zones.
- How the free gas is distributed beneath the three-phase boundary? The answer is undoubtedly complex and require the recovery of a significant number of undisturbed

samples from BSRs and free gas zones in different gas hydrate provinces. The acquisition of in-situ data on the pore fluid pressure would further be crucial to evaluate the presence and the nature of overpressures in natural gas hydrate systems. This data acquisition would imply drilling operation near and, possibly, across BSRs in various provinces, with the recovery of pressurised cores containing free gas-bearing sediment, and the concurrent recording of the in-situ fluid pressure. In this perspective, the results from the forthcoming IODP Expedition 372 along the Hikurangi margin, where I have contributed in evaluating the petrophysical properties of the sediments, could be revealing, and will potentially give to the hydrate community a major awareness on the impact of shallow overpressures on submarine mass movements.

- Finally, the evolution of natural gas hydrate systems through time is probably the most complex and intriguing research unknown. It is possible that, in future, natural gas hydrate systems will be routinely studied with well-logging devices installed in the overburden and capable of providing prolonged real-time measurements of the sediment properties, the pore fluid pressures and the rate of fluid flux. The integration with large-scale geophysical surveys will still be necessary. Analysing, in conjunction, the evolution of the petrophysical and seismic character of a gas hydrate deposit through time, owing to both natural processes and the exploitation of a hydrate reservoir, would undoubtedly represent a milestone in this research field.

# References

Algar, C.K. & Boudreau, B.P. 2010. Stability of bubbles in a linear elastic medium: Implications for bubble growth in marine sediments. *J. Geophys. Res.: Earth Surface,* 115**,** F03012.

Algar, C.K., et al. 2011a. Initial rise of bubbles in cohesive sediments by a process of viscoelastic fracture. *J. Geophys. Res.: Solid Earth,* 116**,** B01104.

Algar, S., et al. 2011b. Mass-transport deposits of the deepwater northwestern Borneo margin (Malaysia)–characterization from seismic-reflection, borehole, and core data with implications for hydrocarbon exploration and exploitation. *In:* Shipp, R.C., Weimer, P. & Posamentier, H.W. (eds.) *Mass-Transport Deposits in Deepwater Settings.* SEPM Special Publication, 96, 351-366.

Anderson, R., et al. 2003. Experimental measurement of methane and carbon dioxide clathrate hydrate equilibria in mesoporous silica. *The Journal of Physical Chemistry B,* 107**,** 3507-3514.

Anderson, R., et al. 2009. Gas hydrate growth and dissociation in narrow pore networks: capillary inhibition and hysteresis phenomena. *Geol. Soc. London, Spec. Publ.,* 319**,** 145-159.

Andreassen, K., et al. 1995. Seismic studies of a bottom simulating reflection related to gas hydrate beneath the continental margin of the Beaufort Sea. *J. Geophys. Res,* 100**,** 12659-12673.

Andreassen, K., et al. 1997. Amplitude versus offset modeling of the bottom simulating reflection associated with submarine gas hydrates. *Mar. Geol.,* 137**,** 25-40.

Andreassen, K., et al. 2000. A double gas-hydrate related bottom simulating reflector at the Norwegian continental margin. *Ann. N. Y. Acad. Sci.,* 912**,** 126-135.

Andreassen, K., et al. 2017. Massive blow-out craters formed by hydrate-controlled methane expulsion from the Arctic seafloor. *Science,* 356**,** 948-953.

Andresen, K.J. & Huuse, M. 2011. 'Bulls-eye'pockmarks and polygonal faulting in the Lower Congo Basin: relative timing and implications for fluid expulsion during shallow burial. *Mar. Geol.,* 279**,** 111-127.

Andresen, K.J. 2012. Fluid flow features in hydrocarbon plumbing systems: What do they tell us about the basin evolution? *Mar. Geol.,* 332**,** 89-108.

Archer, D. 2007. Methane hydrate stability and anthropogenic climate change. *Biogeosci. Disc.,* 4**,** 993-1057.

Archer, D., et al. 2009. Ocean methane hydrates as a slow tipping point in the global carbon cycle. *Proc. Natl. Acad. Sci. USA,* 106**,** 20596-20601.

Archie, G.E. 1942. The electrical resistivity log as an aid in determining some reservoir characteristics. *Transactions of the AIME,* 146**,** 54-62.

Ashi, J., et al. 2002. Distribution of methane hydrate BSRs and its implication for the prism growth in the Nankai Trough. *Mar. Geol.,* 187**,** 177-191.

Attias, E., et al. 2016. Controlled-source electromagnetic and seismic delineation of subseafloor fluid flow structures in a gas hydrate province, offshore Norway. *Geophys. J. Int.,* 206**,** 1093-1110.

Auguy, C., et al. 2017. Seismic evidence of gas hydrates, multiple BSRs and fluid flow offshore Tumbes Basin, Peru. *Mar. Geophys. Res.***,** 1-15.

Avseth, P., et al. 2010. *Quantitative seismic interpretation: Applying rock physics tools to reduce interpretation risk*, Cambridge University Press.

Baba, K. & Yamada, Y. 2004. BSRs and associated reflections as an indicator of gas hydrate and free gas accumulation: An example of accretionary prism and forearc basin system along the Nankai Trough, off central Japan. *Resour. Geol.,* 54**,** 11-24.

Bahk, J.-J., et al. 2011. Core lithologies and their constraints on gas-hydrate occurrence in the East Sea, offshore Korea: Results from the site UBGH1-9. *Mar. Petrol. Geol.,* 28**,** 1943-1952.

Bahk, J.-J., et al. 2013. Gas hydrate occurrences and their relation to host sediment properties: results from second Ulleung Basin Gas hydrate drilling expedition, east sea. *Mar. Petrol. Geol.,* 47**,** 21-29.

Bai, H., et al. 2016. Possible link between weak bottom simulating reflections and gas hydrate systems in fractures and macropores of fine-grained sediments: Results from the Hikurangi Margin, New Zealand. *Mar. Petrol. Geol.,* 71**,** 225-237.

Bakke, S. & Øren, P.-E. 1997. 3-D pore-scale modelling of sandstones and flow simulations in the pore networks. *Spe Journal,* 2**,** 136-149.

Ballard, A.L. & Sloan Jr, E.D. 2000. Structural transitions in methane+ ethane gas hydrates—Part II: modeling beyond incipient conditions. *Chem. Eng. Sci.,* 55**,** 5773-5782.

Bangs, N.L.B., et al. 1991 18. The cause of the bottom-simulating reflection in the vicinity of the Chile Triple Junction. Proceedings of the Ocean Drilling Program: Scientific results, 141, 243-252.

Bangs, N.L.B., et al. 1993. Free gas at the base of the gas hydrate zone in the vicinity of the Chile triple junction. *Geology,* 21**,** 905-908.

Bangs, N.L.B. & Brown, K.M. 1995 19. Regional heat flow in the vicinity of the Chile Triple Junction constrained by the depth of the bottom-simulating reflection. Proceedings of the Ocean Drilling Program, Scientific Results, 141, 253-258.

Bangs, N.L.B., et al. 2005. Upward shifts in the southern Hydrate Ridge gas hydrate stability zone following postglacial warming, offshore Oregon. *J. Geophys. Res.: Solid Earth,* 110, B03102.

Bangs, N.L.B., et al. 2010. Massive methane release triggered by seafloor erosion offshore southwestern Japan. *Geology,* 38**,** 1019-1022.

Bangs, N.L.B., et al. 2011. The mechanics of intermittent methane venting at South Hydrate Ridge inferred from 4D seismic surveying. *Earth Planet. Sci. Lett.,* 310**,** 105-112.

Barnes, P.M., et al. 2010. Tectonic and geological framework for gas hydrates and cold seeps on the Hikurangi subduction margin, New Zealand. *Mar. Geol.,* 272**,** 26-48.

Barry, M.A., et al. 2012. Gas domes in soft cohesive sediments. *Geology,* 40**,** 379-382.

Bauer, K., et al. 2015. Lithological control on gas hydrate saturation as revealed by signal classification of NMR logging data. *J. Geophys. Res.: Solid Earth,* 120**,** 6001-6017.

Benting, M., et al. 2006. Deepwater geohazard and gas hydrate investigation, Gumusut-Kakap development project, offshore Sabah, Malaysia. *Shell International internal report by Fugro GeoServices, Inc.-confidential*.

Berndt, C., et al. 2004. Seismic character of bottom simulating reflectors: examples from the mid-Norwegian margin. *Mar. Petrol. Geol.,* 21**,** 723-733.

Berndt, C., et al. 2012. Repeated slope failure linked to fluid migration: the Ana submarine landslide complex, Eivissa Channel, Western Mediterranean Sea. *Earth Planet. Sci. Lett.,* 319**,** 65-74.

Bertoni, C., et al. 2017. Spectrum of gas migration phenomena across multi-layered sealing sequences. *AAPG Bull.,* in press.

Bhatnagar, G., et al. 2007. Generalization of gas hydrate distribution and saturation in marine sediments by scaling of thermodynamic and transport processes. *Am. J. Sci.,* 307**,** 861-900.

Bhatnagar, G. 2008. *Accumulation of gas hydrates in marine sediments.* Rice University.

Bily, C. & Dick, J.W.L. 1974. Naturally occurring gas hydrates in the Mackenzie Delta, NWT. *B. Can. Petrol. Geol.,* 22**,** 340-352.

Blinova, V.N., et al. 2003. Hydrocarbon gases in deposits from mud volcanoes in the Sorokin Trough, north-eastern Black Sea. *Geo-Mar. Lett.,* 23**,** 250-257.

Boetius, A., et al. 2000. A marine microbial consortium apparently mediating anaerobic oxidation of methane. *Nature,* 407**,** 623-626.

Boetius, A. & Wenzhöfer, F. 2013. Seafloor oxygen consumption fuelled by methane from cold seeps. *Nat. Geosci.,* 6**,** 725-734.

Borowski, W.S., et al. 1996. Marine pore-water sulfate profiles indicate in situ methane flux from underlying gas hydrate. *Geology,* 24**,** 655-658.

Borowski, W.S., et al. 1999. Global and local variations of interstitial sulfate gradients in deep-water, continental margin sediments: Sensitivity to underlying methane and gas hydrates. *Mar. Geol.,* 159**,** 131-154.

Borowski, W.S. 2004. A review of methane and gas hydrates in the dynamic, stratified system of the Blake Ridge region, offshore southeastern North America. *Chem. Geol.,* 205**,** 311-346.

Boswell, R. & Collett, T.S. 2006. The gas hydrates resource pyramid. *Natural Gas & Oil,* 304**,** 285-4541.

Boswell, R. & Collett, T.S. 2011. Current perspectives on gas hydrate resources. *Energy Env. Sc.,* 4**,** 1206-1215.

Boswell, R., et al. 2011. Geologic controls on gas hydrate occurrence in the Mount Elbert prospect, Alaska North Slope. *Mar. Petrol. Geol.,* 28**,** 589-607.

Boswell, R., et al. 2012a. Subsurface gas hydrates in the northern Gulf of Mexico. *Mar. Petrol. Geol.,* 34**,** 4-30.

Boswell, R., et al. 2012b. Architecture of gas-hydrate-bearing sands from Walker Ridge 313, Green canyon 955, and Alaminos canyon 21: northern deepwater Gulf of Mexico. *Mar. Petrol. Geol.,* 34**,** 134-149.

Boswell, R., et al. 2016. Prospecting for marine gas hydrate resources. *Interpretation,* 4**,** SA13-SA24.

Boudreau, B.P. 2012. The physics of bubbles in surficial, soft, cohesive sediments. *Mar. Petrol. Geol.,* 38**,** 1-18.

Bourry, C., et al. 2009. Free gas and gas hydrates from the Sea of Marmara, Turkey: chemical and structural characterization. *Chem. Geol.,* 264**,** 197-206.

Brie, A., et al. 1995 Shear sonic interpretation in gas-bearing sands, SPE 30 595. SPE Annual Technical Conference and Exhibition.

Brooks, J.M., et al. 1983. Molecular and isotopic compositions et hydrocarbons at Site 533, Deep Sea Drilling Project Leg 76. *Initial Reports of the Deep Sea Drilling Projects,* 76**,** 377-389.

Brooks, J.M., et al. 1986. Association of gas hydrates and oil seepage in the Gulf of Mexico. *Org. Geochem.,* 10**,** 221-234.

Brooks, J.M., et al. 1991. Observations of gas hydrates in marine sediments, offshore northern California. *Mar. Geol.,* 96**,** 103-109.

Brothers, D.S., et al. 2014. Seabed fluid expulsion along the upper slope and outer shelf of the US Atlantic continental margin. *Geophys. Res. Lett.,* 41**,** 96-101.

Brown, A. 2000. Evaluation of possible gas microseepage mechanisms. *AAPG Bull.,* 84**,** 1775-1789.

Brown, A.R. 2011. *Interpretation of three-dimensional seismic data,* Society of Exploration Geophysicists and American Association of Petroleum Geologists.

Brown, K.M. & Bangs, N.L.B. 1991 20. Thermal regime of the Chile Triple Junction: constraints provided by downhole temperature measurements and distribution of gas hydrate. Proceedings of the Ocean Drilling Program, Scientific results, 141, 259-275.

Brown, K.M., et al. 1996. The nature, distribution, and origin of gas hydrate in the Chile Triple Junction region. *Earth Planet. Sci. Lett.,* 139**,** 471-483.

Bryndzia, L.T., et al. 2005. Quantitative Integrated Evaluation, (DRhI),Technology Deployment Project For N.W. Borneo. *Shell internal report-confidential*.

Bünz, S. & Mienert, J. 2004. Acoustic imaging of gas hydrate and free gas at the Storegga Slide. *J. Geophys. Res.: Solid Earth,* 109, B04102.

Bünz, S., et al. 2005. Gas hydrates at the Storegga Slide: Constraints from an analysis of multicomponent, wide-angle seismic data. *Geophysics,* 70**,** B19-B34.

Bünz, S., et al. 2012. Active gas venting through hydrate-bearing sediments on the Vestnesa Ridge, offshore W-Svalbard. *Mar. Geol.,* 332**,** 189-197.

Burwicz, E.B., et al. 2011. Estimation of the global amount of submarine gas hydrates formed via microbial methane formation based on numerical reaction-transport modeling and a novel parameterization of Holocene sedimentation. *Geochim. Cosmochim. Acta,* 75**,** 4562-4576.

Burwicz, E.B., et al. 2017. 3-D basin-scale reconstruction of natural gas hydrate system of the Green Canyon, Gulf of Mexico. *Geochem. Geophys. Geosyst.*

Cadena, A.F., et al. 2015. Application of Stratigraphic Grade Concepts to Understand Basin-fill Processes and Deposits in an Active Margin Setting, Magdalena Submarine Fan and Associated Fold-and-Thrust Belts, Offshore Colombia.

Calvès, G., et al. 2008. Three-dimensional seismic analysis of high-amplitude anomalies in the shallow subsurface of the Northern Indus Fan: Sedimentary and/or fluid origin. *J. Geophys. Res.: Solid Earth,* 113.

Carcione, J.M. & Tinivella, U. 2000. Bottom-simulating reflectors: Seismic velocities and AVO effects. *Geophysics,* 65**,** 54-67.

Carroll, J. 2014. *Natural gas hydrates: a guide for engineers,* Gulf Professional Publishing.

Carson, B. & Screaton, E.J. 1998. Fluid flow in accretionary prisms: Evidence for focused, time-variable discharge. *Rev. Geophys.,* 36**,** 329-351.

Cartwright, J.A. & Huuse, M. 2005. 3D seismic technology: the geological 'Hubble'. *Basin Res.,* 17**,** 1-20.

Cartwright, J.A. & Santamarina, C. 2015. Seismic characteristics of fluid escape pipes in sedimentary basins: implications for pipe genesis. *Mar. Petrol. Geol.,* 65**,** 126-140.

Cathles, L., et al. 2010. The physics of gas chimney and pockmark formation, with implications for assessment of seafloor hazards and gas sequestration. *Mar. Petrol. Geol.,* 27**,** 82-91.

Chand, S., et al. 2004. Elastic velocity models for gas-hydrate-bearing sediments—A comparison. *Geophys. J. Int.,* 159**,** 573-590.

Chand, S., et al. 2008. Gas hydrate stability zone modelling in areas of salt tectonics and pockmarks of the Barents Sea suggests an active hydrocarbon venting system. *Mar. Petrol. Geol.,* 25**,** 625-636.

Charlou, J., et al. 2004. Physical and chemical characterization of gas hydrates and associated methane plumes in the Congo–Angola Basin. *Chem. Geol.,* 205**,** 405-425.

Chatterjee, S., et al. 2014. The impact of lithologic heterogeneity and focused fluid flow upon gas hydrate distribution in marine sediments. *J. Geophys. Res.: Solid Earth,* 119**,** 6705-6732.

Chazallon, B., et al. 2007. A comparative Raman spectroscopic study of natural gas hydrates collected at different geological sites. *Chem. Geol.,* 244**,** 175-185.

Chen, D.F. & Cathles, L.M. 2003. A kinetic model for the pattern and amounts of hydrate precipitated from a gas steam: Application to the Bush Hill vent site, Green Canyon Block 185, Gulf of Mexico. *J. Geophys. Res.: Solid Earth,* 108, B1, 2058.

Chen, L.-T., et al. 2017. Hydrate formation in sediments from free gas using a one-dimensional visual simulator. *Fuel,* 197**,** 298-309.

Chen, L., et al. 2014. Two dimensional fluid flow models at two gas hydrate sites offshore southwestern Taiwan. *J. Asian Earth Sci.,* 92**,** 245-253.

Choi, J., et al. 2013. Gas origin and migration in the Ulleung Basin, East Sea: Results from the Second Ulleung Basin Gas Hydrate Drilling Expedition (UBGH2). *Mar. Petrol. Geol.,* 47**,** 113-124.

Choi, J.H., et al. 2011. X-ray computed-tomography imaging of gas migration in water-saturated sediments: From capillary invasion to conduit opening. *Geophys. Res. Lett.,* 38.

Chun, J.-H., et al. 2011. Sediment mounds and other sedimentary features related to hydrate occurrences in a columnar seismic blanking zone of the Ulleung Basin, East Sea, Korea. *Mar. Petrol. Geol.,* 28**,** 1787-1800.

Claypool, G.E. & Kaplan, I.R. 1974. The origin and distribution of methane in marine sediments. *In:* Kaplan, I. (ed.) *Natural gases in marine sediments.* Springer.

Claypool, G.E., et al. 2006 15. Microbial methane generation and gas transport in shallow sediments of an accretionary complex, southern Hydrate Ridge (ODP Leg 204), offshore Oregon, USA. Proceedings of the Ocean Drilling Program, Scientific Results, 204.

Clennell, M.B., et al. 1999. Formation of natural gas hydrates in marine sediments: 1. Conceptual model of gas hydrate growth conditioned by host sediment properties. *J. Geophys. Res.: Solid Earth,* 104**,** 22985-23003.

Clennell, M.B., et al. 2000a. Formation of natural gas hydrates in marine sediments: Gas hydrate growth and stability conditioned by host sediment properties. *Ann. N. Y. Acad. Sci.,* 912**,** 887-896.

Clennell, M.B., et al. 2000b. Movement and accumulation of methane in marine sediments: relation to gas hydrate systems. *In:* Max, M.D. (ed.) *Natural Gas Hydrate in oceanic and permafrost environments, 105-122.* Springer.

Collett, T.S. 1994. Permafrost-Associated Gas Hydrate Accumulationsa. *Ann. N. Y. Acad. Sci.,* 715**,** 247-269.

Collett, T.S. & Ladd, J. 2000 19. Detection of gas hydrate with downhole logs and assessment of gas hydrate concentrations (saturations) and gas volumes on the Blake Ridge with electrical resistivity log data. Proceedings of the Ocean Drilling Program, Scientific Results,164, 179-191.

Collett, T.S., et al. 2009. Natural gas hydrates: a review. *In:* Collett, T.S., Knapp, C.C. & Boswell, R. (eds.) *Natural gas hydrates-Energy Resource Potential and Associated Geologic Hazards.* AAPG Memoir, 89, 146-219.

Collett, T.S. & Lee, M.W. 2011 Downhole well log characterization of gas hydrates in nature–a review. Proceedings of the 7th International Conference on Gas Hydrates (ICGH 2011).

Collett, T.S., et al. 2011. Permafrost-associated natural gas hydrate occurrences on the Alaska North Slope. *Mar. Petrol. Geol.,* 28**,** 279-294.

Collett, T.S., et al. 2012. Gulf of Mexico Gas Hydrate Joint Industry Project Leg II logging-while-drilling data acquisition and analysis. *Mar. Petrol. Geol.,* 34**,** 41-61.

Cook, A.E., et al. 2008. Fracture-controlled gas hydrate systems in the northern Gulf of Mexico. *Mar. Petrol. Geol.,* 25**,** 932-941.

Cook, A.E., et al. 2010. Electrical anisotropy due to gas hydrate-filled fractures. *Geophysics,* 75**,** F173-F185.

Cook, A.E. & Malinverno, A. 2013. Short migration of methane into a gas hydrate-bearing sand layer at Walker Ridge, Gulf of Mexico. *Geochem. Geophys. Geosyst.,* 14**,** 283-291.

Cook, A.E., et al. 2014. Natural gas hydrates occupying fractures: A focus on non-vent sites on the Indian continental margin and the northern Gulf of Mexico. *Mar. Petrol. Geol.,* 58**,** 278-291.

Cook, A.E. & Tost, B.C. 2014. Geophysical signatures for low porosity can mimic natural gas hydrate: An example from Alaminos Canyon, Gulf of Mexico. *J. Geophys. Res.: Solid Earth,* 119**,** 7458-7472.

Corredor, F., et al. 2005. Structural styles in the deep-water fold and thrust belts of the Niger Delta. *AAPG Bull.,* 89**,** 753-780.

Couzens-Schultz, B.A. & Chan, A.W. 2010. Stress determination in active thrust belts: An alternative leak-off pressure interpretation. *J. Struct. Geol.,* 32**,** 1061-1069.

Couzens-Schultz, B.A. & Azbel, K. 2014. Predicting pore pressure in active fold–thrust systems: An empirical model for the deepwater Sabah foldbelt. *J. Struct. Geol.,* 69**,** 465-480.

Crutchley, G.J., et al. 2013. Drivers of focused fluid flow and methane seepage at south Hydrate Ridge, offshore Oregon, USA. *Geology,* 41**,** 551-554.

Crutchley, G.J., et al. 2014. The impact of fluid advection on gas hydrate stability: Investigations at sites of methane seepage offshore Costa Rica. *Earth Planet. Sci. Lett.,* 401**,** 95-109.

Crutchley, G.J., et al. 2015. Gas migration into gas hydrate-bearing sediments on the southern Hikurangi margin of New Zealand. *J. Geophys. Res.: Solid Earth,* 120**,** 725-743.

Crutchley, G.J., et al. 2016. High-resolution seismic velocity analysis as a tool for exploring gas hydrate systems: An example from New Zealand's southern Hikurangi margin. *Interpretation,* 4**,** SA1-SA12.

Cunningham, R. & Lindholm, R.M. 2000. Seismic Evidence for Widespread Gas Hydrate Formation, Offshore West Africa. *In:* Mello, M.R. & Katz, B.J. (eds.) *Petroleum systems of South Atlantic margins.* AAPG Memoir, 73, 93-105.

Dai, J., et al. 2004. Detection and estimation of gas hydrates using rock physics and seismic inversion: Examples from the northern deepwater Gulf of Mexico. *The Leading Edge,* 23**,** 60-66.

Dai, S., et al. 2012. Hydrate morphology: Physical properties of sands with patchy hydrate saturation. *J. Geophys. Res.: Solid Earth,* 117, B11205.

Dai, S. & Santamarina, J.C. 2014. Sampling disturbance in hydrate-bearing sediment pressure cores: NGHP-01 expedition, Krishna–Godavari Basin example. *Mar. Petrol. Geol.,* 58**,** 178-186.

Dai, S. & Seol, Y. 2014. Water permeability in hydrate-bearing sediments: A pore-scale study. *Geophys. Res. Lett.,* 41**,** 4176-4184.

Daigle, H. & Dugan, B. 2010a. Effects of multiphase methane supply on hydrate accumulation and fracture generation. *Geophys. Res. Lett.,* 37**,** L20301.

Daigle, H. & Dugan, B. 2010b. Origin and evolution of fracture-hosted methane hydrate deposits. *J. Geophys. Res.: Solid Earth,* 115, B11103.

Daigle, H., et al. 2011. Transient hydraulic fracturing and gas release in methane hydrate settings: A case study from southern Hydrate Ridge. *Geochem. Geophys. Geosyst.,* 12.

Daigle, H. & Dugan, B. 2011. Capillary controls on methane hydrate distribution and fracturing in advective systems. *Geochem. Geophys. Geosyst.,* 12.

Daigle, H. & Dugan, B. 2014. Pore size controls on the base of the methane hydrate stability zone in the Kumano Basin, offshore Japan. *Geophys. Res. Lett.,* 41**,** 8021-8028.

Dan-Unterseh, G., et al. 2014 3D seismic and AUV data integration for deepwater geohazard assessment: Application to offshore northwest Borneo, Brunei, OTC 24796-MS. Offshore Technology Conference-Asia.

Davidson, D., et al. 1984. The ability of small molecules to form clathrate hydrates of structure II. *Nature,* 311**,** 142-143.

Davie, M.K. & Buffett, B.A. 2001. A numerical model for the formation of gas hydrate below the seafloor. *J. Geophys. Res.: Solid Earth,* 106**,** 497-514.

Davie, M.K. & Buffett, B.A. 2003. A steady state model for marine hydrate formation: Constraints on methane supply from pore water sulfate profiles. *J. Geophys. Res.: Solid Earth,* 108.

Davie, M.K., et al. 2004. Methane solubility in marine hydrate environments. *Mar. Geol.,* 203**,** 177-184.

Davies, R.J., et al. 2006. Giant clastic intrusions primed by silica diagenesis. *Geology,* 34**,** 917-920.

Davies, R.J. & Cartwright, J.A. 2007. Kilometer-scale chemical reaction boundary patterns and deformation in sedimentary rocks. *Earth Planet. Sci. Lett.,* 262**,** 125-137.

Davies, R.J. & Clarke, A.L. 2010. Methane recycling between hydrate and critically pressured stratigraphic traps, offshore Mauritania. *Geology,* 38**,** 963-966.

Davies, R.J., et al. 2012. Deepwater canyons: An escape route for methane sealed by methane hydrate. *Earth Planet. Sci. Lett.,* 323**,** 72-78.

Davies, R.J., et al. 2014. Probable patterns of gas flow and hydrate accretion at the base of the hydrate stability zone. *Geology,* 42**,** 1055-1058.

Davies, R.J., et al. 2015. An irregular feather-edge and potential outcrop of marine gas hydrate along the Mauritanian margin. *Earth Planet. Sci. Lett.,* 423**,** 202-209.

Davis, E.E., et al. 1990. Rates of fluid expulsion across the Northern Cascadia Accretionary Prism: Constraints from new heat row and multichannel seismic reflection data. *J. Geophys. Res.: Solid Earth,* 95**,** 8869-8889.

Davy, B., et al. 2010. Gas escape features off New Zealand: Evidence of massive release of methane from hydrates. *Geophys. Res. Lett.,* 37**,** L21309.

De Prunelé, A., et al. 2017. Focused hydrocarbon-migration in shallow sediments of a pockmark cluster in the Niger Delta (Off Nigeria). *Geochem. Geophys. Geosyst.,* 18**,** 93-112.

Dewangan, P., et al. 2011. Fault system and thermal regime in the vicinity of site NGHP-01-10, Krishna–Godavari basin, Bay of Bengal. *Mar. Petrol. Geol.,* 28**,** 1899-1914.

Dickens, G.R., et al. 1997. Direct measurement ofin situ methane quantities in a large gas hydrate reservoir. *Nature,* 385**,** 426-428.

Dickens, G.R., et al. 2000. Detection of methane gas hydrate in the pressure core sampler (PCS): volume-pressure-time relations during controlled degassing experiments. *In:* Paull, C.K., Matsumoto, R., Wallace, P.J. & Dillon, W.P. (eds.) *Proceedings of the Ocean Drilling Program: Scientific Results, 164, 113-126.*

Dickens, G.R. 2003. Rethinking the global carbon cycle with a large, dynamic and microbially mediated gas hydrate capacitor. *Earth Planet. Sci. Lett.,* 213**,** 169-183.

Domenico, S.N. 1976. Effect of brine-gas mixture on velocity in an unconsolidated sand reservoir. *Geophysics,* 41**,** 882-894.

Du, C. & Yortsos, Y. 1999. A numerical study of the critical gas saturation in a porous medium. *Transport Porous Med.,* 35**,** 205-225.

Duan, Z., et al. 1992. The prediction of methane solubility in natural waters to high ionic strength from 0 to 250 C and from 0 to 1600 bar. *Geochim. Cosmochim. Acta,* 56**,** 1451-1460.

Dugan, B. & Flemings, P.B. 2000. Overpressure and fluid flow in the New Jersey continental slope: implications for slope failure and cold seeps. *Science,* 289**,** 288-291.

Dugan, B. 2012. Petrophysical and consolidation behavior of mass transport deposits from the northern Gulf of Mexico, IODP Expedition 308. *Mar. Geol.,* 315**,** 98-107.

Dumke, I., et al. 2016. Gas hydrate distribution and hydrocarbon maturation north of the Knipovich Ridge, western Svalbard margin. *J. Geophys. Res.: Solid Earth,* 121**,** 1405–1424.

Dvorkin, J. & Nur, A. 1998. Acoustic signatures of patchy saturation. *Int. J. Solids Struct.,* 35**,** 4803-4810.

Dvorkin, J., et al. 2000. Introduction to physical properties and elasticity models. *In:* Max, M.D. (ed.) *Natural Gas Hydrate in oceanic and permafrost environments, 245-260.* Springer.

Ecker, C., et al. 1998. Sediments with gas hydrates: Internal structure from seismic AVO. *Geophysics,* 63**,** 1659-1669.

Edgar, N.T., et al. 1973. 8. Site 153. *Deep Sea Drilling Project (DSDP) Reports and Publications,* 15.

Egeberg, P.K. & Dickens, G.R. 1999. Thermodynamic and pore water halogen constraints on gas hydrate distribution at ODP Site 997 (Blake Ridge). *Chem. Geol.,* 153**,** 53-79.

Ellis, M., et al. 2008. Electromagnetic surveying of seafloor mounds in the northern Gulf of Mexico. *Mar. Petrol. Geol.,* 25**,** 960-968.

Engelder, T. & Fischer, M.P. 1994. Influence of poroelastic behavior on the magnitude of minimum horizontal stress, Sh in overpressured parts of sedimentary basins. *Geology,* 22**,** 949-952.

England, W.A., et al. 1987. The movement and entrapment of petroleum fluids in the subsurface. *J. Geol. Soc. London,* 144**,** 327-347.

Ercilla, G., et al. 2002. The Magdalena Turbidite System (Caribbean Sea): present-day morphology and architecture model. *Mar. Geol.,* 185**,** 303-318.

Escalona, A. & Mann, P. 2011. Tectonics, basin subsidence mechanisms, and paleogeography of the Caribbean-South American plate boundary zone. *Mar. Petrol. Geol.,* 28**,** 8-39.

Fauria, K.E. & Rempel, A.W. 2011. Gas invasion into water-saturated, unconsolidated porous media: Implications for gas hydrate reservoirs. *Earth Planet. Sci. Lett.,* 312**,** 188-193.

Fischer, D., et al. 2013. Subduction zone earthquake as potential trigger of submarine hydrocarbon seepage. *Nat. Geosci.,* 6**,** 647-651.

Flemings, P.B., et al. 2002. Flow focusing in overpressured sandstones: Theory, observations, and applications. *Am. J. Sci.,* 302**,** 827-855.

Flemings, P.B., et al. 2003. Critical pressure and multiphase flow in Blake Ridge gas hydrates. *Geology,* 31**,** 1057-1060.

Fofonoff, N.P. 1985. Physical properties of seawater: A new salinity scale and equation of state for seawater. *J. Geophys. Res.,* 90**,** 3332-3342.

Fohrmann, M. & Pecher, I.A. 2012. Analysing sand-dominated channel systems for potential gas-hydrate-reservoirs using an AVO seismic inversion technique on the Southern Hikurangi Margin, New Zealand. *Mar. Petrol. Geol.,* 38**,** 19-34.

Foschi, M. 2014. *Seismic evidence for hydrocarbon migration.* Cardiff University.

Foschi, M. & Cartwright, J.A. 2016. South Malvinas/Falkland Basin: Hydrocarbon migration and petroleum system. *Mar. Petrol. Geol.,* 77**,** 124-140.

Foschi, M., et al. 2017. Sequential vertical gas charge into multilayered sequences controlled by central conduits. *AAPG Bull.*

Foucher, J.-P., et al. 2002. Observation and tentative interpretation of a double BSR on the Nankai slope. *Mar. Geol.,* 187**,** 161-175.

Fraser, D.R.A., et al. 2016. Gas hydrate accumulations related to focused fluid flow in the Pegasus Basin, southern Hikurangi Margin, New Zealand. *Mar. Petrol. Geol.,* 77**,** 399-408.

Frederick, J.M. & Buffett, B.A. 2011. Topography-and fracture-driven fluid focusing in layered ocean sediments. *Geophys. Res. Lett.,* 38.

Frederick, J.M. & Buffett, B.A. 2014. Taliks in relict submarine permafrost and methane hydrate deposits: Pathways for gas escape under present and future conditions. *J. Geophys. Res.: Earth Surface,* 119**,** 106-122.

Freire, A.F.M., et al. 2011. Structural-stratigraphic control on the Umitaka Spur gas hydrates of Joetsu Basin in the eastern margin of Japan Sea. *Mar. Petrol. Geol.,* 28**,** 1967-1978.

Froelich, P.N., et al. 1995 21. Geochemical evidence for gas hydrate in sediment near the Chile Triple Juction. Proceedings of the Ocean Drilling Program, Scientific Results, 141, 279-286.

Frye, M. 2008. Preliminary evaluation of in-place gas hydrate resources: Gulf of Mexico Outer Continental Shelf, U.S. Department of the Interior, Minerals Management Service Resource Evaluation Division. *OCS Report MMS.*

Frye, M., et al. 2012. Gas hydrate resource potential in the Terrebonne Basin, Northern Gulf of Mexico. *Mar. Petrol. Geol.,* 34**,** 150-168.

Fujii, T., et al. 2015. Geological setting and characterization of a methane hydrate reservoir distributed at the first offshore production test site on the Daini-Atsumi Knoll in the eastern Nankai Trough, Japan. *Mar. Petrol. Geol.,* 66**,** 310-322.

Ganguly, N., et al. 2000. Heat flow variations from bottom simulating reflectors on the Cascadia margin. *Mar. Geol.,* 164**,** 53-68.

Gay, A., et al. 2006. Isolated seafloor pockmarks linked to BSRs, fluid chimneys, polygonal faults and stacked Oligocene–Miocene turbiditic palaeochannels in the Lower Congo Basin. *Mar. Geol.,* 226**,** 25-40.

Gay, A., et al. 2007. Geological controls on focused fluid flow associated with seafloor seeps in the Lower Congo Basin. *Mar. Geol.,* 244**,** 68-92.

Gee, M.J.R., et al. 2007. The Brunei slide: a giant submarine landslide on the North West Borneo Margin revealed by 3D seismic data. *Mar. Geol.,* 246**,** 9-23.

Ghosh, R., et al. 2010. Effective medium modeling of gas hydrate-filled fractures using the sonic log in the Krishna-Godavari basin, offshore eastern India. *J. Geophys. Res.: Solid Earth,* 115, B06101.

Ginsburg, G.D., et al. 1993. Gas hydrates from the continental slope, offshore Sakhalin Island, Okhotsk Sea. *Geo-Mar. Lett.,* 13**,** 41-48.

Ginsburg, G.D. & Soloviev, V.A. 1994. Mud volcano gas hydrates in the Caspian Sea. *Bull. Geol. Soc. Denmark,* 41**,** 100.

Ginsburg, G.D. & Soloviev, V.A. 1997. Methane migration within the submarine gas-hydrate stability zone under deep-water conditions. *Mar. Geol.,* 137**,** 49-57.

Gisler, E.P., et al. 2007. Integrated Site Characterization, Gumusut Deepwater Development, Blocks G, J and K, Offshore Sabah, Malaysia. *Shell International internal report by Fugro GeoServices, Inc.-confidential*.

Goldberg, D.S., et al. 2010. Evaluation of natural gas-hydrate systems using borehole logs. *Geophysical Characterization of Gas Hydrates***,** 239-262.

Gorman, A.R., et al. 2002. Migration of methane gas through the hydrate stability zone in a low-flux hydrate province. *Geology,* 30**,** 327-330.

Gorman, A.R. & Senger, K. 2010. Defining the updip extent of the gas hydrate stability zone on continental margins with low geothermal gradients. *J. Geophys. Res.: Solid Earth,* 115, B07105.

Goto, S., et al. 2016. Simulation of gas hydrate dissociation caused by repeated tectonic uplift events. *J. Geophys. Res.: Solid Earth,* 121.

Grant, C.J. 2004 The upper Miocene deepwater fans of Northwest Borneo, DFE04-OR-047. Deepwater And Frontier Exploration In Asia & Australasia Symposium, 421-428.

Grauls, D. 2001. Gas hydrates: importance and applications in petroleum exploration. *Mar. Petrol. Geol.,* 18**,** 519-523.

Graves, C.A., et al. 2017. Methane in shallow subsurface sediments at the landward limit of the gas hydrate stability zone offshore western Svalbard. *Geochim. Cosmochim. Acta,* 198**,** 419-438.

Greinert, J., et al. 2006. 1300-m-high rising bubbles from mud volcanoes at 2080m in the Black Sea: Hydroacoustic characteristics and temporal variability. *Earth Planet. Sci. Lett.,* 244**,** 1-15.

Grevemeyer, I., et al. 2000. Natural gas hydrates on the continental slope off Pakistan: constraints from seismic techniques. *Geophys. J. Int.,* 140**,** 295-310.

Grevemeyer, I. & Villinger, H. 2001. Gas hydrate stability and the assessment of heat flow through continental margins. *Geophys. J. Int.,* 145**,** 647-660.

Guerin, G., et al. 1999. Characterization of in situ elastic properties of gas hydrate-bearing sediments on the Blake Ridge. *J. Geophys. Res.: Solid Earth,* 104**,** 17781-17795.

Haacke, R.R., et al. 2007. Gas hydrate, fluid flow and free gas: Formation of the bottom-simulating reflector. *Earth Planet. Sci. Lett.,* 261**,** 407-420.

Haacke, R.R., et al. 2008. Controls on the formation and stability of gas hydrate-related bottom-simulating reflectors (BSRs): A case study from the west Svalbard continental slope. *J. Geophys. Res.: Solid Earth,* 113.

Hachikubo, A., et al. 2010a. Molecular and isotopic characteristics of gas hydrate-bound hydrocarbons in southern and central Lake Baikal. *Geo-Mar. Lett.,* 30**,** 321-329.

Hachikubo, A., et al. 2010b. Isotopic composition of gas hydrates in subsurface sediments from offshore Sakhalin Island, Sea of Okhotsk. *Geo-Mar. Lett.,* 30**,** 313-319.

Hachikubo, A., et al. 2015. Molecular and isotopic composition of volatiles in gas hydrates and in sediment from the Joetsu Basin, eastern margin of the Japan Sea. *Energies,* 8**,** 4647-4666.

Hadley, C., et al. 2008 Gumusut-Kakap project: Geohazard characterisation and impact on field development plans, IPTC12554. International Petroleum Technology Conference.

Haines, S.S., et al. 2017. High-resolution seismic characterization of the gas and gas hydrate system at Green Canyon 955, Gulf of Mexico, USA. *Mar. Petrol. Geol.,* 82**,** 220-237.

Hamilton, E.L. 1971. Elastic properties of marine sediments. *J. Geophys. Res.,* 76**,** 579-604.

Hamilton, E.L. 1979. V p/V s and Poisson's ratios in marine sediments and rocks. *J. Acoust. Soc. Am.,* 66**,** 1093-1101.

Hawkins, R.A. & Narkus, A. 1998 New Development in Offshore Geotechnical Investigation. Society of Underwater Technology. Offshore Site Investigation and Foundation Behaviour, New Frontiers.

Hedges, J.I. & Keil, R.G. 1995. Sedimentary organic matter preservation: an assessment and speculative synthesis. *Mar. Chem.,* 49**,** 81-115.

Heeschen, K.U., et al. 2003. Distribution and height of methane bubble plumes on the Cascadia Margin characterized by acoustic imaging. *Geophys. Res. Lett.,* 30.

Heeschen, K.U., et al. 2007. In situ hydrocarbon concentrations from pressurized cores in surface sediments, Northern Gulf of Mexico. *Mar. Chem.,* 107**,** 498-515.

Helgerud, M.B., et al. 1999. Elastic-wave velocity in marine sediments with gas hydrates: Effective medium modeling. *Geophys. Res. Lett.,* 26**,** 2021-2024.

Helgerud, M.B. 2001. *Wave speeds in gas hydrate and sediments containing gas hydrate: A laboratory and modeling study.* Stanford University.

Helgerud, M.B., et al. 2009. Elastic wave speeds and moduli in polycrystalline ice Ih, sI methane hydrate, and sII methane-ethane hydrate. *J. Geophys. Res.: Solid Earth,* 114, B02212.

Henry, P., et al. 1996. Fluid flow in and around a mud volcano field seaward of the Barbados accretionary wedge: results from Manon cruise. *J. Geophys. Res.: Solid Earth,* 101**,** 20297-20323.

Henry, P., et al. 1999. Formation of natural gas hydrates in marine sediments, 2, Thermodynamic calculations of stability conditions in porous sediments. *J. Geophys. Res.,* 104**,** 23005-23022.

Hensen, C., et al. 2003. Control of sulfate pore-water profiles by sedimentary events and the significance of anaerobic oxidation of methane for the burial of sulfur in marine sediments. *Geochim. Cosmochim. Acta,* 67**,** 2631-2647.

Hermanrud, C., et al. 2013. Consequences of water level drops for soft sediment deformation and vertical fluid leakage. *Math. Geosci.,* 45**,** 1-30.

Hesse, S., et al. 2010. The structural evolution of folds in a deepwater fold and thrust belt–a case study from the Sabah continental margin offshore NW Borneo, SE Asia. *Mar. Petrol. Geol.,* 27**,** 442-454.

Hesselbo, S.P., et al. 2000. Massive dissociation of gas hydrate during a Jurassic oceanic anoxic event. *Nature,* 406**,** 392-395.

Hester, K.C. & Brewer, P.G. 2009. Clathrate hydrates in nature. *Annu. Rev. Mar. Sci.,* 1**,** 303-327.

Hildenbrand, A., et al. 2002. Gas breakthrough experiments on fine-grained sedimentary rocks. *Geofluids,* 2**,** 3-23.

Hillis, R. 2000. Pore pressure/stress coupling and its implications for seismicity. *Exploration Geophysics,* 31**,** 448-454.

Hillman, J.I.T., et al. 2017a. Gas hydrate reservoirs and gas migration mechanisms in the Terrebonne Basin, Gulf of Mexico. *Mar. Petrol. Geol.,* 86**,** 1357-1373.

Hillman, J.I.T., et al. 2017b. The character and amplitude of 'discontinuous' bottom-simulating reflections in marine seismic data. *Earth Planet. Sci. Lett.,* 459**,** 157-169.

Ho, S., et al. 2012. Vertical evolution of fluid venting structures in relation to gas flux, in the Neogene-Quaternary of the Lower Congo Basin, Offshore Angola. *Mar. Geol.,* 332**,** 40-55.

Holbrook, W.S., et al. 1996. Methane hydrate and free gas on the Blake Ridge from vertical seismic profiling. *Science,* 273**,** 1840.

Holbrook, W.S. 2001. Seismic studies of the Blake Ridge: Implications for hydrate distribution, methane expulsion, and free gas dynamics. *In:* Paull, C.K. & Dillon,

W.P. (eds.) *Natural gas hydrates: Occurrence, distribution, and detection.* AGU Geophysical Monograph 124, 235-256.

Holland, M., et al. 2008 Observed gas hydrate morphologies in marine sediments. Proceedings of the 6th International Conference on Gas Hydrates (ICGH 2008).

Holland, M. & Schultheiss, P. 2014. Comparison of methane mass balance and X-ray computed tomographic methods for calculation of gas hydrate content of pressure cores. *Mar. Petrol. Geol.,* 58**,** 168-177.

Holtzman, R. & Juanes, R. 2011. Thermodynamic and hydrodynamic constraints on overpressure caused by hydrate dissociation: A pore-scale model. *Geophys. Res. Lett.,* 38**,** L14308.

Holtzman, R., et al. 2012. Capillary fracturing in granular media. *Phys. Rev. Lett.,* 108**,** 264504.

Hong, W.-L., et al. 2014. A kinetic-model approach to quantify the effect of mass transport deposits on pore water profiles in the Krishna–Godavari Basin, Bay of Bengal. *Mar. Petrol. Geol.,* 58**,** 223-232.

Hopkins, H. 1973. Geology of the Aruba Gap abyssal plain near DSDP site 153. *Initial reports of the deep sea drilling project,* 15**,** 1039-1050.

Hornbach, M.J., et al. 2004. Critically pressured free-gas reservoirs below gas-hydrate provinces. *Nature,* 427**,** 142-144.

Hornbach, M.J., et al. 2012. Detecting hydrate and fluid flow from bottom simulating reflector depth anomalies. *Geology,* 40**,** 227-230.

Horozal, S., et al. 2009. Seismic indicators of gas hydrate and associated gas in the Ulleung Basin, East Sea (Japan Sea) and implications of heat flows derived from depths of the bottom-simulating reflector. *Mar. Geol.,* 258**,** 126-138.

Hovland, M., et al. 1997. Gas hydrate and free gas volumes in marine sediments: Example from the Niger Delta front. *Mar. Petrol. Geol.,* 14**,** 245-255.

Hovland, M. & Gudmestad, O.T. 2001. Potential influence of gas hydrates on seabed installations. *In:* Paull, C.K. & Dillon, W.P. (eds.) *Natural gas hydrates: occurrence, distribution, and detection.* AGU Geophysical Monograph 124, 307-315.

Hovland, M. & Svensen, H. 2006. Submarine pingoes: Indicators of shallow gas hydrates in a pockmark at Nyegga, Norwegian Sea. *Mar. Geol.,* 228**,** 15-23.

Hustoft, S., et al. 2007. High-resolution 3D-seismic data indicate focussed fluid migration pathways above polygonal fault systems of the mid-Norwegian margin. *Mar. Geol.,* 245**,** 89-106.

Hustoft, S., et al. 2009. Gas hydrate reservoir and active methane-venting province in sediments on< 20 Ma young oceanic crust in the Fram Strait, offshore NW-Svalbard. *Earth Planet. Sci. Lett.,* 284**,** 12-24.

Hustoft, S., et al. 2010. Three-dimensional seismic analysis of the morphology and spatial distribution of chimneys beneath the Nyegga pockmark field, offshore mid-Norway. *Basin Res.,* 22**,** 465-480.

Hutchison, C.S. 2010. The north-west Borneo trough. *Mar. Geol.,* 271**,** 32-43.

Hyndman, R.D. & Davis, E.E. 1992. A mechanism for the formation of methane hydrate and seafloor bottom-simulating reflectors by vertical fluid expulsion. *J. Geophys. Res.: Solid Earth,* 97**,** 7025-7041.

Hyodo, M., et al. 2013. Mechanical behavior of gas-saturated methane hydrate-bearing sediments. *J. Geophys. Res.: Solid Earth,* 118**,** 5185-5194.

Imbert, P., et al. 2014. How to evacuate 10 km3 of mud: saturate with gas and decrease the pressure! *Geo-Mar. Lett.,* 34**,** 199-213.

Ingram, G.M., et al. 2004. Deepwater North West Borneo: hydrocarbon accumulation in an active fold and thrust belt. *Mar. Petrol. Geol.,* 21**,** 879-887.

Inks, T.L., et al. 2009. Seismic prospecting for gas-hydrate and associated free-gas prospects in the Milne Point area of northern Alaska. *In:* Collett, T.S., Knapp, C.C. & Boswell, R. (eds.) *Natural gas hydrates-Energy Resource Potential and Associated Geologic Hazards.* AAPG Memoir, 89, 555-583.

Iodp. *International Ocean Discovery Program Database:* http://iodp.tamu.edu/database/ [Online].

Ito, T., et al. 2015. Lithological features of hydrate-bearing sediments and their relationship with gas hydrate saturation in the eastern Nankai Trough, Japan. *Mar. Petrol. Geol.,* 66**,** 368-378.

Jain, A.K. & Juanes, R. 2009. Preferential mode of gas invasion in sediments: Grain-scale mechanistic model of coupled multiphase fluid flow and sediment mechanics. *J. Geophys. Res.: Solid Earth,* 114, B08101.

Jenkyns, H.C. 2003. Evidence for rapid climate change in the Mesozoic–Palaeogene greenhouse world. *Philosophical Transactions of the Royal Society of London A: Mathematical, Physical and Engineering Sciences,* 361**,** 1885-1916.

Jin, Z.H., et al. 2015. Crack extension induced by dissociation of fracture-hosted methane gas hydrate. *Geophys. Res. Lett.,* 42**,** 8522-8529.

Johnson, J.E., et al. 2014. Influence of total organic carbon deposition on the inventory of gas hydrate in the Indian continental margins. *Mar. Petrol. Geol.,* 58**,** 406-424.

Johnson, J.E., et al. 2015. Abiotic methane from ultraslow-spreading ridges can charge Arctic gas hydrates. *Geology,* 43**,** 371-374.

Jones, D.M., et al. 2008. Crude-oil biodegradation via methanogenesis in subsurface petroleum reservoirs. *Nature,* 451**,** 176-180.

Jong, J., et al. 2014 Basin Modeling Study of Deepwater Block R (DWR) Offshore Sabah and Its Correlation with Surface Geochemical Analyses, IPTC-18186-MS. International Petroleum Technology Conference.

Jong, J., et al. 2016 A Sequence Stratigraphic Case Study of an Exploration Permit in Deepwater Sabah: Comparison and Lessons Learned from Pre-Versus Post-Drill Evaluations. Proceedungs, Indonesian Petreoleum Association, 40th Annual Convention & Exhibition.

Judd, A.G. & Hovland, M. 2007. *Seabed Fluid Flow: The Impact on Geology, Biology and the Marine Environment*, Cambridge University Press.

Jung, J.-W. & Santamarina, J.C. 2012. Hydrate formation and growth in pores. *J. Cryst. Growth,* 345**,** 61-68.

Jung, J. & Santamarina, J.C. 2011. Hydrate adhesive and tensile strengths. *Geochem. Geophys. Geosyst.,* 12.

Kang, N.-K., et al. 2016. Distribution and origin of seismic chimneys associated with gas hydrate using 2D multi-channel seismic reflection and well log data in the Ulleung Basin, East Sea. *Quatern. Int.,* 392**,** 99-111.

Kannberg, P.K., et al. 2013. Temporal variation of methane flares in the ocean above Hydrate Ridge, Oregon. *Earth Planet. Sci. Lett.,* 368**,** 33-42.

Kastner, M., et al. 1995. 10. Relation between pore fluid chemistry and gas hydrates associated with bottom-simulating reflectors at the Cascadia margin, Sites 889 and 892. *1995. Proceedings of the Ocean Drilling Program, Scientific Results, 146, 175-187,* 146**,** 175-187.

Kastner, M., et al. 1998. Chemistry, isotopic composition, and origin of a methane-hydrogen sulfide hydrate at the Cascadia subduction zone. *Earth Planet. Sci. Lett.,* 156**,** 173-183.

Kelley, P. & Bishop, A. 2003. Isotube Mud Gas Results: Limbayong 1, Sabah, Malaysia. *Shell internal report-confidential*.

Kennett, J.P., et al. 2000. Carbon isotopic evidence for methane hydrate instability during Quaternary interstadials. *Science,* 288**,** 128-133.

Khan, O., et al. 2005 Deepwater Imaging beneath Gas Anomalies–A Case Study. 67th EAGE Conference & Exhibition.

Kida, M., et al. 2006. Coexistence of structure I and II gas hydrates in Lake Baikal suggesting gas sources from microbial and thermogenic origin. *Geophys. Res. Lett.,* 33**,** L24603.

Kida, M., et al. 2009. Natural gas hydrates with locally different cage occupancies and hydration numbers in Lake Baikal. *Geochem. Geophys. Geosyst.,* 10.

Kida, M., et al. 2015. Chemical and crystallographic characterizations of natural gas hydrates recovered from a production test site in the eastern Nankai Trough. *Mar. Petrol. Geol.,* 66**,** 396-403.

Kim, G.Y., et al. 2013a. Fracture orientation and induced anisotropy of gas hydrate-bearing sediments in seismic chimney-like-structures of the Ulleung Basin, East Sea. *Mar. Petrol. Geol.,* 47**,** 182-194.

Kim, J.-H., et al. 2011. Molecular and isotopic signatures in sediments and gas hydrate of the central/southwestern Ulleung Basin: high alkalinity escape fuelled by biogenically sourced methane. *Geo-Mar. Lett.,* 31**,** 37-49.

Kim, J.-H., et al. 2013b. Depressurization experiment of pressure cores from the central Ulleung Basin, East Sea: Insights into gas chemistry. *Org. Geochem.,* 62**,** 86-95.

King, R.C., et al. 2009. Present-day stress and neotectonic provinces of the Baram Delta and deep-water fold–thrust belt. *J. Geol. Soc. London,* 166**,** 197-200.

King, R.C., et al. 2010. Balancing deformation in NW Borneo: Quantifying plate-scale vs. gravitational tectonics in a delta and deepwater fold-thrust belt system. *Mar. Petrol. Geol.,* 27**,** 238-246.

Kinoshita, M., et al. 2009 Expedition 315 Site C0002. Proceedings of the Integrated Ocean Drilling Program, Volume 314/315/316.

Kinoshita, M., et al. 2011. Heat flow estimated from BSR and IODP borehole data: Implication of recent uplift and erosion of the imbricate thrust zone in the Nankai Trough off Kumano. *Geochem. Geophys. Geosyst.,* 12.

Klapp, S.A., et al. 2007. First determination of gas hydrate crystallite size distributions using high-energy synchrotron radiation. *Geophys. Res. Lett.,* 34.

Klapp, S.A., et al. 2010. Microstructures of structure I and II gas hydrates from the Gulf of Mexico. *Mar. Petrol. Geol.,* 27**,** 116-125.

Klaucke, I., et al. 2016. Fluid venting and seepage at accretionary ridges: the Four Way Closure Ridge offshore SW Taiwan. *Geo-Mar. Lett.,* 36**,** 165-174.

Kleinberg, R.L., et al. 2003. Deep sea NMR: Methane hydrate growth habit in porous media and its relationship to hydraulic permeability, deposit accumulation, and submarine slope stability. *J. Geophys. Res.: Solid Earth,* 108.

Kleinberg, R.L., et al. 2005. Magnetic resonance log of JAPEX/JNOC/GSC et al. Mallik 5L-38 gas hydrate production research well: Gas hydrate saturation, growth habit, and relative permeability. *Bull. Geol. Surv. Canada,* 585**,** 114.

Koch, S., et al. 2015. Gas-controlled seafloor doming. *Geology,* 43**,** 571-574.

Koch, S., et al. 2016. Gas migration through Opouawe Bank at the Hikurangi margin offshore New Zealand. *Geo-Mar. Lett.***,** 1-10.

Koh, C.A. 2002. Towards a fundamental understanding of natural gas hydrates. *Chem. Soc. Rev.,* 31**,** 157-167.

Koh, C.A., et al. 2012. State of the art: Natural gas hydrates as a natural resource. *J. Natural Gas Sci. Eng.,* 8**,** 132-138.

Konno, Y., et al. 2015. Effect of methane hydrate morphology on compressional wave velocity of sandy sediments: Analysis of pressure cores obtained in the Eastern Nankai Trough. *Mar. Petrol. Geol.,* 66**,** 425-433.

Krabbenhoeft, A., et al. 2013. Patterns of subsurface fluid-flow at cold seeps: The Hikurangi Margin, offshore New Zealand. *Mar. Petrol. Geol.,* 39**,** 59-73.

Kraemer, L.M., et al. 2000. Lithology of the upper gas hydrate zone, Blake Outer Ridge: a link between diatoms, porosity, and gas hydrate. *In:* Paull, C.K., Matsumoto, R., Wallace, P.J. & Dillon, W.P. (eds.) *Proceedings of the Ocean Drilling Program, Scientific Results, 164, 229-236.*

Kroeger, K.F., et al. 2015. Thermal evolution of the New Zealand Hikurangi subduction margin: impact on natural gas generation and methane hydrate formation–a model study. *Mar. Petrol. Geol.,* 63**,** 97-114.

Kumar, P., et al. 2014. Geologic implications of gas hydrates in the offshore of India: Krishna–Godavari Basin, Mahanadi Basin, Andaman Sea, Kerala–Konkan Basin. *Mar. Petrol. Geol.,* 58**,** 29-98.

Kvenvolden, K.A. & Mcmenamin, M.A. 1980. Hydrates of natural gas: a review of their geologic occurrence. *Geological Survey Circular 825***,** 1-11.

Kvenvolden, K.A., et al. 1984. Geochemistry of a naturally occurring massive marine gas hydrate. *Org. Geochem.,* 6**,** 703-713.

Kvenvolden, K.A. & Kastner, M. 1990. 32. Gas hydrates of the Peruvian outer continental margin. *In:* Suess, E. & von Huene, R. (eds.) *Proceedings of the Ocean Drilling Program, Scientific Results, 112, 517-526.*

Kvenvolden, K.A. 1993. Gas hydrates-geological perspective and global change. *Rev. Geophys.,* 31**,** 173-173.

Kvenvolden, K.A., et al. 1993. Worldwide distribution of subaquatic gas hydrates. *Geo-Mar. Lett.,* 13**,** 32-40.

Kvenvolden, K.A. 1995. A review of the geochemistry of methane in natural gas hydrate. *Org. Geochem.,* 23**,** 997-1008.

Kvenvolden, K.A. & Lorenson, T.D. 2001. The global occurrence of natural gas hydrate. *In:* Paull, C.K. & Dillon, W.P. (eds.) *Natural Gas Hydrates: Occurrence, Distribution and Detection.* AGU Geophysical Monographs Series, 124, 3-18.

Ladd, J.W., et al. 1984. Seismic reflection profiles across the southern margin of the Caribbean. *Geol. Soc. Am. Mem.,* 162**,** 153-159.

Laird, A.P. & Morley, C.K. 2011. Development of gas hydrates in a deep-water anticline based on attribute analysis from three-dimensional seismic data. *Geosphere,* 7**,** 240-259.

Lambeck, K. & Chappell, J. 2001. Sea level change through the last glacial cycle. *Science,* 292**,** 679-686.

Larter, S., et al. 2005 Biodegradation, gas destruction and methane generation in deep subsurface petroleum reservoirs: an overview. Petroleum Geology: North-West Europe and Global Perspectives—Proceedings of the 6th Petroleum Geology Conference, Geological Society, London, 6, 633-639.

Le, A.N., et al. 2015. Seismic characterization of a Bottom Simulating Reflection (BSR) and plumbing system of the Cameroon margin, offshore West Africa. *Mar. Petrol. Geol.,* 68**,** 629-647.

Leduc, A.M., et al. 2013. Fluid flow pipes triggered by lateral pressure transfer in the deepwater western Niger Delta. *Mar. Petrol. Geol.,* 43**,** 423-433.

Lee, G.H., et al. 2003. Opal-A/opal-CT phase boundary inferred from bottom-simulating reflectors in the southern South Korea Plateau, East Sea (Sea of Japan). *Geophys. Res. Lett.,* 30.

Lee, J.Y., et al. 2010a. Parametric study of the physical properties of hydrate-bearing sand, silt, and clay sediments: 2. Small-strain mechanical properties. *J. Geophys. Res.: Solid Earth,* 115**,** B11105.

Lee, J.Y., et al. 2010b. Volume change associated with formation and dissociation of hydrate in sediment. *Geochem. Geophys. Geosyst.,* 11.

Lee, J.Y., et al. 2013. Pressure core based study of gas hydrates in the Ulleung Basin and implication for geomechanical controls on gas hydrate occurrence. *Mar. Petrol. Geol.,* 47**,** 85-98.

Lee, M.W. & Dillon, W.P. 2001. Amplitude blanking related to the pore-filling of gas hydrate in sediments. *Mar. Geophys. Res.,* 22**,** 101-109.

Lee, M.W. 2002. Biot-Gassmann theory for velocities of gas hydrate-bearing sediments. *Geophysics,* 67**,** 1711-1719.

Lee, M.W. 2004. Elastic velocities of partially gas-saturated unconsolidated sediments. *Mar. Petrol. Geol.,* 21**,** 641-650.

Lee, M.W. & Collett, T.S. 2006 22. Gas hydrate and free gas saturations estimated from velocity logs on Hydrate Ridge, offshore Oregon, USA. Proceedings of the Ocean Drilling Program, Scientific results, 204.

Lee, M.W. 2007. Amplitude Variation of Bottom Simulating Reflection with Respect to Frequency—Transitional Base or Attenuation? *USGS Scientific Investigations Report,* 5091**,** 1-12.

Lee, M.W. & Collett, T.S. 2008. Integrated analysis of well logs and seismic data to estimate gas hydrate concentrations at Keathley Canyon, Gulf of Mexico. *Mar. Petrol. Geol.,* 25**,** 924-931.

Lee, M.W. & Waite, W.F. 2008. Estimating pore-space gas hydrate saturations from well log acoustic data. *Geochem. Geophys. Geosyst.,* 9.

Lee, M.W. & Collett, T.S. 2009. Gas hydrate saturations estimated from fractured reservoir at site NGHP-01-10, Krishna-Godavari basin, India. *J. Geophys. Res.: Solid Earth,* 114.

Lee, M.W., et al. 2009. *Seismic-attribute analysis for gas-hydrate and free-gas prospects on the North Slope of Alaska,* AAPG Memoir 89, 541-554.

Lee, M.W. & Collett, T.S. 2011 Three types of gas hydrate reservoirs in the gulf of mexico identified in LWD data. Proceedings of the 7th International Conference on Gas Hydrates (ICGH 2011).

Lee, M.W. & Collett, T.S. 2012. Pore-and fracture-filling Gas hydrate reservoirs in the Gulf of Mexico Gas hydrate Joint Industry Project leg II Green Canyon 955 H well. *Mar. Petrol. Geol.,* 34**,** 62-71.

Lee, M.W. & Collett, T.S. 2013. Characteristics and interpretation of fracture-filled gas hydrate–An example from the Ulleung Basin, East Sea of Korea. *Mar. Petrol. Geol.,* 47**,** 168-181.

Lei, L. 2017. *Gas Hydrate in Fine-grained Sediments—Laboratory Studies and Coupled Processes Analyses.* Georgia Institute of Technology.

Lein, A., et al. 1999. Chemical and isotopic evidence for the nature of the fluid in CH4-containing sediments of the Håkon Mosby Mud Volcano. *Geo-Mar. Lett.,* 19**,** 76-83.

Leslie, S.C. & Mann, P. 2016. Giant submarine landslides on the Colombian margin and tsunami risk in the Caribbean Sea. *Earth Planet. Sci. Lett.,* 449**,** 382-394.

Li, A., et al. 2016. Gas trapped below hydrate as a primer for submarine slope failures. *Mar. Geol.*

Li, L., et al. 2015. BSRs, estimated heat flow, hydrate-related gas volume and their implications for methane seepage and gas hydrate in the Dongsha region, northern South China Sea. *Mar. Petrol. Geol.,* 67**,** 785-794.

Liang, J., et al. 2017. Evaluation of gas hydrate-bearing sediments below the conventional bottom-simulating reflection on the northern slope of the South China Sea. *Interpretation,* 5**,** 1-41.

Ligtenberg, J. 2005. Detection of fluid migration pathways in seismic data: implications for fault seal analysis. *Basin Res.,* 17**,** 141-153.

Lin, C.-C., et al. 2014. Canyon-infilling and gas hydrate occurrences in the frontal fold of the offshore accretionary wedge off southern Taiwan. *Mar. Geophys. Res.,* 35**,** 21-35.

Liu, C., et al. 2012. The characteristics of gas hydrates recovered from Shenhu Area in the South China Sea. *Mar. Geol.,* 307**,** 22-27.

Liu, C., et al. 2015. Characterization of natural gas hydrate recovered from Pearl River Mouth basin in South China Sea. *Mar. Petrol. Geol.,* 61**,** 14-21.

Liu, X. & Flemings, P.B. 2006. Passing gas through the hydrate stability zone at southern Hydrate Ridge, offshore Oregon. *Earth Planet. Sci. Lett.,* 241**,** 211-226.

Liu, X. & Flemings, P.B. 2007. Dynamic multiphase flow model of hydrate formation in marine sediments. *J. Geophys. Res.: Solid Earth,* 112, B03101.

Liu, X. & Flemings, P.B. 2009. Dynamic response of oceanic hydrates to sea level drop. *Geophys. Res. Lett.,* 36, L17308.

Liu, X. & Flemings, P.B. 2011. Capillary effects on hydrate stability in marine sediments. *J. Geophys. Res.: Solid Earth,* 116, B07102.

Lodolo, E., et al. 2002. Assessment of gas hydrate and free gas distribution on the South Shetland margin (Antarctica) based on multichannel seismic reflection data. *Geophys. J. Int.,* 148**,** 103-119.

Londono, J., et al. 2015. Basement Architecture of the Southern Caribbean Basin, Guajira Offshore, Colombia. *In:* Bartolini, C. & Mann, P. (eds.) *Petroleum Geology and Potential of the Colombian Caribbean Margin.* AAPG Memoir, 108, 85-102.

Long, H., et al. 2007. Interpreting in situ pressure and hydraulic properties with borehole penetrometers in ocean drilling: DVTPP and Piezoprobe deployments at southern Hydrate Ridge, offshore Oregon. *J. Geophys. Res.: Solid Earth,* 112, B04101.

Long, P., et al. 2010. Infrared imaging of gas-hydrate-bearing cores: state of the art and future prospects. *In:* Riedel, M., Willoughby, E.C. & Chopra, S. (eds.) *Geophysical characterization of gas hydrates.* SEG geophysical developments series, 217-232.

López, C. & Ojeda, G. 2006. Heat flow in the Colombian Caribbean from the bottom simulating reflector (BSR). *CT&F-Ciencia, Tecnología y Futuro,* 3**,** 29-39.

Lorenson, T.D. 1999. Gas composition and isotopic geochemistry of cuttings, core, and gas hydrate from the JAPEX/JNOC/GSC Mallik 2L-38 gas hydrate research well. *Bull. Geol. Surv. Canada***,** 143-163.

Lorenson, T.D., et al. 2011. Gas geochemistry of the Mount Elbert gas hydrate stratigraphic test well, Alaska North slope: implications for gas hydrate exploration in the Arctic. *Mar. Petrol. Geol.,* 28**,** 343-360.

Lorenson, T.D. & Collett, T.S. under review. National Gas Hydrate Program Expedition 01 Offshore India gas hydrate petroleum systems as revealed by hydrocarbon gas geochemistry. *Mar. Petrol. Geol.*

Loreto, M.F., et al. 2010. Offshore Antarctic Peninsula gas hydrate reservoir characterization by geophysical data analysis. *Energies,* 4**,** 39-56.

Løseth, H., et al. 2009. Hydrocarbon leakage interpreted on seismic data. *Mar. Petrol. Geol.,* 26**,** 1304-1319.

Løseth, H., et al. 2011. 1000 m long gas blow-out pipes. *Mar. Petrol. Geol.,* 28**,** 1047-1060.

Lu, H., et al. 2005. Near-surface Geohazards of the Gumusut-Kakap Field. *Shell internal presentation-confidential*.

Lu, H., et al. 2007. Complex gas hydrate from the Cascadia margin. *Nature,* 445**,** 303-306.

Lu, H. & Shipp, R.C. 2011. Impact of a large mass-transport deposit on a field development in the upper slope of southwestern Sabah, Malaysia, offshore northwest Borneo. *In:* Shipp, R.C., Weimer, P. & Posamentier, H.W. (eds.) *Mass-Transport Deposits in Deepwater Settings.* SEPM Special Publication, 96, 199-218.

Lu, Z., et al. 2011. Gas hydrate occurrences in the Qilian Mountain permafrost, Qinghai province, China. *Cold Reg. Sci. Technol.,* 66**,** 93-104.

Lu, Z., et al. 2013. Gas source for gas hydrate and its significance in the Qilian Mountain permafrost, Qinghai. *Mar. Petrol. Geol.,* 43**,** 341-348.

Lückge, A., et al. 2002. Hydrocarbon gas in the Costa Rica subduction zone: primary composition and post-genetic alteration. *Org. Geochem.,* 33**,** 933-943.

Lüdmann, T. & Wong, H.K. 2003. Characteristics of gas hydrate occurrences associated with mud diapirism and gas escape structures in the northwestern Sea of Okhotsk. *Mar. Geol.,* 201**,** 269-286.

Luff, R. & Wallmann, K. 2003. Fluid flow, methane fluxes, carbonate precipitation and biogeochemical turnover in gas hydrate-bearing sediments at Hydrate Ridge, Cascadia Margin: numerical modeling and mass balances. *Geochim. Cosmochim. Acta,* 67**,** 3403-3421.

Lunne, T., et al. 1997. *Cone penetration testing, Geotechnical Practice*, CRC Press.

Macdonald, I.R., et al. 2004. Asphalt volcanism and chemosynthetic life in the Campeche Knolls, Gulf of Mexico. *Science,* 304**,** 999-1002.

Macelloni, L., et al. 2015. Heat-flow regimes and the hydrate stability zone of a transient, thermogenic, fault-controlled hydrate system (Woolsey Mound northern Gulf of Mexico). *Mar. Petrol. Geol.,* 59**,** 491-504.

Mackay, M.E., et al. 1994. Origin of bottom-simulating reflectors: geophysical evidence from the Cascadia accretionary prism. *Geology,* 22**,** 459-462.

Maia, A.R., et al. 2016. Shallow plumbing systems inferred from spatial analysis of pockmark arrays. *Mar. Petrol. Geol.,* 77**,** 865-881.

Majorowicz, J., et al. 2014. Gas hydrate contribution to Late Permian global warming. *Earth Planet. Sci. Lett.,* 393**,** 243-253.

Makogon, Y.F., et al. 2007. Natural gas-hydrates—A potential energy source for the 21st Century. *J. Petrol. Sci. Eng.,* 56**,** 14-31.

Makogon, Y.F. & Omelchenko, R.Y. 2013. Commercial gas production from Messoyakha deposit in hydrate conditions. *J. Natural Gas Sci. Eng.,* 11**,** 1-6.

Malinverno, A., et al. 2008. Gas hydrate occurrence from pore water chlorinity and downhole logs in a transect across the northern Cascadia margin (Integrated Ocean Drilling Program Expedition 311). *J. Geophys. Res.: Solid Earth,* 113, B08103.

Malinverno, A. 2010. Marine gas hydrates in thin sand layers that soak up microbial methane. *Earth Planet. Sci. Lett.,* 292**,** 399-408.

Malinverno, A. & Goldberg, D.S. 2015. Testing short-range migration of microbial methane as a hydrate formation mechanism: Results from Andaman Sea and Kumano Basin drill sites and global implications. *Earth Planet. Sci. Lett.,* 422**,** 105-114.

Markl, R.G., et al. 1970. Structure of the Blake-Bahama outer ridge. *J. Geophys. Res.,* 75**,** 4539-4555.

Martinez, W., et al. 2015. Tectono-stratigraphic Evolution of the Chichibacoa–Rancherias Basin Offshore Colombia. *In:* Bartolini, C. & Mann, P. (eds.) *Petroleum Geology and Potential of the Colombian Caribbean Margin.* AAPG Memoir, 108, 709-728.

Maslin, M., et al. 1998. Sea-level–and gas-hydrate–controlled catastrophic sediment failures of the Amazon Fan. *Geology,* 26**,** 1107-1110.

Maslin, M., et al. 2004. Linking continental-slope failures and climate change: Testing the clathrate gun hypothesis. *Geology,* 32**,** 53-56.

Matsumoto, R., et al. 2004. Detection and evaluation of gas hydrates in the eastern Nankai Trough by geochemical and geophysical methods. *Resour. Geol.,* 54**,** 53-67.

Matsumoto, R., et al. 2017. Recovery of thick deposits of massive gas hydrates from gas chimney structures, eastern margin of Japan Sea: Japan Sea Shallow Gas Hydrate Project. *Fire in the Ice,* 17**,** 1-6.

Mau, S., et al. 2007. Indications of a link between seismotectonics and $CH_4$ release from seeps off Costa Rica. *Geochem. Geophys. Geosyst.,* 8.

Mavko, G., et al. 2009. *The rock physics handbook: Tools for seismic analysis of porous media*, Cambridge university press.

Mazumdar, A., et al. 2009. Evidence of paleo–cold seep activity from the Bay of Bengal, offshore India. *Geochem. Geophys. Geosyst.,* 10.

Mazumdar, A., et al. 2012. Geochemical and geological constraints on the composition of marine sediment pore fluid: Possible link to gas hydrate deposits. *Mar. Petrol. Geol.,* 38**,** 35-52.

Mazurenko, L.L., et al. 2002. Mud volcano gas hydrates in the Gulf of Cadiz. *Terra nova,* 14**,** 321-329.

Mazurenko, L.L., et al. 2009. Gas hydrate forming fluids on the NE Sakhalin slope, Sea of Okhotsk. *Geol. Soc. London, Spec. Publ.,* 319**,** 51-72.

Mcconnell, D.R., et al. 2012. Review of progress in evaluating gas hydrate drilling hazards. *Mar. Petrol. Geol.,* 34**,** 209-223.

Mcgee, T., et al. 2009. Hydrocarbon gas hydrates in sediments of the Mississippi Canyon Area, northern Gulf of Mexico. *Geol. Soc. London, Spec. Publ.,* 319**,** 29-49.

Meckel Iii, R.D. 2011. Reservoir characteristics and classification of sand-prone submarine mass-transport deposits. *In:* Shipp, R.C., Weimer, P. & Posamentier, H.W. (eds.) *Mass-Transport Deposits in Deepwater Settings.* SEPM Special Publication, 96, 423-452.

Meckel Iii, R.D., et al. 2011. Reservoir characterization of sand-prone mass-transport deposits within slope canyons. *In:* Shipp, R.C., Weimer, P. & Posamentier, H.W. (eds.) *Mass-Transport Deposits in Deepwater Settings.* SEPM Special publication, 96, 391-421.

Mienert, J., et al. 2005. Ocean warming and gas hydrate stability on the mid-Norwegian margin at the Storegga Slide. *Mar. Petrol. Geol.,* 22**,** 233-244.

Milkov, A.V. & Sassen, R. 2000. Thickness of the gas hydrate stability zone, Gulf of Mexico continental slope. *Mar. Petrol. Geol.,* 17**,** 981-991.

Milkov, A.V., et al. 2003. Global gas flux from mud volcanoes: a significant source of fossil methane in the atmosphere and the ocean. *Geophys. Res. Lett.,* 30.

Milkov, A.V. 2004. Global estimates of hydrate-bound gas in marine sediments: how much is really out there? *Earth-Sci. Rev.,* 66**,** 183-197.

Milkov, A.V., et al. 2004a. Ethane enrichment and propane depletion in subsurface gases indicate gas hydrate occurrence in marine sediments at southern Hydrate Ridge offshore Oregon. *Org. Geochem.,* 35**,** 1067-1080.

Milkov, A.V., et al. 2004b. Co-existence of gas hydrate, free gas, and brine within the regional gas hydrate stability zone at Hydrate Ridge (Oregon margin): evidence from prolonged degassing of a pressurized core. *Earth Planet. Sci. Lett.,* 222**,** 829-843.

Milkov, A.V. 2005. Molecular and stable isotope compositions of natural gas hydrates: a revised global dataset and basic interpretations in the context of geological settings. *Org. Geochem.,* 36**,** 681-702.

Milkov, A.V., et al. 2005. Gas hydrate systems at Hydrate Ridge offshore Oregon inferred from molecular and isotopic properties of hydrate-bound and void gases. *Geochim. Cosmochim. Acta,* 69**,** 1007-1026.

Milkov, A.V. 2011. Worldwide distribution and significance of secondary microbial methane formed during petroleum biodegradation in conventional reservoirs. *Org. Geochem.,* 42**,** 184-207.

Miller, D.J., et al. 2015. Natural gas hydrates in the Rio Grande Cone (Brazil): A new province in the western South Atlantic. *Mar. Petrol. Geol.,* 67**,** 187-196.

Miller, J.J., et al. 1991. An Analysis of a Seismic Reflection from the Base of a Gas Hydrate Zone, Offshore Peru. *AAPG Bull.,* 75**,** 910-924.

Minshull, T. & White, R. 1989. Sediment compaction and fluid migration in the Makran accretionary prism. *J. Geophys. Res.: Solid Earth,* 94**,** 7387-7402.

Minshull, T., et al. 1994. Seismic velocity structure at a gas hydrate reflector, offshore western Colombia, from full waveform inversion. *J. Geophys. Res.: Solid Earth,* 99**,** 4715-4734.

Miyazaki, K., et al. 2011. Triaxial compressive properties of artificial methane-hydrate-bearing sediment. *J. Geophys. Res.: Solid Earth,* 116.

Moore, G.T. & Fahlquist, D.A. 1976. Seismic profile tying Caribbean DSDP Sites 153, 151, and 152. *Geol. Soc. Am. Bull.,* 87**,** 1609-1614.

Moore, J.C. & Vrolijk, P. 1992. Fluids in accretionary prisms. *Rev. Geophys.,* 30**,** 113-135.

Moridis, G.J., et al. 2004. Numerical studies of gas production from several $CH_4$ hydrate zones at the Mallik site, Mackenzie Delta, Canada. *J. Petrol. Sci. Eng.,* 43**,** 219-238.

Moridis, G.J., et al. 2011. Gas production from a cold, stratigraphically-bounded gas hydrate deposit at the Mount Elbert Gas Hydrate Stratigraphic Test Well, Alaska North Slope: Implications of uncertainties. *Mar. Petrol. Geol.,* 28**,** 517-534.

Morley, C.K., et al. 2003. Characteristics of repeated, detached, Miocene–Pliocene tectonic inversion events, in a large delta province on an active margin, Brunei Darussalam, Borneo. *J. Struct. Geol.,* 25**,** 1147-1169.

Morley, C.K. 2007. Development of crestal normal faults associated with deepwater fold growth. *J. Struct. Geol.,* 29**,** 1148-1163.

Morley, C.K. & Leong, L.C. 2008. Evolution of deep-water synkinematic sedimentation in a piggyback basin, determined from three-dimensional seismic reflection data. *Geosphere,* 4**,** 939-962.

Morley, C.K. 2009. Growth of folds in a deep-water setting. *Geosphere,* 5**,** 59-89.

Morley, C.K., et al. 2011. Deepwater fold and thrust belt classification, tectonics, structure and hydrocarbon prospectivity: A review. *Earth-Sci. Rev.,* 104**,** 41-91.

Morley, C.K., et al. 2014. Reprint of: Comparison of modern fluid distribution, pressure and flow in sediments associated with anticlines growing in deepwater (Brunei) and continental environments (Iran). *Mar. Petrol. Geol.,* 55**,** 230-249.

Mosher, D.C. 2011. A margin-wide BSR gas hydrate assessment: Canada's Atlantic margin. *Mar. Petrol. Geol.,* 28**,** 1540-1553.

Moss, J.L. 2010. *The spatial and temporal distribution of pipe and pockmark formation.* Cardiff University.

Moss, J.L. & Cartwright, J.A. 2010. 3D seismic expression of km-scale fluid escape pipes from offshore Namibia. *Basin Res.,* 22**,** 481-501.

Mourgues, R., et al. 2011. "Basin scale" versus "localized" pore pressure/stress coupling–Implications for trap integrity evaluation. *Mar. Petrol. Geol.,* 28**,** 1111-1121.

Muggeridge, A. & Mahmode, H. 2012. Hydrodynamic aquifer or reservoir compartmentalization? *AAPG Bull.,* 96**,** 315-336.

Müller, P.J. & Suess, E. 1979. Productivity, sedimentation rate, and sedimentary organic matter in the oceans—I. Organic carbon preservation. *Deep Sea Research Part A. Oceanographic Research Papers,* 26**,** 1347-1362.

Murray, D.R., et al. 2006. Saturation, acoustic properties, growth habit, and state of stress of a gas hydrate reservoir from well logs. *Petrophysics,* 47.

Naudts, L., et al. 2010. Active venting sites on the gas-hydrate-bearing Hikurangi Margin, off New Zealand: Diffusive-versus bubble-released methane. *Mar. Geol.,* 272**,** 233-250.

Nelson, C.H., et al. 2011. Interplay of mass-transport and turbidite-system deposits in different active tectonic and passive continental margin settings: external and local controlling factors. *In:* Shipp, R.C., Weimer, P. & Posamentier, H.W. (eds.) *Mass-Transport Deposits in Deepwater Settings.* SEPM Special Publication, 96, 39-66.

Nelson, P.H. 2009. Pore-throat sizes in sandstones, tight sandstones, and shales. *AAPG Bull.,* 93**,** 329-340.

Netzeband, G.L., et al. 2010. The structures beneath submarine methane seeps: seismic evidence from Opouawe Bank, Hikurangi Margin, New Zealand. *Mar. Geol.,* 272**,** 59-70.

Nimblett, J. & Ruppel, C. 2003. Permeability evolution during the formation of gas hydrates in marine sediments. *J. Geophys. Res.: Solid Earth,* 108.

Noguchi, S., et al. 2011. 3-D internal architecture of methane hydrate-bearing turbidite channels in the eastern Nankai Trough, Japan. *Mar. Petrol. Geol.,* 28**,** 1817-1828.

Nole, M., et al. 2016. Short-range, overpressure-driven methane migration in coarse-grained gas hydrate reservoirs. *Geophys. Res. Lett.,* 43**,** 9500-9508.

Nole, M., et al. 2017. Linking basin-scale and pore-scale gas hydrate distribution patterns in diffusion-dominated marine hydrate systems. *Geochem. Geophys. Geosyst.,* 18.

Nuzzo, M., et al. 2009. Origin of light volatile hydrocarbon gases in mud volcano fluids, Gulf of Cadiz—evidence for multiple sources and transport mechanisms in active sedimentary wedges. *Chem. Geol.,* 266**,** 350-363.

Ochoa, A.E.C. 2013. Characterization of gas hydrate reservoirs in the offshore Caribbean region oF Colombia. *Fire in the Ice,* 13**,** 7-11.

Ogawa, K. & Jong, J. 2016 A Leaking Hydrocarbon Charge System In Deepwater Sabah– Evidence From Reservoir Fluid Geochemistry And Mud-Gas Isotope Analysis. Proceedungs, Indonesian Petreoleum Association, 40th Annual Convention & Exhibition.

Osborne, M.J. & Swarbrick, R.E. 1997. Mechanisms for generating overpressure in sedimentary basins: a reevaluation. *AAPG Bull.,* 81**,** 1023-1041.

Ostanin, I., et al. 2013. Hydrocarbon plumbing systems above the Snøhvit gas field: structural control and implications for thermogenic methane leakage in the Hammerfest Basin, SW Barents Sea. *Mar. Petrol. Geol.,* 43**,** 127-146.

Ostermeier, R.M., et al. 2002. Dealing with shallow-water flow in the deepwater Gulf of Mexico. *The Leading Edge,* 21**,** 660-668.

Pape, T., et al. 2010a. Molecular and isotopic partitioning of low-molecular-weight hydrocarbons during migration and gas hydrate precipitation in deposits of a high-flux seepage site. *Chem. Geol.,* 269**,** 350-363.

Pape, T., et al. 2010b. Gas hydrates in shallow deposits of the Amsterdam mud volcano, Anaximander Mountains, Northeastern Mediterranean Sea. *Geo-Mar. Lett.,* 30**,** 187-206.

Pape, T., et al. 2011. Distribution and abundance of gas hydrates in near-surface deposits of the Håkon Mosby Mud Volcano, SW Barents Sea. *Geochem. Geophys. Geosyst.,* 12.

Pape, T., et al. 2014. Hydrocarbon seepage and its sources at mud volcanoes of the Kumano forearc basin, Nankai Trough subduction zone. *Geochem. Geophys. Geosyst.,* 15**,** 2180-2194.

Paull, C.K., et al. 1995. Methane-rich plumes on the Carolina continental rise: associations with gas hydrates. *Geology,* 23**,** 89-92.

Paull, C.K., et al. 2005. Geochemical constraints on the distribution of gas hydrates in the Gulf of Mexico. *Geo-Mar. Lett.,* 25**,** 273-280.

Paull, C.K., et al. 2007. Origin of pingo-like features on the Beaufort Sea shelf and their possible relationship to decomposing methane gas hydrates. *Geophys. Res. Lett.,* 34.

Paull, C.K., et al. 2008a. Association among active seafloor deformation, mound formation, and gas hydrate growth and accumulation within the seafloor of the Santa Monica Basin, offshore California. *Mar. Geol.,* 250**,** 258-275.

Paull, C.K., et al. 2008b. Origin of pockmarks and chimney structures on the flanks of the Storegga Slide, offshore Norway. *Geo-Mar. Lett.,* 28**,** 43-51.

Paull, C.K., et al. 2015. Seafloor geomorphic manifestations of gas venting and shallow subbottom gas hydrate occurrences. *Geosphere,* 11**,** 491-513.

Pecher, I.A., et al. 1996. Velocity structure of a bottom simulating reflector offshore Peru: Results from full waveform inversion. *Earth Planet. Sci. Lett.,* 139**,** 459-469.

Pecher, I.A., et al. 2001. The link between bottom-simulating reflections and methane flux into the gas hydrate stability zone–new evidence from Lima Basin, Peru Margin. *Earth Planet. Sci. Lett.,* 185**,** 343-354.

Pecher, I.A., et al. 2005. Erosion of the seafloor at the top of the gas hydrate stability zone on the Hikurangi Margin, New Zealand. *Geophys. Res. Lett.,* 32**,** L24603.

Pecher, I.A., et al. 2010. Focussed fluid flow on the Hikurangi Margin, New Zealand—Evidence from possible local upwarping of the base of gas hydrate stability. *Mar. Geol.,* 272**,** 99-113.

Pecher, I.A., et al. 2014 Double BSRs on the Hikurangi Margin, New Zealand—Possible implications for gas hydrate stability and composition. Proceedings of the 8th International Conference on Gas Hydrates (ICGH 2014).

Petersen, C.J., et al. 2010. High-resolution P-Cable 3D seismic imaging of gas chimney structures in gas hydrated sediments of an Arctic sediment drift. *Mar. Petrol. Geol.,* 27**,** 1981-1994.

Peuchen, J. 2000 Deepwater cone penetration tests, OTC 12094. Offshore Technology Conference.

Phrampus, B.J. & Hornbach, M.J. 2012. Recent changes to the Gulf Stream causing widespread gas hydrate destabilization. *Nature,* 490**,** 527-530.

Phrampus, B.J., et al. 2014. Widespread gas hydrate instability on the upper US Beaufort margin. *J. Geophys. Res.: Solid Earth,* 119**,** 8594-8609.

Pindell, J., et al. 2005. Plate-kinematics and crustal dynamics of circum-Caribbean arc-continent interactions: Tectonic controls on basin development in Proto-Caribbean margins. *Geological Society of America Special Papers,* 394**,** 7-52.

Piñero, E., et al. 2013. Estimation of the global inventory of methane hydrates in marine sediments using transfer functions. *Biogeosciences,* 10**,** 959-975.

Plaza-Faverola, A., et al. 2010. Fluid distributions inferred from P-wave velocity and reflection seismic amplitude anomalies beneath the Nyegga pockmark field of the mid-Norwegian margin. *Mar. Petrol. Geol.,* 27**,** 46-60.

Plaza-Faverola, A., et al. 2011. Repeated fluid expulsion through sub-seabed chimneys offshore Norway in response to glacial cycles. *Earth Planet. Sci. Lett.,* 305**,** 297-308.

Plaza-Faverola, A., et al. 2012a. The free gas zone beneath gas hydrate bearing sediments and its link to fluid flow: 3-D seismic imaging offshore mid-Norway. *Mar. Geol.,* 291**,** 211-226.

Plaza-Faverola, A., et al. 2012b. Evolution of fluid expulsion and concentrated hydrate zones across the southern Hikurangi subduction margin, New Zealand: An analysis from depth migrated seismic data. *Geochem. Geophys. Geosyst.,* 13.

Plaza-Faverola, A., et al. 2010. Evidence from three-dimensional seismic tomography for a substantial accumulation of gas hydrate in a fluid-escape chimney in the Nyegga pockmark field, offshore Norway. *J. Geophys. Res.: Solid Earth,* 115, B08104.

Plaza-Faverola, A., et al. 2014. Submarine gas seepage in a mixed contractional and shear deformation regime: Cases from the Hikurangi oblique-subduction margin. *Geochem. Geophys. Geosyst.,* 15**,** 416-433.

Plaza-Faverola, A., et al. 2015. Role of tectonic stress in seepage evolution along the gas hydrate-charged Vestnesa Ridge, Fram Strait. *Geophys. Res. Lett.,* 42**,** 733-742.

Plaza-Faverola, A., et al. 2017. Bottom-simulating reflector dynamics at Arctic thermogenic gas provinces: an example from Vestnesa Ridge, offshore west-Svalbard. *J. Geophys. Res.: Solid Earth,* 122**,** 4089–4105.

Pohlman, J.W., et al. 2005. The origin of thermogenic gas hydrates on the northern Cascadia Margin as inferred from isotopic (13 C/12 C and D/H) and molecular composition of hydrate and vent gas. *Org. Geochem.,* 36**,** 703-716.

Pohlman, J.W., et al. 2009a. Methane sources in gas hydrate-bearing cold seeps: evidence from radiocarbon and stable isotopes. *Mar. Chem.,* 115**,** 102-109.

Pohlman, J.W., et al. 2009b. Methane sources and production in the northern Cascadia margin gas hydrate system. *Earth Planet. Sci. Lett.,* 287**,** 504-512.

Popescu, I., et al. 2006. Multiple bottom-simulating reflections in the Black Sea: potential proxies of past climate conditions. *Mar. Geol.,* 227**,** 163-176.

Posamentier, H.W. & Martinsen, O.J. 2011. The character and genesis of submarine mass-transport deposits: Insights from outcrop and 3D seismic data. *In:* Shipp, R.C., Weimer, P. & Posamentier, H.W. (eds.) *Mass-Transport Deposits in Deepwater Settings.* SEPM Special publication, 96, 7-38.

Prasad, M. 2002. Acoustic measurements in unconsolidated sands at low effective pressure and overpressure detection. *Geophysics,* 67**,** 405-412.

Priest, J.A., et al. 2005. A laboratory investigation into the seismic velocities of methane gas hydrate-bearing sand. *J. Geophys. Res.: Solid Earth,* 110, B04102.

Priest, J.A., et al. 2009. Influence of gas hydrate morphology on the seismic velocities of sands. *J. Geophys. Res.: Solid Earth,* 114, B11205.

Prinzhofer, A., et al. 2000. Geochemical characterization of natural gas: a physical multivariable approach and its applications in maturity and migration estimates. *AAPG Bull.,* 84**,** 1152-1172.

Qian, J., et al. 2014. AVO analysis of BSR to assess free gas within fine-grained sediments in the Shenhu area, South China Sea. *Mar. Geophys. Res.,* 35**,** 125-140.

Rajan, A., et al. 2012. Acoustic evidence for a gas migration and release system in Arctic glaciated continental margins offshore NW-Svalbard. *Mar. Petrol. Geol.,* 32**,** 36-49.

Ramirez, V., et al. 2015. Petroleum systems of the Guajira Basin, northern Colombia. *In:* Bartolini, C. & Mann, P. (eds.) *Petroleum Geology and Potential of the Colombian Caribbean Margin.* AAPG Memoir, 108, 399-430.

Rees, E.V.L. 2009. *Methane gas hydrate morphology and its effect on the stiffness and damping of some sediments.* University of Southampton.

Rees, E.V.L., et al. 2011. The structure of methane gas hydrate bearing sediments from the Krishna–Godavari Basin as seen from Micro-CT scanning. *Mar. Petrol. Geol.,* 28**,** 1283-1293.

Rempel, A.W. 2007. Formation of ice lenses and frost heave. *J. Geophys. Res.: Earth Surface,* 112**,** F02S21.

Rempel, A.W. 2011. A model for the diffusive growth of hydrate saturation anomalies in layered sediments. *J. Geophys. Res.: Solid Earth,* 116**,** B10105.

Riboulot, V., et al. 2013. Sea-level change and free gas occurrence influencing a submarine landslide and pockmark formation and distribution in deepwater Nigeria. *Earth Planet. Sci. Lett.,* 375**,** 78-91.

Riboulot, V., et al. 2014. Control of Quaternary sea-level changes on gas seeps. *Geophys. Res. Lett.,* 41**,** 4970-4977.

Riboulot, V., et al. 2016. Initiation of gas-hydrate pockmark in deep-water Nigeria: Geo-mechanical analysis and modelling. *Earth Planet. Sci. Lett.,* 434**,** 252-263.

Riboulot, V., et al. 2018. Freshwater lake to salt-water sea causing widespread hydrate dissociation in the Black Sea. *Nature communications,* 9**,** 117.

Rice, D.D. & Claypool, G.E. 1981. Generation, accumulation, and resource potential of biogenic gas. *AAPG Bull.,* 65**,** 5-25.

Riedel, M., et al. 2002. Seismic investigations of a vent field associated with gas hydrates, offshore Vancouver Island. *J. Geophys. Res.: Solid Earth,* 107, B9, 2200.

Riedel, M., et al. 2006. Geophysical and geochemical signatures associated with gas hydrate–related venting in the northern Cascadia margin. *Geol. Soc. Am. Bull.,* 118**,** 23-38.

Riedel, M., et al. 2009. Gas hydrate drilling transect across northern Cascadia margin-IODP Expedition 311. *Geol. Soc. London, Spec. Publ.,* 319**,** 11-19.

Riedel, M., et al. 2010a. Seismic imaging of a fractured gas hydrate system in the Krishna–Godavari Basin offshore India. *Mar. Petrol. Geol.,* 27**,** 1476-1493.

Riedel, M., et al. 2010b Expedition 311 synthesis: scientific findings. Proceedings of the Integrated Ocean Drilling Program Expedition, 311.

Riedel, M., et al. 2012. Mass-transport deposits and gas hydrate occurrences in the Ulleung Basin, East Sea–Part 2: Gas hydrate content and fracture-induced anisotropy. *Mar. Petrol. Geol.,* 35**,** 75-90.

Riedel, M. & Rohr, K.M.M. 2012. Gas hydrate within the Winona Basin, offshore western Canada. *Mar. Petrol. Geol.,* 30**,** 66-80.

Riedel, M., et al. 2014. Compressional and shear-wave velocities from gas hydrate bearing sediments: Examples from the India and Cascadia margins as well as Arctic permafrost regions. *Mar. Petrol. Geol.,* 58**,** 292-320.

Riedel, M., et al. 2017. Evidence for gas hydrate occurrences in the Canadian Arctic Beaufort Sea within permafrost-associated shelf and deep-water marine environments. *Mar. Petrol. Geol.,* 81**,** 66-78.

Roberts, H.H., et al. 2006. Seafloor reflectivity—an important seismic property for interpreting fluid/gas expulsion geology and the presence of gas hydrate. *The Leading Edge,* 25**,** 620-628.

Robertson, P.K. 2009. Interpretation of cone penetration tests-a unified approach. *Canadian Geotech. J.,* 46**,** 1337-1355.

Rolfsvåg, T.A. & Danielsen, T.M. 2016 Perched Water Static Model, SPE-180000-MS. SPE Bergen One Day Seminar.

Römer, M., et al. 2016. Tidally controlled gas bubble emissions: A comprehensive study using long-term monitoring data from the NEPTUNE cabled observatory offshore Vancouver Island. *Geochem. Geophys. Geosyst.*

Romero Otero, G.A. 2009. *Deepwater sedimentary processes in an active margin, Magdalena submarine fan, offshore Colombia.* University of Oklahoma.

Rose, K.K., et al. 2014. Anomalous porosity preservation and preferential accumulation of gas hydrate in the Andaman accretionary wedge, NGHP-01 site 17A. *Mar. Petrol. Geol.,* 58**,** 99-116.

Ruffine, L., et al. 2013. Investigation on the geochemical dynamics of a hydrate-bearing pockmark in the Niger Delta. *Mar. Petrol. Geol.,* 43**,** 297-309.

Ruppel, C.D. 1997. Anomalously cold temperatures observed at the base of the gas hydrate stability zone on the US Atlantic passive margin. *Geology,* 25**,** 699-702.

Ruppel, C.D. 2000. Thermal state of the gas hydrate reservoir. *In:* Max, M.D. (ed.) *Natural Gas Hydrate in oceanic and permafrost environments, 29-42.* Springer.

Ruppel, C.D. 2011. Methane hydrates and contemporary climate change. *Nature Education Knowledge,* 3**,** 29.

Ruppel, C.D. & Kessler, J.D. 2017. The Interaction of Climate Change and Methane Hydrates. *Rev. Geophys.,* 55**,** 1-43.

Ryu, B.-J., et al. 2013. Scientific results of the second gas hydrate drilling expedition in the Ulleung basin (UBGH2). *Mar. Petrol. Geol.,* 47**,** 1-20.

Saeki, T., et al. 2008 Extraction of methane hydrate concentrated zone for resource assessment in the eastern Nankai Trough, Japan, OTC 19311. Offshore Technology Conference.

Sain, K., et al. 2000. Evidence for a thick free gas layer beneath the bottom simulating reflector in the Makran accretionary prism. *Mar. Geol.,* 164**,** 3-12.

Santamarina, J.C., et al. 2012. Pressure core characterization tools for hydrate-bearing sediments. *Scientific Drilling,* 14.

Santamarina, J.C., et al. 2015. Hydro-bio-geomechanical properties of hydrate-bearing sediments from Nankai Trough. *Mar. Petrol. Geol.,* 66**,** 434-450.

Sassen, R. & Macdonald, I.R. 1994. Evidence of structure H hydrate, Gulf of Mexico continental slope. *Org. Geochem.,* 22**,** 1029-1032.

Sassen, R., et al. 1999. Thermogenic gas hydrates and hydrocarbon gases in complex chemosynthetic communities, Gulf of Mexico continental slope. *Org. Geochem.,* 30**,** 485-497.

Sassen, R., et al. 2000. Exclusion of 2-methylbutane (isopentane) during crystallization of structure II gas hydrate in sea-floor sediment, Gulf of Mexico. *Org. Geochem.,* 31**,** 1257-1262.

Sassen, R., et al. 2001a. Massive vein-filling gas hydrate: relation to ongoing gas migration from the deep subsurface in the Gulf of Mexico. *Mar. Petrol. Geol.,* 18**,** 551-560.

Sassen, R., et al. 2001b. Gas hydrate and crude oil from the Mississippi Fan Foldbelt, downdip Gulf of Mexico Salt Basin: significance to petroleum system. *Org. Geochem.,* 32**,** 999-1008.

Sassen, R., et al. 2001c. Thermogenic vent gas and gas hydrate in the Gulf of Mexico slope: Is gas hydrate decomposition significant? *Geology,* 29**,** 107-110.

Sassen, R., et al. 2001d. Stability of thermogenic gas hydrate in the Gulf of Mexico: Constraints on models of climate change. *In:* Paull, C.K. & Dillon, W.P. (eds.) *Natural gas hydrates: occurrence, distribution, and detection.* AGU Geophysical Monograph Series, 124, 131-143.

Sassen, R., et al. 2004. Free hydrocarbon gas, gas hydrate, and authigenic minerals in chemosynthetic communities of the northern Gulf of Mexico continental slope: relation to microbial processes. *Chem. Geol.,* 205**,** 195-217.

Sassen, R. & Curiale, J.A. 2006. Microbial methane and ethane from gas hydrate nodules of the Makassar Strait, Indonesia. *Org. Geochem.,* 37**,** 977-980.

Saunders, D.F., et al. 1999. Model for hydrocarbon microseepage and related near-surface alterations. *AAPG Bull.,* 83**,** 170-185.

Sauter, E.J., et al. 2006. Methane discharge from a deep-sea submarine mud volcano into the upper water column by gas hydrate-coated methane bubbles. *Earth Planet. Sci. Lett.,* 243**,** 354-365.

Scandella, B.P., et al. 2011. A conduit dilation model of methane venting from lake sediments. *Geophys. Res. Lett.,* 38.

Schenk, H., et al. 1997. The conversion of oil into gas in petroleum reservoirs. Part 1: Comparative kinetic investigation of gas generation from crude oils of lacustrine, marine and fluviodeltaic origin by programmed-temperature closed-system pyrolysis. *Org. Geochem.,* 26**,** 467-481.

Schmidt, K.a.G., et al. 2007. Calculation of the interfacial tension of the methane–water system with the linear gradient theory. *Fluid Phase Equilib.,* 261**,** 230-237.

Schmidt, M., et al. 2005. Methane hydrate accumulation in "Mound 11" mud volcano, Costa Rica forearc. *Mar. Geol.,* 216**,** 83-100.

Schoell, M. 1983. Genetic characterization of natural gases. *AAPG Bull.,* 67**,** 2225-2238.

Scholl, D.W., et al. 2009. Why Hydrate-linked Velocity-amplitude Anomaly Structures are Common in the Bering Sea Basin: A Hypothesis.

Schowalter, T.T. 1979. Mechanics of secondary hydrocarbon migration and entrapment. *AAPG Bull.,* 63**,** 723-760.

Schubotz, F., et al. 2011. Petroleum degradation and associated microbial signatures at the Chapopote asphalt volcano, Southern Gulf of Mexico. *Geochim. Cosmochim. Acta,* 75**,** 4377-4398.

Schultheiss, P.J., et al. 2006. Pressure coring, logging and subsampling with the HYACINTH system. *Geol. Soc. London, Spec. Publ.,* 267**,** 151-163.

Schultheiss, P.J., et al. 2008 Pressure core analysis: the keystone of a gas hydrate investigation. Proceedings of the 6th International Conference on Gas Hydrates (ICGH 2008).

Schultheiss, P.J., et al. 2010. Borehole pressure coring techniques and core analysis at in situ pressure. *In:* Riedel, M., Willoughby, E.C. & Chopra, S. (eds.) *Geophysical Characterization of Gas Hydrates.* SEG geophysical developments series, 263-278.

Schultheiss, P.J., et al. 2011 PCATS: pressure core analysis and transfer system. Proceedings of the 7th International Conference on Gas Hydrates (ICGH 2011).

Schwalenberg, K., et al. 2005. Marine gas hydrate electromagnetic signatures in Cascadia and their correlation with seismic blank zones. *First Break,* 23**,** 57-63.

Schwalenberg, K., et al. 2010. Evaluation of gas hydrate deposits in an active seep area using marine controlled source electromagnetics: Results from Opouawe Bank, Hikurangi Margin, New Zealand. *Mar. Geol.,* 272**,** 79-88.

Serié, C., et al. 2012. Gas hydrate pingoes: Deep seafloor evidence of focused fluid flow on continental margins. *Geology,* 40**,** 207-210.

Serié, C., et al. 2016. Subsurface fluid flow in the deep-water Kwanza Basin, offshore Angola. *Basin Res.***,** 1-31.

Serov, P., et al. 2017. Postglacial response of Arctic Ocean gas hydrates to climatic amelioration. *Proc. Natl. Acad. Sci. USA***,** 201619288.

Sha, Z., et al. 2015. A seepage gas hydrate system in northern South China Sea: seismic and well log interpretations. *Mar. Geol.,* 366**,** 69-78.

Shankar, U. & Riedel, M. 2011. Gas hydrate saturation in the Krishna–Godavari basin from P-wave velocity and electrical resistivity logs. *Mar. Petrol. Geol.,* 28**,** 1768-1778.

Shankar, U., et al. 2013. Gas hydrate and free gas saturations using rock physics modelling at site NGHP-01-05 and 07 in the Krishna–Godavari Basin, eastern Indian margin. *J. Petrol. Sci. Eng.,* 106**,** 62-70.

Shankar, U. & Riedel, M. 2013. Heat flow and gas hydrate saturation estimates from Andaman Sea, India. *Mar. Petrol. Geol.,* 43**,** 434-449.

Shankar, U. & Riedel, M. 2014. Assessment of gas hydrate saturation in marine sediments from resistivity and compressional-wave velocity log measurements in the Mahanadi Basin, India. *Mar. Petrol. Geol.,* 58**,** 265-277.

Shedd, W., et al. 2012. Occurrence and nature of "bottom simulating reflectors" in the northern Gulf of Mexico. *Mar. Petrol. Geol.,* 34**,** 31-40.

Shin, H. & Santamarina, J.C. 2010. Fluid-driven fractures in uncemented sediments: Underlying particle-level processes. *Earth Planet. Sci. Lett.,* 299**,** 180-189.

Shipley, T.H., et al. 1979. Seismic evidence for widespread possible gas hydrate horizons on continental slopes and rises. *AAPG Bull.,* 63**,** 2204-2213.

Simonetti, A., et al. 2013. Spatial distribution of gas hydrates from high-resolution seismic and core data, Woolsey Mound, Northern Gulf of Mexico. *Mar. Petrol. Geol.,* 44**,** 21-33.

Singh, S.C., et al. 1993. Velocity structure of a gas hydrate reflector. *Science,* 260**,** 204-208.

Skarke, A., et al. 2014. Widespread methane leakage from the sea floor on the northern US Atlantic margin. *Nat. Geosci.,* 7**,** 657-661.

Sloan Jr, E.D. 2003. Fundamental principles and applications of natural gas hydrates. *Nature,* 426**,** 353-363.

Sloan Jr, E.D. & Koh, C. 2007. *Clathrate hydrates of natural gases*, CRC press.

Slowey, N.C. 2007. Gumusut-Kakap geologic sediment core: photographs, lithologic descriptions, X-ray radiographs, and age dating. *Shell International internal report by Fugro GeoServices, Inc.-confidential*.

Smith, A.J., et al. 2014a. The evolution of methane vents that pierce the hydrate stability zone in the world's oceans. *J. Geophys. Res.: Solid Earth,* 119**,** 6337-6356.

Smith, A.J., et al. 2014b. Thermogenic methane injection via bubble transport into the upper Arctic Ocean from the hydrate-charged Vestnesa Ridge, Svalbard. *Geochem. Geophys. Geosyst.,* 15**,** 1945-1959.

Soloviev, V.A. & Ginsburg, G.D. 1997. Water segregation in the course of gas hydrate formation and accumulation in submarine gas-seepage fields. *Mar. Geol.,* 137**,** 59-68.

Spangenberg, E. 2001. Modeling of the influence of gas hydrate content on the electrical properties of porous sediments. *J. Geophys. Res.: Solid Earth,* 106**,** 6535-6548.

Spangenberg, E. & Kulenkampff, J. 2006. Influence of methane hydrate content on electrical sediment properties. *Geophys. Res. Lett.,* 33**,** L24315.

Spangenberg, E., et al. 2014. Are Laboratory-Formed Hydrate-Bearing Systems Analogous to Those in Nature? *J. Chem. Eng. Data,* 60**,** 258-268.

Stern, L.A. & Lorenson, T.D. 2014. Grain-scale imaging and compositional characterization of cryo-preserved India NGHP 01 gas-hydrate-bearing cores. *Mar. Petrol. Geol.,* 58**,** 206-222.

Stolper, D.A., et al. 2014. Formation temperatures of thermogenic and biogenic methane. *Science,* 344**,** 1500-1503.

Subramanian, S., et al. 2000. Structural transitions in methane+ ethane gas hydrates—part I: upper transition point and applications. *Chem. Eng. Sci.,* 55**,** 5763-5771.

Sultan, N., et al. 2004. Effect of gas hydrates melting on seafloor slope instability. *Mar. Geol.,* 213**,** 379-401.

Sultan, N., et al. 2007. Detection of free gas and gas hydrate based on 3D seismic data and cone penetration testing: An example from the Nigerian Continental Slope. *Mar. Geol.,* 240**,** 235-255.

Sultan, N., et al. 2010. Hydrate dissolution as a potential mechanism for pockmark formation in the Niger delta. *J. Geophys. Res.: Solid Earth,* 115, B08101.

Sultan, N., et al. 2011. Dynamics of fault-fluid-hydrate system around a shale-cored anticline in deepwater Nigeria. *J. Geophys. Res.: Solid Earth,* 116, B12110.

Sultan, N., et al. 2014. Pockmark formation and evolution in deep water Nigeria: Rapid hydrate growth versus slow hydrate dissolution. *J. Geophys. Res.: Solid Earth,* 119**,** 2679-2694.

Sun, Q., et al. 2012. Shallow gas and focused fluid flow systems in the Pearl River Mouth Basin, northern South China Sea. *Mar. Geol.,* 315**,** 1-14.

Taladay, K., et al. 2017. Gas-In-Place Estimate for Potential Gas Hydrate Concentrated Zone in the Kumano Basin, Nankai Trough Forearc, Japan. *Energies,* 10**,** 1552.

Taladay, K.B. 2015. *A 3-Dimensional Analysis and Assessment of the Natural Gas Hydrate System in the Kumano Forearc Basin, Offshore Japan, from NanTroSEIZE Drilling and 3D Seismic Data.* University of Hawaii at Manoa.

Taylor, M.H., et al. 2000. Trapping and migration of methane associated with the gas hydrate stability zone at the Blake Ridge Diapir: new insights from seismic data. *Mar. Geol.,* 164**,** 79-89.

Terzaghi, K. 1943. *Theory of consolidation*, Wiley Online Library.

Tingay, M.R.P., et al. 2003. Pore pressure/stress coupling in Brunei Darussalam—implications for shale injection. *Geol. Soc. London, Spec. Publ.,* 216**,** 369-379.

Tingay, M.R.P., et al. 2007. 'Vertically transferred'overpressures in Brunei: Evidence for a new mechanism for the formation of high-magnitude overpressure. *Geology,* 35**,** 1023-1026.

Tingay, M.R.P., et al. 2009. Present-day stress and neotectonics of Brunei: Implications for petroleum exploration and production. *AAPG Bull.,* 93**,** 75-100.

Tinivella, U., et al. 1998. Seismic tomography study of a bottom simulating reflector off the South Shetland Islands (Antarctica). *Geol. Soc. London, Spec. Publ.,* 137**,** 141-151.

Tinivella, U. & Accaino, F. 2000. Compressional velocity structure and Poisson's ratio in marine sediments with gas hydrate and free gas by inversion of reflected and refracted seismic data (South Shetland Islands, Antarctica). *Mar. Geol.,* 164**,** 13-27.

Tinivella, U., et al. 2002. Gas hydrate and free gas distribution from inversion of seismic data on the South Shetland margin (Antarctica). *Mar. Geophys. Res.,* 23**,** 109-123.

Tinivella, U. & Giustiniani, M. 2013. Variations in BSR depth due to gas hydrate stability versus pore pressure. *Global Planet. Change,* 100**,** 119-128.

Tishchenko, P., et al. 2005. Calculation of the stability and solubility of methane hydrate in seawater. *Chem. Geol.,* 219**,** 37-52.

Tohidi, B., et al. 2001. Visual observation of gas-hydrate formation and dissociation in synthetic porous media by means of glass micromodels. *Geology,* 29**,** 867-870.

Torres, M.E., et al. 2004. Gas hydrate growth, methane transport, and chloride enrichment at the southern summit of Hydrate Ridge, Cascadia margin off Oregon. *Earth Planet. Sci. Lett.,* 226**,** 225-241.

Torres, M.E., et al. 2008. Methane hydrate formation in turbidite sediments of northern Cascadia, IODP Expedition 311. *Earth Planet. Sci. Lett.,* 271**,** 170-180.

Torres, M.E., et al. 2011 Occurrence of high salinity fluids associated with massive near-seafloor gas hydrate deposits. Proceedings of the 7th International Conference on Gas Hydrates (ICGH 2011).

Tréhu, A.M., et al. 2004a. Feeding methane vents and gas hydrate deposits at south Hydrate Ridge. *Geophys. Res. Lett.,* 31.

Tréhu, A.M., et al. 2004b. Three-dimensional distribution of gas hydrate beneath southern Hydrate Ridge: constraints from ODP Leg 204. *Earth Planet. Sci. Lett.,* 222**,** 845-862.

Tréhu, A.M., et al. 2006 1. Leg 204 synthesis: Gas hydrate distribution and dynamics in the central Cascadia accretionary complex. Proceedings of the Ocean Drilling Program, Scientific Results, 204.

Tryon, M.D., et al. 2002. Fluid and chemical flux in and out of sediments hosting methane hydrate deposits on Hydrate Ridge, OR, II: Hydrological processes. *Earth Planet. Sci. Lett.,* 201**,** 541-557.

Tsimpanogiannis, I.N. & Yortsos, Y.C. 2004. The critical gas saturation in a porous medium in the presence of gravity. *J. Colloid Interface Sci.,* 270**,** 388-395.

Tsuji, Y., et al. 2009. Methane-hydrate occurrence and distribution in the eastern Nankai Trough, Japan: Findings of the Tokai-oki to Kumano-nada methane-hydrate drilling program. *In:* Collett, T.S., Knapp, C.C. & Boswell, R. (eds.) *Natural Gas Hydrates—Energy Resource Potential and Associated Geologic Hazards.* AAPG Memoir, 89, 228-246.

Uchida, T., et al. 1999a. Raman spectroscopic determination of hydration number of methane hydrates. *AICHE J.,* 45**,** 2641-2645.

Uchida, T., et al. 1999b. Summary of physicochemical properties of natural gas hydrate and associated gas-hydrate-bearing sediments, JAPEX/JNOC/GSC Mallik 2L-38 gas hydrate research well, by the Japanese research consortium. *Bull. Geol. Surv. Canada***,** 205-228.

Underschultz, J. 2007. Hydrodynamics and membrane seal capacity. *Geofluids,* 7**,** 148-158.

Usgs. *https://woodshole.er.usgs.gov/project-pages/hydrates/primer.html* [Online].

Ussler, W. & Paull, C.K. 2001. Ion exclusion associated with marine gas hydrate deposits. *In:* Paull, C.K. & Dillon, W.P. (eds.) *Natural Gas Hydrates: Occurrence, Distribution, and Detection.* AGU Geophysical Monograph Series, 124, 41-51.

Vadakkepuliyambatta, S., et al. 2015. Controls on gas hydrate system evolution in a region of active fluid flow in the SW Barents Sea. *Mar. Petrol. Geol.,* 66**,** 861-872.

Van Rensbergen, P., et al. 2002. Sublacustrine mud volcanoes and methane seeps caused by dissociation of gas hydrates in Lake Baikal. *Geology,* 30**,** 631-634.

Vanneste, M., et al. 2001. Multi-frequency seismic study of gas hydrate-bearing sediments in Lake Baikal, Siberia. *Mar. Geol.,* 172**,** 1-21.

Vanneste, M., et al. 2003. Atypical heat-flow near gas hydrate irregularities and cold seeps in the Baikal Rift Zone. *Mar. Petrol. Geol.,* 19**,** 1257-1274.

Vaughan, A. 2006. Gumusut Kakap Geohazard & Geotechnical Investigation: Phase 1: LWD & Wireline acquisition. *Shell internal report-confidential.*

Vogt, P.R. & Jung, W.Y. 2002. Holocene mass wasting on upper non-Polar continental slopes—due to post-Glacial ocean warming and hydrate dissociation? *Geophys. Res. Lett.,* 29**,** 1341.

Von Huene, R., et al. 1980. Leg 67: the deep sea drilling project Mid-America trench transect off Guatemala. *Geol. Soc. Am. Bull.,* 91**,** 421-432.

Von Huene, R. & Pecher, I.A. 1999. Vertical tectonics and the origins of BSRs along the Peru margin. *Earth Planet. Sci. Lett.,* 166**,** 47-55.

Wadham, J., et al. 2012. Potential methane reservoirs beneath Antarctica. *Nature,* 488**,** 633-637.

Waelbroeck, C., et al. 2002. Sea-level and deep water temperature changes derived from benthic foraminifera isotopic records. *Quaternary Sci. Rev.,* 21**,** 295-305.

Waite, W.F., et al. 2004. Methane hydrate formation in partially water-saturated Ottawa sand. *Am. Mineral.,* 89**,** 1202-1207.

Waite, W.F., et al. 2009. Physical properties of hydrate-bearing sediments. *Rev. Geophys.,* 47.

Wallmann, K., et al. 2006a. Kinetics of organic matter degradation, microbial methane generation, and gas hydrate formation in anoxic marine sediments. *Geochim. Cosmochim. Acta,* 70**,** 3905-3927.

Wallmann, K., et al. 2006b. Methane discharge into the Black Sea and the global ocean via fluid flow through submarine mud volcanoes. *Earth Planet. Sci. Lett.,* 248**,** 545-560.

Wang, H., et al. 2017a. Gas hydrate formation in compressional, extensional and un-faulted structural settings–Examples from New Zealand's Hikurangi margin. *Mar. Petrol. Geol.,* 88**,** 69-80.

Wang, K. & Davis, E.E. 1996. Theory for the propagation of tidally induced pore pressure variations in layered subseafloor formations. *J. Geophys. Res.: Solid Earth,* 101**,** 11483-11495.

Wang, P., et al. 2015. Geochemical dynamics of the gas hydrate system in the Qilian Mountain Permafrost, Qinghai, Northwest China. *Mar. Petrol. Geol.,* 59**,** 72-90.

Wang, S., et al. 2017b. A Review of Formation Mechanism Study on Reservoirs with Tilted Oil-water Contacts. *Acta Geol. Sin. (English Edition),* 91**,** 320-340.

Wang, X., et al. 2011. Elevated gas hydrate saturation within silt and silty clay sediments in the Shenhu area, South China Sea. *J. Geophys. Res.: Solid Earth,* 116, B05102.

Wang, X., et al. 2014. Gas hydrate identified in sand-rich inferred sedimentary section using downhole logging and seismic data in Shenhu area, South China Sea. *Mar. Petrol. Geol.,* 51**,** 298-306.

Wang, X., et al. 2016. Characterization of gas hydrate distribution using conventional 3D seismic data in the Pearl River Mouth Basin, South China Sea. *Interpretation,* 4**,** SA25-SA37.

Warren, J.K., et al. 2010. Organic geochemical, isotopic, and seismic indicators of fluid flow in pressurized growth anticlines and mud volcanoes in modern deep-water slope and rise sediments of offshore Brunei Darussalam: Implications for hydrocarbon exploration in other mud-and salt-diapir provinces. *In:* Wood, L. (ed.) *Shale Tectonics.* AAPG Memoir, 93, 163-196.

Watts, N.L. 1987. Theoretical aspects of cap-rock and fault seals for single-and two-phase hydrocarbon columns. *Mar. Petrol. Geol.,* 4**,** 274-307.

Wegner, S.A. & Campbell, K.J. 2014. Drilling hazard assessment for hydrate bearing sediments including drilling through the bottom-simulating reflectors. *Mar. Petrol. Geol.,* 58**,** 382-405.

Wei, J., et al. 2015. Gas hydrate distributions in sediments of pockmarks from the Nigerian margin–Results and interpretation from shallow drilling. *Mar. Petrol. Geol.,* 59**,** 359-370.

Weinberger, J.L., et al. 2005. Painting a picture of gas hydrate distribution with thermal images. *Geophys. Res. Lett.,* 32**,** L04609.

Weinberger, J.L. & Brown, K.M. 2006. Fracture networks and hydrate distribution at Hydrate Ridge, Oregon. *Earth Planet. Sci. Lett.,* 245**,** 123-136.

Weitemeyer, K. & Constable, S. 2010. Mapping shallow geology and gas hydrate with marine CSEM surveys. *First Break,* 28**,** 97-102.

Wenau, S., et al. 2015. Cold seeps at the salt front in the Lower Congo Basin I: Current methane accumulation and active seepage. *Mar. Petrol. Geol.,* 67**,** 894-908.

Westbrook, G.K., et al. 2008 High-resolution 3D seismic investigations of hydrate-bearing fluid-escape chimneys in the Nyegga region of the Vøring plateau, Norway. Proceedings of the 6th International Conference on Gas Hydrates (ICGH 2008).

Westbrook, G.K., et al. 2009. Escape of methane gas from the seabed along the West Spitsbergen continental margin. *Geophys. Res. Lett.,* 36.

Whiticar, M.J., et al. 1986. Biogenic methane formation in marine and freshwater environments: CO2 reduction vs. acetate fermentation—isotope evidence. *Geochim. Cosmochim. Acta,* 50**,** 693-709.

Whiticar, M.J., et al. 1995 26. Organic geochemistry of gases, fluids, and hydrates at the Cascadia accretionary margin. Proceedings of the Ocean Drilling Program, Scientific Results, 146, 385-397.

Widess, M.B. 1973. How thin is a thin bed? *Geophysics,* 38**,** 1176-1180.

Wilson, R.M., et al. 2014. Subsurface methane sources and migration pathways within a gas hydrate mound system, Gulf of Mexico. *Geochem. Geophys. Geosyst.,* 15**,** 89-107.

Winckler, G., et al. 2002. Noble gases and radiocarbon in natural gas hydrates. *Geophys. Res. Lett.,* 29.

Winters, W.J., et al. 2004. Physical properties and rock physics models of sediment containing natural and laboratory-formed methane gas hydrate. *Am. Mineral.,* 89**,** 1221-1227.

Winters, W.J., et al. 2007. Methane gas hydrate effect on sediment acoustic and strength properties. *J. Petrol. Sci. Eng.,* 56**,** 127-135.

Winters, W.J., et al. 2011. Physical properties of sediment from the Mount Elbert gas hydrate stratigraphic test well, Alaska North Slope. *Mar. Petrol. Geol.,* 28**,** 361-380.

Winters, W.J., et al. 2014. Comparison of the physical and geotechnical properties of gas-hydrate-bearing sediments from offshore India and other gas-hydrate-reservoir systems. *Mar. Petrol. Geol.,* 58**,** 139-167.

Wood, W.T., et al. 2002. Decreased stability of methane hydrates in marine sediments owing to phase-boundary roughness. *Nature,* 420**,** 656-660.

Xu, W. & Ruppel, C.D. 1999. Predicting the occurrence, distribution, and evolution of methane gas hydrate in porous marine sediments. *J. Geophys. Res.: Solid Earth,* 104**,** 5081-5095.

Xu, W. & Germanovich, L.N. 2006. Excess pore pressure resulting from methane hydrate dissociation in marine sediments: A theoretical approach. *J. Geophys. Res.: Solid Earth,* 111**,** B01104.

Yang, J., et al. 2013. Gas migration below gas hydrates controlled by mass transport complexes, offshore Mauritania. *Mar. Petrol. Geol.,* 48**,** 366-378.

Yardley, G. & Swarbrick, R. 2000. Lateral transfer: A source of additional overpressure? *Mar. Petrol. Geol.,* 17**,** 523-537.

Yilmaz, Ö. 2001. *Seismic data analysis: Processing, inversion, and interpretation of seismic data,* Society of exploration geophysicists.

Yoneda, J., et al. 2015. Mechanical properties of hydrate-bearing turbidite reservoir in the first gas production test site of the Eastern Nankai Trough. *Mar. Petrol. Geol.,* 66**,** 471-486.

Yoneda, J., et al. 2017. Pressure-core-based reservoir characterization for geomechanics: Insights from gas hydrate drilling during 2012–2013 at the eastern Nankai Trough. *Mar. Petrol. Geol.,* 86**,** 1-16.

Yoo, D.G., et al. 2013. Occurrence and seismic characteristics of gas hydrate in the Ulleung Basin, East Sea. *Mar. Petrol. Geol.,* 47**,** 236-247.

Yoshioka, H., et al. 2010. Activities and distribution of methanogenic and methane-oxidizing microbes in marine sediments from the Cascadia Margin. *Geobiology,* 8**,** 223-233.

Yuan, J. & Edwards, R. 2000. The assessment of marine gas hydrates through electrical remote sounding: hydrate without a BSR? *Geophys. Res. Lett.,* 27**,** 2397-2400.

Yun, T.S., et al. 2005. Compressional and shear wave velocities in uncemented sediment containing gas hydrate. *Geophys. Res. Lett.,* 32.

Yun, T.S., et al. 2007. Mechanical properties of sand, silt, and clay containing tetrahydrofuran hydrate. *J. Geophys. Res.: Solid Earth,* 112.

Yun, T.S., et al. 2010. Hydrate-bearing sediments from the Krishna− Godavari Basin: physical characterization, pressure core testing, and scaled production monitoring. *Energy & Fuels,* 24**,** 5972-5983.

Zander, T., et al. 2017. Potential impacts of gas hydrate exploitation on slope stability in the Danube deep-sea fan, Black Sea. *Mar. Petrol. Geol.*

Zhang, Z., et al. 2012. Rock physics-based seismic trace analysis of unconsolidated sediments containing gas hydrate and free gas in Green Canyon 955, Northern Gulf of Mexico. *Mar. Petrol. Geol.,* 34**,** 119-133.

Zhang, Z. & Wright, C.S. 2017. Quantitative interpretations and assessments of a fractured gas hydrate reservoir using three-dimensional seismic and LWD data in Kutei basin, East Kalimantan, offshore Indonesia. *Mar. Petrol. Geol.,* 84**,** 257-273.

Zielinski, G.W., et al. 2007. Heat flow and surface hydrocarbons on the Brunei continental margin. *AAPG Bull.,* 91**,** 1053-1080.

Zillmer, M., et al. 2005. Seismic investigation of a bottom simulating reflector and quantification of gas hydrate in the Black Sea. *Geophys. J. Int.,* 161**,** 662-678.